CORNELL LABORATORY FOR ACCELERATOR-BASED SCIENCES AND EDUCATION (CLASSE)

ecloud10

49th ICFA Advanced Beam Dynamics Workshop on Electron Cloud Physics

Oct. 8–12, 2010

Statler Hotel, Cornell University
Ithaca, New York, USA

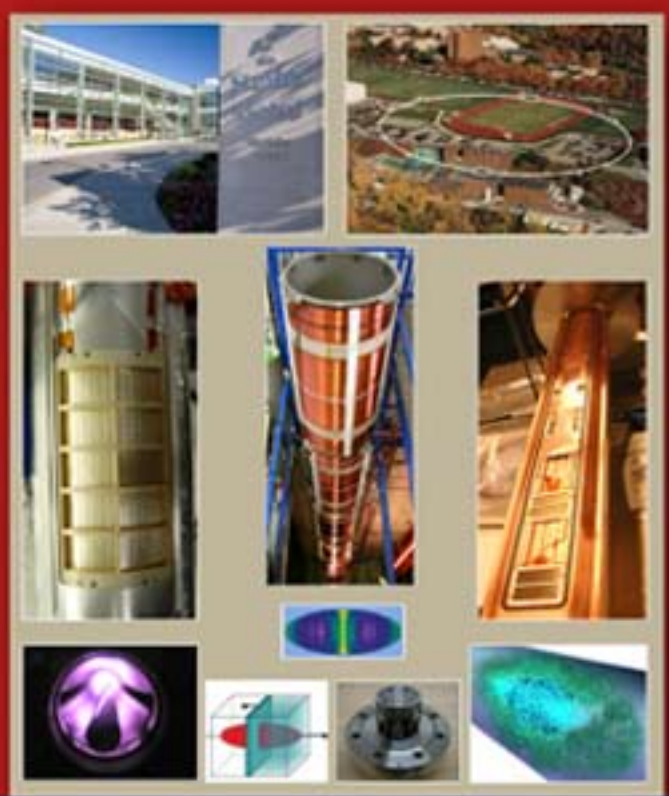

FOR INFORMATION AND TO REGISTER, VISIT: WWW.LEPP.CORNELL.EDU/EVENTS/ECLOUD10/

Dear Colleagues-

The 49th ICFA Advanced Beam Dynamics Workshop on electron cloud physics, ECloud 2010, was held October 8-12, 2010 on the campus of Cornell University, in Ithaca, New York and attracted more than 60 scientists from around the world. It was the fourth workshop in the ECloud series and the 49th ICFA Advanced Beam Dynamics Workshop. Prior ECloud workshops were held at CERN in 2002; Napa, California in 2004; and Daegu, Korea in 2007.

The development of the electron cloud (EC) in accelerator vacuum systems remains a significant issue for the operation of present and planned high intensity accelerators. The interaction of the cloud with the beam can lead to single and multi-bunch instabilities, emittance growth, and betatron tune shifts. The presence of the cloud in the beam chambers can result in a rapid rise in vacuum pressure, significant heat loads on cryogenic surfaces, and can interfere with beam diagnostics. Since the last ECloud workshop in 2007, an intense R&D effort has been underway to further understand the physics of the EC and to investigate new methods to mitigate the EC effects. The ECloud 2010 program will focus on: a review of EC observations at existing machines; recent experimental efforts to characterize the EC (including EC diagnostics, experimental techniques, characterization of mitigation methods, and characterization of beam instabilities and emittance growth); the status of EC physics models and simulation codes and their comparison to recently acquired experimental data; and the mitigation requirements and potential performance limitations imposed by the EC on upgraded and future machines. In addition to the technical reports at the workshop, a set of introductory lectures were held for students and those new to the field on the opening day of the workshop.

We were more than happy that many participants expressed their gratitude and considered the ECloud 2010 workshop a resounding success.

We look forward to seeing you again at the next ECloud workshop.

Mark Palmer, ECloud 2010 Workshop Chair
Karl Smolenski, ECloud 2010 Editor

Contents

Conference Chair

Mark Palmer	Cornell University

Local Organizing Committee

B.J. Bortz	Cornell University
Devin Bougie	Cornell University
Jeanne Butler	Cornell University
Jim Crittenden	Cornell University
Mark Palmer (Chair)	Cornell University
David Rubin	Cornell University
Karl Smolenski (Editor)	Cornell University
Kiran Sonnad	Cornell University
Michael Roman	Cornell University
Monica Wesley	Cornell University

49th ICFA Advanced Beam Dynamics Workshop

ecloud 10

Cornell University, 2010

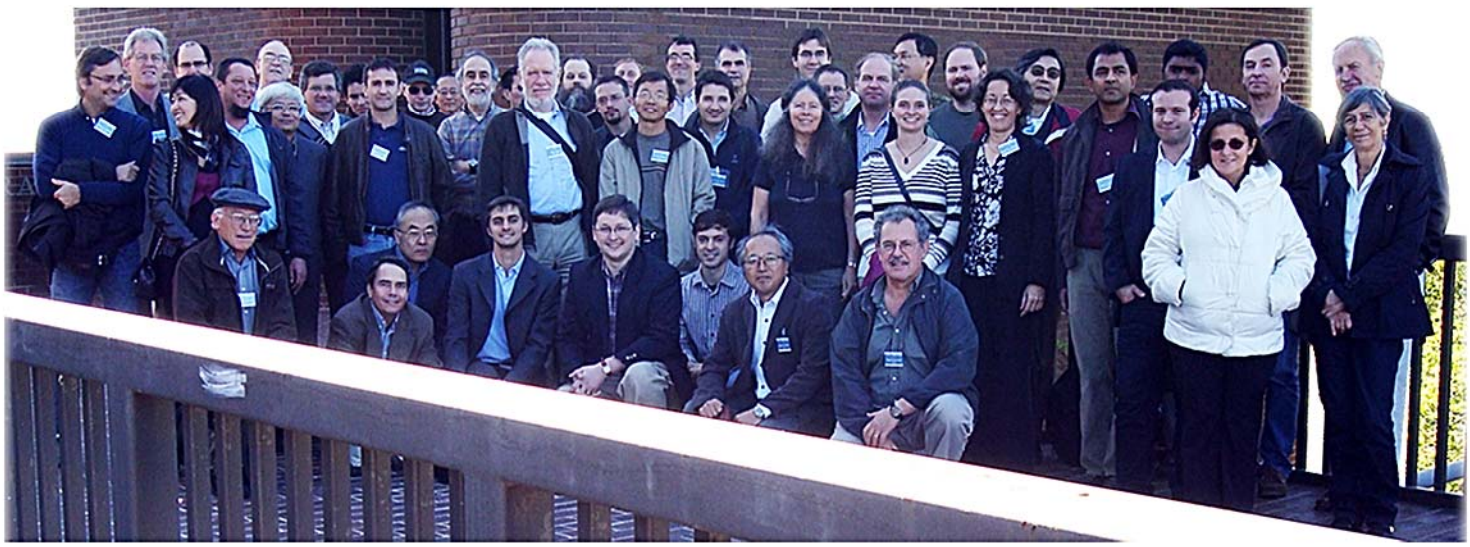

RECENT STUDIES OF THE ELECTRON CLOUD INDUCED BEAM INSTABILITY AT THE LOS ALAMOS PSR*

R. Macek#, L. Rybarcyk, R. McCrady and T. Zaugg,
LANL, Los Alamos, NM 87545, USA
J. Holmes, ORNL, Oak Ridge, TN 37831, USA

Abstract

Recent beam studies have demonstrated that a stable beam with the standard production bunch width of 290 ns and near the e-p instability threshold will become unstable when the bunch width is shortened significantly. This was not the case years earlier when the ring rf operated at the 72.000 integer subharmonic of the Linac bunch frequency. The present operating frequency is set at the 72.070 non-integer subharmonic and appears to be responsible for the recently observed "short pulse instability phenomenon". Experimental characteristics of the short pulse instability are presented along with comparisons to the instability under 72.000 subharmonic operating conditions.

INTRODUCTION

The electron cloud (EC) induced instability, also known as the two-stream e-p instability, has been observed ever since the PSR was commissioned in 1986 [1] and has been extensively studied since then. All the available evidence points to a two-stream instability from coupled motion of the proton beam and a "cloud" of low energy electrons. In our present picture of this instability, primary electrons arising mostly from beam losses are amplified by multipactor on the ~140 ns long trailing edge of the ~290 ns long beam pulse. Sufficient electrons survive the ~70 ns gap between bunch passages to be captured by the next bunch passage to drive the instability. The largest uncertainly in locating the main EC source is the distribution of primary electrons born at the chamber walls from grazing angle beam losses.

For the discussion to follow, it is helpful to understand the process for and signature of the instability threshold shown in Figure 1. During beam instability studies, we store a stable beam for typically 400 μs after the end of accumulation in order to allow the instability to develop at fixed beam intensity and in the absence of losses from H^0 excited states which field strip part way into the first dipole downstream of the injection stripper foil. The ring rf buncher voltage is lowered until a) exponentially growing coherent motion is seen on a beam position monitor (BPM) in the ring and b) a significant beam loss shows on the sum signal from 19 loss monitors and ~5% loss of beam current appears by the time the beam is extracted. Thresholds obtained by the above criteria are reproducible to ~5% of the buncher voltage. For buncher voltages ~5% above the threshold the beam is stable. At lower buncher voltages, the instability is more pronounced in that the losses are typically higher and the coherent motion and losses start earlier and may saturate.

The plot of instability threshold voltage as a function of beam intensity while all other beam parameters are held fixed is designated an **instability threshold curve**. These are typically linear in intensity (Q = charge stored/pulse) and have long been studied as a function of many beam setup parameters (e.g. emittance, bunch width, tune, multipole settings, buncher phase, etc) [2]. For instability threshold curves, the intensity is varied by beam jaws at the linac front end or by periodically chopping out a turn of injection. An example of threshold curves for 3 beam bunch lengths (PW, pattern width of one injected turn or mini-pulse) is shown in Figure 2 for data collected in 2001 when the PSR rf routinely operated at the exact 72.000 subharmonic of the linac frequency.

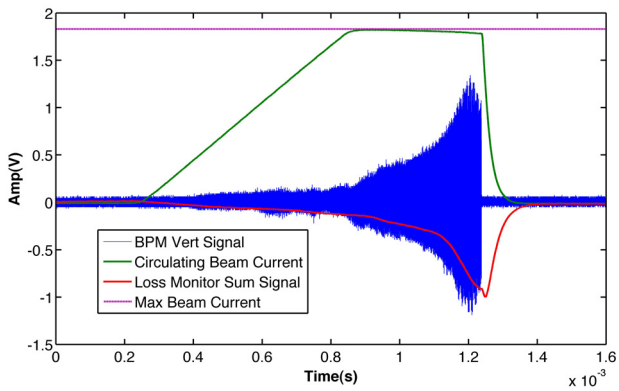

Figure 1: Experimental signature for the e-p threshold.

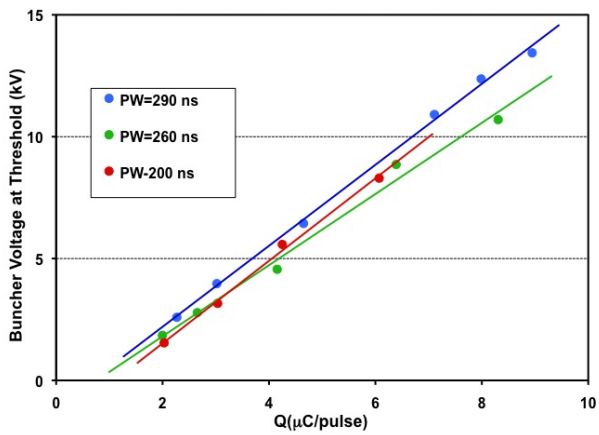

Figure 2: Instability threshold curves for various PW collected 5/26/2001 (72.000 subharmonic operation). Beam was accumulated for 1225 μs and stored for 400 μs after end of injection.

*This work was supported by the U. S. Department of Energy under contract DE-AC52-06NA25396.
#macek@lanl.gov

In Figure 2, the threshold curves show a typical linear behavior as a function of intensity with essentially the same curve for each PW such that the threshold curve depended only on stored charge/pulse and not the bunch width. Note that changing the PW does reduce the charge/macro-pulse (same as charge/turn) in these measurements where the accumulation time and store time after the end of accumulation is fixed along with the beam injection offset, which sets the beam size except for effects from space charge emittance growth. The very weak dependence on PW shown in Figure 2 persisted for several years until a major change in behavior was observed recently and is described in the next section

It should be noted that the dependence on PW in Figure 2 is at considerable variance with the linear stability theory developed by Blaskiewicz et al in ref [3]. In this model the threshold charge depends linearly on the rf voltage and as the third power of bunch length. The bunch-width scaling for the new results discussed below for the non-integer subharmonic (72.070) conditions are found to be considerably more consistent with this model.

RECENT OBSERVATIONS OF EC INSTABILITY FOR SHORT PULSES

In 2009 it was observed that reducing the PW required more buncher voltage to keep the beam stable, which is in striking contrast to the behavior in earlier years. This phenomenon has been studied several times since then and was found to be reproducible for the present ring-operating regime (72.070 subharmonic of the linac bunch frequency). Examples of instability threshold curves for this regime are shown in Figure 3 and should be compared with those in Figure 2 that cover the same range of PWs and storage time (400 μs). The comparison shows that the beams with shorter PW are now significantly less stable i.e., have an instability threshold voltage that is significantly higher for the same stored charge.

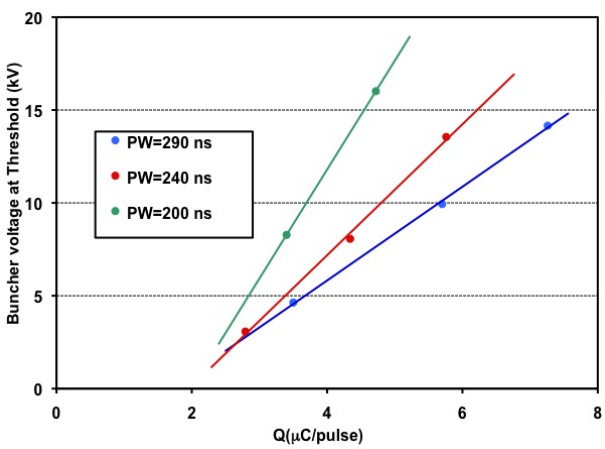

Figure 3: Instability threshold curves for various PW collected 9/25/2010 (72.070 subharmonic operation). Beam was accumulated for 825 μs and stored for 400 μs after end of accumulation.

Another set of threshold curves, covering a wider range of bunch widths (PW), is shown in Figure 4 and was collected with a shorter store time of 200 μs that enabled us to go to even shorter PW without exceeding the maximum voltage on the rf buncher (~17 kV). The threshold curves in Figures 3 and 4 show that beams with shorter PW are progressively less stable as the PW is lowered. Also note that the curve for PW=290 in Figure 4 is somewhat lower than the corresponding curve in Figure 3. This is a typical behavior in that a longer store time requires a slightly higher rf buncher voltage to avoid instability, presumably because the instability has more time to develop after the end of accumulation.

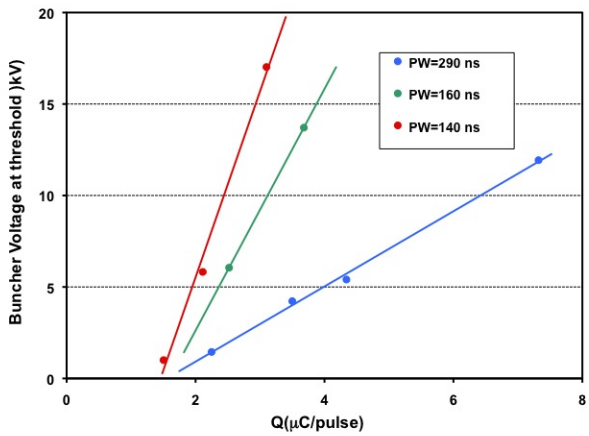

Figure 4: Instability threshold curves for various PW collected 9/24/2010 (72.070 subharmonic). Beam was accumulated for 825 μs and stored for 200 μs after end of accumulation.

The slopes of the instability threshold curves in Figure 3 and 4 are plotted as a function of PW in Figure 5. Fits to the data points using the $(PW)^{-3}$ law predicted in the model of ref [3] are shown. It should be noted that other values of the PW exponent from -2.5 to -4 fit reasonably well. The main point is the strong variation of the instability threshold curves with PW for 72.070 subharmonic operation compared with the no variation for 72.000 integer subharmonic operation of earlier years.

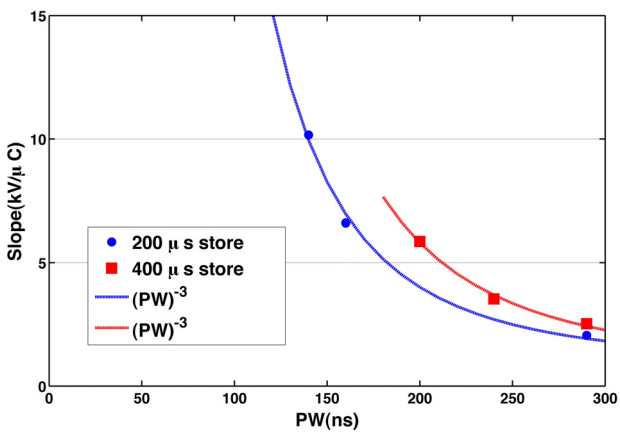

Figure 5: Slopes of the instability threshold curves of Figures 3 (red points) and 4 (blue points) plotted as a

function of PW. The continuous curves are fits [$(PW)^{-3}$ plus a constant] to the respective data sets.

At the start of the 2010 LANSCE/PSR operating cycle the ring was inadvertently set to the 72.009 subharmonic of the linac frequency. This error was discovered when we investigated why the longitudinal beam profile showed more "hash" i.e. high frequency structure. This investigation (7/15/10) also revealed that lowering the PW for a 290 ns beam near threshold no longer made the beam unstable, which was the behavior observed for years when operating the ring at the 72.000 integer subharmonic. The ring was then set up for the 72.070 subharmonic in order to make a contemporaneous comparison with the 72.009 subharmonic data. The main results of this investigation are plotted in Figures 6 and 7 and discussed below.

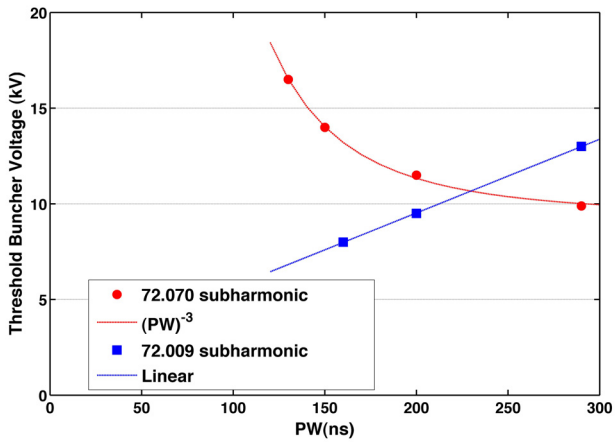

Figure 6: Comparison of instability threshold data plotted as a function of PW for ring operation at the 72.009 and 72.070 subharmonic of the linac bunch frequency. Also shown is a $(PW)^{-3}$ fit to the 72.070 subharmonic data and a linear fit to the 72.009 subharmonic data. The data shown here was collected 7/15/10 for a full accumulation time of 925 μs and 400 μs added store time.

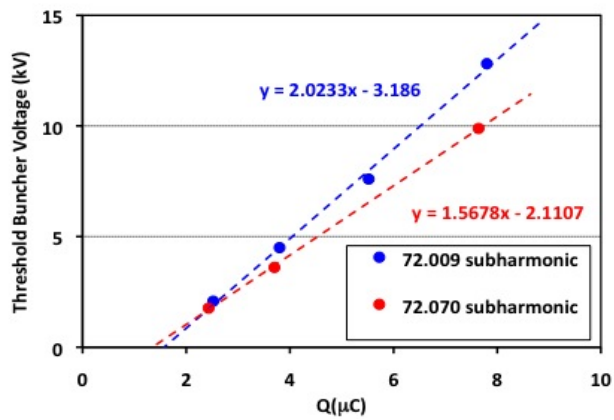

Figure 7: Comparison of instability threshold curves for ring operation at the 72.009 (blue curve) and 72.070 subharmonic (red curve) of the linac bunch frequency. Data plotted here was collected 7/15/10 for a PW = 290 ns, 925 μs accumulation and 400 μs store time after end of accumulation.

During the investigation we did not have enough beam time to take 3 or 4-point threshold curves for every PW. Instead, we took standard threshold curves (where intensity is varied with all other parameters fixed) for the largest PW=290 ns (Figure 7) and collected instability threshold voltage data as a function of PW for the full accumulation and store times (Figure 6). The data of Figure 6 confirm that the short pulse instability still exists for the 72.070 subharmonic frequency and also shows that the behavior at the 72.009 subharmonic frequency is similar to the experience of previous years for 72.000 subharmonic frequency. A more detailed discussion and comparison of the two operating frequencies follows in the next section.

The data in Figure 7 are similar to and consistent with measurements in 2006 where the 72.070 subharmonic frequency systematically lowered the instability threshold voltage. The latter was one reason for adopting the 72.070 subharmonic frequency for routine production beam, i.e., PW = 290 ns. Additional reasons included a reduction in high frequency structure on the longitudinal beam pulse and beam position monitors (BPM) plus a reduction in electron cloud generation in drift spaces.

WHAT IS DIFFERENT NOW?

The search for a beam dynamics explanation of the surprising difference in instability thresholds as a function of PW for the integer and non-integer subharmonic ring frequencies motivates a more detailed comparison of the two setups. The main difference is in the filling of longitudinal phase space as depicted schematically in Figure 8 for the integer subharmonic (72.000) and a non-integer subharmonic (72.100). For the integer subharmonic ring frequency, the micropulses with the linac rf structure are injected on top of the micropulses of previous turns while, for the non-integer subharmonic, the micropulses have a slight delay on each successive turn and fill in the space between microbunches.

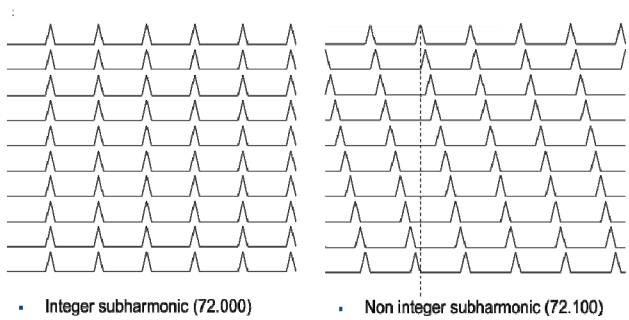

Figure 8: Schematic representation of turn-by-turn injection of micropulses (beam bunches with the time structure of the linac rf, 201.25 MHz) into the ring. The abscissa is the PSR rf phase and sequential turns (mini-pulses which are about 58 micropulses for a PW=290) are shown on the ordinate. Integer subharmonic (72.000) injection is shown on the left and non-integer subharmonic (72.100) on the right.

This "stacking" or "pileup" of micropulses results in large space charge forces at the micropulse locations and very few particles (and little space charge) between them. This effect is shown in the longitudinal phase space distribution of Figure 9 obtained from an ORBIT [4] simulation of production beam accumulation in PSR at the integer subharmonic. The projection of the longitudinal phase space distribution of Figure 9 onto the phase axis is plotted in Figure 10 and shows significant high frequency structure that is also observed experimentally.

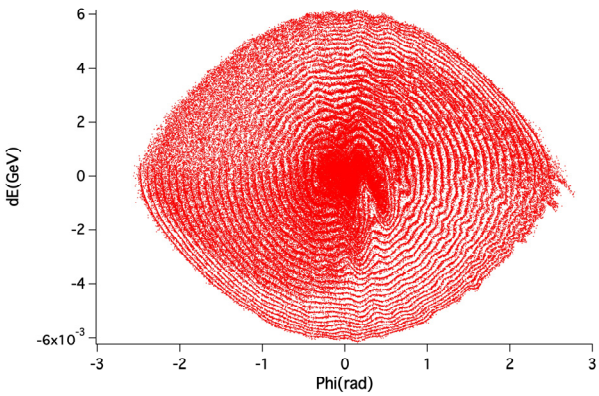

Figure 9: Longitudinal phase space distribution (dE vs. the phase, Phi) obtain from an ORBIT simulation of beam accumulation (625 μs, for 5.2 μC of stored charge) with the integer subharmonic rf (10kV). Energy loss from stored beam particles that traverse the stripper foil (400 microgram/cm^2) is included as is transverse and longitudinal space charge plus the complex impedance of the heated inductive inserts in the ring [5, 6].

For the non-integer subharmonic regime depicted in the right hand graphic of Figure 8, the micropulses on subsequent turns are injected with a slight phase or time shift with respect to the micropulse of the previous turn. This fills the space between micropulses in 10 turns for the 72.100 or 14 turns for the 72.070 subharmonic. The chopping for minipulses is synchronized to the ring frequency such that the pattern repeats every 10 turns for 72.100 or 14 turns for 72.070. This "micropulse painting" leads to a much smoother distribution in longitudinal phase space (no ridge and valley structure) and significantly reduced high frequency structure on the longitudinal bunch profile.

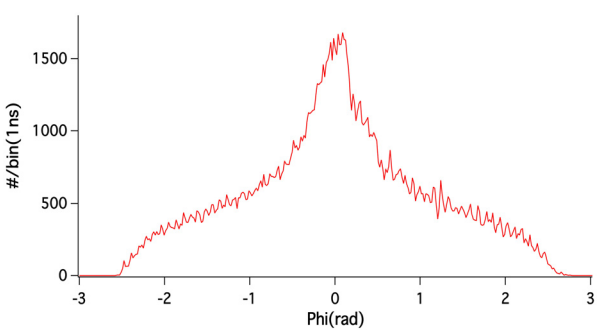

Figure 10: Histogram of the projection of the phase space distribution of Figure 9 onto the phase axis.

A reasonably good approximation to the longitudinal phase distribution obtained with the 72.070 subharmonic ring rf "micropulse painting" can be obtained from an ORBIT simulation with no linac rf bunch structure on the injected beam. Results from such a simulation for accumulation of 5.2 μC of stored charge in 625 μs are plotted in Figure 11. Included in the simulation are energy losses in the stripper foil (400 microgram/cm^2), transverse and longitudinal space charge plus the complex impedance of the heated inductive inserts in the ring.

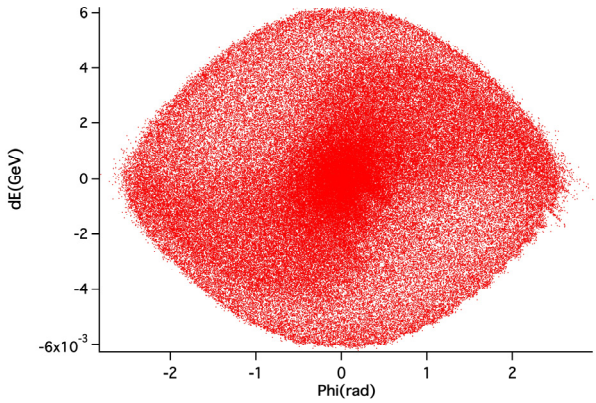

Figure 11: Longitudinal phase space distribution from an ORBIT simulation with no linac 201.25 MHz bunch structure on the injected beam.

A comparison of wall current monitor signals for the two ring frequencies is shown in Figure 12 and reveals the reduced high frequency structure for the non-integer 72.070 subharmonic. Digital fft analysis of the last 20 μs (55 turns) of the wall current signals showed that the frequency spectra (mostly revolution harmonics) in the range 75-225 MHz (revolution harmonics 28-80) were down 12-15 db for the non-integer subharmonic (72.070) compared to the integer subharmonic (72.000).

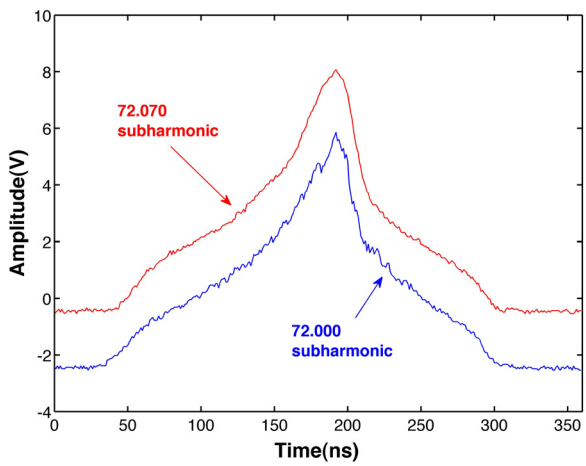

Figure 12: Wall current monitor signals at the last turn in PSR just before extraction for integer subharmonic (72.000) and non-integer subharmonic (72.070) ring frequencies. Data collected 7/15/2006 for 825 μs of accumulation and 200 μs of added store time.

Other benefits of the non-integer (72.070) subharmonic operation include reduced noise in the ring BPMs,

somewhat lower instability threshold curves (e.g., Figure 7) and reduced electron cloud signals in drift spaces (see Figure 13). The electron signal for integer subharmonic (blue trace) in Figure 13 is a factor of 5-10 larger than for the non-integer case (red trace) and shows much greater short-term (tens of turns) fluctuations before the end of accumulation.

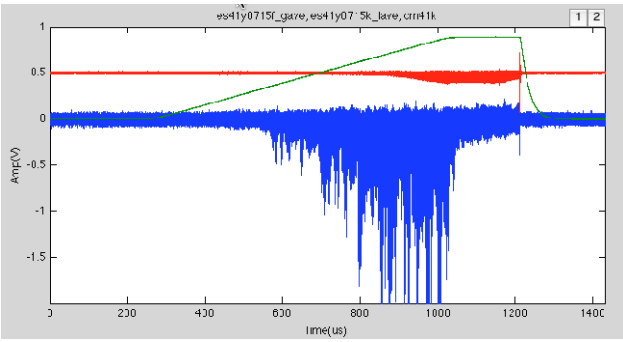

Figure 13: Comparison of electron signals from a drift space diagnostic for integer subharmonic (72.000, blue trace) and non-integer subharmonic (72.070, red trace). They are also compared with the stored current beam current signal (green trace, arbitrary units). The red trace has been displaced 0.5 V in the vertical for clarity. Data shown here were collected 7/15/2006 for 825 μs of accumulation and 200 μs of added store time.

The data, simulations and analysis in this section have provided a more detailed comparison of the beam characteristics for the two ring frequencies but have not established a clear beam dynamics explanation for the large difference in behavior of the instability thresholds as function of PW. The short pulse instability behavior for the non-integer subharmonic is reasonably consistent with the instability model of Blaskiewicz et al [3]. In this model the rf voltage at threshold is proportional to $(PW)^{-3}$, which approximately fits the red (72.070 subharmonic) curve in Figure 6 or the slopes of the instability thresholds of Figures 2 and 3 as shown in Figure 5.

CONCLUSIONS

In 2009 the "short pulse instability" phenomenon was discovered at PSR for the non-integer subharmonic (72.070) ring frequency. It was a surprise because the instability threshold buncher voltage as a function PW was quite different for the integer subharmonic (72.000) frequency in use until 2007. As it turns out, the threshold voltage as a function PW for the non-integer subharmonic frequency is reasonably consistent with the Blaskiewicz model [3]. Thus, the real beam dynamics question is why the integer subharmonic ring frequency leads to more stable short pulses, where the threshold voltage is proportional to PW. Perhaps the answer lies with the space charge effects of the strong ridge and valley structure of the longitudinal phase space distribution or the increased high frequency longitudinal structure for the integer subharmonic (72.000) operating regime. A theoretical investigation along these lines would be valuable.

ACKNOWLEGMENTS

We gratefully acknowledge the excellent support provided by the AOT division at LANL. The expertise and enthusiastic response of the accelerator operators was of immense value during the execution of our beam experiments. One of us (R. Macek) would also like to acknowledge useful discussion with M. Blaskiewicz, M. Plum, and P. Channell.

REFERENCES

[1] D. Neuffer et al, "Observations of a fast transverse instability in the PSR", NIM **A321**, p. 1(1992).

[2] R. Macek, Series of lectures on electron cloud effects at PSR given at the Electron Cloud Feedback Workshop, Indiana University, Bloomington, IN, March 15-18, 2004. website: http://physics.indiana.edu/~shylee/ap/mwapc/epfeedback.html.

[3] M. Blaskiewicz et al, "Electron cloud instabilities in the Proton Storage Ring and Spallation Neutron Source", PRST-AB **6**, 014203 (2003).

[4] J. A. Holmes et al, "ORBIT: Beam Dynamics Calculations for High Intensity Rings", ICFA Beam Dynamics Newsletter **30**, April 2003.

[5] M. Plum et al, "Experimental study of passive compensation of space charge at the Los Alamos National Laboratory Proton Storage Ring", PRST-AB **2**, 064201(1999).

[6] C. Beltran et al, "Calculations and observations of the longitudinal instability caused by the ferrite inductors at the Los Alamos Proton Storage Ring (PSR)", Proceedings of PAC 2003, paper TOPD004, p 326 (2003).

RECENT EXPERIMENTAL RESULTS ON AMORPHOUS CARBON COATINGS FOR ELECTRON CLOUD MITIGATION

C. Yin Vallgren , S. Calatroni, P. Chiggiato, P. Costa Pinto, H. Neupert, M. Taborelli , G. Rumolo, E .Shaposhnikova, W. Vollenberg, CERN, Geneva, Switzerland

Abstract

Amorphous carbon (a-C) thin films, produced in different coating configurations by using DC magnetron sputtering, have been investigated in laboratory for low secondary electron yield (SEY) applications. After the coatings had shown a reliable low initial SEY, the a-C thin films have been applied in the CERN Super Proton Synchrotron (SPS) and tested with Large Hadron Collider (LHC) type beams. Currently, we have used a-C thin film coated in so-called liner configuration for the electron cloud monitors. In addition the vacuum chambers of three dipole magnets have been coated and inserted into the machine.

After describing the different configurations used for the coatings, results of the tests in the machine and a summary of the analyses after extraction will be presented. Based on comparison between different coating configurations, a new series of coatings has been applied on three further dipole magnet vacuum chambers. They have been installed and will be tested in coming machine development runs.

MOTIVATION

In a proton or positron particle accelerator, an electron cloud can be generated by residual gas ionization, by photoemission when synchrotron-radiation photons hit the surface of the vacuum chamber and by subsequent secondary emission via a beam induced multipactoring process [1]. This process reduces the machine luminosity and beam quality. It leads to dynamic pressure rise, transverse emittance blow up, thermal load and beam losses. The goal of this work is to find a method to eliminate the e-cloud in the CERN Super Proton Synchrotron (SPS) in order to make the SPS able to deliver the ultimate beam to Large Hadron Collider (LHC) and reach maximum luminosity for the machine. Four important requirements are: the solution must be implementable in the existing SPS dipoles, does not require any bake out since the SPS has heating limitation, is robust against venting and also has a long life time. Simulations [2], [3] show that the threshold value for the SEY in order to avoid e-cloud in the SPS with nominal LHC beam is = 1.3.

In this work, carbon is chosen as coating material due to its few valence electrons and its non-reactivity. Carbon thin film coatings produced by DC magnetron sputtering in different coating set-ups have been tested for different applications.

christina.yin.vallgren@cern.ch
mauro.taborelli@cern.ch

THIN FILM COATINGS

Four different coating configurations have so far been used due to the different geometries of the chambers to be coated, as listed in Table 1. Different discharge gases (Ne, Kr, Ar) and different coating parameters, such as temperature of substrate, discharge gas pressure, power applied during coatings have been tested. To maximize sputtering efficiency and reduce the risk of implantation of heavy discharge gas ions, such as Argon and Krypton, on the coating surfaces, we chose to use Neon as discharge gas after many tests.

In a perfectly cylindrical vacuum chamber, one graphite rod is used as cathode for the DC magnetron sputtering and this method was used for making most of the lab samples for SEY investigation as well as vacuum characterizations in the lab. In Fig. 1(a), the 7 meters long solenoid used to provide magnetic field parallel to the cathode in the cylindrical tube configuration is shown.

Since the shape of the vacuum chambers in the SPS is not perfectly round, we need to find other solutions to make a homogeneous coating. A configuration of a liner with rectangular cross section in a round tube with 4 graphite rods has been tested, as shown in Fig. 1(b). This configuration has been applied for both lab samples and liners for electron cloud monitors (ECM) used for electron cloud measurements in-situ the SPS, as shown in Fig. 1(c). The surface temperature can go up to 250 C during the coating.

To detect electron cloud we used the same type of monitors as in previous tests [1], [4], [5]. The schematic drawing of the device is shown in Fig. 1(c). The Electron Cloud Monitor (ECM) equipped with stainless steel (SS) liners with or without coating is then installed in a special dipole C magnet which provides a magnetic field perpendicular to the beam direction. Unless otherwise specified, during all the experiments the field was kept at 1.2 kG (the SPS injection value). On one side of the liner, small holes with a transparency of 7% are drilled to pass the electrons generated by e-cloud through the liner. Under those holes there is a multi strip detector to collect the escaped electrons, if any.

After the lab results showed a SEY lower than 1.3, the threshold value calculated by simulations [2] [3], three of the SPS dipole magnets were coated and tested with the LHC type of beams. In Fig. 1(d), an SPS MBB dipole and the vacuum equipment used for coating can be seen. Inside the dipole, the magnetic field during coating was provided by the dipole itself and was perpendicular to the cathodes. The power used during coating was also kept limited not to damage the coil. Three MBB dipoles have been coated in

this way and tested in the machine with beam. A visible disadvantage, as shown in Fig. 1(e), with this type of coating is the non-uniformity. To improve the homogeneity of the coating in the SPS dipole magnet, another three dipole magnet vacuum chambers coated in the same way as ECM have been tested. Indeed this configuration results in more uniform coating, but requires to coat the chamber separated from the dipole coil. For the coating the chamber must be extracted from the dipole and inserted in the coil (Fig. 1(a)) so that the magnetic field this time is parallel to the cathode. With the present SPS magnets such a process is very time and resource consuming.

EXPERIMENTS

The measurements of SEY in the lab are carried out with an electron gun, which sends primary electrons (PE) of 50-2000 eV to the surface of the sample, and a collector for the emitted electrons. The collector is biased to +45 V in order to capture all secondary electrons, whereas the sample is biased to -18 V. All reported SEY measurements were carried out at normal PE angle of incidence. The electron dose was calculated to be below 1 10 C/mm over irradiated areas of about 2 mm for a full SEY measurement. Each sample was measured as received after extraction from the deposition chamber and transfer to the SEY measurement apparatus through air. The time in air during the transfer is approximately 2 hours. The precision of the measured SEY values is estimated to 0.03. After the SEY measurement, an X-ray Photoemission Spectroscopy (XPS) spectrum to determine coating compositions is usually taken after a transfer under UHV from the SEY system to the XPS system. More details about the SEY measurements are given in [6].

Four ECMs can be used at the same time to measure the electron cloud current during one SPS machine development (MD) run. During each MD run, an ECM with an SS liner has been used as reference. The SS liner has been exchanged before certain MD runs in order to have a non-conditioned surface as reference. Various amorphous carbon (a-C) coatings have been tested in several MD runs, as well as a NEG (TiZrV) to compare the various effect on electron cloud elimination.

After successful tests with a-C coated liners in 2008 (see [4]), three dipole magnets of B-type (MBB) have been coated with a thin film of the same material and installed in the SPS in March 2009. Positions of the MBB dipoles installed in the SPS are shown in Fig. 1(f). The total air exposure time of the coating before installation (on the ground and in the tunnel) was around one week. Pressure measurements (1 Hz sampling rate) were performed with Penning gauges installed on the pumping port between two uncoated dipoles used as reference and between a-C coated dipoles. In addition a gauge was placed between a coated and an uncoated dipole. The inter-magnet pumping ports with RF shields are made of bare SS. In some MD runs, the RF shield between the two carbon coated magnets was also coated to maximize the elimination effect on e-cloud.

RESULTS AND DISCUSSIONS

The SEY of a witness sample coated simultaneously with each liner was measured in the laboratory.

For a clear view of how the a-C coating works for e-cloud suppression compared to SS, the SEY curves measured in the lab for the SS and two typical a-C coated liners is shown in Fig. 2(a) and the ECM signals measured in the SPS on SS and on two typical a-C coated liners is shown in Fig. 2(b) on logarithmic scale. The SEY of both a-C liners is well below the SEY of SS, as well as the threshold value (= 1.3) of the SPS with nominal LHC beam [2] [3], e-cloud signal presented on SS liner was clearly shown about 10 times higher compared to that on the a-C coated liners.

Figure 2(c) shows the normalized e-cloud signal on linear scale versus time measured in three different MD runs for one a-C coated liner. This liner was inserted in the SPS with an initial SEY of 1.14 and a visible decrease of measured electron current occurred after 5 hours of operation during MD 1 (3-4 batches of nominal LHC beam accelerated to 450 GeV/c). The measured dose of the electron bombardment on the liner after 5 hours of MD was about 1.2 10 C/mm . After two months in the SPS vacuum (10 mbar, unbaked) and with normal SPS operation (without LHC type beams but with the usual beam delivery to CNGS and other fixed target experiments) a new run with LHC type beam did not reveal any ageing from the e-cloud signal. In addition, this liner was kept in the SPS during the 2008/2009 winter shutdown and was vented to air during two months. After re-pumping and operating the machine during 6 months, the test with the LHC type beam exhibited an even stronger reduction of the electron current signal on the liner. The visible improvement of electron current on the liner cannot be explained by scrubbing effect, since the e-cloud was too low. The pressure from MD1, 2, 3 has been compared and the result confirms a significant improvement in pressure, by a factor of 10. The possible reason of the improvement of electron signal is the improvement of pressure in the SPS which decreased the current measured due to ionization of the residual gas by the beam. In conclusion this liner remained more than one year in the machine, sustained a prolonged venting during shutdown and did not show any sign of deterioration. Testing for longer term is still in progress.

After the successful tests with the liners in 2008, a-C coatings were applied to the three SPS magnet vacuum chambers in March 2009. Microwave transmission measurements detected e-cloud related signals in one of the uncoated magnets and no signal was measurable in one of the coated magnets [7].

The dynamic pressure rise is shown in Fig. 3(a) for an LHC type beam. The resolution of the measurement is only 1 s, but the cycle time (21.6 s) and the effect of the acceleration ramp is well visible. The scattering in the pressure

Table 1: Four different coating configurations were used with DC magnetron sputtering. Different discharge gases (Ne, Kr, Ar) and different coating parameters (temperature of substrate, discharge gas pressure, power) can be used.

Coating configuration	**Magnetic field**	**Samples**
Cylindrical tube with one graphite rod cathode	Parallel to the cathodes	Lab samples for SEY investigations and vacuum characterizations
Liner in tube with 4 graphite rods	Parallel to the cathodes	Lab samples for SEY investigations and liner for e-cloud monitors
MBB magnet chamber in-situ chamber in the dipole with Multi-electrode	Perpendicular to the cathodes and chamber axis	Version I: MBB coating in-situ in SPS dipoles
MBB magnet chamber stand-alone with liner configuration	Parallel to the cathodes	Version II: MBB coating outside SPS dipoles

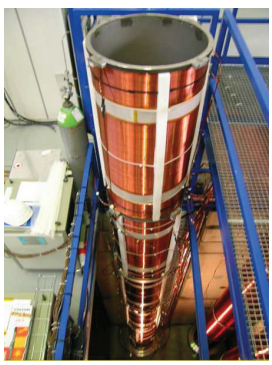

(a)

(b)

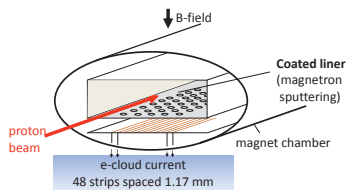

(c)

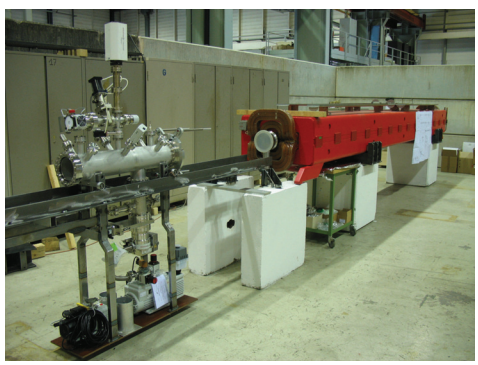

(d)

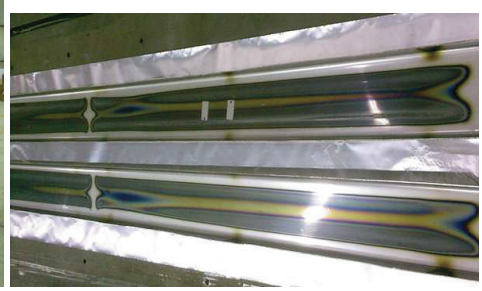

(e)

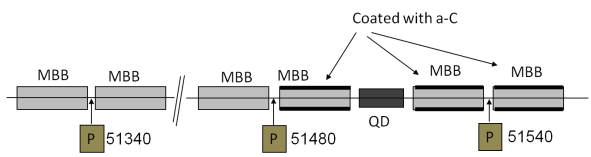

(f)

Figure 1: (a): 7 m long solenoid used to provide a magnetic field parallel to the cathodes used during the coatings. (b): Liner configuration with four carbon cathodes to provide a homogeneous coating. (c): Electron Cloud Monitor used to observe electron cloud activity in-situ the SPS. (d): MBB dipole magnet equipped with vacuum system. Inside the dipole, three graphite cathodes and the same magnetic field provided by the dipole self was used, which was perpendicular to the cathodes. The power used during coating was kept limited not to damage the coil. (e): Inspection of the extracted a-C coated MBB after operation in the SPS. (f): The design of the coated and the uncoated magnets in the SPS. MBB: Magnetic Bender B-type. QD: defocussing quadrupole. P: penning gauge.

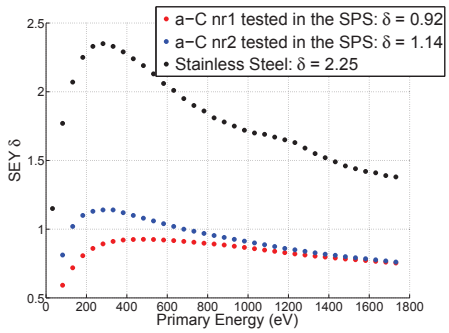

(a)

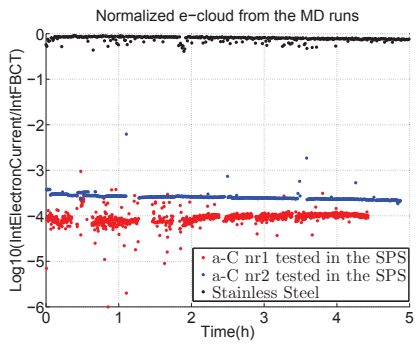

(b)

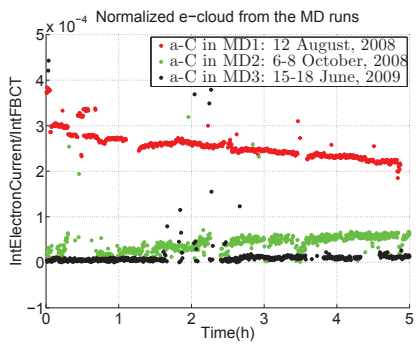

(c)

Figure 2: (a): Comparison of the SEY of SS and a-C coatings measured in the lab. (b): ECM signals from SS and a-C coatings in the base-10 logarithm of integrated electron current signal for each supercycle divided by integrated intensity (FBCT) for each supercycle as a function of supercycle number [nC/10 protons per bunch]. (c): ECM signals from different a-C coatings. EC has a magnitude of 10 . Integrated electron current signal for each supercycle divided by integrated intensity (FBCT) for each supercycle as a function of supercycle number [nC/10 protons per bunch].

rise is large and the pressure also changes with the various parameters (e.g. RF voltage). However it is obvious that the decrease in pressure rise due to the coating, if any, is not as marked as for the e-cloud signal in the ECM.

The result of a recent inspection of one of a-C coated MBB chambers is shown in Fig. 1(e). The coating of the extracted MBB dipole does not look as uniform as expected, and some part of the chamber is even without coating. In the middle part of the chamber, the coating layer is thin and appears very transparent. This laterally non-uniform coating color indicates differences in thickness and possibly composition. The SEY measurement of this magnet has also been performed in the lab, see Fig. 3(b). The highest SEY occurred in the middle part of the shorter side of the chamber with a value of 1.33 as shown in Fig. 3(b).

The same inspection has been done on four a-C coated liners extracted from the SPS. These a-C coated liners have all been tested during MD 2 - MD 9 runs in 2009, with 3-4 batches of nominal LHC beam accelerated to 450 GeV/c. The longest has been inserted in the SPS for more than 1.5 years. In Fig. 4, a perfectly homogeneous, dark coating shows no peeling off and no damage of the beam on all four extracted liners after more than one year operation in the SPS. The SEY measurements of these liners after extraction have also been performed in the lab. The increase of the SEY is negligible as shown in Fig. 5.

These inspections of the coated liners and dipoles confirmed that the coating in the magnets was significantly inferior to the coatings in the liner, which gave a complete suppression of e-cloud. Therefore, to improve the homogeneity and the quality of the coating in the SPS dipole magnet, another three dipole magnet vacuum chambers coated in the same way as ECM have been tested. They have been installed in the SPS and will be tested with beam in coming MD runs.

CONCLUSION AND OUTLOOK

In conclusion the experiments have shown that a complete suppression of e-cloud can be achieved by coating of liners with a thin layer of amorphous carbon, which has an SEY close to 1.0 as measured in the laboratory. The coating does not show ageing after more than one year of exposure in the SPS vacuum with the machine in operation with beams. The inspection of the coated magnet from the first series, which was coated by using the magnetic field of the dipole itself confirmed that the coating was significantly inferior to the coatings in the liner, which gave a complete suppression of e-cloud.

Future activity will now be focused on the development of a configuration to coat beam pipes without dismounting the chamber from the dipole on a large scale with the same quality of coating as in the ECMs. We will also follow the ageing development of the new version of MBB coating and try to understand the relationship between dynamic pressure rise and e-cloud effect.

The first implementation on a large scale with this type

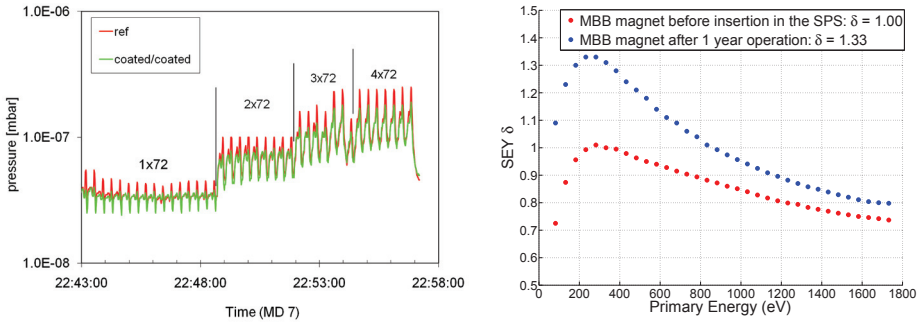

(a) (b)

Figure 3: (a): The comparison of the pressure measurements of the uncoated and coated dipoles. The nominal LHC beam which consisted of 1, 2, 3 and 4 batches with 72 bunches at 25 ns spacing and intensity of 10 protons/bunch. (b): SEY measurement on the coated MBB magnet before and after operation in the SPS.

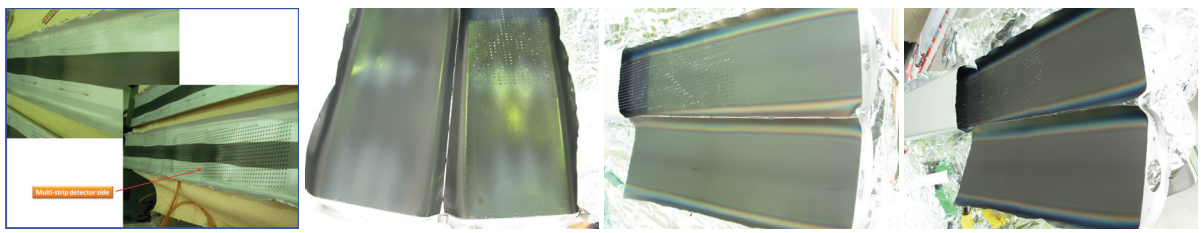

(a) (b) (c) (d)

Figure 4: Inspection of four a-C liners extracted from the SPS. (a): a-C Strip, a-C coating used for confirming necessity of coating width. (b): C-Zr, a-C on rough Zr coating (c): CNe64, a-C number 64. (d): CNe65, a-C number 65.

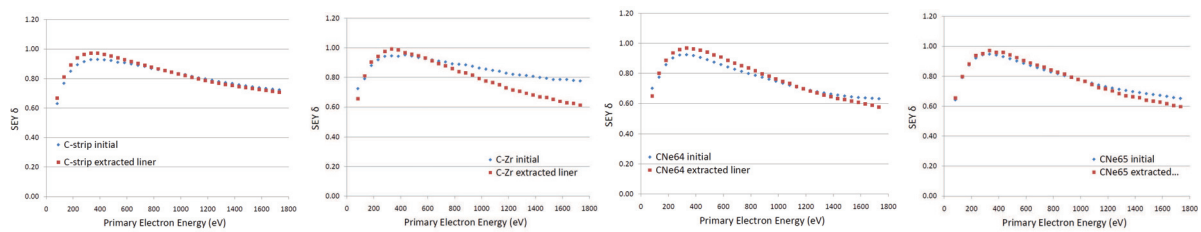

(a) (b) (c) (d)

Figure 5: SEY measurements on four a-C coated liners before and after operation in the SPS. (a): a-C Strip, a-C coating used for confirming necessity of coating width. (b): C-Zr, a-C on rough Zr coating (c): CNe64, a-C number 64. (d): CNe65, a-C number 65.

of a-C coating is now planned to be performed in the SPS magnets of total 200 meters during the shutdown 2012/2013.

ACKNOWLEDGEMENT

We thank all the members of the TE-VSC-group and SPSU Study team for their work. This work would not have been possible without their enthusiasm and help.

REFERENCES

[1] *Measurement of the Electron Cloud Properties by Means of a Multi-Strip Detector in the CERN SPS*
G.Arduini et al. EPAC 2002, Paris, France.

[2] *Which parts of the SPS do we need to coat?*
G.Rumolo, talk at AEC09, 12 October 2009, CERN.

[3] *Amorphous Carbon Thin Films for the mitigation of electron clouds in particle accelerators*
S.Calatroni et al. HHH-2008 Proceedings

[4] *Experimental Studies of Carbon Coatings as Possible Means of Suppressing Beam Induced Electron Multipacting in the CERN SPS*
E.Shaposhnikova et al. PAC09, Vancouver, Canada.

[5] *Low Secondary Electron Yield Carbon Coatings for Electron-cloud Mitigation in Modern Particle Accelerators*
C.Yin Vallgren et al. IPAC10, Kyoto Japan.

[6] *Amorphous Carbon Thin Film for Low Secondary Electron Yield Applications*.
C.Yin Vallgren et al. IPAC10, Kyoto Japan.

[7] *Electron Cloud Measurements of Coated and Uncoated Vacuum Chambers in the CERN SPS by Means of the Microwave Transmission Method*
S.Federmann et al. IPAC10, Kyoto Japan.

Can electron multipacting explain the pressure rise in the ANKA cold bore superconducting undulator?

S. Casalbuoni*, S. Schleede†, D. Saez de Jauregui, M. Hagelstein, P. F. Tavares‡§
Karlsruhe Institute of Technology, Institute of Synchrotron Radiation, Germany

Abstract

Preliminary studies performed with the cold bore superconducting undulator installed in the ANKA (ANgstrom source KArlsruhe) storage ring suggest that the beam heat load is mainly due to the electron wall bombardment. Electron bombardment can both heat the cold vacuum chamber and induce an increase in the pressure because of gas desorption. In this contribution we compare the measurements of the pressure in a cold bore performed in the electron storage ring ANKA with the predictions obtained using the equations of gas dynamic balance in a cold vacuum chamber exposed to synchrotron radiation and electron bombardment. The balance results from two competing effects: the photon and electron stimulated desorption of the gas contained in the surface layer of the chamber wall and of the gas cryosorbed, and the cryopumping by the cold surface. We show that photodesorption alone cannot explain the experimental results and that electron multipacting is needed to reproduce the observed pressure rise. Electron bombardment can at the same time explain the observed beam heat load.

INTRODUCTION

In order to produce synchrotron radiation of highest brilliance, third generation synchrotron sources make use of insertion devices (IDs). The state of the art available today for IDs is the permanent magnet technology with magnet blocks placed inside the vacuum of the storage ring. Following an initial proposal at SPRING8 [1], the concept of Cryogenic Permanent Magnet Undulators (CPMU) is presently considered as a possible future evolution of in-vacuum undulators [2, 3, 4, 5]. Superconducting undulators can reach, for the same gap and period length, higher fields even with respect to CPMU devices, allowing to increase the spectral range and the brilliance. At ANKA we are running a research and development program on superconducting insertion devices (SCIDs). One of the key issues for the development of SCIDs is the understanding of the beam heat load to the cold vacuum chamber. The beam heat load is a fundamental input parameter for the design of SCIDs since it is needed to specify the cooling power.

Studies performed on the cold bore superconducting undulator installed at ANKA indicate that a simple model of electron bombardment could explain the beam heat load and observed pressure rise during normal user operation [6]. In this paper we go a step further solving the equations of gas dynamic balance in a cold vacuum chamber exposed to synchrotron radiation and electron bombardment. We show that the observed pressure rise can be explained by the occurence of electron multipacting and not by photodesorption alone. The paper is organized as follows. For completeness, in the next two sections we summarize respectively the experimental setup and the observations described in more detail in Ref. [6]. Afterwards we present the equations of gas dynamic balance and the input parameters derived from the literature and used to solve the model, and we derive an approximate analytical solution to those equations and discuss its properties. We discuss then the main results of the comparison between observations and simulations, and finally we give some conclusions and outlook.

EXPERIMENTAL SETUP

ANKA is an electron storage ring used as a synchrotron facility [7]. A cold bore superconducting undulator built by ACCEL Instr. GmbH, Bergisch Gladbach, Germany [8], is installed in one of the four straight sections of the ring; the rest of the ring is at room temperature. The vacuum chambers of the warm part of ANKA have been baked before installation at 200°C for 48 hours and vented with nitrogen.

The storage ring compatible cryostat is shown in Fig. 1. The system is cryogen free and is cooled by three Sumitomo cryocoolers (RDK-408D @ 50 Hz) [9]: two of them cool the coils to about 4 K and one cools the UHV (Ultra High Vacuum) tank, which is at 10 K and protects the coils from the external thermal radiation. The cryostat consists of two separate vacuum systems for the cold mass: an UHV vacuum system for the beam and an insulation vacuum system for the coils and the rest of the cold mass. The pressure of the two vacua are monitored by pressure gauges at room temperature. A 300 μm stainless steel foil coated with 30 μm of copper is placed between the cold mass and the beam vacuum. A taper system connects the normal beam pipe with the cold mass and has two func-

* Corresponding author: sara.casalbuoni@kit.edu
† now at the Technische Universität München
‡ on leave from ABTLuS/Brazilian Synchrotron Radiation Laboratory, Campinas, SP - Brazil
§ now at MAX-Lab, Lund, Sweden

tions: 1) smooth transition for wake fields, 2) thermal transition between the cold bore at 4 K and the beam pipe at room temperature. Several temperature sensors are placed on the different elements: coils, UHV tank, taper entrance, taper exit, etc. A pressure gauge (PRT) and a residual gas analyzer (RGA) are located in the room temperature region about 0.5 m upstream from the entrance of the undulator cryostat. A unique diagnostic in this undulator, absent in other cold bore wigglers installed in the different synchrotron light sources [10, 11] (because of the different design) is a pressure gauge with direct access to the cold bore (PCB). The undulator vacuum chamber at 4.2 K is 1.4 m long, it has a rectangular cross section with 66 mm width. The undulator can be operated with different gap sizes: 16, 12, and 8 mm, and it can be opened to 29 mm without current in the coils during injection. The height of the beam vacuum chamber changes accordingly. In this paper we describe results obtained with the beam stay clear height of 29 mm and no current in coils, which means no magnetic field. In order to protect the undulator from the

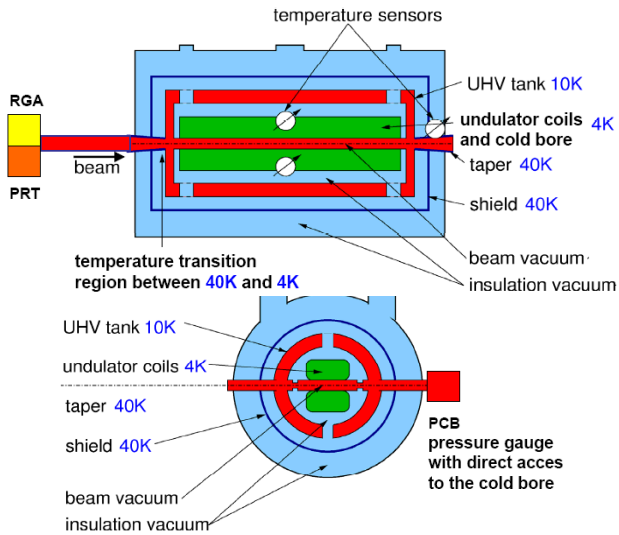

Figure 1: Schematic layout of the vacuum system of the superconducting undulator and the position of the temperature sensors, a pressure gauge (PRT) and a residual gas analyzer (RGA) located in the room temperature region, and a pressure gauge with direct access to the cold bore (PCB).

synchrotron radiation emitted by the upstream magnets a collimator system is located at about 1 m from the entry point of the undulator [14].

OBSERVATIONS

The superconducting undulator has been operating in the ANKA storage ring since 2005 [8]. The beam heat load and the pressure in the cold vacuum chamber have been monitored since then. A typical run is shown in Fig. 2 where the average beam current, the beam energy, the UHV pressure [15] and the temperature of the coils are reported as a function of time. The temperature increase of the coils

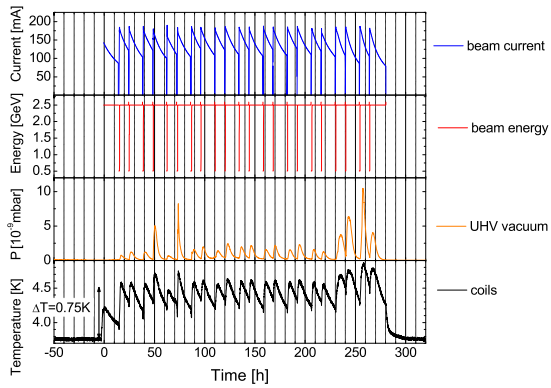

Figure 2: Typical user operation run with open gap (= 29 mm) and no current in the undulator. The beam current, the beam energy, the UHV pressure and the temperature of the coils are reported as a function of time.

can be converted into the deposited beam heat load. The calibration has been performed using a resistor in thermal contact with the coils. The time constant to reach thermal equilibrium is of the order of two hours. The beam heat load to the coils is about 1 W.

A pressure rise is observed after beam injection. A correlation between the heat load and the pressure is observed in several runs, see Fig. 3. In Fig. 4 a comparison of the

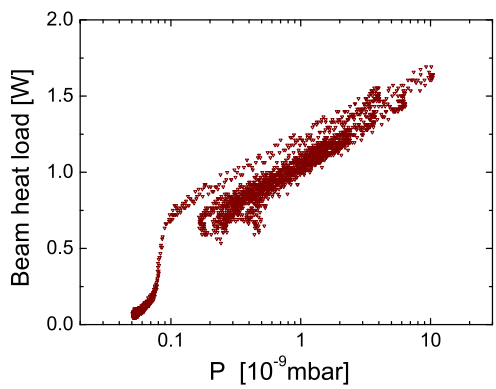

Figure 3: The beam heat load as a function of the UHV pressure in the cold bore from Fig. 2.

pressure behavior in the cold bore (green squares) and in the room temperature region (red triangles) is displayed. In the cold bore the pressure reaches a maximum after 1-3 hours from injection, while in the room temperature region this happens within few minutes. The plot shows also that the decay of the pressure in the cold bore is much faster than the decay of the pressure in the room temperature region. The dynamic pressure increases nonlinearly with the average beam current [6]. A similar pressure rise with cur-

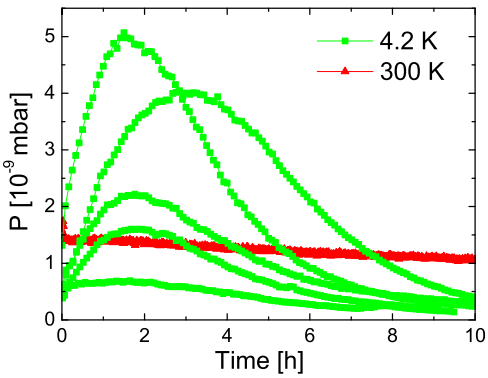

Figure 4: Comparison of the dynamic pressure in the cold bore (green squares) with the one in the room temperature region (red triangles). The static pressure in the cold bore (PCB) is about 2×10^{-11} mbar and in the room temperature region (PRT) is about 2×10^{-10} mbar.

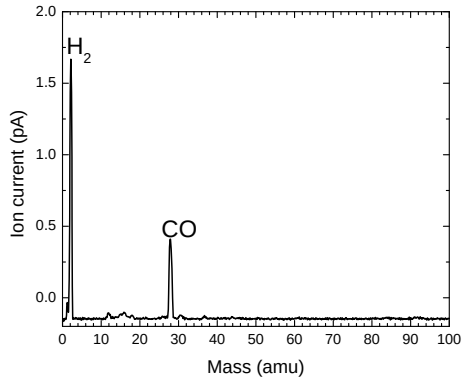

Figure 5: Mass spectrum of the warm vacuum chamber just before the undulator with beam measured with the RGA indicated in Fig. 1.

rent has been observed in positron rings (machines at room temperature) and has been attributed to electron multipacting [12, 13]. We will come back to this in the section where we describe the results.

The mass spectrum (RGA) of the warm vacuum chamber with beam shows, while the undulator is cold, only the H_2 and CO lines, see Fig. 5. CO disappears when there is no beam. In the rest of the ring most of the time no CO is detected. The mass spectrum measured by warming up the undulator to room temperature in absence of electron beam shows together with H_2 the presence of CO, CO_2 and H_2O, indicating that the cryosorbed gas layer might have a more complex gas composition than simply H_2. However, H_2 is the only gas among the ones mentioned above that has a non negligible vapour pressure at 4-20 K and we see that this is the main gas component measured when the undulator is cold.

MODEL AND INPUT PARAMETERS

The equations of gas dynamic balance inside a vacuum chamber can be written as (see Refs. [16, 17] and references therein):

$$\begin{aligned} V\frac{dn}{dt} &= q + q'(s) - \alpha S(n - n_e(s,T)) + u\frac{d^2n}{dz^2}, \\ A\frac{ds}{dt} &= \alpha S(n - n_e(s,T)) - q'(s), \end{aligned} \quad (1)$$

where n is the volume gas density, s the surface density of the cryosorbed gas, V the vacuum chamber volume, A the vacuum chamber wall area, q is the primary beam induced desorption flux, q' the secondary beam induced desorption flux (desorption of cryosorbed molecules), α the sticking coefficient, $S = A\bar{\nu}/4$ is the ideal wall pumping speed, $\bar{\nu}$ is the mean molecular speed, n_e the thermal equilibrium gas density, and u the specific vacuum chamber conductance per unit axial length. In the following, we consider the gas to consist only of H_2.

The specific vacuum chamber conductance per unit axial length is given by $u = A_c D$, where $D = 2A_c\bar{\nu}/3$ is the Knudsen diffusion coefficient and A_c the area of the rectangular cross section of the vacuum chamber. Axial diffusion can be neglected when $DA_c/L^2 \ll S\alpha$ [16], which means:

$$\frac{8}{3}\frac{A_c^2}{AL^2} \ll \alpha\,. \quad (2)$$

Even for the lowest experimental value of the sticking coefficient for H_2 at 4.2 K, $\alpha = 0.02$ [18] condition (2) is satisfied for the geometry of the undulator vacuum chamber where L = 1.4 m and for a gap of 29 mm, $A_c = 0.00191$ m^2 and $A = 0.266$ m^2. Therefore in the following we neglect axial diffusion $ud^2n/dz^2 \approx 0$.

The beam induced desorption flux consists of photon (PSD) and electron (ESD) stimulated desorption:

$$\begin{aligned} q &= \eta\dot{\Gamma} + \phi\dot{\Theta}, \\ q' &= \eta'\dot{\Gamma} + \phi'\dot{\Theta}, \end{aligned} \quad (3)$$

where η and η' are the primary and secondary electron stimulated desorption yields, $\dot{\Gamma}$ is the electron flux, ϕ and ϕ' are the primary and secondary photodesorption yields, and $\dot{\Theta}$ is the photon flux. The photon flux is proportional to the beam current, so we consider it to decay exponentially with time as : $\dot{\Theta} = \dot{\Theta}_0 \exp(-t/\tau)$ where $\tau = 80000$ s is the beam lifetime which is about 22 hours. For the ANKA cold bore vacuum chamber with gap = 29 mm and average beam current $I = 150$ mA, the photon flux impinging on the lower and upper surfaces is $\dot{\Theta}_0 = 5 \times 10^{15}$ photons/s. The photon flux $\dot{\Theta}_0$ is obtained by integrating the angular and spectral distribution of number of photons emitted by the upstream dipole over all photon energies and over the horizontal and vertical acceptance defined by the cold

bore geometry and distance to the upstream bending magnet. We assume that the electron flux also decays exponentially in time: $\dot{\Gamma} = \dot{\Gamma}_0 \exp(-t/\tau_{el})$. In order to estimate $\dot{\Gamma}_0$, we assume that the bombarding electrons are initially generated (e.g. by photo-ionization of the croysorbed H_2 molecules on the cold surface) at rest, and then accelerated against the wall by the transverse electric field of the electron bunch. For a typical 3.6×10^9 electrons/bunch we obtain a mean electron energy $\Delta W = 10$ eV [19] so that if the observed beam heat load $P = 1$ W is to be explained by electron bombardment, then $\dot{\Gamma}_0 = 6 \times 10^{17}$ electrons/s.

The measurements of input parameters such as the photon and electron primary and secondary desorption yields, as well as the sticking coefficient are quite challenging. Several experiments have been performed to measure those parameters for a H_2 layer cryosorbed on a copper substrate at low temperatures and a wide range of values can be found in the literature. The photon and electron primary and secondary desorption yields, as well as the sticking coefficient depend on the temperature, on the surface coverage, on the geometry (closed or open), on the photon and on the electron energy distribution and dose. The different experiments reported in the literature have been performed under a variety of conditions, and it is therefore difficult to compare them with each other and to extract the values needed for a consistent comparison with our experimental situation. Even though a comprehensive review of different experimental results on the above mentioned parameters is beyond the scope of this paper, we list below some of the values obtained in experiments performed in the last 20 years to understand the beam vacuum system of a cold bore accelerator, that started with studies motivated by the 20 TeV Superconducting Super Collider [20] and continued with studies motivated by the Large Hadron Collider (LHC) [21].

The photon primary desorption yield ϕ and the ratio of the secondary photodesorption yield ϕ' to the sticking coefficient α have been measured on a copper electroplated stainless steel liner at 4.2 K in a quasi-closed geometry by Anashin et al. [22] to vary in the range $2 \cdot 10^{-4} \leq \phi \leq 5 \cdot 10^{-2}$ and $5 \cdot 10^{-2} \leq \phi'/\alpha \leq 8$.

In a more recent work [23] measurements of the sticking coefficient α and of the sum of the primary and secondary electron stimulated desorption yields have been reported. The sticking coefficient ranges $0.25 \leq \alpha \leq 0.6$ for surface coverages of about one monolayer $s_m = 3 \times 10^{19}$ molecules/m^2. The sum of the primary and secondary electron stimulated desorption yield for 300 eV electrons has been measured as a function of H_2 coverage at about 2 K on the LHC beam screen to be $50 \leq \eta + \eta' \leq 2000$.

The ratio of the sum of the primary and recycling electron stimulated desorption yield to the sticking coefficient can be estimated from our measurements [6]. Following Ref. [24] we use the equation:

$$\frac{q+q'}{\alpha} = S(n - n_e(s,T)) = SG\Delta P, \qquad (4)$$

where $\Delta P = P_{\max} - P_e$ with $P_e \lesssim 2 \times 10^{-11}$ mbar the thermal equilibrium pressure at 4.2 K and

$$G = \frac{1}{k_B\sqrt{TT_{\rm RT}}} = 2 \times 10^{23}\ \text{m}^{-3}\ \text{mbar}^{-1}$$

with $T = 4.2$ K and $T_{RT} = 300$ K. As mentioned above the photon flux on the ANKA cold bore vacuum chamber with gap=29 mm and $I = 150$ mA, $\dot{\Theta}_0 = 5 \times 10^{15}$ photons/s, and the estimated electron flux to explain a heat load of $P = 1$ W (for 10 eV electrons) is $\dot{\Gamma} \approx 6 \times 10^{17}$ electrons/s. Being $\phi + \phi' \lesssim \eta + \eta'$ [24, 25], we can neglect the contribution of PSD to the beam desorption flux, so that $q = \eta\dot{\Gamma}$ and $q' = \eta'\dot{\Gamma}$. The observed ΔP ranges from 2×10^{-11} mbar to 8×10^{-8} mbar [6]. For H_2 the mean molecular speed at 4.2 K is $\bar{\nu} = 210$ m/s and applying Eq. (4) we find that the sum of the primary and secondary desorption yields $(\eta+\eta')/\alpha$ for H_2 ranges between 10^{-4} molecules/electron to 4 molecules/electron. Our values are in good agreement with the ones measured at COLDEX [24] that range between 10^{-2} molecules/electron for an electron dose of 2×10^{23} electrons/m^2 to 30 molecules/electron for an electron dose of 10^{21} electrons/m^2, considering that in our case the temperature is lower (4.2 K instead of 12 K), the mean electron energy is an order of magnitude smaller (10 eV instead of 100 eV [24]) and that our electron dose is in some cases much higher (after two weeks of normal user operation it is about 2×10^{24} electrons/m^2).

In Ref. [22] it has been shown that the secondary photodesorption yield ϕ' depends linearly on the surface coverage up to one monolayer $\phi' = \phi'_0(s/s_n)$. Similar results have been found by Tratnik [23] for the sum of the primary and secondary electrodesorption yields $\eta + \eta'$ up to one monolayer. Considering the results obtained in Ref. [24], being $5 \cdot 10^{-4} \leq \eta \leq 10^{-1}$, to solve Eqs. (1) we assume $\eta' = \eta'_0(s/s_n)$. In our model we define the normalization of the surface coverage to be $s_n = 10^{18}$ molecules/m^2.

The volume gas density n at a temperature T is related to the pressure measured at room temperature by:

$$n = \frac{P}{k_B\sqrt{TT_{\rm RT}}}\,. \qquad (5)$$

The value of the volume gas density at $t = 0$ (injection time) n_0 is obtained from Eq. (5) with $P = P_0$ [mbar] chosen to fit the experimental data. We have assumed $n_e(s,T) = 4 \times 10^{12}$ molecules/m^3, corresponding to an equilibrium pressure $P_e = 2 \times 10^{-11}$ mbar. The surface coverage at equilibrium is constrained to be $s_0 < 1.5 \times 10^{19}$ molecules/m^2 by the measured adsorption isotherms of H_2 on copper plated stainless steel at 4.2 K from Ref. [26].

APPROXIMATE ANALYTICAL SOLUTIONS TO THE GAS DYNAMIC BALANCE EQUATIONS

Before embarking on a direct numerical computation of the solutions to Eqs. (1), we obtain a closed expression of the solution for a simplified form of these equations, namely when only photodesorption is present (i.e., assuming zero electron flux). Apart from providing a cross-check on the full numerical calculations described in section below, this simplified situation is interesting because, as our analysis will show, it cannot reproduce the experimental data, indicating that the additional ingredient of electron bombardment (and multipacting) is indeed essential. In fact, this approach allows us to obtain several relevant properties of the solutions, as well as an approximate analytical solution, valid in the limit of times short compared to the beam lifetime, which allows us to set bounds on the characteristic time constants associated with the pressure rise when only photons are present.

When the electron flux is zero, Eqs. (1) reduce to

$$\begin{aligned} V\frac{dn}{dt} &= \frac{1}{\tau_\epsilon}e^{-t/\tau} + \frac{A}{\tau_d}e^{-t/\tau}s - \alpha S(n-n_e), \\ A\frac{ds}{dt} &= \alpha S(n-n_e) - \frac{A}{\tau_d}e^{-t/\tau}s, \end{aligned} \tag{6}$$

where we have defined the time constants

$$\begin{aligned} \tau_\epsilon &= \frac{1}{\phi\dot{\Theta}_0} \\ \tau_d &= \frac{As_n}{\phi_0'\dot{\Theta}_0}. \end{aligned} \tag{7}$$

The total number of molecules (on the surface + in the volume)

$$N_T(t) = Vn(t) + As(t) \tag{8}$$

satisfies the equation

$$\frac{dN_T}{dt} = q = \frac{1}{\tau_\epsilon}e^{-t/\tau}, \tag{9}$$

with the trivial solution

$$\begin{aligned} N_T(t) &= \frac{\tau}{\tau_\epsilon}\left(1-e^{-t/\tau}\right) + N_{T0} \\ N_{T0} &= Vn_0 + As_0. \end{aligned} \tag{10}$$

Writing

$$s(t) = \frac{N_T(t) - Vn(t)}{A}, \tag{11}$$

we can now decouple the two equations and write an equation involving $n(t)$ only:

$$\frac{dn}{dt} + g(t)n(t) = k(t), \tag{12}$$

where

$$\begin{aligned} g(t) &= \frac{e^{-t/\tau}}{\tau_d} + \frac{1}{\tau_s} \\ k(t) &= \frac{e^{-t/\tau}}{V\tau_\epsilon} + \frac{n_e}{\tau_s} + \\ &\quad + \frac{1}{V\tau_d}e^{-t/\tau}\left[\frac{\tau}{\tau_\epsilon}\left(1-e^{-t/\tau}\right) + N_{T0}\right], \end{aligned}$$

with

$$\tau_s = \frac{V}{\alpha S}. \tag{13}$$

This can be solved by writing

$$\begin{aligned} g(t) &= \frac{1}{h(t)}\frac{dh}{dt} \\ \frac{1}{h}\frac{d(nh)}{dt} &= \frac{dn}{dt} + g(t)n(t) = k(t) \\ h(t)n(t) - h_0n_0 &= \int_0^t h(t')k(t')dt' \end{aligned}$$

and finally

$$n(t) = \frac{n_0h_0}{h(t)} + \frac{1}{h(t)}\int_0^t h(t')k(t')dt', \tag{14}$$

with

$$\begin{aligned} h(t) &= \exp\left[\frac{\tau}{\tau_d}\left(1-e^{-t/\tau}\right) + \frac{t}{\tau_s}\right] \\ h_0 &= 1\,. \end{aligned} \tag{15}$$

Equation (14) gives the molecular density (and thefore the pressure) as a function of time in the form of a simple integral. Even without solving this integral, we may obtain the limiting behaviour of the solutions for very large time

$$\begin{aligned} N_T(t\to\infty) &\to \frac{\tau}{\tau_\epsilon} + N_{T0} \\ n(t\to\infty) &\to n_e \\ s(t\to\infty) &\to \frac{N_{T0} - Vn_e}{A} + \frac{\tau}{\tau_eA} \end{aligned}$$

Finally, in the limit $\tau \to \infty$, we obtain the approximate solution

$$\begin{aligned} n(t) &= n_0e^{-t/\tau_{ds}} + \tau_{ds}\left(\tfrac{N_{T0}}{V\tau_d} + \tfrac{1}{V\tau_\epsilon} + \tfrac{n_e}{\tau_s}\right)\left(1-e^{-t/\tau_{ds}}\right) + \\ &\quad + \tfrac{\tau_{ds}^2}{V\tau_d\tau_\epsilon}\left(\tfrac{t}{\tau_{ds}} - 1 + e^{-t/\tau_{ds}}\right) \end{aligned} \tag{16}$$

where we have defined yet another time constant

$$\tau_{ds} = \frac{1}{\frac{1}{\tau_d} + \frac{1}{\tau_s}} \tag{17}$$

Noting that, for typical parameters, $\tau_{ds} \ll \tau$, we see from the equation (16) that, for times such that $\tau_{ds} \ll t \ll \tau$, the volume density and therefore the pressure grows linearly with time. Clearly this approximation cannot give us the exact time at which the pressure reaches its maximum value, but it does indicate that such a maximum cannot happen at times much shorter than the beam lifetime τ since for that time range the molecular density is a monotonically increasing function of time. However, this is precisely what

the experimental data show, since the lifetime is typically of the order of 20 hours, whereas the pressure peak happens within just a few hours. This leads us to assume that some other mechanism, apart from photo desorption and with a different characteristic time constants must be involved to explain the experimental observations. In the following section, we discuss this in more detail, using a full numerical solution to the gas dynamic balance equations.

RESULTS

Various simulations have been performed solving Eqs. (1). The idea is to change the input parameters within the range of values found in the literature and to compare the pressure simulated with the one measured.

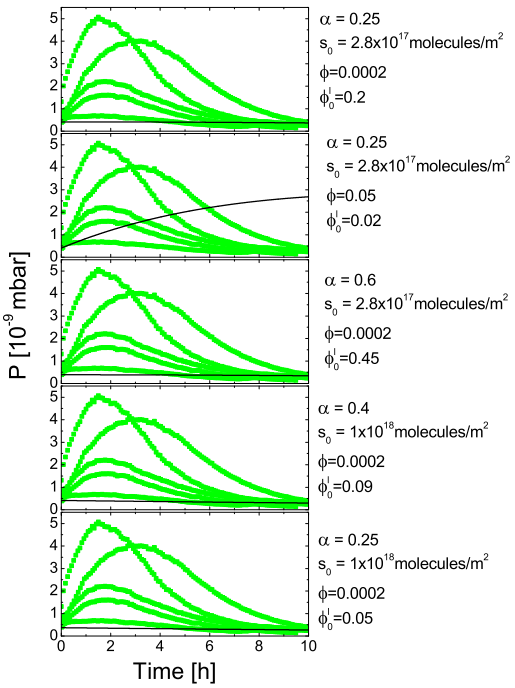

Figure 6: Pressure in the cold vacuum chamber as a function of time. The green squares indicate the typical behaviour and range of measured values. The black line displays the simulations shown in these plots consider only photo-desorption ($\dot{\Gamma}_0 = 0$ electrons/s).

As we have seen above, considering just the contribution of photons ($\dot{\Gamma} = 0$ electrons/s) to desorb molecules from the cold surface it is impossible to reproduce the measured values of the pressure as a function of time. This can also be demonstrated by showing that the first of Eqs. (1) at the time at which the pressure has a maximum t_{max} is not satisfied. Since at t_{max} $dn/dt = 0$ it follows:

$$\exp(-t_{max}/\tau) = \frac{\alpha G S \Delta P}{(\phi + \phi')\dot{\Theta}_0} \qquad (18)$$

The experimental constraints on $2 \cdot 10^{-4} \leq \phi \leq 5 \cdot 10^{-2}$, $5 \cdot 10^{-2} \leq \phi'/\alpha \leq 8$ (Ref. [22]) and on $0.25 \leq \alpha \leq 0.6$ (Ref. [23]) described in the previous section limit $(\phi + \phi')/\alpha$ in the range $0.05 \leq (\phi + \phi')/\alpha \leq 8.2$. With this in mind and recalling from the observations that $\Delta P \simeq 5 \times 10^{-9}$ mbar, the second term of Eq. (18) is always less than 0.02. From our experimental data $t_{max} \simeq 2$ hours and $\tau \simeq 22$ hours, so the first term of Eq. (18) is about 1 and Eq. (18) is not satisfied.

The solutions obtained from Eqs. (1) taking into account only photodesorption with different sets of parameters are reported in Fig. 6. The initial pressure is set to $P_0 = 4 \times 10^{-10}$ mbar. The results obtained considering also electron stimulated desorption are shown in Fig. 7. We have used the values indicated in the column 'fixed' of Table 1 which fit one of the green curves, see Fig. 7. In order to study the effect of the different parameters, we have performed different simulations by varying the parameters shown in Table 1 within the values indicated in the columns 'min' and 'max'. Increasing the sticking coefficient α or decreasing the primary and secondary electron stimulated desorption yield decreases the amount of molecules desorbed and the pressure peak while a change in the surface coverage s_0 does not significantly affect the results. Figure 7 c) also shows that an increase in the decay time of the impinging electrons τ_{el} delays the pressure peak. In

	min	max	fixed
s_0 (10^{17} molecules/m^2)	1	2.5	1.3
α	.1	.6	.3
ϕ			0.0002
ϕ'_0			0.01
η	0.0001	0.0003	0.0001
η'_0	0.001	.01	0.0035
$\dot{\Theta}_0$ (10^{15}photons/s)			5
$\dot{\Gamma}_0$ (10^{17}electrons/s)			6
τ (s)			80000
τ_{el} (s)	5000	15000	9000

Table 1: Values used as input parameters in Eqs. (1) to obtain the values of the pressure as a function of time reported in Fig. 7.

Fig. 8 we show that it is possible to tune the input parameters within the range of values found in the literature to reproduce the different measured curves of the pressure in the cold bore. We conclude that, taking into account the contribution of molecules desorbed by electrons, it is possible to reproduce the observed behaviour of the pressure by varying the input parameters in the range of values found in the literature. The measurements are well reproduced by using a decay time of the electrons desorbing H_2 from the surface in the range 8000 s $< \tau_{el} <$ 13000 s. Since the beam current I_b and the flux of electrons bombarding the wall $\dot{\Gamma}_0$ decay exponentially with time with two different time constants, respectively τ and τ_{el},

$$I_b = I_{b0}\exp(-t/\tau), \quad \dot{\Gamma} = \dot{\Gamma}_0\exp(-t/\tau_{el})$$

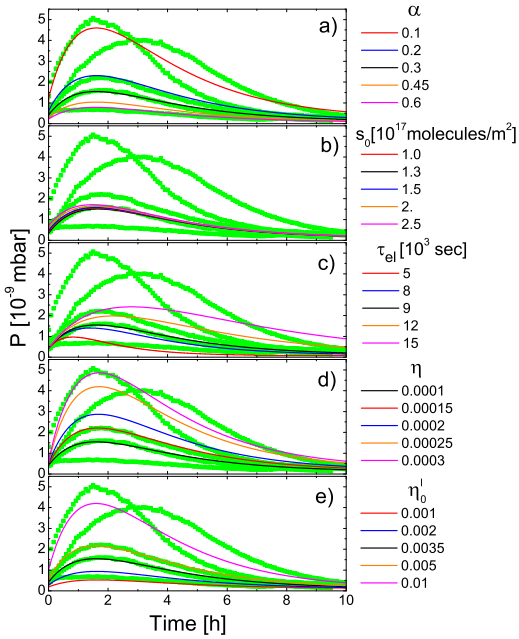

Figure 7: Pressure in the cold vacuum chamber as a function of time. The green squares indicate the typical behaviour and range of measured values. The simulations shwon in these plots are obtained considering also electron stimulated desorption and using the 'fixed' values of the input parameters as in Table I varying a) the sticking coefficient α, b) the initial value of the H_2 surface coverage s_0, c) the decay time of the electrons desorbing H_2 from the surface τ_{el}, d) the primary electron stimulated desorption yield η, e) the secondary electron stimulated desorption yield η'.

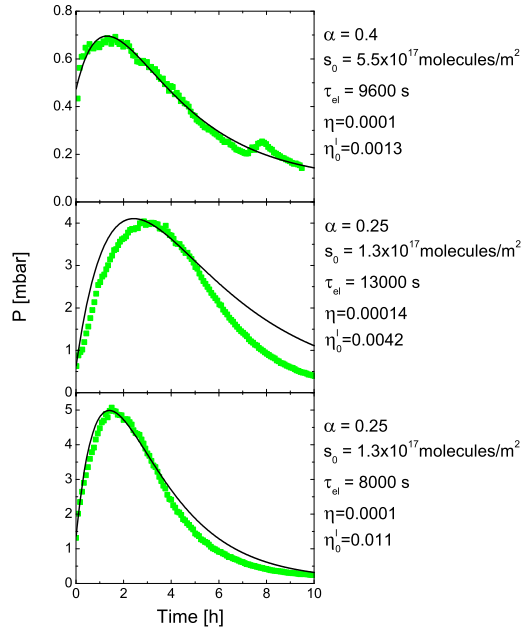

Figure 8: Pressure in the cold vacuum chamber as a function of time. The green squares indicate the typical behaviour and range of measured values. The simulations shown in these plots demonstrate that it is possible to tune the input parameters within the range of values found in the literature to reproduce the different measured curves of the pressure in the cold bore.

where I_{b0} is I_b at $t = 0$ it follows that

$$\dot{\Gamma} = \dot{\Gamma}_0 \exp(\tau/\tau_{el} \ln(I_b/I_{b0})) = \dot{\Gamma}_0 \left(\frac{I_b}{I_{b0}}\right)^{\tau/\tau_{el}} \quad (19)$$

An example of this power law dependence of the flux of the electrons bombarding the wall and desorbing H_2 molecules as a function of the the beam current is shown in Fig. 9. The behaviour of the electron flux $\dot{\Gamma}$ as a function of the beam current I_b displays a growth much faster than linear showing an avalanche effect, which has often been described in the literature as multipacting. The mechanism generating this drastic increase of electrons imping the wall with beam current is still not clear.

CONCLUSIONS AND OUTLOOK

A simple model of electron bombardment appears to be consistent with the beam heat load and pressure rise observed in the cold bore of the superconducting undulator installed at ANKA. A common cause of electron bombardment is the build-up of an electron cloud, which strongly depends on the chamber surface properties. The surface properties as secondary electron yield, photoemission yield, photoemission induced electron energy distribution, needed in the simulation codes to determine the eventual occurrence and size of an electron cloud build-up, have only partly been measured for a cryosorbed gas layer. Even using uncommonly large values for these parameters, the heat load inferred from the ECLOUD simulations [27] is about one order of magnitude lower than the measurements [28]. While electron cloud build-up models have been well bench marked in machines with positively charged beams, in electron machines they do not reproduce the observations satisfactory. This has been shown at the ECLOUD'10 workshop not only in our case, but also by K. Harkay [29] and by J. Calvi [31] comparing the RFA data taken with electron beams in the APS and in CesrTA, respectively, with the simulations performed using the electron cloud build-up codes POSINST [30] and ECLOUD [27]. From these comparisons it seems that the electron cloud build-up codes do not contain all the physics going on for electron beams. In order to fit the data with the simulations, the approach at APS and CesrTA is to change the photoelectron model. At ANKA we tried to study if the presence of a smooth ion background (i.e. a partially neutralized electron beam) can change the photoelectron dynamics so that the photo-electrons can receive a significant amount of kinetic energy from the ion cloud plus electron

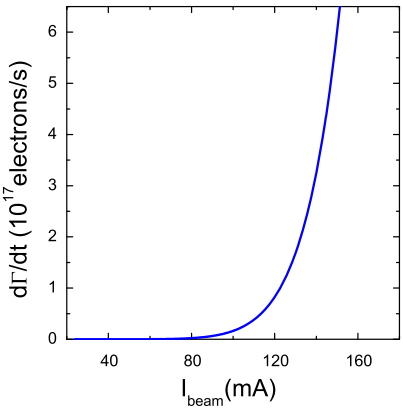

Figure 9: Flux of the electrons desorbing H_2 molecules from the surface a function of the beam current for a decay time $\tau_{el} = 9000$ s. The behaviour of the electron flux $\dot{\Gamma}$ as a function of the beam current I_b displays a growth much faster than linear showing an avalanche effect, which has often been described in the literature as multipacting.

beam system. Encouraged by preliminary analytical results by P. F. Tavares, S. Gerstl will try to fit our data at ANKA by including an ion cloud potential in the ECLOUD code.

We have shown that in order to reproduce the pressure measurements it is necessary to include electron stimulated desorption with a shorter decay time τ_{el} than the beam lifetime τ. This implies a very fast avalanche-like growth of the electron flux $\dot{\Gamma}$ as a function of beam current suggesting electron multipacting. Considering the simplified assumptions, for example, the gas made by H_2 only and the large measurements uncertainties the agreement between simulations and measurements is satisfying. A refinement of the model makes sense once more accurate and controlled measurements will be available with the planned cold vacuum chamber (COLDDIAG) to be installed in a storage ring, implemented with the following diagnostics: i) retarding field analyzers to measure the electron flux, ii) temperature sensors to measure the total heat load, iii) pressure gauges, iv) and mass spectrometers to measure the gas content [32].

ACKNOWLEDGEMENTS

The authors are greatful to Frank Zimmermann (CERN) for useful discussions in the initial phase of this project.

Pedro F. Tavares acknowledges financial support from the Brazilian Research Council - CNPq.

REFERENCES

[1] T. Hara, T. Tanaka, H. Kitamura, T. Bizen, X. Marchal, T. Seike, T. Kohda, and Y. Matsuura, *Phys. Rev. ST Accel. Beams* **7**, 050702 (2004).

[2] C. Kitegi, J. Chavanne, D. Cognie, P. Elleaume, F. Revol, C. Penel, B. Plan, M. Rossat, Proceedings of EPAC 2006, Edinburgh, Scotland 2006.

[3] T. Tanabe, D.A. Harder, G. Rakowsky, T. Shaftan and J. Skaritka, Proceedings of PAC07, Albuquerque, New Mexico, USA 2007.

[4] C. Benabderrahmane, N. Bchu, P. Berteaud, M.E. Couprie, J.M. Filhol, C. Herbeaux, C. Kitegi, J.L. Marlats, K. Tavakoli, A. Mary, Proceedings of EPAC08, Genoa, Italy 2008.

[5] J. Chavanne, M. Hahn, R. Kersevan, C. Kitegi, C. Penel, F. Revol, Proceedings of EPAC08, Genoa, Italy 2008.

[6] S. Casalbuoni, A. Grau, M. Hagelstein, R. Rossmanith, F. Zimmermann, B. Kostka, E. Mashkina, E. Steffens, A. Bernhard, D. Wollmann, and T. Baumbach, *Phys. Rev. ST Accel. Beams* **10**, 093202 (2007).

[7] http://ankaweb.fzk.de/

[8] S. Casalbuoni, M. Hagelstein, B. Kostka, R. Rossmanith, M. Weisser, E. Steffens, A. Bernhard, D. Wollmann, and T. Baumbach, *Phys. Rev. ST Accel. Beams* **9**, 010702 (2006).

[9] SHI Cryogenics Group, http://www.apdcryogenics.com

[10] N.A.Mezentsev, Proceedings of PAC05, Knoxville, Tennessee, USA 2005.

[11] E. Wallén, G. LeBlanc, *Cryogenics* **44**, 879 (2004).

[12] A. Kulikov, J. Seeman, S. Heifets, Proceedings of PAC 2001, Chicago, Illinois, USA 2001.

[13] R. Cimino, A. Drago, C. Vaccarezza, M. Zobov, G. Bellodi, D. Schulte, F. Zimmermann, G. Rumolo, K. Ohmi, M. Pivi, Proceedings of PAC05, Knoxville, Tennessee, USA 2005.

[14] S. Casalbuoni, M. Hagelstein, B. Kostka, R. Rossmanith, E. Steffens, M. Weisser , A. Bernhard, D. Wollmann, T. Baumbach, Proceedings of EPAC 2006, Edinburgh, Scotland 2006.

[15] The pressure values reported in this paper are measured at room temperature. The corresponding values at low temperature can be obtained applying the Knudsen relation $P(T) = (T[\mathrm{K}]/300\ \mathrm{K})^{1/2} P(300\ \mathrm{K})$.

[16] W.C. Turner, Proceedings of PAC 1993, Washington, D.C., USA 1993.

[17] I.R. Collins and O.B. Malyshev, LHC Project Report 274, 2001.

[18] S. Andersson, L. Wilzén, M. Persson, J. Harris, Phys. Rev. B **40**, 8146 (1989);
V.V. Anashin, G.E. Derevyankin, V.G. Dudnikov, O.B. Malyshev, V.N. Osipov, C.L. Foerster, F.M. Jacobsen, M.W. Ruckman, M. Strongin, R. Kersevan,I.L. Maslennikov, W.C. Turner, W.A. Landford, J. Vac. Sci. Techn. **12** (4), 1663 (1994).

[19] O. Gröbner, Proceedings of PAC 1997, Vancouver, Canada 1997.

[20] Conceptual design of the Superconducting super Collider, edited by J. D. Jackson, report No. SSC-SR-2020,1986.

[21] LHC design report, http://lhc.web.cern.ch/LHC/LHC-DesignReport.html

[22] V.V. Anashin, O.B. Malyshev, V.N. Osipov, I.L. Maslennikov and W.C. Turner, J. Vac. Sci. Techn. **12** (5), 2917 (1994).

[23] H. Tratnik, PhD thesis, Wien (2005).

[24] V. Baglin, B. Jenninger, LHC Project Report 721, 2004.

[25] V.V. Anashin, O.B. Malyshev, R. Calder, O. Gröbner, A. Mathewson, Vacuum **48** (7-9), 785 (1997).

[26] E. Wallén, J. Vac. Sci. Techn. **14** (5), 2916 (1996).

[27] G. Rumolo and F. Zimmermann, CERN SL-Note-2002-016.

[28] U. Iriso, S. Casalbuoni, G. Rumolo, F. Zimmermann, Proceedings of the 23^{rd} Particle Accelerator Physics Conference, Vancouver, Canada, 2009.

[29] K. Harkay, these proceedings.

[30] M.A. Furman and M.T. Pivi, Phys Rev ST Accel Beams 5, 124404 (2002).

[31] J. Calvi, these proceedings.

[32] S. Casalbuoni, T. Baumbach, S. Gerstl , A. Grau, M. Hagelstein, D. Saez de Jauregui, C. Boffo, G. Sikler, V. Baglin, R. Cimino, M. Commisso, B. Spataro, A. Mostacci, M. Cox, J. Schouten, E. Wallén, R. Weigel, J. Clarke, D. Scott, T. Bradshaw, I. Shinton, R. Jones, accepted for publication in IEEE Trans. on Appl. Superconductivity.

EMITTANCE GROWTH AND TUNE SPECTRA AT PETRA III

R. Wanzenberg*, DESY, Hamburg, Germany

Abstract

At DESY the PETRA ring has been converted into a synchrotron radiation facility, called PETRA III. 20 damping wigglers have been installed to achieve an emittance of 1 nm. The commissioning with beam started in April 2009 and user runs have been started in 2010. The design current is 100 mA and the bunch to bunch distance is 8 ns for one particular filling pattern with 960 bunches. At a current of about 50 mA a strong vertical emittance increase has been observed. During machine studies it was found that the emittance increase depends strongly on the bunch filling pattern. For the user operation a filling scheme has been found which mitigates the increase of the vertical emittance. In August 2010 PETRA III has been operated without damping wigglers for one week. The vertical emittance growth was not significantly smaller without wigglers. Furthermore tune spectra at PETRA III show characteristic lines which have been observed at other storage rings in the connection with electron clouds. Measurements at PETRA III are presented for different bunch filling patterns and with and without wiggler magnets.

INTRODUCTION

At DESY the PETRA ring has been converted into a synchrotron radiation facility, called PETRA III [1]. Originally, PETRA was built in 1976 as an electron and positron collider which was operated from 1978 to 1986 in the collider mode. From 1988 until 2007 PETRA was used as a preaccelerator for the HERA lepton hadron collider ring. Positron and electron currents of about 50 mA were injected at an energy of 7 GeV and accelerated to the HERA injection energy of 12 GeV. During the conversion to a synchrotron radiation facility from 2007 to 2008 one octant of the PETRA ring has been completely redesigned to provide space for 14 undulators. The new experimental hall is shown in Fig. 1. The commissioning with beam started in April 2009 and user runs have been started in 2010 [2]. PETRA III is presently running in a top up operation mode with *positrons* since PETRA III is sharing the same preaccelrator chain with the synchrotron source DORIS, which is running with positrons to avoid problems with ionized dust particles.

The new facility aims for a very high brilliance of about 10^{21} photons/s/0.1%BW/mm^2/mrad^2 using a low emittance (1 nm rad) positron beam with an energy of 6 GeV. The very low emittance of 1 nm rad has been achieved with the help of 20 damping wigglers with a length of 4 m each

Figure 1: Aerial view of the new experimental hall of PETRA III which was build from 2007 to 2008.

and a peak magnetic field of 1.5 T and a period length of 0.2 m [3].

Beam parameters

A summary of the PETRA III design parameters can be found in Table 1 [1].

Table 1: PETRA III design parameters

Parameter	PETRA III	
Energy /GeV	6	
Circumference /m	2304.0	
Revolution frequency /kHz	130.1	
harmonic number	3840	
RF frequency /MHz	500	
Total current /mA	100	
Bunch Population $N_0/10^{10}$	0.5	12.0
Number of bunches	960	40
Total current /mA	100	100
Bunch separation Δt /ns	8	192
Emittance ϵ_x/nm	1	
ϵ_y/nm	0.01	
Bunch length /mm	12	
Tune Q_x	36.13	
Q_y	30.29	
Q_s	0.049	
Momentum compaction /10^{-3}	1.2	

The design current of 100 mA has been achieved but with a different filling scheme than originally foreseen

* rainer.wanzenberg@desy.de

since a vertical emittance blow-up has been observed for a filling scheme with equidistantly spaced bunches with a bunch to bunch spacing of 8 ns and 16 ns. The emittance blow-up occurred at a total beam current of about 50 mA. Related to the emittance blow-up are additional lines in the tune spectra of the individual bunches. Before the experimental results are discussed the beam current limitation due to coupled bunch instabilities and their cure with powerful multibunch feedback systems are shortly reported in the next subsection.

Beam Instabilities and Feedback Systems

The main reason for beam current limitation due to coupled bunch instabilities is the large parasitic shunt impedance of the seven cell 500 MHz cavities. The measured threshold currents, instability rise times and effective impedances are summarized in Table 2 for PETRA II[1, 4]. PETRA III has almost the same parasitic shunt impedance as PETRA II since presently 12 seven cell 500 MHz cavities are used for PETRA III while in PETRA II 16 cavities of that type were installed. Powerful longitudinal

Table 2: Coupled bunch instabilities

PETRA II	Longt.	Horiz.	Vert.
$I_{\rm thres}$ / mA	7	6	6
$1/\tau$ / Hz	35	50	60
$Z_{\rm eff}$	3.6 MΩ	45 MΩ/m	54 MΩ/m

and transverse feedback systems with a bandwidth larger than 60 MHz have been installed in PETRA III to damp the bunch oscillations due to coupled bunch instabilities. A schematic layout of the feedback system is shown in Fig. 2, see also Ref. [5]. In a lowest order approximation the beam

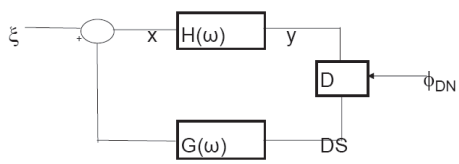

Figure 2: Schematic layout of the PETRA III feedback system [5]: The beam dynamics is described by $H(\omega)$ and the feedback effect by $G(\omega)$ acting on external disturbances of the beam ξ. Φ_{DN} is the noise associated with the feedback detector D.

transfer function $H(\omega) = 1/({\omega_0}^2 - \omega^2)$ may be considered as a harmonic oscillator with a resonant frequency at the tune frequency ω_0 and the effect of feedback is modeled with the function $G(\omega) = i\,\omega\,\Gamma$ with a damping coefficient Γ. The signal from the feedback detector (marked as DS in Fig. 2) is [5]:

$$DS(\omega) = \frac{1}{{\omega_0}^2 - \omega^2 + i\,\omega\,\Gamma}\,\xi + \frac{{\omega_0}^2 - \omega^2}{{\omega_0}^2 - \omega^2 + i\,\omega\,\Gamma}\,\phi_{DN}, \quad (1)$$

where ϕ_{DN} is the detector noise. The detector noise ϕ_{DN} is not transmitted at the tune $\omega = \omega_0$ (see Eqn. 1). Therefore one observes a notch in the tune spectrum at the betatron tune, see Fig. 3. The tune spectra in Fig. 3 were

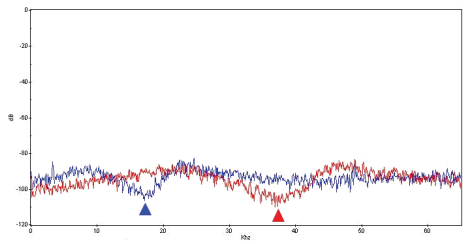

Figure 3: Horizontal (blue line) and vertical (red line) tune spectra of one bunch (#1) in PETRA III. The betatron tunes appear as notches, indicated with arrows in the plot.

recorded for bunch #1 of 40 bunches with a total current of 55 mA, corresponding to a bunch population of $6.6\,10^{10}$ positrons per bunch and a bunch to bunch spacing of 192 ns. This situation may be regarded as a reference where no unusual spectra lines have been observed and the coupled bunch instabilities are well damped with the multibunch feedback system.

MEASUREMENTS

The commissioning of PETRA III [2] with beam started in April 2009 (first stored beam on April 13, 2009). The damping wigglers have been installed on a step by step basis from May 20 to June 25, 2009. After the installation of the damping wigglers the horizontal design emittance of 1 nm has been achieved and the vertical emittance has been $\sim 2\%$ of the horz. emittance. At a diagnostic beam line the horizontal and vertical spot size of the synchrotron light of a bending magnet is analyzed [6]. For some filling schemes a mainly vertical emittance blow-up was observed, correlated with additional lines (sidebands) in the tune spectra. The threshold current of this kind of instability was found to be about 50 mA. Systematic studies of the effect started in May 2010. A filling scheme with 60 short bunch trains with 4 bunches per train was found which avoids any emittance blow-up at the design beam current of 100 mA and is used for user operation.

The main results of the studies with different filling schemes are summarized in this section of this report. The measured tune spectra showed some characteristics which have been observed at other storage rings in connection with electron cloud effects [7, 8, 9]. A unique attribute of the synchrotron light source PETRA III is the large number of damping wigglers (total length 80 m). From Aug. 2 to Aug. 7 PETRA III has been again operated without damping wigglers. It was found that the damping wigglers have no significant influence on the observed emittance growth. In the following subsections the details of the findings are presented.

Studies in May and June 2010

In May 2010 a strong vertical emittance blow-up was observed when a long bunch train of 640 bunches with a bunch-to-bunch distance of 8 ns was stored. The synchrotron light spot at the diagnostic beam line is shown in Fig. 4. This measurement is an average of the beam size of all 640 bunches. There is a strong indication that

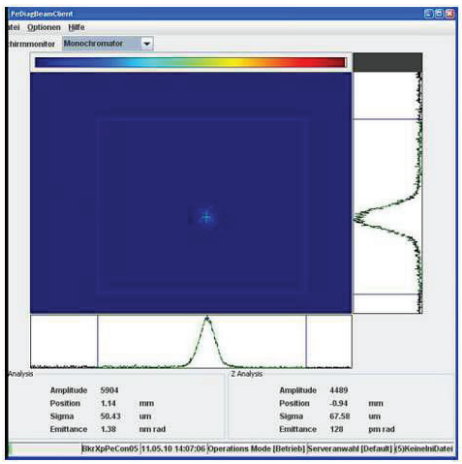

Figure 4: Synchrotron light spot at the diagnostic beam line (May 11, 2010). A significant vertical emittance growth was observed (about a factor 3.5). The total beam current was 65 mA

the large synchrotron light spot results from a single bunch emittance growth and not from a bunch centroid oscillation since the beam life time was growing with beam intensity probably due to a reduced Touschek effect. The emittance growth is correlated with the observation of an extra line (like an upper sideband) in the bunch tune spectrum, which is measured for all individual bunches via the multibunch feedback system. The tune spectrum of bunch #275 is shown in Fig. 5. The notch in the vertical betatron spectrum (red line) indicates the tune (about 39 kHz) and an extra line is clearly seen at a frequency of about 47 kHz. A similar line is observed in the horizontal tune spectrum (blue line) which even seems to be coupled into the vertical plane. The vertical and horizontal tune spectra of a all 640 bunches are shown in Fig. 6 and Fig. 7 using a color code for the spectrum of each bunch. The data are obtained from the multibunch feedback system. The vertical tune is the notch in the tune spectra at about 39 kHz which is not changing along the bunch train, at least within the resolution of the plot.

During the studies in May 2010 a filling scheme with 10 bunch trains of 29 bunches with a bunch to bunch spacing of 8 ns was tried. The filling scheme is shown in Fig. 8. The gap between the bunch trains was larger than 500 ns. Again a vertical emittance growth was observed at a threshold current at about 50 mA. Furthermore additional lines in the tune spectra of the individual bunches were observed, see Fig. 9. The additional line grows in the spectral region

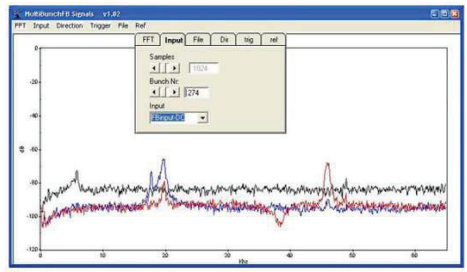

Figure 5: Tune spectrum of bunch #275. The synchrotron tune spectrum (black line) and the betatron tune spectra (horz. blue line, vert. red line) are show.

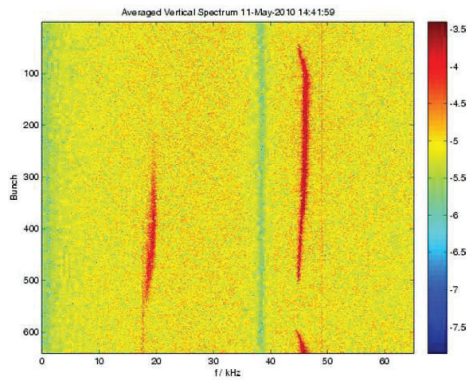

Figure 6: Measured vertical tune spectra of all 640 bunches (May 11, 2010). The total beam current was 62 mA.

of the notch in the spectrum and forms finally a kind of ”upper sideband” of the tune.

Further tests have been done with a bunch train of 200 bunches with a bunch to bunch spacing of 16 ns and a few additional witness bunches behind the bunch train. The goal was to find the minimal distance between a witness bunch and the end of the bunch train at which no addi-

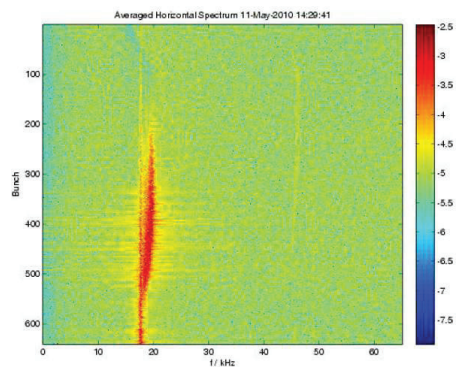

Figure 7: Measured horizontal tune spectra of all 640 bunches (May 11, 2010). The total beam current was 62 mA.

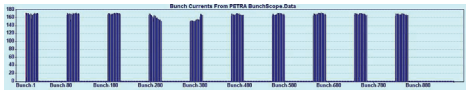

Figure 8: Filling scheme with 10 bunch trains of 29 bunches (May 25, 2010). The bunch to bunch spacing is 8 ns.

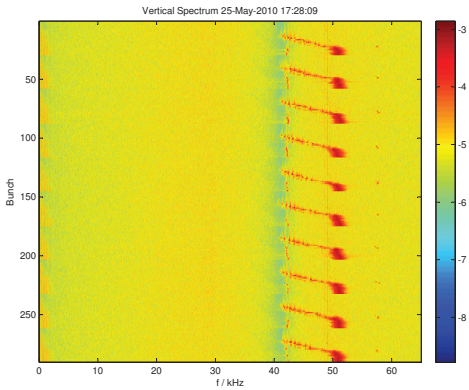

Figure 9: Measured vertical tune spectra of all 10×29 bunches (May 25, 2010). The total beam current was 67 mA.

tional line in the tune spectrum of the witness bunch was observed. It was assumed that the emittance of the witness bunch would not grow since the observed emittance growth was always correlated with additional lines in the tune spectrum. The vertical tune spectra of the 200 bunches are shown in Fig. 10. No additional lines in the spectrum of the witness bunch (not shown in Fig. 10) were observed when the gap between the end of the bunch train and the witness bunch was at least 72 ns or 96 ns (two measurements in May and June 2010).

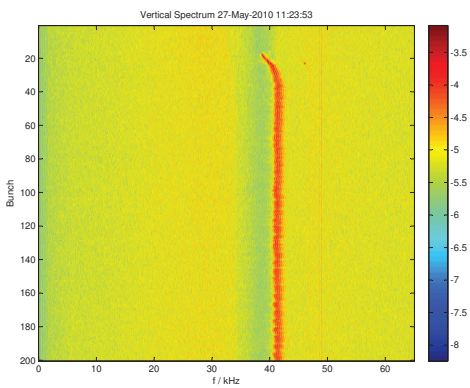

Figure 10: Measured vertical tune spectra of all 200 bunches (May 27, 2010). The total beam current was 47 mA and the bunch to bunch spacing 16 ns.

Based on the measurements with the witness bunches and the observed tune spectra three filling schemes with short bunch trains with only 4 bunches were set-up. The filling patterns are shown in Fig. 11. All schemes use a bunch to bunch distance of 16 ns between the bunches in a train. The number of bunch trains and therefore the gap between the bunch trains differ. The first scheme uses 40 bunch trains with a distance of 144 ns between the bunch trains. The second scheme uses more trains (60) and a distance of 80 ns between the trains. Finally a third scheme with 80 bunch trains and distance of only 48 ns has been used. In May and June 2010 the first scheme was successfully used for user runs with a total bunch current of up-to 70 mA and no vertical emittance blow-up. At the beginning of August a total bunch current of almost 100 mA has been reached with this 60 × 4 filling scheme. The second filling scheme was regularly used for user runs since September 2010 also without any emittance blow-up and a total bunch current of 100 mA. In May a small emittance growth was observed with this scheme indicating that there was some improvement of the situation. The third scheme always showed a significant emittance blow-up and was never used for user runs. A vertical emittance growth has also been ob-

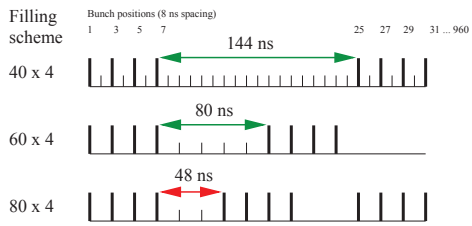

Figure 11: Bunch filling schemes with short bunch trains with 4 bunches and a bunch to bunch spacing of 16 ns.

served when PETRA III was operated with a small number of bunches with a large bunch to bunch spacing. But for these filling schemes it was possible to cure the emittance growth with an increase of the chromaticity from 0.5, the standard setting, to at least a value of 4 and a larger vertical feedback gain. Furthermore a lower sideband instead of a upper sideband was observed in the tune spectra of the bunches. The measured vertical tune spectra of 70 bunches are shown in Fig. 12. PETRA III was operated with one bunch train of 70 bunches with a bunch to bunch spacing of 96 ns between bunches and a gap of 1056 ns at the end of the bunch train. The threshold current for the emittance growth was again about 50 mA when the chromaticity was small (0.5). An increase of the chromaticity helped only for filling schemes with a small number of bunches and a bunch to bunch spacing of at least 96 ns. A larger chromaticity did not help for the filling schemes with a bunch to bunch spacing of 8 ns of 16 ns.

Studies in August 2010 without wigglers

From Aug 2 to Aug 7, 2010 PETRA III was operated with all wigglers moved into the parking position and therefore with an (horz.) emittance of 4.5 nm instead of 1 nm and no magnetic field in the 80 m long wiggler vacuum

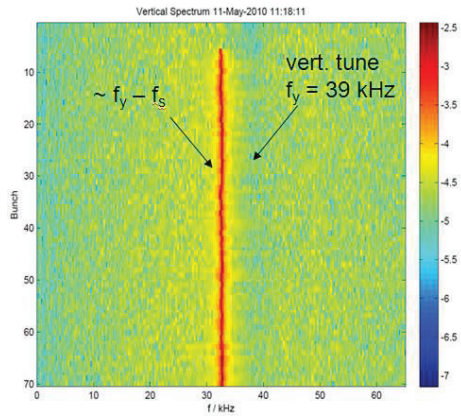

Figure 12: Measured vertical tune spectra of 70 bunches (May 11, 2010). The spacing between the bunches was 96 ns and the total beam current was 55 mA.

chambers. Nevertheless a vertical emittance growth was again observed for several filling schemes at a threshold current of about 50 mA. Additional lines in the tune spectra were also observed.

The vertical tune spectra of a filling scheme with 10 bunch trains of 29 bunches with a bunch to bunch spacing of 8 ns within a train is shown in Fig. 13. The observed spectra are similar to the spectra which have been measured on May 25, see Fig. 9, although some additional lines in the tune spectra were more prominent in May than in the measurements from Aug 5, 2010. The vertical tune spectra of

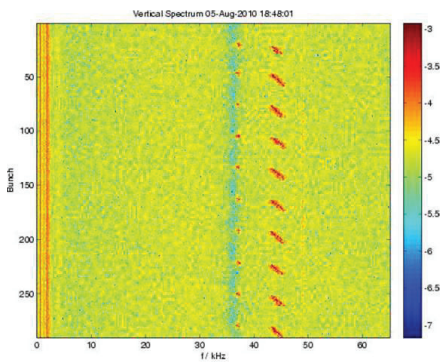

Figure 13: Measured vertical tune spectra of all 10×29 bunches (Aug 5, 2010). The total beam current was 51 mA.

a filling scheme with one bunch train of 200 bunches and a bunch to bunch spacing of 16 ns are shown in Fig. 14. The corresponding measurement with wigglers is shown in Fig. 10. Again several similarities between the spectra from May and from Aug. 5, 2010 are clearly visible. The tune spectra of the first 100 bunches from the two filling schemes of Fig. 13 and Fig. 14 are presented with a different color scheme and in a 3D-plot in Fig. 15 and Fig. 16. In both plots it is visible that an additional line grows in the spectral region of the notch to form finally some type

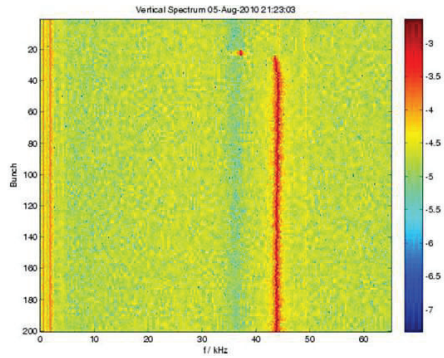

Figure 14: Measured vertical tune spectra of all 200 bunches (Aug 5, 2010). The total beam current was 47 mA and the bunch to bunch spacing 16 ns.

of upper sideband to the tune.

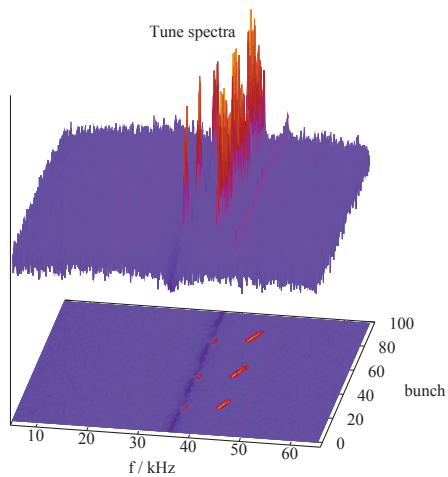

Figure 15: Measured vertical tune spectra of the first 100 bunches of a filling scheme with 10 × 29 bunches (Aug 5, 2010). The total beam current was 51 mA and the bunch to bunch spacing 8 ns.

Studies in August and September 2010

After Aug 7, 2010 all wiggler magnets were placed back into the standard operation position in PETRA III. Further studies have been performed investigating the three filling schemes which are shown in Fig. 11. There was no vertical emittance growth observed for the schemes with 40×4 and 60×4 bunches but there was an emittance growth for the scheme with 80×4 bunches. In Fig. 17 the vertical tune spectra are shown for a filling scheme with 80 trains of 4 bunches. Again some additional lines above the vertical tune notch are visible in the spectra.

In September a similar filling scheme with a gap was used. In Fig. 18 the bunch pattern is shown. In total 40

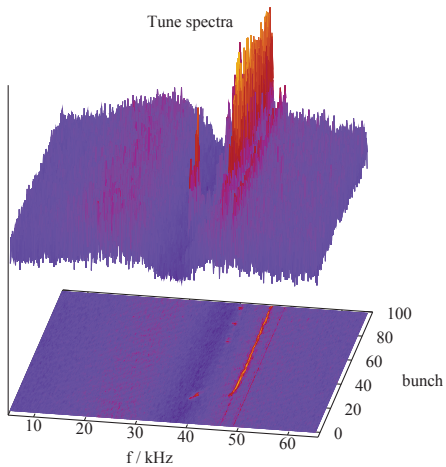

Figure 16: Measured vertical tune spectra of the first 100 bunches of a filling scheme with 200 bunches (Aug 5, 2010). The total beam current was 47 mA and the bunch to bunch spacing 16 ns.

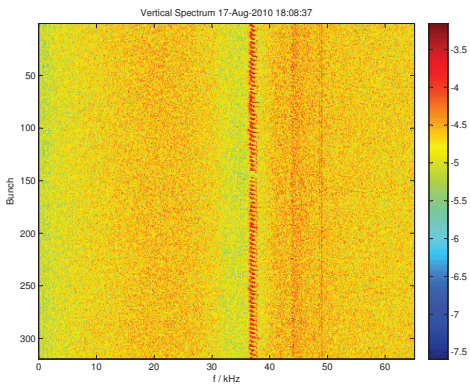

Figure 17: Measured vertical tune spectra of all 80×4 bunches (Aug 17, 2010). The total beam current was 75 mA.

bunch trains of 4 bunches were used with a bunch to bunch spacing of 16 ns. The spacing between the bunch trains was 48 ns. At the end of the bunch trains there was a long gap corresponding to half the circumferences of the PETRA III ring. Also for this filling scheme a vertical emittance

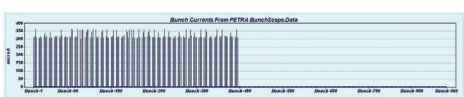

Figure 18: Filling scheme with 40 bunch trains of 4 bunches (Sep 15, 2010). The bunch to bunch spacing was 16 ns and the spacing between the bunch train was 48 ns

growth was observed which was again correlated with additional lines in the tune spectra. The tune spectra are shown in Fig. 19 for all bunches. The spectra of the first bunch trains did not show the additional lines in the tune spectra. But after about 7 bunch trains (or 28 bunches) the additional lines are visible.

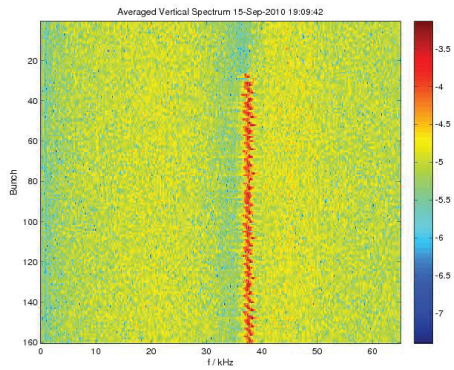

Figure 19: Measured vertical tune spectra of all 40×4 bunches (Sep 15, 2010). The spacing between the short bunch trains was 48 ns The total beam current was 50 mA.

SIMULATIONS

In positron storage rings electrons produced by photoemission and secondary emission form an electron cloud with a charge density which depends on the filling scheme [8, 9]. From the charge density of the electron cloud a broad band impedance model [10] can be obtained which can be compared with the observed threshold currents for the vertical emittance growth at PETRA III and can help to interpret the measurements which are summarized in the previous sections of this report.

Simulation of the build-up of an electron cloud

In 2003 the first simulation for the build-up of electron clouds for PETRA III were done with the computer code ECLOUD 2.3 [11, 12, 13, 14]. More recent simulations of the build-up of an electron cloud in dipole vacuum chambers have been made with the new version 4.0. The vacuum chamber in the dipole magnets is basically an ellipse with a width of 80 mm and a height of 40 mm, see Fig. 20, and is made from aluminum [15, 16]. As an integrated vacuum pump a NEG strip is integrated in an ante chamber, which is placed inside the ring. Synchrotron radiation hits the outer side of the vacuum chamber which is water cooled . For all simulations a primary photo electron emission of 0.065 electrons per meter and positron has been used which is based on a bending radius of about 192 m of the PETRA III dipole magnets (in seven octants without insertion devices) and an assumed effective photo-electron yield of 10 %, see also Ref. [13].

Simulation results for the design parameters of Table 1 (960 bunches) are presented in Fig. 21 and Fig. 22 using $\delta_{max} = 2.5$ for the maximum of the secondary emission

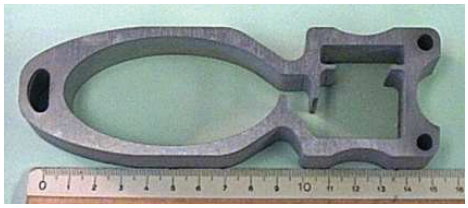

Figure 20: Cut through the vacuum chamber in the PETRA III dipole magnets. The dimension of the ellipse are 80 × 40 mm.

yield (SEY) at an energy of 300 eV of the primary electron. For these parameters one obtains a center density (ρ_c) of about $1.5 \cdot 10^{12}\,\mathrm{m}^{-3}$ which is a factor 1.8 larger than the average beam charge volume density of

$$\langle \rho_b \rangle = \frac{N}{c\,\Delta t\,A} = 0.83 \cdot 10^{12}\,\mathrm{m}^{-3}, \qquad (2)$$

where N is the positron bunch population, Δt the bunch spacing and A the area of the cross section of the vacuum chamber ($A = \pi \times 20\,\mathrm{mm} \times 40\,\mathrm{mm}$). Simulations with version 2.3 of the ECLOUD code gave a center density of about $1.0 \cdot 10^{12}\,\mathrm{m}^{-3}$ [13], which is closer to the result $\langle \rho_b \rangle \approx \langle \rho_c \rangle$ expected from the condition of neutrality for average charge densities of the cloud and the beam.

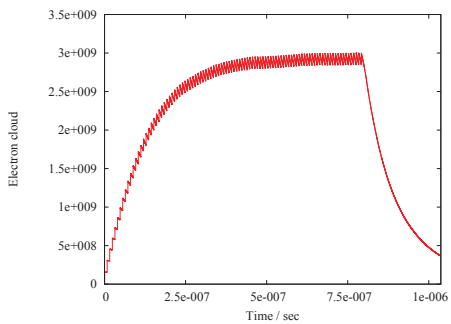

Figure 21: Simulation of electron cloud build-up for a bunch train with a bunch to bunch spacing of 8 ns and bunch population of $0.5 \cdot 10^{10}$ (SEY: $\delta_{max} = 2.5$)

The center density can be translated into a tune shift [17] of

$$\Delta Q = \frac{1}{2}\frac{C}{\gamma}\, r_e\, \langle \beta \rangle\, \langle \rho_c \rangle, \qquad (3)$$

where C is the circumference of the ring, γ the relativistic γ-factor, r_e the classical electron radius and $\langle \beta \rangle$ the average betatron function. For PETRA III one obtains for the vertical betatron frequency:

$$\Delta f_y = 0.54\,\mathrm{kHz}\,10^{-12}\,\mathrm{m}^3 \langle \rho_c \rangle. \qquad (4)$$

A center density of $1.5 \cdot 10^{12}\,\mathrm{m}^{-3}$ will therefore give a tune shift of 0.81 kHz.

Further simulations have been done for the filling schemes with 60×4 and 80×4 bunches from Fig. 11

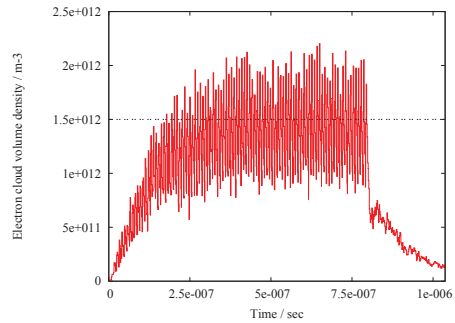

Figure 22: Center density of the electron cloud build-up for a bunch train with a bunch to bunch spacing of 8 ns and bunch population of $0.5 \cdot 10^{10}$ (SEY: $\delta_{max} = 2.5$)

since for the 60×4 filling scheme no emittance blow-up was observed while the bunches from the 80×4 filling scheme clearly showed an increase of the emittance. The results for these filling schemes are presented in Fig. 23 and Fig. 24. In both cases a total bunch current of 50 mA have been assumed resulting in bunch population of $1.0 \cdot 10^{10}$ and $0.75 \cdot 10^{10}$ positrons per bunch. This total current was just the threshold current for the observed emittance growth for the 80×4 filling scheme. The bunch to bunch spacing between the four bunches of one train was 16 ns while the distance between the bunch trains was 80 ns and 48 ns as shown in Fig. 11. The simulation did not show any significant difference between the center density for the two schemes which could explain the observed results. In both cases the center density was about $1.0 \cdot 10^{12}\,\mathrm{m}^{-3}$.

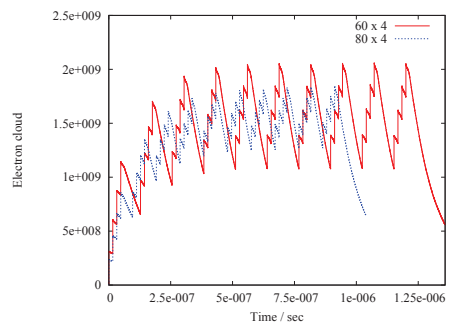

Figure 23: Simulation of electron cloud build-up for a 60x4 and 80x4 bunch filling and bunch population of $1.0 \cdot 10^{10}$ and $0.75 \cdot 10^{10}$ (SEY: $\delta_{max} = 2.5$)

Electron cloud threshold density

The simulated electron cloud densities can be compared with the threshold density $\rho_{e,th}$ for an instability which are obtained from an approach by K. Ohmi [18] which is based on a combination of a broad band resonator model for the impedance [10] and a coasting beam model for the insta-

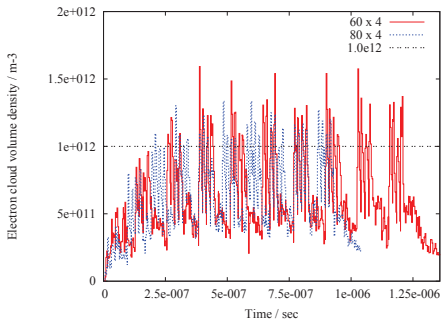

Figure 24: Center density of the electron cloud build-up for a 60x4 and 80x4 bunch filling and bunch population of $1.0 \cdot 10^{10}$ and $0.75 \cdot 10^{10}$ (SEY: $\delta_{max} = 2.5$)

bility:

$$\rho_{e,th} = \frac{2\,\gamma\,Q_s\,\omega_{e,y}\,\sigma_z/c}{K\,Q_{res}\,\sqrt{3}\,r_e\,\langle\beta_y\rangle\,C}, \qquad (5)$$

where Q_s is the synchrotron tune, $Q_{res} \approx 5$ is the Q-value of the broad band impedance model, K is a factor to take into account the pinch effect and $\omega_{e,y}$ is the oscillation frequency of the electrons in the bunch potential. All other parameters have the same meaning as in Eqn. 3. For the design parameters of PETRA III (960 bunch operation mode) one obtains the following threshold densities (see Table 3):

Table 3: PETRA III threshold density

PETRA III	$K = 1$	$K = \omega_{e,y}\,\sigma_z/c$
$\rho_{e,th}$	$8.9 \cdot 10^{12}\,\mathrm{m}^{-3}$	$1.4 \cdot 10^{12}\,\mathrm{m}^{-3}$

Table 3 summarizes the threshold density for two values of the parameter K. According to Ref. [18] a parameter K about $\omega_{e,y}\,\sigma_z/c$ is usually a good approximation. For $K = \omega_{e,y}\,\sigma_z/c = 6.4$ the threshold density of $1.4 \cdot 10^{12}\,\mathrm{m}^{-3}$ is just a bit smaller than the electron cloud density obtained from the simulations with version 4.0 of the computer code ECLOUD (see Fig. 22). This indicates that the observed emittance growth for the filling scheme with 640 bunches, observed in May 2010, is due to an instability driven by an electron cloud. But from simulations for the filling schemes with 60×4 and 80×4 bunches one obtains an electron cloud density which is below the threshold density while the measurements show an emittance growth for the filling scheme with 80×4 bunches.

CONCLUSION

At PETRA III a strong vertical emittance increase has been observed which depends strongly on the bunch filling pattern. The measured tune spectra showed some characteristics (see Fig. 6 and Fig. 7) which have been observed at other storage rings in connection with electron cloud effects. In seven octants of PETRA III the vacuum chambers in the dipole magnets are made from aluminum which has initially ('as received') a maximum secondary emission yield of about 3 which goes done to 1.5 after intense scrubbing of the surface [19]. The simulated electron density for the PETRA III design parameters in the 960 bunch operation mode is just above the threshold density according the model from Ref. [18] when the results from version 4.0 of the ECLOUD code and a K equal to $\omega_{e,y}\,\sigma_z/c$ are used. These facts indicate that the observed vertical emittance increase in PETRA III could be due to an electron cloud driven instability.

But there are several observations which do not fit well with the results obtained from simulations of electron clouds. One would expect that the frequency of the notch in the tune spectra would depend on the bunch number along the bunch train according to Eqn. 3 for the tune shift. This was not observed, but an additional line in the spectra was found to grow in the region of the notch, finally forming a type of upper sideband. The location of the line saturates after about 25 bunches (see Fig.9) while the electron cloud density saturates after about 50 bunches (see Fig.21). No emittance growth has been observed for the filling schemes with 60×4 bunches while there was a significant emittance growth for the filling scheme with 80×4 bunches. These observations could not be explained with the simulation results for these filling schemes. It is very unlikely that the emittance growth for the filling scheme with 70 bunches is related to electron cloud effects since the bunch spacing is 96 ns. It is not yet understood whether and how the multibunch feedback system is also acting on the single bunch in a way which influences the single bunch emittance.

For the user operation with design current of 100 mA a filling scheme with 60×4 bunches was found which avoids any emittance growth. Nevertheless further studies using TE-wave transmission measurements, using the techniques from [20] are planned to obtain a better understanding of the observations.

ACKNOWLEDGMENTS

I would like to thank J. Crittenden for discussions and his electron cloud simulations for PETRA III. Thanks go also to R. Cimino for the measurement of the secondary electron yield of Aluminum samples from the PETRA III vacuum chamber. Further thanks go to my colleagues from DESY: K. Balewski, M. Bieler, J. Keil, A. Kling, G.K. Sahoo who provided valuable data and facts for my talk and the report. Last but not least I would like to thank M. Lomperski for carefully reading the manuscript.

REFERENCES

[1] Editors: K. Balewski, W. Brefeld, W. Decking, H. Franz, R. Röhlsberger, E. Weckert, "PETRA III: A low Emittance Synchrotron Radiation Source", DESY 2004-035, February 2004.

[2] K. Balewski, "Commissioning of Petra III," Proceedings of

1st International Particle Accelerator Conference: IPAC'10, Kyoto, Japan, 23-28 May 2010.

[3] M. Tischer *et al.*, "Damping Wigglers at the PETRA III Light Source," Proceedings of 11th European Particle Accelerator Conference (EPAC 08), Magazzini del Cotone, Genoa, Italy, 23-27 Jun 2008.

[4] K. Balewski and R. Wanzenberg, "Beam current limitations in the synchrotron light source PETRA III," Proceedings of 9th European Particle Accelerator Conference (EPAC 2004), Lucerne, Switzerland, 5-9 Jul 2004.

[5] K. Balewski *et al.*, "Commissioning Results of Beam Diagnostics for the PETRA III Light Source", Proceedings DIPAC'09, Basel, Switzerland, May 2009

[6] G. Kube *et al.*, "Petra III Diagnostics Beamline for Emittance Measurements," Proceedings of 1st International Particle Accelerator Conference: IPAC'10, Kyoto, Japan, 23-28 May 2010.

[7] K. Cornelis, "The electron cloud instability in the SPS," Mini Workshop on Electron Cloud Simulations for Proton and Positron Beams (ECLOUD'02), Geneva, Switzerland, 15-18 Apr 2002.

[8] K. Ohmi, "Beam and photoelectron interactions in positron storage rings", Phys. Rev. Lett. **75** (1995) 1526.

[9] F. Zimmermann, "The electron cloud instability: Summary of measurements and understanding," Proceedings of IEEE Particle Accelerator Conference (PAC 2001), Chicago, Illinois, 18-22 Jun 2001, pp 666-670.

[10] K. Ohmi, F. Zimmermann, E. Perevedentsev, "Wake-Field And Fast Head - Tail Instability Caused By An Electron Cloud", Phys. Rev. E **65** (2002) 016502.

[11] G. Rumolo and F. Zimmermann, "Electron-cloud simulations: Buildup and related effects," Mini Workshop on Electron Cloud Simulations for Proton and Positron Beams (ECLOUD'02), Geneva, Switzerland, 15-18 Apr 2002.

[12] G. Rumolo and F. Zimmermann, "Practical User Guide for ECLOUD", CERN-SL-Note-2002-016, CERN, Geneva, Switzerland, 2002.

[13] R. Wanzenberg, "Prediction of Electron Cloud Effects in the Synchrotron Light Source PETRA III", Internal Report, DESY M 03-02, Dec. 2003.

[14] R. Wanzenberg, "Prediction of Electron Cloud Effects in the Synchrotron Light Source PETRA III", Proceedings ECLOUD'04, Napa, April 2004, CERN-2005-001, p. 169 (2005).

[15] M. Seidel, R. Böspflug, J. Boster, W. Giesske, U. Naujoks and M. Schwartz, "The vacuum system for PETRA III," Proceedings of Particle Accelerator Conference (PAC 05), Knoxville, Tennessee, 16-20 May 2005, pp 2473.

[16] R. Böspflug *et al.*, "Vacuum system design of the third generation synchrotron radiation source PETRA III," J. Phys.: Conf. Ser. **100** 092012, 2008

[17] K. Ohmi, S. Heifets and F. Zimmermann, "Study of coherent tune shift caused by electron cloud in positron storage rings," Proceedings of 2nd Asian Particle Accelerator Conference (APAC '01), Beijing, China, 17-21 Sep 2001.

[18] K. Ohmi, "Electron cloud effect in damping rings of linear colliders," 31st ICFA Beam Dynamics Workshop on Electron Cloud Effects (ECLOUD04), Napa, California, 19-23 Apr 2004

[19] R. Cimino, "private communication", LNF-INFN, Frascati, Italy, 2010

[20] S. De Santis, J. M. Byrd, F. Caspers, A. Krasnykh, T. Kroyer, M. T. F. Pivi and K. G. Sonnad, "Measurement of Electron Clouds in Large Accelerators by Microwave Dispersion," Phys. Rev. Lett. **100** (2008) 094801.

CESR-TA PROGRAM OVERVIEW*

D. Rubin, Cornell University, Ithaca, NY 14850, USA

Abstract

The Cornell Electron/Positron Storage Ring has been configured as a damping ring test accelerator. The principle objective of the CesrTA program is to investigate electron cloud physics in the ultra-low emittance regime characteristic of a linear collider positron damping ring. The storage ring is equipped with 12 superferric damping wigglers to increase the radiation damping rate and decrease the emittance. At a beam energy of 2GeV, the 1.9T wigglers increase the damping rate by an order of magnitude and decrease the emittance by a factor of 5 to 2.6nm. Instrumentation to measure, and techniques to minimize sources of transverse coupling and vertical dispersion routinely yield sub 10pm vertical emittance. More than two dozen multi-channel retarding field analyzers have been installed throughout the magnetic guide field in order to characterize cloud buildup. Shielded button pickups have been deployed to measure cloud decay and energy spectra. Techniques to measure electron cloud induced tune shift, instability, and emittance dilution have been developed. We are building and extending simulations of electron cloud phenomena in order to interpret the measurements and to establish the predictive power of the models. We give an overview of the CesrTA ring parameters, the diagnostic instrumentation for low emittance tuning and electron cloud studies. Details will appear in the references to other articles in this proceedings.

CESRTA PROGRAM OBJECTIVES

The damping ring is the source of low emittance bunches of positrons for the international linear collider. The damping ring is required to store the full complement of bunches that will be delivered to the collision point in each linac cycle. The circumference of the damping ring is determined by the spacing of the bunches in the ring. And the spacing is limited by electron cloud effects. CesrTA aims to measure the development of the electron cloud and the dependence of that development on bunch spacing and bunch charge, on local magnetic field, and on the chemistry and geometry of vacuum chambers. Retarding field analyzers are used to measure the time averaged density of the electron cloud. Shielded button pickups yield a measure of the growth and then decay time of the cloud. In addition, we measure the effect of the electron cloud on the beam. We observe cloud induced tune shift, emittance growth, and head tail instability.

Measurements of the sensitivity of the beam-cloud dynamics to the beam size require that we achieve ultra-low vertical emittance, as near to that of the linear collider damping ring as possible. Beam based instrumentation and techniques for identifying and then compensation of sources of vertical dispersion and transverse coupling have been developed. An xray beam size monitor yields bunch by bunch and turn by turn measurement of vertical beam heights of order 10 microns with a few micron precision.

Vacuum chamber materials are characterized in terms of secondary (electron) emission yield (SEY). Knowledge of SEY is essential to predictions of electron cloud growth and equilibrium electron density. At CesrTA we have implemented an in situ SEY measuring device that provides a means of determining the secondary yield of sample materials at various stages of beam processing with no intermediate exposure to atmosphere.

CESRTA LAYOUT AND OPTICS

The Cornell Electron Storage Ring (CESR) layout is based on simple FODO optics. There are two diametrically opposed straights in which low beta insertions focused colliding beams of electrons and positrons. Superconducting damping wigglers, located in the machine arcs, served to reduce the radiation damping rate in low energy (2GeV/beam) operation from 500ms to 50ms, and to increase the horizontal emittance to order 100nm. The decreased damping time and increased emittance were necessary in order to maintain a high beam-beam current limit and to maximize luminosity. At the conclusion of the colliding beam program, the guide field optics were modified for low emittance operation as a damping ring test accelerator. The low beta optics were removed. Half of the damping wigglers were moved to one of the former low beta straights. The opposite straight was instrumented for measuring electron cloud effects.

The storage ring lattice is reconfigured with zero horizontal dispersion in all of the damping wiggler straights. The effect of the wigglers is to decrease the damping time as before, but to decrease horizontal emittance as well. At 2GeV, with the 12, 1.3m long damping wigglers operating at 1.9T, we achieve horizontal emittance of 2.6nm. Because the CESR quadrupoles and sextupoles are all independently powered, there is extraordinary flexibility of the lattice. As required by the experimental program we operate the storage ring over the energy range of 1.8-5.3GeV, with from zero to 12 damping wigglers, and with integer part of the betatron tune ranging from 10 to 14 with corresponding range of emittances, momentum compaction and bunch length. Parameters of a few of the many CesrTA

* Work supported by the National Science Foundation and by the US Department of Energy under contract numbers PHY-0734867 and DE-FC02-08ER41538.

Table 1: CesrTA Lattice Parameters

Energy[GeV]	2.085	4.0	5.0	5.3
No. Wigglers	12	6	6	0
Wiggler Field [T]	1.9	1.9	1.9	0
Q_x	14.57	14.57	14.57	10.59
Q_y	9.6	9.6	9.6	9.6
Q_z	0.055	0.051	0.043	0.045
V_{RF}[MEV]	4.5	8.1	8	4.6
ϵ_x[nm-rad]	2.6	23	40	144
$\tau_{x,y}$[ms]	57	32	19.6	23.9
α_p	6.76×10^{-3}	6.29×10^{-3}	6.23×10^{-3}	11.2×10^{-3}
σ_l[mm]	12.2	9	15.8	20.1
σ_E/E[%]	0.81	0.89	0.93	0.656
bunch spacing [ns]		≥ 4, steps of 2		

lattice configurations are summarized in Table 1.

LOW EMITTANCE TUNING

Principle sources of vertical emittance are residual vertical dispersion and transverse coupling. Transverse coupling is generated by tilted quadrupoles and vertical misalignment of sextupoles. Vertical dispersion arises from coupling in regions of horizontal dispersion, and vertical kicks from offset quadrupoles and tilted dipoles. Careful alignment of the guide field elements is crucial to achieving ultra-low vertical emittance. As of our most recent survey we have achieved the alignment tolerances shown in Table 2.

Table 2: CESR magnet alignment

Element	misalignment
Quadrupole tilt [μrad]	126
Quadrupole offset [μm]	36
Sextupole offset [μm]	300
Dipole tilt [μrad]	73

We measure residual coupling and vertical dispersion by resonant excitation of the normal mode frequencies. We drive the beam at the normal mode tunes (horizontal, vertical and longitudinal) and measure the amplitude and phase of the vertical and horizontal motion at each beam position monitor for each of the three frequencies. We extract betatron phase advance, coupling of horizontal and vertical motion, and coupling of transverse and longitudinal motion (dispersion). By this method we measure phase with precision of about 0.2 degrees, coupling at the 0.1% level, and vertical dispersion with mm precision. Three minutes of machine time are all that is required to collect a complete set of data to identify sources of vertical emittance. Then based on a fit to the measured data, corrector magnets, (100 quadrupoles, 24 skew quadrupoles and 60 vertical dipoles) are deployed to correct betatron phase advance and to minimize coupling and vertical dispersion. The technique routinely yields vertical emittance < 20 pm in a single iteration. We have developed and refined beam based methods for centering the beam position monitors and calibrating BPM electrode gains[15]. The vertical beam size is measured with an xray camera. x-ray photons from a bend magnet are imaged through a pinhole, fresnel zone plate, or a coded aperture onto a linear photo - diode array, yielding a measurement of the size of a single bunch in a single pass[5, 8].

ELECTRON CLOUD DIAGNOSTIC INSTRUMENTATION

The storage ring has been extensively instrumented for the study of the electron cloud. Retarding field analyzers are used to measure the time average density of electrons near the surface of the vacuum chamber[2]. RFAs are the essential tool for determining the effectiveness of various mitigations[1]. Shielded button pickups give information about the growth and decay of the cloud on the time scale of a few nanoseconds[13]. The x-ray beam size monitor has the capability to measure the size of a bunch with micron resolution in a single pass. Thus we can measure the dilution of the emittance of bunches in the tail of the train due to the cloud generated by bunches at the head. We can further distinguish real emittance growth from the apparent growth that arises due to beam motion. The beam position monitor system also has single pass measurement capability and local processors that can store the data for many thousands of beam passages. The turn by turn position data for the individual bunches in a train yields information about the cloud induced tune shift and instabilities[11, 8].

Retarding Field Analyzers

A retarding field analyzer is a simple detector for measuring the density of the electron cloud near the wall of the vacuum chamber. A variety of geometries have been deployed in CESR. An example of an RFA designed to measure electron density in a standard CESR dipole mag-

net is shown in Figure 1. There are 9 sets of small holes in the wall of the vacuum chamber. Immediately beyond the holes there is a grid, (here in 3 parts) and beyond the grid, the collectors. A negative bias on the grid determines the energy of electrons that will make it to the collector. Then collector current is proportional to the electron density. Although it is not visible in this picture, the collector is segmented into 9 sections, to coincide with the nine sets of holes in the chamber wall, thus providing information about the dependence of the density on the horizontal position. There is some subtlety in interpreting the energy spectra of the cloud electrons and a detailed model of the RFA has been developed for that purpose[2]. The device is deliberately compact so that it will fit between the poles of the arc dipole. RFAs have been installed in wiggler chambers, drifts, quadrupoles, and in the dipole chicane that permits a measure of the dependence of cloud density on dipole field.

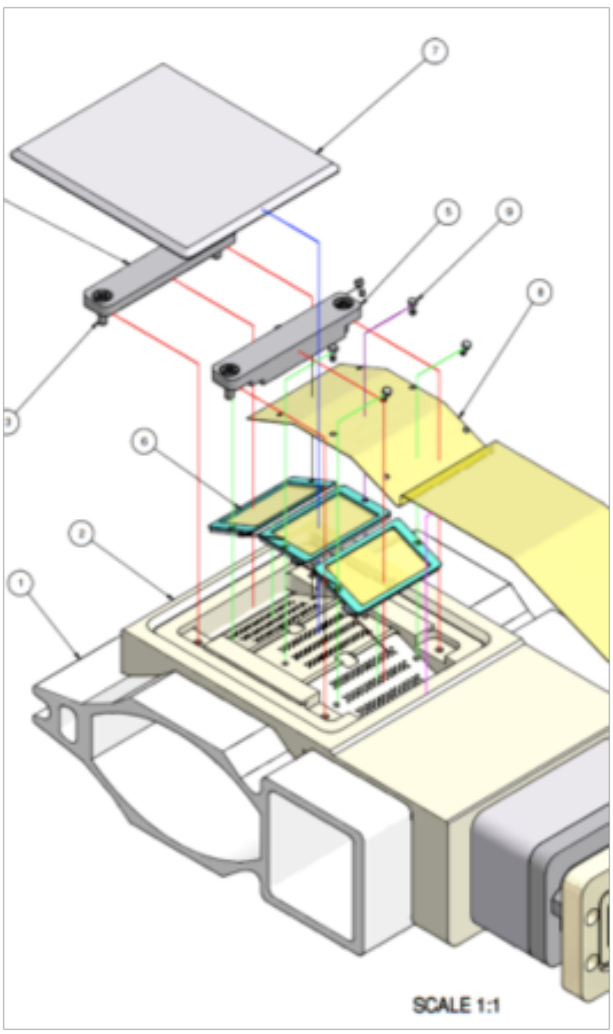

Figure 1: Exploded view of a dipole RFA.

Cloud development in Drifts RFA data for a drift (zero magnetic field) is shown in Figure 2. The RFA has

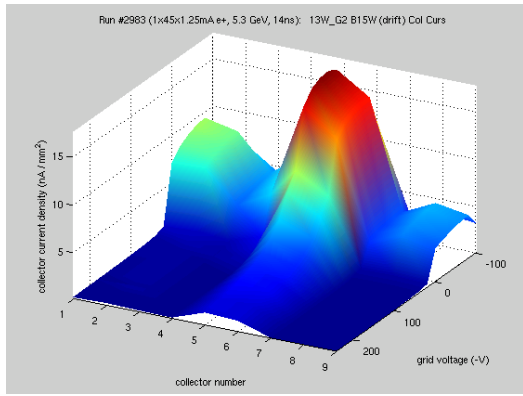

Figure 2: Drift RFA. There is a single train of 45 bunches with 14ns spacing and 1.25mA/bunch at 5.3GeV

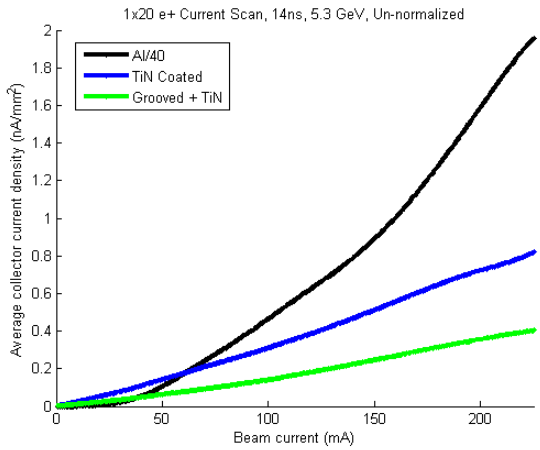

Figure 3: Dipole RFA data for three different chamber treatments. RFA collector current is measured as a function of total current in a 20 bunch train. Collector current for plain aluminum is divided by 20.

nine segments, and the grid voltage is varied from -250 Volts to 100 Volts. The 3-d plot shows the current on each of the nine collectors (horizontal position) vs grid voltage (electron energy). Evidently the electron density is greatest near the center (horizontally) of the chamber and it falls off rapidly with energy to something greater than 250eV.

Mitigation in Dipoles We use the RFA measurements to determine the effectiveness of mitigations. Data from dipole RFAs is shown in Figure 3. The plot shows the collector current density (averaged over the 9 collectors), as a function of beam current for three different chamber treatments. The black line is for the standard aluminum chamber, blue for TiN coated aluminum and green for TiN coated and grooved aluminum. Note that the data in the black line (bare aluminum) is divided by 20. Otherwise it would be off the scale of this plot.

Cloud development in Wigglers The vertical component of the magnetic field in the superconducting damping

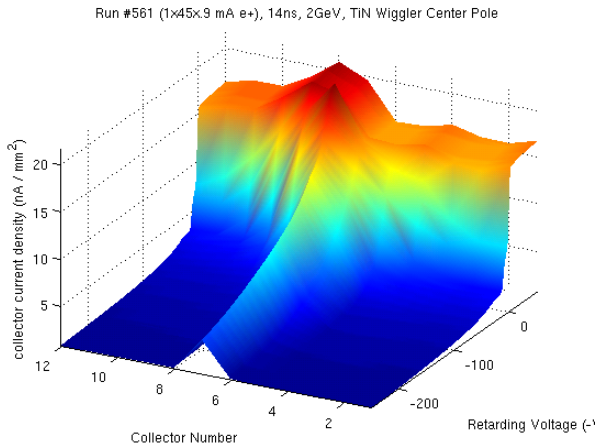

Figure 4: Collector current vs grid voltage for a wiggler RFA at the peak of the magnetic field (1.9T) in a TiN coated copper chamber.

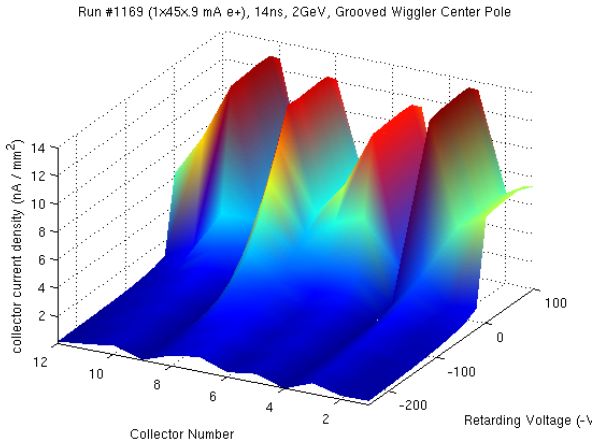

Figure 5: Collector current vs grid voltage for a wiggler RFA at the peak of the magnetic field (1.9T) in a grooved copper chamber. The grooves are cut longitudinally in the floor of the chamber, the RFA is on the ceiling. There is a single train of 45 bunches, with 0.9mA/bunch and 14ns spacing.

wigglers varies sinusoidally with longitudinal position. In order to understand the dependence of the electron cloud density on the field, the wiggler chamber is designed with three distinct RFAs located at the position of the peak field, half of peak, and at zero vertical field. Each of the three RFAs has 12 collectors to provide information about the transverse dependence. We show measurements from an RFA at the peak wiggler field for a chamber that is coated with TiN in Figure 4. The maximum density is at the center of the chamber (collectors 6-7) and for the lowest energy electrons. Comparison of the collector currents shows that the grooves are a bit more effective at mitigating the electron cloud than the TiN coating.

Measurements of the electron spectrum in a copper wiggler chamber with grooves is shown in Figure 5 for the RFA at the peak of the field. The grooves effectively suppress the electron density. Nevertheless the evidence of the grooves (the grooves are cut longitudinally in the floor of the chamber) is apparent in the dependence of collector current on collector number.

Table 3 summarizes the mitigation tests completed and underway. To learn more about RFA measurements, modeling, and comparison with simulation see the articles by J.Calvey in these proceedings.

Shielded button pickup

The RFA gives a time averaged measurement of the electron cloud density. The shielded pickup has a much higher bandwidth, essentially that of a beam positon monitor (nanoseconds), so can inform details of the time evolution of the cloud. A schematic of the shielded pickup is shown in Figure 6 in a cross section of the vacuum chamber. The three button electrodes arrayed transversely across the chamber provide some coarse position information. The electrodes are shielded from the wall current and direct beam pulse by a screen. Low energy electrons are

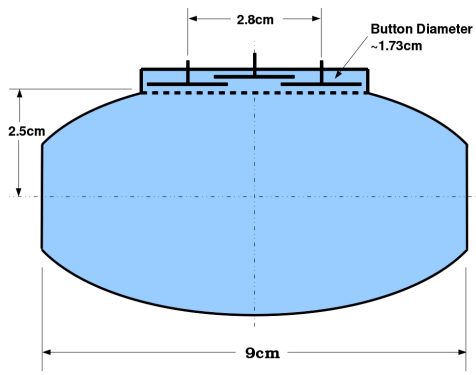

Figure 6: The 3 pickup electrodes are shielded from the direct beam signal by a screen.

detected as a current on the electrodes. An example of the shielded pickup measurement is shown in Figure 7. The probe bunch generates the cloud and the witness bunch that trails the probe by 14ns kicks the cloud electrons into the pickup. The passage of the first 8mA probe bunch is marked by the early pulse in the plot with peak just past the 20ns (the second) time division. This small pulse is the direct beam signal that is imperfectly shielded by the screen. The current in the witness bunch is varied from 1mA to 8mA. The (positive) witness bunch drives the electrons from the floor of the chamber towards the detector, the velocity increasing with the witness bunch charge.

The shielded pickup[13] gives us information about the decay time of the cloud. As we learned from the witness bunch measurement in Figure 7, the witness bunch signal is a measure of the cloud density at the time of passage. If we vary the delay of the witness with respect to the probe

	Drift	Quad	Dipole	Wiggler	VC Fab
Al	×	×	×		CU, SLAC
Cu	×			×	CU,KEK,LBNL,SLAC
TiN on Al	×	×	×		CU,SLAC
TiN on Cu	×			×	CU,KEK,LBNL,SLAC
Amorphous C on Al	×				CERN, CU
NEG on SS	×				CU
Solenoid Windings	×				CU
Fins w/TiN on Al	×				SLAC
Triangular Grooves on Cu				×	CU,KEK,LBNL,SLAC
Triangular Grooves w/TiN on Al			×		CU, SLAC
Triangular Grooves w/TiN on Cu				◯	CU,KEK
Clearing electrode				×	CU,KEK,LBNL,SLAC

Table 3: Surface characterization and mitigation tests. × indicates that the chamber and accompanying RFA is deployed and ◯ that the test is planned.The last column names the laboratories that contributed to the design and fabrication of the chamber.

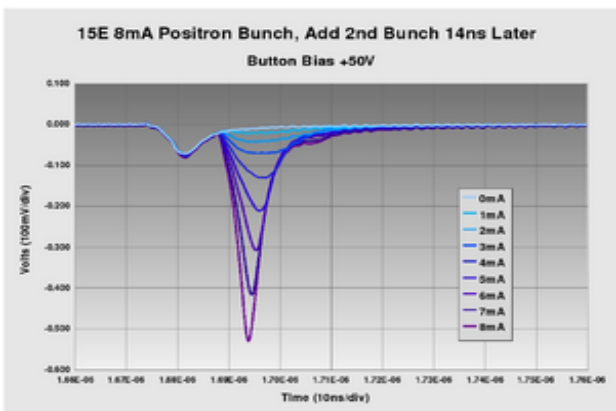

Figure 7: The small pulse just past the second time division is the direct signal from the probe. The pulse that follows 14ns later is the electrons that are accelerated off of the floor of the chamber towards the detector.

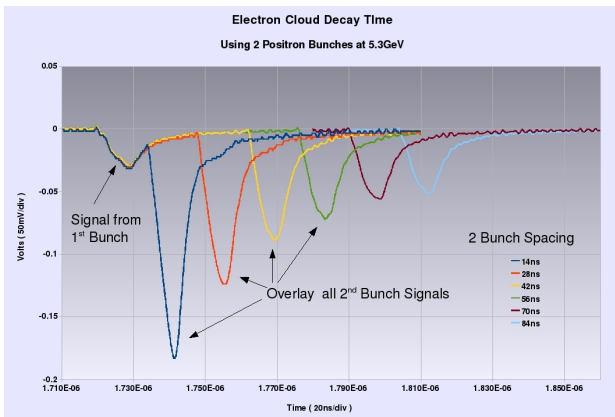

Figure 8: The witness bunch follows the probe at 14ns, 28ns, 42ns,56ns,70ns, and 84ns. The current in both probe and witness is fixed at 8mA

we measure the evolution of the cloud density. Such a witness bunch measure of the cloud decay is shown in Figure 8. The delay time of the witness with respect to probe is varied in 14ns steps. The exponential decay of the cloud is evident.

Measurements with the shielded pickup in the field of a solenoid tell us something about the energy spectrum of the photo-electrons. Figure 9 is a schematic of the detector in a longitudinal magnetic field. The holes in the screen that shield the electrodes are 2.5mm long and 0.76mm in diameter. Therefore, the screen is only transparent to electrons with trajectories very nearly perpendicular to the screen. And since most of the electrons are produced when the synchrotron radiation strikes the outside wall of the chamber, the detector becomes a momentum analyzer.

TE wave

We are exploring both theoretically and experimentally the so-called TE wave technique for measuring electron cloud density. A carrier electromagnetic wave is injected into the vacuum system at a beam position monitor and then detected at a nearby monitor. The electron cloud density modifies the wave number associated with the propagation of electromagnetic waves through the beampipe. Gaps in the fill pattern result in a modulation of the phase shift. In the frequency domain this results in sidebands of the fundamental frequency. The amplitude of the sidebands is related to the cloud density[4, 10]. The method has the advantage

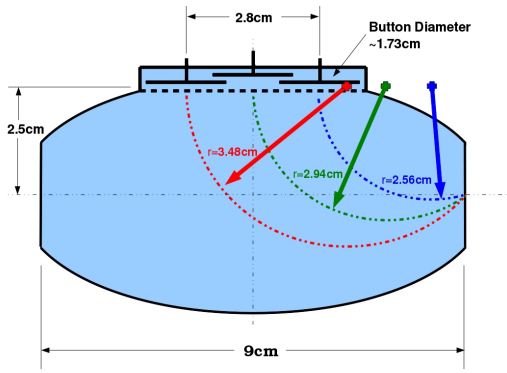

Figure 9: The shielded pickup in a longitudinal magnetic field becomes a momentum analyzer. The schematic shows that photo-electrons emitted from the outside wall of the vacuum chamber will be detected by one of the three shielded buttons depending on their energy and the local magnetic field.

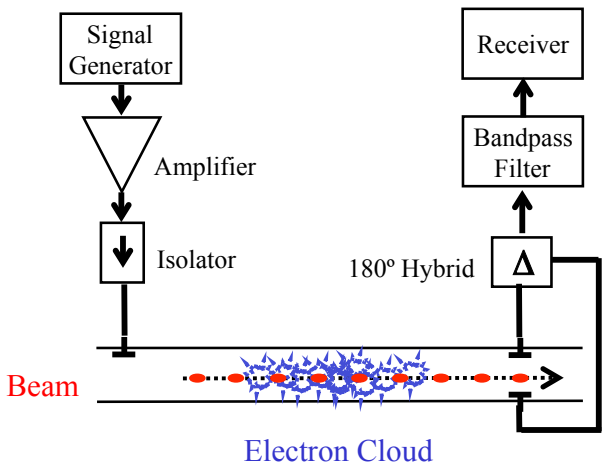

Figure 10: The TE wave measurement method

that no special vacuum instrumentation is required. The disadvantage is that interpretation of the results is complicated. The TE wave method is illustrated in Figure 10.

Beam Dynamics

Tune shift The positron beam is focused by the electrostatic field of the electron cloud[6]. The effect of the focusing is to shift the tune of the positron bunches. The tune shift then serves as the principle measurement of the electron cloud density around the ring. In a long train, the bunches near the tail of the train are focused by the cloud generated by bunches near the head. We have developed two techniques for measuring the spectrum of each bunch in a train. One strategy is to kick the entire train coherently, exciting betatron oscillations, and then to collect turn by turn position data for each bunch. We use an FFT to extract the tune. The results of a measurement by the coherent excitation method are shown in Figure 11. We circulate a

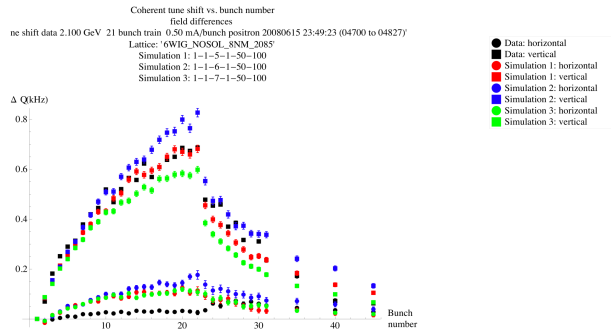

Figure 11: The vertical tuneshift (square points) is much larger than the horizontal tune shift (round points). The data are the black points. Simulation requires knowledge of the secondary (electron) emission yield. The simulation was performed with SEY=2.0 (red), SEY=2.2 (blue), and SEY=1.8 (green). The best fit to the data is SEY=2.0

.

train of 21 bunches spaced at 14ns intervals and a witness bunch at some number of 14ns intervals beyond the end of the train. We see the increasing cloud density, (increasing shift in tune), along the train and then the decay of the cloud as measured by the shift in the tune of the witness bunch. The measurements are in reasonably good agreement with the POSINST simulation[3, 6, 12].

Instability - head tail mode Another technique for extracting information about the bunch spectra and the interaction of the circulating positrons and the electron cloud is to use a gated spectrum analyzer. We thus measure the power spectrum of each of the bunches in the train. In addition to the induced tune shift we observe synchrobetatron sidebands for bunches near the tail of the train. Evidently, the cloud induces a head tail instability[6, 9].

Emittance Growth Another effect of the increasing cloud density along the train is the dilution of the vertical emittance. We use the x-ray beam size monitor to measure the vertical size of each of the bunches in the train[5, 8]. A measurement of the emittance growth in a 20 bunch train is shown in Figure 12 for bunch currents from 0.3mA to 0.75mA. The emittance of the first few bunches is $\sim$ 7pm. We see no emittance growth at the lowest current of 0.3mA/bunch and certainly no significant growth with 0.4mA. But with 0.5mA/bunch emittance dilution is observed in bunch 15 and at 0.75mA at bunch 11. The cloud induced emittance growth is anticipated by simulations[9].

MEASUREMENT OF SECONDARY EMISSION YIELD

The development and equilibrium density of the electron cloud is critically sensitive to the secondary emission yield

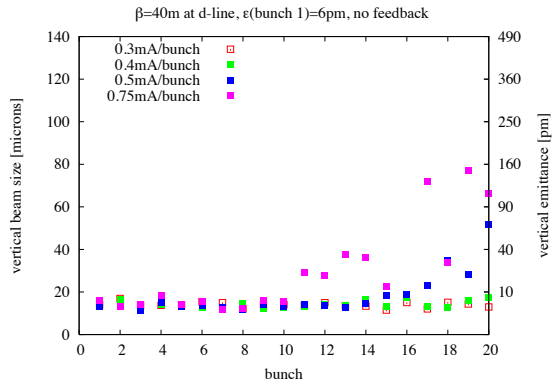

Figure 12: Vertical size of each bunch in a 20 bunch train is measured with the x-ray beam size monitor. Emittance growth is observed in bunch 15 for the train with 0.5mA bunches and at bunch 11 at 0.75mA/bunch.

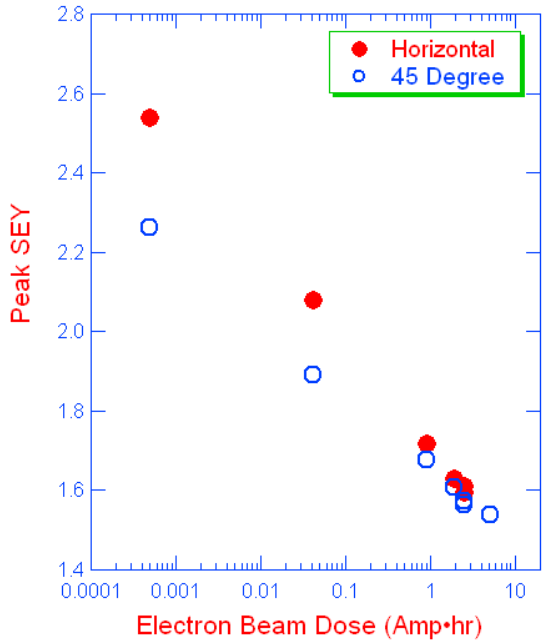

Figure 13: SEY versus electron beam dose. The horizontal (red) points are for sample material that is in the mid plane and recieves direct synchrotron radiation. The blue points are for a sample that is at 45 degrees above the midplane.

of the vacuum chamber material. And the SEY is typically reduced with beam processing. Of course, exposure to atmosphere after beam processing immediately contaminates the surface. Therefore, in order to determine the effective secondary yield it is useful to be able to measure SEY in situ. We have implemented an in situ station that allows for the extended exposure of a sample to synchrotron radiation and associated electron bombardment, and then measurement of the SEY while it remains in the CESR vacuum[14]. A plot of the SEY for TiN coated aluminum versus exposure is shown in Figure 13.

CONCLUSION

The instrumentation that has been deployed in CESR for the CesrTA experimental program provides the capability for characterization of the development of the electron cloud and the interaction of the electron cloud with circulating beams of positrons and electrons. Low emittance tuning techniques have been employed to minimize vertical emittance to facilitate exploration of electron cloud phenomena in the ultra-low emittance regime typical of damping rings. In this article we present an overview of the CesrTA instrumentation and a very brief sampling of the measurements. The interested reader is directed to the references to other articles in these proceedings for more details.

REFERENCES

[1] J.Calvey, "Electron Cloud Mitigation Investigations at CesrTA", *these proceedings*

[2] J.Calvey, Methods for Quantitative Interpretation of Retarding Field Analyzer Data, *these proceedings*

[3] D. Kreinick, "Using Coherent Tune Shifts to Evaluate Electron Cloud Effects on Beam Dynamics at CesrTA", *these proceedings*

[4] J.Sikora, "TE Wave Measurements at CesrTA", *these proceedings*

[5] J.Flanagan, "xBSM bunch-by-bunch measurements in EC conditions at CesrTA", *these proceedings*

[6] Dugan, G., "CESR TA Electron Cloud induced beam dynamics", *these proceedings*

[7] Li, Y., " Implementation and operation of electron cloud diagnostics for Cesr TA", *these proceedings*

[8] Rider, Nathan, " Bunch by bunch instrumentation upgrades for CESR based on requirements for the CESR TA research program", *these proceedings*

[9] S., Kiran, " Simulation of electron cloud induced instabilities and emittance growth", *these proceedings*

[10] S., Kiran, "Simulations using VORPAL on the effect of imperfections and non-uniformities in TE wave", *these proceedings*

[11] M. Billing, "Beam dynamics techniques" , *these proceedings*

[12] G. Dugan, "Synrad3D photon propogation and scattering simulation" , *these proceedings*

[13] J. Crittenden, "Electron cloud modeling results for time resolved shielded pickup measurements at Cesr TA" , *these proceedings*

[14] J. Kim, "In situ SEY measurements in CesrTA" , *these proceedings*

[15] D. Rubin, et.al., "CesrTA Low Emittance Tuning", *these proceedings*

E-CLOUD ACTIVITY OF DLC AND TIN COATED CHAMBERS AT KEKB POSITRON RING

S. Kato #, M. Nishiwaki, KEK, Tsukuba, Japan

Abstract

A TiN coated copper chamber and diamond like carbon (DLC) coated aluminium chambers were installed to an arc section of the KEKB positron ring to make comparisons of electron cloud activity as well as total pressure and residual gas components during the beam operation under the same condition. For the DLC coating, two different types of surface roughness: smooth and rough were prepared. The chamber with large surface roughness that was obtained with cost-effective simple abrasive of the large grain before the coating was installed in the same arc section and exposed to the electron cloud until the KEKB shutdown. The measured electron cloud activity in the DLC coated chamber with smooth surface showed half and one-sixth of those in the TiN coated chamber and the copper chamber, respectively at the operation of around 1000 Ah. Much more reduction of the e-cloud activity owing to the DLC on the roughed chamber surface was found, that is a reduction of one-fifth and one-tenth, respectively, in comparison with the DLC on non-roughed chamber and the TiN coating on non-roughed chamber at around 1000 Ah.

INTRODUCTION

After we found reduction of secondary electron yield (SEY) due to electron beam induced graphitization at surfaces of many metals, alloys and compounds, we have been performing comparative investigation to show validity of carbon materials such as graphite, diamond, amorphous carbon, electron induced graphite layer and so on with other metals and compounds in order to reduce e-cloud activity in accelerators [1-6].

One can find a couple of advantages of carbon materials for mitigating e-cloud in the following: (a) low δmax and low SEYs at higher incident energies and at oblique incident angles of electrons are shown due to mainly the low mass density of carbon materials, (b) low outgassing is achievable, depending on the method to make the films, (c) carbon materials show less adsorption (low sticking coefficient) and quick desorption (low activation energy of desorption), (d) hard coating with good adhesion is possible, (e)carbon raw materials are inexpensive[1-3, 7-9].

EXPERIMENTAL

Surface roughing was done before DLC coating on the inner surface of a 0.9 m-long Al beam chamber. For this purpose, cost-effective simple abrasive of the large grain with an average size of 30 microns was adopted with a process speed of 100 mm/min along with the chamber.

The DLC coating for the chamber shown in Fig. 1 was carried out mainly with acetylene gas of 1Pa in a pulsed DC plasma-CVD (chemical vapor deposition) chamber which allows us to coat DLC on a less than 3.5m-long chamber. The measured chamber temperature was not larger than 140 degrees C during the coating. Sample coupons were set inside of the envelopes that were connected to the Al chamber to confirm the film quality and the film thickness. The DLC deposition rate was measured to be 100 nm/min and the coating homogeneity was measured to be ±5%.

Figure 1: 0.9m long DLC coated Al Chamber after the surface roughing.

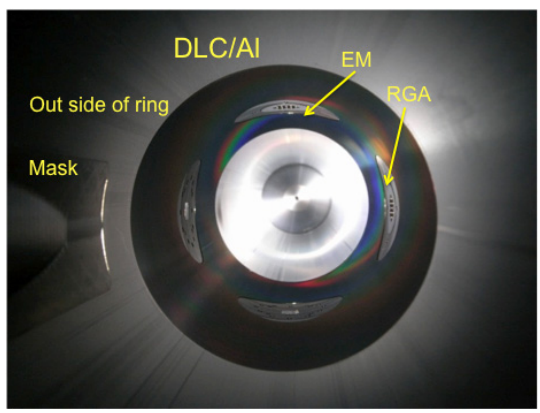

(a)

(b)

#shigeki.kato@kek.jp

Figure 2: (a) Inside of the non-roughed DLC chamber. (b) The DLC coated surface after roughing.

While the total thickness of the film was 3.4 μm, the pure DLC was in a thickness of 0.2 μm because of the multi layer system in order to enhance the film adhesion.

Some of measured characteristics show an atomic hydrogen composition of about 0.3, a Vickers hardness of 700~800 (a measured Hv of the A5052 Al chamber was 97), a resistivity of $10^{10\sim11}$ Ωcm. The measured Rys after the coating with a mechanical surface profile meter were 1.3 μm and 21 μm for the non-roughed and roughed surfaces, respectively.

In addition to a previous report of e-cloud activities for differently treated chambers at the KEKB positron ring [6], the surface-roughed DLC coated chamber was also installed to the same arc section together with a cold cathode gauge (CCG) a residual gas analyser (RGA), a retarding filed analyser (RFA) and sample coupons of which SEYs can be measured via UHV suitcases at lab.

RESULTS AND DISCUSSIONS

Table 1 shows an exposure history of the four types of beam chambers to the e-cloud with a positron beam current of 1.5 - 1.7 A in a period from Feb. 8, 2008 to June 30, 2010 at the same arc section. In Fig. 3, a pressure trend for four beam chambers is shown as a function of the integrated positron beam current.

Table 1: Exposure history of the four types of beam chambers to the e-cloud of the KEKB positron ring.

YYYY-MMDD	Coating / Beam Chamber
2008-0208 ~ 2009-0630	Cu
2009-1014 ~ 2009-1116	DLC / Al
2009-1117 ~ 2009-1224	TiN / Cu
2010-0513 ~ 2010-0630	DLC/ Roughed Al Surface

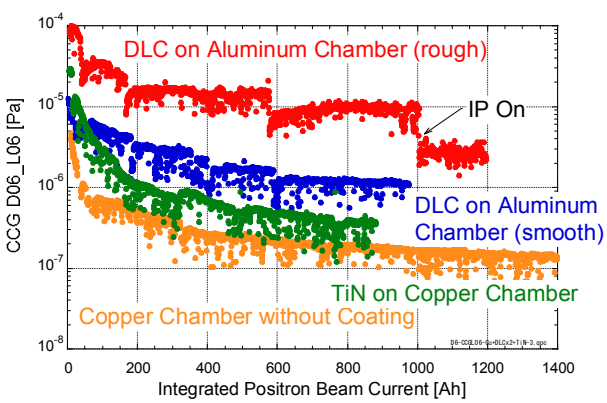

Figure 3: Total pressure measured with CCG for four different beam chambers is shown as a function of the integrated positron beam current.

Large outgassing from the surface-roughed DLC coated chamber as shown in Fig. 3 was expected before the beam operation because of the relatively thick coat and the large surface roughness. However it turned out later that a sputter ion pump (SIP) for the chamber had been out of order due to the controller breakdown just after the beam operation started. The high pressure had been thought to be intrinsic to the surface-roughed DLC film and nobody had doubt of the pump. After replacing the controller at 1000Ah, the pressure at the chamber dropped one-third, that is roughly 10 times and 3 times higher pressure compared with copper chamber and the non-roughed DLC chamber, respectively. This result of the surface-roughed DLC coat is not anymore surprising and this might be acceptable for the beam operation if hydrogen gas is dominant and the mitigation for e-cloud is remarkable, that is trade-off. In any case, it took roughly 1000Ah to get reasonable conditioning in a viewpoint of outgassing.

Comparison of the RGA spectra as shown in Fig.4 was made at the different integrated beam current unfortunately because of the SIP trouble. However the pressures in the chambers were almost constant for those integrated beam current and all the other conditions like the beam current were almost the same during the measurements.

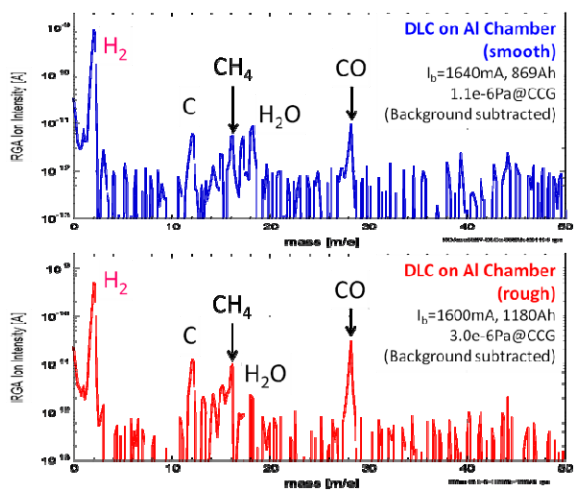

Figure 4: RGA Spectra for the non-roughed and the roughed DLC coated chambers. Background spectra acquired without the beam operation were subtracted.

These two spectra where hydrogen gas is dominant are similar each other and no hydrocarbon gas component except CH_4 that is usually seen in any accelerator to a certain extent was observed up to m/e 100. The detailed

difference in ion current intensities of four gas species is shown in Table 2 also using the data of the other types of coating[6]. Here one sees higher intensities for the roughed DLC chamber than the intensities of the others as expected. However the measured CCG pressure was not so high as the expectation considering the actual rough-surface area. The relatively large ratios of C, CH_4 and CO/N_2 to H_2 for the roughed DLC chamber might be due to partially uncoated areas on the quite rough surface or partial decomposition of the DLC film at the top edges specially in an area which is irradiated with the synchrotron light. In Table 2, it is also noticeable that the residual gas species except hydrogen from the non-roughed DLC chamber are equivalent to the gas species from the TiN chamber. The m/e 28 current of 2.0e-11 A for the TiN coat includes contribution of nitrogen outgassing from the TiN film to some extent due its decomposition since nitrogen of m/e 14 was found only in the spectra of TiN coated chamber. Hydrogen outgassing which mainly affect to the total pressure would be only the issue in case of the DLC chambers. Even concerning to this issue, the hydrogen outgassing might not be eventually a problem of the accelerator operation because its low Z.

Table 2: RGA ion current intensities for the three different types of coating. Because of degradation of the RGA electron multiplier in the measurement for roughed DLC chamber, the ion intensities were corrected based on the CCG data.

$\times 10^{-12}$ A

	H_2	C	N	CH_4	CO/N_2
TiN	65	5.0	7.0	5.0	20
DLC (smooth)	900	6.0	N.D.	6.0	10
DLC (rough)	2700	70	N.D.	54	160

Fig. 5 shows monitored currents at the RFA for the four types of chamber as a function of the integrated beam current. The e-cloud mitigation with the roughed DLC surface seems to be outstanding. At the beginning of the beam operation, the reduction factor of e-cloud activity for the roughed DLC chamber showed 60 when the activity in the copper chamber is defined to be one. While the activity gradually increased during the beam operation, the reduction factor was saturated to be 30.

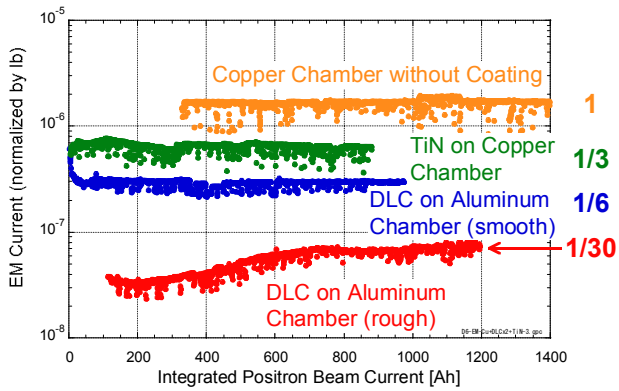

Figure 5: Monitored currents at the RFA for the four types of chamber as a function of the integrated beam current.

The gradual increase of the e-cloud activity in the roughed DLC chamber might be due to partial decomposition or partial exfoliation. In a visual check of the inside of the roughed DLC chamber after the KEKB shutdown at the end of June, 2010, light reflection change at the surface along with a line that is irradiated with the synchrotron light was found. Some partial exfoliation was also found at the circular boundary line between the non-roughed surface with the old DLC coating and the roughed surface followed with the DLC coating. This might be because of two sorts of geometric mismatching, that is mismatching of the old and new coating layers and mismatching of the smooth and rough coating substrates. This geometric mismatching would have caused mechanical stress at the circular boundary. Some cure should have been done before the roughing. However this was only the position where the partial exfoliation was found for the roughed DLC chamber.

CONCLUSION

The e-cloud activity as well as the total pressure and the RGA spectra in the newly installed DLC coated chamber with rough surface into the KEKB positron ring were measured in comparison with those in the copper, TiN and non-roughed DLC chambers. A remarkable reduction of the e-cloud activity of around 30 was achieved when the activity in the copper chamber is defined to be one. The dominant hydrogen outgassing from the surface-roughed DLC chamber might be acceptable for the beam operation if the mitigation for e-cloud is significant, that is trade-off. However further effort to reduce the outgassing should be made.

ACKNOWLEDGEMENTS

The authors would like to thank Dr. K. Shibata (KEK) for his cooperation in the TiN coating for the copper chamber.

We deeply appreciate H. Hisamatsu and M. Shirai (KEK) for their technical cooperation.

REFERENCES

[1] Shigeki KATO, edited by Y.Yamazaki, Accelerator Technical Design Report for J-PARC Accelerator Group JAERI/KEK Joint Project Team, KEK Report 2002-13.
[2] M. Nishiwaki and S. Kato, American Vacuum Society the 49th International Symposium, Denver, CO, 2002.
[3] M. Nishiwaki and S. Kato, 16th International Vacuum Congress, Venice, Italy, 2004.
[4] M. Nishiwaki and S. Kato, J. Vac. Soc. Jpn. **48** (2005) 118.
[5] S. Kato and M. Nishiwaki, Workshop of Anti e-cloud Coatings, CERN, Oct. 2009.
[6] M. Nishiwaki and S. Kato, Proc. of IPAC-2010, Kyoto, Japan, 23-28 May 2010, pp THPEA079.
[7] S. Kato, K. Josek and E. Taglauer, Vacuum **42**(1990)253.
[8] S. Kato, H. Oyama and H. Odagiri, Vacuum **41**(1990)1998.
[9] C. Yin Vallgren, G. Arduini, J. Bauche, S. Calatroni, P. Chiggiato, K. Cornelis, P. Costa Pinto, E. Me´tral, G. Rumolo, E. Shaposhnikova, M. Taborelli, G. Vandoni, Proc. of IPAC-2010, Kyoto, Japan, 23-28 May 2010, pp TUPD048

ELECTRON CLOUD MITIGATION INVESTIGATIONS AT CESR-TA*

J.R. Calvey, J. Makita, M.A. Palmer, R.M. Schwartz,
C.R. Strohman, CLASSE, Cornell University, Ithaca, NY, USA
S. Calatroni, G. Rumolo, CERN, Geneva, Switzerland
K. Kanazawa, Y. Suetsugu, KEK, Ibaraki, Japan†
M. Pivi, L. Wang, SLAC, Menlo Park, CA, USA

Abstract

As part of an effort to understand and mitigate the electron cloud effect, the CESR storage ring at Cornell has been reconfigured into a damping ring-like setting, as well as instrumented with a large number of electron cloud diagnostic devices. In particular, more than 30 Retarding Field Analyzers (RFAs) have been installed. These devices, which measure the local electron cloud density and energy distribution, have been deployed in drift, dipole, quadrupole, and wiggler field regions, and have been used to evaluate the efficacy of cloud mitigation techniques in each element.

INTRODUCTION

The density, energy distribution, and transverse profile of the electron cloud can depend strongly on several parameters that can vary substantially throughout an accelerator. These include local photon flux, vacuum chamber shape and material, primary and secondary emission properties of the material, and magnetic field type and strength. Therefore it is useful to have a detector that can sample the electron cloud locally. At CesrTA we have primarily used Retarding Field Analyzers (RFAs) for this purpose [1]. RFAs can measure the energy distribution of the cloud by applying a retarding potential between two grids, rejecting any electrons below a certain energy[2]. In addition, most RFAs are segmented across the top of the beam pipe, effectively measuring the transverse distribution of the cloud.

We have used these devices to probe the local behavior of the cloud in the presence of different mitigation schemes. Several such schemes have been proposed, including beam pipe coatings (TiN, amorphous Carbon, NEG) [3, 4], grooved beam pipes [5], solenoids, and clearing electrodes [6].

Table 1 provides a list of the mitigation techniques that have been evaluated so far at CesrTA.

Table 1: Mitigation techniques at CesrTA

Field Type	Base Material	Mitigation
Drift	Aluminum, Copper	TiN, Carbon, NEG coatings, solenoids
Dipole	Aluminum	TiN coating, grooves
Quadrupole	Aluminum	TiN coating
Wiggler	Copper	TiN coating, grooves, clearing electrode

DRIFT MEASUREMENTS

Fig. 1 shows a typical retarding voltage scan in an TiN coated drift chamber for a 45 bunch train of positrons, at 1.25 mA/bunch (corresponding to a bunch population of 2×10^{10}), 14ns spacing, and beam energy 5.3 GeV. The plot shows the RFA response as a function of collector number and retarding voltage. The RFA signal is expressed in terms of current density in nA/mm^2, normalized to the transparency of the RFA beam pipe and grids. In principle, this gives the time averaged electron current density incident on the beam pipe wall. The signal is peaked at low energy and in the central collectors, though some current remains at high energy in the central collectors and at low energy in all collectors.

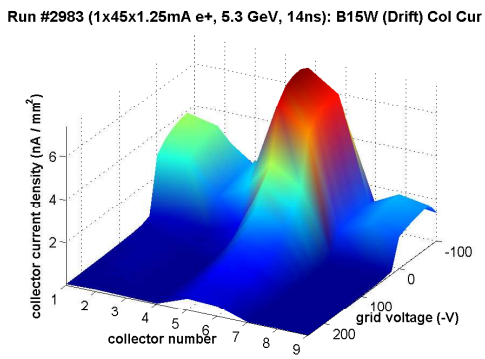

Figure 1: Example voltage scan: TiN coated drift RFA

We have taken RFA data in both TiN and amorphous Carbon coated drift chambers, as well as an uncoated Aluminum chamber. All three of these chambers have been installed at the same location in the ring at different times. This ensures that the comparison is done with the exact same beam conditions, including photon flux and beam size.

A comparison of different beam pipe coatings in a drift region can be found in Fig. 2. It shows the average collector current density as a function of beam current (in this case

* Work supported by the US National Science Foundation (PHY-0734867) and Department of Energy (DE-FC02-08ER41538)
† Work supported by The Japan/US Cooperation Program

for a 20 bunch train of positrons), for all of the chamber coatings mentioned. There are two sets of data shown for the TiN chamber, one taken shortly after it was installed, and one taken after four months of beam processing. The Carbon chamber did not show significant processing.

Both TiN and Carbon coatings show a largely suppressed signal relative to Aluminum. The Carbon chamber falls in between unprocessed and processed TiN.

Fig 3 shows the same comparison for data taken with an electron beam. Though the scale is smaller on this plot, the relative performance of the three chamber types is roughly the same.

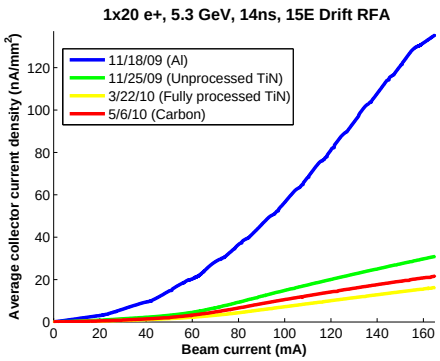

Figure 2: Drift RFA comparison, positron beam

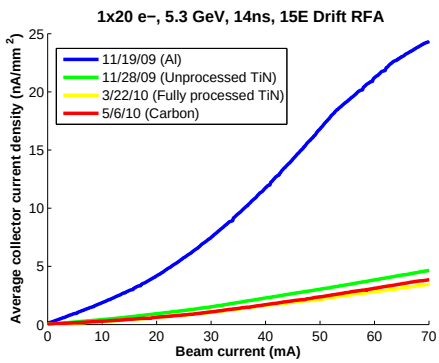

Figure 3: Drift RFA comparison, electron beam

NEG Coated Chamber

We have also installed a NEG coated chamber in our L3 straight region. This chamber is instrumented with three single collector RFAs, located at different azimuthal positions. Fig. 4 shows the current measured by one of these RFAs, comparing the signal before activation of the NEG, after activation, and after processing. Both activation and processing reduce the current measured by this RFA; the other two detectors behave similarly.

DIPOLE MEASUREMENTS

Most of our dipole RFA measurements were done using a chicane of four magnets built at SLAC [7]. The

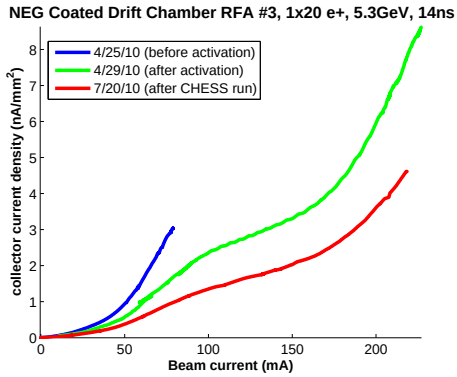

Figure 4: NEG RFA comparison

field in these magnets is variable, but most of our measurements were done in a nominal dipole field of 810G. Of the four chicane chambers, one is bare Aluminum, two are TiN coated, and one is both grooved and TiN coated. The grooves are triangular with a depth of 5.6mm and an angle of 20°. A retarding voltage scan, done in the Aluminum chamber and with the same beam conditions as Fig. 1, can be seen in Fig. 5. Here one can see a strong central multipacting spike.

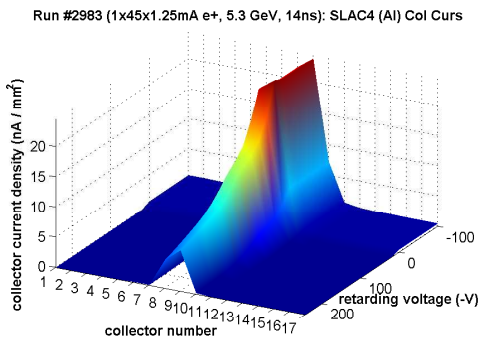

Figure 5: Typical dipole RFA measurement

Fig. 6 shows a comparison between three of the chicane RFAs. We found the difference between uncoated and coated chambers to be even stronger than in a drift region. At high beam current, the TiN coated chamber shows a signal smaller by two orders of magnitude than the bare Al chamber, while the coated and grooved chamber performs better still.

Bifurcation

For high bunch currents, one actually observes a bifurcation of the central multipacting peak into two peaks with a dip in the middle. This is demonstrated in Fig 7, which shows the signal in all 17 RFA collectors vs beam current. Bifurcation occurs when the average energy of electrons in the center of the beam pipe is past the peak of the SEY curve, so that the effective maximum yield is actually off

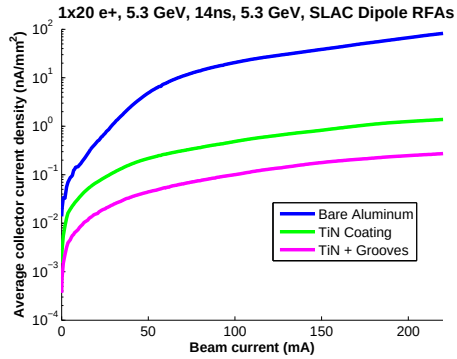

Figure 6: Dipole RFA comparison

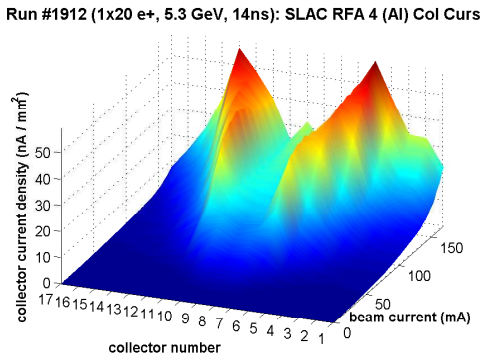

Figure 7: Bifurcation of peak density in a dipole

center. The higher the bunch current, the further off center these peaks will be.

QUADRUPOLE MEASUREMENTS

Another development at CesrTA has been the incorporation of an RFA into a quadrupole chamber. This RFA wraps azimuthally around the chamber, from about 70 to 150 degrees (taking zero degrees to be the source point). A typical quadrupole RFA measurement is shown in Fig. 8. We find that the collector that is lined up with the quad pole tip (no. 10) sees a large amount of current, while the rest of the collectors see relatively little. This suggests that the majority of the cloud in the quad is streaming between two pole tips.

Fig. 9 shows a comparison of a bare Aluminum (both processed and unprocessed) quadrupole chamber with the TiN coated chamber that has replaced it. In this comparison only collector 10 is being plotted. The signal in the TiN chamber was found to be reduced by well over an order of magnitude.

Long Term Cloud Trapping

One potential side effect of the cloud mirroring between the quad pole tips is that it may become trapped for a long time. We have seen some evidence of this at CesrTA. Fig 10 shows the signal in collector no. 10 for a voltage scan done with a 45 bunch train of positrons at 1mA/bunch. Also

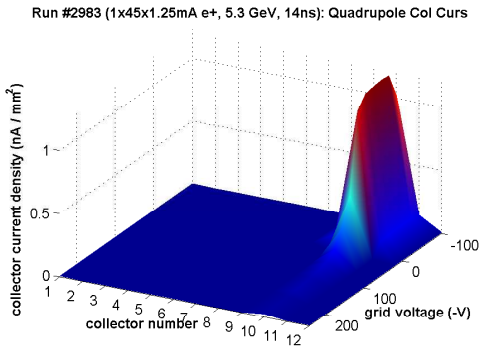

Figure 8: Quadrupole RFA measurement

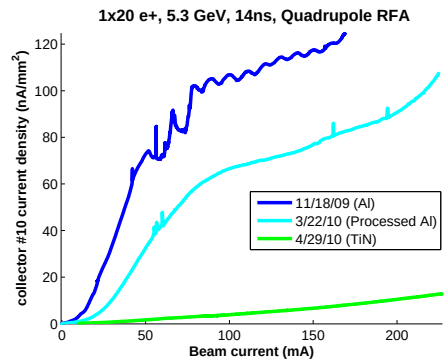

Figure 9: Quadrupole mitigation comparison

plotted are simulations done in ECLOUD [8] of these conditions. If one does a simulation for only one beam revolution period (2.56μs), the simulated signal is too low at all energies by over an order of magnitude. However, if one continues the simulation for multiple turns of the beam, one finds that the data and simulation start to get closer. By 19 turns, they are in very good agreement at high energy, and within a factor of 2 at low energy. This implies that the cloud is building up over several turns, and that the RFA is sensitive to this slow buildup.

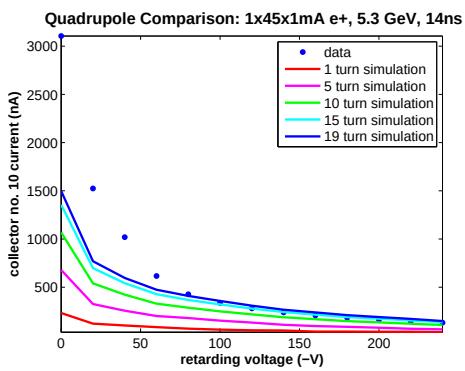

Figure 10: Long term cloud buildup in a quadrupole

WIGGLER MEASUREMENTS

The L0 straight section of CESR has been reconfigured to include six superconducting wigglers, three of which are instrumented with RFAs [9]. Each wiggler has an RFA in the center of one of the wiggler poles (where the transverse field is largest), half way between poles (where the field is longitudinal), and in an intermediate region. This paper will focus on the center pole RFA, which can roughly be considered to be in a 1.9T dipole field.

Fig. 11 shows a typical Cu wiggler RFA voltage scan for a 45 bunch train of positrons at 1.25mA/bunch, 14ns spacing, and 2.1 GeV. The signal is fairly constant across all the collectors at low retarding voltage, but does become peaked at the center at high energy. There is also an anomalous spike in current at low (but nonzero) retarding voltage; we believe this is due to a resonance between the bunch spacing and retarding voltage [10].

As with the drift RFAs, cycling the location of the different wigglers has allowed us to compare the RFA response with different mitigation techniques in the same longitudinal position in the ring. We have tested chambers with bare Copper, TiN coating, triangular grooves (with no coating, 2mm depth and 20° angle), and a clearing electrode. Fig. 12 shows the average collector current vs beam current in three chambers with mitigation; the copper wiggler is adjacent to this location, and is shown for a rough comparison. Note that, unlike the other measurements presented so far in this paper, beam pipe coating does not appear to lead to a significant reduction in RFA current, and grooves lead only to a small improvement. The chamber instrumented with a clearing electrode, however, shows a sizable reduction in signal. The electrode was set to 400V for this measurement.

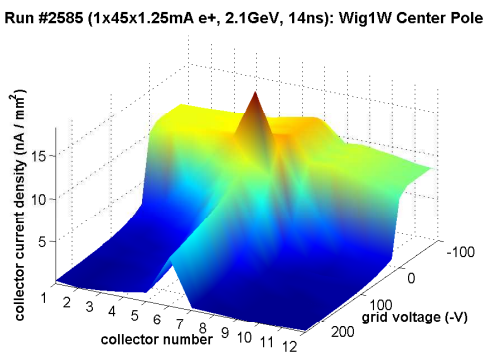

Figure 11: Wiggler RFA measurement, Cu chamber

Wiggler Ramp

Another interesting measurement that has been done with our wiggler RFAs is a "wiggler ramp", in which the RFA signal is monitored while the field in all six wigglers is ramped down from full (1.9T) to zero. Fig. 13 shows the signal in our three center pole wiggler RFAs vs wiggler

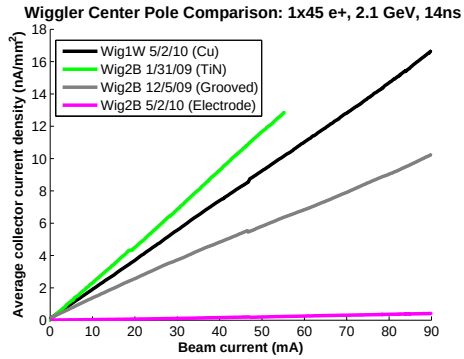

Figure 12: Wiggler mitigation comparison

field. We observe a "turn on" of the signal in each detector at a specific wiggler field value. Note that the detectors that are further downstream (i.e. have a higher s value) turn on first. This is because as the wiggler field in increased, the radiation fan becomes wider, and photons generated by the wiggler will collide with the beam pipe wall sooner. The farther downstream a detector is, the less wide the fan must be for photons to hit at that location. This measurement can help us understand the scattering properties of photons generated in this region, since only photoelectrons produced on the top or bottom of the beam pipe will be detectable by the RFA.

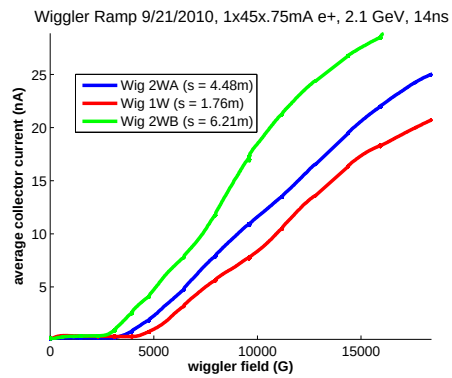

Figure 13: Wiggler ramp measurement

CONCLUSIONS

A great deal of RFA data has been taken at CesrTA, in a wide variety of beam conditions and magnetic field elements. Many interesting phenomena have been observed, including bifurcation of the peak density in a dipole, long term cloud trapping in a quadrupole, and a resonance with retarding voltage in a wiggler.

In terms of the effectiveness of mitigation types, several qualitative comments can be readily made:

- We have found beam pipe coatings (TiN, Carbon, and NEG) to be effective at mitigating the cloud in drifts.

- TiN coating was also found to be effective in a dipole and quadrupole; using a grooved and coated chamber in a dipole is even more effective.
- In a wiggler, a clearing electrode appears to be the most effective mitigation technique.

A systematic study to obtain more quantitative information about the different chambers, in particular their primary and secondary electron yield properties, is currently underway [11].

REFERENCES

[1] M. Palmer et. al., PAC09, Vancouver, TH5RFP030

[2] R.A. Rosenberg, K.C. Harkay, Nucl. Instrum. Meth. A 453, 507 (2000).

[3] E. Shaposhnikova et. al., PAC09, Vancouver, MO6RFP008

[4] F. Le Pimpec et. al., http://arxiv.org/abs/physics/0405098v1

[5] L. Wang, T. O. Raubenheimer and G. Stupakov, NIM-PR-A, 571, 588 (2007).
M. Pivi, F. K. King, R. E. Kirby, T. O. Raubenheimer, G. Stupakov and F. Le Pmpec, J. Appl. Phys., 104, 104904 (2008).

[6] Y. Suetsugu, H. Fukuma, L. Wang, M. T. F. Pivi, A. Morishige, Y. Suzuki, M. Tsukamoto, NIM-PR-A, 598, 372.

[7] M. T.F. Pivi, J. S.T. Ng et al. Nucl. Instr. Methods A, doi:10.1016/j.nima.2010.04.052.

[8] F. Zimmermann and G. Rumolo, ICFA Beam Dynamics Newsletter No. 33, eds. K. Ohmi and M.A. Furman (2004).

[9] Y. Li et. al., PAC09, Vancouver, TH5RFP029.

[10] J. Calvey et. al., IPAC10, Kyoto, TUPD022.

[11] J. Calvey et. al., “Methods for Quantitative Interpretation of Retarding Field Analyzer Data”, these Proceedings.

EXPERIMENTAL EFFORTS AT LNF TO REDUCE SECONDARY ELECTRON YIELD IN PARTICLE ACCELERATORS

R. Cimino[#], M. Commisso, T. Demma, D.R. Grosso
LNF- INFN, Frascati, Italy
N. Mahne, A. Giglia, CNR-IOM, Trieste, Italy

Abstract

A common effort in most accelerator centres is to develop new technologies to produce and test beam pipe inner walls of particle accelerators with an as low as possible Secondary Electron Yield (SEY). This item, in fact, is crucial in controlling Electron Cloud formation and in reducing its effects that are well known to be a potential bottle-neck to the performances obtainable from present and future accelerators. Frascati has a longstanding experience in qualifying materials in terms of surface parameters of interest to e-cloud issues. We are routinely measuring SEY, its dependence from electron energy, temperature and scrubbing. We are about to be ready to study not only the Photo Electron Yield (PEY), but more importantly, to characterize in situ the surface chemical composition and eventual modifications occurring during electron or photon irradiation by using synchrotron radiation beamlines in construction at DAΦNE. Our experimental measurements of the relevant parameters can be also confidently compared to simulations, performed by running the EC codes, in order to elucidate the final consequences on machine performances. Such a combined characterization effort is also suggesting ways to produce low SEY materials coatings. This issue is particularly important in view of the possible construction in Italy of a Super-B high luminosity collider [1], where e-cloud issues are foreseen to be a potential bottleneck to operational machine performances.

INTRODUCTION

In accelerator rings beamlines with positively charged beams, an electron cloud [2] may be initially generated by photoelectrons or ionization of residual gas and increased by the surface secondary emission process. If an electron cloud (EC) forms, it may couple with the circulating beam and cause beam instabilities, tune shift, and vacuum pressure rise, ultimately affecting the machine performances. Electron cloud detrimental effects have been observed at many storage rings [3] and are expected to be a serious issue for future machines like ILC-DR and Super-B.

EC build-up and evolution depend strongly on the surface properties of the accelerator walls such as Secondary Electron Yield (SEY), defined as the number of emitted electrons per incident electron and commonly denoted by δ. Generally for metal surfaces used in accelerators, the value of SEY ranges from 1 to 3 in the 0-500 eV energy range, and reaches a maximum (δ_{max}) around 200 eV. The SEY of technical surface materials for accelerator vacuum chambers has been extensively measured in the past years at CERN [4, 5], KEK [6, 7], SLAC [8, 9, 10] and other laboratories [11].

A low SEY is essential for the operation of particle accelerators, since their design luminosity and performances relies on a SEY value of about 1.3 or less. Clearly, an industrial surface with such a low yield should be stable in time and during operation, and have the necessary requirements in terms of vacuum compatibility, impedance, surface resistance, etc.. Up to now, unfortunately the significant effort done by many laboratories to find suitable surface coatings or systems, has not yet given satisfactory and conclusive results. LHC, for instance, does not count on a specific low yield material coating but on the experimental evidence that the SEY of the chosen Cu surface is strongly reduced by surface conditioning during initial operations (or commissioning). In this framework, the understanding of the conditioning process is needed to predict the conditioning time and beam parameters required to reach accelerator design performances. To this scope we have measured SEY reduction (scrubbing) not only versus the dose (the number of impinging electrons per unit area on sample surfaces) of the impinging electrons, but also versus their energy, with special attention to low energy primary electrons (<50 eV) which have been recently shown to have peculiar behavior in terms of reflectivity [4]. Such studies, performed on Cu prototype of the beam screen adopted for the Large Hadron Collider (LHC), have shown that scrubbing efficiency depends not only on the dose but also on the energy of incident electron beams [12,13].

So, while it is clear that scrubbing is one possible solution to obtain low SEY beam pipe accelerators, it seems very useful to study the actual chemical phenomena occurring at the real surfaces and causing the observed SEY reduction. Such careful surface analysis can not only clarify some important functional aspects related to the scrubbing process, but also can individuate new strategies in producing stable low SEY materials.

In this context Surface science techniques and synchrotron radiation spectroscopies are ideal tools to perform “in situ” characterization of the chemical composition of a relevant surface material and its eventual modifications occurring during electron or photon irradiation. To convince ourselves that such research line could indeed give significant insight to the scrubbing

[#]roberto.cimino@lnf.infn.it
Oral Session

process itself, before having access to the XUV beamlines in construction at DAΦNE [14] we performed preliminary experiments at Elettra focussing on the relation between the SEY and the surface condition of representative LHC samples. We correlate the SEY reduction obtained by electron bombardment with the surface chemical composition by using photoemission spectroscopy. Such characterization suggests also ways to produce low SEY materials.

EXPERIMENTAL

The measurements were performed at the BEAR beamline at ELETTRA in Trieste. This is a bending magnet beamline, which can provide a monochromatic beam with energies ranging from 3 to 1600 eV with a resolving power between 2200 and 5800 [15], and a white light with a spectral distribution similar to that of LHC. The actual energy resolution in our experiments was about 100 meV at 300 eV, this value being experimentally derived by measuring the exciton line-width at the C K edge on a diamond sample.

The experimental station has been described elsewhere [16]. Briefly, the UHV analysis chamber is equipped with a 6-degrees freedom manipulator, covering both the entire azimuth and polar angle ranges, with an angle resolution better that 1/100 degree.

The samples studied, co-laminated Cu for the LHC beam screen, were introduced into the measurement chamber without any treatment and characterized by photoemission and absorption spectroscopies. It was necessary to polarize the sample to a negative bias voltage since the transmission function of the CMA, used for the photoemission measurements is not constant at low energies. The bias voltage was chosen as that voltage that maximizes the transmission function of the CMA at low energies.

Absorption measurements were performed in the total electron yield (TEY) mode. As the radiation impinges on the sample, the absorption spectra are given by the ratio between current intensity flowed through the sample and the current intensity of a W mesh monitoring the radiation flux.

The SEY (δ) is determined from: $\delta=I_e/I_0 = (I_0-I_S)/I_0$ where I_e is the current due to electrons emitted by the sample; I_0 is the impinging electron current and I_s is the drain current measured from sample to ground, both measured with a Keithley picoammeter.

The SEY has been measured before and after the irradiation with a source of electrons made of a filament with barium oxide, which being not collimated, allows a more uniform bombardment on a larger zone of the sample surface and can provide a large current on the sample. During the bombardment the filament was biased at –390 V and the sample at + 50 eV, in order to collect the total amount of electrons emitted by the filament. Therefore the electrons hit the sample with an energy of 440 eV. Electron dose is determined from: $D=Q/A=I_0t/A$, where Q is the total charge incident per unit area on sample surface, I_0 is the impinging beam current and t is time period for which the sample was exposed to the beam. Unit chosen here for dose are Cmm^{-2}. All SEY and doses have been performed at normal incidence.

RESULTS AND DISCUSSION

In Fig. 1 we present the overview photoemission spectra measured on the LHC sample before (as received sample) and after the electron bombardment. These spectra have been acquired with a photon of energy 650 eV.

The as received sample was conditioned with a dose of $10mCmm^{-2}$ at the energy of 440 eV. As it was shown in previous papers [12, 13], this electron dose is sufficient to reduce the maximum value of SEY yield, δ_{max}, from 2.1 to ~1.1 (not shown).

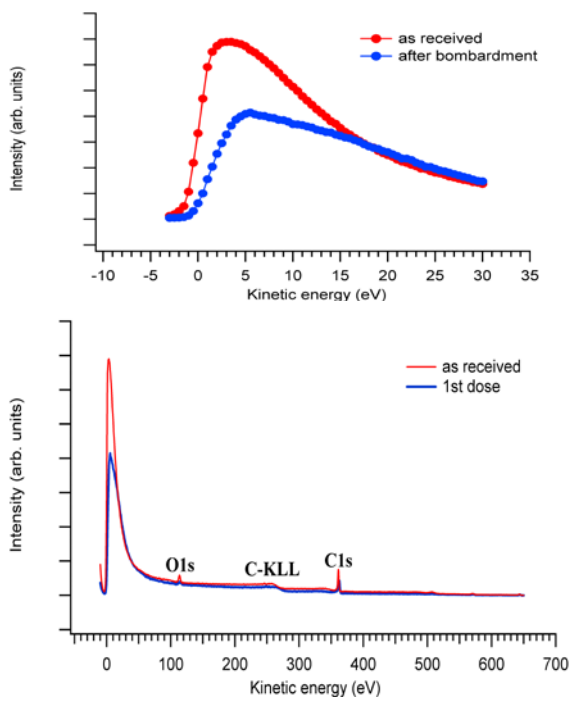

Figure 1: Top: Photoemission overview spectra of the sample (as received) and after electron bombardment. Bottom: peak of secondary electrons before and after the bombardment with electrons.

In the photoemission spectra we can distinguish the high peak of secondary electrons, centered at 3 eV, the O1s core level peak due to oxygen atoms at the kinetic energy of ~ 110 eV (labelled with A), and the broad KLL Auger line at the kinetic energy of ~ 258 eV (labelled with B) and the C1s

core level peak at the kinetic energy of ~ 358 eV (labelled with C) due to C atoms.

It is clear that electron irradiation causes a decrease of the secondary electron peak, as better evidenced in the bottom side of Fig.1. This reduction is due to the chemical modification induced by electron bombardment on the surface of the sample.

In order to better observe the changes in the contaminants induced by electron bombardment, Fig. 2 shows the O1s and C1s spectra measured at higher energy resolution. The behavior of these peaks shows that there is not only a pure reduction of the intensities due to the cleaning of incident electrons, but there is also a changing in the chemical state of these contaminants. This is particularly evident in the case of carbon, whose C1s peak after the exposure to the electron beam is shifted toward higher kinetic energies, indicating that the carbon impurities (mainly hydrocarbons) have changed to graphitic carbon.

The chemical changes induced by the electron bombardment are also reflected by the absorption spectra taken on the oxygen and carbon K-edges, reported in Fig.3. The absorption spectrum of the oxygen shows only a reduction of signal, but not great changes in the shape. This suggests that the electron bombardment causes some oxygen desorption from the sample surface but does not significantly modify its chemical environment. Modifications of the C K-edge are more evident. Very important is to note the increase of the peak at 285 eV: this feature is generally considered a strong fingerprint of the formation of π bonds between carbon atoms, hence suggests a transition to a flat rearrangement of carbon atoms on the substrate surface. This is a clear signal of a graphitization of the carbon on the surface.

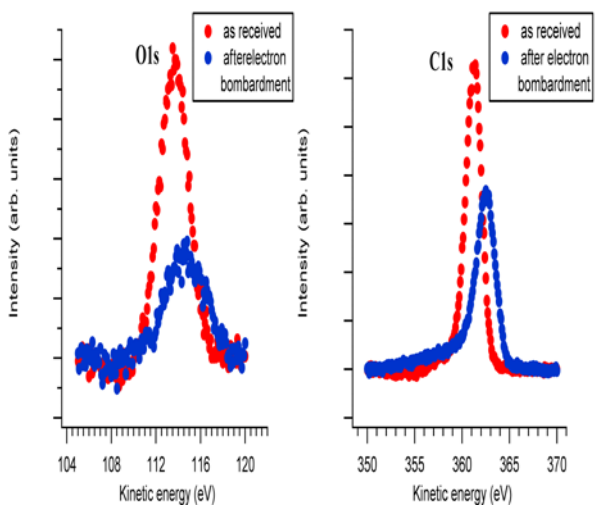

Figure 2: O1s (left) and C1s (right) core level spectra measured before and after electron bombardment.

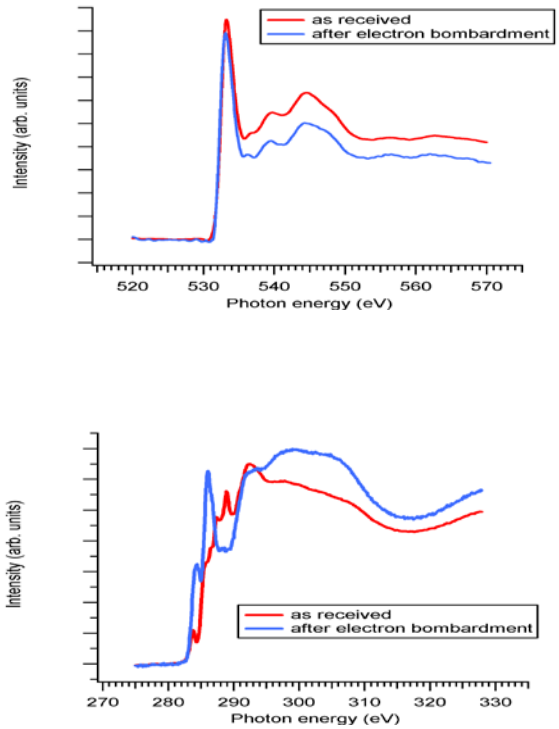

Figure 3: Absorption spectra measured at the K-edges of oxygen (top) and carbon (bottom).

Both photoemission and absorption measurements confirm that the electron bombardment results in the graphitization of the carbon impurities on the copper surface. At the same time, δ_{Max} of SEY curves (not shown) [12, 13], decreases to ~1.1 after the electron doses. Similarly, graphitization and decrease in SEY were also observed in other materials [17] after the irradiation with primary electron beams of 5 keV [7, 9]. Thus we conclude that the electron beam-induced graphitization results in the decrease of the SEY.

These results show that the SEY reduction can be confidently associated to the formation, on the surface, of a graphitic layer and suggest new researches directed to develop novel technologies to produce and test innovative materials, such as graphitic coatings, with low intrinsic SEY to be used in accelerators to mimic what is actually happening during scrubbing. This line is also consistent with carbon coatings techniques under development at CERN and in other Laboratories. Such Carbon coatings may allow to suppress e-cloud effects down to comfortable levels. Some experimental efforts are already undergoing at LNF and in other accelerator centres like CERN, SLAC, CESR-TA and KEK-B and will be subject of future publications.

CONCLUSION

We report preliminary experimental results on the relation between the surface properties of LHC samples conditioned with a dose of electrons at 440 eV and the reduction of SEY. Photoemission and absorption measurements performed on samples before (as received) and after electron irradiation, confirm that the electron bombardment results in the graphitization of the carbon impurities on the copper surface. As a consequence of this chemical modification we observe a SEY decreasing to 1.1. This opens up the possibility of producing stable graphite films to lower SEY values of industrial materials to the desired values.

ACKNOWLEDGEMENT

We acknowledge the substantial help of V. Baglin, R. Flammini and R. Larciprete during the definition of the project and discussion of the data.

The experiments were funded by the group V committee of the INFN.

REFERENCES

[1] M.E. Biagini, R. Boni, M. Boscolo et. al, proceedings of European Particle Accelerator Conference (EPAC08), and references therein p. 2605.

[2] M. Izawa, Y. Sato, T. Toyomasu, Phys. Rev. Lett. 74 (1995) 5044; K. Ohmi, Phys. Rev. Lett. 75, (1995) 526.

[3] Proceedings of ECLOUD'02, ECLOUD'04, ECLOUD'07 and references therein.

[4] R. Cimino, I. R. Collins, M. A. Furman, M. Pivi, F. Ruggiero, G. Rumolo, F. Zimmermann, Phys. Rev. Lett. 93 (2004) 014801.

[5] C. Scheuerlein, M. Taborelli, J. Vac. Sci. Technol. A 20 (1) (2002) 93-101; C. Scheuerlein, M. Taborelli, N. Hilleret, A. Brown, M. A. Baker, Appl. Surf. Sci. 202 (2002) 57-67.

[6] M. Nishiwaki, S. Kato, J. Vac. Sci. Technol. A 25 (2007) 675.

[7] M. Nishiwaki, S. Kato, Vacuum 84 (2010) 743.

[8] R.E. Kirby, F.K. King, Nucl. Instr. And Meth. A 469 (2001) 1-12.

[9] F. Le Pimpec. R. E. Kirby, F. K. King, M. Pivi, J. Vac. Sci. Technol. A 23 (2005) 1610.

[10] M. Pivi, G. Collet, F.K King, R. E. kirby et al. Nucl. Instr. And Meth. A 621 (2010) 47.

[11] P. He et al., in proceedings of European Particle Accelerator Conference (EPAC04), p. 1804.

[12] R. Cimino, M. Commisso, T. Demma, A. Grilli, M. Pietropaoli, L. Ping, V. Sciarra, V Baglin, P. Barone, A. Bonanno, proceedings of European Particle Accelerator Conference (EPAC08), p. 1592.

[13] M. Commisso, R. Cimino et al., to be published.

[14] Balerna et al. LNF Annual report 2008 and 2009.

[15] http://www.iom.cnr.it/

[16] BEAR: a Bending Magnet for Emission Absorption and Reflectivity, S. Nannarone, A. Giglia, N. Mahne, A. De Luisa, B. Doyle, F. Borgatti, M. Pedio, L. Pasquali, G. Naletto, M.G. Pelizzo, G. Tondello, NOTIZIARIO NEUTRONI E LUCE DI SINCROTRONE-Vol. 12 (2007) 8-19.; The UHV Experimental Chamber For Optical Measurements (Reflectivity and Absorption) and Angle Resolved Photoemission of the BEAR Beamline at ELETTRA, L. Pasquali, A. De Luisa, S. Nannarone, CP705, Synchrotron Radiation Instrumentation: Eight International Conference.

[17] M. Nishiwaki, S. Kato in proceedings of ECLOUD'07, 2007. p.82.

Feedback Control of SPS E-clouds / Transverse Mode Coupled Instabilities*

C. Rivetta †, A. Bullit, J.D. Fox, T. Mastorides, G. Ndabashimiye, M. Pivi, O. Turgut (SLAC, USA),
W. Hofle, B. Savant (CERN, Switzerland), and R. Secondo, J.-L. Vay (LBNL, USA)

Abstract

The CERN SPS at high intensities exhibits single bunch transverse instabilities induced by electron clouds and strong head-tail interactions. One proposal to mitigate these instabilities is to use feedback systems with enough bandwidth to sense the transverse position and apply correction fields to multiple sections of the nanosecond-scale bunch. To develop the feedback control prototype, different research areas has been pursed to model and identify the bunch dynamics, design the feedback control and implement the GigaHertz bandwidth hardware. This paper presents those R & D lines and reports the progress until present time.

INTRODUCCION

Intrabunch instabilities induced by electron clouds and strong head-tail interactions are one of the limiting factors to reach the maximum beam currents in SPS and LHC rings [1]. The effect of coating the chambers and adding grooves to the surface of those structures has been studied to mitigate intrabunch and collective effect instabilities induced by electron clouds (e-clouds) [2]. CERN is proposing a plan to coat large part of the SPS and LHC chambers in order to mitigate e-cloud instabilities. Continuous testing of the limitations of these techniques and the design of the necessary infrastructure to apply the coating are currently conducted al CERN [3]. These techniques cannot mitigate transverse mode coupled instabilities (TMCI) and research is conducted at CERN SPS to evaluate the maximum stable beam current that is possible to accelerate adjusting the beam chromaticity.

Feedback techniques can stabilize bunch instabilities induced not only by e-clouds but also induced by strong head-tail interactions (TMCI). Complementary to the plan previously described, US LHC Accelerator Research Program (LARP) is supporting a collaboration between US Labs and CERN to study the viability of controlling intrabunch instabilities using feedback control techniques. A collaboration among SLAC / LBNL / CERN (under the DOE LARP program) started evaluating the limitations of this technique to mitigate both instabilities and other possible head-tail distortions in bunches [4].

The application of feedback control to stabilize the bunch is challenging because it requires bandwidth sufficient to sense the transverse position and apply correction fields to multiple sections of a nanosecond-scale bunch. These requirements impose technology challenges and limits in the design [5]. Additionally, the intra-bunch dynamics is more challenging than the beam dynamics involving the interaction between bunches. The collaboration has defined different interdependent working lines to study the problem, to design a feedback control channel and to develop the hardware of a control system prototype to prove principles and evaluate the limitations of this technique by stabilizing a few bunches in the CERN SPS machine. This paper gives an overview of the research areas and plans, measurements and results of present studies, and goals and future directions.

RESEARCH & DEVELOPMENT PLAN - GOALS

The US and CERN collaboration was proposed recently (in October 2008) to mitigate via feedback e-clouds, TMCI, and other intra-bunch distortions and instabilities at SPS and LHC. The motivation of this collaboration is to control e-clouds and TMCI via GigaHertz bandwidth feedback systems. The immediate goal is to analyze and define design techniques for the system, study the limitations of the feedback technique to mitigate those instabilities, and build the hardware of a minimum prototype to control a few bunches and measure the limiting performance. The design of a final system is based on the results of this first stage.

The collaboration has defined different working lines that involve:

1. Development of reduced mathematical models of the bunch dynamics interacting with e-clouds and machine impedances. Identification of those reduced models based on machine measurements. Design of control feedback algorithms based on the reduced models.
2. Inclusion of realistic feedback models in advanced multi-particle simulation codes to test the models, possible feedback designs and diagnostic tools.
3. Measurements in the SPS machine to validate both the reduced and multi-particle models
4. Development of hardware prototypes to sense and drive the transverse position of different sections of the bunch. Development of hardware prototype of feedback control processing channel.

* Work supported by the US-DOE under Contract DE-AC02-76SF00515

† rivetta@slac.stanford.edu

The main goal is to model the bunch dynamics using both reduced mathematical models and multi-particle non-linear models and validate them via real measurements in the machine. It allows to perform model-based design of the feedback control system including uncertainties, signal perturbations and noise in the channel. Multi-particle codes will define a test-bench for both the designed control algorithms and also the diagnostic tools used during the machine measurements. Based on validated and realistic models of the system, the design can be translated directly to the hardware prototype. The final performance of the system will be tested by controlling a few bunches in the CERN SPS machine. A simplified chart of this Research and Development (R & D) plan is depicted in Fig. 1. After validating and testing the feedback control prototype and evaluating cost and performance a final design, production and commissioning of the system will be conducted.

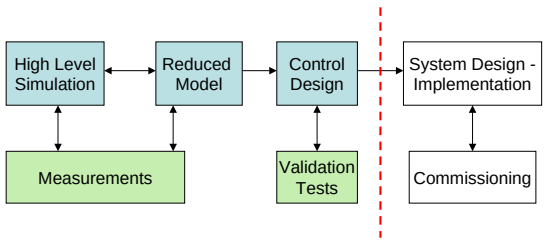

Figure 1: Simplified R & D chart for the development of the wideband feedback control system.

GENERAL OBSERVATIONS FROM MEASUREMENTS AND SIMULATIONS

Several machine measurements where conducted at SPS during summer 2009 and 2010 [5]. The main purpose was to capture the data to analyze different signatures of the bunch dynamics when it interacts with electron clouds. Part of this data has been used to validate multi-particle simulation results, comparing the measurements with simulation results describing similar conditions that the machine. Some representative results form the measurements are shown in the following figures. During the measurements on June 2009, two batches with 72 bunches each were injected to the SPS at 26GeV and $1x10^{11}$protons/bunch. The first batch was stable but the second batch exhibited groups of bunches with e-cloud instabilities. Fig. 2 depicts the vertical pick-up signals after equalization to recover the original bunch profile. The SUM signal is the sum of the upper/lower plates of the pick-up and it is proportional to the bunch profile. The DIFF signal is the difference between upper/lower plates and it is proportional to the vertical position of the bunch. The extracted vertical signal shows the vertical position of different sectors of the bunch. It is important to notice that bunch 47 in the first batch is stable but the same bunch in the second batch (bunch 119) shows oscillations. This oscillation is larger in the tail of the bunch (bunch tail : right side of the bunch). It also gives an idea of the bandwidth required for the feedback system. The feedback channel has to sense signals that have a few periods in the bunch span (3 ns.), compute and apply correction signals through the kicker in the same time span.

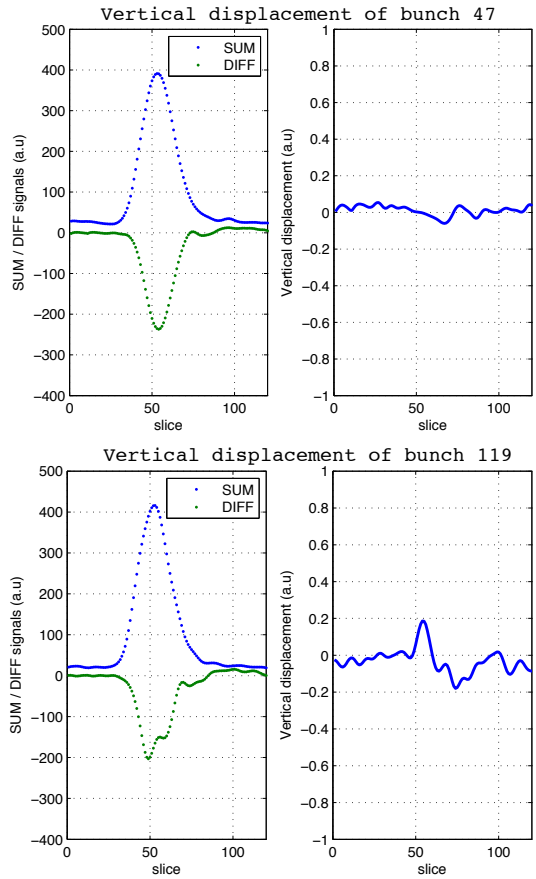

Figure 2: *Upper*: SUM-DIFF signals, vertical displacement for bunch 47. - *Lower*: SUM-DIFF signals, vertical displacement for bunch 119. (*time scale: 2ps/slice*)

Other valuable information from these measurements is that the dynamics for different sectors of the bunch is different. Figure 3 shows the unstable vertical motion for several turns of three representative areas of the bunch. Measuring the frequency spectrum of different sectors in the tail of the bunch, it was observed that the fractional tune shifts due to the e-cloud interaction with the bunch. Fig. 4 depicts the frequency shifting from the nominal tune 0.185 for this machine to 0.197. Simulations have shown larger tune shifts at different energies for sectors in the tail of the bunch.

FEEDBACK STABILIZATION OF INTRA-BUNCH INSTABILITIES

General Considerations for Feedback Design

The proposed digital feedback control topology to stabilize the transverse vertical oscillations within the bunch due to the interaction with the electron clouds and machine impedances is depicted in Fig. 5. The vertical dis-

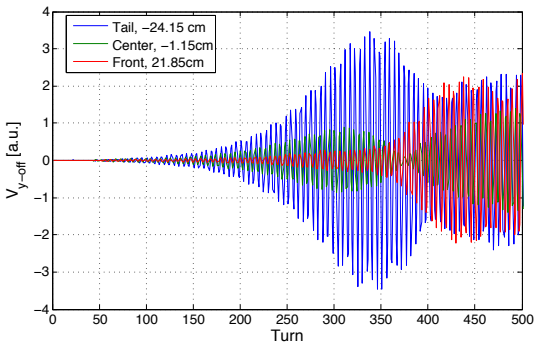

Figure 3: Vertical motion in time domain for different sections of the bunch.

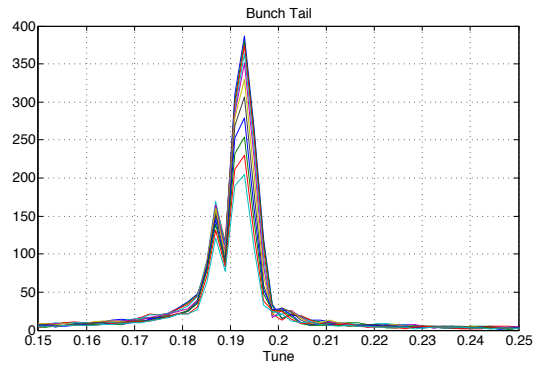

Figure 4: Spectrum corresponding to a few sections of the bunch tail.

placement of different sections along the longitudinal axis of the bunch is estimated and converted to a digital signal V_y by the receiver and ADC. Those samples are processed to generate the control signal V_C and converted to analog signal by the DAC. This signal drives the amplifier and kicker to apply correction fields to multiple sections of the nanosecond-scale bunch.

Based on previous observations, the bunch dynamics interacting with the machine impedance (TMCI) and e-clouds is non linear and unstable. The design of an stabilizing feedback control will have multiple constraints due to the complex bunch dynamics. The original instability of the bunch will set a minimum open loop gain in the feedback system, while the intrinsic delay in the control action will limit the maximum gain. Bunch dynamic characteristics as the growth rate or tunes change intrinsically and also the beam dynamics change with the machine operation. These parameter or dynamic variations force to design robust or adaptive controllers in order to preserve the stability and performance of the feedback system in presence of those variations during operation. Additionally, the feedback control system has to reject noise and perturbations, like horizontal signals cross-talked with the vertical signals detected.

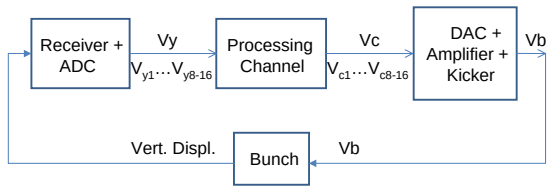

Figure 5: General block diagram of wideband feedback control to stabilize e-clouds/TMCI bunch instabilities.

Hardware prototype

To evaluate the minimum hardware prototype required to control a few bunches in the SPS ring, in addition to the data previously presented, it is possible to analyze the spectrum of the unstable bunches measured during the e-clouds study. Figure 6 depicts the spectrum of the stable bunch 45 (first batch) and the unstable bunch 119 (bunch 47-second batch) for turns 1 - 600. Based on the unstable bunch, it suggests that the bunch spectrum presents frequency components that extent up to near 1 GHz, requiring such a processing capability in the feedback system.

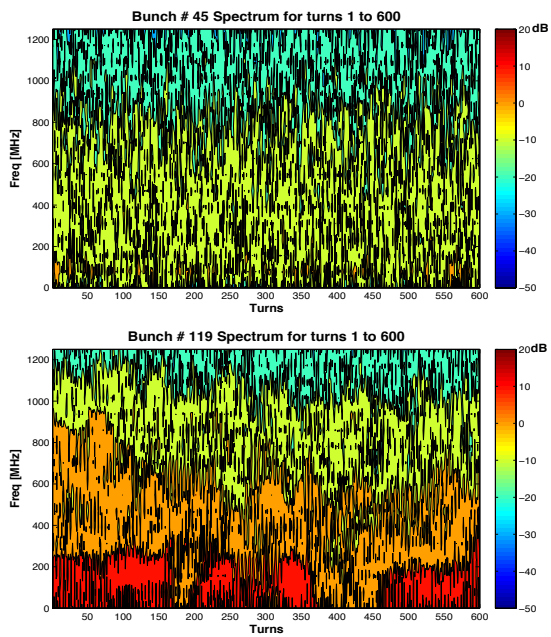

Figure 6: Frequency spectrum for bunch 45 (stable) and bunch 119 (unstable)

The hardware under development consists of a digital processing channel, sampling the signals at 4 Giga Samples/sec. This sampling rate is 8 times higher than actual commercial bunch-by-bunch feedback units. A general block diagram of the proposed hardware is depicted in fig. 7. The amount of multiplication/accumulate (MACs) operations in the processing channel, assuming simple architectures for the control algorithm, can exceed 5-8 Giga-MACs/sec setting to the limit the complexity of the digital processing channel. Wideband pick-ups already installed in the SPS accelerator (exponential strip-lines) have

been used as horizontal and vertical beam position monitors (BPM) for the measurements [6]. One of the pick-ups is planned to be used as a kicker to conduct studies driving the bunch. The existent pick-ups have been characterized and exhibit limitations to use them effectively as part of the feedback system. Mainly, there are resonances in the chambers holding the pick-ups, limiting the maximum frequency of the signal detected up to 1.7 GHz. Similarly, the pick-up used as kicker has a limited bandwidth of about 200 MHz. It is planned to develop and build new BPMs and kickers with required bandwidth above 1-2 GHz. and install them in the machine during the one year shut-down starting in 2012.

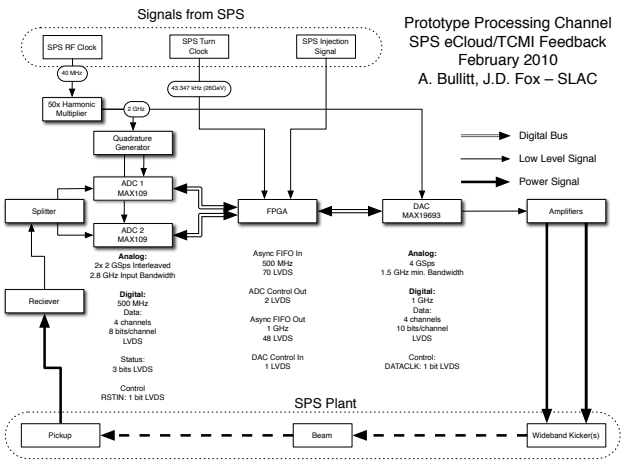

Figure 7: Block diagram of the proposed hardware prototype

.

Multi-particle Simulation Codes - Feedback Control Models

Given the actual limitations both in time and in the hardware installed in the SPS ring to test the feedback system, non-linear simulators based on multi-particle description of the bunch and e-clouds (WARP, HeadTail, CMAD) have been very useful to analyze the bunch dynamics and reduced models as well as to generate analysis tools to process the measured data [7]. The effort now is to include in those simulation codes realistic models of the feedback system to have a test-bench to analyze the impact in the stability and final emittance of the bunch of finite number of samples per bunch, hardware limitations, bandwidth and noise. Figure 8 depicts a block diagram of the model included in multi-particle simulation codes to represent a realistic feedback channel and analyze the principal limitations in the feedback control introduced by the hardware. The receiver, amplifier and kicker are modeled introducing the real frequency response. Additionally, the amplifier and kicker have limited power capabilities, and noise and spurious signals perturbs the feedback signal detected representing the vertical displacement of different parts of the bunch. In that figure, it is important to observe that the bunch is modeled using multiple particles but the main information linking the bunch dynamics and the feedback system is described by the coordinates of 64 longitudinal slices. The feedback channel uses the information of 8 samples that correspond to a sampling frequency of 4 G Samples/sec (More samples, *e.g. 16 samples*, can be included to represent higher sampling rates in the processing channel). All these constraints affects the stability and performance of the system.

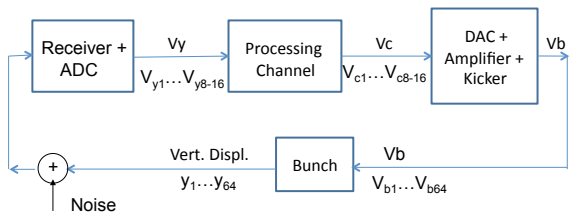

Figure 8: Block diagram of the feedback system modeled in multi-particle code simulators (CMAD-Warp-HeadTail)

.

Reduced Mathematical Models of Bunch Dynamics - Identification

Development of reduced mathematical models to describe the bunch dynamics is important to design the feedback control taking into account not only the intrinsic bunch dynamic but also noise, system perturbations and other uncertainties and limitations. Simple models consisting of a set of coupled oscillators have been evaluated comparing their behavior with results from simulations based on multi-particle codes and measurements. Presently a set of oscillators with time-variant parameters is under study to model the vertical displacement of different areas of the bunch and take into account the synchrotron motion of the particles within the bunch.

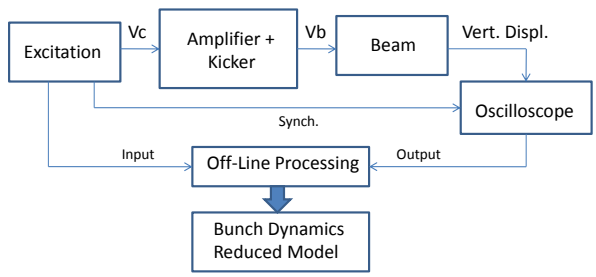

Figure 9: Set-up for reduced model identification of bunch dynamics.

.

The parameters of the reduced model are identified from measurements. A research effort is in place to generate tools to be able to identify the bunch dynamics directly form measurements in the machine based on the reduced models. An identification technique has been used to define the growth rate and fractional tunes of different sections of

the bunch using the measurement of unstable oscillations as those depicted in Figs. 3 and 4. It is planned to identify the bunch dynamics in a more controlled behavior stabilizing the beam and driving the bunch by injecting sequences of random noise. The parameters of the reduced model can be calculated by analyzing the vertical displacement response of the bunch to that stimulus. Figure 9 depicts the block diagram of the system identification set-up. The bunch is driven by a random sequence V_C generated by the excitation and the bunch vertical displacement is estimated by post-processing the oscilloscope measurements. Off line processing using identification routines based on a reduced model of the bunch are used to calculate the model parameters. Based on data generated by using multi-particle simulation codes, an example of the identification test is shown in Fig. 10. This figure depicts the vertical displacement of different longitudinal bunch slices (Samples 9 - 11) when the bunch is driven by a random sequence (Measured Output - Solid Lines). The estimated output depicts the response of the identified reduced model of the bunch to the same random excitation.

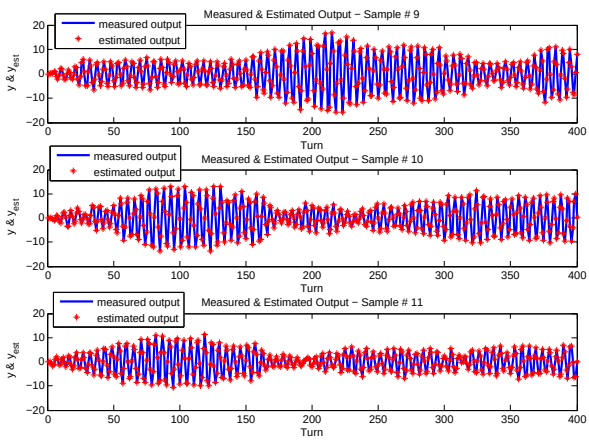

Figure 10: Response of identified reduced model.

.

SPS MACHINE MEASUREMENTS

Data collected and results from SPS machine developments and measurements (MD) have been very useful to validate results and adjust parameters in the multi-particle simulation codes. Conducted MDs have measured the natural behavior of the bunch dynamics interacting with electron clouds. To improve the multi-particle simulation codes and incorporate the feedback processing channel, more measurements in the machine are necessary to characterize the dynamics when the bunch is driven by an external excitation. In the next MD (Spring 2011), it is planned to drive the beam with the existent kicker installed in the SPS machine using a set-up similar to the one depicted in Fig. 9. The main goal with these tests is to drive different longitudinal sections of the bunch near the e-cloud instability threshold. These tests will allow measuring vertical tune shifts due to the e-cloud interaction with the bunch and also collect data to test the bunch dynamics identification algorithms. Driving tests are important to validate previous measurements conducted to estimate the kicker gain and strength and the power levels necessary to drive the beam. These results will give solid data necessary for the design of the new wide-band kicker. Additionally, because the excitation board depicted in Fig. 9 has the basic functions of the back-end of the feedback control system prototype, this MD will be very useful to test the timing and synchronization with the SPS machine and quantify timing errors.

Plans for SPS shutdown

The dedicated hardware installed in the SPS to be used by the wideband feedback system has limited frequency response and power capability. The goal during the SPS shutdown is to replace this hardware. New wideband BPM is being designed at CERN and an accelerated research program to study different kicker options is conducted by the collaboration. After choosing the best option for the kicker technology, the idea is to build a prototype and install it in the SPS ring during the shutdown.

CONCLUSIONS

This paper presented the R& D plan and progress directed toward the control of transverse intrabunch instabilities using Giga Hertz bandwidth feedback techniques. To design and build a prototype to control a few bunches in the SPS ring, a collaboration between US Labs and CERN has been established. This collaboration has identified different important areas that includes the modeling and measurement of the bunch dynamics interacting with e-clouds and the machine impedance, the model-based design of the control feedback algorithms and the development of wideband hardware to implement the feedback system. Part of this hardware will be installed during the SPS shutdown to have the appropriated feedback control implementation to control a few bunches and demonstrate the feasibility and quantify the limitations of this feedback technique.

ACKNOWLEDGEMENTS

We thanks the SLAC AARD, CERN AB RF departments and the US LARP for the support.

REFERENCES

[1] G. Arduini *et al.* 31^{st} Advanced ICFA Beam Dynamics Workshop Napa, CA, USA, CERN-2005-001.

[2] F. Caspers, S. Federmann, E. Mahner, P. Pinto, D. Seebacher, M. Taborelli, B. Salvant, C. Yin Vallgren, "Electron Cloud Measurements of Coated and Uncoated Vacuum Chambers in the CERN SPS by Means of the Microwave Transmission Method," 1^{st} International Particle Accelerator Conference: IPAC'10, Kyoto, Japan, May 2010, pp TUPEA076.http://www.JACoW.org.

[3] Christina Yin Vallgren, *et al.* "Amorphous Carbon Coatings for Mitigation of Electron Cloud in the CERN SPS," 1^{st} International Particle Accelerator Conference: IPAC'10, Kyoto, Japan, May 2010, pp TUPD048. http://www.JACoW.org.

[4] J.D. Fox, T. Mastorides , G. Ndabashimiye, C. Rivetta, D. Van Winkle, J. Byrd, J-L Vay, W. Hofle, G. Rumolo, R. De Maria,"Feedback Techniques and Ecloud Instabilities - Design Estimates," Particle Accelerator Conference PAC 2009, Vancouver, BC, Canada, May 2009. http://www.JACoW.org.

[5] J.D. Fox, A. Bullitt, T. Mastorides , G. Ndabashimiye, C. Rivetta, O. Turgut, D. Van Winkle, J. Byrd, M. Furman, J-L Vay, W. Hofle, G. Rumolo, R. De Maria. "SPS Eclouds Instabilities - Analysis of Machine Studies and Implications for Eclouds Feedback," 1^{st} International Particle Accelerator Conference: IPAC 2010, Kyoto, Japan, May 2010, pp. WEPEB052.http://www.JACoW.org.

[6] R. Di Maria *et al.*, "Performance of Exponential Coupler in the SPS with LHC Type Beam for Transverse Broad-band Instability Analysis," 2009 DIPAC MOPD17.

[7] Jean-Luc Vay *et al.*, "Update on Electron-Cloud Simulations Using the Package WARP-POSINST," Particle Accelerator Conference PAC 2009, Vancouver, BC, Canada, May 2009, pp. FR5RFP077 http://www.JACoW.org.

SIMULATED PERFORMANCE OF AN FIR-BASED FEEDBACK SYSTEM TO CONTROL THE ELECTRON CLOUD SINGLE-BUNCH TRANSVERSE INSTABILITIES IN THE CERN SPS*

R. Secondo†, J.-L. Vay, J. M. Byrd, M. A. Furman, M. Venturini (LBNL, USA),
J. D. Fox, C. H. Rivetta (SLAC, USA), and W. Höfle (CERN, Switzerland)

Abstract

The operation at high current of high-energy proton machines like the SPS at CERN is affected by transverse single-bunch instabilities due to the Electron Cloud effect [1]. As a first step towards modeling a realistic feedback control system to stabilize the bunch dynamics, we investigate the use of a Finite Impulse Response (FIR) filter to represent the processing channel. The effect of the processing channel on the bunch dynamics is analyzed using the macro-particle simulation package Warp-Posinst. We discuss the basic features of the feedback model, report on simulation results, and present our plans for further development of the numerical model.

INTRODUCTION

Electron clouds in the SPS at CERN are responsible for the occurrence of large and fast growing transverse instabilities in high-intensity proton beams. A feedback (FB) control system to damp transverse instabilities has been proposed and is currently under study [2]. The particle-in-cell, macroparticle simulation code suite Warp-Posinst is being used to model the dynamics of the beam-electron interaction and the action of the feedback system on the beam with the intent to determine the basic requirements for the FB system such as minimum bandwidth and amplitude of the kicker signal necessary to achieve stability.

Figure 1 shows a schematic of the control loop.

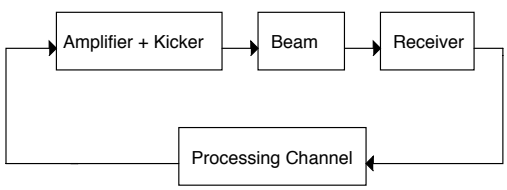

Figure 1: General scheme of the SPS Ecloud Feedback Control System.

The processing channel discussed in this paper is based on a simple bandpass FIR filter, which is more realistic than the model utilized in previous studies [3]. The filter limits the bandwidth around the nominal betatron tune frequency, eliminating spurious signals and advancing the phase at the tune frequency. Single-bunch simulation results are presented comparing open (FB off) and closed (FB on) loop cases and analyzing the vertical motion of bunch slices. The model of the kicker is ideal and has no bandwidth limitation. As a first pass towards evaluating the gain requirement of the amplifier driving the kicker, we performed several simulations limiting the kick signal to a nominal saturation level and studied how this affects the control of the beam dynamics. Conclusions and future developments of the numerical model are discussed in the last section.

FEEDBACK MODEL

The simple $5-$tap band-pass FIR filter used in our studies damps the beam vertical motion while limiting the bandwidth around the nominal fractional tune $[Q_y] = 0.185$ and performing a phase advance of 90 deg around the nominal tune value. The filter has 5 taps, *i.e.* it is based on 5 previous measurements $y_i(k)$ of the bunch vertical displacement taken at a fixed location around the ring. The output $z_i(k)$ is calculated as

$$z_i(k) = a_1 y_i(k-1) + a_2 y_i(k-2) + ... + a_n y_i(k-n) \quad (1)$$

where $i = 1, \cdots, N_{\text{slices}}$ identifies the bunch slice, k is the machine turn no., $n = 5 =$ is the # of taps, and the set of coefficients $a_1, a_2 ... a_n$ define the impulse response of the filter. This set of coefficients depends on the design of the transfer function chosen. The FIR Bode plot is reported in Fig. 2.

The output signal of the filter is used to kick each slice of the bunch. The kick is applied on a one-turn delay basis at the position along the accelerator where the beam is sampled.

The action of the feed-back system can be represented in terms of the following simplified linearized model of bunch dynamics

$$y'' + \omega^2 y = K(y_e - y) + \Delta_{p_\perp}, \quad (2)$$

where y is the amplitude of the transverse oscillation of a beam slice and y_e the transverse offset of the electron cloud baricenter corresponding to that slice; the constant K is a measure of the interaction between the beam and the electron cloud and $\Delta_{p_\perp}$ the signal from the kicker. A functioning feed-back will force the vertical displacement

* Work supported by the US-DOE under Contract DE-AC02-05CH11231, the SciDAC program ComPASS and the US-LHC Accelerator Research Program (LARP). Used resources of NERSC and the Lawrencium cluster at LBNL

† rsecondo@lbl.gov

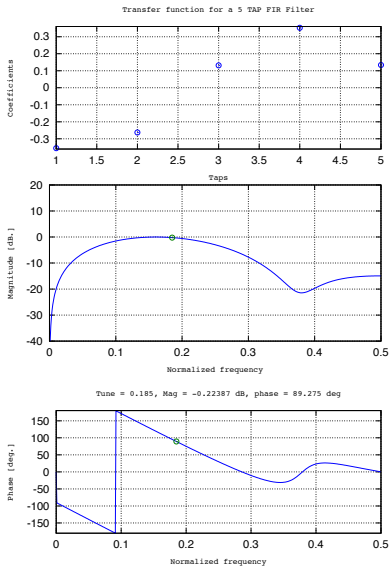

Figure 2: FIR filter Bode Plot. The frequency response has maximum magnitude 0 dB and phase 90 deg around $[Q_y] = 0.185$

of each slice of the bunch toward zero $y \simeq 0$, reducing (2) to

$$K y_e \simeq \Delta_{p_\perp}, \tag{3}$$

suggesting that analyzing $\Delta_{p_\perp}$ will give a measure of the interaction between the e-cloud and the bunch.

SIMULATION RESULTS

Single-bunch simulations were performed at the SPS injection energy $E = 26$ GeV, assuming a uniform distribution of electrons $n_e = 10^{12} m^{-3}$ in all stations around the ring. In all cases discussed here we applied an initial uniform vertical offset to the bunch with 10% amplitude relative to σ_y. The feedback loop is closed in order to damp the beam using the FIR filter. The kicker is ideal and has no bandwidth limitation. The beam dynamics in the ring assumes a smooth approximation for the lattice. For more details on the physics model implemented in Warp-Posinst we refer to [3].

Table 1 reports the beam parameters used in all runs.

Figure 3 shows the vertical displacement of one slice in the tail of the bunch both in the open and closed loop cases. In open loop the bunch develops a strong instability due to the electron cloud, while in closed loop the oscillation is controlled and the beam transverse oscillations are well damped.

Figure 4 reports the momentum change imparted by the kicker to each bunch slice at each machine turn. Notice that in spite of the apparent stabilization of beam centroid motion (see red curve in Fig. 3) a finite signal of the kicker is still required, particularly in the head and tail of the bunch, with the tail needing a stronger kick compared to the head. We plan to carry out further studies to determine the physical basis of this behavior or a possible dependence on spurious numerical effects in the simulations.

Table 1: WARP Parameters used in the SPS simulations

Parameter	Symbol	Value
beam energy	E_b	26 GeV
bunch population	N_b	1.1×10^{11}
rms bunch length	σ_z	0.23 m
rms transversal emittance	$\epsilon_{x,y}$	2.8, 2.8 mm.mrad
rms momentum spread	σ_{rms}	2×10^{-3}
beta functions	$\beta_{x,y}$	33.85, 71.87 m
betatron tunes	$Q_{x,y}$	26.13, 26.185
chromaticities	$Q'_{x,y}$	0, 0
cavity Voltage	V	2 MV
mom. compact. factor	α	1.92×10^{-3}
circumference	C	6.911 km
# of beam slices	N_{slices}	64
# of stations/turn	N_s	20

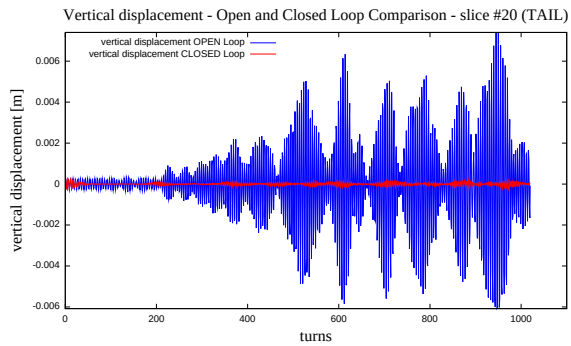

Figure 3: Comparison between open and closed loop cases of a slice vertical displacement in the tail of the bunch.

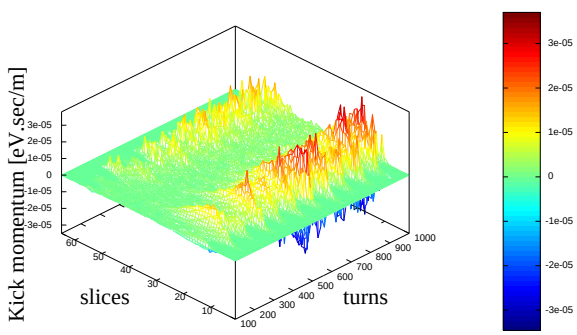

Figure 4: Momentum slices vs. turns, applied to the bunch by the kicker. The first 100 turns are cut off to avoid displaying the initial offset. Slices close to 0 represent the tail of the bunch, while slices close to 64 represent the head.

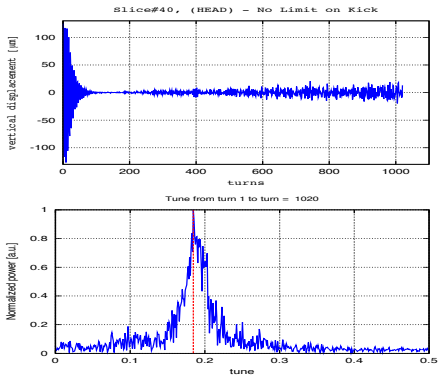

Figure 5: Vertical displacement vs. turns and fractional tune of a slice in the head of the bunch. The fractional tune has a maximum peak at $[Q_y] = 0.185$.

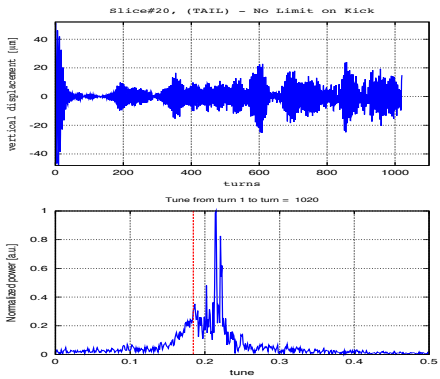

Figure 6: Vertical displacement vs. turns and fractional tune of a slice in the tail of the bunch. The fractional tune is shifted and has a maximum peak at $[Q_y] = 0.2149$.

Figures 5 and 6 show the vertical displacement and fractional betatron tune of a slice, respectively in the head and tail of the proton bunch. After the initial offset oscillation the instability is well damped in both cases. The fractional tune of the tail is characterized by a large shift, similar to the one in open-loop case, Figure 7. For the moderate value of the electron density considered in this study the filter appears to perform well in damping the instability, however we have yet to try to optimize its design.

An important issue of the system is given by the limits in terms of power of the amplifier that drives the kicker. If the amplifier saturates the value of the kicker signal could not be sufficient to control the instability. We ran simulations with the purpose of understanding the limits of the kicker efficiency in controlling the instability by forcing the kicker signal to saturate at a pre-set value.

Figure 8 shows the momentum applied to the bunch in the case of a saturation value of $2.874 \cdot 10^{-5}$ eV.sec/m in momentum units. With this constraint the beam looks initially stable but a vertical instability soon appears and

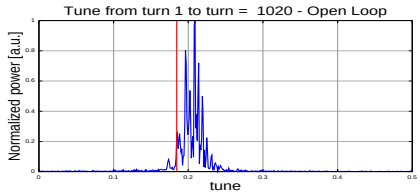

Figure 7: Fractional betatron tune of a slice in the tail of the bunch in Open Loop case. The tune is shifted and has a maximum peak at $[Q_y] = 0.20903$.

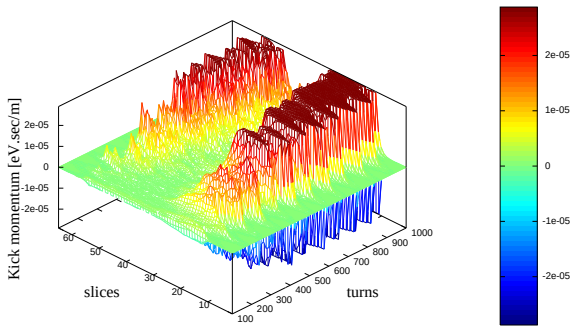

Figure 8: Momentum, slices vs. turns, applied to the bunch by the kicker, the signal is set to saturate at $2.874 \cdot 10^{-5}$ eV.sec/m. Slices close to 0 are in the tail of the bunch, while slices close to 64 are in the head.

grows exponentially as the simulation progresses. As already noticed in reference to Figure 4, even if the proton bunch is initially stabilized by the feedback the kicker needs to keep applying a momentum kick to the bunch to maintain stability. However, in this case the kicker cannot provide all the required correction signal due to the imposed limitation on the maximum voltage allowed. Finally, notice that the instability appears larger in the bunch tail, Figure 9, compared to the bunch head, Figure 10, and in both cases the beam tune is shifted.

CONCLUSION

Transverse single-bunch instabilities have been observed in the SPS at CERN due to e-cloud effects and are acknowledged as possible serious limitation to any future intensity upgrade of the LHC injection complex. A feedback control system could help overcome these limitations and represents an attractive potential solution. As part of the R&D required for a feasibility study we have started to carry out numerical simulations using the Warp-Posinst code to model the effect of a feed-back system on the beam in the presence of e-cloud. See also [5]. A simple FIR filter has been used as an improvement on previous approaches to represent the processing channel in the feedback loop model.

Single-bunch simulations using an ideal kicker show that the feedback system is effective at suppressing the vertical instability that would otherwise appear in the presence of

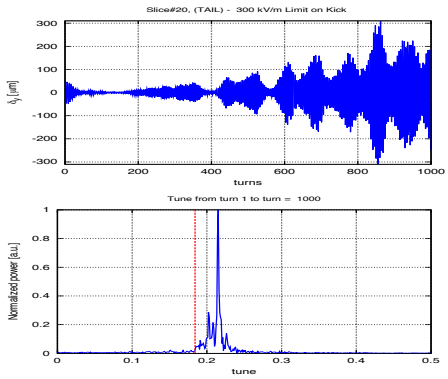

Figure 9: Vertical displacement vs. turns and fractional tune of a slice in the Tail of the bunch. The kicker signal saturates at $2.874 \cdot 10^{-5}$ eV.sec/m. The instability grows larger and faster compared to the head. The tune is shifted to $[Q_y] = 0.2152$.

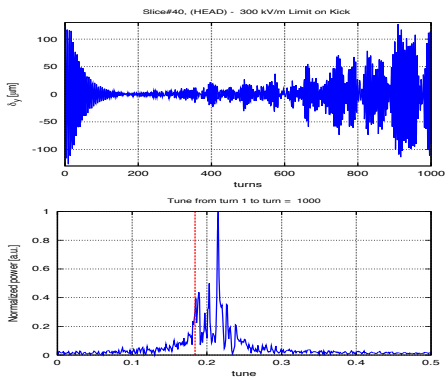

Figure 10: Vertical displacement vs. turns and fractional tune of a slice in the head of the bunch. The kicker signal saturates at $2.874 \cdot 10^{-5}$ eV.sec/m. The beam becomes increasingly unstable and the fractional tune maximum peak is shifted to $[Q_y] = 0.2152$.

a $n_e = 10^{12} m^{-3}$ e-cloud density. The vertical motion of the bunch is well damped when no limitation is imposed to the amplitude of the kick signal but a vertical instability eventually reappears in the case where a saturation level of $2.874 \cdot 10^{-5}$ eV.sec/m in momentum is imposed on the kicker field.

Future improvements of the numerical model will include the frequency response of the receiver and the kicker, downsampling the beam from $N_{slices} = 64$ to a more realistic $N_{slices} = 8$, and adding noise in the loop to investigate the minimum gain required for stability.

REFERENCES

[1] G. Arduini et al., CERN-2005-001, 31-47 (2005)

[2] J. D. Fox et al., SPS Ecloud Instabilities - Analysis of machine studies and implications for Ecloud Feedback. Proceedings of IPAC 2010, Kyoto, Japan.

[3] J.-L. Vay et al., Simulation of E-Cloud Driven Instability and its Attenuation Using a Feedback System in the CERN SPS, Proceedings of IPAC 2010, Kyoto, Japan.

[4] J. M. Byrd, Simulations of the PEP-II transverse coupled-bunch feedback system, PAC95, Proceedings, (1996).

[5] C. H. Rivetta et al., Feedback Control of SPS E-Cloud/TMCI Instabilities, Proceedings of ECLOUD10, Cornell, Ithaca, USA.

STUDIES OF THE ELECTRON-CLOUD-INDUCED BEAM DYNAMICS AT CESR-TA*

G. Dugan, M. G. Billing, R. Meller, M. Palmer, G. A. Ramirez, J. Sikora, K. Sonnad, H. Williams,
CLASSE, Cornell University, Ithaca, NY 14853 USA
R. L. Holtzapple, California Polytechnic State University, San Luis Obispo, CA

Abstract

At CesrTA, we have developed the capability to make automated measurements of the self-excited frequency spectra of individual bunches, to look for signals for single-bunch instabilities. We can also drive single bunches and measure the rate of decay of selected lines in their frequency spectra. We have used these capabilities to explore the dynamics of the interaction of a multi-bunch beam with the electron cloud. The basic observation is that, under conditions of sufficiently high current and sufficiently low chromaticity, the multi-bunch frequency spectra exhibit vertical $m = \pm 1$ synchrobetatron (head-tail) lines, separated from the vertical betatron line by the synchrotron frequency, for many of the bunches along the train. The amplitude of these lines typically (but not always) grows along the train. The dependence of this effect on many of the parameters of the beam has been explored.

OVERVIEW

Introduction

To continue our studies of electron cloud related phenomena, we have developed the capability to make automated measurements of frequency spectra of individual bunches, to look for signals for single-bunch instabilities.

In this measurement, a button BPM at 33W (sensitive to both vertical and horizontal motion) is gated on a single bunch, and the signal is routed to a spectrum analyzer. Several frequency spectra are acquired, covering a range which spans the lowest betatron sidebands. Machine conditions, such as bunch current, magnet settings, feedback system parameters, etc. are automatically recorded and stored before and after each single-bunch spectrum is taken.

Using this system, during the recent July-August, 2010, and September runs, a number of observations were made which illuminate the dynamics of the electron-cloud/beam interaction at CesrTA. This paper will review results from these experiments.

General remarks

All experiments discussed here were done at 2.085 GeV in a low emittance lattice. The machine parameters are shown in Table 1.

Trains having bunches numbering from 30-45, with a bunch spacing of 14 ns, and bunch currents in the range of $0.5 - 1.25$ mA ($0.8 - 2.0 \times 10^{10}$ particles) per bunch were studied. In all cases, except where specifically noted, the beam particles were positrons.

Table 1: Nominal machine parameters. The emittances and tunes are those of a single bunch in the machine.

Parameter	Unit	Value
Energy	GeV	2.085
Lattice		2085mev_20090516
Horizontal emittance	nm	2.6
Vertical emittance	pm	~ 20
Bunch length	mm	10.8
Horizontal tune		14.55
Vertical tune		9.58
Synchrotron tune		0.065
Momentum compaction		6.8×10^{-3}
Revolution frequency	kHz	390.13

Several systematic checks were undertaken:

- Checks were made to rule out intermodulation distortion in the BPM electronics and in the BPM itself.
- The betatron and synchrobetatron (head-tail) lines moved as expected when the vertical, horizontal, and synchrotron tunes were varied.

The longitudinal feedback was off for these measurements. The vertical and horizontal feedback were turned down to 20% of full power. Some experiments explored the effect of turning the vertical feedback fully off.

More details on the experimental technique can be found in [2].

General observations

The basic observation is that, under a variety of conditions, the frequency spectra exhibit the vertical $m = \pm 1$ synchrobetatron (head-tail) lines, separated from the vertical betatron line by the synchrotron frequency, for many of the bunches along the train. The amplitude of these lines typically (but not always) grows along the train.

Typically, for the bunch at which the vertical synchrobetatron lines first appear above the noise floor (which is about 40 db below the vertical betatron line), we observe (on a bunch-by-bunch X-ray beam size monitor) growth in the beam size, which continues to increase along the train [3].

*Work supported by the US National Science Foundation (PHY-0734867) and Department of Energy (DE-FC02-08ER41538)

Under some conditions, the first bunch in the train also exhibits a synchrobetatron line ($m = -1$ only). The presence of a "precursor" bunch, placed about 180 ns before the train, eliminates the $m = -1$ signal in the first bunch.

Subsequent sections will present the details of these observations, together with their dependence on machine and beam parameters such as bunch current, number of bunches, chromaticity, synchrotron tune, beam emittance, vertical feedback, and particle species. In the final section, some preliminary observations on measurements of bunch-by-bunch damping rates are presented.

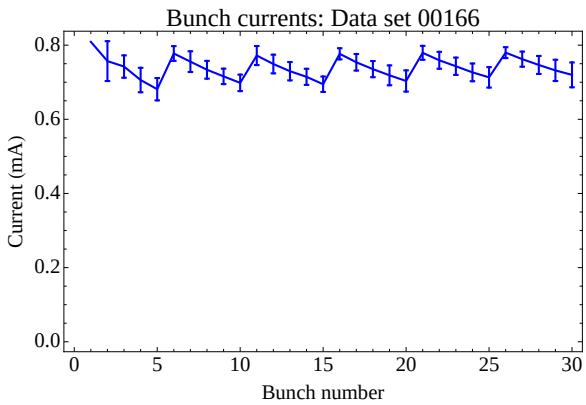

Figure 1: Data set 166: Bunch-by-bunch currents. See text for an explanation of the error bars.

BUNCH-BY-BUNCH POWER SPECTRUM

To measure a bunch-by-bunch power spectrum, the machine is loaded with a bunch train with a uniform current per bunch, and software is run to automatically collect frequency spectra from a button BPM gated on the first bunch. The data acquisition takes a few minutes, and the gate is then moved to the second bunch, and so on through the train. The gate width is much smaller than the bunch spacing, so only the motion of the gated bunch is observed. The frequency spectra are 10 s averages, acquired in 4 measurements, each with a 40 kHz span, covering the range from 170 to 330 kHz.

Since the beam has a relatively short lifetime, it is necessary to periodically pause the measurements and "top off" the bunch train. Typically, this is done after data acquisition is completed for a group of 5 bunches. Fig. 1 shows the beam current as a function of bunch number during a specific data set. In this figure, the current per bunch plotted for bunch n corresponds to the average value of the bunch current for all bunches earlier than bunch n; the error bar represents the rms variation in this number, principally due to irregularities in the fill. The dips at bunches 5, 10, ..., and peaks at 6, 11, ..., correspond to when the train is "topped off."

The bunch-by-bunch power spectrum observed in data set 166 is shown in Fig. 2. The figure plots the power spectrum for each bunch, as measured at the button BPM, vs. frequency. The four prominent peaks seen correspond, from lower to higher frequency, to the $m = -1$ vertical synchrobetatron line, the horizontal betatron line, the vertical betatron line, and the $m = +1$ vertical synchrobetatron line. Fig. 3 shows the spectrum of the last bunch, bunch 30, in greater detail. For this data set, the vertical chromaticity[1] was 1.16, and the horizontal chromaticity was 1.33.

The principal features exhibited in Fig. 2 and Fig. 3 are discussed in more detail in the next subsections.

POWER SPECTRUM FEATURES NEAR THE BETATRON LINES

Horizontal betatron lineshape

Fig. 4 shows the bunch-by-bunch power spectrum near the horizontal betatron line. There is a major peak which shifts up in frequency by about 4 kHz during the bunch train. This shift is attributable to the electron cloud. A quantitative comparison with simulations is presented below. In addition, there is a lower amplitude "shoulder", which appears to be roughly constant in frequency during the bunch train (i.e., there is no tune shift). A plausible explanation for this shoulder is the following: tune shift measurements and simulations[4] have shown that, when the all the bunches in the train are oscillating in-phase, the horizontal tune shift due to the electron cloud in a dipole-dominated ring such as CesrTA is very small. However, for the data set shown in Fig. 4, the bunches in the train are spontaneously excited, so a mixture of multibunch modes will be present. This mixture of multibunch modes will exhibit a spectrum of electron-cloud-induced tune shifts, ranging from nearly zero tune shift for the mode in which the bunches are oscillating in phase, to large tune shifts for modes in which bunches are oscillating with different phases. Qualitatively, this should produce a spectrum similar to that shown in Fig. 4.

Vertical betatron lineshape

Fig. 5 shows the bunch-by-bunch power spectrum near the vertical betatron line. In this case, there is a shift up in frequency of the major peak by about 2 kHz during the bunch train, which is again attributable to the electron cloud. In addition, there is a smaller peak at a higher frequency, present even on the first bunch, which appears to grow in amplitude and merge with the main peak near the end of the bunch train. Since this peak is present even for the first bunch, it is unlikely that it is due to a multibunch mode dependence of the vertical electron cloud tune shifts. Also, measurements and simulations[4] have shown that the dependence of the *vertical* tune shifts on the multibunch mode is much smaller than for the horizontal tune

[1] The chromaticity is defined as

$$\chi = \frac{dQ}{d\delta},$$

where δ is the relative momentum shift and Q is the tune.

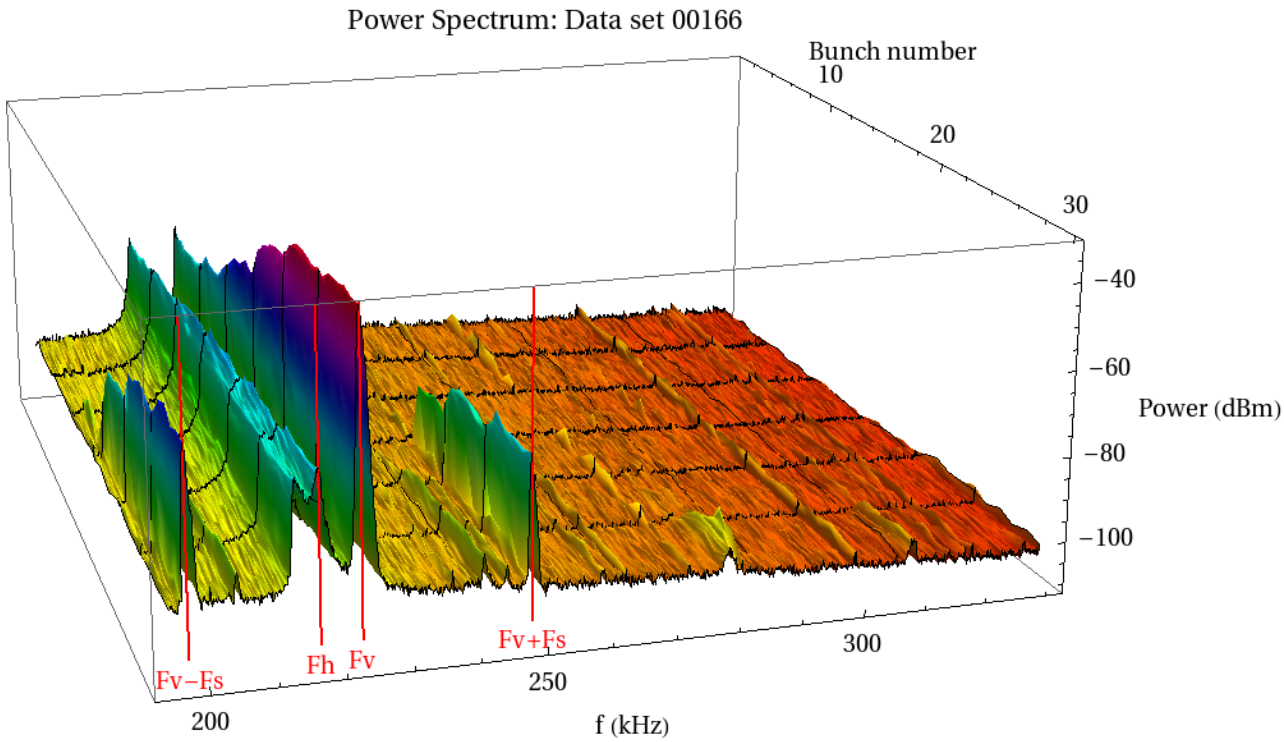

Figure 2: Data set 166: Bunch-by-bunch power spectrum.

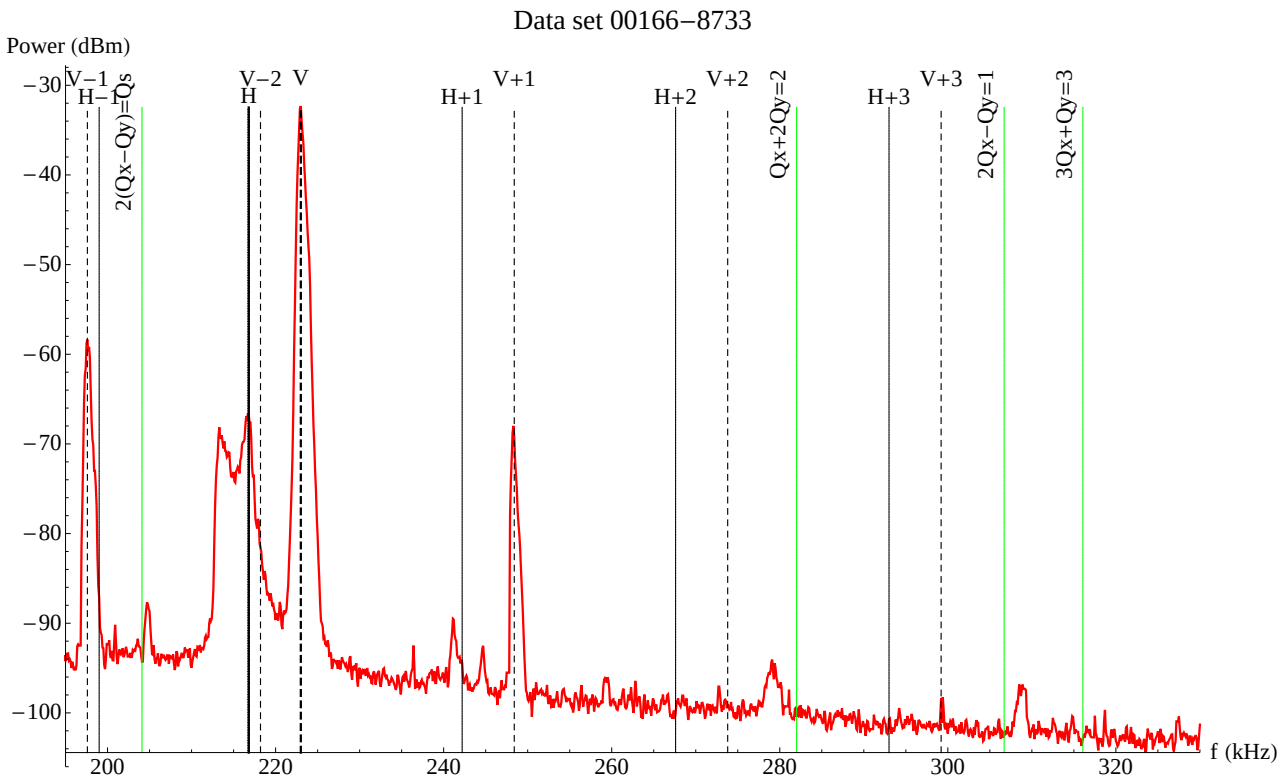

Figure 3: Data set 166: Power spectrum for bunch 30. The lines labelled, for example,"V+1" and "V-1" are shown at frequencies of $\pm f_s$ from the vertical betatron line ("V"), in which f_s is the synchrotron frequency. The locations of several machine resonances are also indicated.

shifts. This suggests that the structure in the vertical plane may be a single-bunch effect, but we have no good explanation for it.

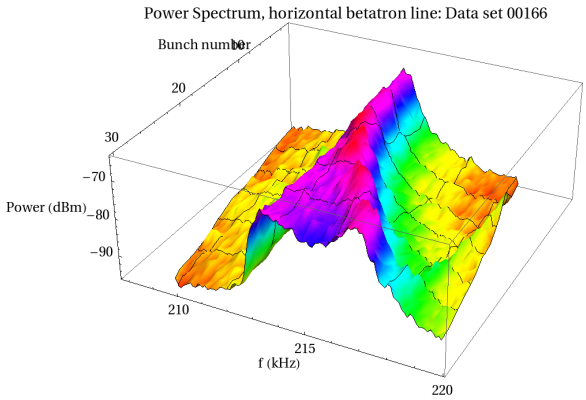

Figure 4: Data set 166: Bunch-by-bunch power spectrum: detail at horizontal betatron line. Chromaticity: (H,V) = (1.33, 1.16). Bunch current = 0.74 mA.

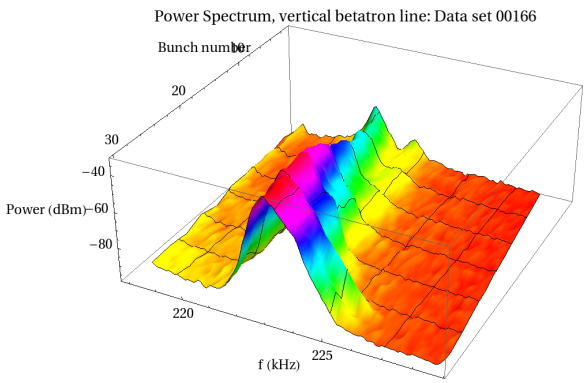

Figure 5: Data set 166: Bunch-by-bunch power spectrum: detail at vertical betatron line. Chromaticity: (H,V) = (1.33, 1.16). Bunch current = 0.74 mA.

Horizontal and vertical betatron lines: peak power and frequency

In Fig. 6, the peak power point[2] for each of the horizontal and vertical betatron lines is shown, as a function of bunch number. The strong excitation of vertical dipole motion is evident in the increase in vertical betatron line power along the train. There is minimal if any additional excitation in the horizontal plane.

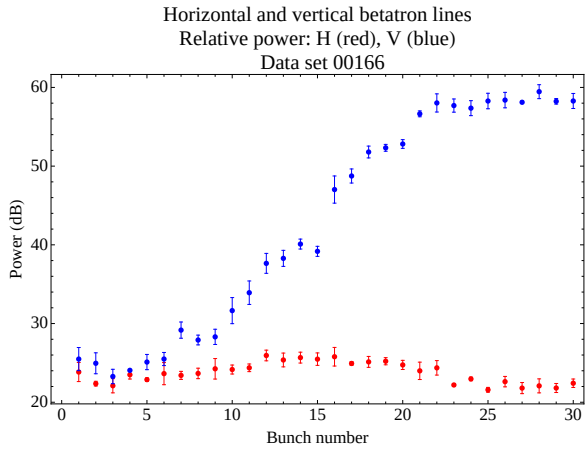

Figure 6: Horizontal and vertical peak power vs. bunch number, data set 166. Chromaticity: (H,V) = (1.33, 1.16). Bunch current = 0.74 mA.

In Fig. 7, the frequency of the peak power point is given, relative to the frequency of the first bunch. Thus, Fig. 7 illustrates the tune shift[3] along the train, which is primarily due to the electron cloud effect.

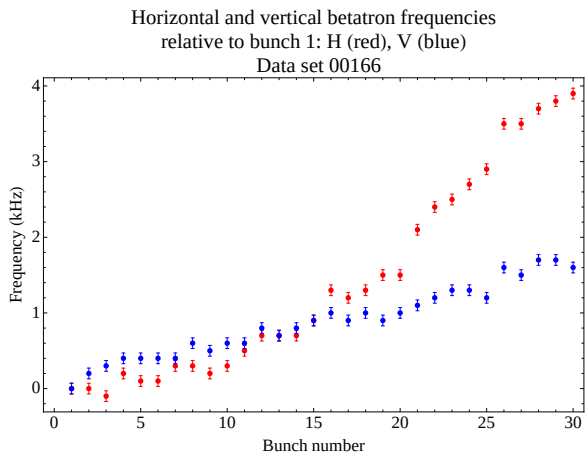

Figure 7: Horizontal and vertical tune shifts vs. bunch number, data set 166. Chromaticity: (H,V) = (1.33, 1.16). Bunch current = 0.74 mA.

Comparison with electron cloud buildup simulations

The cloud buildup program `POSINST` [1] can be used to compute the cloud density corresponding to a set of beam and vacuum chamber properties at CesrTA, and from this density the tune shifts can be computed. For this data, in

[2]For all the relative power plots shown in this paper, the plotted points were obtained as follows: A frequency region is selected, 10 kHz wide, centered approximately on the frequency of interest. The average background power level in this region is determined. Then, the maximum value of the power in this region is found, and subtracted from the background power level, to obtain the relative power.

Because of this background subtraction, if the relative power is close to zero (as in the plots of head-tail line power later in the paper), this signifies the absence of any significant peak.

The frequency plots correspond to the frequencies of the peak power points.

The errors shown in the frequency plots correspond to the bin widths of the frequency spectra (100 Hz). The errors shown in the relative power plots are estimated from the variation in the power over a spectral bin width.

[3]The tune shift is given in frequency units.

which the betatron lines are self-excited, it is reasonable to suppose that the dominate mode of oscillation of the bunches in the train is one in which each bunch is oscillating with a different phase than other bunches in the train. Under this condition, a good estimate of the tune shift can be calculated from the field gradient of the electron cloud's electric field, averaged over the transverse distribution of the bunch, and evaluated before the beam "pinches" the cloud [5].

These calculations (see [4] for details of the assumptions and methodology) can be compared with the measured tune shifts shown in Fig. 7. Comparisons between simulations and measurements are shown in Fig. 8 and Fig. 9. The key parameters used in the POSINST simulation are given in Table 2.

The error bars on the simulated points are due to macroparticle statistics; for the vertical tune shifts, the comparison would benefit from an increased number of macroparticles, which was not feasible due to computer run time limitations. Nevertheless, inspection of Fig. 8 and Fig. 9 indicates that the simulation compares well with the data.

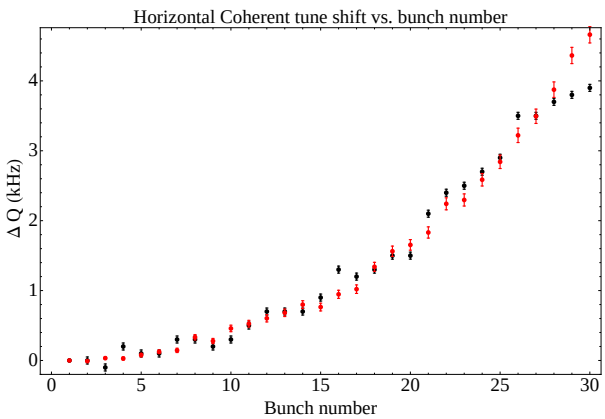

Figure 8: Data set 166: Horizontal tune shift vs. bunch number, comparison between data (black) and simulation (red) from POSINST with parameters given in Table 2.

ESTIMATES OF THE ELECTRON CLOUD DENSITY

Cloud density from measured betatron tune shifts

In this section, the measured tune shift is used to estimate the average electron cloud density. For a lattice in which the beta functions are equal in both planes, the electron-cloud-induced tune shifts δQ_x and δQ_y may be directly related to the average electron cloud density $\langle \rho_c \rangle$ via the relation

$$\langle \rho_c \rangle = \gamma \frac{\delta Q_x + \delta Q_y}{r_e \langle \beta \rangle C},$$

in which $\langle \beta \rangle$ is the average beta function, C is the ring circumference, γ is the beam Lorentz factor, and r_e is the classical electron radius. This relation may be used to obtain an estimate of the cloud density along the train. For CesrTA, we use $C = 649$ m (sum of all drift and dipole lengths) and $\langle \beta \rangle = 16$ m. The cloud densities for each bunch resulting from this calculation are shown as the red points in Fig. 10.

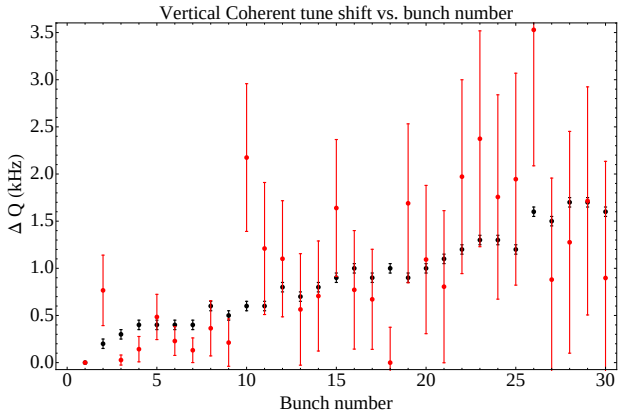

Figure 9: Data set 166: Vertical tune shift vs. bunch number, comparison between data (black) and simulation (red) from POSINST with parameters given in Table 2.

Comparison with electron cloud buildup simulations

We can compare the cloud density, obtained from the measured tune shifts, with the density obtained from the POSINST simulations discussed in the previous section. This comparison is shown in Fig. 10. For the simulation result, shown as black dots in the figure, the cloud density is evaluated at the time corresponding to the leading edge of the bunch (i.e., before the "pinch"), and is averaged over the transverse profile of the beam. The density shown is the weighted average over drifts (total length 175 m) and dipoles (total length 474 m). It is clear from Fig. 10 that the cloud density computed directly from the tune shifts is quite close to the simulation result.

VERTICAL HEAD-TAIL LINES

Head-tail line power and frequency characteristics

As shown in Fig. 2 and Fig. 3, there are two lines which appear in the bunch-by-bunch power spectrum, starting part way along the train, which have frequencies which are close to the betatron frequency plus and minus the synchrotron frequency. In Fig. 11 and Fig. 12, we plot the power and frequency (relative to the vertical betatron line, $\pm$ the synchrotron frequency) of these lines . We associate the lower frequency line with the $m = -1$ head-tail line, which arises as a result of head-tail bunch motion driven by the broadband impedance of the electron cloud. Similarly, we associate the higher frequency line with the $m = +1$

Table 2: POSINST simulation parameters (aluminum chamber, 2 GeV CesrTA positron beam)

POSINST **Parameter**	**Description**	**Unit**	**Value**
photopbppm (drift)	Photons/beam particle/meter (in a drift)	m^{-1}	0.272
photopbppm (dipole)	Photons/beam particle/meter (in a dipole)	m^{-1}	0.522
queffp	Quantum efficiency	%	12
refleff	Reflectivity	%	15
ek0phel	Peak photoelectron energy	eV	5
eksigphel	RMS photoelectron energy	eV	5
E0tspk	Energy of peak secondary yield	eV	310
dtotpk	Peak secondary yield		2.05
P1epk	Elastic yield at zero energy		0.5
P1rinf	Rediffused yield at high energy		0.19

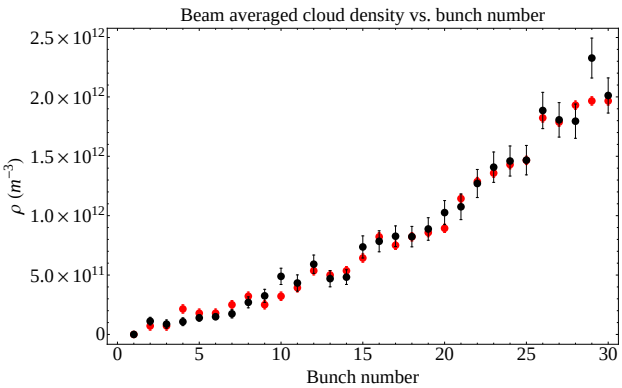

Figure 10: Data set 166: Average initial (i.e., before the "pinch") electron cloud density vs. bunch number, comparison between estimate from measured tune shifts (red), and simulation (black) from POSINST with parameters given in Table 2.

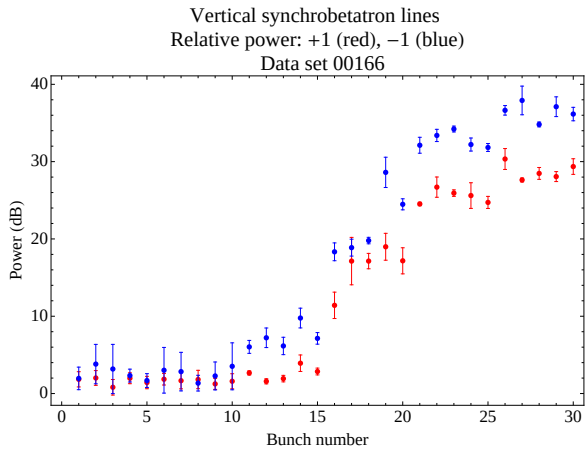

Figure 11: Data set 166: Vertical head tail lines: peak power vs. bunch number. Chromaticity: (H,V) = (1.33, 1.16). Bunch current = 0.74 mA.

head-tail line. From Fig. 11, we see that these lines appear above the noise level around bunch 15 or 16. The $m = -1$ line is somewhat more strongly excited than the $m = +1$ line.

Observations of beam size growth under similar beam conditions [3] see rapid emittance growth starting at about the same point in the train.

Fig. 12 shows that, for bunch numbers greater than about 15, where the head-tail lines appear above the background, the frequency of these head-tail lines, relative to the vertical line, is equal to the synchrotron frequency (within the errors).

Head-tail lines: correlation with cloud density

Comparing Fig. 10 and Fig. 11, the average electron cloud density at which the head-tail lines are first observed can be established. For the conditions of data set 166, the head-tail lines emerge at an initial (i.e., before the "pinch") beam-averaged cloud density around 8×10^{11} m^{-3}.

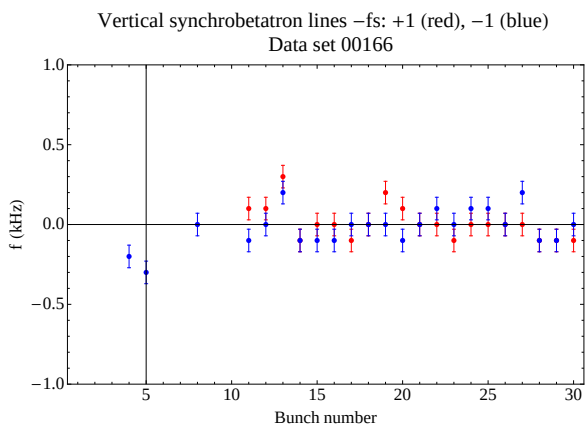

Figure 12: Data set 166: Vertical head tail lines: frequency difference from vertical betatron line vs. bunch number, with the synchrotron frequency removed from the offset.

REPRODUCIBILITY

The reproducibility of the observations of the head-tail lines is illustrated in Fig. 13 and Fig. 14. These plots show

the power in the vertical head-tail lines for two data sets taken on different dates (data set 147 on 9/25/2010, and data set 157 on 9/26/2010) but under the same nominal machine and beam conditions as data set 166. Comparing Fig. 13 and Fig. 14 with each other and with Fig. 11 indicates good consistency between the observations of the head-tail lines.

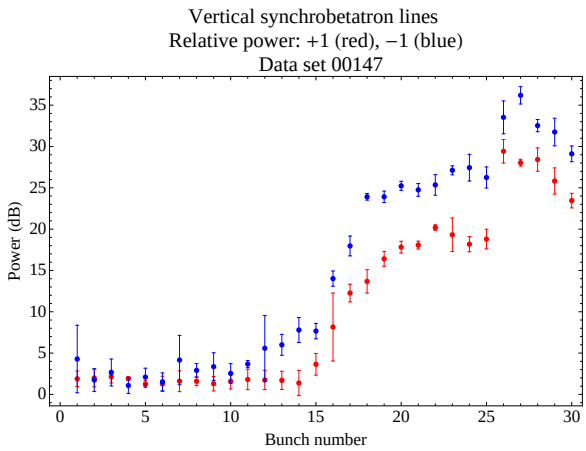

Figure 13: Data set 147: Vertical head tail lines: peak power vs. bunch number. Chromaticity: (H,V) = (1.33, 1.16). Bunch current = 0.74 mA.

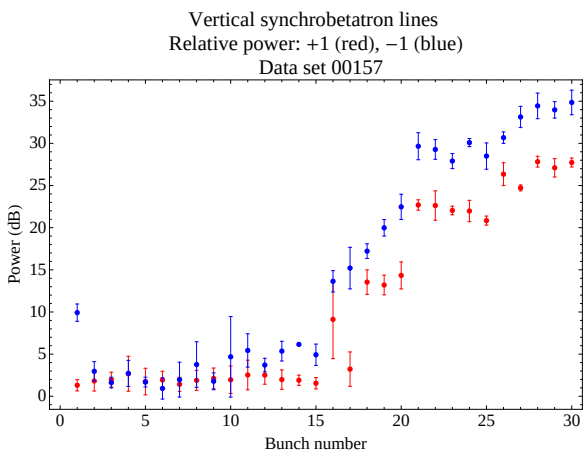

Figure 14: Data set 157: Vertical head tail lines: peak power vs. bunch number. Chromaticity: (H,V) = (1.33, 1.16). Bunch current = 0.73 mA.

CHROMATICITY DEPENDENCE

The chromaticity dependence of the head-tail lines is illustrated by comparing Fig. 13, Fig. 15 and Fig. 16. For all data sets, the nominal bunch current was abut 0.74 mA. We see that for data set 142 (Fig. 15), with a higher value of the vertical chromaticity than data set 147, there are no head-tail lines observed. For data set 129 (Fig. 16), with lower values of both chromaticities than data set 142, but a higher value of the vertical chromaticity than data set 147, head-tail lines are observed, but their onset is a few bunches later in the train than in data set 147, which has the lowest vertical chromaticity.

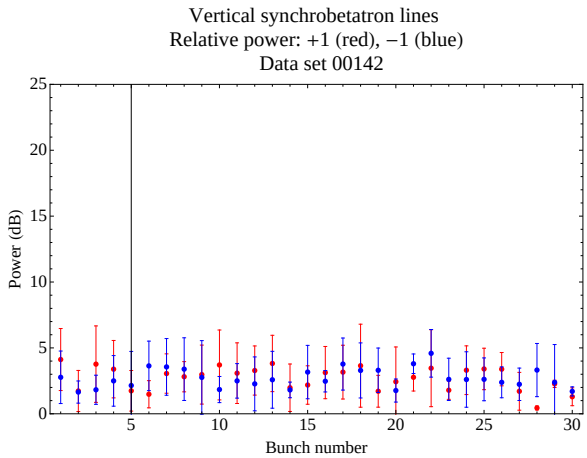

Figure 15: Data set 142: Vertical head tail lines: peak power vs. bunch number. Chromaticity: (H,V) = (1.34, 1.99). Bunch current = 0.74 mA.

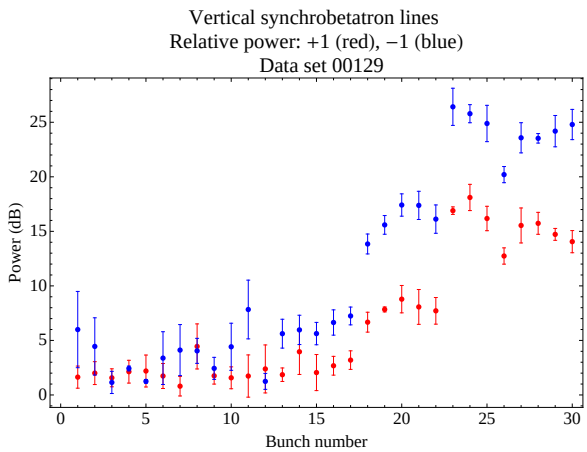

Figure 16: Data set 129: Vertical head tail lines: peak power vs. bunch number. Chromaticity: (H,V) = (1.07, 1.78). Bunch current = 0.74 mA.

CURRENT DEPENDENCE

The current dependence of the head-tail lines is illustrated by comparing Fig. 15 and Fig. 17. Both data sets have the same chromaticity, but the data set with the lower bunch current (data set 142) shows no head-tail lines, while the higher current data set (data set 150) shows head-tail lines staring to emerge around bunch 12. Similarly, we can compare Fig. 13 and Fig. 18. Again, both data sets have the same (lower) chromaticity, but the data set with the lower bunch current (data set 178) shows no head-tail lines, while the higher current data set (data set 147) shows head-tail lines staring to emerge around bunch 16.

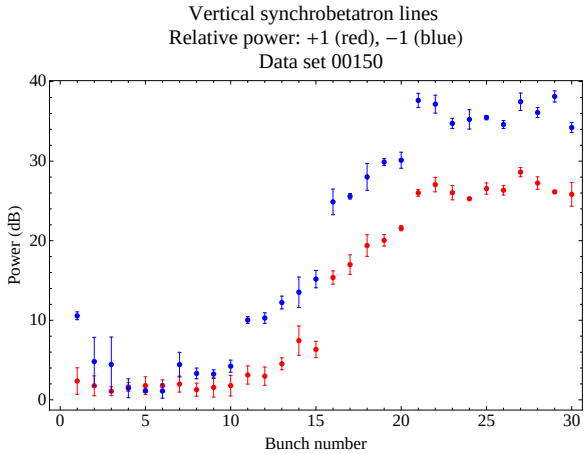

Figure 17: Data set 150: Vertical head tail lines: peak power vs. bunch number. Chromaticity: (H,V) = (1.34, 1.99). Bunch current = 0.95 mA.

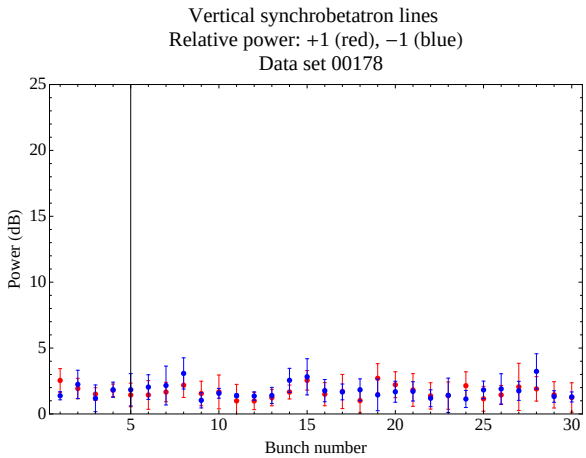

Figure 18: Data set 178: Vertical head tail lines: peak power vs. bunch number. Chromaticity: (H,V) = (1.34, 1.11). Bunch current = 0.5 mA.

BUNCH NUMBER DEPENDENCE

The bunch number dependence of the head-tail lines is illustrated by comparing Fig. 15 with Fig. 19. Both data sets have the same chromaticity and bunch current, but data set 156 contains 45 bunches in the train. The vertical tunes of the first bunch were slightly different for the two runs: for run 142, it was about 227 kHz, while for run 156 the tune was about 221 kHz. No head-tail lines are observed in data set 142 (Fig. 15) out to the end of the train, bunch 30. But with 45 bunches, head-tail lines are observed starting around bunch 18, then growing to a peak around bunch 25, and falling off at the end of the train. The fact that the head-tail lines are seen with a 45 bunch train with the same bunch current as a 30 bunch train for which no lines are seen, is suggestive that there is a residual cloud density which lasts more than one turn, and which depends on the total current.

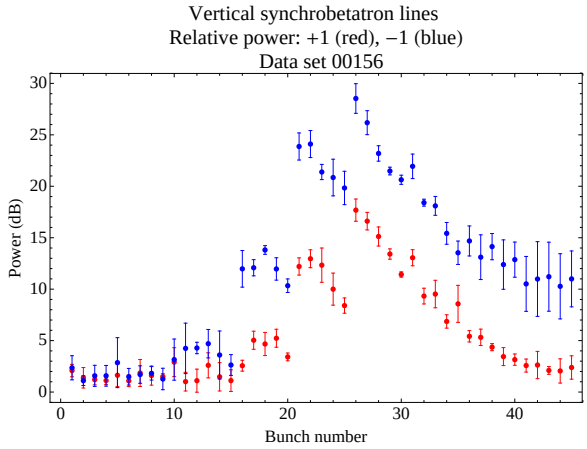

Figure 19: Data set 156: Vertical head tail lines: peak power vs. bunch number. Chromaticity: (H,V) = (1.34, 1.99). Bunch current = 0.73 mA. The increased amplitude at bunches 21 and 26 is an artifact due to refilling of the train at these bunch numbers.

45 bunch train: Correlation with cloud density

In Fig. 20, we show the cloud density as a function of bunch number, computed from the measured tune shifts, as discussed above. Comparison with Fig. 19 shows that the head-tail lines emerge from the background at a cloud density of about 8×10^{11} m^{-3}, which is the same as the threshold density found for data set 166, even though the vertical chromaticity was higher for data set 156. The fall-off of the head-tail lines after bunch 25 suggests that the instability is saturating. Yet the cloud density continues to increase after bunch 25 (at least until around bunch 35) as Fig. 20 shows. The head-tail instability threshold is expected to be sensitive to the beam size, so what may be happening is that the instability is driving beam size growth along the train, and the increase in the threshold as the beam size increases provides a mechanism for the instability to saturate.

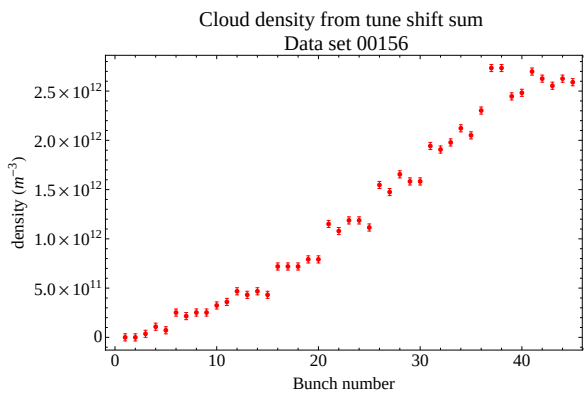

Figure 20: Average initial electron cloud density vs. bunch number, estimate from measured tune shifts, data set 156

SYNCHROTRON TUNE DEPENDENCE

The synchrotron tune dependence of the head-tail lines is illustrated by comparing Fig. 13 and Fig. 21. Both data sets have the same chromaticity and bunch current, but data set 151 (Fig. 21) has a reduced synchrotron frequency of 20.7 kHz, and an increased bunch length of 12.8 mm. The nominal frequency and bunch length, for data set 147 (Fig. 13) are 25.4 kHz and 10.8 mm.

For both data sets, the separation between the vertical betatron lines and the head-tail lines equals the synchrotron frequency. A comparison of Fig. 13 and Fig. 21 shows that the head-tail line threshold is about the same in both cases, but the power in the lines grows more slowly with bunch number for the data set with a reduced synchrotron tune.

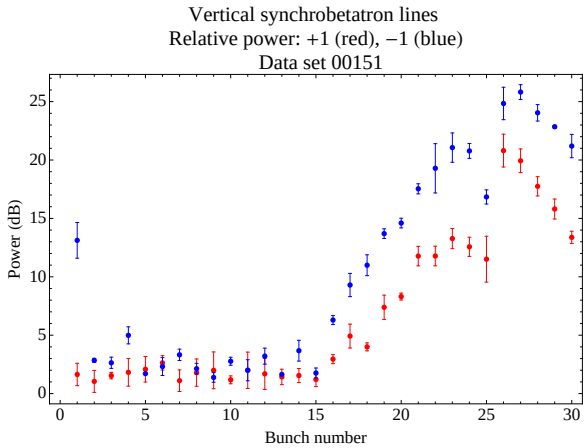

Figure 21: Data set 151: Vertical head tail lines: peak power vs. bunch number. Chromaticity: (H,V) = (1.33, 1.16). Bunch current = 0.74 mA. Synchrotron frequency 20.7 kHz, bunch length 12.8 mm

SINGLE-BUNCH VERTICAL EMITTANCE DEPENDENCE

The vertical emittance dependence of the head-tail lines is illustrated by comparing Fig. 13 and Fig. 22. Both data sets have the same chromaticity and bunch current, but data set 158 (Fig. 22) has an increased single-bunch vertical emittance of 300 pm[4]. The nominal single-bunch vertical emittance, for data set 147 (Fig. 13), is $\sim$ 20 pm.

A comparison of Fig. 13 and Fig. 22 shows that the head-tail line threshold is a few bunches earlier for the data set with increased vertical emittance, but the power in the lines grows more slowly with bunch number for data set 158. Generally, there is not a great deal of difference, which is peculiar, since the electron cloud head-tail instability is expected to considerably more severe for smaller vertical emittance. It is possible that, due to emittance growth along the train, the vertical emittance of the bunch at which the instability starts is larger than the single-bunch vertical emittance.

[4]This number was estimated from a lattice model, not directly measured.

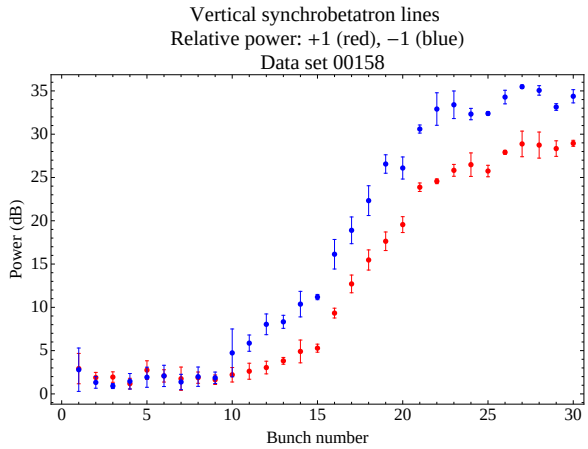

Figure 22: Data set 158: Vertical head tail lines: peak power vs. bunch number. Chromaticity: (H,V) = (1.33, 1.16). Bunch current = 0.77 mA. Single-bunch vertical emittance $\sim$ 300 pm (estimated).

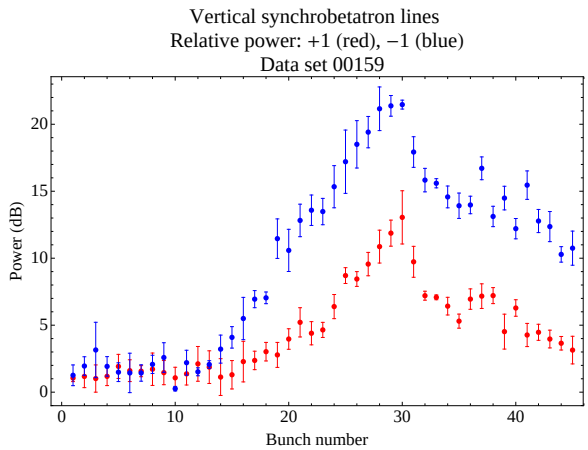

Figure 23: Data set 159: Vertical head tail lines: peak power vs. bunch number. Chromaticity: (H,V) = (1.34, 1.99). Bunch current = 0.75 mA. Single-bunch vertical $\sim$ 300 pm (estimated).

Another observation which explores the vertical emittance dependence of the head-tail lines is illustrated by comparing Fig. 19 and Fig. 23. Both data sets have 45 bunches and have the same chromaticity and bunch current, but data set 159 (Fig. 23) has an increased single-bunch vertical emittance of $\sim$ 300 pm. The single-bunch vertical emittance, for data set 156 (Fig. 19), is $\sim$ 20 pm.

Again, a comparison of Fig. 19 and Fig. 23 shows that the head-tail line threshold is a few bunches earlier for the data set with increased vertical emittance, but the power in the lines grows more slowly with bunch number for data set 159. In this case, the power peaks later in the train, and at a smaller value, for the data set with increased emittance. The saturation effect is observed for both values of

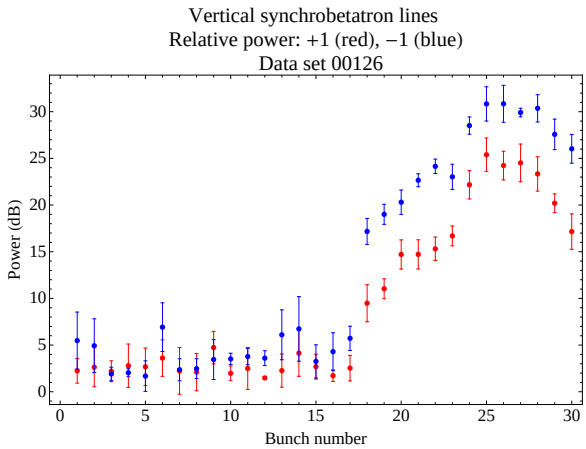

Figure 24: Data set 126: Vertical head tail lines: peak power vs. bunch number. Chromaticity: (H,V) = (1.07, 1.78). Bunch current = 0.72 mA. Vertical feedback off.

the single-bunch vertical emittance.

VERTICAL FEEDBACK DEPENDENCE

The vertical feedback dependence of the head-tail lines is illustrated by comparing Fig. 16 and Fig. 24. Both data sets have the same chromaticity and bunch current, but data set 126 (Fig. 24) has the vertical (dipole) feedback off. For data set 129 (Fig. 16), as for all the other data sets discussed here (except 126), the vertical feedback is set to 20% of full gain.

A comparison of Fig. 16 and Fig. 24 shows that the head-tail line threshold is about in the same place for these two data sets. But for data set 129, the peak power rises to about 25 db by bunch 22, and then plateaus. For data set 126 (feedback off), it increases to about 32 db by bunch 25, and then starts to decay.

PARTICLE SPECIES DEPENDENCE

The species dependence of the bunch-by-bunch power spectrum is illustrated by comparing data set 166 (Fig. 2) and data set 154 (Fig. 25). Both data sets have the same chromaticity and bunch current, but data set 154 is for electrons. For electrons, we see less vertical excitation along the train, and smaller head-tail line excitation, than for positrons. The large tune shifts observed with the positron beam are also absent.

The details of the different structures of the head-tail lines for electrons and positrons can be seen by comparing Fig. 11 and Fig. 26. For electrons, the head-tail lines start later in the train, and at their maxima are 20 dB lower than the positron head-tail lines.

The positron head-tail excitation is presumably due to electron cloud effects. The physical mechanism responsible for the head-tail excitation in the electron case is not likely to be either electron cloud or positive ions. It may be due to the broad-band impedance of the machine itself.

PRECURSOR BUNCH EXPERIMENT

In Fig. 27, the power spectrum of bunch 1 for data set 151 is shown. Note the presence of a prominent $m = -1$ head-tail line. This line disappears for the second bunch, and does not re-appear until much later in the train, as shown in Fig. 21. Moreover, beam size measurements[3] indicate that the first bunch in the train is frequently larger in size than the next few bunches.

This suggests that the cloud density near the beam, which persists after the train ends, may be sufficiently high, even for the first bunch in the train, that spontaneous head-tail motion occurs. However, the interaction of the first bunch with this cloud evidently decreases the cloud density near the beam, so that bunch 2 does not suffer from spontaneous head-tail motion.

Simulations and witness bunch measurements indicate that the electron cloud lifetime in dipoles and drifts is much shorter than one turn in CesrTA. Cloud density which persists for many turns may be due to trapped cloud in quadrupoles and wigglers. Simulations and RFA measurements in quadrupoles have both indicated that trapped cloud may be present.

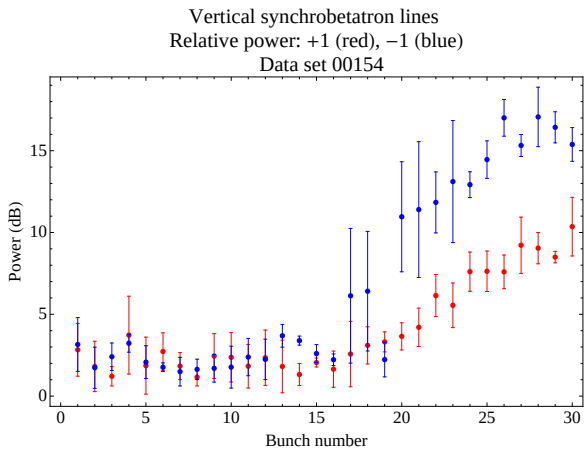

Figure 26: Data set 154: Vertical head tail lines: peak power vs. bunch number. Chromaticity: (H,V) = (1.33, 1.16). Bunch current = 0.76 mA. Electrons.

To test this hypothesis, in data set 153, a 0.75 mA "precursor" bunch was placed 182 ns before bunch 1. Otherwise, conditions were the same as for data set 151. The spectrum of the first bunch for data set 153 is shown in Fig. 28. Note that the head-tail line is now absent. In addition, the structure seen on the upper edge of the vertical betatron line in Fig. 27 is also absent. In Fig. 29, the power in the vertical head-tail lines is shown as a function of bunch number, for data set 153. Comparing with data set 151 (Fig. 21), it can be seen that the power in the lines near the end of the train is somewhat lower (perhaps 5 db) when the precursor bunch is present.

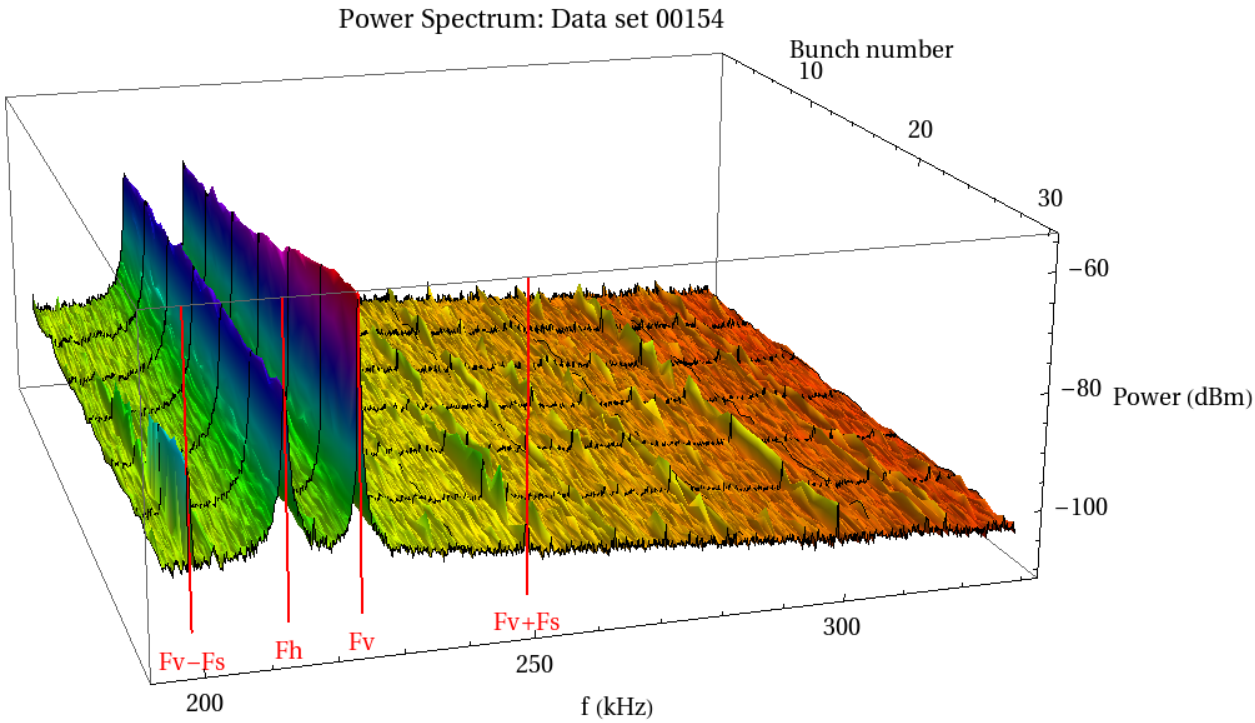

Figure 25: Data set 154: Bunch-by-bunch power spectrum. This data set is for electrons, but has the same chromaticity and bunch current parameters as data set 166 (Fig. 2).

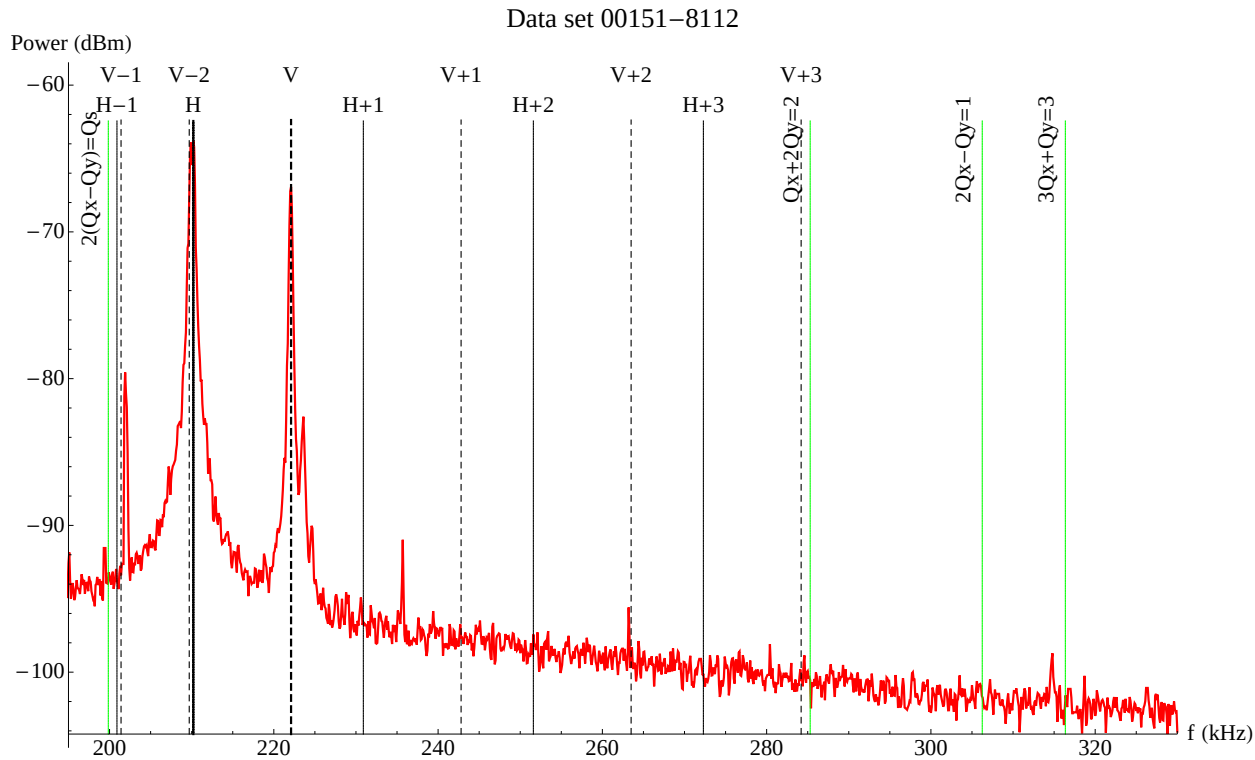

Figure 27: Data set 151: Power spectrum, bunch 1. The lines labelled, for example,"V+1" and "V-1" are shown at frequencies of $\pm f_s$ from the vertical betatron line ("V"), in which f_s kHz is the synchrotron frequency. The location of several machine resonances are also indicated.

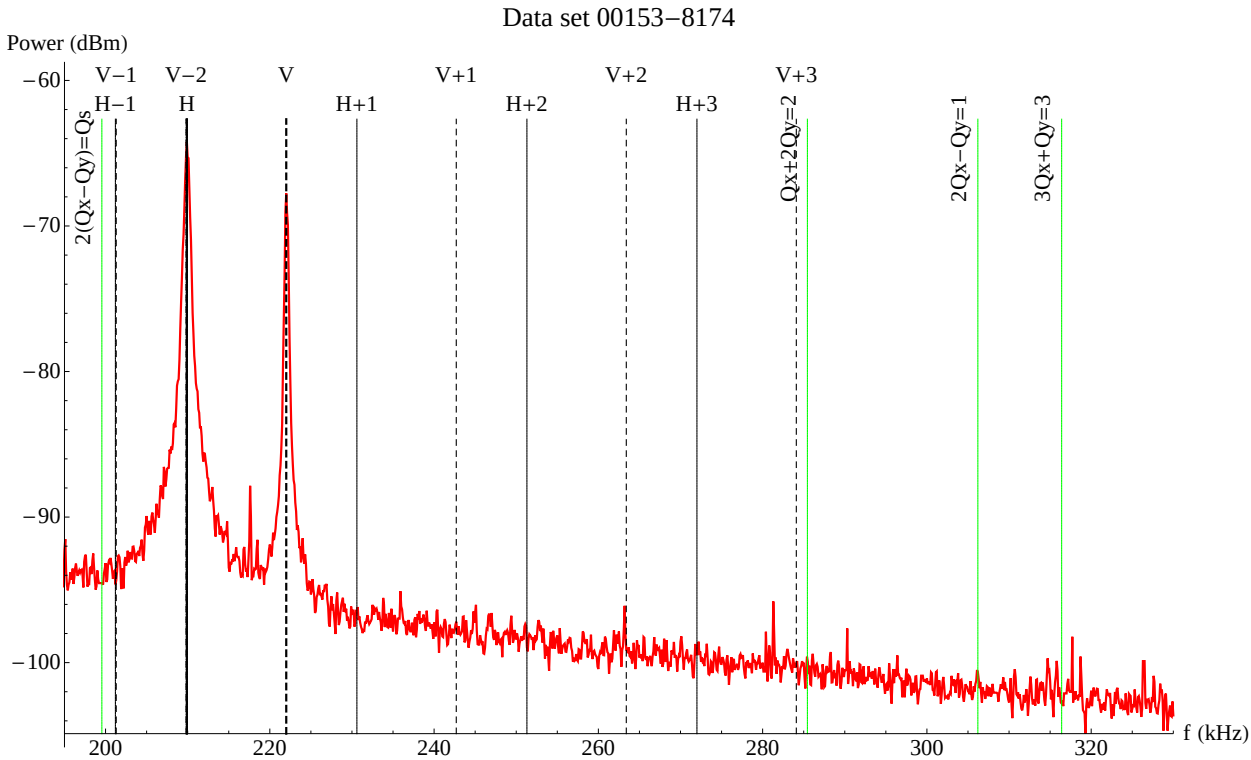

Figure 28: Data set 153: Power spectrum, bunch 1. This data set has the same conditions as data set 151, except for the presence of an additional 0.75 mA "precursor" bunch placed 182 ns before bunch 1.

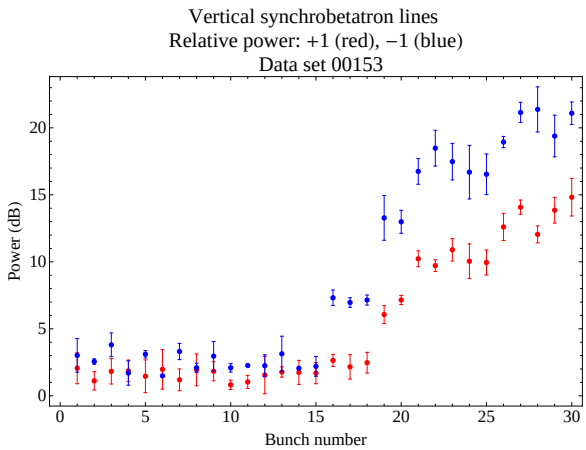

Figure 29: Data set 153: Vertical head tail lines: peak power vs. bunch number. Chromaticity: (H,V) = (1.33, 1.16). Bunch current = 0.74 mA. Precursor bunch present.

SINGLE BUNCH CURRENT VARIATION EXPERIMENT

To explore further the dynamics of the interaction of the last bunch in the train with the cloud, a series of power spectral measurements were made, in which the current in the first 29 bunches in a 30 bunch train was fixed, but the current in the last bunch was varied. The power spectrum with the last bunch at 0.25 mA is shown in Fig. 30, while the power spectrum with the last bunch at 1.25 mA is shown in Fig. 31.

The vertical excitation of the bunch, both at the vertical betatron line and at the head-tail lines, is much larger for the higher current bunch. The $m = +1$ head-tail line appears to acquire a low-frequency shoulder at the higher current.

In addition, while it is hard to see from these figures, the frequency of the vertical betatron line is almost independent of the current in the bunch. The shift from 0.25 mA to 1.25 mA is less than 0.2 kHz. Note that this behavior is very different from what would be expected for a conventional machine impedance, for which one would expect a strong current dependence for the tune.

BUNCH-BY-BUNCH DAMPING RATES: METHODOLOGY

In addition to the power spectrum measurements described above, in which spontaneous excitations of single bunches are passively monitored, we have also made measurements in which we actively excite a single bunch in a train, and measure the rate at which the bunch damps after the excitation is turned off. These bunch-by-bunch damping rate measurements come in two varieties:

- $m = 0$ *(dipole mode).* In this case, we drive a single bunch by delivering a narrow pulse to the transverse feedback system's kicker. We observe the $m = 0$

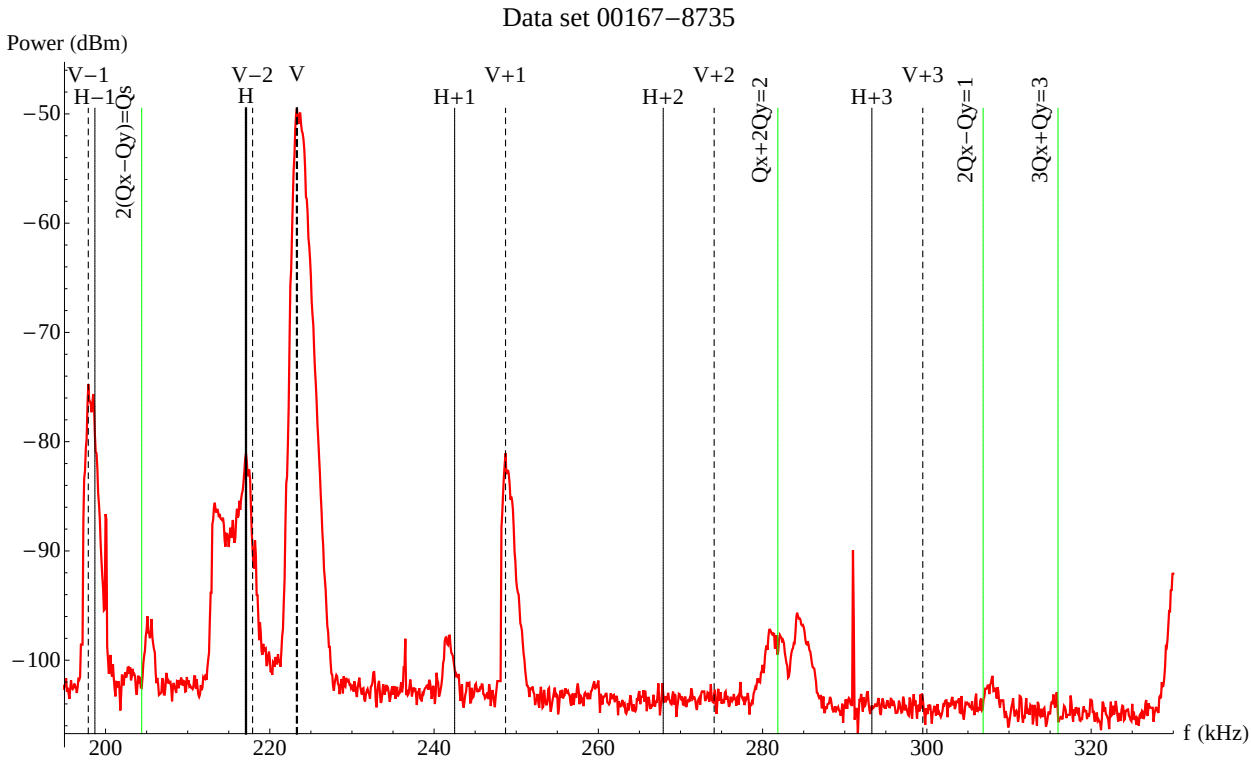

Figure 30: Data set 167: Power spectrum, bunch 30. Bunch 30 current = 0.25 mA. The first 29 bunches had a nominal current of 0.75 mA/bunch. Chromaticity: (H,V) = (1.33, 1.16).

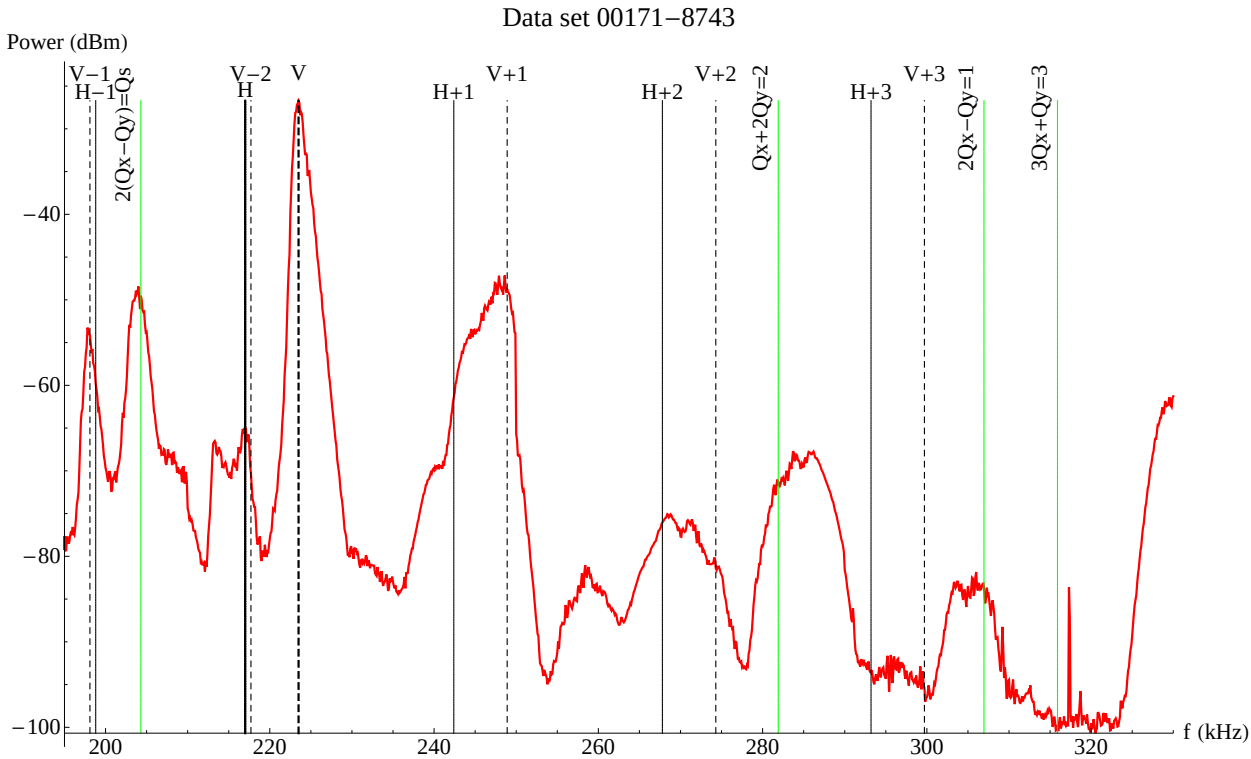

Figure 31: Data set 171: Power spectrum, bunch 30. Bunch 30 current = 1.25 mA. The first 29 bunches had a nominal current of 0.75 mA/bunch. Chromaticity: (H,V) = (1.33, 1.16).

motion (betatron line) on a button BPM, gated on the same bunch. Using a spectrum analyzer in zero span mode, tuned to the betatron line, we measure the damping rate of the $m = 0$ line's power after the drive is turned off.

- $m = \pm 1$ *(head tail modes).* In this case, we apply a CW drive to the RF cavity phase, to provide a large amplitude longitudinal excitation. We then perform a transverse drive-damp measurement, as in the previous case, but with the spectrum analyzer tuned to the head-tail line's frequency.

A number of measurements were made to investigate the systematics of this technique. More details can be found in [2].

Results will be shown here for two data sets in which 30 bunch trains with currents of about 0.75 mA/bunch were studied. (For these conditions, the self-excited head-tail lines first appear above background around bunch 15).

DRIVE-DAMP MEASUREMENTS

For the two data sets, we show the line power as a function of time, and bunch number. For data set 182 (Fig. 32), the $m = 0$ mode was excited and monitored. For data set 177 (Fig. 33), the $m = -1$ mode was excited and monitored.

In data set 182, the first bunch is more easily excited than the next few bunches, but the damping rates are similar. But further along the train, the excitation level increases and the damping time gets very long near the end of the train. This is consistent with reduced stability for the later bunches.

In data set 177, we see a similar trend, except that the first few bunches all appear to have similar damping times and excitation levels. Again, further along the train, the excitation level increases and the damping time gets very long near the end of the train.

Generally, the fastest damping rates observed in these data sets are on the order 200 s^{-1}, which is much larger than the radiation damping rate. The feedback system was set to 20% of maximum for these measurements. At this level, and for 0.75 mA/bunch, the feedback system provides a damping rate of a few hundred s^{-1}. Thus, the fastest rates observed are consistent with what is expected from the feedback system. Future measurements are planned in which the feedback system will be gated off for the bunch being excited and measured.

CONCLUSIONS

The basic observation is that, under a variety of conditions, single-bunch frequency spectra in multi-bunch positron trains exhibit the $m = \pm 1$ head-tail (HT) lines, separated from the vertical line by the synchrotron frequency, for some of the bunches during the train. A summary of more detailed observations follows in the following bullets.

- For a 30 bunch train with 0.75 mA/bunch, the onset of the HT lines occurs at a ringwide initial (i.e., before the "pinch") beam-averaged cloud density of around 8×10^{11} m^{-3} (assuming no cloud density at the start of the train).
- The betatron lines exhibit structure which varies along the train. The vertical line power grows along the train and has a fine structure that is not understood.
- The onset of the HT lines depends strongly on the vertical chromaticity, the beam current and the number of bunches.
- For a 45 bunch train, the HT lines have a maximum power around bunch 30; the line power is reduced for later bunches.
- There is a weak dependence of the onset of the HT lines on the synchrotron tune, the single-bunch vertical emittance, and the vertical feedback. The relatively weak dependence of the HT line onset on the single-bunch vertical emittance is contrary to expectations for the electron cloud effect. It is possible that, due to incoherent emittance growth along the train, the vertical emittance of the bunch at which the instability starts is larger than the single-bunch vertical emittance.
- Under identical conditions, HT lines also appear in electron trains, but the onset is later in the train, and develops more slowly, than for positrons. The HT excitation for electrons may be due to the broadband impedance of the ring.
- Under some conditions, the first bunch in the train also exhibits a head-tail line ($m = -1$ only). The presence of a "precursor" bunch can eliminate the $m = -1$ signal in the first bunch, and also leads to the onset of the HT lines at a later bunch in the train. The implication is that there is a significant cloud density near the beam which lasts many turns. Indications from RFA measurements and simulations indicate this "trapped" cloud may be in the quadrupoles and wigglers.
- There is a strong dependence of the HT line structure observed on last bunch in a 30 bunch train, as a function of the current in that bunch. But the frequency of the vertical betatron line of this bunch is only very weakly dependent on the current in the bunch.
- We have made preliminary measurements of damping rates of single bunches in 30 bunch trains. A more comprehensive set of measurements in the future will shed more light on the effective electron cloud impedance.
- Future work will include more checks for systematics (looking at different BPMs, for example), as well as measurements at different bunch spacings and beam energies.

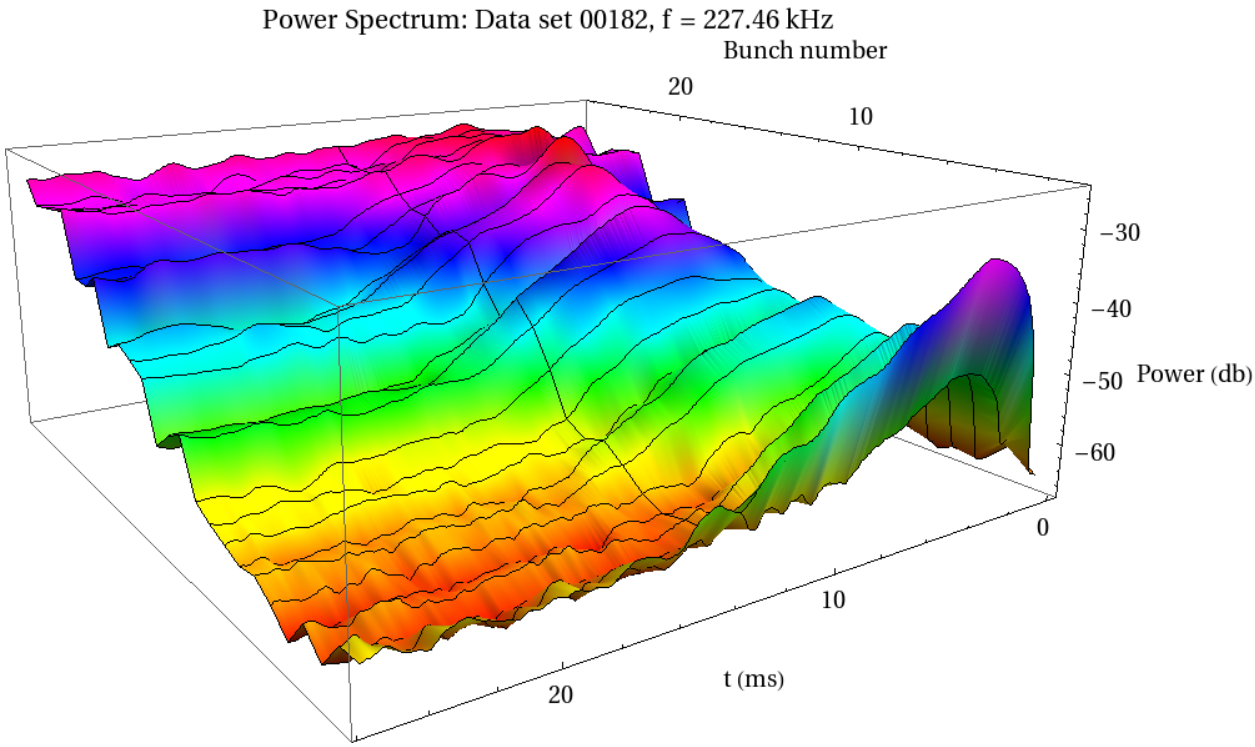

Figure 32: Data set 182: Grow-damp measurements for $m = 0$ mode. Chromaticity: (H,V) =(1.28,2.39). Bunch current = 0.72 mA

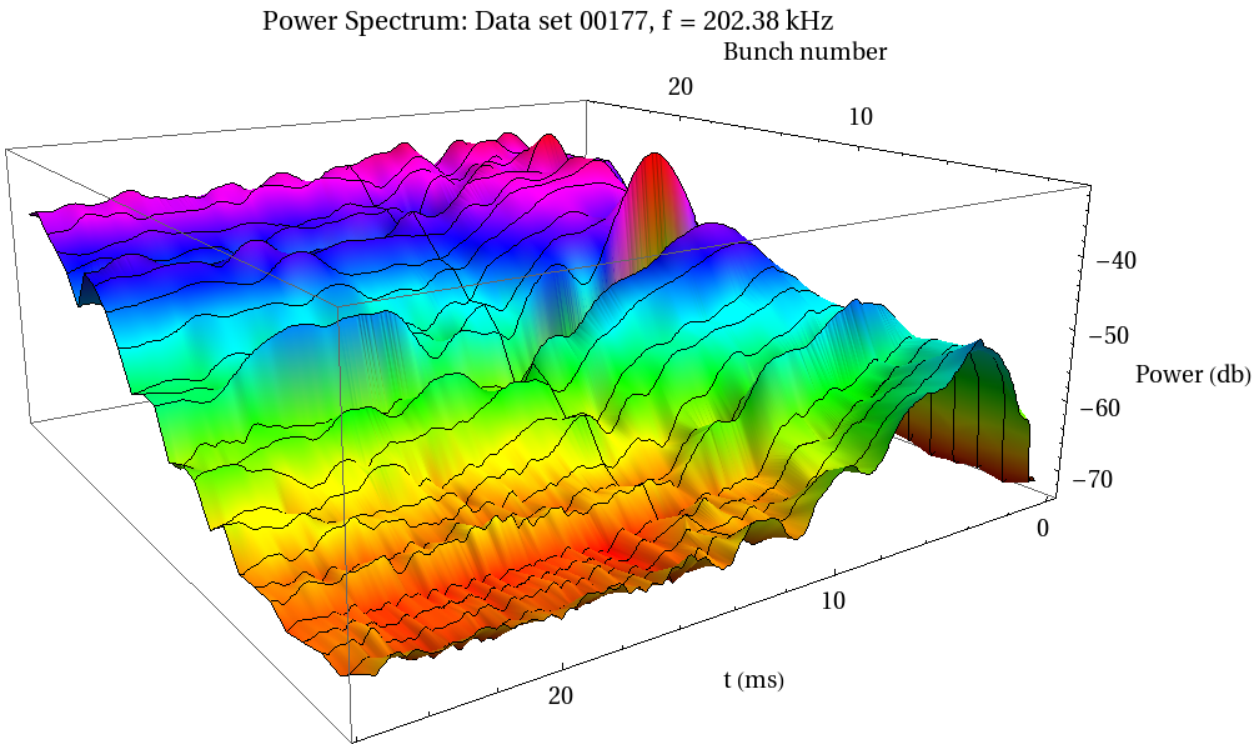

Figure 33: Data set 177: Grow-damp measurements for $m = -1$ mode. Chromaticity: (H,V) =(1.28,2.39). Bunch current = 0.75 mA

REFERENCES

[1] M. A. Furman and G. R. Lambertson, Proc. MBI-97, KEK Proceedings 97-17, p. 170; M. A. Furman and M. T. F. Pivi, Oral Session PRST-AB 5, 124404 (2002).

[2] M. Billing et. al., "Techniques for Observing Beam Dynami-

cal Effects Caused by the Presence of Electron Clouds", contribution to this workshop

[3] J. Flanagan et. al., contribution to this workshop

[4] D. Kreinick et. al., "Using Coherent Tune Shifts to Evaluate Electron Cloud Effects on Beam Dynamics at CesrTA ", contribution to this workshop

[5] K. Ohmi, S. Heifets, F. Zimmerman, "Study of Coherent Tune Shift Caused by Electron Cloud", APAC2 (2001), p. 445

ELECTRON CLOUD INSTABILITY IN LOW EMITTANCE RINGS

K. Ohmi, H. Jin and Y. Susaki

KEK, Tsukuba, Japan, Postech, Pohang, Korea

Abstract

Electron cloud instability, especially single bunch instability, is crucial issue for the emittance preservation in low emittance positron rings. In Super B factories and ILC damping ring, the emittance preservation is directory connected to their performance. Cesr-TA in Cornell has been operated to study the electron cloud effects in a low emittance ring. We discuss threshold density and unstable mode for the single bunch instability in low emittance rings, Cesr-TA and Super KEKB.

INTRODUCTION

The single bunch instability induced by electron cloud in Cesr-TA has been studied. Cesr-TA can be operated low and normal emittance. It is interesting to observed and analyze the both emittance cases in a ring. The simulation results were published in Reference [1]. We review the results of Cesr-TA in the paper [1] and discuss Super KEKB case.

The single bunch electron cloud instability is caused by coherent motion of electrons in a bunch. The angular frequency of electrons is expressed by

$$\omega_e = \sqrt{\frac{\lambda_p r_e}{\sigma_y(\sigma_x+\sigma_y)}}c$$

This formula is derived from taking into account of electric field in the bunch. Space charge between electrons is negligible because beam field is much stronger than the space charge field. The instability is caused by corrective motion of electrons in a cloud and positrons in a bunch with the frequency.

The phase factor $\omega_e\sigma_z/c$ characterizes how many oscillation electrons experience in a bunch. The phase factor is around 3-7 for KEKB, while more than 10 for ILC damping ring and Super B factories, because of the very small beam size. We discuss the electron cloud instability with focusing the phase factor, $\omega_e\sigma_z/c$.

Cesr-TA is operated at very low emittance (ε_x=2.6 nm) in 2GeV, while is high (ε_x=40 nm) in 5 GeV. The phase factors are 11 and 3.2 in 2 and 5 GeV, respectively, where the average beta function is $\beta=L/2\pi\nu$=12 m. The factor is 18 for Super B factories.

ANALYTICAL ESTIMETE OF THE INSTABILITY THRESHOLD

The electron oscillation gives correlation of transverse motion between different longitudinal positions z. The correlation is represented by wake field, which is expressed by [2]

$$W(z) = K\frac{\gamma\omega_p^2\omega_e L}{\lambda_p r_e c^3}e^{\omega_e z/2Qc}\sin\omega_e z/c \qquad (1)$$

Electrons oscillate with a frequency spread due to the longitudinal and horizontal profile of the bunch. The quality factor (Q) characterizes how many period the electron oscillate for the damping due to the spread. A numerical analysis for the electron induced wake field gave Q_{nl}~7 [2]. The effective quality factor should be minimum of $Q=\min(Q_{nl}, \omega_e\sigma_z/c)$.

The electron density near the beam is uniform before the interaction. The electrons are attracted by the beam electric force, which behaves 1/r for a long distance interaction, where r is the distance of bunch and an electron. The factor K characterizes how far electrons are gathered to the beam. The factor is assumed to be equal to the phase factor, $K=\omega_e\sigma_z/c$.

The threshold of the fast head-tail instability is estimated by analytical and simulation methods.

$$U = \frac{\sqrt{3}\lambda_p r_0\beta}{\nu_s\ \gamma\ \omega_e\sigma_z/c}\frac{|Z_\perp(\omega_e)|}{Z_0} = \frac{\sqrt{3}\lambda_p r_0\beta}{\nu_s\ \gamma\ \omega_e\sigma_z/c}\frac{KQ}{4\pi}\frac{\lambda_e}{\lambda_p}\frac{L}{\sigma_y(\sigma_x+\sigma_y)} = 1 \qquad (2)$$

where Z is the transverse impedance correspond to the wake field in Eq.(1). The threshold density is solved using the relation $\lambda_e=2\pi\sigma_x\sigma_y\rho_{e.th}$, as follows:

$$\rho_{e,th} = \frac{2\gamma\nu_s\omega_e\sigma_z/c}{\sqrt{3}KQr_0\beta L} \qquad (3)$$

The threshold densities of the electron cloud are estimated for the existing and proposed positron rings in Table 1. The threshold density for Cesr-TA is ρ_{th} =0.82x10^{12} and 5.0x10^{12} m^{-3} for 2 and 5 GeV, respectively. The threshold is 0.27 x10^{12} and 0.54x10^{12} m^{-3} for of Super KEKB and Super B, respectively.

SIMULATION OF THE INSTABILITY THRESHOLD

The threshold should be crosschecked using simulations, since the analytical estimate is somewhat ambiguous for K and Q. The simulation in this paper is performed by PEHTS, which is a particle in cell code for motion of macro-positrons in the beam and macro-electrons in the cloud.

Figure 1 shows the evolution of the vertical beam size for various electron density in Cesr-TA. The threshold is 1.0 x10^{12} and 6.0x10^{12} m^{-3} for 2 and 5 GeV, respectively. Slow beam blow up below the threshold seen in 5 GeV

case is unphysical incoherent emittance growth. The blow up depends on the number of beam-electron cloud interaction point. To evaluate physical incoherent emittance growth, it is necessary to perform simulations using realistic lattice [1,3].

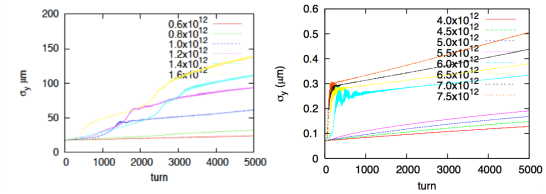

Figure 1: Evolution of the vertical beam size for various electron densities in Cesr-TA. Left and right plots are for 2 and 5 GeV, respectively.

Coherent motion of positrons and electrons should be monitored to distinguish the instability from the incoherent emittance growth. Figure 2 shows variations of vertical bunch position and size, and electron position during an interaction.

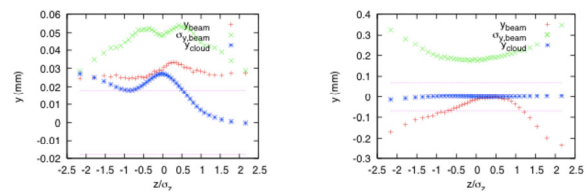

Figure 2: Coherent motion between electron cloud and bunch. Left and right plots are for 2 and 5 GeV, respectively.

Figure 3 shows the evolution of the vertical beam size for various electron densities in Super KEKB. The threshold, which is obtained 0.24×10^{12} m^{-3}, agrees well with the analytic estimate in Table 1. Super KEKB is being designed to satisfy the electron density.

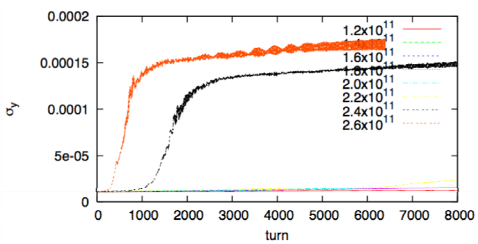

Figure 3: Evolution of the vertical beam size for various electron densities in Super KEKB.

BEAM SPECTRUM OF THE ELECTRON CLOUD INDUCED HEAD-TAIL INSTABILITY

The beam spectrum is given by Fourier transformation of the dipole motion, averaged vertical position of the bunch <y>. The beam spectrum caused by the electron cloud has been measured in KEKB [4]. Upper side band signal, $\nu_y+a\nu_s$, where $1<a<2$, has been observed. Appearance of the sideband spectrum depends on the interaction of beam-electron cloud, especially the phase factor $\omega_e\sigma_z/c$ characterize head-tail mode.

Figure 4 shows the Fourier spectra for 2 (top) and 5 GeV (bottom), respectively. Lower side band is dominant for 2 GeV, while upper sideband is dominant for 5 GeV. Figure 5 shows betatron and sideband frequencies as function of electron cloud density. The dotted line indicates the tune shift given by the formula,

$$\Delta\nu = \frac{r_e}{2\gamma}\rho_e\beta L \quad (4)$$

Tune shift in the betatron frequency is not seen in 2GeV case, while tune shift is consistent with the formula (4). Distance from sideband is smaller than synchrotron tune in 2 GeV case, while larger in 5 GeV case. The behaviour in 2 GeV case changes with taking into account of the bunch by bunch feedback system in the simulation. More detailed studies are necessary.

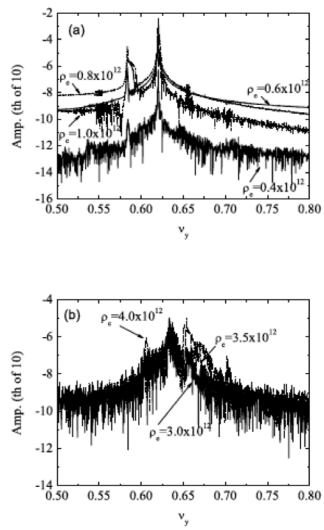

Figure 4: Fourier spectra of the vertical dipole amplitude for various electron cloud densities. Top and bottom plots are for Cesr-TA/2GeV and 5GeV.

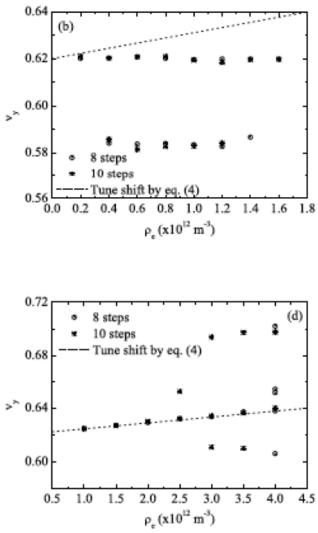

Figure 5: Betatron and sideband spectra of the vertical dipole amplitude as function of the electron cloud densities. Top and bottom plots are for Cesr-TA/2GeV and 5GeV. The number of step in the plots is integration step for one revolution in the simulation. The dotted line indicates tune shift due to electron cloud.

SUMMARY

Thresholds of electron cloud density for the fast head-tail instability were estimated by using analytic formula and computer simulation. The threshold density given by the formula and simulation agree well. The density agree with measurements in KEKB [4] and Cesr-TA[5]

Synchro-beta side band, which is induced by the fast head-tail instability, is studied by the simulation. Upper sideband is stronger for Cesr-TA/5 GeV (low $\omega_e\sigma_z/c <$ 10), while lower sideband is stronger for 2 GeV (high $\omega_e\sigma_z/c >$10). Upper sideband is seen in KEKB [4] and PETRA-III [6], and both sideband are seen in CesrTA/2GeV[5]. These observations seem to agree with the simulation results qualitatively. However the agreement is not perfect, tune shift for large $\omega_e\sigma_z/c$ is not seen in the simulation.

REFERENCES

[1] H. Jin, M. Yoon, K. Ohmi, J. Flanagan, M. Palmer, Jpn. J. Appl. Phys. **50**, 026401 (2011).
[2] K. Ohmi, F. Zimmermann, E. Perevedentsev, Phys. Rev. E . **65**, 016502 (2001).
[3] Y. Susaki and K. Ohmi,. Proceedings of IPAC'10.
[4] J. Flanagan et al., Phys. Rev. Lett. 94, 054801 (2005).
[5] R. Wanzenberg et al., in this proceedings.
[6] G. Dugan et al., in this proceedings.

Table 1: Parameter list for positron rings and their threshold for electron cloud head tail instability

	KEKB	KEKB	PETRA-III	Cesr-TA/2	Cesr-TA/5	SuperKEKB	Super B
Circumference (m)	3016	3016	2304	768	768	3160	1260
Energy (GeV)	3.5	3.5	6	2	5	4	6.7
Bunch population	3	8	0.5	2	2	9	5
Beam current (A)	0.5	1.7	0.1	-	-	3.6	1.9
Emittance	18	18	1	2.6	40	3.2	2
Coupling (%)	1	1	1	1	1	0.3	0.25
Mom. Comp. (10^{-4})	3.4	3.4	12.2	67.6	62	3.5	-
Bunch length (mm)	6	7	12	12.2	15.7	6	5
Energy spread(10^{-3})	0.73	0.73	1.31	0.8	0.94	0.8	0.64
Synchrotron tune	0.025	0.025	0.049	0.055	0.0454	0.025	0.0126
Bunch spacing (ns)	8	6	4	4-14	14	4	4
Average beta (m)	10	10	10	12	12	10	10
Electron frequency f_e(GHz)	28	40	35	35	11	150	175
Phase angle, $\omega_e\sigma_z/c$	3.6	5.9	8.8	8.9	3.7	18.8	18.3
Threshold density (10^{12} m^{-3})	0.63	0.38	0.95	0.82	5.02	0.27	0.54
Tune shift at the threshold	0.0078	0.0047	0.0053	0.009	0.014	0.003	0.0015

E-CLOUD EFFECTS ON SINGLE-BUNCH DYNAMICS IN THE PROPOSED PS2 *

M. Venturini†, M. Furman, and J.-L. Vay, LBNL, CA 94720, USA

Abstract

One of the options considered for future upgrades of the LHC injector complex entails the replacement of the PS with the PS2, a longer circumference and higher energy synchrotron. Electron cloud effects represent an important potential limitation to the achievement of the upgrade goals. We report the results of numerical studies aiming at estimating the e-cloud density thresholds for the occurrence of single bunch instabilities.

INTRODUCTION

The requirement for PS2 is to accelerate bunch trains up to 50 GeV kinetic energy (twice the energy reach of PS) in either the 25 ns or the 50 ns bunch spacing configuration, with 4×10^{11} and 5.9×10^{11} particles per bunch respectively.

In addition to space-charge effects [1] and classical instabilities [2], a potential limiting factor to the machine performance is the accumulation of electron cloud. E-cloud can affect the beam dynamics by triggering single or multi-bunch instabilities, or cause a growth of the beam emittance through incoherent effects. Extensive studies of electron cloud formation in the PS2 for various lattice elements, bunch-train structures were reported elsewhere [3]. Here we focus on the investigation of the impact of the electron cloud on the single-bunch dynamics. The study was carried out by macroparticle simulations using the Warp/POSINST code [4]. Preliminarily results were reported in [5].

PHYSICS MODEL

The physics model implemented in Warp is similar to that implemented in other already established codes for the analysis of e-cloud effects on the beam, like HEADTAIL [6]. Warp and HEADTAIL have been extensively benchmarked in the past and further spot-checks were carried out during these studies confirming a generally good agreement with each other. In the model, beam/e-cloud interactions occur at a finite number of discrete interaction points (or 'stations') along the machine circumference, where electrons are effectively confined to a transverse plane orthogonal to the beam orbit. An initially cold and transversely uniform electron distribution is assumed to exist before, and refreshed after, each bunch passage. In an actual machine the form of the distribution and peak value of the e-cloud density is generally strongly dependent on the lattice element type, and often on the exact location along the machine. However, for these studies it is assumed that the electron cloud, concentrated on uniformly distributed stations along the ring circumference, has the same density (peak value and form of transverse distribution) at all stations. The more realistic scenario in which the electron density can vary along the machine, reflecting, in particular, differences of e-cloud accumulation in dipoles and field-free regions as determined by e-cloud build-up codes like POSINST [7] or ECLOUD [8], should be investigated in future work for improved accuracy.

Table 1: Selected lattice/beam parameters used in the Warp simulations

	Extraction	Injection
Kinetic energy (GeV)	50	4
Trans. tunes $Q_{x,y}$	11.8, 6.71	11.8, 6.71
Rms emittance $\gamma\varepsilon_\perp$ (μm)	3	3
Trans. rms sizes $\sigma_{x,y}$ (mm)	1.33, 1.43	4.27, 4.59
Synch. tune Q_s (10^{-3})	1.24	12.1
Long. rms size σ_z (m)	0.30	1.41
Slippage η (10^{-3})	-1.82	-37.5

The electron dynamics during the bunch passage is determined by the self-fields and the fields generated by the beam particles, with an option to pin the electron motion to vertical lines to mimic the dynamics in a dipole magnet. The dynamics of the beam particles is determined by their response to the electron fields at the stations in the 'quasistatic' approximation [4] and optionally to the beam's own fields. The beam particles motion from station to station is modelled by linear transfer maps in the smooth approximation with chromatic effects accounted for by introduction of a phase-advance dependance on the particle momentum. The Poisson equation, yielding the fields generated by the electrons and the protons in the beam slices as the beam steps through each station, is solved on a rectangular grid with metallic boundary conditions. The horizontal and vertical dimensions $2a$=12.5 and $2b$=6.5 cm of the grid were chosen to match the values of the two axes of the proposed elliptical vacuum chamber design.

The goal of the study is to identify threshold values of the e-cloud density for the appearance of single-bunch instabilities. These can generally be captured by relatively short time-scale simulations. The results shown in the following were obtained by simulating the beam dynamics through 10^3 turns (corresponding to about 4.5 ms storage time) at injection and extraction on the assumption of steady (no energy ramping) machine conditions. We did not attempt to assess secular slow-rate emittance growth below instability

* Work supported by DOE under Contract No. DE-AC02-05CH11231 and the US LHC Accelerator Research Program (LARP).

† mventurini@lbl.gov

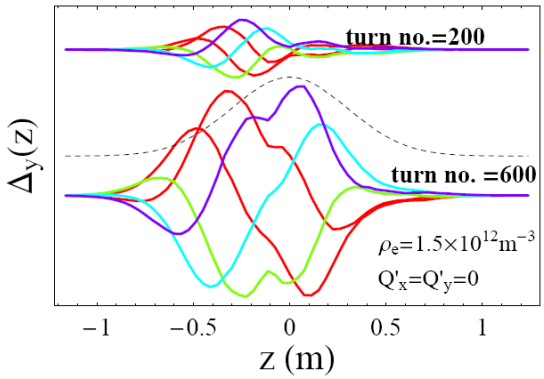

Figure 1: The beam vertical dipole moment along a bunch showing the signature of the head-tail like instability induced by e-cloud. The signal is monitored at one location along the ring for 5 successive bunch passages starting from turn no. 200 (upper set of curves) and 600 (lower set of curves). The dashed line represents the initial bunch longitudinal profile (beam head at $z > 0$).

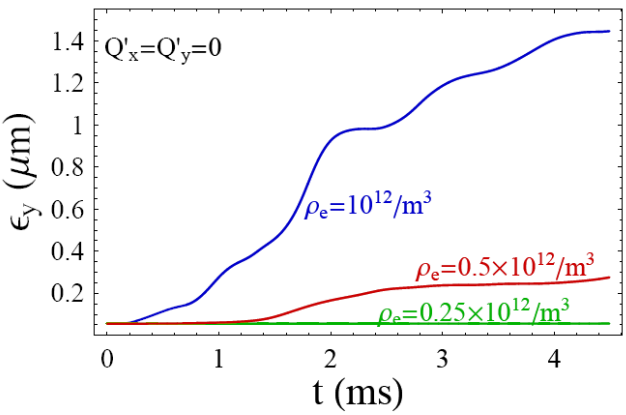

Figure 2: Evolution of the unnormalized vertical emittances for various choices of the e-cloud density ρ_e and vanishing chromaticities at $E = 50$ GeV beam energy.

threshold, which would require implementing a model for energy ramping and a considerably larger computational effort.

Selected machine parameters at injection and extraction used in the present simulations are summarized in Table 1. The beam transverse sizes reported in the table correspond to the nominal rms sizes averaged over the ring circumference for the given design emittances and betatron functions. The negative slippage factors correspond to a purely imaginary value $\gamma_t = 26i$ of the transition gamma factor.

The initial proton beam distribution is assumed gaussian in the 6D phase space (truncated at $\pm 4\sigma$ in the longitudinal direction), matched to the lattice in the absence of e-cloud and space-charge effects. We primarily assumed a nominal bunch population $N_p = 5.9 \times 10^{11}$ protons/bunch but considered a smaller population $N_p = 4.2 \times 10^{11}$ as well for comparison.

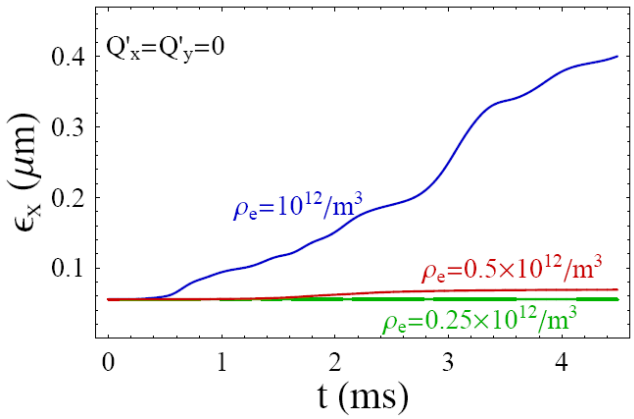

Figure 3: Evolution of the unnormalized horizontal emittances for various choices of the e-cloud density ρ_e and vanishing chromaticities at $E = 50$ GeV beam energy.

SIMULATION RESULTS

Monitoring of the emergence of the instability is primarily done by inspecting the evolution of the bunch centroid in the horizontal and vertical planes. Above threshold the bunch dynamics displays the classic signature of the head-tail instability [9, 10]. This is illustrated by Fig. 1, where we show five turn-by-turn snapshots of the beam slices vertical centroid weighted by the beam longitudinal density after 200 and 600 turns, showing the expected increase in oscillation amplitude in the presence of an instability. Growth in the amplitude of the centroid motion is invariably accompanied by a growth in the beam transverse emittance. Fig.'s 2 and 3 show examples of the evolution of vertical and horizontal emittances at extraction for vanishing chromaticities and various choices of the e-cloud density. The results of a systematic search for the instability threshold are shown in Fig. 4. For vanishing chromaticities the simulations place the instability threshold in the neighborhood of e-cloud density $\rho_e \simeq 0.4 \times 10^{12}$ m^{-3} in the vertical plane (pictures to the right) and slightly above that value in the horizontal plane ($\rho_e \simeq 0.5 \times 10^{12}$ m^{-3}, pictures to the left). We ascribe the discrepancy in the onset of the instability between the two planes to the different values of the transverse tunes, although we would have expected that the significantly larger tune in the horizontal plane would have resulted in a relatively more stable beam motion. The two top-pictures in Fig. 4 report the maximum relative emittance growth measured over 10^3 turns, while the pictures at the bottom report the maximum detected amplitude of centroid oscillation in units of the amplitude of the initial centroid offsets over the same number of turns. (Here and in the other simulations discussed in this paper we generally started the calculation with small beam centroid offsets equal to 10% of the beam rms transverse size). Negative chromaticities of a few units are shown to stabilize the motion as expected for a head-tail like instability in a lattice with negative slippage [11]. Specifically, for the

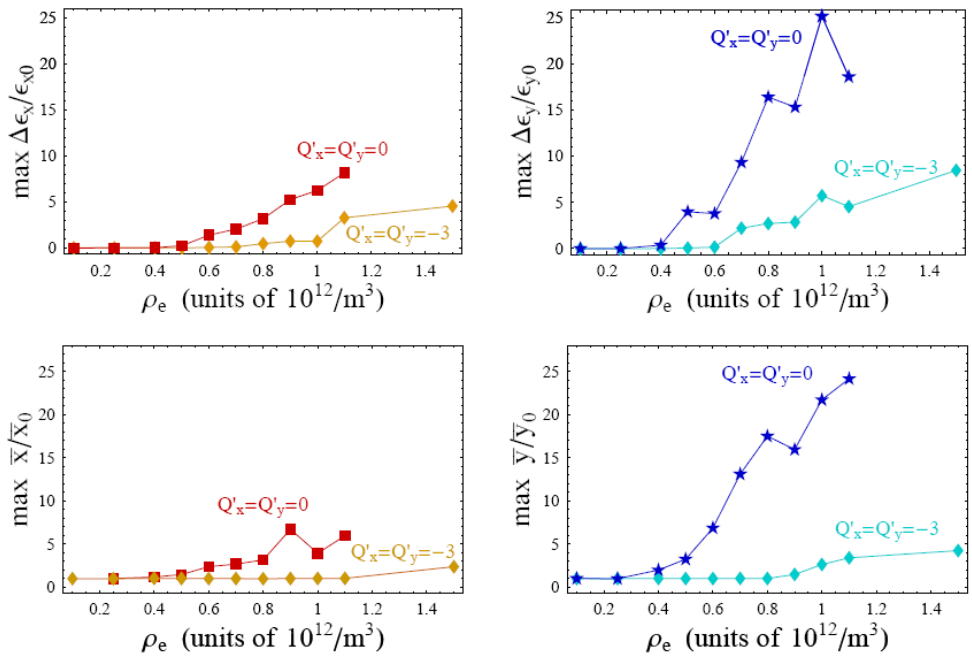

Figure 4: The instability threshold is detected by monitoring the max. variation of emittances (top pictures) and amplitude of the bunch centroid oscillations (bottom pictures) over 1000 turns for increasing values of e-cloud density. Finite negative chromaticities are shown to stabilize the motion. Left and right pictures are for horizontal and vertical motion respectively. $E = 50$ GeV beam energy.

case reported in Fig. 4 chromaticities $Q'_x = Q'_y = -3$ are shown to increase the threshold for emittance growth by 50% while the threshold measured in terms of centroid motion moves upwards by about 100%. We verified that inverting the sign of the chromaticity does not cure and, in fact, may aggravate the instability ($Q'_\alpha = \xi_\alpha Q_\alpha$, with $\alpha = x, y$, where ξ_α is the *relative* chromaticity). The simulations of Fig. 4 were carried out with the motion of the electrons unconstrained in the transverse plane, as is the case in free-field regions. In contrast, in dipoles the electrons gyrate along the vertical field lines effectively suppressing the onset of the instability in the horizontal plane. To approximate this behavior we carried out simulations using the Warp option that enables the pinning of the electron orbits to vertical lines. Results of these simulations are shown in the left picture of Fig. 5, showing the maximum amplitude of the vertical centroid motion oscillations over 10^3 turns (vanishing chromaticities). While there is no sign of instability (or significant emittance growth) in the horizontal plane (data not shown) we can observe a noticeable stabilization of the beam motion in the vertical plane as well, with the instability threshold now moved to about $\rho_e \simeq 0.8 \times 10^{12}$ m^{-3}. Because about half of the PS2 circumference is occupied by dipoles estimates based only on the calculations presented in Fig. 4 (field-free regions) are somewhat pessimistic. Instead, extrapolating these results to a model of machine that combines field free and dipole-occupied regions in the ratio 1:1 we can roughly estimate that, on the assumption that the electron density be the same in bends and field-free regions, we should expect the instability to occur for densities $\rho_e \simeq 2 \times 0.5 \times 10^{12}$ m^{-3} in horizontal plane and $\rho_e \simeq 1.5 \times 0.4 \times 10^{12}$ m^{-3} in the vertical plane.

Varying the bunch population from $N_p = 5.9$ to 4.2×10^{11} did not result in a significant variation in the the instability threshold in the vertical plane while resulting in a somewhat higher threshold in the vertical plane (Fig. 5, center picture).

Finally, we found that at injection the instability is generally milder than at extraction, with the threshold instability in the vertical plane appearing to be about 50% higher, see Fig. 5, right picture. In the same picture also observe a more noticeable difference of behavior in the two planes than observed at extraction, with the horizontal motion appearing relatively more stable. This is not unexpected [12] as the generally unfavorable scaling of instabilities that one would anticipate at lower energy is offset by larger transverse beam sizes that soften the interaction of the beam with the e-cloud. We should caution, however, that the linear approximation assumed for the longitudinal dynamics and a gaussian form assumed for the longitudinal distribution are not necessarily good approximations for the longitudinal dynamics of PS2 at injection, where the bunches fully occupy the rf buckets.

The simulations were carried out using a fairly large number of macroparticles (500k) to represent the proton beam in order to stabilize the simulations outcome from run to run. We used up to 65k macroelectrons to repre-

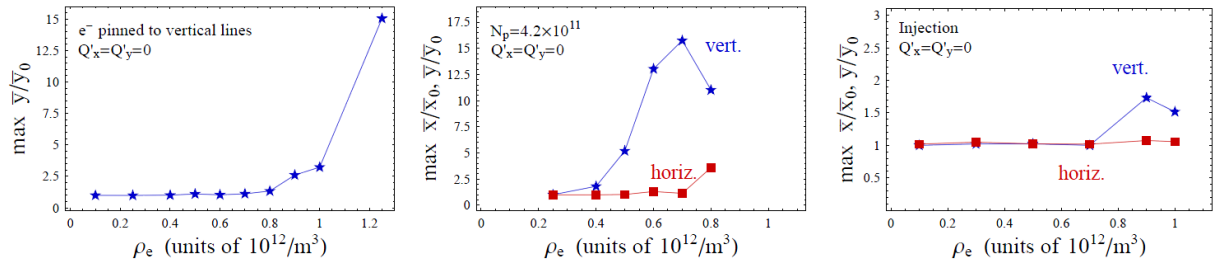

Figure 5: Left picture: max. amplitude of the beam centroid oscillations in the vertical plane *vs.* electron cloud density, with pinning of the electron orbits to vertical lines. Middle picture: decreasing the bunch population from $N_p = 5.9$ to 4.2×10^{11} proton/bunches does not affect the vertical motion significantly while increasing the threshold in the horizontal plane. Right picture: at injection the motion is more stable in both transverse planes. (Left and middle pictures are for the beam at extraction.)

sent the electron cloud starting with realizations of the initial e-cloud density obtained by depositing the macroelectrons on a regular grid. We used 40 stations/turn corresponding to 4 station/betatron wavelength in the vertical plane. Doubling the number of stations did not seem to result in substantially different results. We subdivided the $[-4\sigma_z, 4\sigma_z]$ longitudinal beam support into 64 slices, and generally used a 128×128 grid in the transverse plane. In selected cases we verified that increasing the transverse grid size to 256×256 resulted in somewhat different estimates of emittance growth and amplitude of centroid oscillation above instability threshold but not in a significant difference in the estimate of the critical density at which the instability occurs.

CONCLUSION

The critical values of e-cloud density for the onset of single-bunch instabilities found in this study are within, or close to, the range of densities expected from the e-cloud build-up studies [3].

In particular, the lowest threshold value ($\rho_e = 0.6 \times 10^{12}$ m^{-3}, in the vertical direction) is at the low-end of the interval of estimated e-cloud densities for the case with the more aggressive bunch train structure (25 ns bunch separation). Our results indicate that measures to mitigate the e-cloud accumulation (*e.g.* by decreasing the effective maximum secondary-electron yield below the $\delta_{\max} = 1.3$ reference value used in [3]) would have to be considered for a successful operation of the PS2 ring.

REFERENCES

[1] J. Qiang *et al.*, "Studies of Space Charge Effects in the Proposed CERN" PS2, IPAC 2010, Proceedings.

[2] K. Bane *et al.*, "Impedance Considerations for the Design of the Vacuum System of the CERN PS2 Proton Synchrotron", IPAC 2010, Proceedings.

[3] M. Furman *et al.*, "Electron-cloud Build-up Simulations in the Proposed PS2: Status Report", IPAC 2010, Proceedings.

[4] J-L Vay *et al.*, "Update on E-Cloud Simulations using the Package Warp/Posinst", PAC09 Proceedings (2009).

[5] M. Venturini *et al.*, "E-cloud Driven Single-bunch Instabilities in PS2", IPAC 2010, Proceedings.

[6] G. Rumolo and F. Zimmermann, PRST-AB **5** 121002 (2002).

[7] M. A. Furman and G. R. Lambertson, KEK Proc. 97-17; M. A. Furman and M. T. F. Pivi, PRSTAB **5**, e124404 (2003).

[8] G. Rumolo and F. Zimmermann, "Practical User Guide for ECLOUD," CERN-SL-Note-2002-016 (AP), May 13, 2002.

[9] K. Ohmi, F. Zimmermann, and E. Perevedentsev, Phys. Rev. E, **65** 016502 (2001).

[10] F. Zimmermann, PRST-AB, **7** 124801 (2004).

[11] A. Chao, Physics of Collective Instabilities in High Energy Accelerators, John Wiley & Sons, Inc., New York, 1993.

[12] G. Rumolo *et al.*, Phys. Rev. Lett. **100** 144801 (2008).

IMPLEMENTATION AND OPERATION OF ELECTRON CLOUD DIAGNOSTICS FOR CESRTA*

Y. Li#, X. Liu, V. Medjidzade, J. Conway, M. Palmer
CLASSE, Cornell University, Ithaca, NY 14853, U.S.A.

Abstract

The vacuum system of Cornell Electron Storage Ring (CESR) was successfully reconfigured to support CesrTA physics programs, including electron cloud (EC) build-up and suppression studies. One of key features of the reconfigured CESR vacuum system is the flexibility for exchange of various vacuum chambers with minimized impact to the accelerator operations. This is achieved by creation of three short gate-valve isolated vacuum sections. Over the last three years, many vacuum chambers with various EC diagnostics (such as RFAs, shielded pickups, etc) were rotated through these short experimental sections. With these instrumented test chambers, EC build-up was studied in many magnetic field types, including dipoles, quadrupoles, wigglers and field-free drifts. EC suppression techniques by coating (TiN, NEG and a-C), surface textures (grooves) and clearing electrode are incorporated in these test chambers to evaluate their vacuum performance and EC suppression effectiveness. We present the implementation and operations of EC diagnostics.

INTRODUCTION

With the successful reconfiguration of Cornell Electron Storage Ring (CESR) [1], CesrTA provides unique opportunities for study electron cloud growth and mitigation, and ultra-low emmittance lattice development and tuning, as well as beam instrumentation R&D, that are critical for the global design efforts of the International Linear Collider Damping Rings. As depicted in Fig 1, two long straight experimental sections and two very short experimental sections were created to provide flexibility of the CesrTA studies, to continue to support X-ray users at CHESS (Cornell High-Energy Synchrotron Sources). These experimental sections may be isolated via gate valves, so that test chambers could be exchanged without significantly impact overall accelerator operations. In these experimental sections, many new vacuum chambers were deployed with various EC diagnostics, such as retarding field analyzers (RFAs) for measuring steady-state EC build-up [2], RF shielded pickups [3] for studying EC growth, and TE wave transducer/receiver beam buttons [4]. With these EC diagnostics, effectiveness of many types of EC suppression techniques was evaluated in the test chambers. The details of these EC diagnostics and the corresponding measurements are described in separated papers in these proceeding. This paper is focussed on vacuum aspects of the implementation and the operational performances of these diagnostics and test chambers.

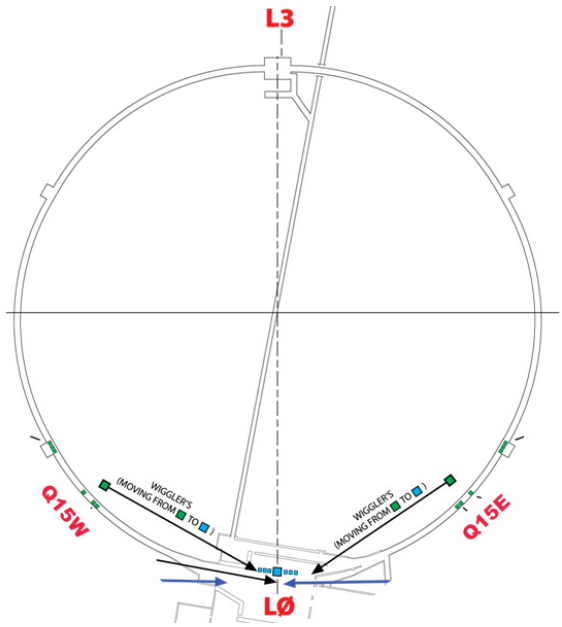

Figure 1: Four experimental sections were created after re-configuration of CESR vacuum system, including two long straights in south IR (L0), the north IR (L3) and two short sections in the arcs (namely, Q15W and Q15E). These sections may be isolated by gate valves to allow flexibility in deployments of various test chambers.

SOUTH IR EXPERIMENTAL SECTION

After removal of the center CLEO HEP Detector package, the South IR experimental section (~17.6 m in length), as shown in Fig 2, hosts a string of six superconducting wigglers (SCWs). The three SCWs in the West of L0 were fitted beampipes equipped with the thin-style RFAs [5]. A total of four RFA SCWs were constructed and rotated through this experimental section. The four RFA SCWs have different beampipe interior features, and they are (1) bare copper, (2) copper with TiN coating, (3) copper with a copper grooved bottom plate (which was later coated with TiN), and (4) copper with a EC clearing electrode at the bottom.

* Work supported by the US National Science Foundation (PHY- 0734867), the US Department of Energy (DE-FC02-08ER41538), and the Japan / US Cooperation Program
# YL67@Cornell.edu

RFA SCW with a grooved plate

Fig 3 shows the structure of the RFA SCW with a Cu-groove plate, and details of the grooves. Simulations [6] showed that in order to suppress secondary electron emission yield (SEY), the tips and valleys of the triangular grooves must be very shard, with radius less than 0.1mm. The required sharpness was achieved via a special milling process. The groove plate is e-beam welded to the bottom of the RFA SCW beampipe.

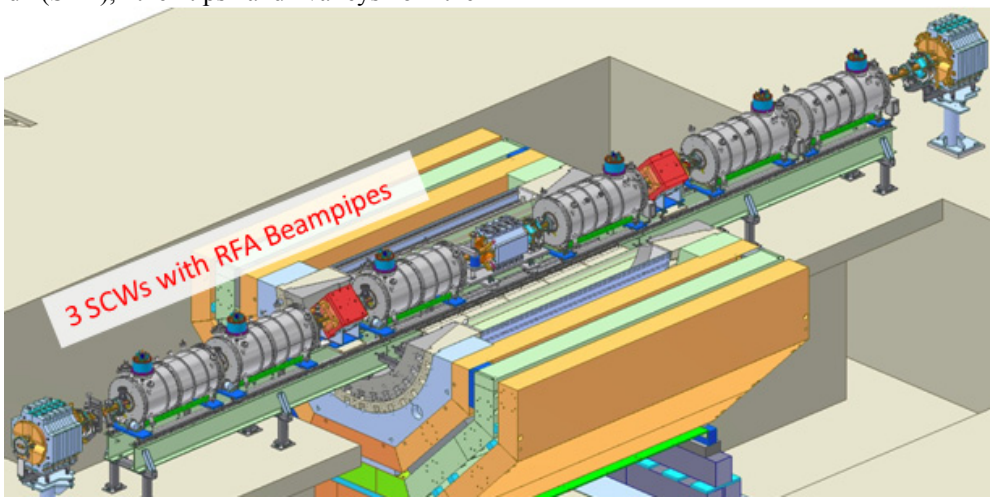

Figure 2: CESR South IR straight section with six super-conduction wigglers (SCWs). Three of these SCWs in the west side are fitted with RFA-instrumented beampipe. Various mitigation techniques, including TiN coating, grooved beampipe and clearing electrode, were tested with these three SCWs

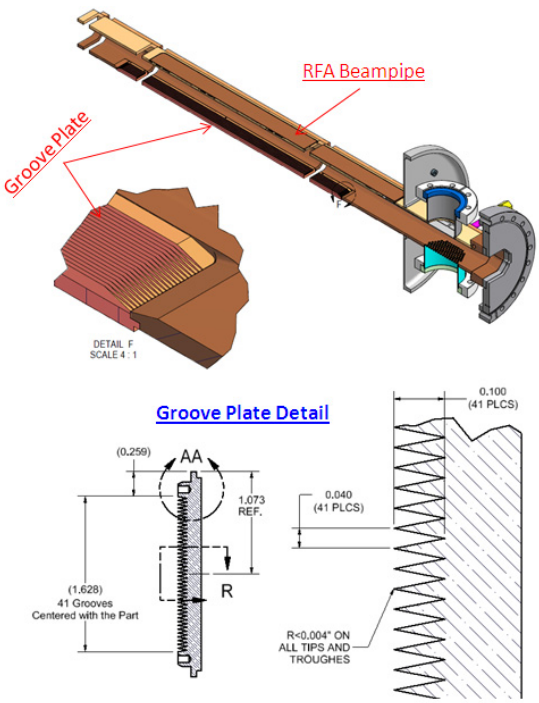

Figure 3: RFA SCW beampipe with a copper grooved plate. The groove plate has 41 triangular grooves of 1-mm spacing, and is integrated to the bottom beampipe via E-beam weld.

The grooved RFA SCW was installed in the South IR section between July 2009 and March 2010 for CesrTA experiment runs. After the 2009-2010 CesrTA experiment runs and CHESS high current runs, the grooved assembly was removed from CESR during an accelerator shutdown in March 2010. A careful optical close-up inspection was performed on the groove plate over its entire length, and the inspection did not detect any beam-induced damage to the groove tips.

TiN coating was then applied to the interior surfaces of the grooved beampipe, via DC sputtering process. With careful arrangement of multiple titanium electrodes, a uniform TiN coating (~0.5μm in thickness) was deposited onto the grooves without visible shadowing. The TiN coated RFA SCW assembly was re-installed in the west South IR for further CesrTA experiments.

RFA SCW with Clearing Electrode

An electron cloud clearing electrode is deployed on one of the RFA SCW. The clearing electrode is based on the KEK design [7], using thermal spray thin film technique. As illustrated in Fig.4, the electrode is formed by a 0.2-mm thick alumina base film and a 0.2-mm thick tungsten film. DC voltage up to 1.5 kV can be applied to the electrode through an N-type vacuum feedthrough and a low profile contact button. This clearing electrode has very low higher-order-mode loss (HOML), which is critical for both the CesrTA and the CHESS operations. This RFA SCW was installed in the South IR region in March 2010, and has successfully operated through two CesrTA experiment runs and the CHESS X-ray runs. A thermocouple was attached immediately underneath the electrode, bear the contact button. No measurable beam induced heating was detected with stored total beam current as high as 430mA. A close-up inspection during

January 2011 shutdown found that the electrode and the electric contact are in excellent condition.

Vacuum Performance

The South IR section is pumped by six non-evaporable getter (NEG) pumps (as primary pumps) and six small ion pumps (for non-gettable gases). Vacuum performance of this section is monitored by six evenly spaced cold-cathode ion gauges (CCGs) and a residual gas analyzer (RGA) at center of the section.

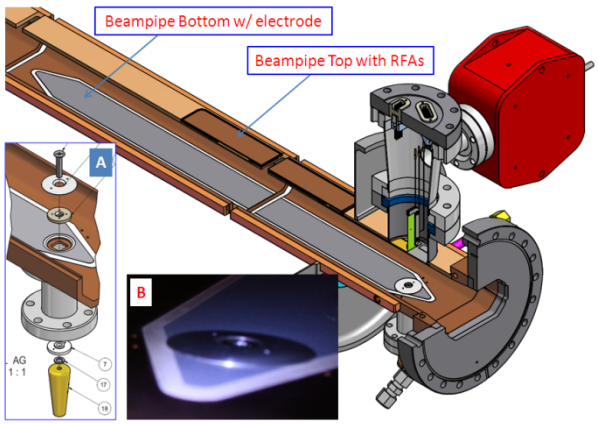

Figure 4: RFA SCW beampipe with a clearing electrode. The electrode was deposited onto the bottom half of the beampipe via thermal-spray technique. Insert A illustrates structure of low-profile electric contact, and insert B is a image of the contact button taken during post operation inspection in January 2011.

The beam processing of the vacuum chambers is monitored during CHESS X-ray runs, where the conditions for the stored beams are constant and stable. The measure synchrotron radiation (SR) induced pressure rises at three CCGs are plotted in Fig. 5 as a function of total beam dose. During the CHESS runs, the east side and the west side of the section receive comparable SR flux. However, the west sides had much higher SR-induced outgassing. One plausible source of higher outgassing rate in west side is due to the TiN coating..

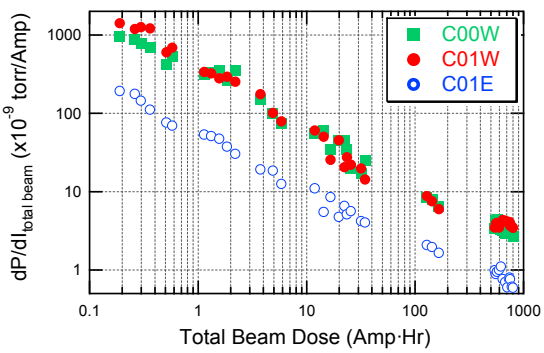

Figure 5: Beam conditioning of vacuum chambers in the South IR experimental section, as measured by cold cathode ion gauges at the center of the section (C00W) and at east- and west-side (C01E and C01W).

Typical RGA spectra in the region clearly indicate desorption of N_2, from the TiN coated surfaces. As shown in Fig. 6, significant high N_2 desorption is related to high-energy photons generated the SCWs in the section. To further demonstrate the point, the ratio of N_2 and H_2 was measured with increasing SCW magnetic field. The results in Fig.7 clearly showed increase of N_2 desorption with SCW SR fan striking the TiN coated surfaces.

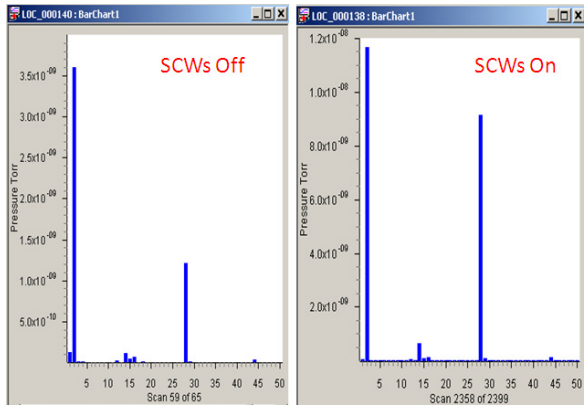

Figure 6: Two typical RGA spectra taken at the center of the South IR, with positron beam energy at 4 GeV.

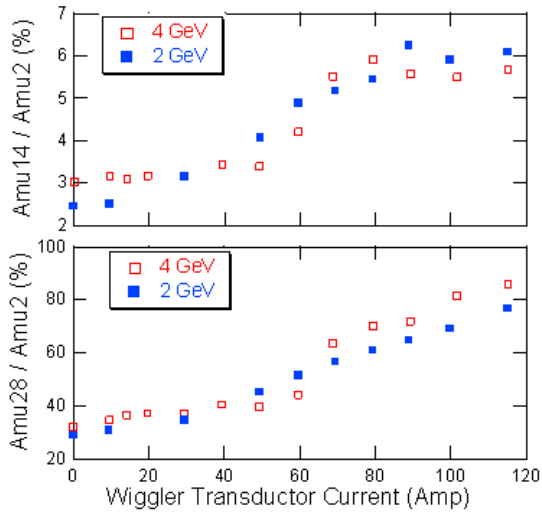

Figure 7: Increased desorption of N_2 from TiN coated surfaces with increasing magnetic field in the SCWs. The measurements were taken with 35 mA positron beam at beam energies of 2 and 4 GeV.

NORTH IR EXPERIMENTAL SECTION

The North Experimental Section (L3) is another long straight, that host (1) SLAC Chicane dipole magnets with RFA on grooved and TiN coated aluminium chambers; (2) RFA equipped quadrupole chamber; (3) NEG coating tests, (4) TE wave measurement, and (5) in-situ SEY measurement system. Fig. 8 depicts the L3 experimental section.

NEG Coating Tests

NEG coating test setup is shown in Fig. 9. To measure effectiveness of NEG coating in EC suppression, a NEG coated stainless steel chamber is equipped with 3 RFAs and a RF-shielded pickup (designed and fabricated by LBNL team). To prevent influences of un-coated beampipes, the test chamber is 'guarded' by a pair of NEG coated 1-m long stainless steel beampipes. (The beampipe string was NEG coated by SAES Getters.)

The vacuum performance of the NEG coating was monitored four CCGs and one RGA. After a brief beam conditioning, the NEG coating was activated at 250°C for 24-hour. The beam processing of the NEG coated beampipes is displayed in Fig.10.

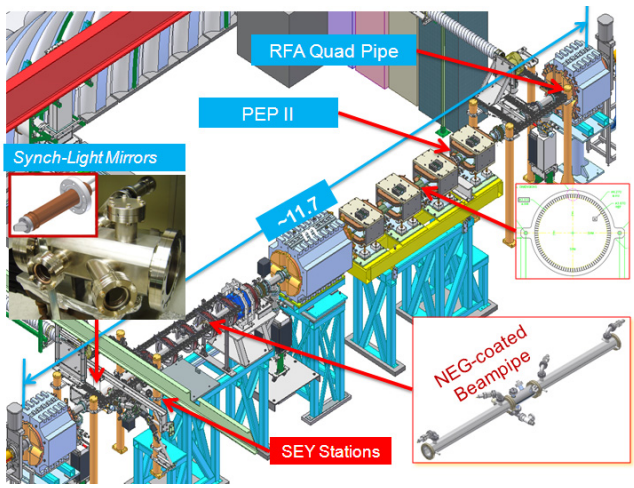

Figure 8. North Experimental Section

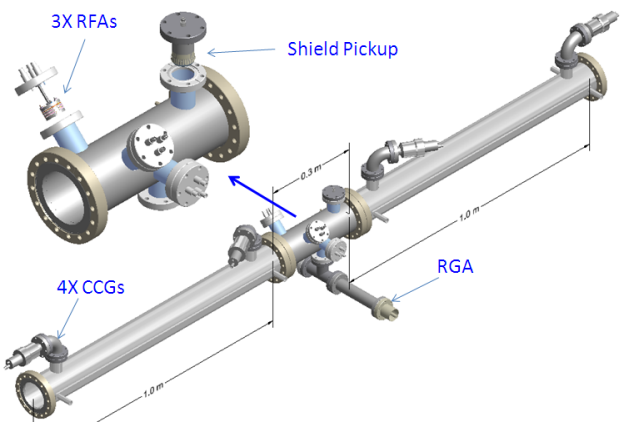

Figure 9. NEG Coating test setup

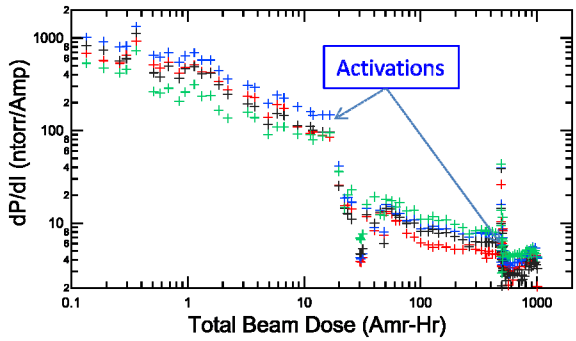

Figure 10. Beam processing of NEG coated beampipes

RFA Quadrupole Chamber

Cornell thin-style RFA was implemented in a bare aluminium quadrupole, as illustrated in Fig.11. The RFA structure consisted of a curved high-transparency Au-plated copper mesh as retarding grid and a flexible circuit detector with 12 segments that provides ~76° coverage. After CesrTA experimental runs from July 2009 to March 2010, the quad RFA beampipe was coated with TiN coating at Cornell. The TiN-coated chamber was re-installed in April 2010 at the same location in L3 for further experiments.

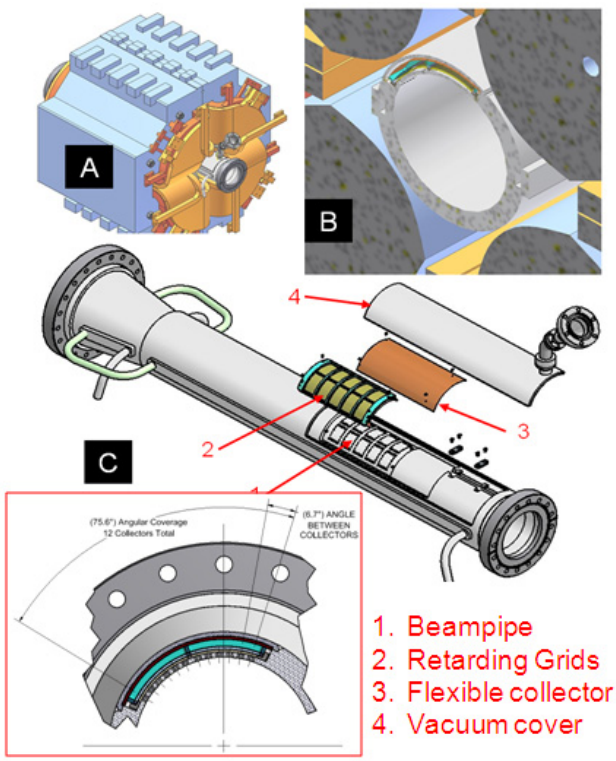

Figure 11. Implementation thin RFA in a quadrupole vacuum chamber

Secondary Emission Yield System

Two SEY systems were installed on a SLAC-build housing chamber. With load-locks, samples of different materials and different coatings can be inserted for SR exposure, without interrupting CESR operations. The

detail description of the *in-situ* SEY system and results are given in this proceeding [8].

SHORT EXPERIMENTAL SECTIONS

Two very short experimental sections (namely Q15W and Q15E sections) were created in the arc of CESR. Each section contains only one bending magnet/chamber and a short straight. With gate valves, many test chambers may be rotated through these sections without significant impact to the CESR operations. So far, many EC-suppression coatings were evaluated on aluminium beampipes. The design of the aluminium beampipe, as shown in Fig 12, incorporated a segmented RFA, two sets of RF-shielded pickups. With this design, bare aluminium, TiN coated and amorphous carbon coated aluminium chambers have been evaluated. The beam conditioning history of these test chambers are summarized in Fig 13, which showed very similar vacuum performances of these surfaces.

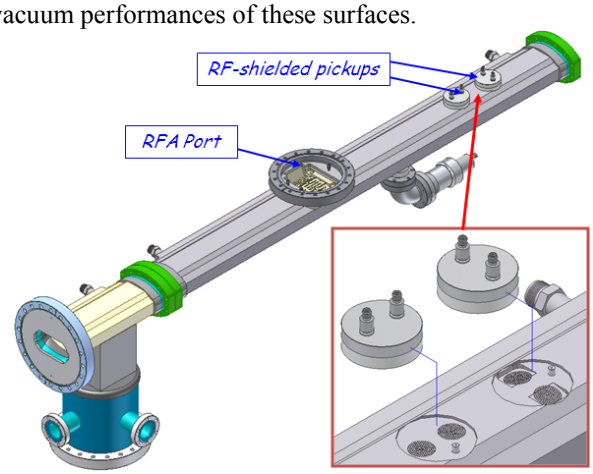

Figure 12. This design of aluminium chamber is used in the short experimental sections at Q15W and Q15E in CESR.

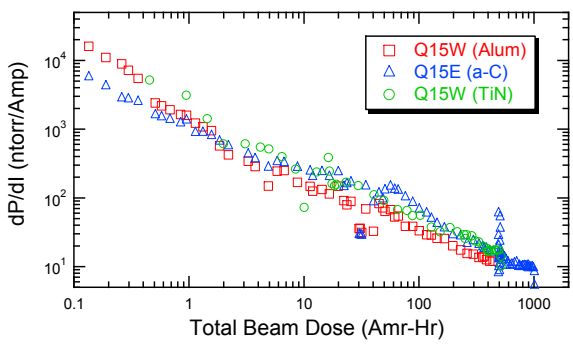

Figure 13. Beam conditioning of bare aluminium, TiN- and amorphous carbon coated aluminium beampipes.

SUMMARY

The reconfigured CESR vacuum system provided flexibility needed for many EC studies for CesrTA. We have successfully implemented RFAs in all major types magnets (including dipole, quadrupole and wigglers) and drifts. Other EC diagnostics, such as RF-shielded pickups, TE-wave beam buttons, were also deployed in many experimental sections. With these diagnostics, many EC-suppression techniques were evaluated at CesrTA, such as various coatings (TiN, amorphous- and diamond-like carbon, and NEG), grooved surfaces (both triangular and rectangular shaped grooves), and clearing electrode. The vacuum performances of the EC-suppression features were also evaluated.

ACKNOWLEDGEMENT

The Vacuum Group (Brent Johnson, Tobey Moore, William Edward and Brian Kemp) provided excellent technical support throughout the project. It would be impossible to achieve what is described in this paper, without their dedicated assistances.

Ms. Dawn Munson of Lawrence Berkeley National Laboratory (LBNL) and many technical staff member fabricated all the RFA beampipes of the SCWs deployed in the South IR in this study. Their assistances are greatly appreciated.

Dr. Y. Suetsugu of KEK introduced the technique of thermal sprayed EC clearing electrode, and arranged thermal spray of EC clearing electrode for the CesrTA SCW beampipe.

Dr. S. Calatroni and his colleagues at CERN provided assistance in amorphous carbon coating on two Q15 EC-study vacuum chambers.

REFERENCES

[1] Y. Li, et al, "CESRTA VACUUM SYSTEM MODIFICATIONS" Proceedings of PAC09, Vancouver, BC, Canada, p.357.

[2] J. Calvey et al, "Electron cloud mitigation investigations at CESRTA", these proceedings.

[3] D. Rubin, et al, "Overview of the CESR TA R&D Program", these proceedings.

[4] S. De Santis, et al, "TE wave measurements at CESR TA", these proceedings.

[5] Y. Li, et al, "Design and Implementation of CesrTA SuperConducting Wiggler Beampipes with Thin Retarding Field Analyzers", Proceedings of PAC09, Vancouver, BC, Canada, p. 3507.

[6] L. Wang, SLAC, private communications.

[7] Y. Suetsugu, et al., "Demonstration of electron clearing effect by means of a clearing electrode in high-intensity positron ring". Nucl. Instr & Methods in Phy. Res. Sec. A, 2009. 598(2), p. 372.

[8] J.S. Kim, et al, "In situ SEY measurements in CesrTA", these proceedings.

.

BUNCH-BY-BUNCH INSTRUMENTATION UPGRADES FOR CESR, BASED ON REQUIREMENTS FOR THE CESR TEST ACCELERATOR RESEARCH PROGRAM*

N. Rider#, J. Alexander, M. Billing, C. Conolly, N. Eggert, E. Fontes, W. Hopkins, B. Kreis, A. Lyndaker, R. Meller, M. Palmer, D. Peterson, M. Rendina, P. Revesz, D. Rubin, J. Savino, R. Seeley, J. Shanks, C. Strohman, CLASSE, Cornell University, Ithaca, NY 14853, U.S.A.
R. Holtzapple, California Polytechnic State University, San Luis Obispo, CA 93407, U.S.A.,
J. Flanagan, KEK, Japan

Abstract

The research focus of the CESR Test Accelerator program requires new instrumentation hardware, software and techniques in order to accurately investigate beam dynamics in the presence of electron cloud effects. These new instruments are also required to develop low emittance beam conditions which are key to the success of the damping ring design for the International Linear Collider. This paper will detail some of the architecture and tools which have been developed to support these efforts. Emphasis will be placed on the 4 ns bunch-by-bunch Beam Position Monitoring system as well as the 4 ns capable x-ray Beam Size Monitor.

CESR INSTRUMENTATION SUPPORT

A structure of supporting hardware and software has been developed to support the instrumentation required for the CESR Test Accelerator (CesrTA) program.. Some of the components of this structure are listed below:

- Matlab based control and analysis software
- Custom C based control and analysis software
- Standardized data formats with shared file input/output routines
- Common low level communication interfaces
- Common timing synchronization and triggering

BPM DEVELOPMENT

A new turn-by-turn beam position monitoring system has been developed. This system allows for turn-by-turn multi-bunch measurements of 4 nS spaced bunches. Some of the key design goals of the new system are as follows:

- Front-end bandwidth of 500 MHz
- Absolute position accuracy of 100 um
- Single-shot position resolution of 10 um
- Differential position accuracy of 10 um
- Channel to channel sampling accuracy of 10 pS
- BPM tilt errors of 10 mrad or less

Performance of the bpm system has been shown to be in line with these goals. Fig.1 shows vertical orbit differences between pairs of detectors located close together on a single vacuum chamber. The histogram contains 256k turns of data. The single unit sigma is shown on each plot and is substantially consistent with our design goals.

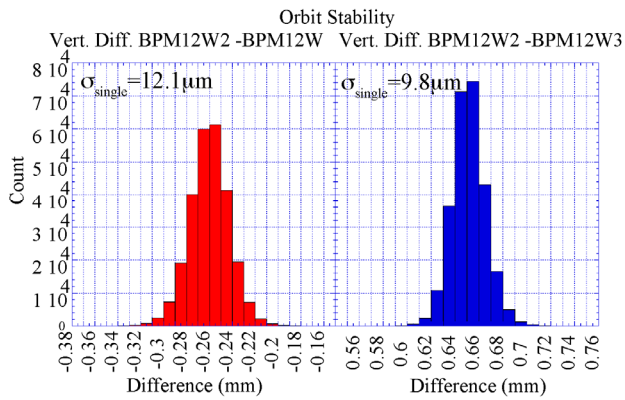

Fig 1: BPM Stability Measurement Results

XBSM HARDWARE

The x-ray Beam Size Monitor (xBSM) [1,2,3,4] has been developed in conjunction with the Cornell High Energy Synchrotron Source. Existing beam lines have been utilized while optics and detectors were designed specifically for the monitor. The x-ray source is a dipole magnet which is part of CESR. X-rays pass through the evacuated beam line and a set of optics elements. There are three optics elements that can be used: a vertically limiting slit, a Fresnel zone plate and a coded aperture. The layout of the XBSM experimental set up is shown in figure 2.

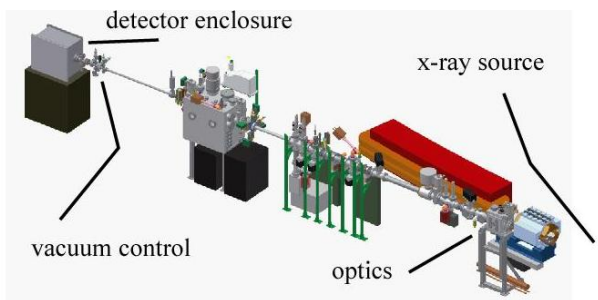

Fig 2: XBSM Layout

* Supported by the US National Science Foundation (PHY-0734867) and Department of Energy (DE-FC02-08ER41538)
# NTR7@Cornell.edu

The **vertically limiting slit** operates as a pin-hole lens. The slit has been adjusted to be about 50μm in height, which gives the minimum image height. This slit size creates an image with width about (20 um x magnification). A smaller slit height would cause the image to broaden due to diffraction while a larger slit height would cause the image to broaden due to transmission.

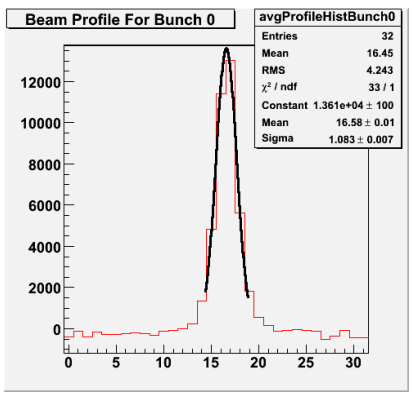

Fig 3: Vertically limiting Slit Image

Advantage:

The pin-hole image is largely insensitive to the x-ray wavelength within the synchrotron radiation spectrum.

Disadvantage:

While the pin-hole provides a simple peak, as shown in figure 3, the image is a convolution of the beam height and the slit height resulting in large uncertainties for beam size measurements below about 16μm.

The image of the **Fresnel Zone Plate** (FZP) is a diffraction pattern and sensitive to the x-ray wavelength. There is a central peak due to designing the x-ray beam and FZP to focus near the maximum of the x-ray wavelength distribution.

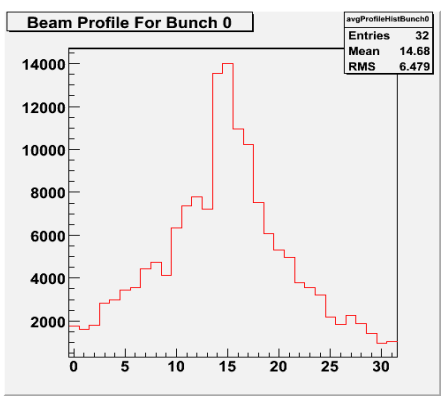

Fig 4: Fresnel Zone Plate Image

Disadvantage:

The image shown in figure 4 is without the use of a monochromator; it has a broad underlying distribution of out-of-focus x-rays. Use of a monochromator eliminates the broad component but does not allow enough x-ray flux for useful turn-by-turn measurements.

Advantage:

The central peak of the image is a focus with natural width less than one pixel width; it provides useful beam size measurements to the smallest beam size. Turn averaging and fitting procedures to extract this information are being developed.

The image of the **Coded Aperture** shown in figure 5 is a combination of transmission and diffraction resulting from the 8 slits ranging in size from 10 to 40μm.

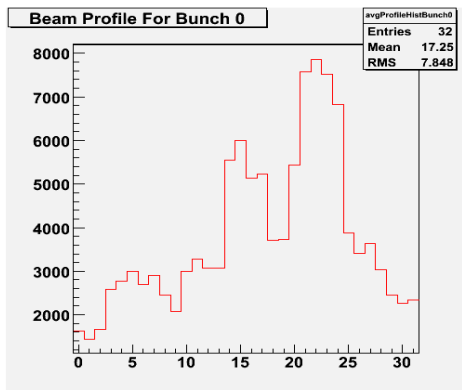

Fig 5: Coded Aperture Image

Advantage:

As in the case of the vertically limiting slit, the imaging is relatively insensitive to variations in the wavelength. The resolving power of the coded aperture has been compared to that of the Fresnel zone plate both without the use of a monochromator. Data was collected in "slow scans" for the two imaging devices, for two beam sizes. For each imaging device, the RMS of the difference between images from different beam sizes is an indication of the resolving power. The RMS difference for the coded aperture was 1.7x greater than that of the Fresnel zone plate (for the same change in beam size and normalized for incident photon flux), indicating that the beam size resolving power of the coded aperture is superior. The coded aperture is discussed in further detail elsewhere [5].

A Challenge:

In the future, we will develop the fitting procedures necessary to exploit the improved information provided by the multiple-peaked image.

HIGH SPEED DIGITIZER DEVELOPMENT

To match the characteristics of the ILC damping ring design, CESR is being upgraded to operate with 4ns bunch spacing. The new readout system for the XBSM provides 32 parallel 250MHz digitizers. Variable gain amplifiers have a range of 24dB. Digitization of the amplifier output, shown in figure 6, demonstrates

successful operation of the digitizers and optimization of the amplifiers for 4 ns operation.

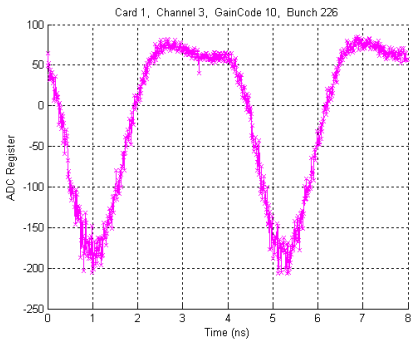

Fig 6: 4 nS Spaced Bunch Digitization

DETECTOR DEVELOPMENT

The detector is a vertical array of 32 InGaAs diodes with pitch 50µm and horizontal width 400µm. The InGaAs layer is 3.5 µm thick, which absorbs 73% of photons at 2.5keV; there is a 160nm Si_3N_4 passivation layer. The time response of the detector is sub-nanosecond. As shown in figure 7, sequential diodes are read out on opposite sides of the array with 100 µm spacing; diodes are connected, via wire bonds, to a conventional 250 µm center-to-center printed circuit board.

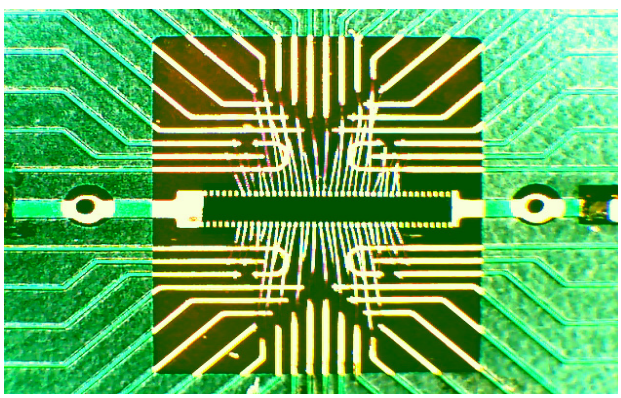

Fig 7: xBSM Detector

SUMMARY

The CesrTA program has necessitated the development of many pieces of instrumentation software and hardware. These pieces have all been integrated into a supporting framework upon which the Beam Position Monitors and X-ray Beam Size Monitors depend.

The upgraded 4 ns x-ray Beam Size Monitor is undergoing commissioning and development while providing useful experimental results for the program. Future developments in analysis techniques will allow the program to achieve the program goals in support of the International Linear Collider design effort.

REFERENCES

[1] J.P. Alexander *et al*, TH5RFP026, PAC09
[2] J.P. Alexander *et al*, TH5RFP027, PAC09
[3] J.W. Flanagan *et al*, TH5RFP048, PAC09
[4] D. P. Peterson *et al*, MOPE090, PAC10
[5] J.W. Flanagan *et al*, MOPE007, PAC10

METHODS FOR QUANTITATIVE INTERPRETATION OF RETARDING FIELD ANALYZER DATA*

J.R. Calvey, J.A. Crittenden, G.F. Dugan, M.A. Palmer, CLASSE, Cornell University, Ithaca, NY, USA
K. Harkay, ANL, Argonne, Il, USA †

Abstract

A great deal of Retarding Field Analyzer (RFA) data has been taken as part of the CesrTA program at Cornell. Obtaining a quantitative understanding of this data requires use of cloud simulation programs, as well as a detailed model of the RFA itself. In a drift region, the RFA can be modeled by postprocessing the output of a simulation code, and one can obtain best fit values for important simulation parameters using a systematic method to improve agreement between data and simulation.

INTRODUCTION

RFAs essentially consist of three elements [1]:

- Holes drilled into the beam pipe to allow electrons to pass through
- A retarding grid to which a negative voltage can be applied, rejecting any electrons which have less than a certain energy
- A collector which captures any electrons that make it past the grid. Often there are several collectors arranged transversely across the top of the beam pipe.

In principle, a single RFA measurement gives a great deal of information about the local behavior of the electron cloud. A typical "voltage scan," in which the retarding voltage of the RFA is varied while beam conditions are held fixed, is a measurement of the density, energy distribution, and transverse structure of the cloud [2]. In practice, however, it is a highly nontrivial task to map a data point from a voltage scan to any of these physical quantities. Typically, this gap is bridged through the use of cloud simulation programs, which track the motion of cloud particles during and after the passage of a bunch train. At CesrTA we have primarily used two such programs, POSINST [3] and ECLOUD [4].

The simplest method for simulating the output of an RFA for a given set of beam conditions is post-processing the output of one of these programs. More specifically, these codes can output a file containing information on each macroparticle-wall collision, and one can perform a series of calculations on this output to determine what the RFA would have seen had one been present.

A basic postprocessing script does the following:

- Determine if the macroparticle has hit in the azimuthal region where one of the RFA collectors exists.
- Calculate an efficiency (probability of passing through the beam pipe hole) based on the incident angle.
- Determine if the macroparticle has enough energy to make it past the retarding field.
- Deposit an appropriate amount of current on the grid and collector.

Note that by proceeding in this way one impicitly assumes that the presence of the RFA has no effect on the development of the cloud. This assumption is probably justified for a drift RFA, but may not be in the presence of a magnetic field [5]. This paper will focus on the drift case.

METHODOLOGY

The sheer volume of RFA data obtained so far at CesrTA necessitates a systematic method for detailed analysis. The goal is, given a set of voltage scan data, to find a set of simulation parameters that bring data and simulation into as close to agreement as possible. The best fit parameters obtained from this method should be close to the real values for the material under study. The following method was employed to accomplish this:

1. Choose a set of voltage scan data.
2. Choose a set of simulation parameters.
3. Do a simulation with the nominal values of each parameter.
4. Postprocess the output of the simulation to obtain a predicted RFA signal.
5. For each voltage scan and each parameter, do a simulation with a high and low value of the parameter, and determine the predicted RFA signals.
6. For each point in the simulated voltage scan, do a best linear fit to the curve of RFA signal vs parameter value. The slope of this line determines how strongly this point depends on the parameter.
7. Find a set of new parameters that should minimize the difference between data and simulation, assuming linear dependence of each voltage scan point on each parameter.
8. Repeat the process with this new set of parameters.

Table 1 lists one set of beam conditions that has been subjected to this method. All of these data were taken on the same day, at a beam energy of 5.3GeV. Note that it includes 20 and 45 bunch trains at different bunch currents,

* Work supported by the US National Science Foundation (PHY-0734867) and Department of Energy (DE-FC02-08ER41538)
† Work supported by the US Department of Energy (DE-AC02-06CH11357)

as well as 9 bunches equally spaced around the ring. It also includes both electron and positron beams. So a broad region of beam conditions can be studied within one round of analysis.

Table 1: Set of Beam Conditions Under Study

Bunches	Spacing (ns)	Bunch Cur (mA)	Species
20	14	2.8	e^+
20	14	10.75	e^+
45	14	.75	e^+
45	14	1.25	e^+
45	14	2.67	e^+
9	280	4.11	e^+
20	14	2.8	e^-
20	14	10.75	e^-
45	14	.8	e^-
45	14	1.25	e^-
9	280	3.78	e^-

PARAMETERS

In principle this method can be used to obtain a best fit value for any number of primary and secondary electron yield parameters. In practice, due to time and disk space constraints, it is better to choose a few important parameters to fit. Table 2 lists a standard set of parameters used for this method. Note that the cloud simulations in this case were done in POSINST, so the POSINST name for each parameter is given [3]. The photon flux and reflectivity for each RFA are fixed, based on simulations of photon production and reflection in the CesrTA vacuum chamber [6]. Where two values are given for the nominal value of the parameter, the first refers to an uncoated (Aluminum) chamber, and the second to a (TiN, Carbon, or NEG) coated one. Also note that dt0pk (the total peak yield) is not an independent parameter, but rather the sum of the three secondary yield components (the "true secondary," "rediffused," and "elastic" yield) at peak energy.

Parameter Domains

We want to understand where each parameter matters the most, so we can determine their values as independently as possible. One could think of this as "diagonalizing" the problem by choosing to look at voltage scan points that depend more strongly on one parameter than any other. This is best accomplished by using data taken in a wide variety of beam conditions. Figure 1 shows the strongest parameter for a few different conditions, as a function of retarding voltage and collector number, color coded according to legend on the top left. Specifically, the colors indicate the parameter for which a small fractional variation will have the largest effect on the simulated voltage scan. For example, the RFA signal for a 20 bunch train of electrons at high bunch current (Fig. 1(c)) depends strongly on the

Table 2: Parameters Under Study

Parameter	Description	Nominal
dtspk	Peak "true secondary" yield	1.8, .8
P1rinf	"Rediffused" yield	0.2
dt0pk	**Total peak yield** (δ_{max})	**2.0, 1.0**
P1epk	Low energy elastic yield	0.5
E0tspk	Peak yield energy	310, 500
queffp	Quantum efficiency	0.1
eksigphel	Primary energy width	150

"true secondary" yield, while for 9 widely spaced bunches of positrons (Fig. 1(d)) the quantum efficiency and photoelectron energy distribution are the most important parameters. Note that for this analysis, primary electron yield parameters were allowed to be different for electron and positron beams, to help compensate for uncertainties in the local photon flux, as well as the fact that the energy of the incident photons can be different for the two species.

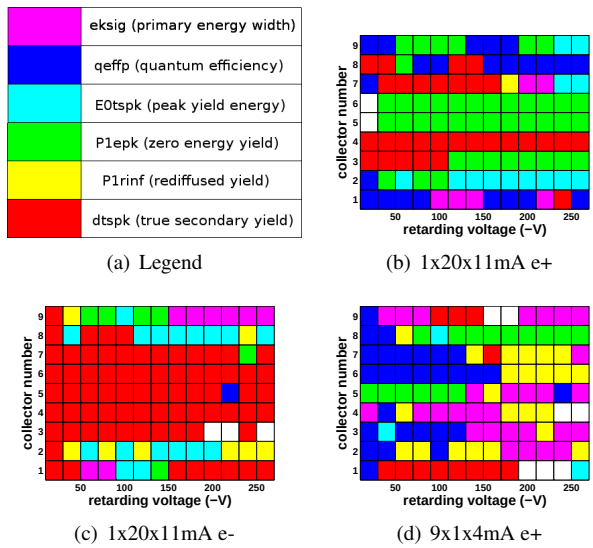

(a) Legend (b) 1x20x11mA e+

(c) 1x20x11mA e- (d) 9x1x4mA e+

Figure 1: Parameter "Domains", 5.3 GeV

SUBTLETIES

Several subtle difficulties arise when trying to understand RFA data on a detailed, quantitative level.

Beam Pipe Hole Secondaries

Secondary electrons can be generated in the beam pipe holes below the RFA, leading to a low energy enhancement in the RFA signal. We have developed a specialized particle tracking code to quantify this effect [5], which is included in the analysis described above.

Photoelectron Model

We have found that the traditionally used low energy photoelectrons do not provide sufficient signal for electron beam data with high bunch current. This is because high energy particles are needed to overcome the initial beam potential in order for the cloud to develop. Similar conclusions can be drawn based on measurements done with a shielded pickup detector [7]. As a first step, a Lorentzian photoelectron energy distribution with a wide width (150 eV) has been added to POSINST to provide some energetic primaries. However, it is likely we will need to develop a more sophisticated model of photoelectron production to obtain complete agreement with the electron data.

Interaction with Cloud

In high magnetic field regions, the presence of the RFA can have an effect on the development of the cloud. In particular, a resonance between bunch spacing and retarding voltage can occur [5]. Fully understanding this effect requires an RFA model that is integrated into the simulation code itself. This is under development.

PRELIMINARY RESULTS

Fig. 2 shows the effect of employing the method described above for an RFA in an uncoated Aluminum drift chamber, for a few of the conditions in Table 1. These plots show the central collector in blue (collector 5 in a 9 collector RFA), the sum of the two intermediate collectors (4 and 6) in red, and the outer collectors (1-3 and 7-9) in green. Data are shown as dots, while simulations are plotted with solid lines. Plotted on the left are simulations done with the nominal values of each parameter (Table 2), and on the right are simulations done with the "best fit" parameters.

Generally speaking this method has had some success in bringing data and simulation into agreement. In fact, for the Aluminum chamber the agreement was able to be simultaneously improved for 10 of the 11 conditions listed in Table 1.

This method was then repeated for RFA data taken in TiN, Carbon, and NEG coated chambers, with comparable results.

As stated above, the goal of this analysis is to obtain a set of simulation parameters that leads to the best agreement with data. Table 3 shows the best fit secondary emission values for each chamber.

Table 3: Best fit parameters

Parameter	Aluminum	Carbon	NEG	TiN
dtspk	2.18	0.618	0.715	.42
P1rinf	0.227	0.221	0.173	.212
dt0pk	**2.447**	**0.879**	**0.928**	**.672**
P1epk	0.416	0.26	0.452	.298
E0tspk	314	486	500	428

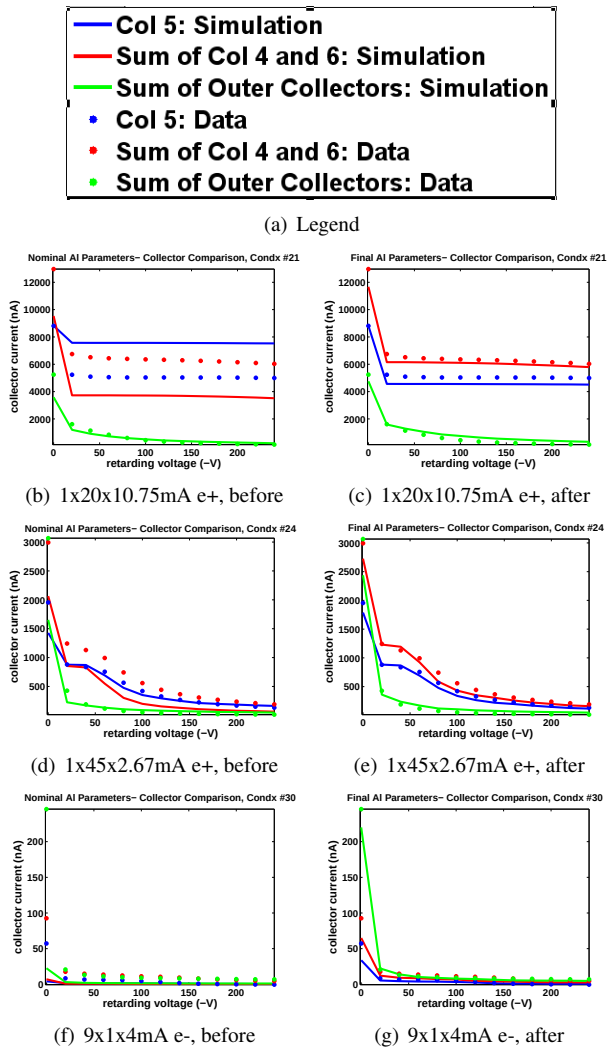

(a) Legend

(b) 1x20x10.75mA e+, before

(c) 1x20x10.75mA e+, after

(d) 1x45x2.67mA e+, before

(e) 1x45x2.67mA e+, after

(f) 9x1x4mA e-, before

(g) 9x1x4mA e-, after

Figure 2: Improvement of agreement with data for 5.3 GeV, Aluminum chamber

There are several things to take away from this table. First, according to this analysis, TiN, Carbon and NEG coated chambers all have a very low ($< .9$) peak secondary yield, while Aluminum has a very high one. Comparing the three coatings to each other, TiN appears to come out slightly ahead. However, errors and correlations between the different parameters need to be quantified before any definitive comparisons can be made at this level. So this evaluation should be taken as preliminary.

There is some question of the ability of this method to distinguish the true secondary and elastic yield, since both produce low energy secondaries. Thus one may be able to obtain similarly good agreement with data by using, for example, a somewhat lower true secondary yield and a somewhat higher elastic yield.

Also note that due to large uncertainties in the modeling of photoelectrons, final primary emission values are of questionable utility, and consequently are not quoted here.

CONCLUSIONS

A systematic method has been used to improve agreement between RFA data and simulation, and best fit simulation parameters have been obtained. A great deal of work remains to be done, including:

- Quantifying errors and correlations in these parameters
- Repeating the analysis for RFAs in magnetic fields, including dipoles, quadrupoles, and wigglers.
- Repeating the analysis for other beam conditions.
- Investigating the effect of other parameters.
- Comparing with other local cloud measurements, such as shielded pickups.
- Continuing development of integrated RFA models.
- Incorporating a more complete description of photoelectron emission, as well as improving the estimate of incident photon flux.

If successful, the end result of this analysis will be a detailed and self-consistent description of the in situ primary and secondary emission properties of the materials under investigaiton.

REFERENCES

[1] R.A. Rosenberg, K.C. Harkay, Nucl. Instrum. Meth. A 453, 507 (2000)

[2] M. Palmer et. al., TH5RFP030, Proc. of PAC09.

[3] M.A. Furman and G.R. Lambertson, Proc. MBI-97, KEK Proceedings 97-17, p. 170.
M.A. Furman and M.T.F. Pivi, PRST-AB 5, 124404 (2002).

[4] F. Zimmermann and G. Rumolo, ICFA Beam Dynamics Newsletter No. 33, eds. K. Ohmi and M.A. Furman (2004).

[5] J. Calvey et. al., TUPD022, Proc. of IPAC10.

[6] G. Dugan, S. MIlashuk, D. Sagan, "Synrad3D Photon propagation and scattering simulation", these Proceedings.

[7] J.A. Crittenden et. al., these Proceedings.

TE Wave Measurements at CesrTA*

J.P. Sikora#, CLASSE, Ithaca, NY 14853 U.S.A.
S. De Santis, LBNL, Berkeley, CA 94720 U.S.A.
K. Hammond, Harvard University, Cambridge, MA 02138 , U.S.A.

Abstract

TE Wave measurement stations have been installed in the L0 and L3 regions of CesrTA. The L0 region has quasi-rectangular beam pipe and is the location of 6 superconducting wiggler magnets. The L3 region has round beam pipe with a chicane dipole magnet (from PEPII). At both locations, coaxial relays are used to multiplex an rf signal from a signal generator output, through the beam pipe, to the input of a spectrum analyzer. Software is used to monitor accelerator conditions and can be triggered to take data on demand, or on changes in conditions such as beam current or wiggler fields. This paper will describe the TE Wave measurement technique, the installation of hardware at CesrTA and some measurement examples. It will also outline some problems in the interpretation of data, specifically the results of reflections and standing waves.

INTRODUCTION

Microwaves that are transmitted through a waveguide will be phase shifted by the presence of a plasma. The beam pipe of an accelerator, although not an ideal waveguide, can also transmit microwaves and the electron cloud produced by a train of bunches will phase shift microwaves transmitted through the beam pipe. Since the cloud lifetime is a fraction of a revolution period at CesrTA, a phase modulation of the carrier is produced at the beam revolution frequency. This results in phase modulation sidebands of the received carrier frequency, spaced at the revolution frequency of 390kHz [1].

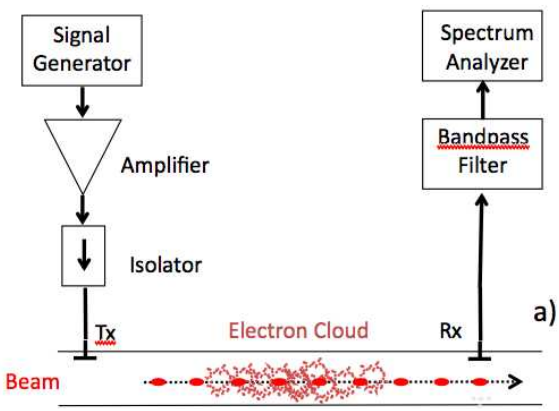

Figure 1: The basic TE Wave technique: a carrier is injected at Tx and the modulated signal detected at Rx.

*This work is supported by the US National Science Foundation PHY-0734867, and the US Department of Energy DE-FC02-08ER41538.
jps13@cornell.edu

Beam position monitor (BPM) button detectors are used to couple microwaves into and out of the beam pipe. These detectors were originally installed at many location around CesrTA for the purpose of orbit and trajectory measurements. Some of these buttons were borrowed from the BPM system; others were installed specifically for TE Wave measurements. Thus far, we have only used the transverse electric $TE_{1,0}$ mode, since it is relatively easy to excite in the beam pipe and has a maximum electric field in the center of the pipe. A sketch of the method of coupling is given in figure 2. For convenience in making combinations of measurements, a transmitting and receiving pair are available at each location. While hybrid combiners can be used, many of the detectors at CesrTA use 0 degree combiners, with cable lengths chosen to give a differential signal at the desired frequency, usually at about 2GHz.

Notice that the button pairs are offset from the center of the pipe. Given this geometry, it would also be possible to excite the $TE_{2,0}$ mode, but this higher frequency has not been used. The $TE_{1,0}$ mode is sensitive to the electron cloud near the beam, in the center of the pipe, while the $TE_{2,0}$ mode is not. Also, the 5 watt amplifier that we are presently using is limited to a little over 2GHz.

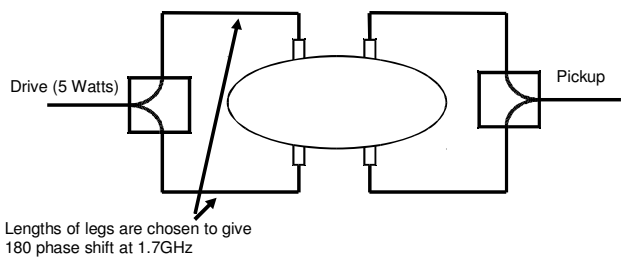

Figure 2: Top and bottom buttons are combined to give differential signals at the measurement frequency. This selects the TE microwaves while helping to reject direct beam signal sidebands. The button electrodes are ~1.7cm dia with a horizontal spacing of 2.8cm.

As an aid in analysis, the transmitted carrier is phase modulated at 410kHz with a depth of .001radian so that reference sidebands are visible near the cloud induced modulation sidebands. The carrier frequency is chosen to be somewhat above the cutoff frequency of the beam pipe's $TE_{1,0}$ mode, which at CesrTA is close to 2 GHz. As will be seen in a later section, the cutoff frequency for the beam pipe at CesrTA is not very clear and has many resonances. This feature has a significant effect on our ability to obtain a convincing calibration of the electron cloud density.

Figure 3 shows a typical spectrum. While the carrier is set to be somewhat above the cutoff frequency, the exact frequency is chosen so that the response is close to a local maximum and the modulation sidebands are between the beam induced revolution harmonics.

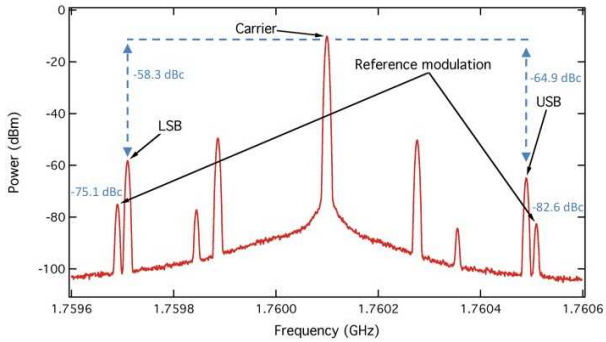

Figure 3: A spectrum of the received signal showing both reference modulation and cloud induced sidebands (labeled LSB and USB). The peaks closest to the carrier are the beam revolution harmonics, while the smaller peaks are from a noisy power supply for the 5 watt amp.

MEASUREMENT STATIONS

Figure 4 shows the location of two stations used for TE Wave measurement at CesrTA. At each station, there is an Agilent N5181A signal generator followed by a Mini-Circuits ZHL-5W-2G amplifier. As show in figure 5, the drive signal is routed with ½ inch heliax to a mechanical relay that can route the drive to the available detector locations. In the same way, the received signals are selected by a relay and routed with heliax to an Agilent MXA-9020A spectrum analyzer.

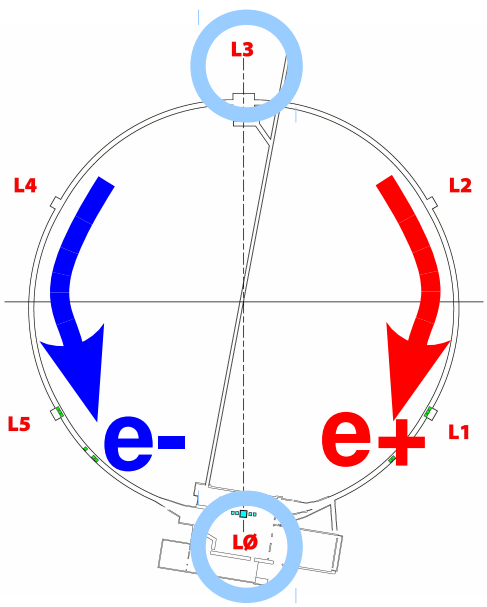

Figure 4: The L3 region is at the north end and the L0 region at the south end of the CesrTA storage ring. In L0, the positron beam travels from east to west.

The instruments are connected to the accelerator control system with network cables for configuration and data taking. For each measurement, software configures the station hardware following a list of drive/detector pairs, collects data for each pair and updates an html table. The table has links to the data files that contain the station configuration, spectra, and relevant accelerator data such as bunch current, beam energy, wiggler fields, etc., as well as links to plots of the spectra. The table allows easy browsing of the data, but additional software is required for further analysis. In a typical plot shown in the next section, each data file represents a single point. Work is now underway to load relevant data summaries into a database that can be more easily searched.

Data has been routinely collected using both the standard transmission measurements - where different detectors are used for drive and received signals - as well as resonant measurements where the drive and detection are at the same location.

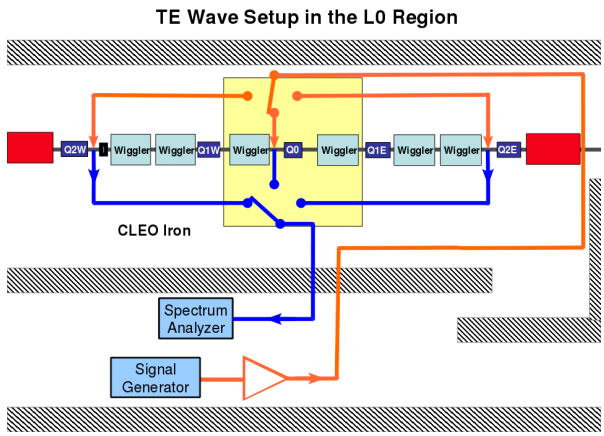

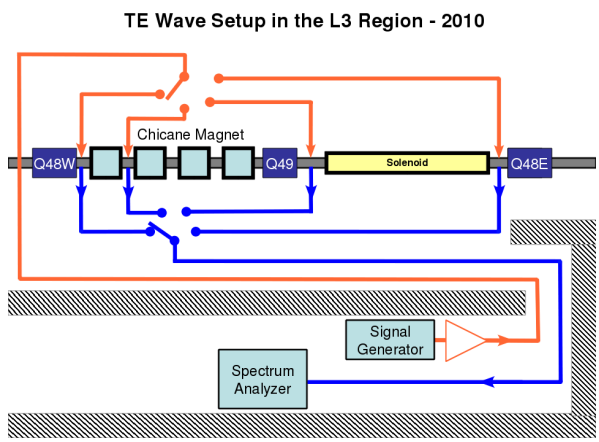

Figure 5: The layout of measurement stations at L0 and L3 is given above. In the L3 region with round beam pipe, the detectors are often oriented to give a horizontal electric field. This allows the rf to excite cyclotron resonances of electrons in the Chicane's dipole magnets.

MEASUREMENT EXAMPLES

Below are examples of some recent measurements made at CesrTA. Figures 6 and 7 show the general behavior of the electron cloud induced phase modulation sidebands at 2GeV and at 5GeV.

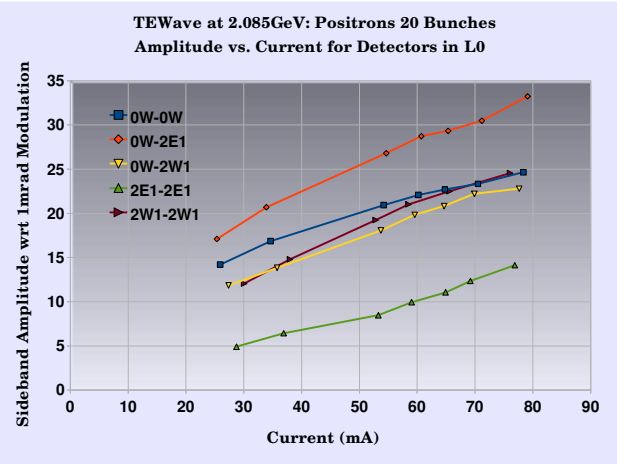

Figure 6: At 2 GeV, six superconducting wigglers are on in the L0 region. There is a general increase in cloud intensity for measurements that are further downstream (westward) along this series of wigglers.

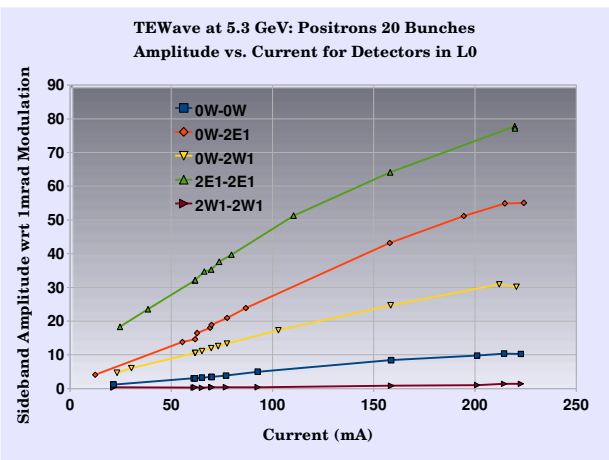

Figure 7: At 5 GeV with the wigglers off, there is a general decrease in cloud intensity for measurements that are further downstream of the positron beam. The source of light is the last dipole magnet in the east before the wiggler straight section.

The next two measurements are more specialized. Figure 8 shows the change in sideband amplitude of detectors in L0 as the superconducting wigglers are ramped up from zero to a full field of 1.9 Tesla. This data was taken with 45 bunches of positrons, whose trajectory is from east to west. Notice that the eastern resonant detector 2E1-2E1 shows no change in amplitude with wiggler field because the wigglers are all down stream of this detector. Figure 9 shows another very specialized measurement, where the magnetic field of the Chicane magnet in L3 was ramped through the value that corresponds to the electron cyclotron resonance. Across this resonance, there is a nearly 30dB increase in the magnitude of the phase modulation sideband. At the same magnetic field, there is a small (0.5dB) decrease in the amplitude of the carrier frequency.

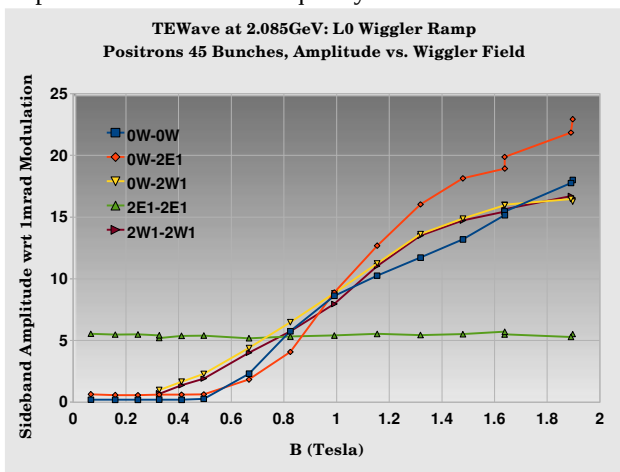

Figure 8: During a ramp of wiggler fields there is an increase in the cloud intensity with increased field. This increase begins slightly earlier at the 2W1 which is furthest downstream. The 2E1 detector signal is unaffected since it is upstream of all wigglers.

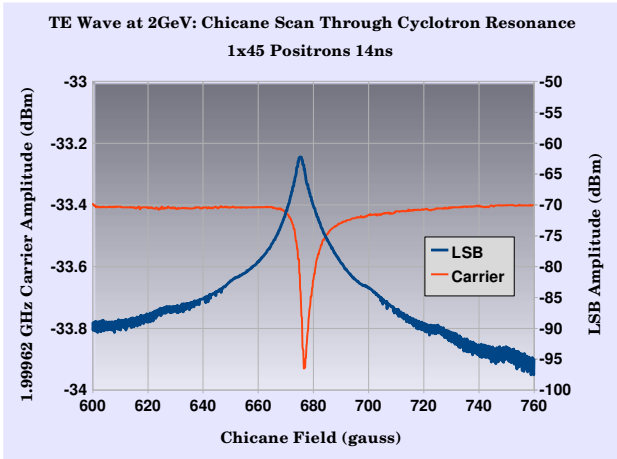

Figure 9: During a scan of the chicane magnet in L3, a strong resonance is seen both in the sideband and carrier amplitudes of the TE Wave signal. This occurs at a field corresponding to the electron cyclotron resonance.

So there is data available that shows a correlation between the sideband amplitudes and the expected relative density of the electron cloud. Treating the beam pipe as a wave guide, the phase modulation depth can be obtained through the relation below, that gives the phase shift of a $TE_{1,0}$ wave through a plasma, where ω_p is the

$$\Delta\varphi = \frac{L\omega_p^2}{2c(\omega^2-\omega_c^2)^{1/2}} \qquad (1)$$

plasma frequency, ω_c is the cutoff frequency of the wave guide and L is the distance of propagation[1].

IMPERFECT WAVE GUIDE

Beam Pipe Response

In an ideal rectangular waveguide, there is a definite cut off frequency, below which there is no propagation and above which a wave can propagate freely. When using accelerator beam pipe as a waveguide, the response function is noticeably non-ideal with a large number of resonances as shown in figure 10, that are probably due to reflections. There are many discontinuities in the beam pipe: gate valves, longitudinal slots for vacuum pumps, transitions in dimensions, etc. Figure 11 shows the superposition of a number response functions, where the drive is applied to the center of L0 and observed at other detectors.

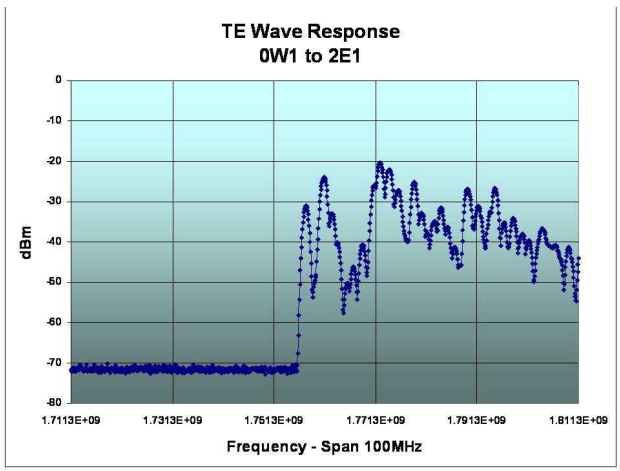

Figure 10: The response function of a TE wave transmitted through the beam pipe in the L0 region.

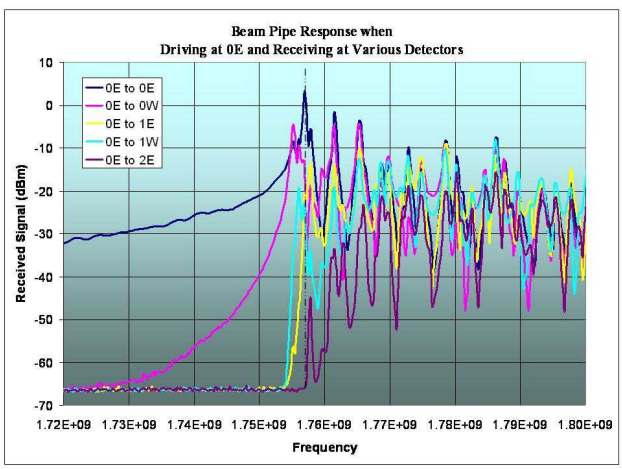

Figure 11: This is an overlay of the measured response functions from 0E to several other detectors in L0 (data from 2008). The complex pattern of resonances suggests that there is more than one set of reflections. However, there are frequencies where the resonances of several detectors coincide. Notice that the largest peak is 0E to 0E, where the drive and pickup are at the same location.

Model: A Waveguide with Reflections

If a wave guide contains two discontinuities, a standing wave is set up at particular frequencies. Because of the change in phase velocity near the cutoff frequency, the spacing of the resonances is not uniform but is given by the relation below where f_c is the cutoff frequency, L is the distance between discontinuities and n is an integer[2].

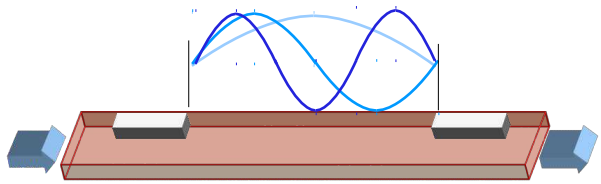

$$f^2 = \frac{c^2}{4L^2}n^2 + f_c^2$$

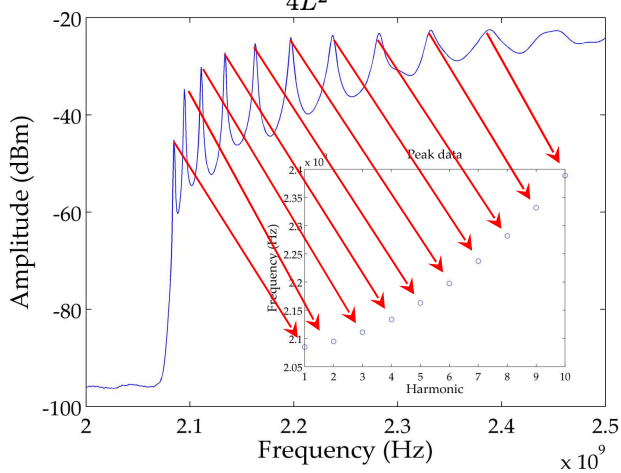

Figure 12: The measured response function of a waveguide with a single pair of discontinuities is given above (upper curve). Arrows connect the spectral peaks with the calculated resonances (circles).

The Effect of Reflections on the Calibration

The published relation between the sideband amplitude and the density of the electron cloud is based on a single pass transmission of the TE Wave between two points in the beam pipe[1]. However, reflections result in multiple passes of the wave through the plasma so that the phase shift becomes magnified. A more relevant model for electron cloud measurement would be the perturbation of the resonant frequency of a cavity by the presence of a plasma[3], where the shift in resonant frequency is proportional to the integral of E^2 over the volume of the dielectric. Work on this approach was carried out as a Research Experience for Undergraduates (REU) project (2009), where the resonant detector mode was modeled as wave guide that is excited at the cutoff frequency[4].

Using some lengths of wave guide, another REU (2010) project measured the amplitude and phase of transmission in a wave guide with discontinuities, where a dielectric could be inserted in the region of the standing waves[2]. The measurements of figures 13 and 14 show the phase *difference* with and without the dielectric inserted.

In figure 13 the dielectric is inserted at the midpoint between the two discontinuities. Although it is difficult to measure on this scale, there is a very small difference in phase shift anywhere in between the resonances. This would correspond to non-resonant wave guide transmission. On resonance, the phase difference

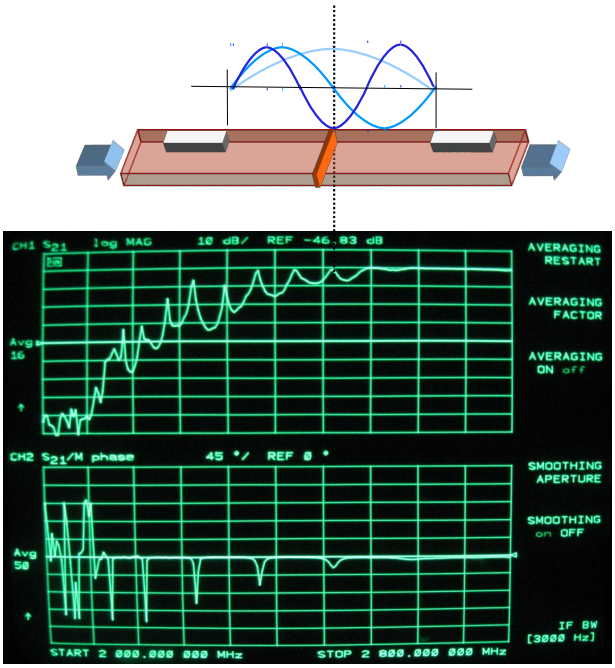

Figure 13: If the dielectric is inserted at the midpoint of the discontinuities, the even numbered harmonics will have no phase shift, since the dielectric will be at a voltage minimum. Frequency span: 2.0 to 2.8GHz.

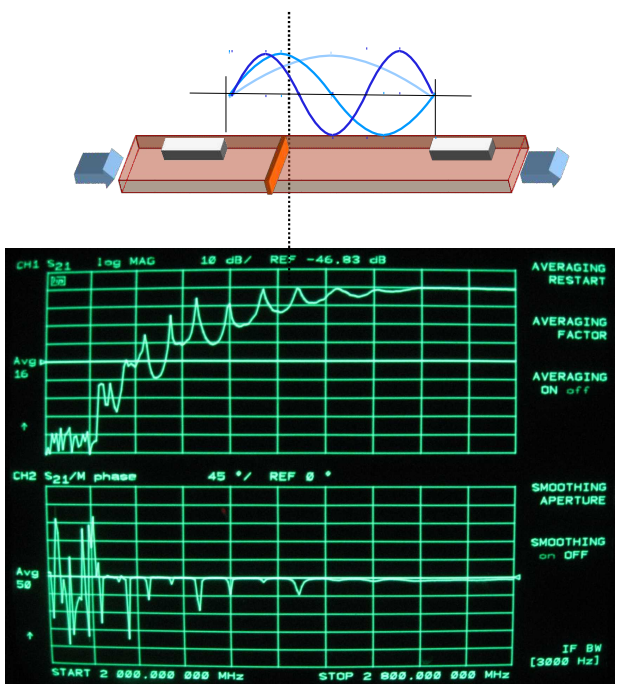

Figure 14: If the dielectric is inserted off center, the phase shifts for both the even and odd harmonics are visible, but their magnitudes vary. Frequency span: 2.0 to 2.8GHz

alternates between being large and being near zero, because the location of the dielectric is at a voltage maximum for odd *n* and a voltage minimum for even *n*. Where E is zero the resonant frequency shift is zero.

Another measurement was made with the dielectric displaced from the center of the discontinuities at a position that was roughly one third of the distance. In this case, all of the resonances show a somewhat enhanced difference in phase shift with the dielectric, as can be seen in figure 14.

From these simple examples, it seems clear that the phase shift can be enhanced by resonances. It also shows that the sensitivity can vary greatly along the length of the beam pipe – becoming zero at some locations – depending on which resonance is used for the measurement. This needs to be taken into account, especially when looking for highly localized electron cloud densities. In the example of the cyclotron resonance measurement of the previous section (figure 9), the effect was not visible at all with a carrier frequency of 2.00470Ghz, but was quite pronounced at 1.99962GHz .

SUMMARY

Data shows that the TE Wave technique is sensitive to the electron cloud density. However, given the typical response functions as shown in figures 10 and 11, it seems likely that almost *all* detectors pairs are resonant, whether the drive and pickup are at the same detector or not. These resonances are presumed to be from discontinuities in the beam pipe and can magnify the electron cloud induced modulation sidebands. So a quantitative analysis of reflections seems to be critical in order to obtain believable measurements of electron cloud densities. Once a field profile is obtained, calculations should follow the model of the *frequency modulation* due to a plasma in resonant cavities rather than the *phase modulation* of a plasma in single pass wave guide transmissions.

REFERENCES

[1] S. De Santis, J. M. Byrd, F. Caspers, A. Krasnykh, T. Kroyer, M. T. F. Pivi, and K. G. Sonnad Phys. Rev. Lett. 100, 094801 (2008).

[2] K. Hammond, “Effects of Reflections on TE Wave Measurements of Electron Cloud Density”, Internal Report, Cornell University (2010).

[3] Saxton, W. A., Yeh, Y. S., “Modified Theory for Cavity Perturbation Measurement of Plasma Parameters”, NASA-CR-107473, SR-5 (1969).

[4] B.T. Carlson, “Implementation and Comparison of Electron Cloud Measurements at the Cornell Electron Storage Ring”, Internal Report, Cornell University (2009).

Progress on simulation of beam dynamics with electron cloud effects: An update*

K.G. Sonnad† CLASSE, Cornell University, Ithaca, NY, USA
M.T.F. Pivi, SLAC, Menlo Park CA USA
J-L Vay, LBNL, Berkeley, CA USA
G. Rumolo, R. Tomas, F. Zimmermann, CERN, Geneva, Switzerland
G. Franchetti, GSI, Darmstadt, Germany

Abstract

This paper provides a brief review of progress on the simulation methods associated with studying the beam response to electron cloud effects. Comparison of results obtained from the program CMAD and other similar programs are reported. An update on recent developments and future planned upgrades to CMAD are discussed.

INTRODUCTION

Studying the influence of electron clouds on the dynamics of beams in storage rings has made steady progress in the last few years. Earlier methods involved using a constant focusing model with interacting points (IPs) at discrete locations around the ring. This was followed by modifying the transport mechanism to that of a simple FODO lattice in a ring with the strengths of the quadrupole magnets adjusted so that the betatron tunes of the model matched with the actual tunes. The latter model helps include several features not to be found in the former one. More recently, considerable progress had been made toward using the full lattice rather than an idealized one. The programs used to produce the results in this paper, namely HEADTAIL [1], WARP [2], and CMAD [3], are capable of all the simulation methods mentioned above.

Dedicated experiments are being performed on a regular basis at CesrTA to study the interaction between positron beams and electron clouds over a wide range of parameters [4]. These experiments are not only helping us understand the physics of electron effects, but also providing information on the extent of detail that needs to be introduced in order to reproduce the observed effects in the simulation. We have been regularly performing simulations using CMAD in our efforts to validate them with observations being made at CesrTA. The outcome of this effort will prove very valuable when studying future accelerators such as the ILC and CLIC damping rings, the super B factories and the upgrade of hadron machines such as the Fermilab MI, LHC and SPS.

The general method of performing these simulations involves tracking a certain number of beam particles around the ring with the help of transfer maps, and including electron cloud effects at discrete ”interacting points” (IPs) in the ring. The electron cloud is represented on a two dimensional grid and the beam represents a finite number of 2D grids referred to as slices. The beam is made to pass through the cloud slice by slice and both the electrons and beam particles are evolved dynamically with every cloud-beam slice interaction. This procedure is repeated at every IP. The electron cloud distribution gets refreshed after every interaction but the beam distribution evolves throughout the process. One also has the option of using a “frozen field” approximation where the electric field produced by the electron can be reused for a given time period before refreshing it again with a Poisson solver. The beam is usually tracked for several turns, the number depending upon the characteristic time scale of the phenomenon to be understood. For example, simulating head-tail interaction requires tracking for several synchrotron periods.

Despite the overall features of the simulation methods being fairly common, subtle differences exist in ways the calculations are carried out by different programs. For example, the program, CMAD divides the beam into slices such that the total charge on each slice is the same. Some other programs such as WARP and HEADTAIL divides the beam into slices of equal length. Both methods have their own advantages and disadvantages. Since the different programs have been developed independently by different groups, it is unlikely that a trivial mistake made in one of them would be repeated in another. Thus it very important to validate the results of such programs to (1) eliminate the possibility of a mistake or bug (2) to ensure that none of the subtle differences in calculation methods such as the one mentioned above lead to significant numerical errors.

There has been a continued effort in comparing results from different programs [5, 6] and this paper is meant to provide a summary of the latest on this. Besides comparing results from different programs, we are making an effort to study the effect of numerical noise on emittance growth. Emittance growth has been experimentally observed and very similar dependencies to physical parameters have been seen in simulations for CesrTA. At the same time, it is well known that particle-in-cell simulations cause numerical noise. The numerical noise could cause a particle confined on a trajectory exhibiting stable motion to artificially wander into a region of unstable motion. To study the possibility of this happening, one needs to compare emittance growth rates over a number of computational parameters. If emittance growth rate varies significantly with

* Work supported by DOE DE-FC02-08ER41538 and NSF PHY-0734867
† kgs52@cornell.edu

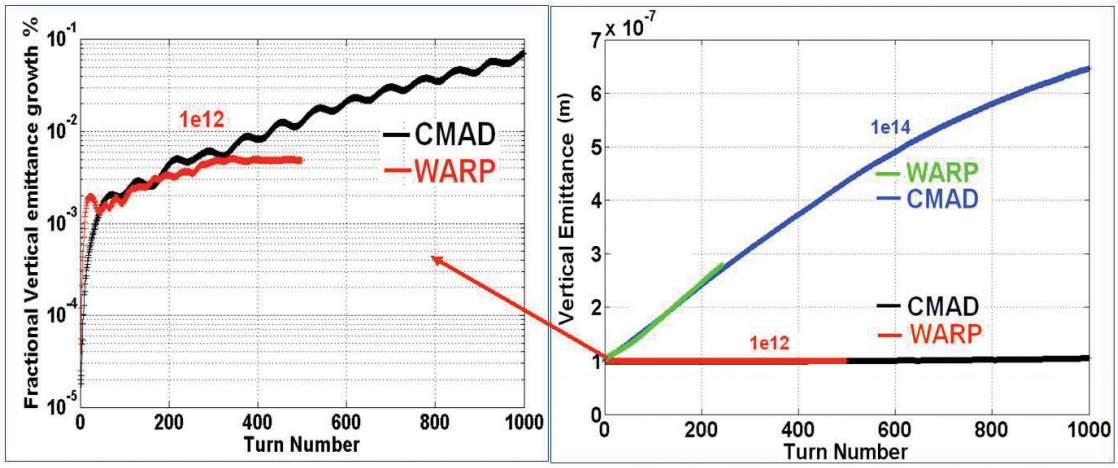

Figure 1: SPS FODO model.

varying number of macroparticles, one can deduce that the result is being dominated by numerical effects. It is important to ensure that such effects are insignificant even if it is not possible to eliminate them.

COMPARISON OF RESULTS FROM DIFFERENT PROGRAMS

Agreement between the programs HeadTail and WARP has been reported for a constant focusing system [6]. Although the parameters used for this study were extreme and not representative of real accelerator conditions, they were well suited for comparison of results from different simulation programs. This is because small inaccuracies are expected to be amplified when conditions such as electron cloud density and chromaticity are exaggerated since both contribute to nonlinearity in the transport system. One case of this study was verified against results obtained from CMAD. This is shown in Fig 2, which was done for parameters corresponding to an LHC type proton beam in the SPS. Emittance growth is tracked for varying electron densities. It may be noticed that the results from CMAD deviate slightly for an electron density of $10^{13}/m^3$ but overall there is reasonable agreement between the three programs.

Another case for benchmarking such results from different programs was initiated by Frank Zimmermann [5] for the SPS, represented by an idealized FODO lattice. This consisted of a FODO structure with thin lens quadrupoles. The strengths of the quadrupoles are adjusted so that the tune of this idealized system matched with the real tunes. Figure 3 gives the twiss functions generated by MADX. Details of all the accelerator parameters of this case can be found in [5] including results obtained using HEADTAIL for the same set of parameters. The comparisons between WARP and CMAD for this case is shown in Fig 1. Unfortunately, at that time we were unable to perform the calculation for a 1000 turns with WARP. Given the available results both the programs show that the emittance growth is very small for the $10^{12}m^{-3}$ electron density case, probably witin the extent of contribution from numerical noise. For the $10^{14}m^{-3}$ electron density case however, both programs show a rapid growth in emittance, with very good quantita-

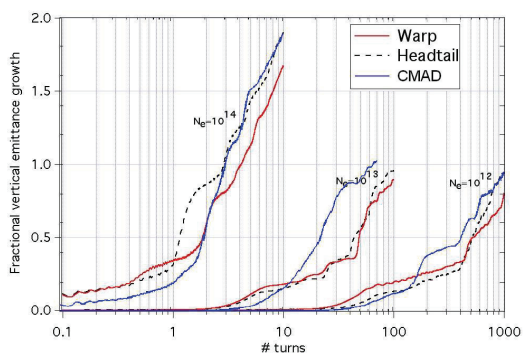

Figure 2: Comparison of results from three simulation programs for a continuous focusing case for an LHC type beam in the SPS.

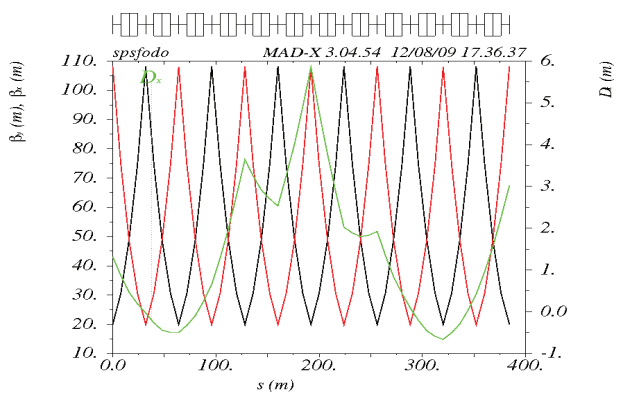

Figure 3: Twiss functions of one FODO cell of the idealized SPS lattice model

tive agreement. The computational parameters used in both the calculations were as follows - The beam was cut into 64 slices, a 64×64 grid was used, 300000 macro protons, and $64^2 = 4096$ macro electrons were used. A "quiet start" (uniform distribution of cold electrons) was considered for the initial electron distribution with 1 electron/cell.

SOME DETAILS ON CMAD

The program CMAD is being actively developed and at the same time being used for simulating electron cloud effects in various machines. This program is capable of parallel simulations which becomes necessary when including the complete lattice for tracking. Calculation pertaining to a specific slice is handled by a separate processor and so ideally the number of processors a job runs on should be equal to the number of slices the beam is divided into, which is typically around a hundred. Inclusion of the complete lattice will take into account variation of the twiss functions around the ring. This is important because the physical size of the beam is influenced by the beta functions and the dispersion, and the response of the electron cloud depends on the physical beam size. The electrons respond to an external magnetic field via the Boris push scheme. Thus in the presence of a dipole field, the electrons move along the field lines with a cyclotron motion, provided the resolution of the grid spacing is within the cyclotron radius.

In the current version of CMAD, the electron cloud is uniformly distributed before the start of an interaction with the beam. We are in the process of improving this so that one could use a more realistic electron distribution as an initial condition. Along with adding features in the simulation program CMAD, we are also developing useful data output routines that can provide useful information of the dynamics at different levels. Examples include tracking trajectories of individual particles and tracking the transverse displacement of individual slices in order to understand electron cloud induced head-tail motion. A more detailed report of the physics results obtained using CMAD for CesrTA is given in [7]

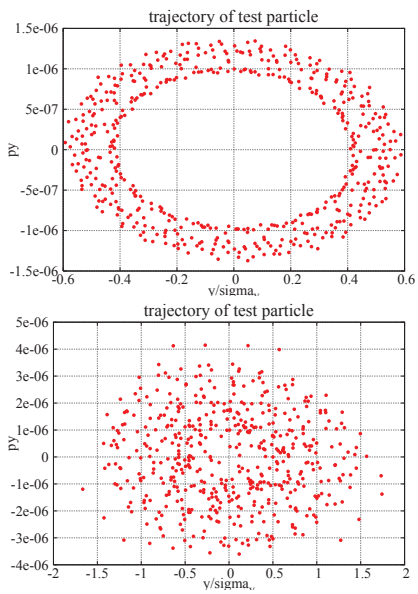

Figure 4: Vertical phase space trajectory of a single positron in a beam with cloud density of $10^{11}/m^3$ and $10^{12}/m^3$ respectively

Figure 4 shows the trajectories of a particle at two cloud densities. The calculation was done for a CesrTA 2GeV energy lattice with a positron bunch current of 1mA. The results clearly show that with increasing cloud densities, the motion of the particle becomes increasingly nonlinear. This is more so in the vertical plane where the beam size is much smaller. The vertical emittance was 50pm and the horizontal 2.6nm. The bunch length was 1.2cm.

CONCLUSION

Simulation of electron clouds effects on the dynamics of beams is a very involved procedure. Several assumptions and approximations need to be made and the extent of their validity needs to be carefully studied. The results obtained from independent simulation programs need to be verified against each other to eliminate possible programming errors and to gauge the accuracy of subtle differences in implementation of the same algorithm. This effort of comparison of results needs to be continued and extended to a more detailed set of calculations. We are in the process of comparing analytic estimates of tune shift with CMAD results. Comparisons between CMAD results and those obtained by measurements at CesrTA are also underway. The eventual goal of this study is to build sufficient confidence so that simulations from these programs can offer guidance in the design of future accelerator facilities and upgrades of existing ones.

REFERENCES

[1] G Rumolo and F. Zimmermann, "Electron cloud simulations: beam instabilities and wakefields" Phys. Rev. ST Accel. Beams 5, 121002 (2002)

[2] J.-L. Vay, A. Friedman and D. P. Grote, "Proceeding of the 9th International Computational Accelerator Physics Conference" Vol 1, page 262.

[3] M.T.F. Pivi, "A new self-consistent parallel code to simulate the electron cloud build-up and instabilities", Proceedings of PAC07, Albuquerque, New Mexico, USA

[4] G. Dugan, *et al*, "Studies of Electron-Cloud-Induced Beam Dynamics at CesrTA" In these proceedings

[5] E. Benedetto, *et al* "Modeling Incoherent Electron Cloud Effects" Proceedings of PAC07, Albuquerque, New Mexico, USA

[6] J-L Vay, *et al*, "Update On Electron-Cloud Simulations Using the Package WARP-POSINST", Proceedings of PAC09, Vancouver, BC, Canada

[7] M. T. F. Pivi, K. G. Sonnad, *et al*, "Single-Bunch instability simulations for CesrTA using CMAD" In these proceedings.

Effects of reflections on TE-wave measurements of electron cloud density *

K. Hammond, Harvard University, Cambridge MA,
J. Sikora, K. G. Sonnad† CLASSE, Cornell University, Ithaca NY,
S. Veitzer, TechX Corp, Boulder CO

Abstract

The TE-wave transmission technique is a method for measuring the electron cloud (EC) density in an accelerator beam pipe. It involves transmitting an RF signal through the pipe and detecting the intensity of the phase modulation caused by the fluctuating EC density. Using physical and simulated data, the experiments described in this paper explore the effects of reflections on the phase advance of TE-waves. It is shown that introducing reflections to a waveguide can significantly distort phase measurements in some cases.

INTRODUCTION

This paper focuses on the TE-wave transmission method for determining Electron Cloud (EC) density. This method, first proposed for the SPS at CERN [1, 2], involves using beam position monitor (BPM) buttons to transmit electromagnetic waves at microwave-range frequencies through a length of beam pipe. The method later was demostrated to work at the SLAC PEP II Low Energy Ring by using solenoid field setting to control the electron cloud density. [3] We explore the influence of internal reflections within the beam pipe on these measurements. Accelerator beam pipes are far from ideal waveguides, and the EC is not the only perturbation that the TE-waves encounter. Numerous measurement instruments alter the beam pipe walls, and the overall dimensions of the pipe change periodically as the beam passes through different regions of CESR. Such effects are likely to cause reflections and, possibly, resonances. If some waves reflect between two protrusions one or more times before reaching a detector, they will undergo a greater phase advance than those that transmit without reflection. Under such circumstances, phase shift measurements would not accurately represent the EC if reflections are ignored. The experiments and simulations described in the following sections wereintended to help elucidate the effects of reflections on guided waves in accelerator beam pipes.

EXPERIMENTAL SETUP

The effects of nonuniformities on TE-wave transmission were studied with physical waveguides and with numerical simulation software.

Physical Model

The physical waveguides were copper pipes with rectangular cross sections. The pipes had flanges affixed to each end, allowing for pipes to be connected to one another to increase overall length. Transverse dimensions were 0.072m x 0.034m; pipe lengths were on the order of one meter. On some occasions, washers were added between flanges at the junction of two lengths of pipe to allow an opening for the introduction of nonuniformities such as metal strips or Lexan plastic. The presence of the narrow ($\sim$0.002m) space between adjoined pipes itself had no noticeable effect on the TE-wave signal.

TE-wave signals were generated and recorded with an Aeroflex 3281A spectrum analyzer for some experiments and a Hewlett Packard 8753B network analyzer for others. The signal reached the waveguide through a coaxial cable with a characteristic impedance of 50Ω, and was transmitted to the pipe through an antenna. A receiving antenna picked up the signal at the other end, returning the signal to the generator through a similar cable that terminated at a 50Ω resistor. The signal generator repeatedly swept through a specified frequency range (less than 3 GHz) with a sampling period on the order of tens of microseconds. Signal intensity was about -20 dBm.

Simulation

VORPAL, a particle-in-cell plasma simulation code [4], was used for the numerical models described in this paper. VORPAL software maps three-dimensional space onto a grid, assigning values for physical quantities such as EM field components to each set of coordinates. Boundary conditions, as well as physical attributes such as current density, may be programmed directly into the simulation code. Yee's algorithm [5] was employed in these simulations to solve Maxwell's equations for the coordinates at each time step. Particle positions and velocities were updated using the relativistic Boris algorithm [6].

The boundary conditions used for these simulations were characterized by two types of cross-sectional geometry and two types of end behavior. The cross-sections were either those of the rectangular pipe described above or of the CESR beampipe. The latter consists of two circular arcs (radius 0.075m) connected with flat side planes. It is about 0.090m from side to side and 0.050m between the apices

* Work supported by NSF grants PHY-0849885 and PHY-0734867 and DOE grant DE-FC02-08ER41538
† kgs52@cornell.edu

of the arcs. For both cross-sections, VORPAL constrained the values of the parallel electric field components to zero (the boundary conditions for a perfect conductor).

The ends of the pipes were either perfect conductors or perfectly-matched layers (PMLs) designed to fully absorb any transmissions. Applying the conducting boundaries created a resonant cavity; using PMLs simulated a section of a longer, continuous beam pipe. PML boundaries, first developed by J. Berenger [7], ascribe a parabolically increasing electrical and (nonphysical) magnetic conductivity to the regions at the ends of the beam pipes. These regions had significant thickness, sometimes as much as one-fourth the length of the entire pipe.

VORPAL maintains an electron cloud by generating a specified initial distribution of particles in the simulation grid and tracking their subsequent motion due to field interactions. The simulation uses macroparticles of high mass and charge to represent groups of nearby electrons. Cells on the boundary of the EC region are made to delete particles that pass through them to prevent the particles from escaping. Secondary particle sources (such as metallic surfaces) are also available, but none were used in these tests. Instead, electrons were set to initially have zero velocity (a cold plasma). They were also artificially constrained to cross no more than one cell per time step, a restriction that in practice has does not significantly limit the physicality of the simulation.

Waves were excited in the simulations by ascribing a transverse-direction current density to a section of the beam pipe. These sections covered the full cross-sectional area and were two cells thick in the longitudinal dimension.

In addition to recording all EM field data at user-specified intervals, VORPAL can record the time evolution of a number of different quantities over the entire simulation. Known in the code as Histories, recordable quantites include the potential difference between two given points, energy flux through a specified cross section, and the number of particles in a given region. The energy flux history is especially useful for testing the effectiveness of the PML boundaries, since all flux is expected to point away from the source current in the absence of reflections.

One aspect of the simulation that is very different from the actual TE-wave measurements both in the rectangular pipe and the beam pipe is the time scale. While the physical measurements occurred over arbitrarily long periods of time during which the received signals were steady, the simulations modeled systems over periods no longer than one to two hundred nanoseconds. Simulations longer than that tended to exhibit roundoff error, with all field component values increasing exponentially without bound.

RESONANT CAVITY MEASUREMENTS

The resonant cavity experiments conducted with the physical beam pipe and the simulations accomplished two main objectives: to test the accuracy of the simulations and to determine a cutoff frequency for the CESR beam pipe,

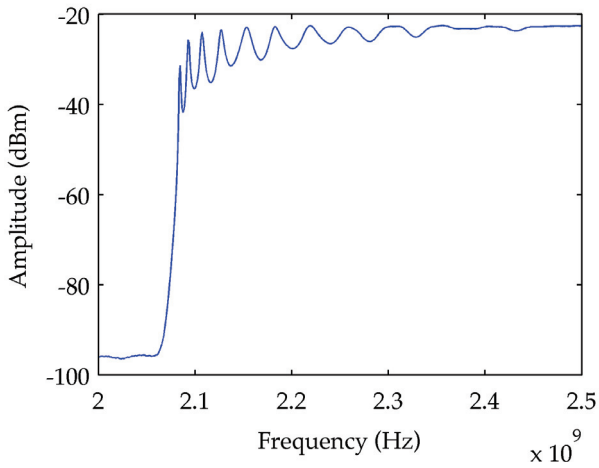

Figure 1: The frequency domain of a 1.219m pipe with a cutoff frequency of approximately 2.08 GHz. Reflections, whose presence is indicated by the resonant frequency peaks, arose because the receiving antenna could not fully absorb the signal.

which would be difficult to derive analytically due to its geometry.

The resonant frequencies of a cavity are those for which the pipe length is a multiple of the half-wavelength. The wavelength λ of a given frequency f (in Hz) in a guide with cutoff frequency f_c can be found from the phase velocity

$$v_\phi = \frac{cf}{\sqrt{f^2 - f_c^2}}, \tag{1}$$

which arises directly from the dispersion relation (Eq. 1) for an empty pipe. The resonant wavelengths must satisfy

$$\lambda = \frac{v_\phi}{f} = \frac{2L}{n}, \tag{2}$$

where L is the pipe length and n is an integer. Consequently, the frequency of the nth resonant harmonic satisfies the hyperbolic relationship

$$f^2 = \frac{c^2}{4L^2} n^2 + f_c^2. \tag{3}$$

The spectrum analysis for a 1.219m rectangular pipe (Fig. 1) showed a series of peaks in the frequency domain in agreement with Eq. 9.

Simulating the frequency sweep used to produce the distribution function in Fig. 1 would not be practical due to the limited time frame and discrete time steps. However, transmitting a single frequency will still produce a full distribution in the frequency domain because the signal is effectively a pulse in the time scale of the simulation. Although the carrier frequency's magnitude in the distribution is at least 10dBm stronger than that of any other frequency and much greater if the carrier resonates, the peaks representing the harmonics are still clearly visible (see Fig. 2).

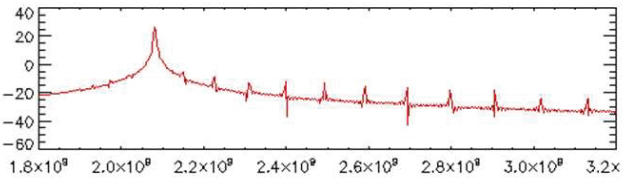

Figure 2: The distribution function from the VORPAL simulation for a 1m resonant cavity. The greatest peak is at the carrier frequency (2.081GHz, which is also a resonant harmonic). Note that other peaks at resonant frequencies are clearly visible.

The locations of the peaks in the simulation's frequency domain tended to suggest a cavity length greater than the programmed length of 1.219m. Increasing the number of grid points per unit distance improved the accuracy of the peak locations, and the suggested length was accurate within 0.5% when the longitudinal distance between grid points was $\leq$ 1cm. It was also noted that the peaks in the Fourier transform did not obey the hyperbolic relationship (Eq. 9) indefinitely. For frequencies past 9 GHz the spacing between the peaks began to decrease, and no peaks were visible for frequencies greater than 12 GHz. This is to be expected, because at high frequencies the wavelength λ falls to a level comparable with the grid point spacing and thus precludes an accurate simulation.

With some confidence established in the accuracy of the simulated frequency peak data, the simulation could then be used to produce an estimate of the CESR beam pipe cutoff frequency. The locations of the first twenty-one frequency peaks were recorded for a one-meter resonant cavity with CESR cross-sectional geometry. The squares of the frequencies f^2, accompanied by their corresponding harmonic numbers n^2, were fit to the hyperbolic form of Eq. 9 ($f^2 = an^2 + b$). a, the coefficient of n^2, was solved for the length L and returned a value of 1.015m. The square root of b, corresponding to the cutoff frequency f_c, was 1.888 GHz. Based on the value of L with respect to the actual simulation length, this value for f_c is taken to be within a 1.5% margin of error.

PHASE SHIFT MEASUREMENTS

To observe small phase shifts in the physical waveguide, two pipes were connected with a small gap (as described in Section II-A) through which a plastic strip could be inserted. Metal blocks were added to both ends of the pipe as perturbations to increase reflections. (Nevertheless, reflections still would have occurred without the metal blocks - they cannot be avoided with the equipment used in this experiment.) The Lexan plastic, like the low-density cold electron plasma, behaves as a linear dielectric under the experimental conditions.

To produce a phase shift measurement, TE-waves were transmitted through the pipe (without the dielectric) and

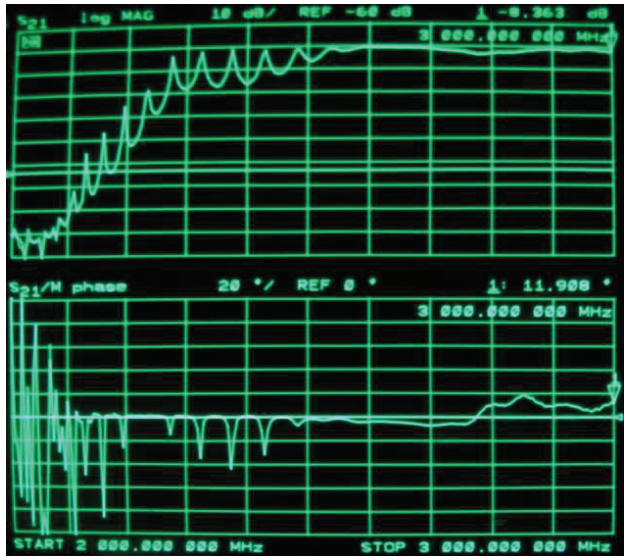

Figure 3: Network analyzer data for the phase shifts caused by a Lexan plastic dielectric in the physical conductor. The amplitude for each frequency is shown on top at 10dBm per division; the corresponding phase shifts are shown on the bottom at 20° per division.

measured by the network analyzer. The frequency was swept between two and three gigahertz. The phase shift at each frequency value was recorded in the analyzer's memory. The dielectric was then added, and the analyzer displayed the difference between the dielectric-effected phase shift data and the stored data. The result, as shown on the bottom half of Fig. 3, was a plot of $\Delta\Phi$ versus frequency.

The top half of Fig. 3 plots amplitude versus frequency, similar to Fig. 1. The cutoff is less abrupt in this distribution, most likely due to the presence of the metal perturbations. The analyzer recorded background noise in the first division (from 2GHz to roughly 2.1GHz); hence the erratic data for $\Delta\Phi$ versus frequency in that range. Note, however, that spikes in phase shift appear at about the same frequencies as peaks in the amplitude distribution. This is indicative of greater phase shifts at resonant harmonics, as predicted.

It is also apparent that the effect of the dielectric on the signal's phase is not the same for all frequencies. Most notably, the harmonic at $\approx$2.23GHz (where a peak in amplitude is recorded on the top half) exhibited no noticeable phase shift from the pipe without the dielectric.

The simulation of a particle beam or even a time-varying EC was beyond the scope of the code used for these simulations, so all phase shifts were calculated based on data from an EC-containing pipe as compared to an empty pipe with all other features the same. For phase comparison, the apex-to-apex potential difference was recorded for each time step at the end of the pipe opposite the current source. For every phase comparison, these two voltage functions were essentially the same for the EC-filled pipe

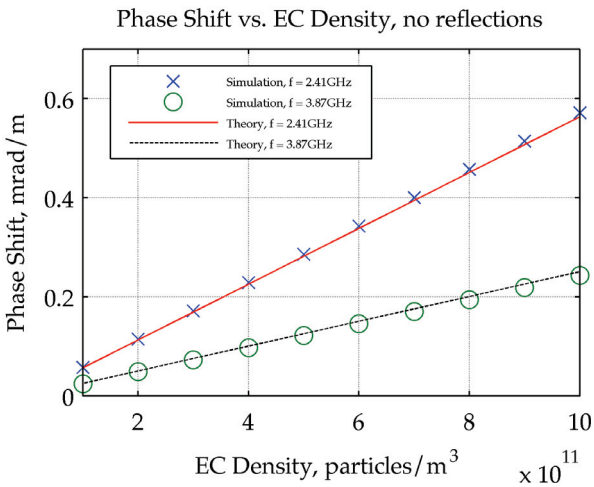

Figure 4: Phase shift data from reflection-free simulations against values predicted by Eq. 11. Electron densities are typical of those seen in CESR.

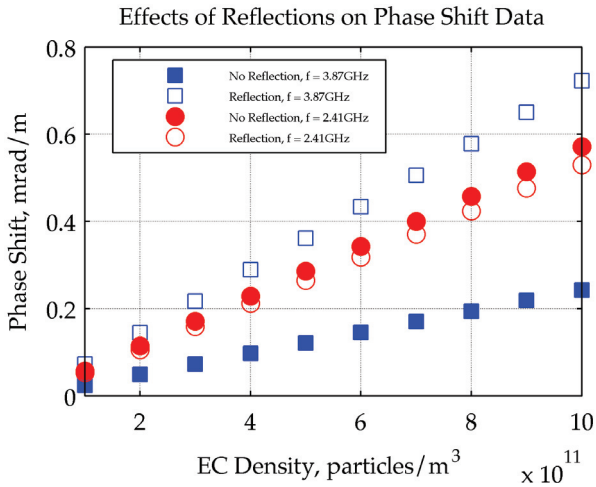

Figure 5: Phase shift data from simulations with and without reflections.

and the empty pipe (except for a small phase shift). Since these functions were essentially sinusoids at the carrier frequency, the following method could be employed to derive the phase shift $\Delta\Phi$.

Both sets of data were normalized by dividing their respective quantities by $\sqrt{2}$ times the RMS amplitude. For normalized sinusoids that differ by a small change in phase $\Delta\Phi$, the difference between them can be expressed as follows:

$$\begin{aligned} &sin(\omega t + \Delta\Phi) - sin(\omega t) \\ &= 2sin(\tfrac{\Delta\Phi}{2})cos(\tfrac{2\omega+\Delta\Phi}{2}) \\ &\approx \Delta\Phi cos(\tfrac{2\omega+\Delta\Phi}{2}) \end{aligned} \quad (4)$$

Thus, small phase shifts are approximately equal to $\sqrt{2}$ times the RMS of the difference between corresponding values in the two normalized sets of data.

All simulations used for phase-shift data were conducted with 0.5m CESR pipes. Drawing upon Eq. 4, the formula for the plasma frequency $\omega_p = 2\pi f_p$, and CESR's cutoff frequency f_c, the phase shift for a pipe without reflection is expected to be [8]

$$\Delta\Phi = \frac{n_e e^2 L}{4\pi c\epsilon_0 m_e \sqrt{f^2 - f_c^2}} \quad (5)$$

for low values of $\Delta\Phi$.

As shown in Fig. 4, the phase shift data collected from the simulations for reflection-free pipes corresponded well to the theoretically-predicted values in Eq. 11. Similar success with a VORPAL-simulated pipe with a square cross-section has been reported befor [8].

To test for the effects of reflections, the simulations were altered to include two protruding conductors. The protrusions were slabs in the transverse plane, extending from the bottom to one centimeter above the apex of the lower arc. They were spaced 0.4 meters apart, and the frequencies (2.41GHz and 3.87GHz, the same as the above simulation) were chosen to be the resonant harmonics ($n = 4$ and $n = 9$, respectively) of a 0.4 meter resonant cavity in order to maximize reflections. As evidence that reflections were in fact occurring between the protrusions, the energy flux (not shown) fell periodically below zero (positive flux points away from the source current), whereas the flux at the end opposite the source was always positive.

Fig. 5 shows the results. The solid shapes represent the data for no reflections and are the same data that appear in Fig. 4. The open shapes represent the phase shifts in the presence of reflection. In all cases the phase advance appears to increase in direct proportion to EC density, which is consistent with Eq. 11. The nature of the overall change in phase shift due to reflections, however, is unclear. Although we expected reflections to greatly increase the phase shift in all cases, $\Delta\Phi$ actually decreased a bit for f = 2.41GHz ($n = 4$). Nevertheless, these results do not necessarily conflict with the physical data in Fig. 3, which suggests that $\Delta\Phi$ is liable to vary significantly with frequency.

DISCUSSION AND CONCLUSION

The TE-wave transmission technique requires an accurate measure of phase shift in order to successfully predict the spacial average EC density. If beam pipe reflections are capable of significantly changing the average phase advance of a TE signal, their affects must be accounted for. The results from both the physical experiments and simulations have shown that subjecting a waveguide transmission to reflections can have a major effect on phase shift, in one case causing more than a twofold increase.

The nature of the effect of reflections, however, is poorly understood. The data shown in Figs. 3 and 5 suggest that

phase shift can be greatly altered at resonant frequencies, but that this is not always the case. Further work is needed to better characterize these effects. In particular, simulations should be run on a spectrum of frequencies beginning at the cutoff to create a distribution function. Such distributions should be obtained for different varieties of reflection-generating perturbations.

The VORPAL code used for simulations with CESR beam pipe geometry has been shown to accurately portray physical systems according to waveguide theory. Although it has some limitations, in particular the short time frame of its simulations, it will be a valuable tool in future experiments.

ACKNOWLEDGEMENT

This research was supported by NSF grants PHY-0849885 and PHY-0734867, as well as DOE grant DE-FC02-08ER41538.

REFERENCES

[1] T. Kroyer, F. Caspers, W. Höfle, M. M. Jimenez, M.-F. Malo, J. Tückmantel, and T. U. Wien. "Unexpected results on microwave waveguide mode transmission measurements in the SPS beam pipe." *Proceedings of the 31st ICFA Beam Dynamics Workshop: Electron Cloud Effects (ECLOUD04), Napa, California 2004*, CERN Report No. CERN-2005-001, 2004

[2] T. Kroyer, F. Caspers, and E. Mahner. "The CERN SPS experiment on microwave transmission through the beam pipe." *Proceedings of the 2005 Particle Accelerator Conference, Knoxville TN.*

[3] S. De Santis, J.M. Byrd, F. Caspers, A. Krasnykh, T. Kroyer, M.T.F. Pivi, and K.G. Sonnad, Phys. Rev. Lett. 100, 094801 (2008)

[4] C. Nieter and J. R. Cary. "VORPAL: a versatile plasma simulation code." J. Comp. Phys. 196, 448 (2004)

[5] K. Yee. "Numerical solution of initial boundary value problems involving Maxwell's equations in isotropic media." IEEE Transactions on Antennas and Propagation, AP-14, 302 (1966)

[6] J. P. Boris. "Relativistic plasma simulation-optimization of a hybrid code." Proc. Fourth Conf. Num. Sim. Plasmas, Naval Res. Lab, page 3 (1970)

[7] J. Berenger. "A perfectly matched layer for the absorption of electromagnetic waves." Journal of Computational Physics 114, 185 (1994)

[8] K. Sonnad, M. Furman, S. Veitzer, P. Stoltz, and J. Cary. "Simulation and analysis of microwave transmission through an electron cloud: a comparison of results." *Proceedings of PAC07, Albuquerque, NM* (2007)

TECHNIQUES FOR OBSERVING BEAM DYNAMICAL EFFECTS CAUSED BY THE PRESENCE OF ELECTRON CLOUDS*

M. Billing, G. Dugan, R. Meller, M. Palmer, G. Ramirez, J. Sikora, H. Williams, Cornell Laboratory for Accelerator-based Sciences and Education, Cornell University, Ithaca, NY, U.S.A.,
R. Holtzapple, California Polytechnic State University, San Luis Obispo, CA, U.S.A.

Abstract

During the last several years CESR has been studying the effects of electron clouds on stored beams in order to understand their impact on future linear-collider damping ring designs. One of the important issues is the way that the electron cloud alters the dynamics of bunches within the train. Techniques for observing the dynamical effects of beams interacting with the electron clouds have been developed. The methodology and examples of typical measurements are presented here.

OVERVIEW OF MEASUREMENT REQUIREMENTS

The storage ring CESR has been reconfigured and operates as a test accelerator Cesr-TA, studying the effects electron clouds in the presence of trains of positron or electron bunches[1]. With a 500 MHz RF acceleration system, CESR can store bunches with as little as a 2 nsec spacing, however for higher current operation the beam position monitor (CBPM) system and beam stabilizing feedback (BSF) systems are configured for bunches with at least a 4 nsec spacing. The most common bunch spacings employed during machine studies have been 4 nsec and 14 nsec, however higher multiples of 2 nsec spacing also have been utilized. The range of several Cesr-TA operating parameters are given in Table 1.

Table 1: Cesr-TA Operating Parameters

Parameter	Typical Range	Units
Beam Energy	2.0 - 5.3	GeV
Circulation Time	2.56×10^{-6}	sec
Number of Superconducting (SC) Wiggler Magnets	0 - 12	
Horizontal Emittance	1×10^{-6}	m-rad
Bunch Spacing	4, 6, 8, 10, 12, 14, …	
Maximum Bunch Charge	25.6	nC
Maximum Single Beam Current	3 – 200 (depending on beam species and powering of SC wigglers)	mA

* Work supported by the US National Science Foundation (PHY- 0734867) and Department of Energy (DE-FC02-08ER41538)

There are several beam parameters, which are particularly relevant for the study of electron cloud effects. Since the electron cloud can produce focusing of the stored beam, measuring the betatron tunes of bunches through the train gives information about the density of the cloud along the length of the train. The electron cloud can also produce unstable motion in bunches later in the train. To observe the unstable motion, it is necessary to detect the amplitude of the betatron frequency and any other frequencies representing different modes of oscillation (e.g. head-tail modes) of bunches within the train. The unstable motion may also result in enlargement of the vertical beam size, so the measurement of the vertical beam size for each bunch in the train is important.

MEASUREMENT HARDWARE

Several instruments have been added or modified for use with the CESR-TA program. They include the bunch-by-bunch beam position monitors, position detectors, which measure the tunes and detect some of the internal modes of oscillation, vertical beam size monitors and beam kickers.

Beam Position Monitors

During the Cesr-TA project the beam position monitoring system underwent an upgrade throughout the entire storage ring. The new CBPM system[2] has independent processing electronic readout modules at or near each of the quadrupole magnets, which can measure the position of every bunch, spaced by as little as 4 nsec, with better than 10 μm turn-by-turn resolution. As shown in figure 1, each module incorporates four front end boards with dual parallel 16-bit digitizer chains based on the Analog Devices AD9461 operating at digitization rates of 125 MHz. When operating with 4 nsec-spaced bunch trains, digitizing is interleaved between the two chains while, for times when CESR operates for synchrotron light users with dual species of 14 nsec-spaced bunches, each digitizer chain handles either the electron or positron bunches. The front-end boards have both a fixed gain amplifier optimized for precision measurements for bunches with approximately 1×10^{10} particles per bunch and a digital variable gain amplifier for measurements over a wide dynamic range. The triggering and timing configurations are carried out by a dedicated timing board integral to each module. This board takes a turn marker signal from the CESR master timing system and provides overall digitization rate control, adjustment capability for channel-to-channel digitization times, and global adjustment capability for the module digitization time

relative to the bunch arrival time at the detector. This fine degree of local timing adjustment is required in order to maintain the resolution and noise performance of each device. Communications, operational control, and onboard data processing for each device is provided through a digital board and its TigerSharcß digital signal processor (DSP). Communications are by both Ethernet and a dedicated CESR field bus.

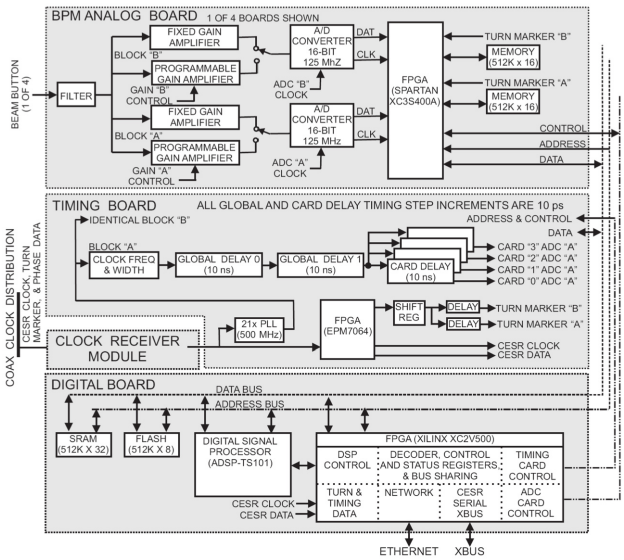

Figure 1: Functional diagram of the CBPM module.

Tune and Motion Detector

The variation of the tunes of individual bunches carries information about the global electron cloud density. Different methods have been employed to measure the tunes of the bunches during the beam dynamics studies.

A simple method for determining the tunes for each bunch in a train of bunches is to use a subset of the complete number of CBPM modules to measure the beam position turn-by-turn for each bunch. The block diagram for this configuration is shown in figure 2a. The data is read out from the CBPM modules and written into a raw data file. Each BPM's position data is then analyzed offline by performing a Fourier transform, which yields the spectral lines of the beam's transverse motion. This method is most often used in conjunction with a kicker that deflects all of the bunches within the train.

A second method is shown in the block diagram in figure 2b. This detection method makes use of a few BPM detectors, which are still connected to CESR's original relay-based BPM system processors. The signal from one BPM button is routed via coaxial relays to one of the analog processors, where fixed gain amplifiers and/or attenuators may be inserted in the signal path to maintain the peak signal level within a factor of five over a wide range of currents. After the gain adjustment the signal passes on to an RF gating circuit, which is triggered by the Fast Timing System, allowing the selection of the signal from a single bunch, sending it to a peak rectifier circuit (with approximately 700 MHz bandwidth) and then routing its output video to a spectrum analyzer in the Control Room. In top plot of figure 3 the timing aperture for the gating circuit was measured by sweeping the gate delay for the signal coming from a single bunch to observe the signal amplitude vs. gate delay. A second method for observing the signal crosstalk between bunches is seen in the bottom plot of figure 3. This plot is obtained by shaking the beam vertically and observing the spectrum analyzer's signal amplitude as a function of gate delay. This second observation gives the base timing aperture as 7.5 nsec wide, giving more than 20 dB isolation of the signal crosstalk from adjacent 4 nsec-spaced bunches and a signal isolation of greater than 50 dB for 14 nsec-spaced bunches.

The initial setup of the storage ring parameters for the tune measurements is performed with a single stored bunch. The betatron tune instrumentation configuration, capable of detecting the beam's tune in both planes, is shown in the block diagram in figure 2c. In this mode the single bunch is excited with the relatively narrow bandwidth shaker magnets (described below) and detected with a swept spectrum analyzer.

a)

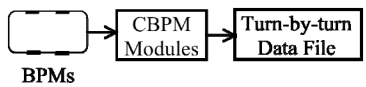

b)

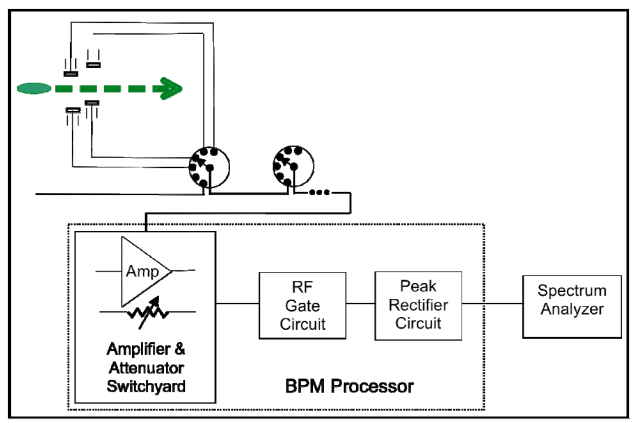

c)

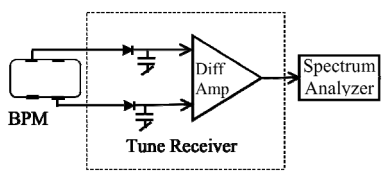

Figure 2: Block diagrams for three different betatron tune receiver configurations: a) Utilizing the bunch-by-bunch and turn-by-turn readout capabilities of the CBPM system. b) Relay BPM system able to gate on a single bunch's BPM signal. c) Simple block diagram of a narrow-band tune receiver, shown in the mode where it can detect both the horizontal and vertical betatron tunes.

Beam Excitation

To measure the tune spectra of bunches it is necessary to observe them undergoing coherent motion. In some cases their self-excitation is sufficient for a good tune measurement, but in other cases the beam must be driven with some type of dipole kicker. There are three types of dipole kickers used in CESR for the measurements described here.

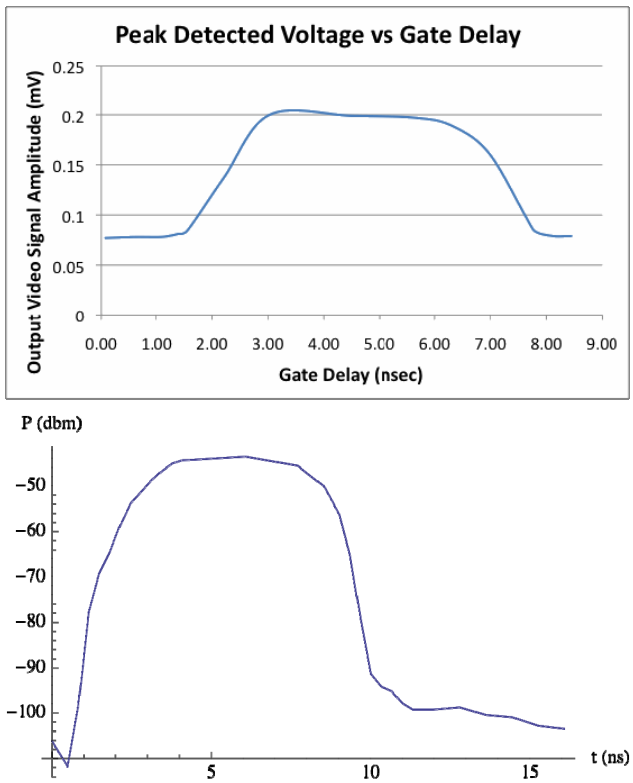

Figure 3: Relay BPM processor's gate timing aperture as measured (Top) with the video signal in the Control Room showing a 77 mV DC offset from its peak rectifier circuit and (Bottom) by driving a single bunch vertically and measuring its response vs. gate delay.

One type of kicker is called a pinger magnet and it is used for single impulse deflection for the beam. There are three pingers installed in CESR: two are horizontal and one is vertical. A horizontal pinger is shown in figure 4 as a single-turn ferrite-core pulsed magnet, which surrounds a Kovar-coated ceramic vacuum chamber. The horizontal pingers are excited using a thryatron with a approximately square pulse, having a flattop region about a 2 μsec long. This is more than long enough to deflect all bunches in one train with the same angle. The pulse shape for the vertical pinger has a different waveform; the magnet is driven with a half sine-wave pulse of approximately 2.5 μsec duration. The pingers can be triggered via CESR's Fast Timing System at repetition rates as high as 60 Hz and the triggers can be synchronized with the CBPM turn-by-turn and bunch-by-bunch data acquisition. Because of its half sine-wave shape, the vertical pinger is timed to have the train of bunches arrive straddling the peak of its deflection.

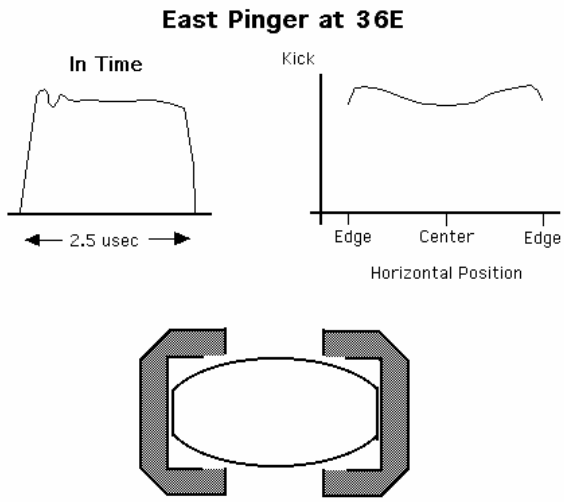

Figure 4: Horizontal pinger. This is a pulsed ferrite magnet surrounding a metalized coated ceramic vacuum chamber, which provides deflection to the beam with a single turn's duration.

The second type of deflection element, utilized for beam dynamics measurements, is a stripline kicker, an example of which is shown in figure 5. There are two (one horizontal and one vertical) stripline kickers installed in CESR. They are the deflectors for the transverse dipole bunch-by-bunch BSF systems for the ring. They have a 3.5 nsec long transit time and are excited with 250W 250 MHz RF amplifiers. As a part of the transverse feedback system for 14 nsec-spaced bunches, the amplifiers are modulated with 14 nsec single period sine-wave, producing a "constant" (±5%) deflection to the beam for about 1 nsec. Each feedback system modulator has an external modulation input and when it is enabled, the input will allow the deflection of any combination of 14 nsec-spaced bunches. For beam dynamics measurements, the stripline kickers are most often used to deflect individual bunches within the train.

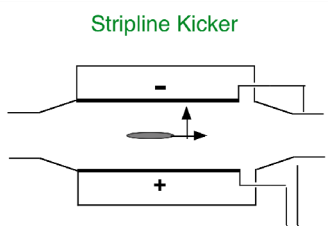

Figure 5: Stripline kicker, having two plates that are driven differentially to deflect the bunch.

For completeness we will mention a third type of deflection component in the storage ring. This is low-frequency shaker magnet, a multi-turn coil wound around a H-frame ferrite core surrounding a metalized coated ceramic vacuum chamber. Although this shaker magnet is not in use during beam dynamics measurements, since it is unable to distinguish motion of individual bunches, it is important for the detection of the tunes as conditions are

re-established at the beginning of each measurement period.

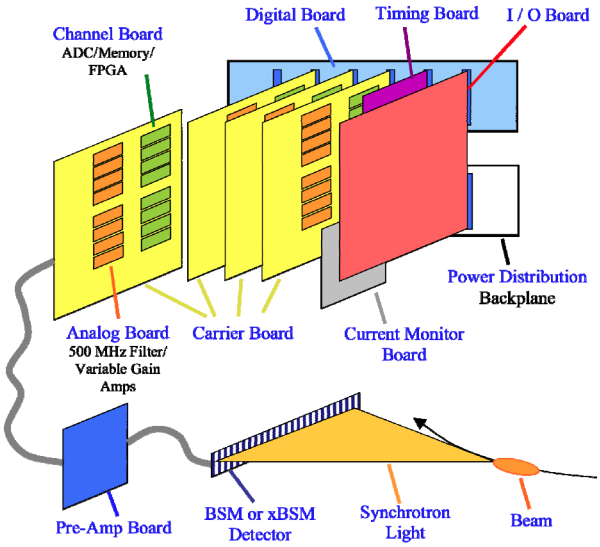

Figure 6: Mechanical layout for the 4 nsec X-ray beam size monitor and its readout electronics

Beam Size Measurement

To study the growth of the vertical beam size due the electron cloud, CESR has installed X-ray beam size monitors (xBSM) on CHESS beam lines for both electron and positron beams. Described elsewhere in detail[3], these detectors consist of upstream X-ray optics configurable as an adjustable slit (AKA a pinhole), a Fresnel zone plate optics chip and a coded aperture optic chip, any of which may be moved into the X-ray beam emanating from one of the hardbend dipole magnets in CESR. A mechanical block diagram of the xBSM system is visible in figure 6. After passing through the X-ray optics, the X-ray beam illuminates a vertical-oriented 32-channel linear pixel detector array having a 50 μm pitch. The detector is capable of measuring the signal from bunches spaced as closely as 4 nsec. After passing through a pre-amplifier, the bunch-by-bunch signals for the 32 channels are digitized and can be recorded turn-by-turn. Utilizing the same timing hardware as the CBPM modules, the xBSM system can be triggered synchronously with the CBPM modules allowing for turn-by-turn beam size measurements correlated between the two systems. The analysis of the xBSM data yields vertical centroid position of the bunch and the vertical beam size for each bunch on each turn.

SCOPE OF BEAM DYNAMICS STUDIES

The beam dynamics studies have focused attention on three specific types of measurements. The first of these is the measurement of the betatron dipole-mode tunes for the bunches within the train, yielding information about the electron cloud density build-up along the train via the localized focusing effect of the cloud on the stored beam. The second class of measurements is associated with determining the onset of unstable motion for stored bunches within the train. The development of the dynamical effects along the train are observed for each bunch using a BPM to detect the spectral composition of centroid motion and the bunch-by-bunch and turn-by-turn xBSM to characterize any vertical beam size enlargement. This set of observations identifies the number of the bunch within the train, at which the unstable motion begins and the rate of growth of the instability. A third set of measurements allows the examination along the train of the damping rates for individual bunches of dipole and head-tail transverse modes below the onset of unstable motion. The measurement techniques, developed for Cesr-TA, will be described in the next three sections.

As part of the beam dynamics measurements, it is necessary to vary the beam conditions. In CESR the spacing and number of bunches within trains can be arranged with great flexibility. The most common spacings are 4 nsec and 14 nsec, but any multiple of 2 nsec greater than 4 nsec is possible. During operation of the storage ring, longitudinal and transverse bunch-by-bunch BSF may be employed.

TUNE SHIFT ALONG THE TRAIN

Over the Cesr-TA project several different techniques have been utilized for making tune shift measurements for individual bunches within trains of bunches. These techniques, their benefits and limitations will be described in the following subsections.

Multi-bunch Large Amplitude Excitation

This method for observing the tunes of different bunches within the train pulses a pinger magnet with a single-turn excitation to deflect all of the bunches within the train and thus start an oscillation of their centroids. The CBPM system is then is timed to read out a number of BPMs over several thousand turns for all bunches in the train (see block diagram in figure 2a); the data acquisition is synchronized with the triggering of the pinger magnet's deflection. After recording the turn-by-turn bunch positions, the data is analyzed offline with a Fast Fourier transform (FFT), from which the betatron tunes are determined. During these measurements the peak vertical beam displacements, for example, were typically 7 mm and 2 mm at 2.1 GeV and 5.3 GeV, respectively.

Since data from all bunches is recorded at the same time, it is relatively rapid to take data in one set of conditions and, since the data from all bunches is taken on the same turns, this method is relatively insensitive to any drifts in the storage ring tunes. However, the fact that all bunches are excited at the same instant implies that the lowest coupled bunch mode is excited for the train of bunches. This makes later bunches in the train susceptible to being excited at the natural oscillation frequencies of preceding bunches, producing multiple spectral peaks in close proximity and confusing the identification of the

later bunch's oscillation frequency. It is also the case that the pinger excitations are relatively large with respect to the stored beam's size, e.g. typically the vertical oscillation amplitude may exceed many ten's of the vertical sigma. So the beam's oscillation is exploring a fairly large volume of the electron cloud's distribution.

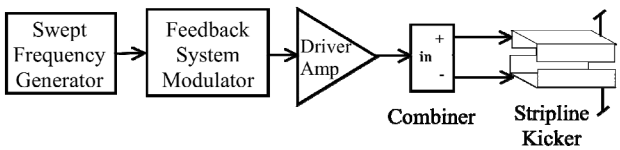

Figure 7: Single bunch excitation method using the stripline kicker, driven by a swept frequency source via the feedback system's external modulation port.

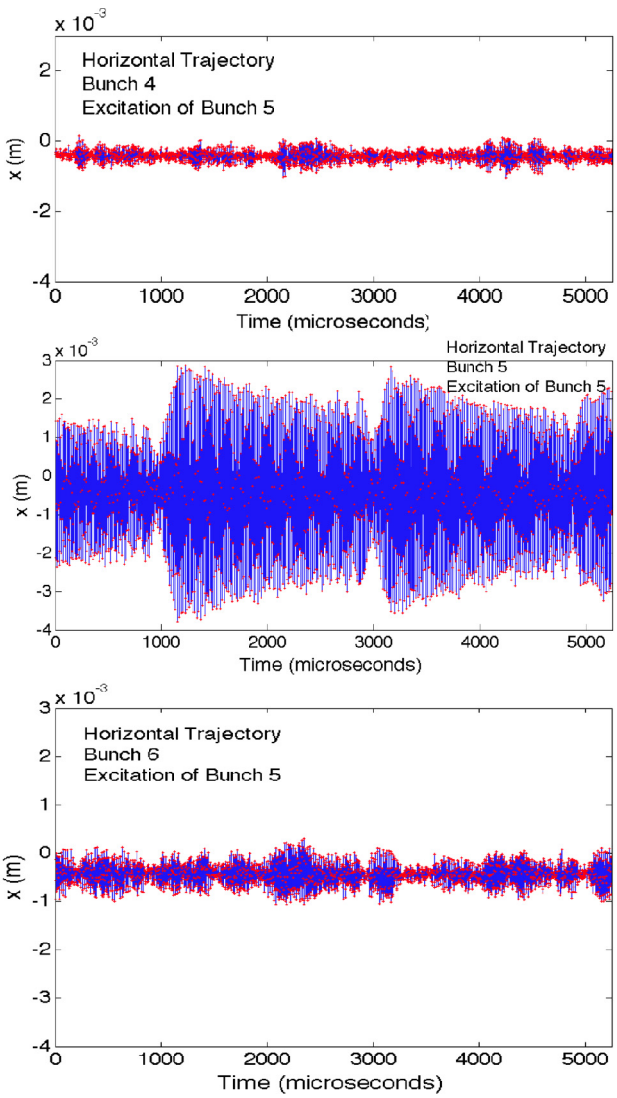

Figure 8: Horizontal position of bunches 1, 5 and 10 (respectively for the top, middle and bottom plots) for a 10-bunch train when only bunch number 5 was driven.

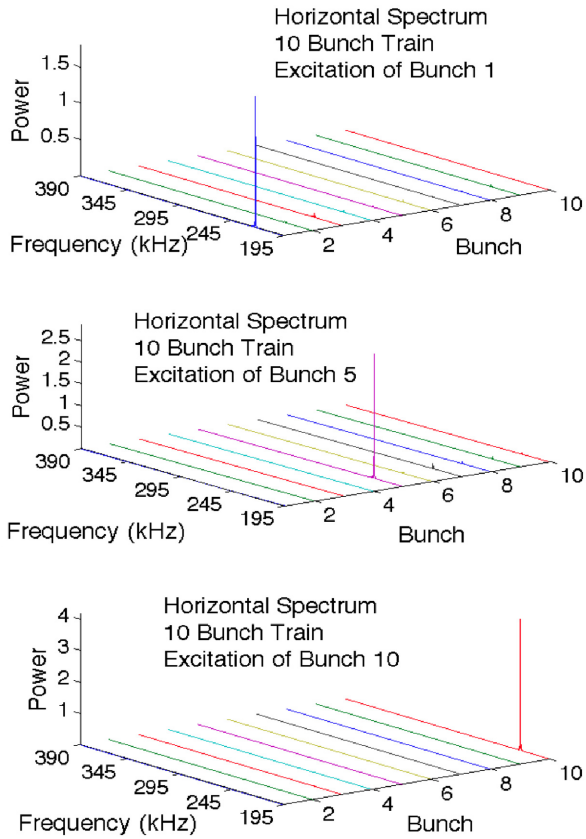

Figure 9: Horizontal position spectra of all bunches in a 10-bunch train when bunches number 1, 5 and 10 (respectively for the top, middle and bottom plots) were driven individually.

Single Bunch Small Amplitude Excitation

Another approach has been developed for bunch-by-bunch tune measurements. This approach focuses on reducing the coupling from preceding bunches to the bunch that one is trying to measure. As shown schematically for one stripline kicker in figure 7, this is accomplished by driving both the horizontal and vertical stripline kickers only for the bunch being measured by making use of the external modulation input for the BSF system. The source for the signal for the external modulation port comes from a frequency synthesizer, whose output frequency is swept across the range of betatron oscillation frequencies for the bunches. The frequency is swept with a saw-tooth at 500 Hz, driving the bunch in the dipole oscillation mode when the excitation frequency crosses the betatron resonance. Again the turn-by-turn position data is recorded for a number of BPMs using the CBPM system readout (as shown in the block diagram in figure 2a) with the total turn record length long enough to capture at least one excitation and damping cycle. The measurement process is repeated as the excitation's delay is stepped from one bunch to the

next, resulting a set of positions for all bunches at each delay. The data is analyzed offline with a FFT to give the oscillation frequency of the excited bunch and coupling of its motion to subsequent bunches via the electron cloud.

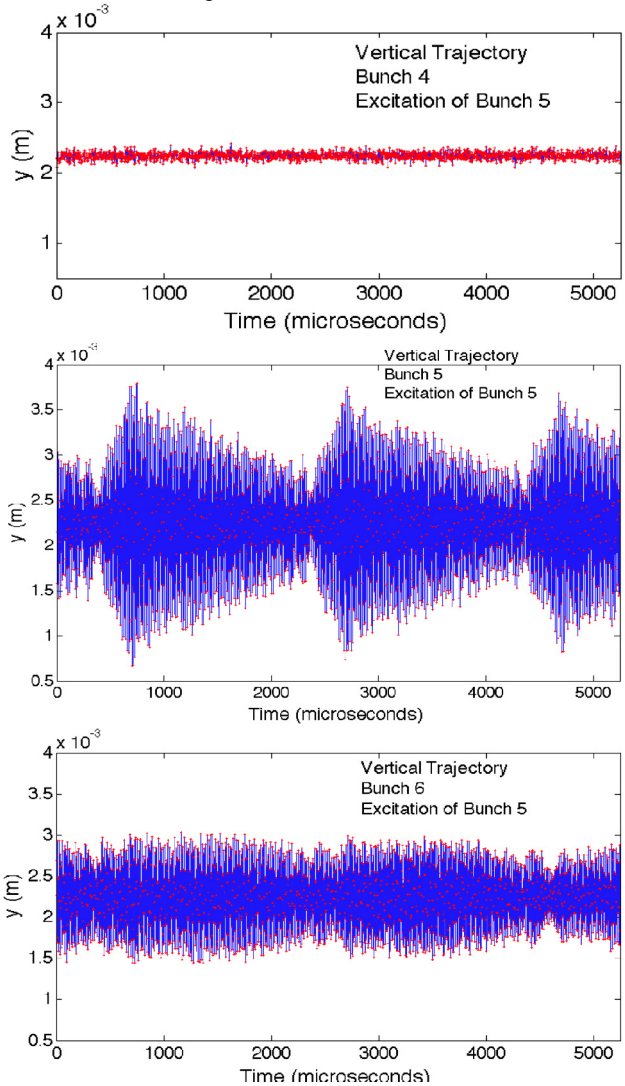

Figure 10: Vertical position of bunches 1, 5 and 10 (respectively for the top, middle and bottom plots) for a 10-bunch train when only bunch number 5 was driven.

Some results are presented here for illustration of this technique; the data were taken with a 10 bunch train with a 14 nsec spacing in 2.1 GeV conditions. Figure 8 shows the horizontal position data for the first, fifth and tenth bunch, when only bunch number 5 was being excited. During the 2048-turns of the data-samples taken on simultaneous turns for the three bunches, it is clear that bunch 5 was excited with two complete cycles of the swept signal source. This is even clearer in figure 9 when viewing the horizontal spectra of all 10 bunches when bunch numbers 1, 5 and 10 were being driven individually. The fact that the stripline kicker is exciting only one bunch is quite evident in both figures 8 and 9.

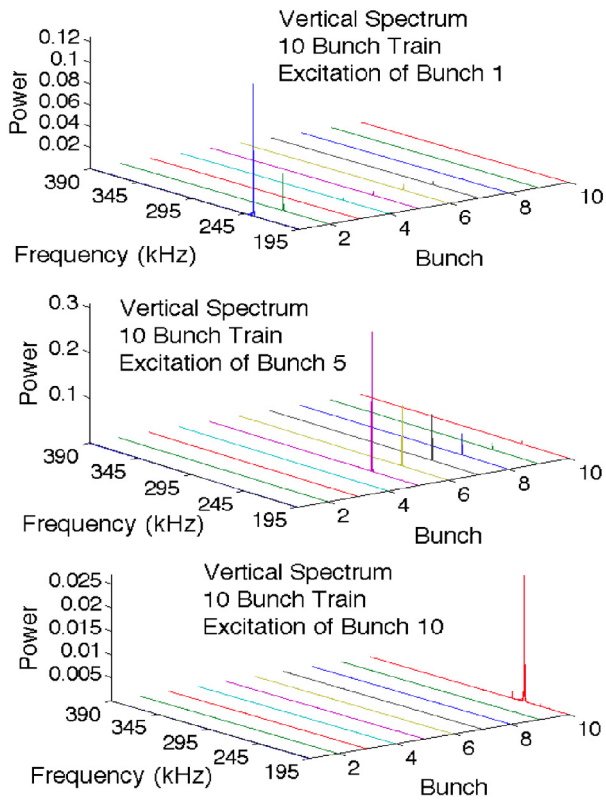

Figure 11: Vertical position spectra of all bunches in a 10-bunch train when bunches number 1, 5 and 10 (respectively for the top, middle and bottom plots) were driven individually.

For comparison with the horizontal data, the matching set of vertical data is presented here for the same storage ring and electron cloud conditions as above. The vertical position data for bunches 1, 5 and 10 is shown in figure 10, when only bunch 5 is driven. Also the vertical spectra for all bunches are shown in figure 11, when bunches 1, 5 and 10 are individually excited. The interesting feature, visible in the vertical data, is that even though only one bunch is being driven, its motion is coupling the subsequent bunches in the train. Figure 11 presents evidence that this coupling increases along the train, suggesting that the electron cloud may be playing some part in this bunch-to-bunch vertical dipole coupling.

This technique has the advantage of avoiding cross-coupling from preceding bunches to the bunch being studied, while also providing information about the coupling of the motion of one bunch to later bunches via the electron cloud. The excitation level can, in principle, be tailored for the bunch that is being driven; the ability to keep a relatively fixed amplitude for the bunch's oscillation could be important for conditions when the first bunches in the train are more stable but the latter bunches are not. This method has the drawback that it slower that the preceding method as it requires collecting turn-by-turn position data for every bunch times the number of bunches within the train, and is, therefore, sensitive to drifts in the tunes of the storage ring.

Feedback System Response

Another approach for tune measurements became apparent after the installation of the Dimtel[4] feedback electronics, capable of damping bunches with spacings down to 4 nsec. While looking at the FFT of the position for a single bunch as part of the feedback system diagnostics, it was observed that the signal response varied as a function of the feedback gain. At low gains the betatron peak is visible, but as the gain is increased the amplitude of the peak decreases until it become a notch in the spectrum at high gain. The explanation for this effect is that there is a broadband excitation of the beam and the feedback system is phased to suppress the bunch's response preferentially at the betatron frequency. When the feedback settings have been fully optimized, the notch in the spectrum for each bunch marks the location of its betatron oscillation frequency.

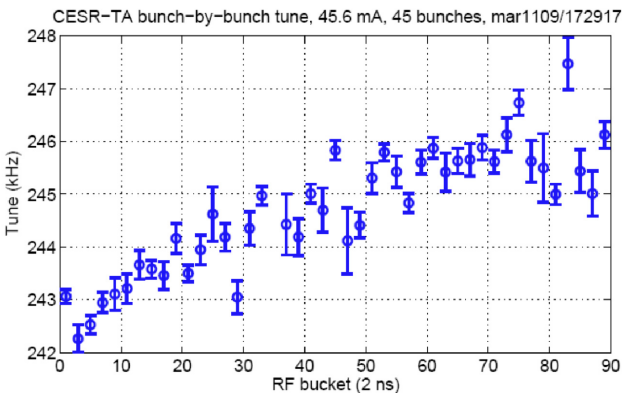

Figure 12: Vertical tune vs. RF bucket number for a train of 45 bunches with 4 nsec bunch spacing determined from notches in the spectra from the feedback error signal.

The position data generally represents the effect of probing the electron cloud in a regime when the bunches are moving at small amplitudes. An example of data taken using this method is seen in figure 12. There is a very clear trend for the vertical focusing effect from the accumulating electron cloud, which is visible the plot. Although this method is quite appealing, only a few tune shift measurements have been performed via this method. This technique works well for 4 nsec-spaced bunches, but it requires fairly exact adjustments of the feedback system parameters to be able to clearly identify the notches in the bunch spectra. To obtain the most accurate spectra, the data for each bunch is averaged typically for 30 seconds, allowing some uncertainty in the tunes due to longer–term drifts in the storage ring focusing.

Self-Excitation

The last method for bunch-by-bunch tune shift measurements to be presented here is a by-product of the observation of beam instabilities, described in the next section. In this set of measurements the position spectrum of each bunch is measured with a spectrum analyzer. Two of the peaks that are visible in these self-excited spectra are the horizontal and vertical dipole modes. The shift of the tunes from bunch to bunch are easily detected via this method. Since most of these measurements are taken in conditions when the beam is above or near an instability threshold for at least some of the bunches within the train, the self-excited amplitudes of the dipole motion will vary along the train. This method is quite sensitive to low signal levels with the noise floor for small amplitude oscillations at the level of 0.4 μm-rms horizontally and 0.2 μm-rms vertically. Due to averaging in the spectrum analyzer, the data acquisition requires about 1 minute for each bunch, leaving this method sensitive to drifts in the storage ring tunes.

MEASURING BEAM INSTABILITIES

An important set of Cesr-TA measurements study beam instabilities due to the electron cloud. This study focuses on the growth of self-excited oscillations of the bunch's centroid and the growth of vertical beam size along the train under various accelerator and electron cloud conditions. The first part of the hardware utilized for these measurements is a monitor for the bunch-by-bunch beam position. The other detection system required is the xBSM monitor for determining vertical beam of each bunch.

Bunch-by-bunch Position Spectra

For instability studies the bunch-by-bunch position measurements are accomplished by a BPM detector connected to one of CESR's original relay-based BPM system processors, which in turn passes its video output signal to a spectrum analyzer in the control room. (For further description see text above and the block diagram shown in figure 2b.) BPM33W, which is located at a higher vertical beta point, has generally been used as the detector for these observations. The signal is taken from one button, making it sensitive to both the horizontal and vertical motion. The data taking software sets the trigger delay for the sampling gate to select a particular bunch within the train. For almost all of the data, an RG-174 coaxial cable is placed within the signal path to limit the bandwidth of the button signal (giving an effective 20 dB of signal attenuation) and to this an additional 12 dB of amplification is added. The signal is then sent to the biased peak rectifier circuit, which has an effective bandwidth of 700 MHz, and a decay time constant of approximately 10 nsec. The resulting video signal is buffered and sent on a wideband coaxial cable to a spectrum analyzer in the control room.

The spectrum analyzer is an Hewlett Packard model 3588A, operating in the baseband (in these studies the center frequency ranges from 190 kHz to 210 kHz) in Narrowband Zoom mode with a 40 kHz span. This mode of operation performs a ±20 kHz FFT on time slices of the signal and these spectra are averaged for 100 time slices, taking about 10 seconds for each 40 kHz step of the center frequency. At 2.1 GeV the position sensitivity of the signal from the BPM at 33W was measured to be

$$x_{rms} = x_0 \left(\frac{1\ \text{mA}}{I_b} \right) 10^{A_x/20\ \text{dBm}} \qquad y_{rms} = y_0 \left(\frac{1\ \text{mA}}{I_b} \right) 10^{A_y/20\ \text{dBm}}$$

where $x_0 = 81.3$ mm and $y_0 = 45.3$ mm. With this gain configuration and over the frequency range of study, the noise baseline falls from -95 dBm to -105 dBm (corresponding in the vertical direction, respectively, to displacements of 1.1 µm-rms to 0.33 µm-rms for a 1 mA bunch.)

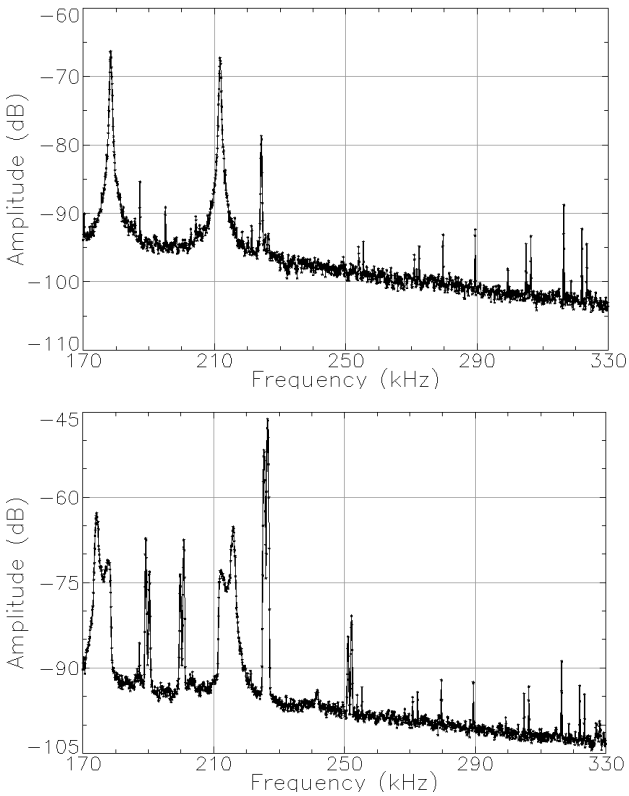

Figure 13: Self-excited beam power spectra for bunch 1 (top) and bunch 30 (bottom) in a 30 bunch-long positron train at 2.1 GeV.

Representative self-excited spectra of the first and last bunch in a 30-bunch positron train at 2.1 GeV are shown in figure 13. For this train the horizontal tunes are in the range from 212 kHz to 218 kHz, and the vertical tunes are in the range from 224 kHz to 227 kHz. Since this spectrum overlaps the ½-integer resonance at 195 kHz, this frequency is a reflection point for the spectra. For bunch 30, additional lines are visible in the ranges 198-201 kHz and 250-252 kHz; these correspond to vertical head-tail modes as their frequencies are plus and minus the synchrotron oscillation frequency added to the vertical tune. The baseline is seen to be falling as roughly a 1/f noise spectrum. There are also a number of unrelated noise lines, scattered throughout the spectra assumed to be due to "cultural noise sources." A "mountain-range" plot of the spectra of all 30 bunches within a 30 bunch-long train is plotted in figure 14. A cut of the spectrum has been made at the half integer resonance (195 kHz) to suppress the "reflected" spectral lines. In this plot the self-excited vertical tune amplitude begins to grow at approximately bunch 10 and continues to grow in amplitude until near bunch 20. In this region the two vertical head-tail lines appear above the noise background. Also around bunch 15 the spectral peak of the horizontal tune appears to bifurcate, something which is also seen in the bottom plot of figure 13, and on close examination these data also show bifurcation of the vertical tune and the vertical head-tail lines for the latest bunches in the train. Figure 14 also shows a number of "fences", i.e. peaks in the spectrum at fixed frequencies due to external "cultural" noise sources.

Many tests have examined the self-consistency and interpretation of the data. The identification of the vertical and horizontal tunes was checked by changing the controls for each separately and verifying which spectral peak moved. They were also checked using BPMs at other locations, which had buttons summed to produce dominantly horizontally- or vertically-sensitive detectors. The interpretation that the vertical head-tail lines were not inter-modulation distortion components coming from the processing electronics was tested [5] by switching an attenuator into the signal path upstream of the peak detector and observing that all spectral peaks decreased by 9±1 dB. If the head-tail lines were actually inter-modulation cross-products from the non-linearity of the electronic processing, then they would have decreased by 18 dB and they only decreased by 9 dB.

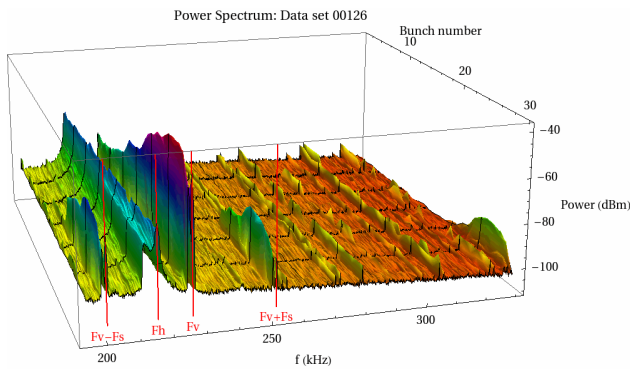

Figure 14: Self-excited beam power spectra for bunches 1 through 30 in a 30 bunch-long positron train at 2.1 GeV. The horizontal axis is the frequency, the vertical axis is the spectral power in dB and the axis into the page is the bunch number with bunch 30 being in the foreground. Red vertical lines in the foreground denote in ascending order the location of the m = -1 vertical head-tail line, the horizontal tune, the vertical tune and the m = +1 vertical head tail line.

This method for detecting the frequency spectra of the bunches is fairly sensitive, however measurements must be made for each individual bunch. The measurement time is about 1 minute per bunch for the frequency range, over which we choose to take data. This means that the data represents the equilibrium state of any unstable motion. It also implies that due the typical beam lifetimes, the beam must be refilled a number of times during the set of data for one observation. In our case we choose typically to refill after measuring five bunch

spectra, which, when plotted, gives the amplitude of peaks within the spectrum a slightly scalloped shaped over five bunches. This refilling cycle coordinates fairly well with the cycle to measure and readout the bunch-by-bunch and turn-by-turn xBSM data.

We have tried to readout the turn-by-turn and bunch-by-bunch positions from a number of BPMs via the CBPM system (giving a much faster data acquisition time.) Unfortunately the head-tail lines are not visible in the CBPM data. Our explanation is that the relay BPM system peak rectifies the position signal and, if there is a temporal variation due to synchrotron motion, the arrival time of the signal varies correspondingly. This gives a frequency modulation to the position signal when viewed by the spectrum analyzer. The CBPM processing is different; the signal is sampled at a fixed time corresponding to the positive peak of the button BPM pulse. Any variation in the arrival time produces only a second order variation in amplitude and, even if one moved the sampling time significantly off of the peak, it does not produce any signal at the head-tail line frequencies.

Bunch-by-Bunch Beam Size

The second detection system in use during these experiments for determining vertical beam size of each bunch is the xBSM monitor (described above with its block diagram in figure 6). The hardware for the xBSM system is explained in greater detail elsewhere[3]. During a given set of instability measurements typically data are taken using all three sets of optics, the adjustable slit (AKA pinhole), the Fresnel zone plate optics chip and the coded aperture optic chip. This allows the greatest range of sensitivity for measurements of the vertical size and centroid motion of the beam. During the measurement cycle, the beam size data are taken bunch-by-bunch and turn-by-turn generally immediately after the train has been topped off, usually occurring after taking the spectrum for every fifth bunch.

MEASURING COHERENT MODE DAMPING RATES

A complement to the instability measurements, described in the preceding section, are the damping rate measurements for the coherent transverse modes. The instability measurements easily record the large amplitude signals as the bunches become unstable and ultimately limit due to non-linearities in the bunch's dynamics. However, the damping measurements give information about the stability of the bunch at small amplitudes before the bunch goes unstable, the regime in which storage rings and damping rings will actually operate. These studies will give some insight about how the beam instability begins developing as one looks from bunch to bunch along the train.

Drive-Damp Excitation

The basic idea for these observations is to employ the same relay BPM configuration as is used for the instability measurements. However, the spectrum analyzer's center frequency is adjusted to be at either the vertical betatron dipole-mode frequency or one of the head-tail mode frequencies while the spectrum analyzer is set to be in Zero Span mode. In this mode the analyzer functions as a tuned receiver with its display producing signal amplitude vs. time. The spectrum analyzer's tracking generator's output is sent to the vertical feedback system's external modulation input. Aside from the spectrum analyzer's control settings, this is quite similar to the hardware configuration shown in figure 7. By adjusting the digital timing controls for the modulator's external input, it possible to drive only one bunch as long as bunch spacing is greater than 6 nsec. (If the bunch spacing is 4 nsec, then the timing of the pulse on the BSF system's stripline kicker will the deflect the bunch under study and slightly kick the following bunch.) To permit the drive-damp modulation of the beam, there is one additional element added to figure 7's block diagram. This element is a modulating gate for the spectrum analyzer's tracking generator signal. This modulator gate is timed with the spectrum analyzer's timing sweep to pass the tracking generator output for 3 msec at the beginning of the sweep and then to gate off its output until the start of the next sweep.

An illustration of the timing and the expected signal response are shown in figure 15. The red curve shows that the amplitude of the transverse excitation of the bunch vs. time is an impulse. The expected beam response initially grows during the driving impulse, usually reaching a saturated level, and then decays exponentially after the drive is switched off (shown in the logarithmic plot as a linear decrease vs. time.) If the spectrum analyzer's tracking generator's frequency is tuned away from the bunch's resonant frequency, the decaying response will have periodic oscillatory beats. So during the measurement it is necessary to make small tuning adjustments to the excitation frequency to produce the most exponential decay possible.

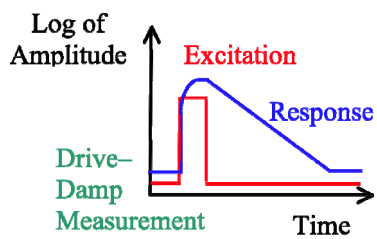

Figure 15: Illustration of the drive-damp measurement: The red trace is the amplitude of the excitation driving the bunch. The blue trace is the bunch's response.

The excitation of the bunch is accomplished in a somewhat different manner for the betatron dipole mode and the head-tail modes. In the both cases the spectrum analyzer is set to drive the coherent mode frequency being measured. However, for the head-tail modes it is necessary to also continuously drive the external modulation input for RF cavity phase at the synchrotron

oscillation frequency. This imposes a longitudinal energy oscillation on all of the bunches within the train, causing them to uniformly shift their arrival times and displace the train's centroid horizontally proportional to the storage ring's dispersion. The typical amplitude of this oscillation is relatively large, with the peak fractional energy varying as much as $\pm 7.6 \times 10^{-3}$. One explanation of the driving mechanism for head-tail modes is that with a constant deflecting field in the stripline kicker, the energy oscillation causes the head of the bunch (at lower energy) to be deflected more than the tail of the bunch (at higher energy.) Although this is a fairly small differential effect, the bunch is being driven on the head-tail resonance allowing the oscillation amplitude to build up.

Two examples of the actual measurements are found in figure 16. In the upper plot the betatron dipole mode's amplitude ramps up for the first 3 msec and then decays exponentially thereafter. The lower plot shows one of the head-tail modes being excited. After the drive turns off, the initial 7 dB drop represents the component of the signal, which represents the excitation of the dipole mode; the roughly exponential shape thereafter is the head-tail mode's decay. If the longitudinal drive to the RF cavity's phase were to be turned, then off the head-tail mode's signal would go away.

This type of measurement may be very useful for understanding the behavior of bunches within the train before their motion becomes unstable. However, even though much of the data acquisition is automated, there are a few steps, which must be accomplished by the personnel taking data. In particular the fine adjustment of the spectrum analyzer's frequency, centering it on the coherent mode's frequency, is necessary to produce the exponential damping curve. The manual adjustment of the frequency makes this type of measurement fairly time-consuming. Routinely, after data is taken for several bunches, the beam is topped off. Beam size measurements are typically taken immediately after topping off.

CONCLUSIONS

This paper has presented details for the beam dynamics measurements performed in the Cesr-TA project. Different techniques for measuring the tunes, the coherent mode amplitudes and damping rates have been described. Information about the strengths and weaknesses of these techniques provide useful ways to rate the different strategies employed for these measurements.

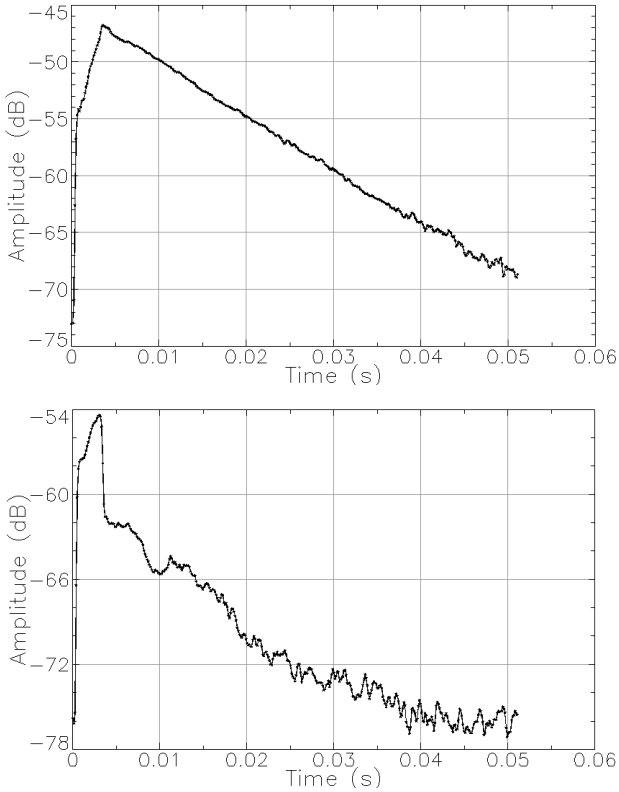

Figure 16: Drive-damp measurements: The upper trace is the response for the bunch being driven at the vertical betatron frequency. The lower trace is the response when one of the head-tail modes is excited. The vertical and horizontal scales are 5 dB and 10 msec per division, respectively.

REFERENCES

[1] M. Palmer, these proceedings.
[2] M. Palmer, "CESR Beam Position Monitor System Upgrade for CesrTA and CHESS Operations", Proceedings of 1st International Particle Accelerator Conference: IPAC'10, Kyoto, Japan, 23-28 May 2010
[3] N. Rider, these proceedings.
[4] Dimtel Inc., www.dimtel.com.
[5] CTA log entry 779.

Synrad3D Photon propagation and scattering simulation *

G. Dugan, D. Sagan
CLASSE, Cornell University, Ithaca, NY 14853 USA

Abstract

As part of the Bmad software library, a program called Synrad3D has been written to track synchrotron radiation photons generated in storage rings. The purpose of the program is primarily to estimate the intensity and distribution of photon absorption sites, which are critical inputs to codes which model the growth of electron clouds. Synrad3D includes scattering from the vacuum chamber walls using X-ray data from an LBNL database. Synrad3D can handle any planar lattice and a wide variety of vacuum chamber profiles.

INTRODUCTION

The Bmad software library[1] has been used very successfully at Cornell for modeling relativistic charged particles in storage rings and linacs. Associated with this library are a number of programs used for lattice design and analysis. Recently, a new program that uses the Bmad library, called Synrad3D, has been developed to track synchrotron radiation photons generated in storage rings and linacs.

The motivation for developing Synrad3D was to estimate the intensity and distribution of photon absorption sites, which are critical inputs to codes which model the growth of electron clouds. Synrad3D includes scattering from the vacuum chamber walls using X-ray data from an LBNL database[2]. Synrad3D can handle any planar lattice and a wide variety of vacuum chamber profiles.

In the following sections, the general approach used in Synrad3D will be described, and two examples of its use will be presented.

APPROACH

Synrad3D uses Monte Carlo techniques to generate photons based on the standard synchrotron radiation formulas for dipoles, quadrupoles and wigglers, in the lattice of an accelerator. Any planar lattice can be handled. The lattice can be specified using Bmad, MAD, or XSIF formats. Photons are generated with respect to the particle beam's closed orbit, so the effect of variations in the orbit can be studied. In a linear accelerator lattice, since there is no closed orbit, the orbit is calculated from the user supplied initial orbit. The particle beam size is also taken into account when generating the photon starting positions. The emittance needed to calculate the beam size can be supplied by the user or is calculated from the standard radiation synchrotron radiation formulas.

* Work supported by the US National Science Foundation (PHY-0734867) and Department of Energy (DE-FC02-08ER41538)

REFLECTIVITY MODEL

Photons are tracked to the wall, where the probability of being scattered is determined by the angle of incidence and the energy of the photon. The model used to determine the scattering angle, which is taken from an X-ray database [2], is shown in Fig. 1. This is for an aluminum vacuum chamber surface, but a model for a different surface could be used.

For comparison, we also show in the figure the relative synchrotron radiation spectra for a 2 GeV beam in an arc dipole and a wiggler at CesrTA. Also shown is a direct measurement [3] of reflectivity at 5° from an aluminum surface made at DAPHNE.

Currently, only specular reflection is included, but diffuse scattering can also be simulated by altering the reflectivity model.

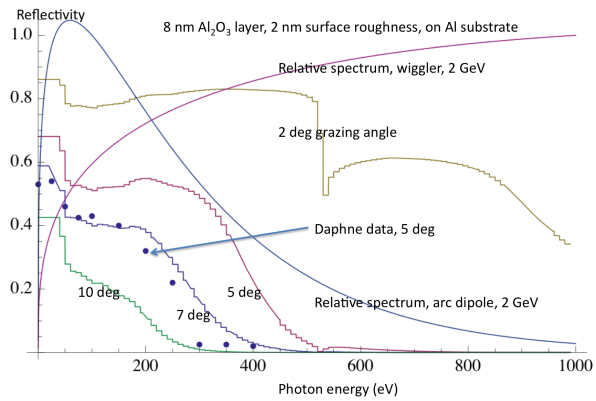

Figure 1: Reflectivity model from LBNL X-ray database

VACUUM CHAMBER MODEL

The vacuum chamber wall is characterized at a number of longitudinal positions by its cross-section. The cross section model is shown in Fig. 2. As shown in the figure, antechambers can be included. A vacuum chamber wall cross-section may also be characterized using a piecewise linear outline.

In between the cross-sections, linear interpolation or triangular meshing can be used. Linear interpolation is faster but is best suited for convex chamber shapes.

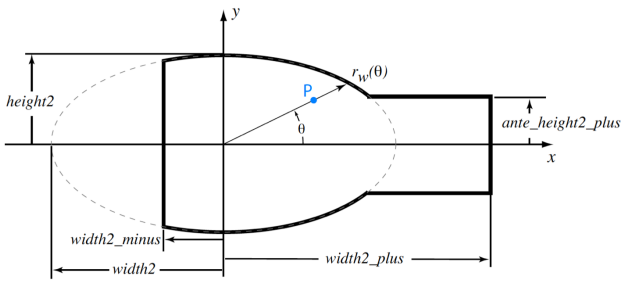

Figure 2: Vacuum chamber model

EXAMPLE 1: PHOTON EMISSION IN A DIPOLE

As the first example, we consider the CesrTA ring with a 5.3 GeV positron beam, and use Synrad3D to simulate photon emission only in the arc dipole at B12W. The vacuum chamber is a simple ellipse. The photons are generated only in the upstream end of this dipole but propagate downstream and can scatter.

In Fig. 3, we show a collection of photon trajectories, projected onto the bend plane. Photons generated by the beam in B12W strike the B12W vacuum chamber a short distance downstream. Some are absorbed here, but most scatter and strike the vacuum chamber further downstream, in B13W. More are absorbed here, but many others scatter again.

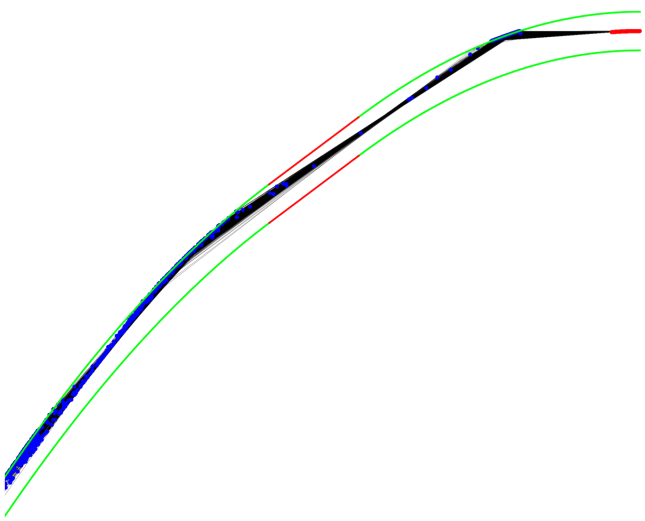

Figure 3: Photon trajectories from B12W: projections onto bend plane. The red dots at the top right are the photon source (the radiating beam in a section of the dipole). Black lines are photon trajectories, and blue dots are photon absorption sites. The upper green lines are the edges of the vacuum chamber in B12W; the red lines are the edges in a straight section, and the lower green lines are the edges of the vacuum chamber in the next dipole, B13W. The geometry has been distorted for purposes of illustration.

These photon trajectories in three dimensions are shown in Fig. 4. Photons from the source (on the right) propagate and strike the vacuum chamber. Blue dots represent absorption sites. For this simple example, in which the photon source is localized longitudinally, the absorption site locations tend to be clumped in several clusters, with decreasing intensity as we get further from the source.

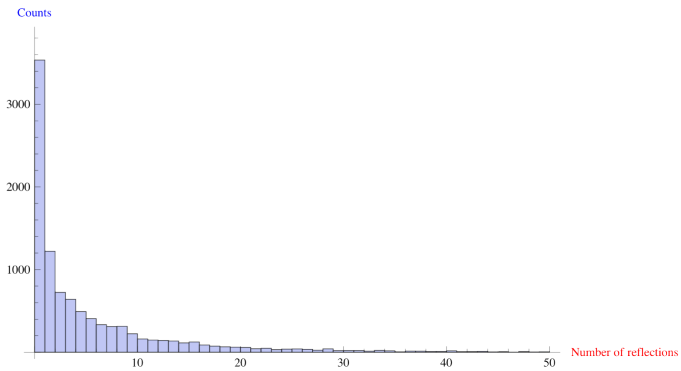

Figure 5: Reflection distribution. The mean number of reflections is 5.4

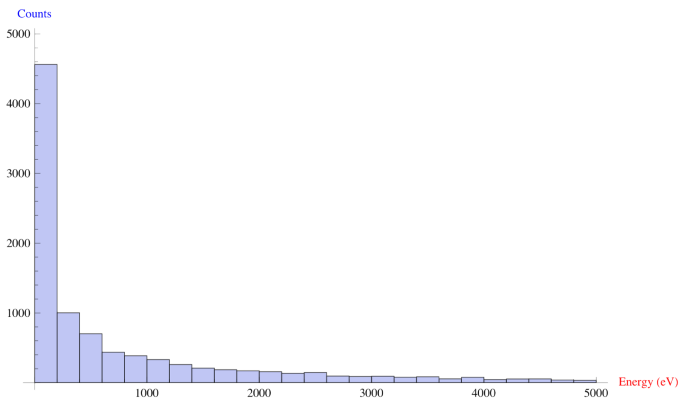

Figure 6: Energy distribution

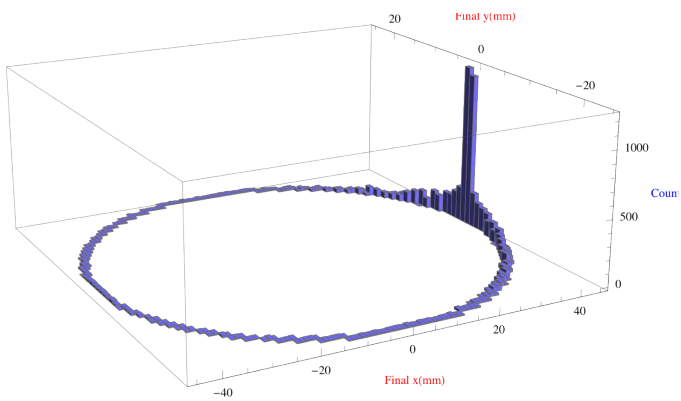

Figure 7: Distribution of photon absorption sites around the vacuum chamber perimeter

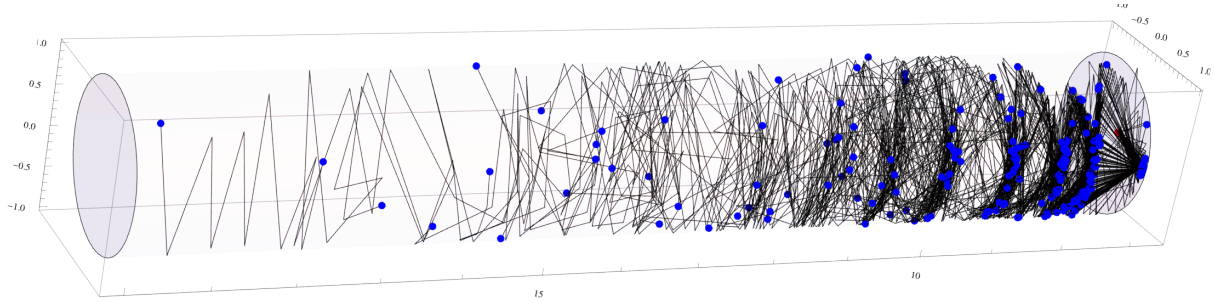

Figure 4: Photon trajectories from B12W in three dimensions. The photon source is on the right. Black lines are trajectories, and blue dots are photon absorption sites. The transverse geometry has been distorted from an ellipse to a circle, and the longitudinal dimension has been rectified and divided by 10, for purposes of illustration.

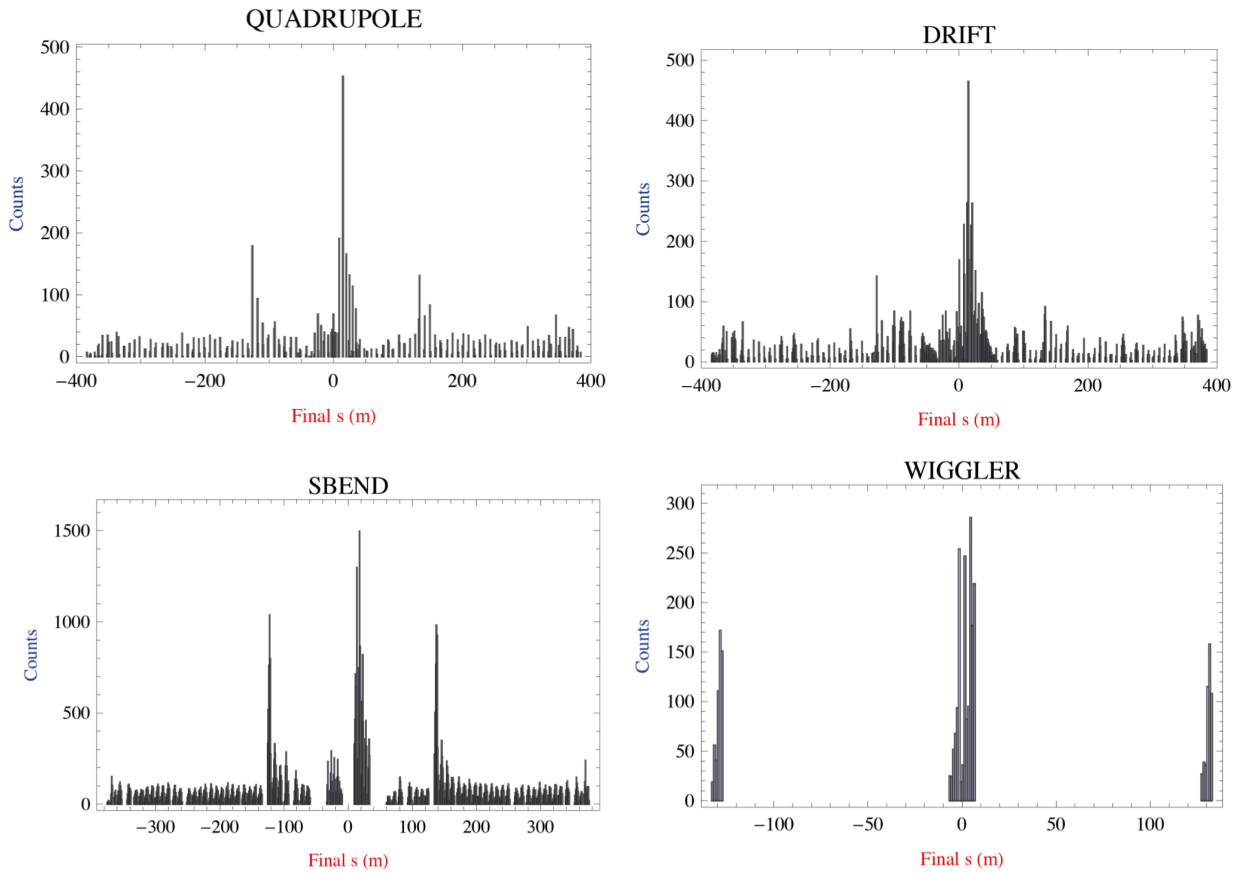

Figure 8: Distribution of photon absorption sites vs. longitudinal position, for different magnetic environments. The origin for the longitudinal coordinate is the center of the L0 straight section. The ring circumference is about 760 m.

Other features of the photon scattering and absorption process are shown in Fig. 5, Fig. 6, and Fig. 7.

In Fig. 5, a histogram of the number of photons, vs. the number of reflections, is presented. Many photons suffer no reflections, that is, they are absorbed as soon as they hit the vacuum chamber, but most are reflected several times before being absorbed. The mean number of reflections is 5.4.

In Fig. 6, a histogram of the number of photons, vs. photon energy, is presented. This is strongly peaked at zero but has a long tail out to at least 5 keV.

In Fig. 7, a two dimensional histogram of the number of photons, vs. location of the absorption site on the vacuum chamber perimeter, is presented. This is is peaked at the outside edge of the vacuum chamber, where the direct photon strikes occur, but there is long tail extending around the entire surface of the vacuum chamber, due to the reflected photons.

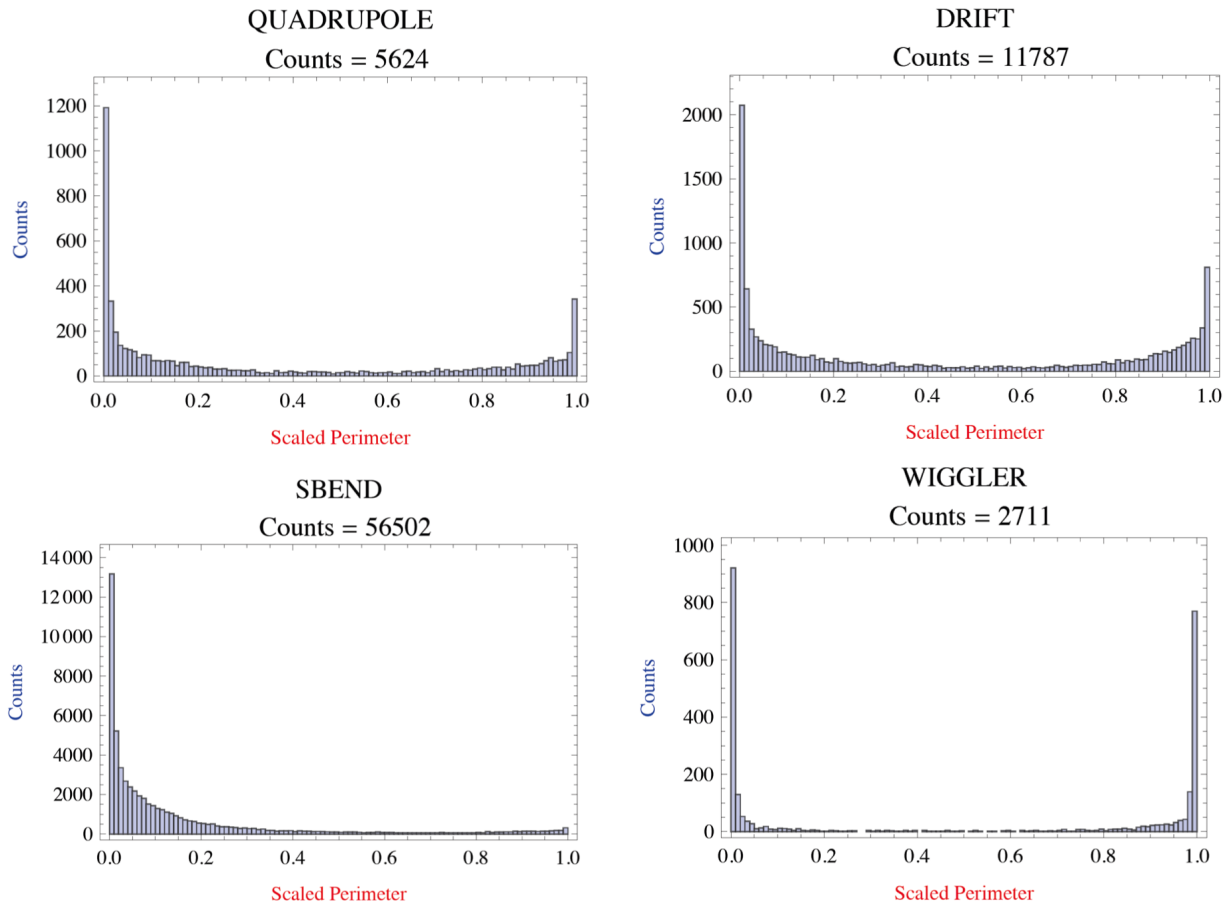

Figure 9: Distribution of photon absorption sites vs. scaled perimeter along the vacuum chamber, for different magnetic environments. The scaled perimeter coordinate varies from zero at the radial outside edge of the vacuum chamber, to 1 at the radial inside edge. Top-bottom symmetry is assumed.

EXAMPLE 2: PHOTON EMISSION THROUGHOUT THE RING

For the second example, photon emission throughout the CesrTA ring from a 2.1 GeV positron beam is simulated. The vacuum chamber is again a simple ellipse.

In Fig. 8, the distribution of photon absorption sites around the ring is shown, sorted by the type of magnetic environment in which the absorption occurs. This information is important for simulations of electron cloud growth, which is strongly influenced by the magnetic environment.

The wigglers in the L0 straight section are responsible for the large peaks in the longitudinal region near $s = 0$. The large peaks near $s = \pm 130$ m are due to wigglers in the arcs near these locations. The small peaks in the arcs are due to the regular Cesr dipoles.

In Fig. 9, we see the distribution of photon absorption sites vs. scaled perimeter along the vacuum chamber, again sorted by the type of magnetic environment in which the absorption occurs.

In the wigglers, most of the photons come from the radiation fans in an upstream wiggler region, so there are strong peaks on both edges of the vacuum chamber. In the bends, most of the radiation is from direct strikes from upstream dipoles, so there is only a strong peak on the radial outside edge, together with a long tail, due to scattering. In the quadrupoles and drifts, there are two peaks, with the higher one at the radial outside, and a distribution between the peaks due to scattering.

SUMMARY

As part of the Bmad software library, a program called Synrad3D has been written to track synchrotron radiation photons generated in storage rings. Synrad3D includes scattering from the vacuum chamber walls using X-ray data from an LBNL database. It can handle any planar lattice and a wide variety of vacuum chamber profiles. Two examples of the application of this program to radiation in CesrTA have been shown and discussed.

REFERENCES

[1] D. Sagan, "Bmad: A relativistic charged particle simulation," Nuc. Instrum. Methods Phys. Res. A, **558**, pp 356-59 (2006)

[2] B.L. Henke, E.M. Gullikson, and J.C. Davis. X-ray interac-

tions: photoabsorption, scattering, transmission, and reflection at E=50-30000 eV, Z=1-92, Atomic Data and Nuclear Data Tables Vol. 54 (no.2), 181-342 (July 1993)

[3] N. Mahne, A. Giglia, S. Nannarone, R. Cimino, C. Vaccarezza, EUROTEV-REPORT-2005-013

ELECTRON CLOUD MODELING RESULTS FOR TIME-RESOLVED SHIELDED PICKUP MEASUREMENTS AT CesrTA

J.A. Crittenden, Y. Li, X. Liu, M.A. Palmer, J.P. Sikora
CLASSE*, Cornell University, Ithaca, NY 14850, USA

S. Calatroni, G. Rumolo
CERN, Geneva, Switzerland

N. Omcikus
University of California at Los Angeles, Los Angeles, CA 90095-1597

Abstract

The Cornell Electron Storage Ring Test Accelerator (CesrTA) program [1] includes investigations into electron cloud buildup, applying various mitigation techniques in custom vacuum chambers. Among these are two 1.1-m-long sections located symmetrically in the east and west arc regions. These chambers are equipped with pickup detectors shielded against the direct beam-induced signal. They detect cloud electrons migrating through an 18-mm-diameter pattern of holes in the top of the chamber. A digitizing oscilloscope is used to record the signals, providing time-resolved information on cloud development. Carbon-coated, TiN-coated and uncoated aluminum chambers have been tested. Electron and positron beams of 2.1, 4.0 and 5.3 GeV with a variety of bunch populations and spacings in steps of 4 and 14 ns have been used. Here we report on results from the ECLOUD modeling code which highlight the sensitivity of these measurements to model parameters such as the photoelectron azimuthal and energy distributions at production, and the secondary yield parameters including the true secondary, rediffused, and elastic yield values. In particular, witness bunch studies exhibit high sensitivity to the elastic yield by providing information on cloud decay times.

INTRODUCTION

The CesrTA program includes the installation of custom vacuum chambers with retarding-field-analyzer (RFA) ports and shielded pick-up detectors of the type shown in Fig. 1. The RFA port is shown on the left end, and two circular shielded pickup modules are shown on the right end of the chamber, each with two ports. In one case the two ports are placed longitudinally, with only one of the two being read out, and in the other case the two ports are arranged transversely, providing laterally segmented sensitivity to the cloud electrons. Thus the centers of buttons are 0, and ± 14 mm from the horizontal center of the chamber. The ports consist of 169 30-mil-diameter holes arranged in concentric circles up to a maximum diameter of 18 mm. The top of the vacuum chamber has been machined such that the holes point vertically. The transparency factor for vertical trajectories is 27%. The approximate 3:1 depth-to-diameter factor is chosen to effectively shield the detectors from the signal induced directly by the beam.

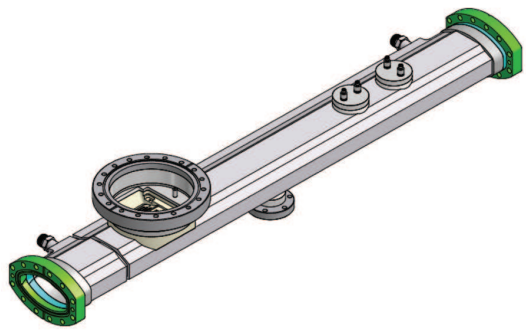

Figure 1: Custom vacuum chamber with RFA port and shielded pickup detectors.

Time-resolved measurements provide time structure information on cloud development, in contrast to the time-integrated RFA measurements [2]. However, they have relatively primitive energy selection, since they have no retarding grid and position segmentation is more coarse, the charge-collecting electrodes being of diameter 18 mm. Data has been recorded with biases of 0 and ± 50V relative to the vacuum chamber. The studies described here address exclusively the data a with bias $+50$ V in order to avoid contributions to the signal from secondary electrons escaping the pickup. Such secondaries generally carry kinetic energy insufficient to escape a 50 V bias. This choice of bias obviously provides sensitivity to cloud electrons which enter the port holes with low kinetic energy. The front-end readout electronics comprise operational amplifiers with $50\ \Omega$ input impedance and a gain factor of 100. Digitized oscilloscope traces are recorded with 0.1 ns step size.

USE OF A WEAK SOLENOIDAL MAGNETIC FIELD

One type of measurement which has been obtained with the shielded-pickup detectors is illustrated schematically

* Work supported by the U.S. National Science Foundation, the U.S. Department of Energy, and the Japan/USA Cooperation Program

in Fig. 2. The vacuum chambers have been outfitted with windings to approximate a solenoidal field in the region of the cloud with magnitude up to 40 G. Since signal contributions require nearly vertical arrival angles, the centers of the corresponding circular trajectories for any given magnetic field value lie in the horizontal plane of the ports. The three trajectories originating at the primary impact point of the synchrotron radiation and leading to the center of each electrode thus select different regions of photoelectron energy and production angle, as shown. Experiments to date

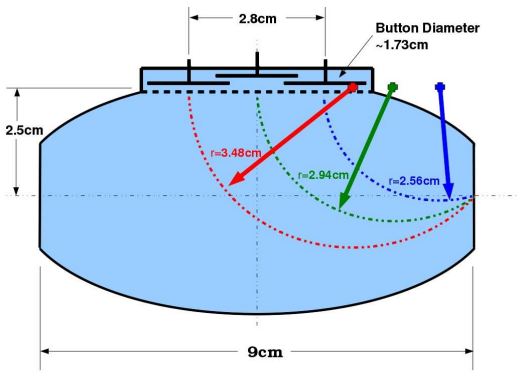

Figure 2: Vacuum chamber wall cross section with circular trajectories of photoelectrons contributing to the pickup signals.

have shown that the 40 G field magnitude range suffices to cover the full energy range of the photoelectrons produced by a 2.1 GeV beam ($E_{critical} \approx 300$ eV) (i.e. no pickup signal is observed for field values of 0 and 40 G), in contrast to the case of a 5.3 GeV beam ($E_{critical} \approx 5$ keV), where photoelectron energies suffice to produce an observable signal even at 40 G. Furthermore, reversal of the solenoidal field provides information on the production of photoelectrons at a point on the vacuum chamber opposite the primary source point and thus relevant to the reflective characteristics of the vacuum chamber wall. This paper does not discuss in detail the measurements obtained with solenoidal field, which remain under analysis, but instead concentrates on an alternative method to measure photoelectron energy.

SENSITIVITY TO PHOTOELECTRON ENERGY DISTRIBUTION

The upper row of Fig. 3 shows examples of shielded pickup signals for two bunches of 5.3 GeV positrons (left) and electrons (right) separated by 14 ns. The population of the first bunch is 1.3E11e while that of the trailing bunch varies up to a similar value. The trailing bunch accelerates cloud particles into the detector, producing the second signal. The arrival time and structure of the earlier signal corresponds to photoelectrons produced at the time of bunch passage on the lower chamber wall. The kick from the positron bunch accelerates such photoelectrons toward the detector, whereas in the case of an electron beam the signal electrons must carry sufficient kinetic energy to overcome the repulsion of the beam bunch.

The lower row of Fig. 3 shows an initial attempt to model the case of two 1.3E11e bunches using the electron cloud simulation code ECLOUD [3]. The calculation of cloud kinematics including space charge forces and beam kicks determines arrival times, momentum vectors and charges of the macroparticles reaching the upper surface of the chamber at the positions of the pickups. This early attempt at simulating the observed signals included a rather crude model of the port hole acceptance, leading to poor approximation of the magnitude of the signal, but it was sufficient to diagnose the obviously discrepancy with the observed signals. The positron case shows moderate time structure differences, but the modeling of the electron beam kick exhibited a dramatic discrepancy. The arrival times of the observed signals indicate photoelectron production on the lower wall of the chamber, which is effected in the simulation via a reflectivity parameter distributing 20% of the photoelectrons uniformly in azimuth. The prompt signal from each electron bunch corresponds to photoelectrons produced on the upper wall repelled into the detector during the bunch passage. The photoelectrons produced on the lower wall in the ECLOUD simulation are similarly reabsorbed, and these are the ones needed to produce the observed signal! In other words, the measurement shows that photoelectrons of sufficient energy to overcome the repulsion of the beam bunch must be present. The photoelectron energy distribution in this original default model is common to many successful simulations of a wide variety of experimental observations [3, 4, 5], namely a Gaussian with average and rms values of 5 eV limited by truncation to positive values. Figure 4 compares such a distribution (blue) to a power-law modification adequately reproducing the observed signal shapes (red). Low-energy and high-energy regions are shown normalized on logarithmic scales to illustrate the dramatically higher energies needed.

This new high-energy distribution was determined by matching single-bunch models to the measured signals for various electron bunch currents as shown in Fig. 5. The measured signals for a single bunch of 5.3 GeV electrons are shown in the left column. A bunch current of 1 mA corresponds to a bunch population of 1.6E10e. The model successfully reproduces the increase of signal magnitude with bunch current. While some time structure discrepancies remain, the improvement relative to the results shown in Fig. 3 is remarkable. The overall normalization of the modeled signals is proportional to the assumed reflectivity value, which in this case was 20%. In addition, the model also exhibits a prompt signal arising from photoelectrons produced nearby the detector repelled into it during the passage of the bunch, increasing with bunch current similarly to the observed signals.

Extensive work continues on refining the energy distributions, studying the consequences on earlier successful modeling of various physical phenomena, and exploiting the information provided by data taken in solenoidal mag-

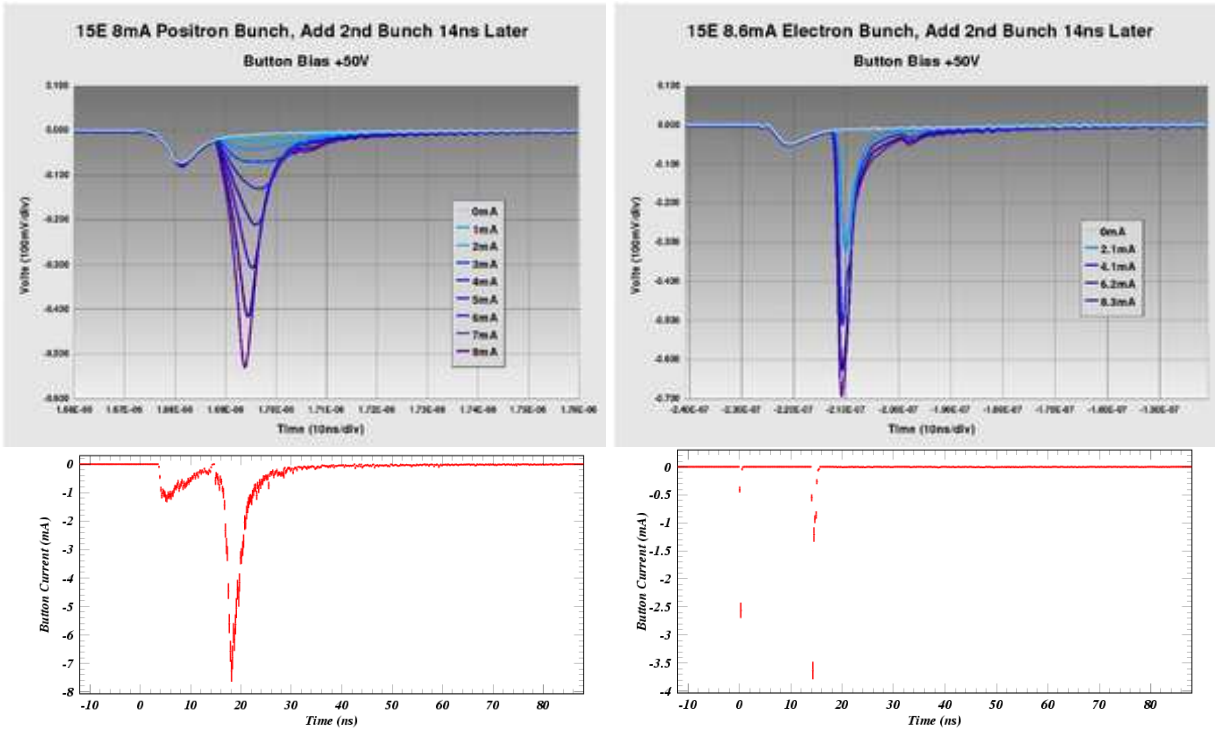

Figure 3: Upper row: shielded pickup signals produced by two 5.3 GeV positron (left) and electron (right) bunches separated by 14 ns. The leading bunch population is 1.3E11e . The population of the second bunch varies up to a similar value. Lower row: initial ECLOUD model results exhibiting discrepancies with the measured signals which are quite dramatic in the case of the electron beam.

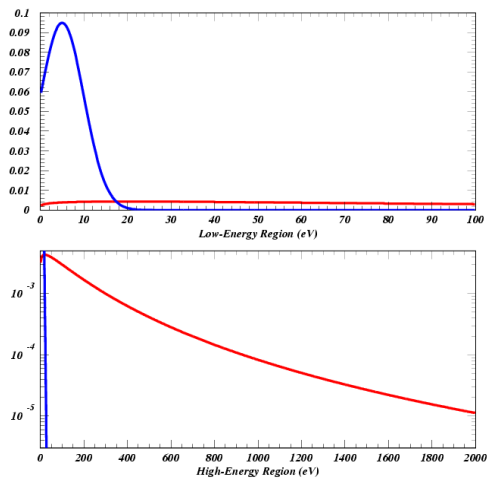

Figure 4: Low- and high-energy regions of the photoelectron energy distributions used to model the measured signals shown in Fig. 3. The original low-energy distribution shown in blue results in dramatic discrepancy with the signals observed in the case of an electron beam. The modified distribution shown in red provides good agreement with the observed signals.

netic fields.

This analysis presents an intriguing opportunity to relate the obtained photoelectron energy distribution to the incident synchrotron energy spectrum and thus derive an estimate of the energy dependence of the quantum efficiency. Since the source of the direct radiation at the primary point of incidence on the outside wall of the beampipe is well known, the critical energy is well defined. However, these signals do not arise from the direct radiation, but rather from a reflected portion of the spectrum. Detailed work on modeling reflected photon trajectories has been undertaken [6]. Preliminary results of this model [7] indicate that the energy dependence of the reflectivity results in an impact energy distribution for the reflected portion of the photon spectrum which is much lower than would be expected from the critical energy of the direct synchrotron radiation. It may be conjectured the high energies needed to explain the shielded pickup signals arise from an interaction of high-energy photons with the wall other than reflection.

Cloud Lifetime Studies Using Witness Bunches

While the awareness of the sensitivity of the shielded pickup measurements to the parameters of photoelectron production was largely motivated by inadequacies of the model discovered in its application to recent measurements, the original intended use of these time-resolved cloud measurements was to provide a quantitative estimate of the elastic yield parameter in the secondary electron yield model. A similar investigation was performed

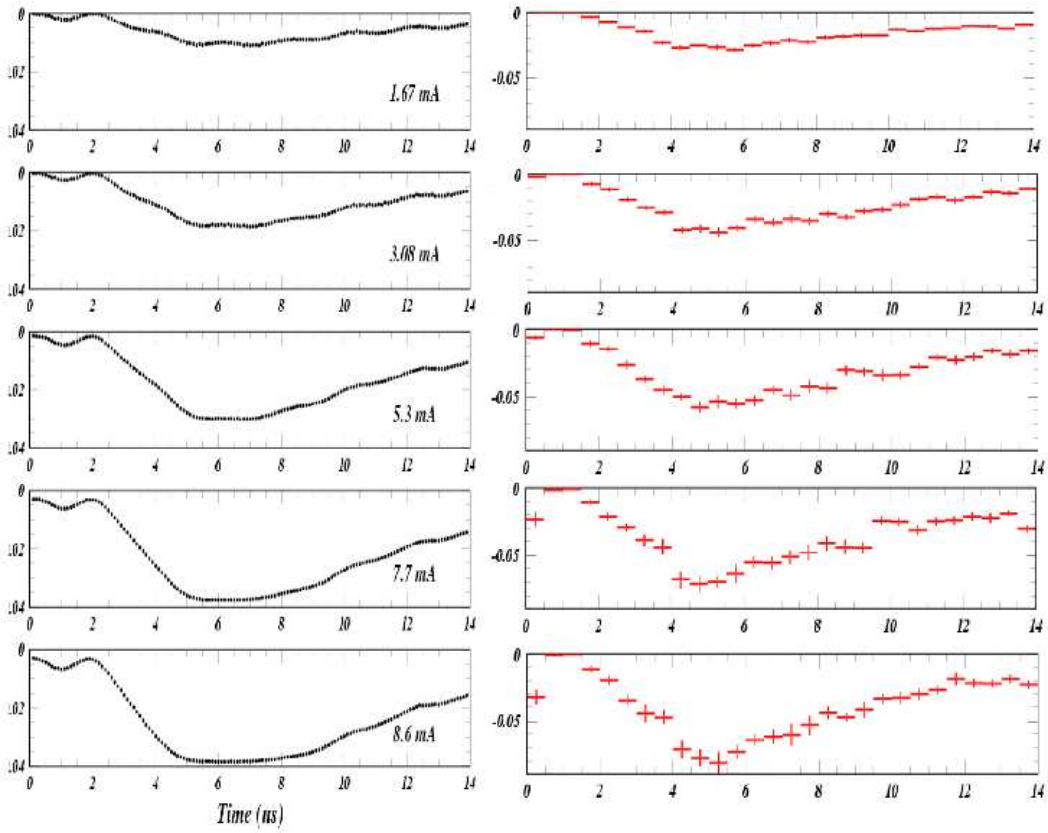

Figure 5: Comparison of measured single bunch signals for various electron bunch currents (left column) to the ECLOUD model (right column) after improving the modeled photoelectron energy distributions.

at RHIC [8]. The basic concept is that the mature cloud long after passage of any beam bunch is dominated by low-energy electrons which suffer predominantly elastic interactions with the vacuum chamber wall. The elastic yield parameter describes the ratio of outgoing to incoming macroparticle charge in probabilistic models [9], and carries a value typically 0.5-0.7, determining the decay time of the cloud density, typically around 100 ns. High-energy electrons of more than 100 eV, produced by synchrotron radiation, beam kicks, or the rediffused component of the secondary yield process, undergo primarily the so-called "true" secondary yield process, in which the produced secondary carries only a few electron volts of kinetic energy, resulting in the dominance of low-energy electrons late in the cloud development.

Figure 6 shows an ECLOUD secondary yield population curve typical of the shielded pickup signal simulations.The true secondary yield maximum at 400 eV ranges from a minimum of 0.9 to a maximum of 1.5 owing to the dependence on incident angle. At low energy the yield value is dominated by the elastic interactions with the chamber wall. This case exhibits an elastic yield parameter of 0.55.

The witness bunch experimental method consists of generating a cloud with a leading bunch, then accelerating cloud electrons into the shielded pickup detector with a trailing bunch at various delay times. The magnitude and time structure of the signal from the leading bunch is determined by the reflective properties of the vacuum chamber and by the energy-dependent quantum efficiency, as described in the preceding section. The signal induced by the witness bunch has a contribution similar to that of the leading bunch added to the contribution from the existing cloud kicked into the detector. The latter contribution is sensitive to the cloud density and the spatial and kinematic distributions of the cloud electrons. Figure 7 shows the results of six sets of simulations with various values for the elastic yield parameter δ_0. In each of the six plots, eleven two-bunch (5.3 GeV, 4.8E10e positrons each) pickup signals are superposed, whereby the delay of the witness bunch varies from 12 to 100 ns. The modeled signals are shown with the statistical error bars corresponding to the number of macroparticles contributing to the signal. The magnitudes of the modeled signals at large witness bunch delay clearly show the dependence on the elastic yield parameter δ_0 as it is varied from 0.05 to 0.75. The most consistent description of the measured signals is given by a value of $\delta_0 = 0.75$. This value can be compared to the value of $\delta_0 = 0.5$ used in the modeling of CesrTA coherent tune shift measurements as described in Refs. [4, 5], where the measurements had much less discriminating sensitivity to the elastic yield.

Figure 8 shows a similar study, but for a titanium-nitride-

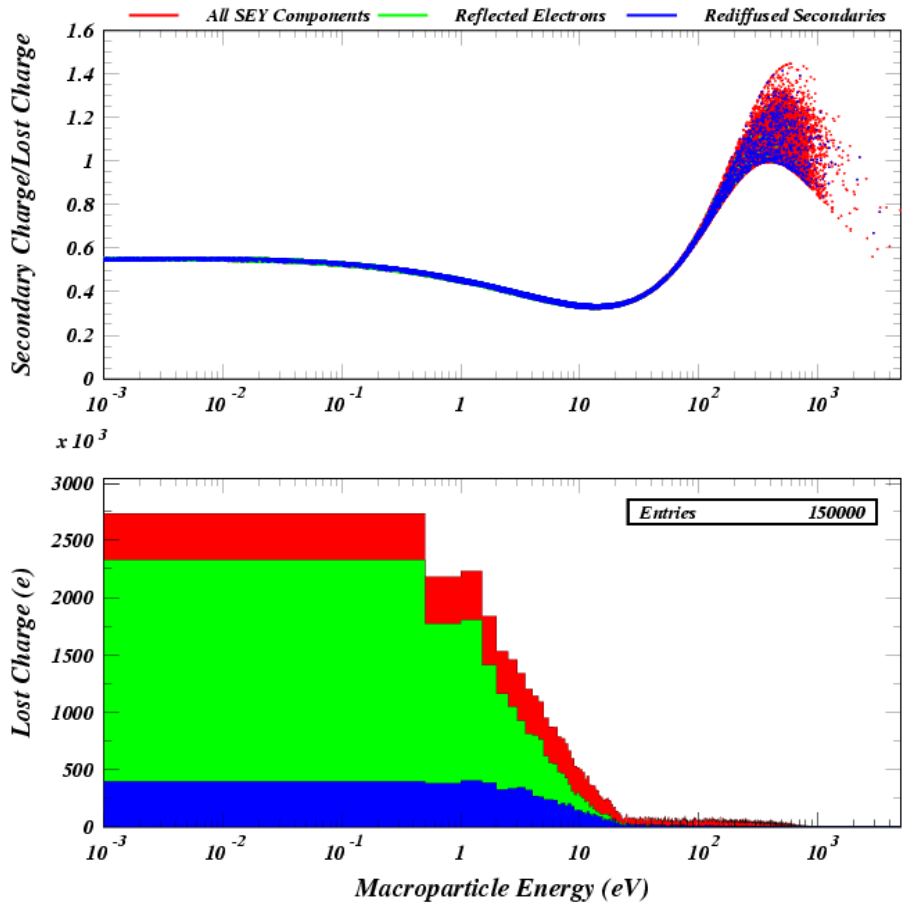

Figure 6: Secondary yield population curve typical of the ECLOUD model for the shielded pickup signals.The upper plot shows the yield value (ratio of secondary macroparticle charge to that of the incident charge) as a function of the incident kinetic energy. At low energy the yield value is dominated by the elastic interaction with the chamber wall. This case exhibits an elastic yield parameter of 0.55. The lower plot shows the incident energy distribution. The elastic and rediffused components are shown in green and blue, respectively. The sum of all three components, true, elastic and rediffused, is shown in red. Since the three colors are plotted on top of each other, the upper plot shows primarily blue at low energy, even though the elastic process dominates, as is seen in the lower plot.

coated aluminum chamber. For each of the six values assumed for the elastic yield, thirteen two-bunch (5.3 GeV, 8.0E10e positrons each) pickup signals are superposed, whereby the delay of the witness bunch is varied from 14 to 84 ns. The optimal value for the elastic yield is clearly less than the value determined for the uncoated aluminum chamber, with $\delta_0 = 0.05$ providing the best description of the measurements.

These comparisons show a number of intriguing discrepancies. The leading bunch signal shape exhibits the need for further tuning of the photoelectron energy distribution. The signal widths tend to be wider than observed. In addition, such a low value of 0.9 for the secondary yield of an uncoated aluminum surface cannot be easily understood, since the tune shifts measurements require an average value around the CESR ring of about 1.8. A wide variety of systematic studies have been undertaken since the ECLOUD'10 workshop, discovering sensitivity to many detailed characteristics of the cloud. For example, the signal widths for early witness signals depend strongly on the azimuthal production distribution of photoelectrons, as was observed by implementing in ECLOUD the distributions calculated by the photon-tracing reflectivity model for the CESR ring described in Ref. [6]. Nonetheless, the dramatic improvements in consistency obtained via such systematic studies have not changed the quantitative conclusions concerning the sensitivity to the value for the elastic yield. Generally one can say that the choice of peak true secondary yield value relative to the effective reflectivity value determines the ratio of the early witness bunch signal magnitudes to that from the leading bunch. However, for witness bunches late enough that the signal magnitude becomes comparable to that of the leading bunch, there is little sensitivity to the true secondary yield. Instead, those signal magnitudes are determined by the value assumed for the elastic yield.

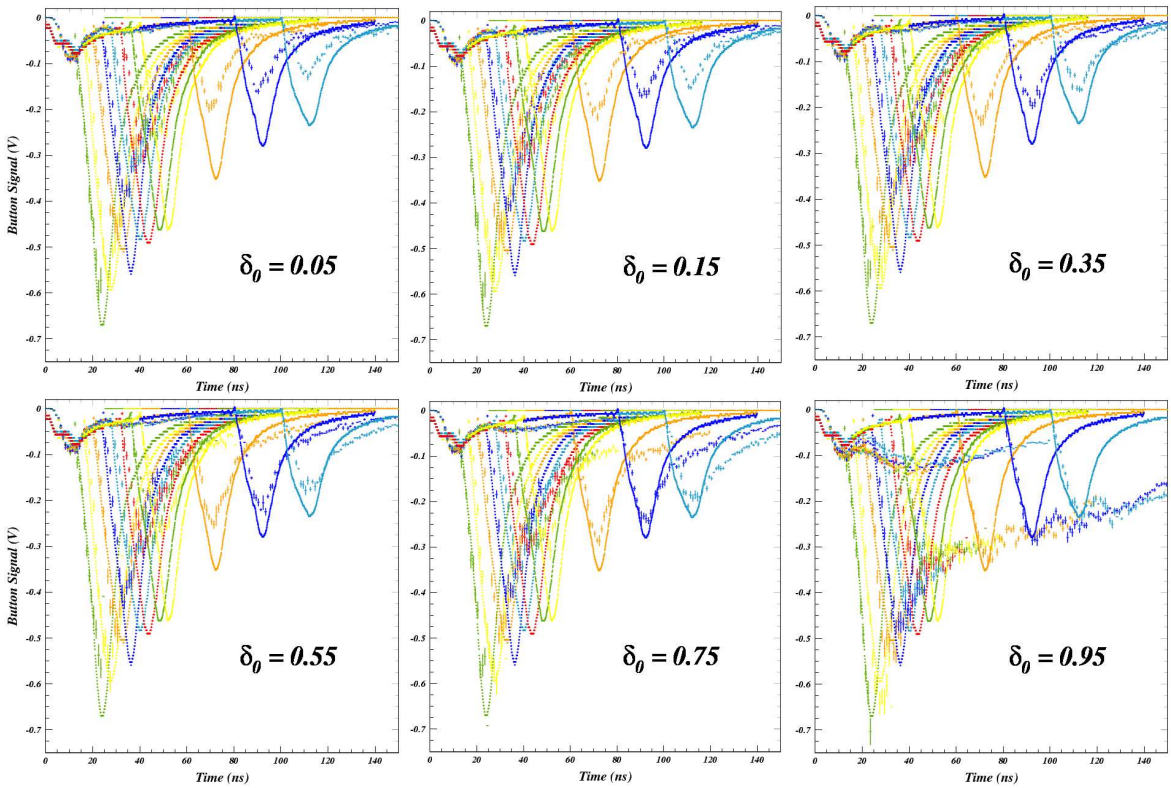

Figure 7: Witness bunch study with the uncoated aluminum chamber. Eleven two-bunch scope traces are superposed in each of the six plots, whereby the delay of the witness bunch ranges from 12 to 100 ns. The modeled signals are shown with the statistical error bars corresponding to the number of macroparticles contributing to the signal. The magnitudes of the modeled signals at large witness bunch delay clearly show the dependence on the elastic yield parameter δ_0 as it is varied from 0.05 to 0.75. The most consistent description of the measured signals is given by a value of $\delta_0 = 0.75$.

SUMMARY

The shielded pickup detectors installed in the CESR ring in 2010 have begun providing a wide variety of time-resolved measurements of electron-cloud-induced signals. Measurements with custom vacuum chambers incorporating cloud mitigation techniques such as carbon and titanium-nitride coatings have been obtained and compared to the case of an uncoated aluminum chamber. Weak solenoidal magnetic fields have been employed to study photoelectron production kinematics. A model for the shielded pickup acceptance has been developed in the context of the electron cloud simulation code ECLOUD. The shielded pickup data have proven remarkably sensitive to model parameters poorly constrained by any other experimental means, such as the azimuthal production distribution for photoelectrons and their energy distributions. The measurements with 5.3 GeV electron and positron beams indicate the need for a high-energy component previously absent in the photoelectron generation model. In addition, the design purpose of the shielded pickup detectors has been experimentally confirmed, as the cloud lifetime has been accurately measured using witness bunches at various delays. Sensitivity to the elastic yield parameter in the secondary yield model has been shown to be less than 0.05 and remarkably robust against variation of other model parameters. Data taken with an uncoated aluminum chamber provide a best estimate for the elastic yield of about 0.75. The cloud lifetime studies in a titanium-nitride-coated aluminum chamber exclude such a high value, yielding an optimal value of 0.05.

REFERENCES

[1] G.F. Dugan, M.A. Palmer, and D.L. Rubin, *ILC Damping Rings R&D at CesrTA*, ICFA Beam Dynamics Newsletter No. 50, eds. J. Urakawa and W. Chou (2009)

[2] J.R. Calvey *et al.*, *Methods for Quantitative Interpretation of Retarding Field Analyzer Data*, these proceedings

[3] F. Zimmermann and G. Rumolo, *Electron Cloud Effects in Accelerators*, ICFA Beam Dynamics Newsletter No. 33, eds. K. Ohmi and M.A. Furman (2004)

[4] J.A. Crittenden *et al.*, *Studies of the Effects of Electron Cloud Formation on Beam Dynamics at CesrTA*, proceedings of PAC09, 4-8 May 2009, Vancouver, British Columbia, Canada

[5] J.A. Crittenden *et al.*, *Progress in Studies of Electron-Cloud-Induced Optics Distortions at CesrTA*, proceedings of IPAC10, 2010, Kyoto, Japan

[6] G.F. Dugan, S. Malishuk and D.C. Sagan, *SYNRAD3D Pho-*

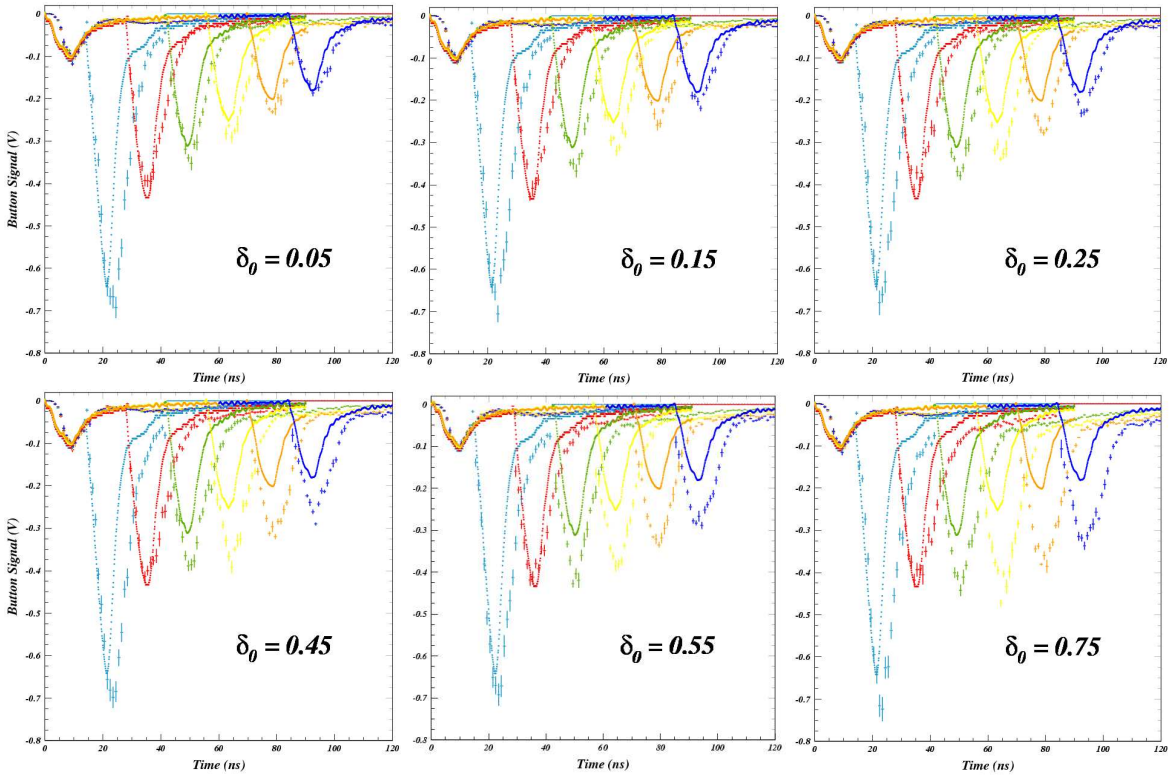

Figure 8: Witness bunch study with the titanium-nitride-coated aluminum chamber. The smooth curves are the digitized shield pickup signals. Six two-bunch scope traces are superposed in each of the six plots, whereby the delay of the witness bunch ranges from 14 to 84 ns. The magnitudes of the modeled signals at large witness bunch delay clearly show the dependence on the elastic yield parameter δ_0 as it is varied from 0.05 to 0.95. The most consistent description of the measured signals is given by a value of $\delta_0 = 0.05$.

ton Propagation and Scattering Simulation, these proceedings

[7] G.F. Dugan, private communication

[8] U. Iriso and G. Rumolo, *Benchmarking Electron Cloud Data With Computer Simulation Codes*, proceedings of EPAC 2006, Edinburgh, Scotland

[9] M.A. Furman and M.T.F. Pivi, *Probabilistic Model for the Simulation of Secondary Electron Emission*, Phys Rev ST-AB 5, 124404 (2002)

USING COHERENT TUNE SHIFTS TO EVALUATE ELECTRON CLOUD EFFECTS ON BEAM DYNAMICS AT CESRTA*

D.L.Kreinick#, J.A.Crittenden, G.Dugan, Z.Leong, M.A.Palmer, CLASSE, Ithaca, NY, USA,
R.L.Holtzapple, M.Randazzo, California Polytechnical State University, San Luis Obispo, CA, USA,
M.A.Furman, M.Venturini, LBNL, Berkeley, CA, USA

Abstract

One technique used at CesrTA for studying the effects of electron clouds on beam dynamics is to measure electron and positron bunch tunes under a wide variety of beam energies, bunch charge, and bunch train configurations. Comparing the observed tunes with the predictions of various simulation programs allows the evaluation of important parameters in the cloud formation models. These simulations will be used to predict the behavior of the electron cloud in damping rings for future linear colliders.

THE MEASUREMENTS

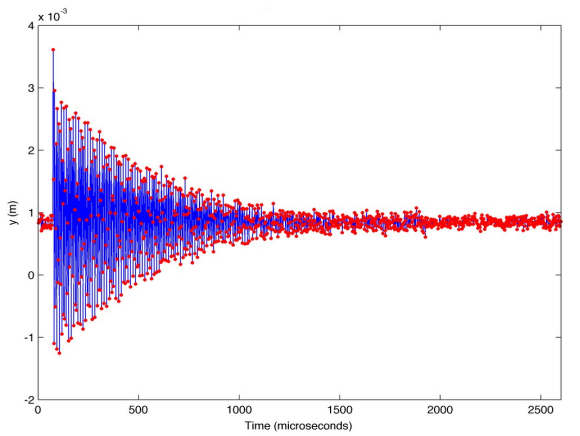

Figure 1: Sample beam position data.

Beams were set into oscillation by displacing them horizontally or vertically for one turn. We measure their turn-by-turn positions at up to six places around the ring for up to 4096 (but typically 1024) turns, and then Fourier transform. Tunes of the bunches of the cloud-inducing train and of "witness" bunches spaced 14 to 490 nsec after the train's passage allowed the cloud buildup and decay to be followed. Figure 1 shows the vertical displacement vs. time taken at one of the six beam position monitors used for this measurement. The 1024 red dots represent the y displacement of bunch 1 on successive turns around the CESR ring. A measurement involves six beam position monitors times 45 bunches. The tune shifts we use are the tunes of subsequent bunches minus the tune of the first bunch. We are tacitly assuming that the cloud dissipates in the 2.5 μsec it takes for the first bunch to go around the ring.

DETERMINING PARAMETERS

Initial parameters for driving the POSINST[1] simulations were determined by trial and error on measurements made at 1.9 GeV with $1.2\text{x}10^{10}$ positrons per bunch. In simulating the ring-averaged tune shifts, we ignored all ring elements except the drift regions and the dipoles, and used the calculated number of synchrorotron-radiated photons weighted by beta values[2]. The parameters we varied and their initial values were

· Total SEY yield (2.0)

· Energy at which the SEY is maximal (310 eV)

· Elastic SEY peak (0.5)

· Quantum efficiency of photoelectron production (0.12)

· Fraction of photons reflected (0.15)

· Yield of rediffused electrons (0.19)

54 data runs with electron and positron beams at 1.9, 2.1, 4.0, and 5.3 GeV energy, in trains of 3 to 45 bunches, with bunch populations of 0.32 to $2.60\text{x}10^{10}$ were simulated and matched to the data. All six parameters were varied ~±10% individually and in selected pairs. As an example, shown in figure 2 are data (in black) for a 21-bunch train of $0.8\text{x}10^{10}$ positrons per bunch at 2.1 GeV followed by 12 witness bunches. Three different POSINST simulations (in color) with total secondary emission yields of 1.8 , 2.0 (nominal), and 2.2 were run.

The program did not lead to a significantly improved parameter set because 1) the original set did surprisingly well describing all data and 2) it is hard to find an optimum in a 6-dimensional space when the parameters are highly correlated and the error bars on the data are not reliably determined.

*Work supported by the US National Science Foundation PHY-0734867 and the US Department of Energy DE-FC02-08ER41538.
dlk8@cornell.edu

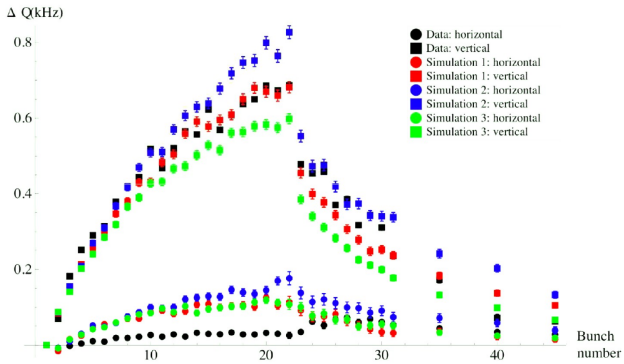

Figure 2: An example of fits to data achieved with various parameters. Black dots are data, colored are simulations.

POSINST AND ECLOUD

Two independent simulation codes POSINST[1] and ECLOUD[3] were used to match the data. It was found that the secondary emission model in ECLOUD was too simple, not accounting for the "rediffused" component. Once the more complex model was added to ECLOUD, the two models generally agreed with one another and with the data. The plots in figure 3 show horizontal and vertical tune shifts vs. time for 0.64×10^{10} (top) and 1.28×10^{10} bunch occupancy.

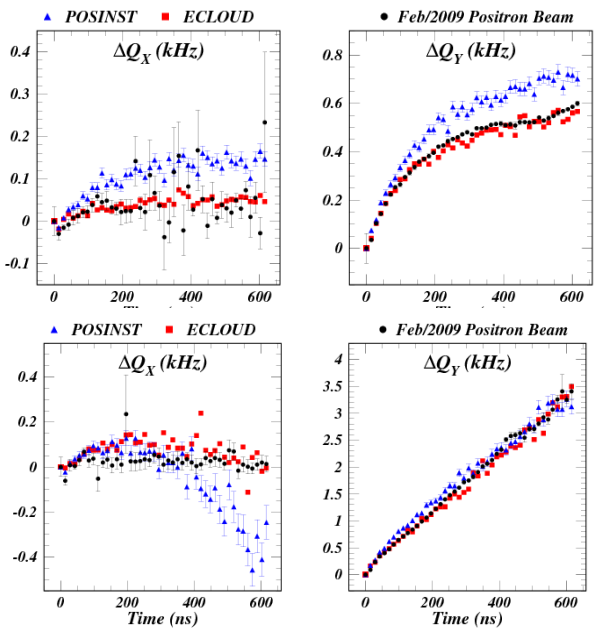

Figure 3: Horizontal (left) and vertical (right) tune shifts vs. time for 0.64×10^{10} (top) and 1.28×10^{10} (bottom) positron beam occupancy.

Data were taken with 45 bunches of 2.1 GeV positrons and bunch spacing 14 ns. Although the bunch populations differ only by a factor of two in the upper and lower plots, the vertical tune shifts differ by a factor of five. The simulations reproduce this behavior and explain why the vertical tune shifts in the upper right portion of figure 3 look different from the lower right. At lower bunch occupancy, the field-free regions dominate the tune shift, and their effects saturate after about bunch 20. At the higher current, the dipole region dominates and its tune shifts continue to grow linearly with time. (Horizontal tune shifts are a different story; see SPONTANEOUS OSCILLATIONS, below.)

SOLENOIDS IN THE DRIFT REGIONS

Attempts have been made to separate the tune effects in the dipoles as opposed to the drift regions by introducing a 40-Gauss solenoidal field in the drift regions. By keeping photoelectrons from hitting the walls, the effects of secondary emission should be neutralized in the drift regions. In the plots of figure 4, the green and blue dots represent data taken with solenoids off and on, respectively. Data are shown for 2.1 GeV positrons (top left) and electrons (bottom left) and 5.3 GeV positrons (top right) and electrons (bottom right). The solid curve is the POSINST simulation including both dipoles and drifts, and the dotted curve includes only dipoles.

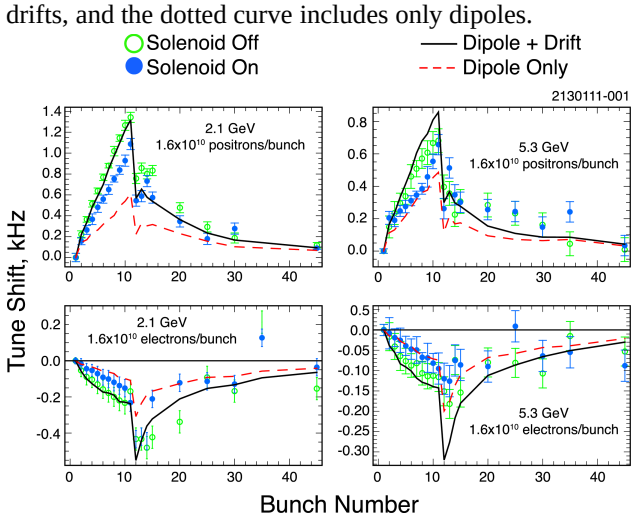

Figure 4: Positron (top) and electron (bottom) vertical tune shifts vs. bunch for 2.1 (left) and 5.3 GeV (right) beams.

SPONTANEOUS OSCILLATIONS

As can be seen in the plots of figures 2 and 3, horizontal tune shifts are suppressed in the usual pinging technique[2]. This technique gives all the bunches in the train the same kick, suppressing the tune shifts in the horizontal plane due to the strong correlation between the horizontal location of the cloud centroid and the beam centroid in the dipoles. Unpinged (self-excited) data allow the observation of sizeable horizontal tune shifts.

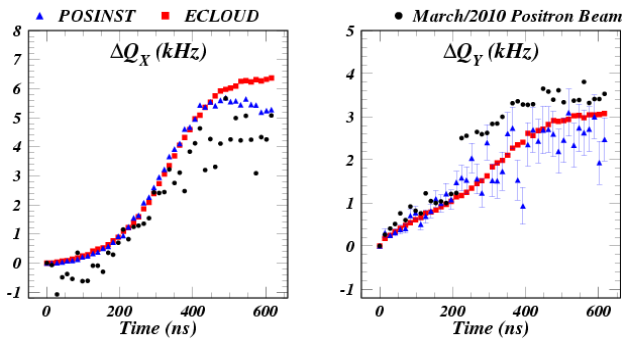

Figure 5: Horizontal (left) and Vertical (right) tune shifts for spontaneous oscillations. Unlike the pinged measurements of figures 2 and 3, the horizontal tune shifts are not suppressed.

The oscillations in the unpinged bunches are less reliably excited, so the data are less stable. Nevertheless usable tune shifts can be observed. The data shown in figure 5 were taken with 45-bunch trains of 2.1 GeV positrons with a bunch occupancy of 2.1×10^{10} and a bunch spacing of 14 ns. Note that the tune shifts saturate after about 400 ns (~25 train bunches), a behavior that is modeled by the simulations.

FURTHER MEASUREMENTS

To help parameter determination, we try to create conditions where one of the parameters may dominate. For example, the reflectivity is particularly important in the dipoles, since only reflected photons can produce photoelectrons above the beamline, where they can be pinned on the magnetic field lines and multipact on the top and bottom of the vacuum pipe. Figure 6 shows six of the most recent measurements and the default POSINST simulations. Only vertical tune shifts are shown. In each case a train of 10 bunches is followed by witness bunches. Data (black) and simulation (red) are shown for 2.1 GeV positron and electron beams (left top and bottom), 5.3 GeV positrons and electrons (middle top and bottom), and 4.0 GeV positrons beams at higher bunch occupation than we have formerly been able to achieve. The nominal POSINST simulations generally reproduce this wide range of data well. At the highest bunch occupancy (3.2×10^{10} at the lower right), the qualitative behavior is simulated, but the quantitative discrepancy represents an opportunity to further refine the POSINST input parameters.

PLANNED IMPROVEMENTS

SYNRAD3D[5], a new synchrotron radiation modeling code, should allow for improvement of the estimates of photon fluxes in the drift and dipole regions. It also provides a much better description of the magnitude and azimuthal distribution of reflected photons.

More careful estimation of the errors in the incoming data should provide more stability for the goodness-of-fit comparisons used to optimize parameters.

Parameter space still remains to be explored in some of the newer data, for example the 4.0 GeV high-bunch-occupancy positron data shown in figure 6. Simulations thus far have mostly concentrated on data with bunch spacings of 14 ns. There are existing 4-ns data that can be modeled.

Recently, instrumentation to excite bunches individually has been deployed in order to further stress the models[6].

REFERENCES

[1] M. Furman and G. Lambertson, "The electron-cloud instability in the arcs of the PEP-II positron ring," http://repositories.cdlib.org/lbnl/LBNL-41123.
M. A. Furman and M. T. F. Pivi, Probabilistic Model for the Simulation of Secondary Electron Emission, Phys. Rev. ST-AB 5, 124404 (2002).

[2] G. F. Dugan, M. A. Palmer, and D. L. Rubin, ILC Damping Rings R&D at CesrTA, ICFA Beam Dynamics Newsletter No. 50, eds. J. Urakawa and W. Chou (2009).
J. A. Crittenden, *et al.*, Studies of the Effects of Electron Cloud Formation on Beam Dynamics at CesrTA, proceedings of PAC09, 4-8 May 2009, Vancouver, British Columbia, Canada.

[3] F. Zimmermann and G. Rumulo, Electron Cloud Effects in Accelerators, ICFA Beam Dynamics Newsletter No. 33, eds. K. Ohme and M.A. Furman (2004).

[4] J. A. Crittenden, *et al.*, Progress in Studies of Electron-Cloud-Induced Optics Distortions at CesrTA, proceedings of IPAC10, 2010, Kyoto, Japan.

[5] G. Dugan, S. Milashuk, D. Sagan, "Synrad3D Photon propagation and scattering simulation", contribution to this workshop.

[6] M. Billing, *et al.*, contribution to this workshop.

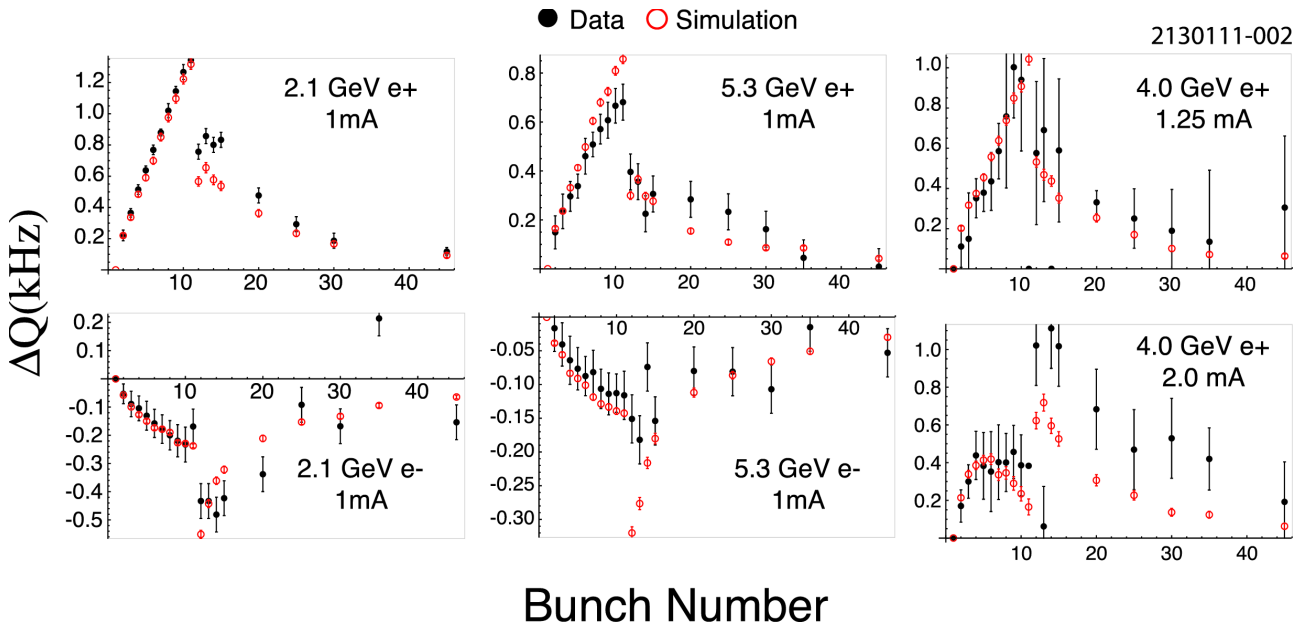

Figure 6: Comparison of measured vertical tune shifts with simulations at a variety of beam energies, beam particles, and beam currents.

CesrTA LOW EMITTANCE TUNING*

D. Rubin, D. Sagan, J.P. Shanks, Y. Yanay, Cornell University, Ithaca, NY 14850, USA

Abstract

Low emittance tuning and characterization of electron cloud phenomena are central to the CesrTA R&D program. A small vertical emittance is required in order to be sensitive to the emittance-diluting effects of the electron cloud. We have developed techniques to systematically and efficiently compensate optical and alignment errors that are the sources of vertical emittance. Beam–based measurements are utilized for centering Beam Position Monitors (BPMs) with respect to adjacent quadrupoles, determining relative gains of BPM button electrodes, and measuring BPM tilts. These calibrations allow for precision measurement of transverse coupling and vertical dispersion. Achieving low emittance also requires the tune plane be relatively clear of nonlinear coupling resonances associated with sextupoles. We report on tests of a sextupole distribution designed to minimize resonance-driving terms. We also report on beam-based measurements of sextupole strengths.

BEAM BASED QUADRUPOLE CENTER MEASUREMENT

The Beam Position Monitors (BPMs) are referenced with respect to the center of their adjacent quadrupole magnets. Magnet survey and repositioning is an ongoing process, therefore it is essential that beam-based calibration of BPM offsets require a minimum of beam time. The new CesrTA BPM system[1] allows for simultaneous measurement of the orbit and betatron phase at each BPM. With this measurement technique, orbit and phase data taken at two quadrupole settings can be combined quickly to accurately determine the quadrupole center with respect to BPM center. This reduces the number of orbit difference measurements that need to be taken, and therefore reduces the time required to center BPMs.

The procedure for centering quadrupoles is illustrated in Figure 1-3.

1. Begin with a model of the lattice. Measure the orbit and betatron phase and fit the model betatron phase advance to the measured phase advance by varying the strengths of the model quadrupoles as shown in Fig. 1. This will be referred to as the base fit.

2. Change the strength of the target quadrupole in the machine and remeasure phase and orbit. In the model, vary the strength of that quadrupole until the newly–measured and model phases agree as shown in Fig. 2.

3. Horizontal and vertical kicks are superimposed on the target quadrupole. Starting from the model fit to the second data set, vary these kicks such that the modeled orbit difference matches the measured difference as shown in Fig. 3.

The orbit difference dx is

$$dx(s) = (\tilde{x} - x_0(\bar{s}))dK_1 L \frac{\sqrt{\beta(s)\beta(\bar{s})}}{2\sin\pi\nu}\cos(|\phi(s) - \phi(\bar{s})| - \pi\nu)$$

and the quadrupole center is given by

$$\tilde{x} = \frac{\text{kick}}{L\,dK_1} + x_0(\bar{s})$$

The ability to simultaneously measure the orbit and betatron phase provides a fast and accurate method for measuring quadrupole centers with respect to BPMs. This technique avoids problems with hysteresis and quadrupole calibration inaccuracies. Presently, a single iteration of this procedure takes roughly 20 seconds.

BEAM-BASED MEASUREMENT OF BPM ELECTRODE GAINS AND TILTS

Non-uniformity in the response of BPM electrodes and physical misalignment or tilts of the BPMs will introduce a systematic error into measurements of coupling and vertical dispersion. We can determine the relative gain of the four electrode BPMs by sampling the response of the electrodes to a beam that is scanned over the cross-section of the BPM[2]. The sampling is accomplished by resonantly exciting the horizontal and vertical normal modes of the beam and collecting turn-by-turn position measurements. The best-fit gains based on three distinct sets of turn-by-turn data are combined and shown in Figure 4.

The distribution of the fitted gains is shown in Figure 5

Determination of BPM tilts

The transverse coupling is measured by resonant excitation of the horizontal and vertical normal modes. Measurement of the relative phase and amplitude of the motion at the normal mode frequencies at each of the BPMs gives the $\bar{C}_{11}, \bar{C}_{12}$, and $\bar{C}_{22}$ elements of the coupling matrix. The measured coupling after correcting $\bar{C}_{12}$ but before gain correction is shown in Figure 6. Coupling after gain correction is shown in Figure 7. $\bar{C}_{12}$ measures the out-of-phase component of the coupling and is therefore very nearly independent of BPM tilts. $\bar{C}_{11}$ and $\bar{C}_{22}$ measure the in-phase components. If $\bar{C}_{12}$ is small, then $\bar{C}_{22}$ is a measure of the BPM tilt. We may therefore fit the gain-corrected coupling data to determine BPM tilts. The fitted tilts are shown in Figure 8.

* Work supported by the National Science Foundation and by the US Department of Energy under contract numbers PHY-0734867 and DE-FC02-08ER41538.

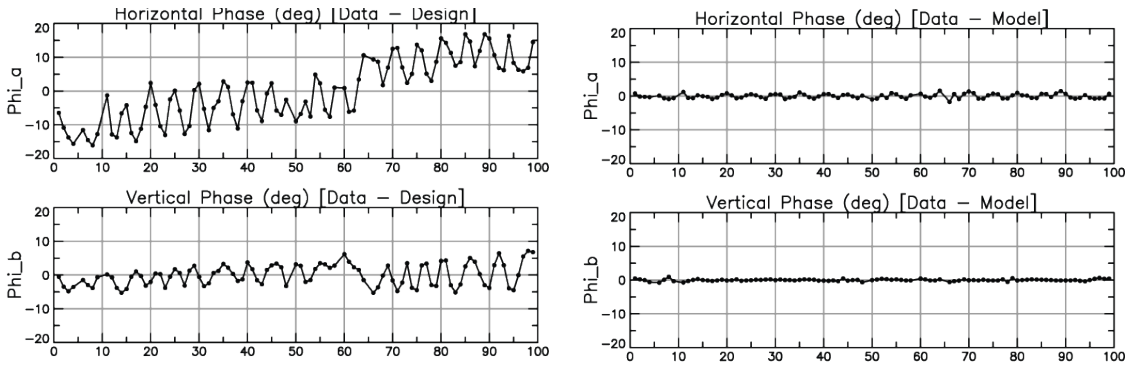

Figure 1: Vary the strengths of all quadrupoles in the lattice model until the model betatron phase matches the measured phase for the nominal K_1 of the quadrupole being calibrated. This is referred to as the "base fit". Left: Difference between the measured horizontal and vertical betatron phase and the design values of the phase. Right: Difference between the measured and the fitted model values.

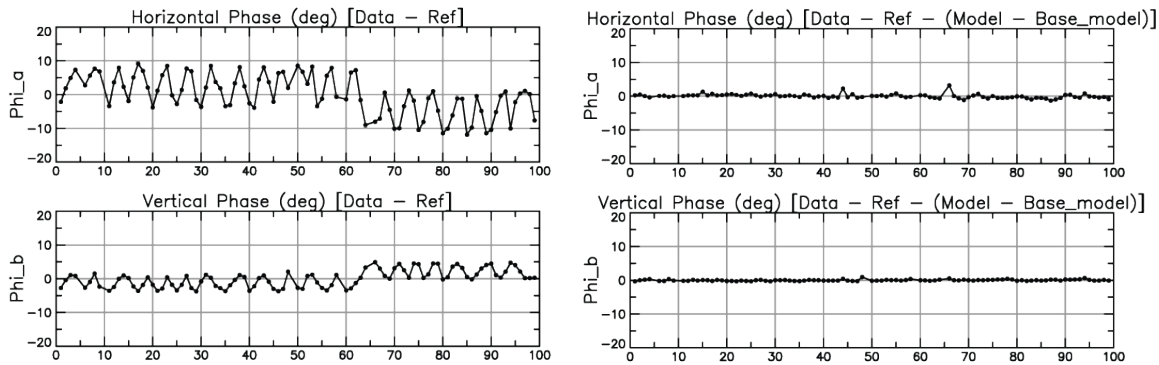

Figure 2: The strength of the target quadrupole is varied in the machine, and the phase and orbit are remeasured. The K_1 of the target quadrupole is varied in the model until the modeled phase most nearly matches the measured phase. Left: Difference in phase between the measurements. Right: Difference between measured and fitted differences.

Measurement of Vertical Dispersion

The effect of gain errors and BPM tilts on the measurement of vertical dispersion are subtle but discernible. We measure vertical dispersion by longitudinally exciting the beam at the synchrotron tune and measuring phase and amplitude of the resulting horizontal and vertical motion at each of the beam position monitors. Figure 9 shows an example of a vertical dispersion measurement without correction of BPM gain errors or BPM tilts. Transverse coupling and vertical dispersion have been jointly minimized through an optimization of skew quadrupoles and vertical steerings. The standard deviation of the residual is 20mm. (Recall that vertical dispersion is nominally zero) The same data is shown in Figure 10, now including correction of BPM button gains. The residual is reduced to 18mm. Finally, we include the fitted BPM tilts (from Figure 11), and the residual is further reduced to 17mm.

SEXTUPOLE RESONANCES AND TURN-BY-TURN DATA

To first order, the transverse motion of a freely oscillating beam is characterized by the tunes, Qx and Qy, and the linear Twiss parameters. Nonlinear components such as sextupole magnets introduce higher-order resonances at frequencies $Q_{nonlin} = nQ_x + mQ_y$. We can extract a phase and amplitude of the beam's response at the frequencies Q_{nonlin} from turn-by-turn data collected at all BPMs. An example of the Fourier spectrum from the horizontal position at one BPM is shown in Figure 12. The logarithmic plot of the Fourier spectrum of 4096 turns clearly shows the dominant response at Q_x, as well as the nonlinear response at higher harmonics.

The nonlinear effects of the sextupoles can be modeled using normal form analysis. The in-phase component of the horizontal response at $2Q_x$ is shown in Figure 13. The blue line denotes the measurement at each beam position monitor and the red line shows the model analytic calculation.

Figure 14 shows the difference in the in-phase compo-

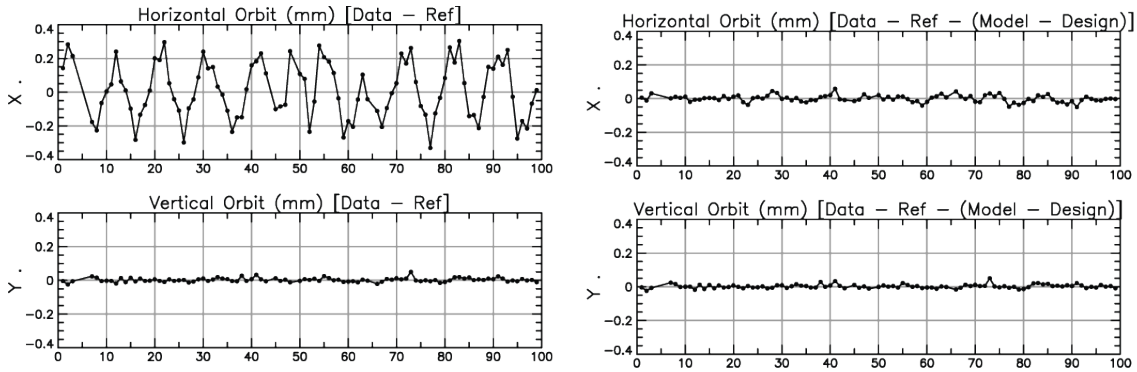

Figure 3: SHorizontal and vertical kicks are superimposed on the target quadrupole. Starting from the model fit to the second data set, vary these kicks such that the modeled orbit difference matches the measured difference. Left: Difference in measured orbits due to the change in the quadrupole strength. Right: Difference between measurement and best-fit orbit generated by the vertical kickers.

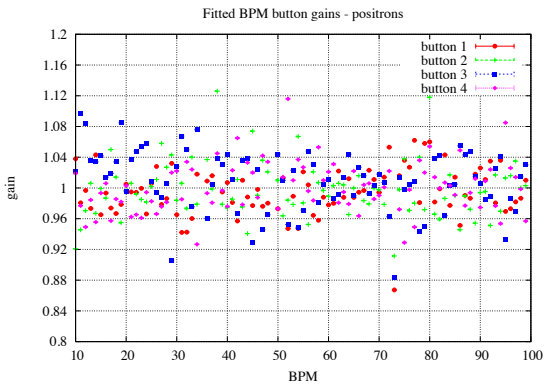

Figure 4: Fitted BPM electrode gains based on turn-by-turn data for a positron beam. The horizontal and vertical normal modes are resonantly excited and we collect data at each BPM electrode for 1024 turns. Three distinct sets of turn-by-turn data are independently fit and combined for this figure. The error bar (nearly invisible) represents the spread in fitted gains for the different data sets.

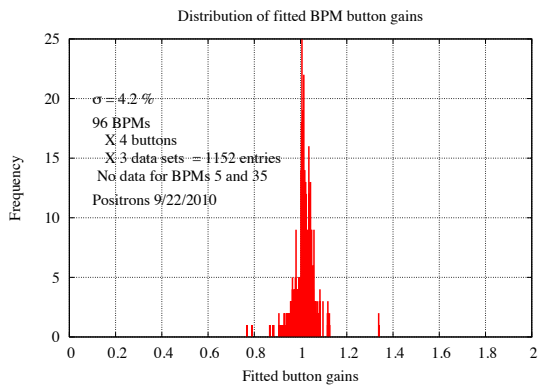

Figure 5: A histogram for the distribution of fitted gains shown in figure 4.

nent of the $2Q_x$ signal due to a known change in the field strength of a single sextupole. The measured difference is shown in blue and the calculated difference in red.

Initial studies of the sextupole driven resonances yield measurements in reasonable agreement the theoretical model. Our goal is to use the phase and amplitude of the motion characterized by linear combinations of horizontal and vertical tune (such as $2Q_x$) to measure and correct the field strengths of all sextupoles in the lattice.

TUNE SCANS OF VERTICAL BEAM SIZE

Our X-ray Beam Size Monitor (xBSM) is capable of measuring bunch-by-bunch, turn-by-turn beam sizes for a 14ns bunch spacing. To reduce the effects of turn by turn jitter, the profile is fitted on each turn to a Gaussian and the standard deviations are averaged over 100 turns. We utilize the xBSM to measure the effects of changing the optics in real-time. We have developed an automated method for scanning the tune plane and sampling the beam size at a specified interval. We use a simple pinhole optic for the xBSM. The pinhole width $16\mu m$ determines the resolution limit of the optic. A tune scan was performed on a lattice with sextupole distribution optimized[3] to reduce resonance-driving terms and increase dynamic aperture. We simulate the dependence of beam size on tune by tracking a particle for 1024 turns and determining its maximum vertical amplitude for a specified grid of horizontal and vertical tunes. The simulation includes quadrupole tilt and offset errors of $\sigma_{tilt} = 200\mu$-rad tilts and $\sigma_{off} = 125\mu$m, typical for the present alignment in CESR. Quadrupole strength errors comparable to those typical of the corrected optics are found to have negligible effect on the results.

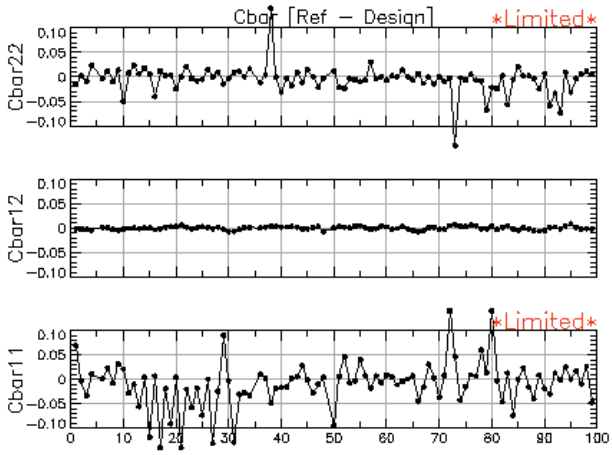

Figure 6: Coupling data after $\bar{C}_{12}$ correction but before BPM gain corrections.

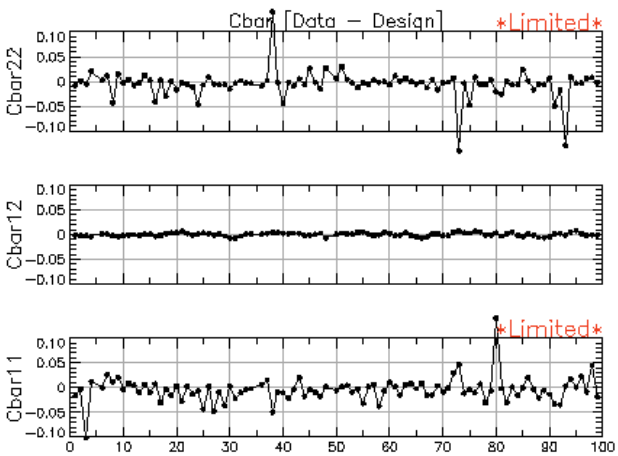

Figure 7: Coupling data after BPM gain corrections.

A tune scan has enabled us to identify the working point corresponding to minimum vertical beamsize (and thus emittance). The measured resonance structure is in reasonable agreement with simulation, indicating the sextupoles have had the expected effect.

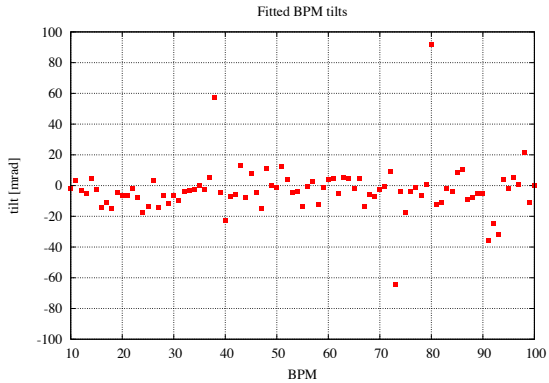

Figure 8: BPM tilts as determined from fitting the gain-corrected coupling data.

CONCLUSION

In order to identify and compensate sources of vertical emittance it is essential to calibrate and characterize the BPM system. We have reported on the status of a new technique for precisely measuring BPM-quadrupole offsets that is made possible by the CesrTA digital BPM electronics. We show that there is a significant variation in the electrode gains in each BPM, the effect of the gain errors on the coupling measurement, and have successfully compensated for this effect. We are able to extract BPM tilts from the gain-corrected coupling data, and the gain and tilt errors have a non-negligible effect on our measurement of vertical dispersion. Scans of vertical beam size vs betatron tune are used to identify the minimum beam size operating point. Finally, we describe a technique for extracting information about the sextupole optics from turn-by-turn data.

REFERENCES

[1] M.Palmer et al., “CESR Beam Position Monitor System Upgrade for CesrTA and CHESS Operations”, Proceedings of the 2010 International Particle Accelerator Conference, Kyoto, Japan.

[2] D.Rubin, M.Billing, R.Meller, M.Palmer, M.Rendina, N.Rider, D.Sagan, J.Shanks, and C.Strohman, Phys. Rev. ST Accel. Beams, 13, 092802 (2010).

[3] J. Bengtsson, ”The Sextupole Scheme for the Swiss Light Source (SLS): An Analytic Approach”, SLS Note 9/97

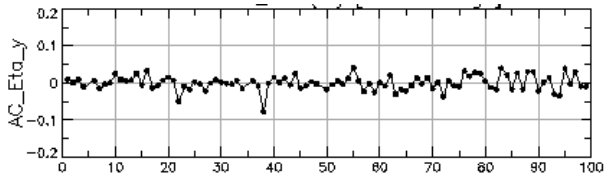

Figure 9: Measured vertical dispersion with no gain or tilt correction. Transverse coupling and vertical dispersion have been jointly minimized through an optimization of skew quadrupoles and vertical steerings. The residual dispersion is 20mm RMS.

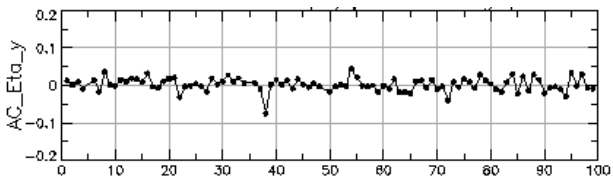

Figure 10: The same measured vertical dispersion, now with BPM button gain corrections. The residual is reduced to 18mm RMS.

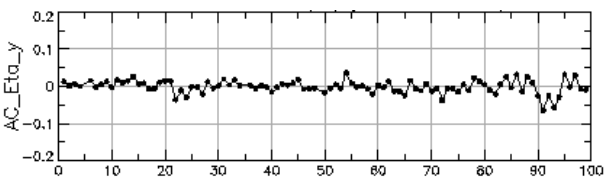

Figure 11: Again, the same measured vertical dispersion with both BPM button gain and BPM tilt corrections. The residual is now reduced to 17mm RMS.

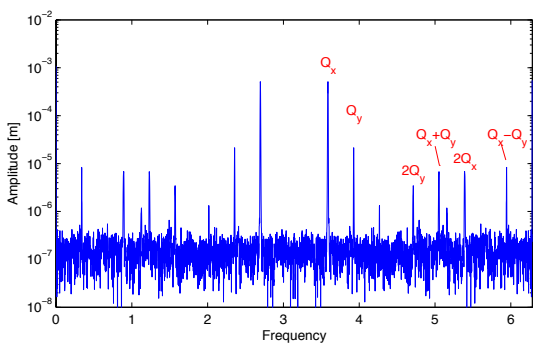

Figure 12: Fourier spectrum of 4096 turns of horizontal turn-by-turn BPM signal.

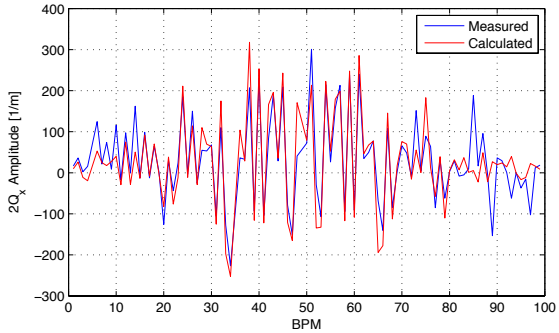

Figure 13: Amplitude of the in-phase response at $2Q_x$. The blue line is the measurement and the red the model.

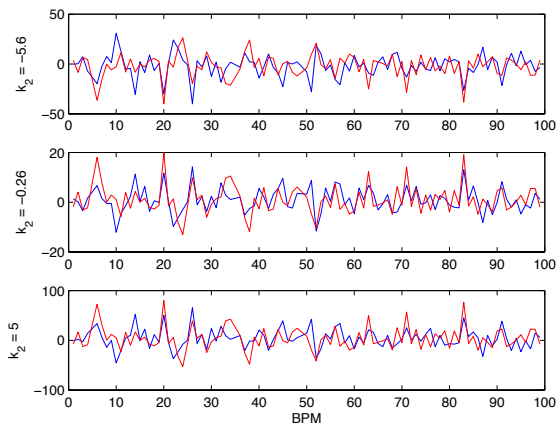

Figure 14: Difference in the in-phase component due to a known change in field strength of a single sextupole. Data is in blue and model in red.

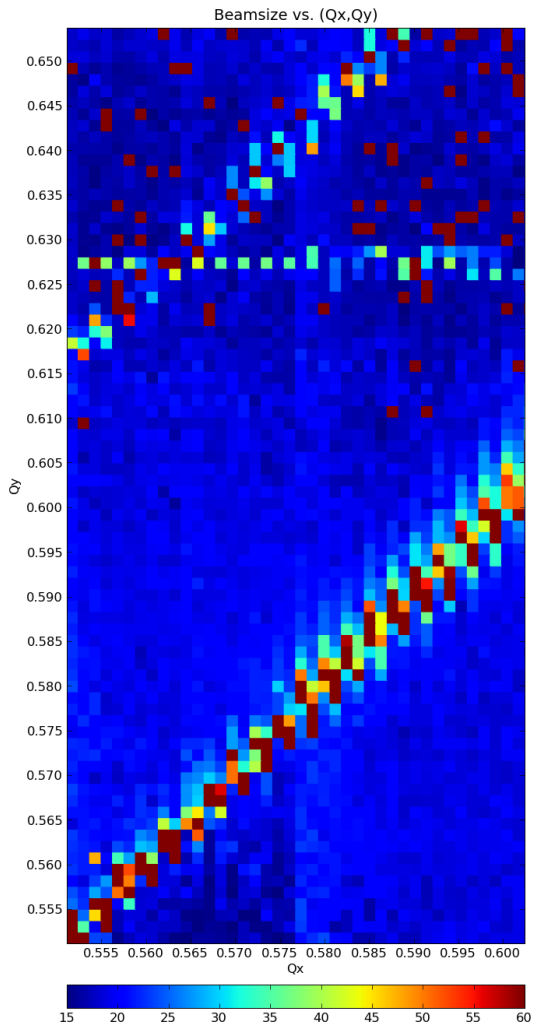

Figure 15: Measured vertical beam size versus horizontal and vertical tune.

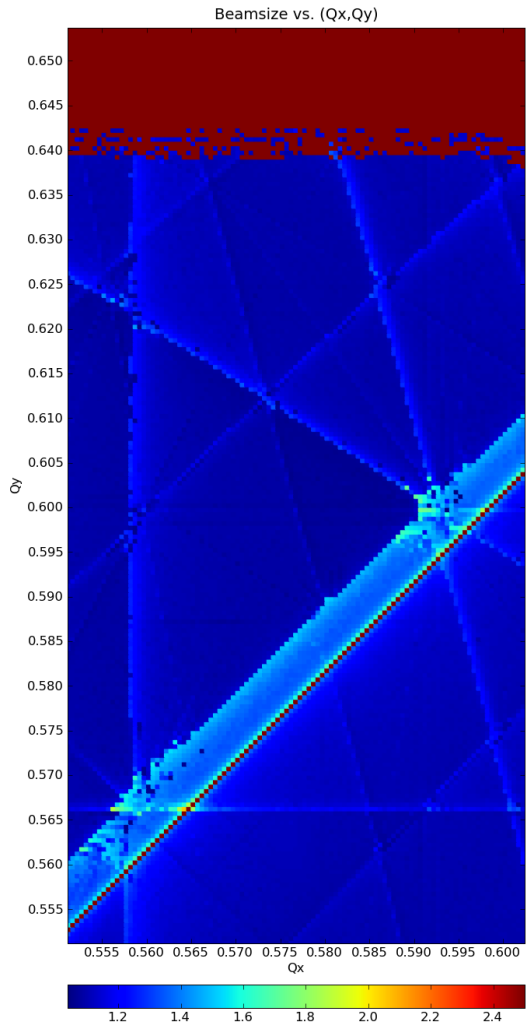

Figure 16: Simulated vertical beam size versus horizontal and vertical tune.

IN SITU SEY MEASUREMENTS AT CesrTA*

J. Kim, D. Asner,† J. Conway, S. Greenwald, Y. Li, V. Medjidzade, T. Moore, M. Palmer, C. Strohman, CLASSE, Cornell University, Ithaca, New York, USA

Abstract

Two in-situ secondary electron yield (SEY) measurement stations were developed at Wilson Laboratory and installed in the L3 section of the Cornell Electron Storage Ring (CESR) in order to track the evolution over time of the SEY peaks of technical surfaces in an accelerator environment, with exposure to direct and scattered synchrotron radiation (SR). Samples were positioned flush with the inner diameter of the beam pipe with one positioned horizontally in the radiation stripe, exposing the sample to direct and scattered radiation, and one at 45° beneath the radiation stripe, exposing the sample to only scattered radiation. Additionally, both samples are exposed to bombardment by electrons from the "electron cloud" in the stainless steel beam pipe. In this paper, we describe the in-situ SEY measurement systems and the initial results on bare aluminum (6061-T6) and TiN-coated aluminum samples.

INTRODUCTION

One mechanism that can limit the performance of a particle accelerator is associated with the formation of an electron cloud inside the vacuum chamber. The electron cloud can disrupt the beam, limit the current, or degrade the beam quality. Electron cloud issues are particularly important for rings, because the impact of small perturbations from the cloud can have a large effect on the stored beam over many turns around the ring. Consequently, control and mitigation of electron cloud effects are an important part of the design effort for the damping rings for the International Linear Collider (ILC) [1] and other future accelerators.

Emission of secondary electrons from the inside surface of the accelerator vacuum chamber is one source of electrons for the cloud. A key quantity is the secondary electron yield (SEY), the ratio of emitted secondary electrons to incident "primary" electrons striking the surface. The SEY depends on the kinetic energy and incident angle of the primary electrons. Because the secondary electrons must leave the surface, the surface characteristics, including surface contaminants, influence the SEY. In order to make accurate predictions about electron cloud effects, it is important to know the SEY under realistic surface conditions.

Because secondary emission happens at the surface, it is possible to change the SEY of a material. Methods to reduce the SEY include coatings [2], grooving the surface [3], and processing the surface with electron bombardment [4]. Lowering the SEY can reduce the number of secondaries contributing to the electron cloud, thereby lessening the adverse impact on the beam.

A research program with the Cornell Electron Storage Ring (CESR) was established to study effects that will impact future rings such as the ILC damping rings. Electron cloud studies are a major part of this CESR Test Accelerator (CesrTA) program [5]. One aspect of the CesrTA program is the study of the SEY of technical surfaces in a realistic accelerator environment.

SEY studies have been previously done on samples exposed to an accelerator environment [2]. However, the time between measurements has often been several months, because the sample must be physically removed from the accelerator vacuum chamber for SEY analysis, an operation which can be done only infrequently. Hence, the SEY as a function of SR dose is difficult to determine with good resolution. One goal of the CesrTA program was to study surface conditioning with improved time resolution.

In our studies, we measure the SEY on samples as a function of the SR dose from a bending magnet, using an in-situ SEY station to take measurements roughly once a week. The typical CESR energy is 5.3 GeV and typical beam currents are 200 mA for electrons and 180 mA for positrons. The SEY station is located in CESR L3 East, so the SEY samples are exposed predominantly to SR from the electron beam. As shown in Figure 1, measurements are taken at 9 points of a 3×3 grid (6.4 mm $\times$ 6.4 mm) on

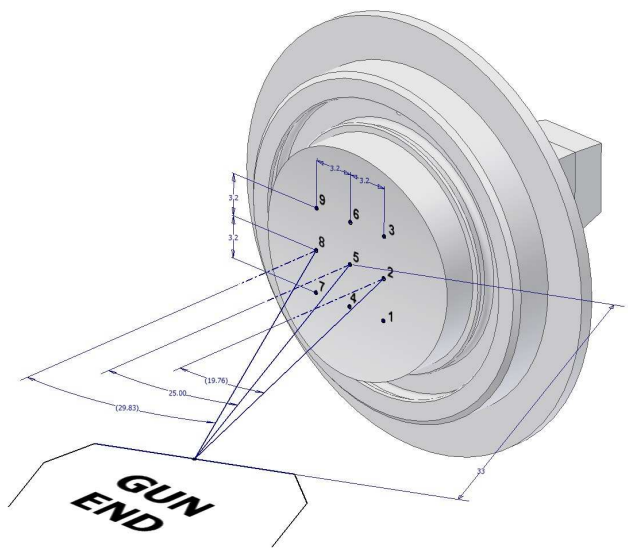

Figure 1: Isometric view of a sample showing the 9 grid points where the SEY is measured.

† Work supported by National Science Foundation Grant PHY-0734867 and Department of Energy Grant DE-FC02-08ER41538.

† Present address: Pacific Northwest National Laboratory, Richland, Washington, USA.

each sample. Measurements have been done on samples coated with SEY-reducing films and bare metal samples.

The in-situ SEY station allows SEY measurements without removal of the sample from the vacuum system. Measurements can be taken in approximately 1.5 hours. This allows us to use the (approximately) weekly CESR maintenance access to measure the SEY as a function of SR dose. In this paper, we will discuss the in-situ measurement apparatus, techniques, and initial results.

IN-SITU MEASUREMENT STATION

Our in-situ measurement station, shown in Figure 2, consists of a sample mounted on an electrically isolated magnetic manipulator and a dc electron gun[1] positioned at 25° to the manipulator. Two of these setups were installed in the CESR beam pipe, one mounted at the horizontal radiation stripe and one mounted at 45° from the horizontal plane, below the radiation stripe.

During accelerator operation, the sample is inserted flush with the inside of the beam pipe and is exposed to SR (Figure 2, upper left). During access periods, the sample is retracted from the beam pipe such that the center of the sample is aligned with the center line of the electron gun (Figure 2, lower left). The electron gun is positioned 32 mm from the center of the sample for the measurements. The SEY measurement circuit is the same as that used in previous studies [6]. A picoammeter[2] is used to measure the current from the sample; the sample dc bias is provided by a power supply internal to the picoammeter. During the SEY measurements, the two gate valves are closed to isolate the CESR vacuum system from the SEY system. The SEY station's vacuum system was designed to allow us to replace samples with minimal tunnel access time.

The SEY stations were assembled and tested prior to installation into CESR. Stray magnetic fields were found to be a major source of uncertainty, causing a distortion in the position and size of the electron beam, especially at low beam energy. Stray fields were minimized by adding mu metal shielding inside the SEY vacuum chamber, which reduced the stray magnetic field to a few milligauss.

SECONDARY ELECTRON YIELD

The SEY is defined as

$$SEY = I_{SEY}/I_p \,, \tag{1}$$

where I_p is the current of the primary electrons incident on the sample and I_{SEY} is the current of the secondary electrons expelled by the bombardment of primary electrons. The SEY depends on the energy and angle of incidence of the primary electron beam. The primary current I_p is measured by firing electrons at the sample with the electron gun and measuring the current from the sample with a positive

[1]Model ELG-2, Kimball Physics, Inc., Wilton, NH.

[2]Model 6487, Keithley Instruments, Inc., Cleveland, OH.

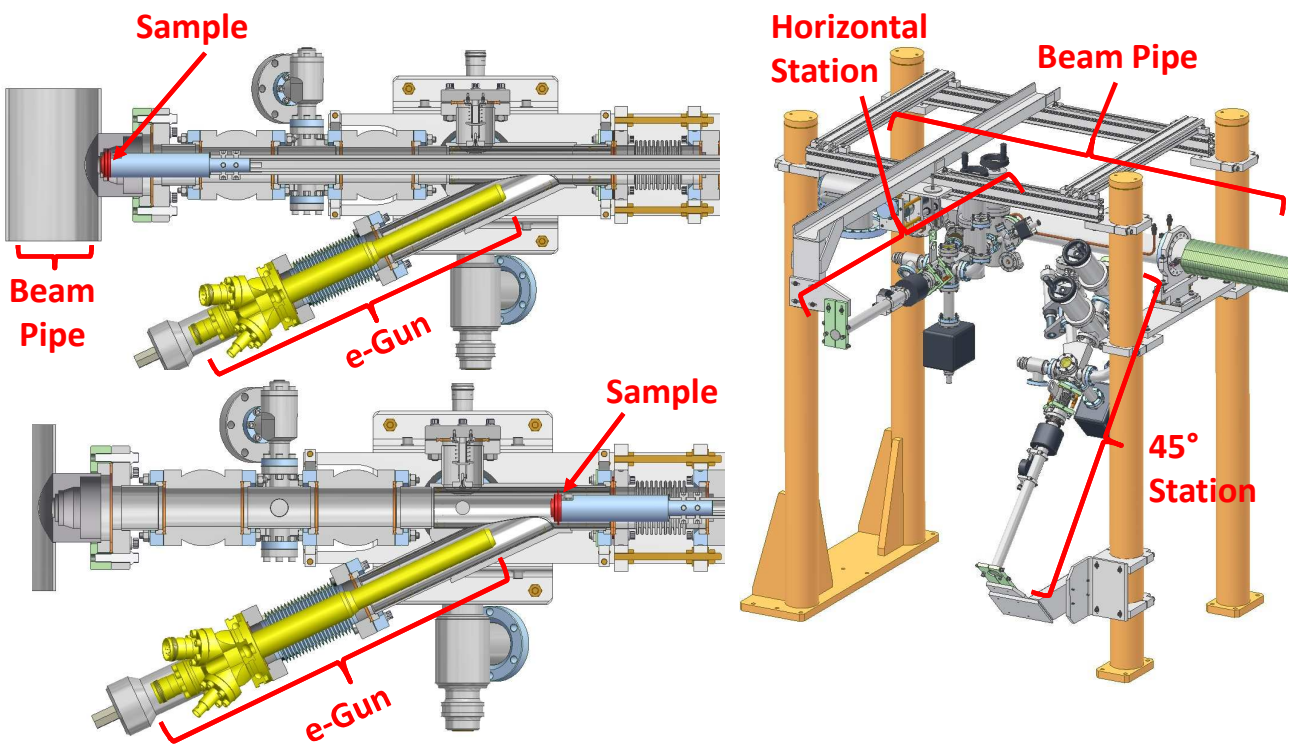

Figure 2: Left: Cross-sectional view of in-situ measurement station with the sample inserted into the beam pipe (top left) and with the sample retracted for SEY measurements (bottom left). Right: external view of horizontal and 45° stations.

bias voltage. A high positive biasing voltage of ∼150 V is used to recapture secondaries produced by the primary beam, so that the net current due to secondaries is zero.

The current I_{SEY} due to secondary electrons is measured indirectly. The total current I_t is measured by again firing electrons at the sample, but with a low negative bias (~ -20 V) on the sample to repel secondaries produced by the primary electron beam, and also to repel secondaries from "adjacent parts of the system that are excited by the elastically reflected primary beam" [7]. Since I_t is effectively the sum of I_p and I_{SEY} ($I_t = I_p + I_{SEY}$, with I_{SEY} and I_p having opposite signs), we calculate SEY as

$$SEY = (I_t - I_p)/I_p \, . \qquad (2)$$

Some SEY systems include a third electrode for a more direct measurement of I_{SEY}, for example the system at KEK [3]. Our in-situ setup cannot accommodate the extra electrode, so we cannot use the more direct method; we must use the indirect method described above.

DATA ACQUISITION SYSTEM

Figure 3 shows an electrical schematic of the system. With the sample retracted from the beam pipe, the current from the sample is measured during three separate electron beam energy scans with the electron gun. Each scan automatically steps the gun energy from 20 eV to 1500 eV in increments of 10 eV. This process is controlled by a data acquisition program we developed in LabVIEW (see Figure 4), using LabVIEW driver programs from Kimball Physics and Keithley. The first scan is done with a 150 V biasing voltage on the sample to measure I_p, with gun settings for $I_p \approx 2$ nA. This measurement is taken between

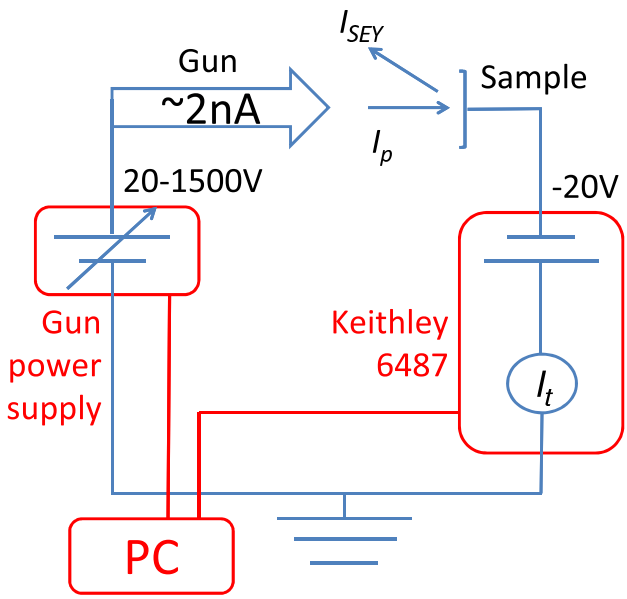

Figure 3: Schematic of electrical system for SEY measurements.

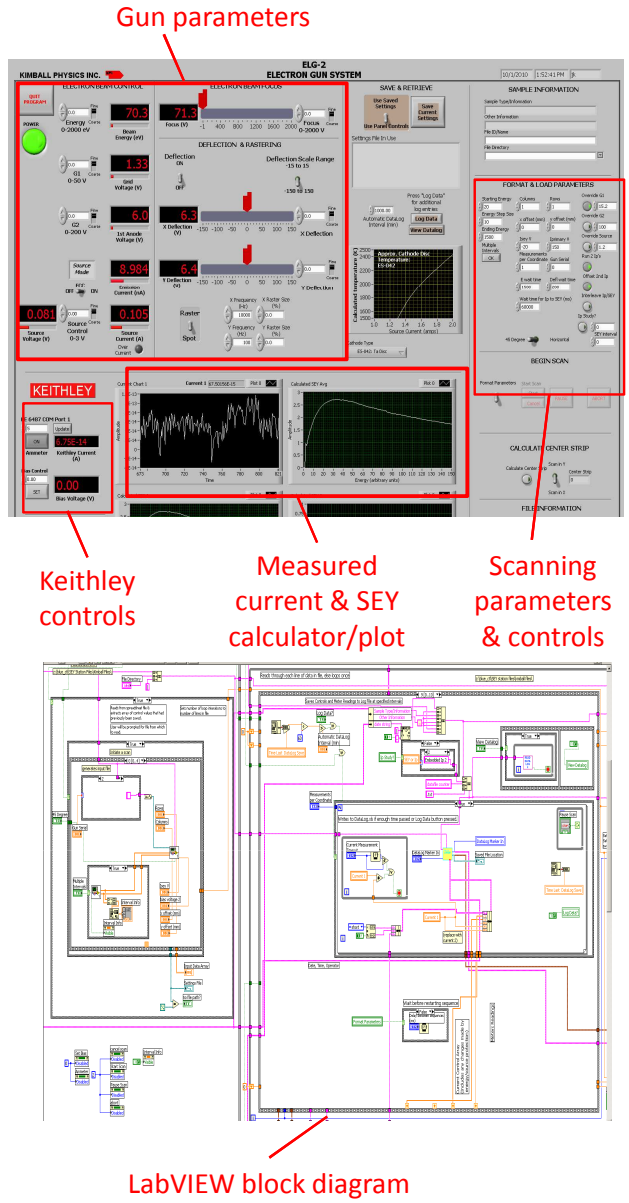

Figure 4: LabVIEW interface and user controls for SEY measurements.

grid points 5 and 9 (see Figure 1) to avoid processing the measurement points with the electron beam during the I_p measurement.

The second scan steps through the same gun energies with a bias voltage of -20 V on the sample to measure I_t. At each gun energy, the beam is rastered across all 9 grid points while the data acquisition system records the current for each point.

The gun has a current drift of $\sim$ 10% per hour. There is an "emission control" mode for the gun with a 0.1% beam stability, but this mode of operation is not compatible with a continuously changing beam energy, as is the case for our measurements. Because of the current drift, the I_p measured in the first energy scan is not exactly the same as the I_p in the second energy scan in which we measure I_t. Be-

cause of the current drift, we repeat the I_p measurement after measuring I_t and average the I_p values for each gun energy when calculating SEY for each energy.

Our LabVIEW software performs all of the measurements, calculates the SEY at each energy from I_t and the average I_p using Equation (2), displays the SEY as a function of energy, and saves the data. Identical measurements are performed on the horizontal system and the 45° system.

INITIAL RESULTS

Aluminum Samples with TiN Coatings

Aluminum samples with titanium nitride coatings provided by M. Pivi (SLAC National Accelerator Laboratory) were installed in CESR in both the horizontal and 45° stations from January to August 2010 and their SEYs were measured roughly once a week. These results are summarized in Figure 5. There is a peak in the SEY for an incident electron energy near 400 eV. A significant decrease in the SEY is evident between the first round of measurements and subsequent measurements. As the SEY decreases, there is a slight upward shift in the energy at which the peak in the SEY occurs, as indicated by the dotted lines in Figure 5.

The value of the SEY peak and the energy E_{max} at which the peak occurs are useful metrics for tracking the SEY behavior as a function of exposure. The beam conditioning behavior of the samples is illustrated in Figure 6, which shows the peak SEY and E_{max} for the center grid point as a function of accumulated dose. The bottom axis indicates the electron beam current integral in ampere·hours; the top axis indicates the calculated SR dose to the vacuum chamber wall in photons per meter. Neither of these values includes a contribution from the positron beam, because the dominant source of SR for the SEY stations is the electron beam. The SR photon dose in Figure 6 accounts for direct SR from the beam onto the chamber wall at the location of the SEY stations: it represents the "source term" and does not attempt to include the effects of scattering of photons (or production of photo-electrons). The dose calculation does not differentiate between the horizontal and 45° stations, even though the 45° station does not receive direct SR and the stations' distance from the bending magnet is not exactly the same.

As can be seen in Figure 6, the sample in the horizontal station began with a peak SEY of almost 1.8 and reached a minimum SEY peak of just under 1. The sample in the 45° station started with a peak SEY of just above 1.7 and reached a minimum SEY peak of around 1.2. As indicated above, E_{max} increased slightly as the peak SEY decreased.

Aluminum Alloy Samples

In August 2010, aluminum alloy samples (Al6061-T6) were installed in the in-situ systems. The results are shown in Figures 7 and 8. The sample in the horizontal setup began with a peak SEY of 2.5 for the center grid point, and reached an SEY peak of 1.6 after 3 ampere·hours of exposure. The sample in the 45° station began with a peak SEY of 2.25 in the center and reached a peak SEY of 1.6 after the same exposure, arriving at a peak SEY of 1.5 after 20 ampere·hours of exposure. The difference in the initial SEY between the two samples is presumably due to differences in the initial surface condition. We did not observe very significant changes in the E_{max} values.

Discussion

Our measurements at the center of the sample demonstrate a steady decrease in SEY peak with increasing beam dosage, D. As an example, for a "fresh" TiN-Al sample in the horizontal system, the measured peak SEY is proportional to $D^{-0.034}$. In each case, the 45° system has a consistently higher SEY than the horizontal system. For Al6061 samples, we observed a lower peak SEY than previously measured in other aluminum samples [4].

We observed small, consistent differences between the peak SEYs for different grid points, correlated with the incident angle of the beam from the electron gun. The incident angle (measured relative to the normal to the sample surface) is 20° for Points 1, 2, and 3; 25° for Points 4, 5, and 6; and 30° for Points 7, 8, and 9 (Figure 1). Higher SEYs were observed at points with larger incidence angles for the electron gun beam, as can be seen in Figure 9, which shows repeated measurements of the peak SEY for all grid points over several weeks. There is reasonably good consistency between different grid points, with a small but systematic increase in the peak SEY between the first three points, middle three points, and last three points.

Our observation that the SEY depends on angle of incidence is qualitatively consistent with the observations that, as the primary electron angle goes from normal incidence toward grazing incidence, the SEY increases; this has been reported in recent secondary emission studies [7] as well as early experiments [8].

It should be pointed out that the initial peak SEY for this sample was about 1.8; the initial measurements are not included in Figure 9 in order to highlight the small variations between points (note that all of the values shown in Figure 9 are within 10% or so of one another).

The last measurements in Figure 9 (gray bars, marked with an asterisk in the legend) were done after a total of 63 days of accelerator operation plus 14 days with the sample under vacuum without beam (at a pressure of order 10^{-8} torr). These last measurements show a small increase in the peak SEY. This may be due to surface contaminants having been slowly removed from the surface in the presence of the beam, with a small amount of recontamination from residual gas in the 2 weeks without beam.

CONCLUSION AND FUTURE WORK

For TiN-Al samples and bare Al6061 alloy samples, we observed a weekly decrease in SEY peaks for both the 45° system and the horizontal system. The main processing

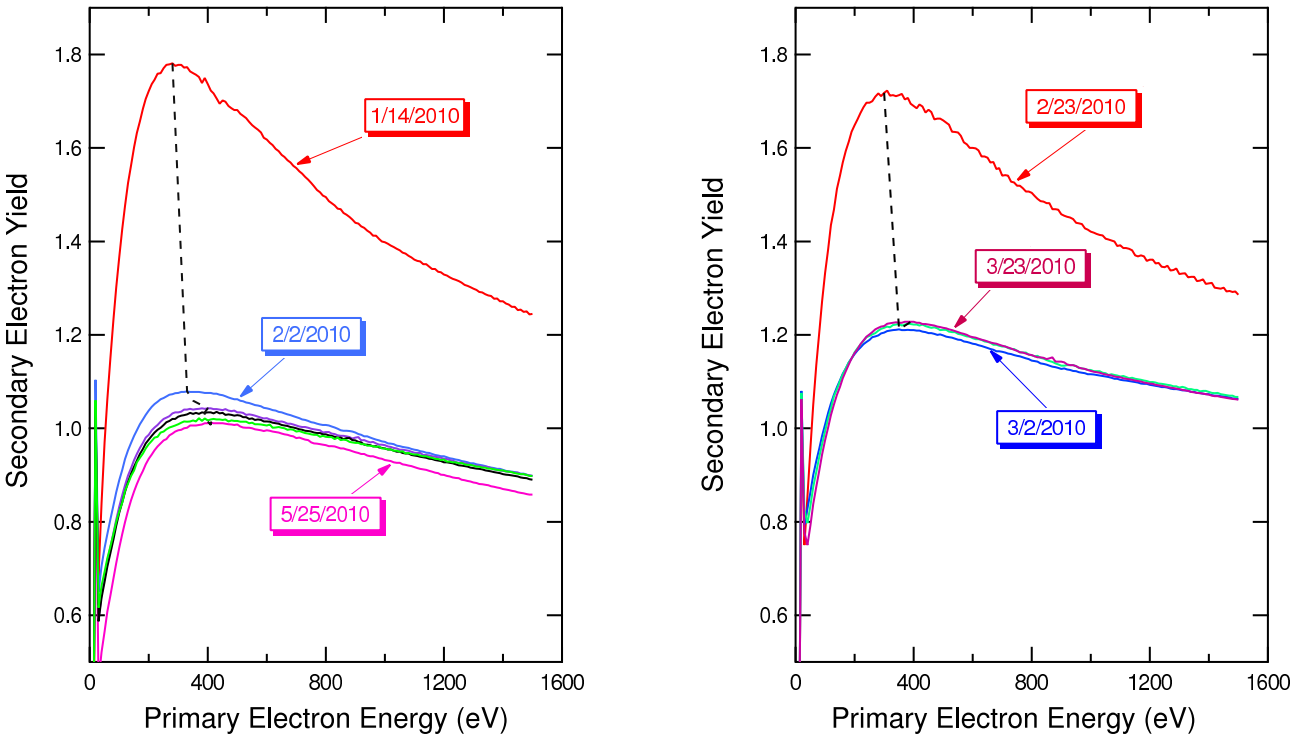

Figure 5: Repeated measurements of SEY as a function of energy for TiN-Al samples in the horizontal station (left) and the 45° station (right).

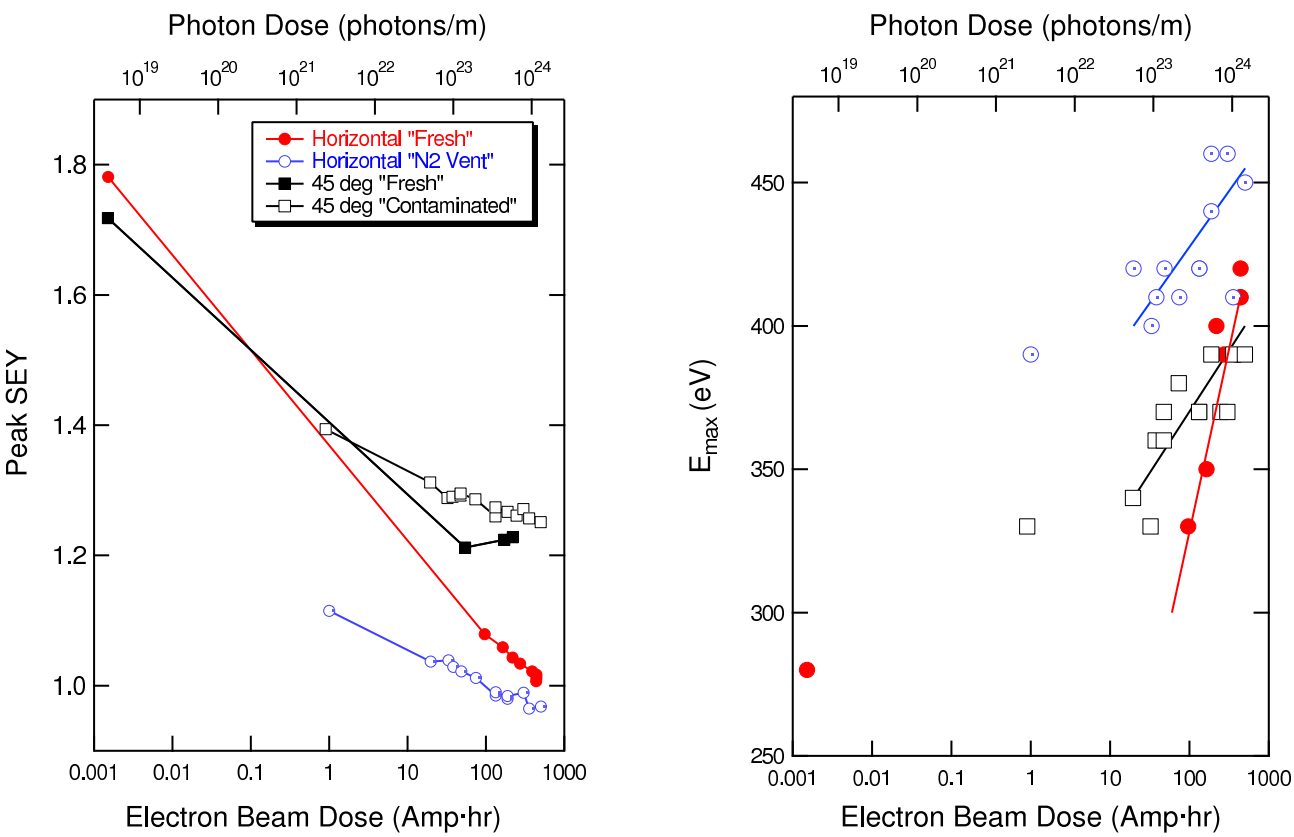

Figure 6: Progression of SEY peak (left) and corresponding energy (right) for TiN-Al samples in the horizontal and 45° stations.

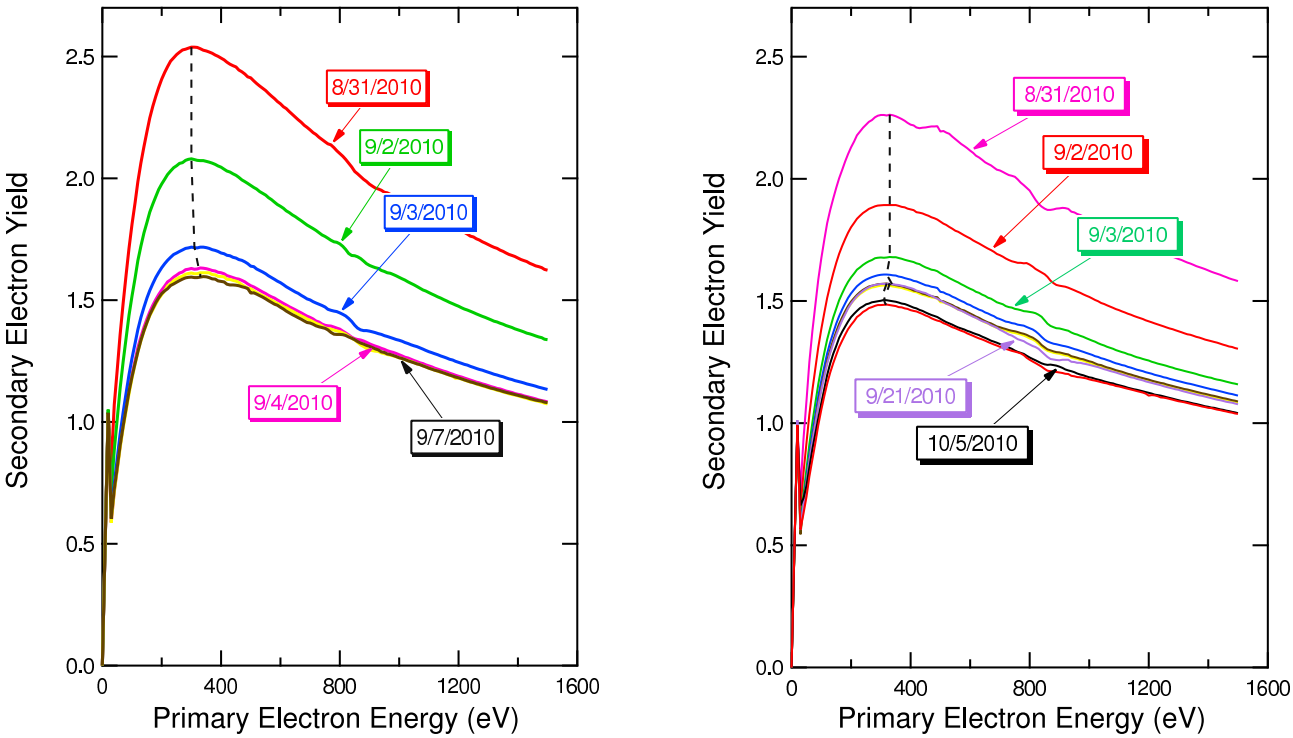

Figure 7: Repeated measurements of SEY as a function of energy for Al6061-T6 samples in the horizontal station (left) and the 45° station (right).

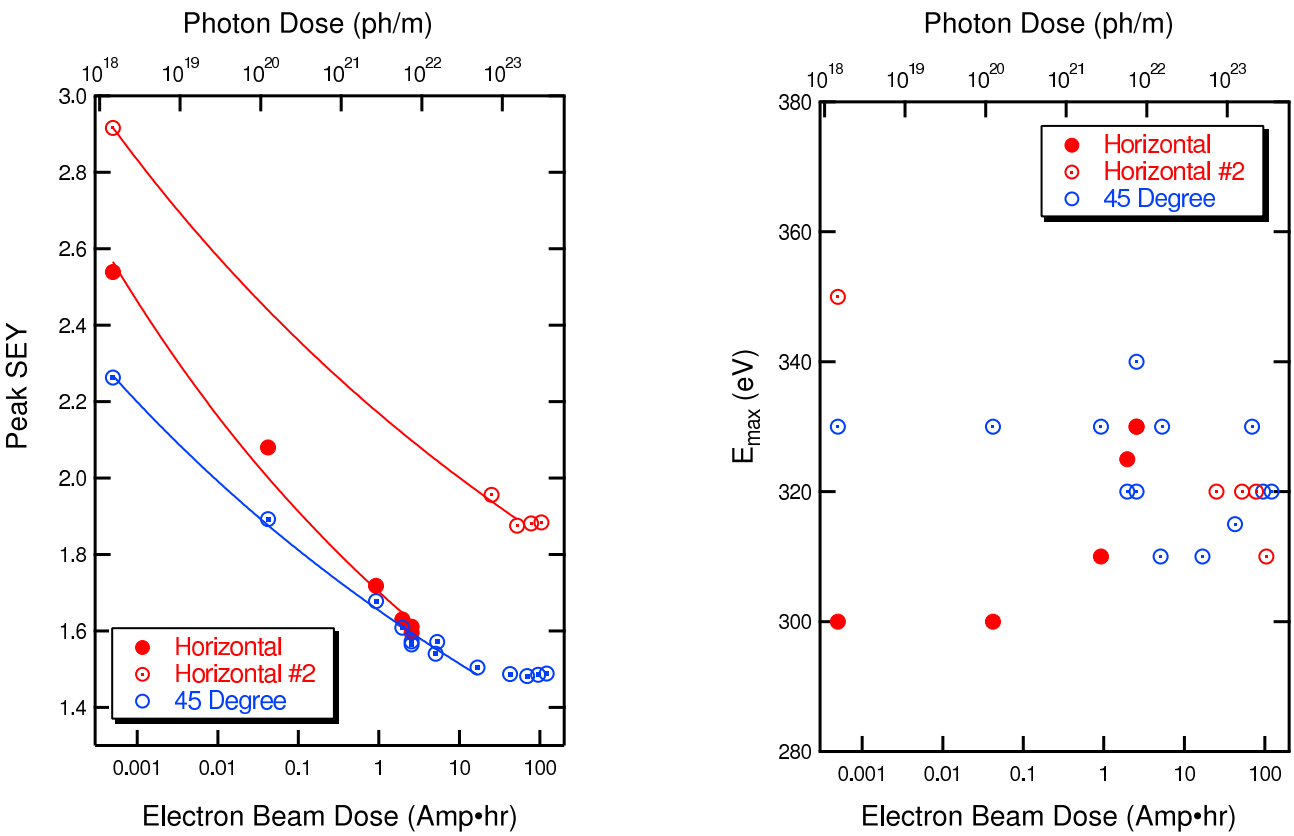

Figure 8: Progression of SEY peak (left) and corresponding energy (right) for Al6061-T6 samples in the horizontal and 45° stations.

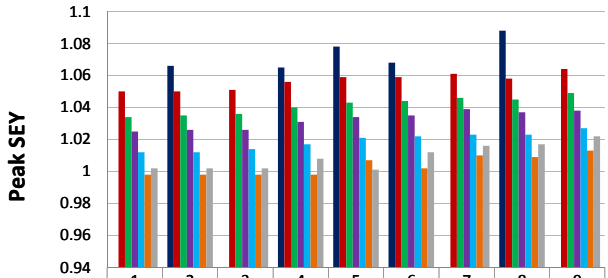

	1	2	3	4	5	6	7	8	9
14 days		1.066		1.065	1.078	1.068		1.088	
21 days	1.05	1.05	1.051	1.056	1.059	1.059	1.061	1.058	1.064
28 days	1.034	1.035	1.036	1.04	1.043	1.044	1.046	1.045	1.049
35 days	1.025	1.026	1.026	1.031	1.034	1.035	1.039	1.037	1.038
49 days	1.012	1.012	1.014	1.017	1.021	1.022	1.023	1.023	1.027
56 days	0.998	0.998	0.998	0.998	1.007	1.002	1.01	1.009	1.013
63 + 14 days*	1.002	1.002	1.002	1.008	1.0011	1.012	1.016	1.017	1.022

Figure 9: Measured SEY peaks of all 9 grid points for the TiN-Al sample in the horizontal system. Different colors correspond to different measurement times.

occurred within the first two weeks, with a total photon dose of 10^{22} photons/m, while, after that, the SEY decrease was about 1% per week. For Al6061, we observed that the SEYs after processing are lower than the minimum SEY value of 1.8 for Al6063 reported by SLAC [4].

We are able to observe a small dependence of the SEY on the angle of the incident electron beam. This indicates that the statistical errors are small enough for us to be able to resolve differences of a few percent.

Initially, TiN-Al samples were installed in an "as received" condition and the processing was monitored. When one sample was exposed to nitrogen gas, the peak SEY increased and then slowly improved to about the same value as had been reached previously. With "as received" samples, we observed differences in the sample processing between the horizontal and 45° systems. For bare Al, the processing rates were different; for TiN-Al, the samples reached different peak SEY values after about 9 weeks of exposure. We plan to check the reproducibility of these results and do additional checks for systematic effects. We are designing additional experiments to determine whether SR bombardment or electron cloud bombardment is the main source of processing.

We are working on mitigating the effects of the drift in the electron gun current. The drift causes a systematic error of around 2 to 4% in the calculated SEY. One method we are investigating is to measure I_p at a given gun energy, then change the bias voltage to measure I_t at the same energy, before stepping to the next energy and repeating the process. However, when we switch the biasing voltage from 150 V to −20 V, we must account for the charging and discharging of the capacitance of the SEY system and cables connecting the picoammeter to the sample, which can dramatically distort the current readings. The charging and discharging of the cables and SEY system can take on the order of several minutes. Using our normal scanning method, the biasing voltage is only switched twice, adding just a few minutes to the total measurement time. However, the method we are investigating switches the bias voltage at every energy; with 150 gun energy changes per scan, the measurement time for this method may be prohibitively long. Consequently, we are investigating SEY system modifications to reduce the stray capacitance and a measurement algorithm with longer energy intervals between changes in the bias voltage.

We have done preliminary measurements on amorphous carbon-coated samples from S. Calatroni and C. Yin Vallgren (CERN), and diamond-like carbon (DLC) coated samples from S. Kato (KEK). An issue we are addressing with the DLC samples is the charging of the insulating surface. Initial measurements have shown a distortion in the SEY curve due to charging of the sample. We can mitigate the charging effect with longer waiting times between energy points to allow the sample to discharge. We are developing software to automate this process.

We plan to do an in-situ comparison of Al6063 and Al6061 alloys to resolve the cause of the discrepancy between our measurements of peak SEY and previously reported results. Other future work will include the study of additional materials, including samples cut from an extruded, aged (30+ years) 6063 aluminum CESR chamber. In addition, we plan to perform in-situ measurements of SEY for materials coated in non-evaporable getter (NEG) thin film, and continue to study amorphous carbon and diamond-like carbon samples.

We have built and tested two additional in-situ SEY systems for studies in the Main Injector at Fermilab.

REFERENCES

[1] M. Pivi *et al.*, in *Proceedings of the 2005 Particle Accelerator Conference*, p. 24–28.

[2] M. T. F. Pivi *et al.*, in *Proceedings of the 2008 European Particle Accelerator Conference*, p. 691–693.

[3] Y. Suetsugu *et al.*, in *Proceedings of the 2010 International Particle Accelerator Conference*, p. 2021–2023.

[4] F. Le Pimpec *et al.*, "Electron Conditioning of Technical Aluminum Surfaces," Tech. Rep. LCC-0153/SLAC-TN-04-051, SLAC (Sep. 2004).

[5] M. A. Palmer *et al.*, in *Proceedings of the 2010 International Particle Accelerator Conference*, p. 1251–1255.

[6] F. Le Pimpec *et al.*, "Secondary Electron Yield Measurements of TiN Coating and TiZrV Getter Film," Tech. Rep. LCC-0128/SLAC-TN-03-052 (v2), SLAC (Aug. 2004).

[7] F. Le Pimpec *et al.*, *Nucl. Instrum. Methods Phys. Res.* **A551**, p. 187–199 (Jul. 2005).

[8] K. G. McKay, in *Advances in Electronics*, L. Marton, Ed., Academic Press, New York, vol. I, p. 65–130 (1948).

ANALYSIS OF SYNCHROTRON RADIATION USING SYNRAD3D AND PLANS TO CREATE A PHOTOEMISSION MODEL

L. Boon, A. Garfinkel, Purdue University, West Lafayette, IN, USA
K. Harkay, ANL, Argonne, IL, USA

Abstract

Using current models of synchrotron radiation production and propagation, work is being done on a realistic photoelectron model from Retarding Field Analyzer (RFA) data. This proposed photoelectron production model will be better able to predict the level of electron cloud density in the vacuum chamber. In this paper SYNRAD3D is used to simulate the production and propagation of photon radiation in in International Linear Collider(ILC) Damping Rings. Analysis of this radiation with photon reflections off the chamber wall has been completed. This data will be used in the future to study photoelectron production as a function of parameters such as minimum absorbed photon energy and lattice element type. The results show that wigglers are regions which create the most photons and therefore have the ability to produce the most photoelectrons.

INTRODUCTION

SYNRAD3D provides a 3-dimensional model of synchrotron radiation, allowing a study of radiation reflection around the perimeter of the chamber as a function of the longitudinal position, s [1]. This program will allow us to study various antechamber designs and other photon absorbers. The final goal is to have a photoelectron model which includes photoelectron emission energy. Comparison will be made to the photoemission in various lattice elements such as dipoles and wigglers to RFA data.

SYNRAD3D

SYNRAD3D is an extension of SYNRAD, a 2-dimensional program which calculates the radiation on the inner and outer most point of the chamber wall. SYNRAD3D uses the Better Methodical Accelerator Design(BMAD) library [1]. SYNRAD3D is a photon production and propagation code, which tracks photons. It uses radiation integrals to determine the probable initial position and energy of a specified number of photons around the ring. It then tracks the photons as they move and reflect in the chamber. SYNRAD3D uses data from the Berkeley's Center for X-Ray Optics to determine the probability of reflection and absorption of each photon as a function of energy and grazing angle (seen in Figure 1 [2]) As seen in the figure the chamber wall is assumed to have an 8 nm Al_2O_3 (aluminum oxide) layer on an Al substrate with 2nm surface roughness. Currently all scatters are specular and elastic.

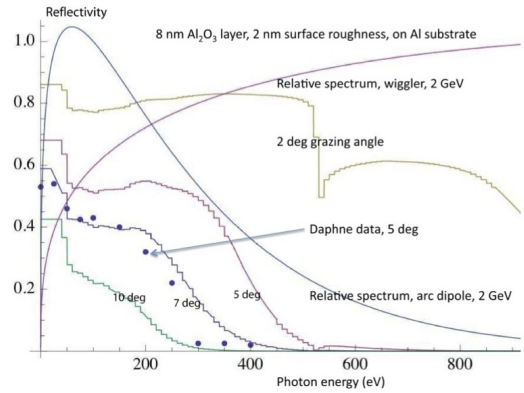

Figure 1: An example of the reflectivity of photons on a specified surface. The reflectivity is based on the photon energy and grazing angle. Data was taken from the Berkeley Center for X-Ray Optics [2] [1].

INTERNATIONAL LINEAR COLLIDER (ILC)

To decrease the cost of the ILC damping rings (DR) it has been proposed to decrease the circumference of the damping rings from 6.4 km to 3.2 km [4]. One of the concerns with a smaller ring is the build up of the electron cloud from photoemission and other effects.

A general schematic of the DR can be seen in figure 2 [4]. The main source of synchrotron radiation are wigglers (to cool the beam) and sector bends in the arcs. To make a better comparison of the photon flux between the current and proposed damping ring the first cut in data ignored all photons with energy less then 4 eV. 4eV was chosen because it is the work function for the chamber wall, which is Al. In addition to the energy cut all wiggler magnets are modeled as alternating dipoles and drifts. Normalization was done using equation 1.

$$\text{photons/m/beam particle} = \frac{N_L * I}{L} \qquad (1)$$

L is the length of the section to average over, and N_L is the number of photons incident on the wall in length L [1]

Analysis for the 3.2 km proposed ring (DSB3)

For the analysis of the 3.2 km ring 101,000 photons were generated. Figure 3 a&b show the normalized photon flux along the inside and outside wall of the damping ring, respectively, where s = 0 is between the injection and extraction points as seen in Figure 2. The main feature of the

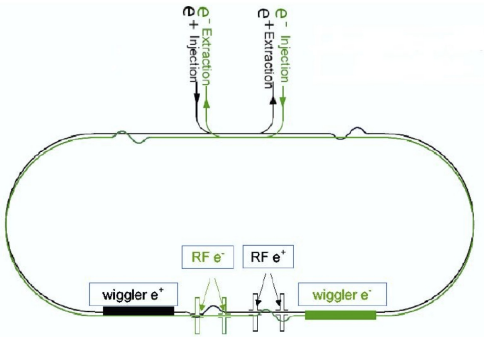

Figure 2: A schematic of the ILC damping ring. [4]

photon flux is a sharp spike at s = 2100. This heightened flux is created by the radiation in the wigglers that is radiated in the direction of the beam, this radiation is then absorbed directly downstream in the first dipole. Besides the photon spike at s = 2100m the inner and outer chamber walls receive similar amounts of photon radiation without antechambers present as seen in figure 4; a graph of the normalized photon radiation through the wigglers. Comparing Figure 4(a) and Figure 4(b) it can be seen that the photon flux for the wigglers on both the inside and outside wall of the chamber is the same when no antechamber is present.

The opening angle of the wiggler radiation with respect to the beam is defined by the equation:

$$\Psi = \begin{cases} 1/\gamma \left(\frac{\omega_c}{\omega}\right)^{1/3} & \omega << \omega_c \\ 1/\gamma & \omega = \omega_c \\ 1/\gamma \left(\frac{\omega_c}{\omega}\right)^{1/2} & \omega >> \omega_c \end{cases} \quad (2)$$

where Ψ is the opening angle, ω_c is the critical photon energy, ω is the energy of the photon, and γ is the relativistic gamma. For the ILC ω_c is —keV. Figures 5 & 6 compare the photon absorption distribution around the perimeter of the chamber wall in the wiggler(figure 5) and — after the wiggler(Figure 6). Zero has been defined as on the positive x-axis, with positive values above the axis x-axis and negative values below the x-axis. The narrow distribution seen in figure 5 corresponds to a smaller opening angle. Because photons are absorbed closer to the wiggler radiation source. Figure 6 is the distribution around the chamber at the high photon flux in the first dipole after the wigglers, at s = 2100m. The distribution around the zero point is wider here. This spread is consistent with the opening angle.

Analysis of the current 6.4 km ring(DCO4)

A similar analysis was completed of the 6.4 km ring so that a comparison between the two could be made. To keep the photons normalized with those of the smaller 3.2 km ring 560,000 photons were produced in the simulation.

The initial graphs of the entire ring show similar features as seen in the 3.2 km ring, with just a few differences in magnitude, compare figures 7 and 3. The main difference is in the photon spike after the wigglers. In the 3.2 km ring the maximum value of photon flux reached is 72 photons/m/beam particle, while in the 6.4 km ring the flux is about half that at 37 photons/m/beam particle. The difference in photon flux is due to the shape of the ring, the smaller ring has a sharper turn in each of the dipoles so there are more photons incident on a shorter section of the ring then there are in the larger 6.4 km ring.

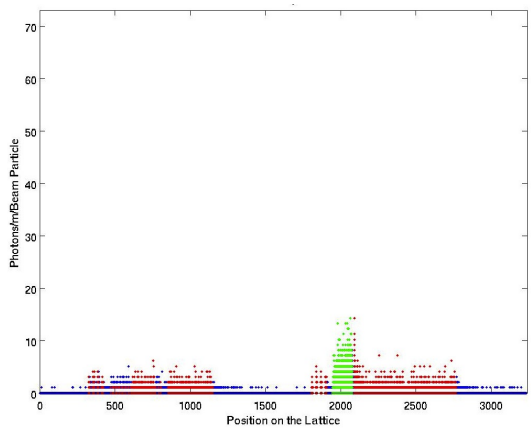

(a) Inside chamber wall

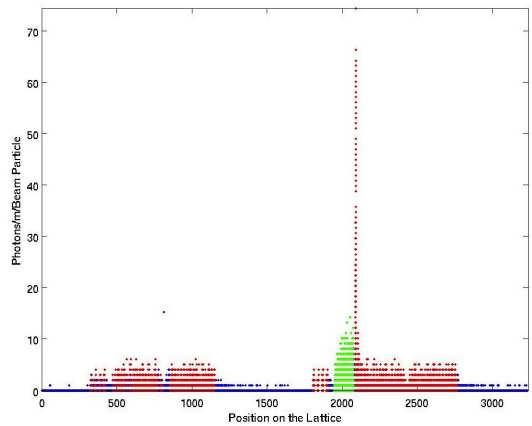

(b) Outside chamber wall

Figure 3: A graph of the photon flux along the inside and outside of the 3.2 km damping ring chamber wall, the individual photons have been normalized by equation 1

An analysis of the photon flux as a function of the perimeter yields the same results as the 3.2 km ring with respect to the opening angle of the generated photons. However similar the shape of the flux there is a higher flux of photons with higher energies than seen in the 3.2 km ring in both the wiggler and spike sections of the chamber wall. (not shown)

RETARDING FIELD ANALYZERS (RFA)

Retarding Field Analyzers [3] are detectors placed in the Advanced Photon Source (APS) and Cornell's CesrTA that measure the energy of free electrons in the chamber. In APS there were 10 detectors in one of the straight sections of the storage ring, the placement is seen in Figure 8. A

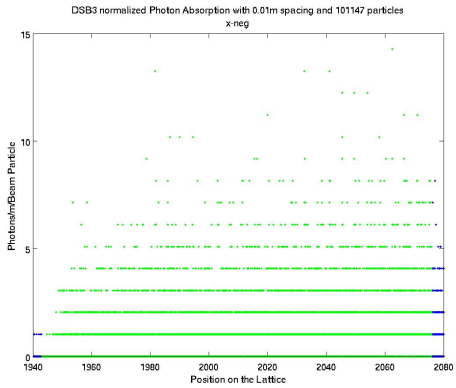

(a) Inside chamber wall

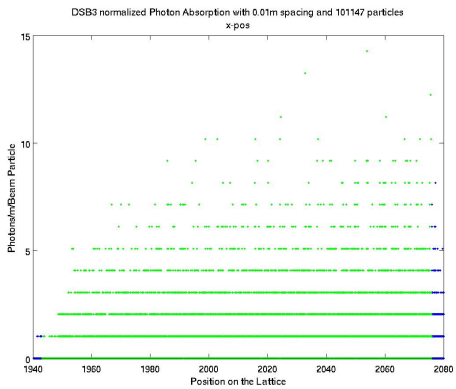

(b) Outside chamber wall

Figure 4: Zoomed in view of the photon flux in the wiggler for the inside and outside of the chamber wall. Both sides have the same photon flux when no antechamber is present.

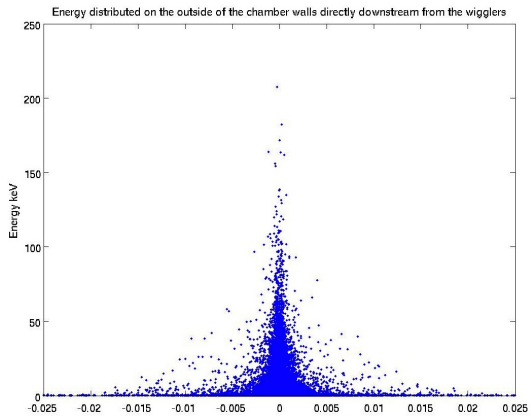

Figure 5: Photon flux along the chamber wall as a function of the perimeter in the wiggler, the tight peak indicates a small opening angle consistent with the photons being generated close to the location they were absorbed.

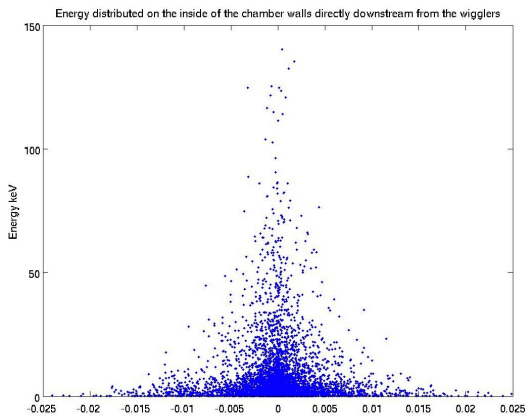

Figure 6: Photon flux along the chamber wall as a function of the perimeter in the photon flux spike near s = 2100m, the wide peak indicates a large opening angle consistent with the photons being generated far from the location they were absorbed.

schematic of the detector can be seen in Figure 9. It has a grounded plate to shield the beam, and a retarding voltage to allow only free electrons with a given energy to be detected.

Data was taken at APS in 1998 and 1999 for both positron and electron beams. The data is believed to fit a lorentzian function (Figure 10)

$$L = \frac{\frac{C_1\Gamma}{2}}{(\frac{\Gamma}{2})^2 + (E - \langle E \rangle)^2}. \quad (3)$$

However for detectors close to the end absorber (EA) such as detector 1, there appears to be a tail after the main peak which decreases more slowly than for data from detectors farther away from the EA. This can be seen in Figure 11. This extra shape is believed to be an exponential and currently an analysis program is being written to calculate the best fit for the sum of a lorentzian and exponential decay.

$$L = \frac{\frac{C_1\Gamma}{2}}{(\frac{\Gamma}{2})^2 + (E - \langle E \rangle)^2} + C_2 e^{-\frac{E}{C_3}} \quad (4)$$

Once this is complete the archived data from APS will be used to study the production of photoelectrons over time, and location relative to the EA. The fitted data will be used as input to a photoelectron model to be incorporated into SYNRAD3D. The RFA's near the EA most resemble the no-antechamber design analyzed earlier in this paper.

CONCLUSION/SUMMARY

Using SYNRAD3D synchrotron radiation models have been studied of both the current and proposed ILC DR. These models show that with the smaller ring there will be more photon flux in the wigglers and in the first dipole downstream from the wigglers. This can be reduced with the use of antechambers, but these simulations have not yet been done. The simulations presented here are consistent with theory. High energy photons are produced in the wigglers and have a small opening angle. The effect of the high photon flux will be studied further with the proposed

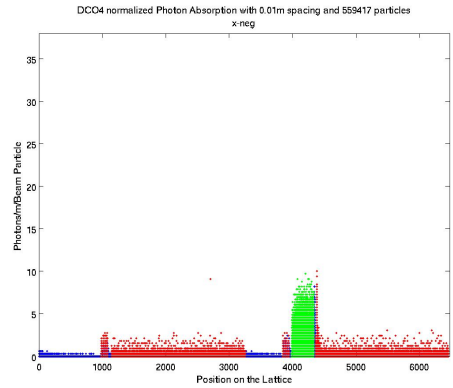

(a) Inside

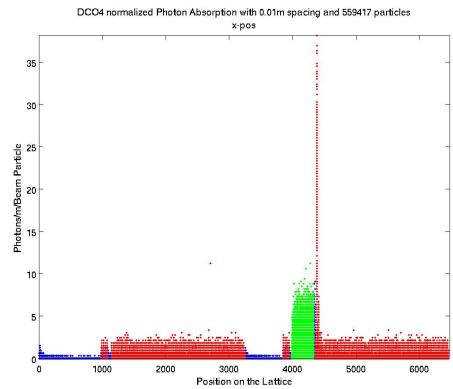

(b) outside

Figure 7: A graph of the photon flux along the inside and outside of the 6.4 km damping ring chamber wall, the individual photons have been normalized by equation 1

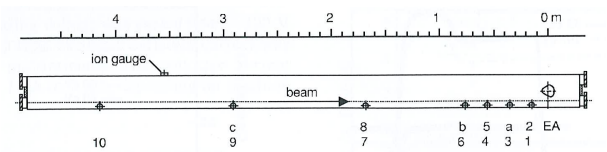

Figure 8: Location of the RFA detectors labeled 1-10 in the APS ring. [3] EA is an end absorber.

photoemission model being created.

ACKNOWLEDGEMENTS

The authors would like to thank D. Sagan and G. Dugan who write SYNRAD3D. And the entire electron cloud group based at Cornell University who gave feedback on this work as it progressed. Thanks also to thank M. Harrison, Director, ILC Global Design Effort Americas Regional Director for financial support.

This work is supported by U.S. Department of Energy, Office of Sciences under contract no. DE-AC02-06CH11357

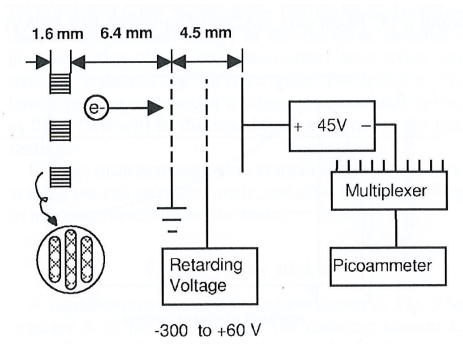

Figure 9: A schematic of the RFA detector. [3]

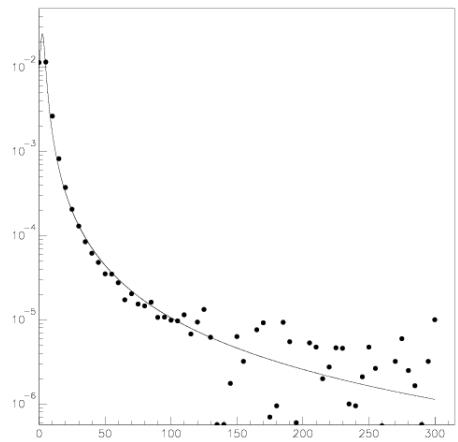

Figure 10: Demonstrates the lorentzian fit used to determine the peak electron energy generated by photons in detector 6.

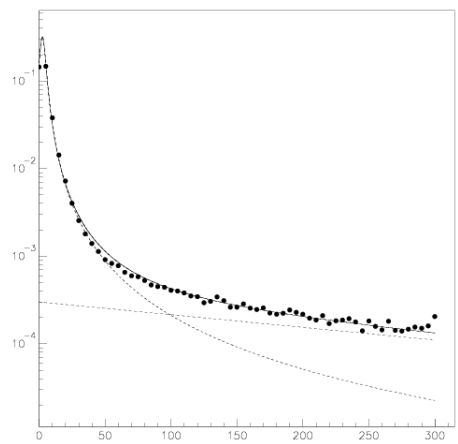

Figure 11: A plot of the readout from detector 1 (near the end absorber); notice need to add a second function to fit the data, this second function is an exponential decay. These added electrons are produced by the proximity to the EA.

REFERENCES

[1] Dugan, G., D, Sagan, "Synrad3d photon propagation and scattering simulation", ECLOUD10 proceedings.

[2] Gullikson, E. "X-Ray Interactions With Matter", http://henke.lbl.gov/optical_constants/mirror2.html

[3] Harkay, K., R. A. Rosenberg. "Properties of the Electron Cloud in a High-Energy Positron and Electron Storage Ring" Physical Review Special Topics-Accelerators and Beams Vol 6, 034402, 2003

[4] Pivi, M. T. F., et al. "Recommendation for the Feasibility of More Compact LC Damping Rings," IPAC'10, Kyoto, Japan, May 2010, p. 3578, www.jacow.org.

ACCURATE SIMULATION OF THE ELECTRON CLOUD IN THE FERMILAB MAIN INJECTOR WITH VORPAL*

Paul L. G. Lebrun, Panagiotis Spentzouris, Fermilab, IL 60510, USA†
John R. Cary, Peter Stoltz, Seth A. Veitzer, Tech-X, Boulder, Colorado, USA‡

Abstract

We present results from a precision simulation of the electron cloud (EC) in the Fermilab Main Injector using the code VORPAL. This is a fully 3d and self consistent treatment of the EC. Both distributions of electrons in 6D phase-space and E.M. field maps have been generated. This has been done for various configurations of the magnetic fields found around the machine have been studied. Plasma waves associated to the fluctuation density of the cloud have been analyzed. Our results are compared with those obtained with the POSINST code. The response of a Retarding Field Analyzer (RFA) to the EC has been simulated, as well as the more challenging microwave absorption experiment. Definite predictions of their exact response are difficult to obtain, mostly because of the uncertainties in the secondary emission yield and, in the case of the RFA, because of the sensitivity of the electron collection efficiency to unknown stray magnetic fields. Nonetheless, our simulations do provide guidance to the experimental program.

MOTIVATION

The electron cloud (EC) phenomena in high intensity proton storage rings and synchrotrons can limit the performance of such machines [1], [3]. This phenomena is characterized by an exponential growth of the number of low energy (eV) electrons emitted at the surface of the beam pipe wall. Such electrons are then accelerated by the field induced by the passage of the proton beam, which itself causes more secondary emission of electrons at the beam pipe wall. This is reminiscent to the multipacting phenomena observed in R.F. cavities, where one field emission region is replaced the proton beam itself. Such EC can generate fast beam instabilities, as they strongly perturb the electric field in the vicinity of the proton beam. This has been predicted by many models, observed in many e^+e^- storage rings, and studied in detail at CesrTA [4]. The Fermilab Main Injector (MI) is no exception. In the "Project X"[5] era, the delivered beam power on target will go from the current value of 300 MW to 2.1 GW. In a first upgrade, the MI cycle time will be reduced to 1.33 seconds from its current value of 2.2 seconds, thereby increasing the 120 GeV beam power to 700 kW. The second upgrade will require a new injector as the bunch charge will increase by a factor of three. While the MI currently delivers the designed beam intensity, we are concerned that a significant increase of the bunch charge will trigger the formation of a much denser EC, and significantly increase beam losses due to fast instabilities that are hard to control.

Therefore, an R&D initiative has started aiming at providing a robust mitigation strategy. Unlike some e^+e^- storage rings (e.g. KEKB), the MI has relatively short straight sections compared to the length of the arcs, which almost entirely consist of dipoles and quadrupole. Thus, an EC solution based on the use of solenoidal fields that confine the EC away from the beam is simply not applicable. A well established solution would consist in coating the beam pipe with a thin layer of either TiN or amorphous carbon [10], but such a solution could be expensive. Thus, despite the success of numerous previous effort in describing the EC, further R&D on the EC in the MI is well justified, because both the phenomenology and the mitigation strategy have always been site specific.

Furthermore, we present here detailed results on the EC morphology and related fields. This is acccomplished using VORPAL [11]. This is a code used for accurate simulation of plasma and beams problems where complicated collective effects are important. Unlike POSINST [3, 7] and QuickPic [6], two distinct codes originally written to simulate "positrons beam instabilities" and used extensively to simulate the response of the beam to the perturbation due to EC, VORPAL is a fully consistent, 3D electromagnetic code using relativistic electrons. Results on a specific benchmark POSINST vs VORPAL will be briefly discussed. While VORPAL allows us to obtain a more precise description of the EC, this can only be done for relatively short sections (2 to 16 m.) of the machine, due to computational limitations. Over such short distances and for relatively short periods of time compared to a full synchrotron cycle, ($\approx 1.0\,\mu$ sec), the electromagnetic fields induced by the EC are not strong enough to perturb the trajectories of the ≈ 20 GeV proton beam. Therefore, the proton beam is assumed to be perfectly rigid, i.e., no changes to its associated current occur throughout the simulation.[1]

*Work by Fermi Research Alliance, LLC under Contract No. DE-AC02-07CH11359 with the United States Department of Energy.

† lebrun@fnal.gov,spentz@fnal.gov

‡ cary@txcorp.com, pstoltz@txcorp.com, veitzer@txcorp.com

[1] Evidently, this is not true over long distances and many turns. However, our simulation produces field maps that can and hopefully will be

Finally, new detectors have been developed in the recent past to characterize the EC. In this paper, we report on both the simulation of the EC phenomena and two distinct instruments: the Retarding Field Analyzer (RFA) [8] and the measurement of phase shifts in microwaves propagating in the MI beam pipe [9].

CONFIGURATIONS

The Fermilab Main Injector

The Fermilab Main Injector (MI) is a strong focusing high energy synchrotron. A complete description of it is evidently beyond the scope of this paper, but can be found in our Fermilab operating manuals[12]. The relevant features of the MI are summarized on table 1. Note that one essential parameter, the Secondary Emission Yield (SEY) at the beam pipe wall, is poorly known. While the SEY can be determined on the bench, it is known to be affected by the complicated surface chemistry in presence of residual gas and irradiation due to beam losses, and the electron cloud itself [13, 14].

The pressure is listed for sake of completeness but is not used in this calculation. That is, we limit our study to the exponential-like growth of the EC due to the interaction of the EC with proton beam and the beam pipe walls, skipping over the generation of the seed electrons. It is assume that some electrons are present in the beam pipe at the beginning of a batch, either due to beam losses or gas ionization. This "seed EC" is much thinner [2]than the EC due to multipacting between the beam and beam pipe wall. That is, the steady-state EC due to gas ionization is much too thin to cause beam instabilities, by at least 5 order of magnitude, as obviously shown later on. However, other sources for seed electrons, such as those due to beam losses, are harder to determine. This simplification implies that our simulation will not give any ab-initio estimate for the timing of the onset of the disturbing EC.

Regarding the transverse emittance, most of the calculations have been done for the worst case scenario for EC, when the emittance remains small and the transverse fields are the strongest.

Modeling of the relevant section of the machine.

A simulation of the EC throughout the full 3.2 km ring is both unnecessary and unrealistic, as it would require too much compute power. The following setups have been implemented in our simulation:

- Short sections with the large radius beam pipe and with small stray magnetic fields. Such straight sections contain one meter coated beam pipe that have been instrumented with RFA's.
- Short (0.25 to 1 m. long) sections of a MI dipole, with uniform dipole fields and an elliptical beam pipe.
- Long ($\sim$ 16 m.) sections of the elliptical beam pipe with a uniformed magnetic field. The length is determined by the distance between antenna used in the microwave experiment. While such a perfectly uniform magnetic field is not realistic, it is has been implemented in the simulation for simplicity and benchmarking purpose.
- Long ($\sim$ 16 m.) sections of the elliptical beam pipe with a MI dipole followed by a MI quadrupole, then a dipole. Realistic fringe fields have been implemented.

Throughout this calculation, the MI is assumed to be at $\approx$ 20 GeV, close to transition, where the bunch length is shortest. This energy has been chosen because the EC effect is most pronounced when the electric fields created the proton bunch are most intense, that is, when the bunches are short. The transverse beam size quoted on table 1 are realistic as they are based on real measurements [18, 19][3]. This emittance is in part dictated by the performance of the Fermilab 8 GeV Booster and associated transfer beam lines, the resistive wall instability (mitigated by the use of a damper system [20]), and possibly by the EC effect.

As shown later, the EC is a localized phenomena, particularly in a strong confining magnetic field. Thus, the short sections can be used to study in detail the some dynamical aspect of the cloud with limited compute power. The long section allows us to study the EC for a variety of magnetic fields and are also used for the simulation of the microwave experiment.

The propagation of a bunch train is simulated for about a fraction of one microsecond. Such a short time with respect to the cycle time of the synchrotron or even the duration of one Fermilab Booster batch (1.6 μ sec) is justified because the EC quickly reaches saturation ($\sim$ 100 ns), if dense enough. If the EC is thin, or evanescent, then longer simulation are needed, but such cases are of little interest, as such ECs will not cause beam instabilities.

Our main simulation tool: VORPAL

VORPAL[11] is a fully 3D code and self-consistent. By this we mean that, within the precision dictated the cell size and the time step, the kinematics of the electrons is correctly dictated by the e.m. field configuration and all fields are taken into account. All such calculations are 3D without requirements on symmetries of the boundary condition. The Courant condition that sets the consistency of the time step regarding to the cell size is always satisfied.

incorporate into the Synergia framework where numerous collective effect can be studied. This will allow us to study the impact of the EC on the beam itself.

[2]Assuming an ionization production $\approx$ 28 ions/cm at STP (assuming a typical Hydrogen, water, Nitrogen, CO mixture[15, 16]), per minimum ionizing protons, the seed density due to gas ionization is estimated to be $1.2\,10^6\ e/m^3$

[3]This is based on recent measurements using the ion profile monitor. Such measurement are a within 10 % of the advertised performance stated in reference [19]

Table 1: Current MI machine and beam parameters.

Parameter	**Value**
Dipole lengths	6.096 m and 4.064 m
Magnetic Field in dipole (20 GeV)	0.234 Tesla
Number of dipoles	216 and 128
Quadrupole Lengths	2.134, 2.539, and 2.945 m
Quadrupole gradient (20 GeV)	2.25 T/m
Number of quadrupole	128, 32 and 48
Length of all dipoles and quadrupole	2332.7 m
Total Length of MI	3319.4 m
Beam Pipe in the arcs minor/major radii	$2.39 \,/\, 5.88$ cm
Beam Pipe radius in straights	7.46 cm
Beam Pipe Material	16 gauge 316L stainless steel
Secondary Emission Yield 300 eV	$1.0 - 3.0$
Vacuum	$\approx 2.0\,10^{-8}$ Torr
Max. Num. of Protons per bunch	$1.0\,10^{11}$
Longitudinal emittance per bunch	$0.8 - 2.6$ eVs
Bunch Length	1 m to 0.3 m
Bunch Spacing	18.9 ns
Number of bunch per batch	70
Number of empty bunches between gaps	4
Abort gaps	$2 \times 0.8\mu$sec
Maximum number of batch	6
Number of bunches per batch	82
Empty bunches at end of batches	3
Normalized transverse emittance	15 to 25 π mm mRad
$\beta_x \sim \beta_y$ in the arcs	11 to 56 m
Bunch transverse size 20 GeV (r.m.s.)	≈ 3 to ≈ 6 mm
Beam Pipe Frequency Cutoff (in dipoles)	1.49 GHz
Microwave Frequency	1.538 GHz
Space between Emitter/Receiver	~ 13 m

The Furman & Pivi[21] model for secondary emission has been implemented in the Tech-X library [22], which is extensively used by the VORPAL code. In addition, the Vaughan model [25] has been implemented and an arbitrary SEY can be uploaded, allowing us to quantitatively determine the sensitivity of the EC effect to the so-called "true secondary" emission yield.

VORPAL runs on leadership class machine, such as the Blue-Gene P or the Cray. Parallelism is implemented in such a way that the casual user does not need to know nor understand the message passing interface MPI. However, targeted problem decomposition have been used to optimize performance, as discussed below.

EC VORPAL scripts and running conditions. As any general purpose codes, VORPAL needs to be customized to the specific problem at hand. This is done by writing specific scripts, which define the physical configuration of the currents and boundaries, initial condition of the cloud and electron emitters. A summary of the salient parameter is given on table 2

The cell size is dictated by the smallest feature in the problem, which, in our case is either the transverse beam size, or the physical size of the slits in the RFA's. Systematic uncertainties are estimated by simply looking at relative changes of the relevant quantities, such as the electron density of the EC, or the voltage on the simulated antenna in the case of the microwave absorption experiment, as a function of grid size. Those listed on table 2 are therefore typical and were not rigidly set at the onset of the calculations.

Two distinct types of boundaries are used: The elliptic (or cylindrical) beam pipe, transverse to the beam and the Perfectly Matched Layers (PML). These later types of boundaries simulate an infinitely long beam pipe on either end of the region of interest. They are particularly needed in detecting quasi plasma wave and the simulation of the microwave absorption experiment.

The initial state of the electron cloud is defined as follow. All electrons have negligible velocities, and are distributed uniformly along the beam axis, awaiting the passage of the first bunch. On the transverse plane we have a simple 2D Gaussian distribution, $\approx 3\times$ broader than the beam. Fortunately, the details of this initial state are inconsequential, as they are completely forgotten after the passage of a few bunches. The initial density is set typically

set at $2.5\,10^{11} m^{-3}$ and the maximum of macro-electrons per cell is initially set to 15. Results at saturation are found to be stable against an increase of such initial conditions.

The static magnetic field configurations (stated above) as well as the current sources are implemented via VORPAL functions and macros. There are two distinct types of current source in the problem: the proton beam itself and the current source responsible for the emission of the microwave generation, only used in the case of the simulation of the microwave absorption experiment.

The electromagnetic solver for cell close to the curved boundary (e.g., the beam pipe) uses the Dey-Mittra [23] cut cell method. A Boris integrator/propagator is used for the relativistic macro-electrons particle. These macro-particles are weighted: as their number grows exponentially at the beginning, the EC is culled and the weights are re-assigned. The probability for a macro-particle to disappear or being re-weighted is flat across the 6D phase space occupied by the EC. At any given time, all weights for all macro-electrons are identical.

The decomposition (i.e., the mapping of PIC cells to computer nodes) is regular and cells that are physically close to each others along the beam axis are preferably implemented on the same processors. This specific decomposition is advantageous because, in most cases, the transverse magnetic field is strong enough to confine the electrons close to the field lines, thereby limiting the transport of electrons along the beam axis. Thus, it make sense to sparsify the problem along the beam axis.

Finally, VORPAL generates multiple output files. Beside the usual log file, the state of the EC is given as a collection of 6D phase space coordinates, the e.m. fields value for each cell and the so-called VORPAL *History* files are extensively used throughout this simulation. These files contain user-specified quantities recorded at every time steps, such the e.m. potential between two points, the number of macro-electrons, allowing us to get a precise detailed picture of selected quantities throughout the simulation.

POSINST

The EC phenomena in the Fermilab MI has been simulated prior to this work [7] using the POSINST. Since VORPAL is a newcomer, it makes sens to compare the results obtained with VORPAL to previous results, and attempt to understand the differences. This benchmark must be at the same time relatively simple and yet relevant to the problem at hand. Thus, a realistic configuration of the beam pipe (elliptical see table 1) and the static magnetic (0.234 T.) is agreed upon. The same grid size transverse and the same SEY parameters are used. To avoid over-simplification, the beam is displaced vertically by 2.5 mm with respect to the center of the beam pipe. A relatively high SEY is used (reaching 2.2 at 300 eV) allowing us to shorten the growth time period and stress the codes, and the final density is higher than for evanescent ECs.

RESULTS

POSINST vs VORPAL: a specific benchmark.

A difference between VORPAL and POSINST relates to the dimensionality: VORPAL can either run as a 2D or 3D code, while POSINST is strictly a 2D+ code. This approximation is fully justified as long as the confining magnetic field is much larger than the transient magnetic field produced by the proton beam: net acceleration of the electrons occurs only along the field lines. Therefore a 2D, time dependent, "electrostatic" calculation is allowed. This has been tested in the VORPAL context, where the 4D proton beam current has been reduced to a time dependent charge density, neglecting the longitudinal current and thereby the magnetic induced by the beam. The VORPAL number of spatial dimension is set to 2. Indeed, the EC density obtained in VORPAL in this 2D and the usual 3D case are consistent.

As shown later, this density changes rapidly near the walls of the beam pipe. Consequently, one has to refine the grid near the curved surface to maintain accuracy. Integrated over the entire volume, changing the transverse grid size from 32×32 to 64×64 changes the estimate of the EC density by 20%. Fortunately, what counts is the EC density in the beam region: the e.m. forces on the protons induced by either free electrons very close to the beam pipe or on the beam surface are small, and nearly identical. Thus, we focused out attention on a 1 beam sigma cylinder centered on the beam. There, the a change of a factor 2^2 in grid size gives at most a 14% change in density.

Since the seed EC are completly different in VORPAL vs POSINST, the onset of the exponential growth can not be compared. Therefore, the POSINST and VORPAL curves have been shifted along the horizontal axes, and only the growth rate (exponential in both codes) and the saturation value can be compared. The details of the EC density at saturation, for POSINST and VORPAL are shown on figure 1. The EC densities in the beam region differ by a factor of ≈ 2. In addition, the growth rate is slower in POSINST. The root-causes of these discrepancies are currently under investigation.

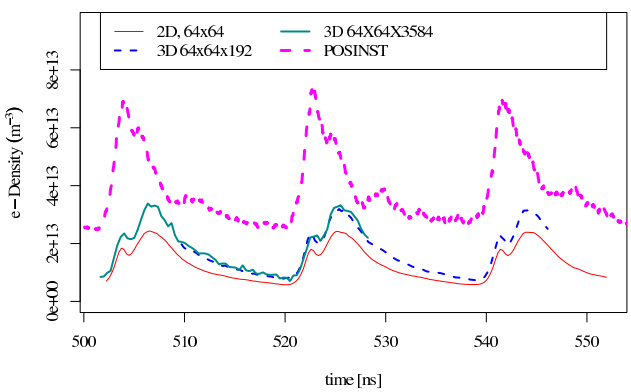

Figure 1: The EC density vs time, once saturation is nearly achieved, for POSINST and VORPAL, in the beam region.

Table 2: Relevant Simulation parameters.

Parameter	**Value**
Phyla Length	from 0.25 m to 16 m
Beam Pipe geometry	elliptical, or cylindrical, as real
Magnetic fields	See above
Number of Grid cells (small con fig.)	720 X 48 X 24
Number of Grid cells (large con fig.)	6144 X 48 X 48
PM Ls length	$\approx$ 1 to 3 m
Typical Time step	3.12 ps
Typical Num. of time steps	10^5
Typical Num. electrons/cell	20
Typical Nnum of processors	32 to 512
Beam Pipe geometry	elliptical, or cylindrical, as real
Bunch Length	0.3 m
Microwave frequency	1.538 GHz
Microwave Electric Field	20 to 100 V/m
BPM dist. emitter/receiver	3.5 m

Growth rate, saturation and decay rate of the EC.

The EC density, based on a VORPAL calculation, for a few different SEYs is shown on figure 2. The SEY curve follow the Vaughan model[25]. The long section of the beam pipe comprising two dipoles and one quadrupole has been used. A proton bunch intensity of $7.\,10^{10}$ is assumed. Evidently, both the growth rate and the saturation value of the density depends on the assumed SEY. Cases where the initial EC has a very long growth time, or the seed EC diffuses away, have not been studied extensively, as they correspond to an nonexistent EC problem. This occurs for $SEY_{max} \leq 1.3$. Despite the factor ≈ 2 discrepancy in the EC density stated above, this critical SEY_{max} value is consistent with the other 2D codes.

For relatively large SEY_{max} ($\geq$ 2.), the saturation is reached after just a few bunches. Low energy secondary electrons emitted from the wall are no longer accelerated efficiently by the proton beam as they are repulsed by the pre-existing electrons from the cloud. This screening effect is a result of the self-consistency of the PIC simulation. No ad hoc processes have been added to reach, or tune, this saturation. Average over ≈ 1 bunch width, the linear density along the beam axis (i.e., integrated over the transverse dimension) of the EC is about $70 \pm 10\%$ of the linear charge density in the bunch.

In absence of beam, electrons drift back the walls of the beam pipe. The decay rate of the EC is dictated by the average velocity along the magnetic field line. Typical values for this decay time range from 30 to 100 ns. Deviation for a simple exponential are substantial, because this decay is not a stochastic process, but a causal change, where fast electrons disappear first.

Sensitivity of the EC density to the SEY_{max} and the bunch intensity.

A critical issue for the Fermilab High Intensity frontier program[5] is to determine the additional beam disturbances and losses that are putatively caused by an enhanced EC problem. Unfortunately, given the uncertainty in the SEY_{max} for the "scrubbed" (i.e., processed by the beam) MI beam pipe, no reliable *ab-initio* predictions for the EC density and the related electric field maps can be generated at this point in time. However, if a moderate value for SEY is assumed - and this is justified by the fact that the EC problem does not currently limit the performance of the MI -, our result indicates that increasing the bunch intensity will not trigger a significant, non-linear, rise in the EC density, as shown on figure 3. This happens despite an increase of the peak electric field because the SEY no longer increases above ≈ 300 eV.

This happy conclusion seems robust against changes in the beam parameters: More intense bunches is likely to cause an increase the beam emittance (via space charge effects at injection, for instance), which itself implies weaker accelerating fields for the electrons in the cloud. Again, in this regime, the SEY weakly depends on the kinetic energy of the electrons.

Some detailed results on electron kinematics, Electric Field and plasma waves

Prior to discuss the experimental program, various observations on the morphology in 6D phase space of the EC are noteworthy. The spatial (longitudinal and transverse) distribution of the electrons in the cloud are shown on figure 4 and figure 5, respectively. The dynamics is also illustrate there via the rapid ($\approx$ ns) change in the local density of cloud. Except for about one ns just after the passage of the bunch, the highest density is always close to the wall

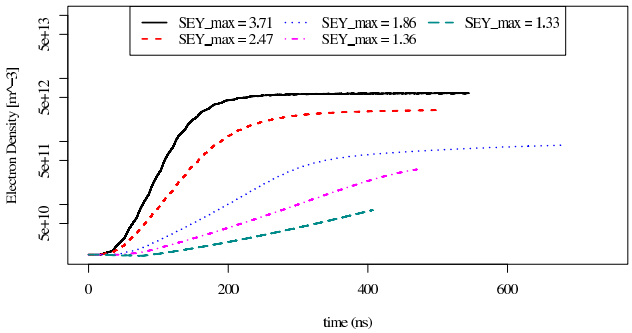

Figure 2: The EC density vs time, at the beginning of a bunch train, for about 10 to 25 MI bunch spacing, illustrating the initial exponential growth and it's saturation, if the SEY is high enough. The seed density is arbitrary, but realistic. This illustrates the sensitivity to the maximum of the SEY.

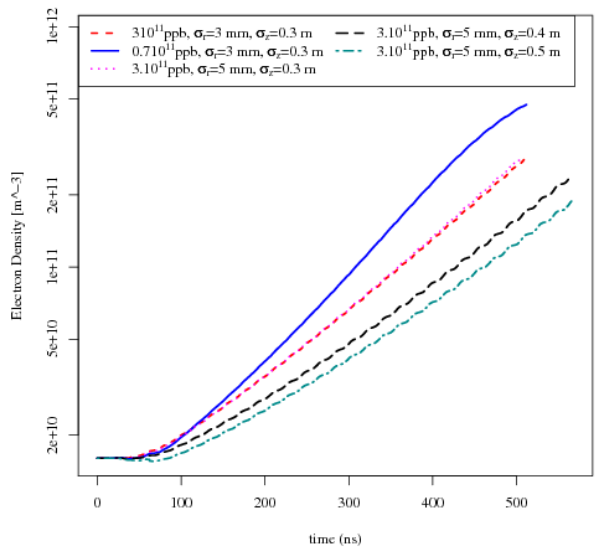

Figure 3: Similarly to the previous plot, The EC density is shown vs time, for various beam conditions. σ_r and σ_z corresponds to the average beam radius and bunch length, respectively. For a moderate value of SEY of 1.36, the worst case scenario corresponds to the current operating conditions and not those expected in the Project-X era.

and can be almost two orders of magnitude higher than at the center of the beam pipe.

The EC density depends on the confining magnetic field, even when the EC is nearly saturated. The fluctuations of the density during and in-between bunches has a non-trivial dependence on this magnetic field, as shown on figure 6 for large SEY_{max} and at stable saturation (i.e., the density averaged over one bunch crossing is stable over time). Also shown on this figure is the mean kinetic energy vs distance from the closest bunch. Highest densities occurs in the drift regions, because net acceleration along the electric field lines induced by the passage of the proton bunch can occur in all transverse directions. The average kinetic energy is highest in the dipoles, presumably because the electric field created by the bunch, tends to be parallel to the magnetic field lines, allowing for efficient acceleration. Except in the fringe regions, the mean velocity along the beam axis is negligible compared the transverse velocities, even in absence of magnetic field.

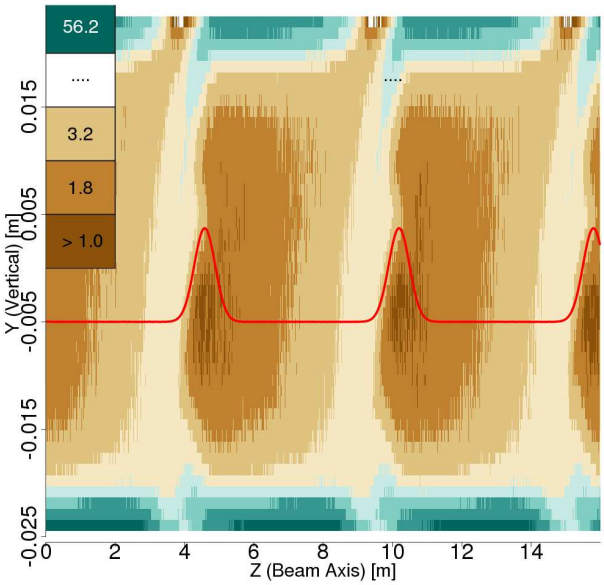

Figure 4: An false color map of the longitudinal profile of the EC density in a dipole and for a continuous bunch train. The color scale is logarithmic. infinitely long dipole and a continuous sequence of bunches. The EC is fully saturated with $SEY_m \approx 2.2$. The proton bunch intensity is $0.7\,10^{11}$. The proton beam (red line) is displaced by 5 mm downwards, which makes the EC top-down asymmetric.

For near critical SEY, the EC will vanish in the quadrupoles and be the highest in the field free regions, as shown on figure 7[4]

From these results, it is clear that the EC density fluctuates at 53 MHz (the bunch crossing frequency), with frequency components up to a few GHz (related to the bunch length.) It is also strongly anisotropic, with at least a strong quadrupole component, if not higher multipoles. Thus the EC will produce electromagnetic wave. While the low frequency component can not propagate in the beam pipe (the cutoff for the fundamental mode being at 1.56 GHz), higher order modes are induced and could be detected. In our simulation, the "pseudo-potential"[5] in between the top and bottom plates of BPMs is recorded for every time step. A straightforward Fourier transform reveals these electromagnetic waves produced by the EC, as shown on figure 8. Evidently, such calculations must be done with the E.M.,

[4]By "field free", we mean the external $B_x = B_y = B_y = 0.$, exactly.

[5]The line integral of the electric field along a specific (and easy to compute) and fixed path, i.e., in our case, along the vertical axis.

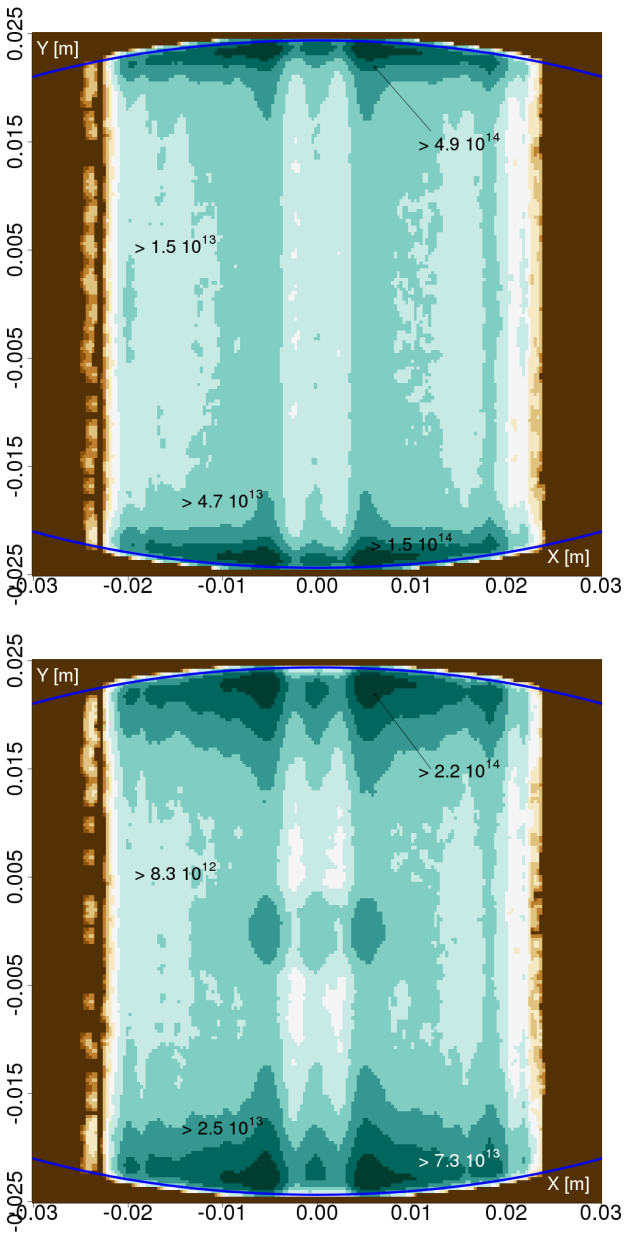

Figure 5: Transverse profile of the EC density. Top: at the beginning of the relaxation phase, when the density reaches a maximum. Bottom: during the pinch phase, when the density is minimum, as the electrons have just migrated away from walls and a diffused excess is seen around the beam spot.

3D VORPAL code and not the relatively 2D code.

As in any complete PIC E.M. code, VORPAL also provided e.m. field maps. Of particular interest is the electric field induced by both the proton beam and the EC, as our ultimate goal is to model these fields such that they can be incorporated in advanced accelerator simulation codes that model non-linear and collective effects [27] Such an example field map is given on figure 9.

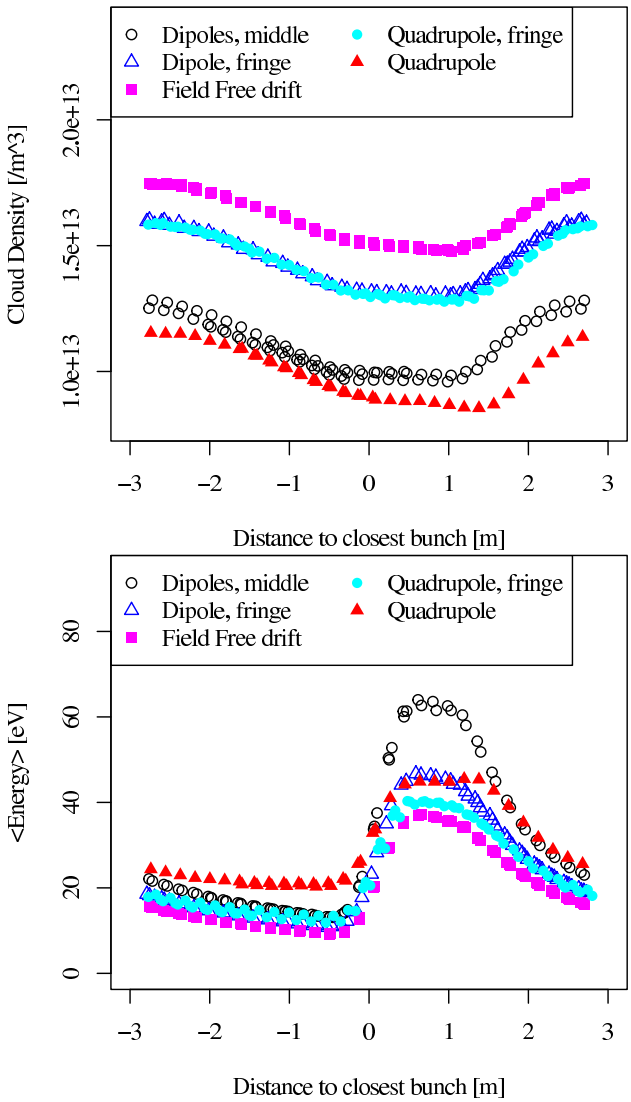

Figure 6: Top: Fluctuation of the EC density averaged over a 40 cm long section of the beam pipe as a function of the distance to the closest proton bunch, for different magnetic field configurations and $0.7\,10^{11}$ Bottom: based on the same configuration the average kinetic energy of the electrons in the cloud.

On the RFA response

A few Retarting Field Analyzers (RFA) have been recently installed in a field free of the Main Injector, where the beam pipe is cylindrical, 6" diameter [8]. Slits allowing electrons to drift into these devices are located on top or bottom of the pipe and have transverse (longitudinal) openings of about 4 mm (2.5 cm), respectively. In VORPAL, such slits are simulated by simply setting the SEY to zero at their location. Fluctuations of the EC density at the slit location can then be extracted from the simulation and are expected to reflect the electron count in these RFAs. An energy cut can be applied to the VORPAL macro-electrons, thereby simulating the effect of the voltage applied on the RFA grid.

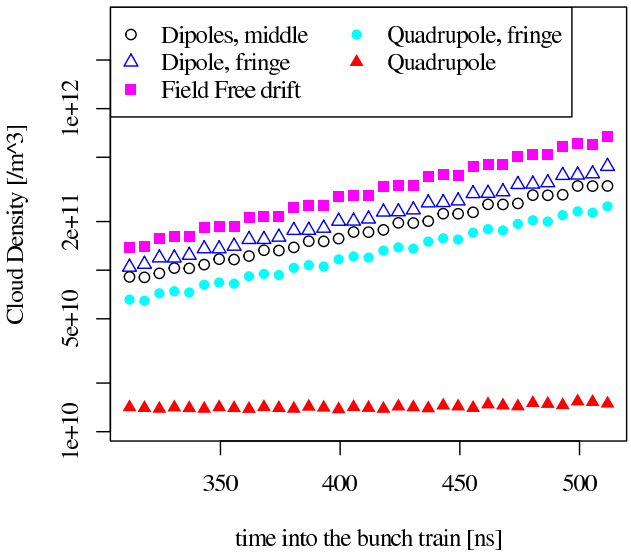

Figure 7: Dependence of the EC exponential growth on the magnetic field configuration, in the case where the SEY is near critical.

Abrupt variations of the electric field near the slits (Edge effects) are ignored in this crude simulation. A more exact implementation would include the precise geometry of the RFA grid and its detector. Since these detectors are quite small with respect to the total size of the beam pipe and VORPAL PIC grid has to be uniform, this refinement has not been implemented. However, a much bigger uncertainty comes from the largely unknown stray magnetic fields due to the dipole and quadrupole bus that are running along the beam line. A field of ≈ 3 to 6 Gauss at one of the RFA location has been detected. More detailed maps will be required to compare data to simulation. Meanwhile, as to illustrate the importance of weak magnetic fields in relation to the spatial distribution of the EC, figure 10 shows the transverse distributions of the electrons in the beam pipe for a uniform stray field of 10 Gauss oriented at 45 degrees, perpendicular to the beam axis.

The Microwave absorption experiment

Multiple types of instrument are needed to characterize the EC. Microwave transmission measurements are non-invasive and relatively cheap to implement. The absorption and re-emission of microwave photons by the e-cloud causes a detectable phase shift in this microwave field. This phase shift is related to the density of the e-cloud [28]. Our original intend was to compare our simulation results to real data taken at the MI [9]. However, significant problems were found at a later stage with the measurement technique: The chosen frequency was very close to the cut-off frequency of the elliptical beam pipe ($\approx$ 1.54 GHz) and, consequently, the transmission efficiency was found to be depend critically on the details of beam pipe (pressure valves, bellows, etc) and to actually change during data taking. That is, the effective length between the receiving and emitting antennas was difficult to determine. Yet, for sake of completion, the phase shift calculated for the long (dipole, quadrupole, dipole) section of the MI is shown on figure 11. As in the simple linearized theory, the phase shift is a good measure of the density.

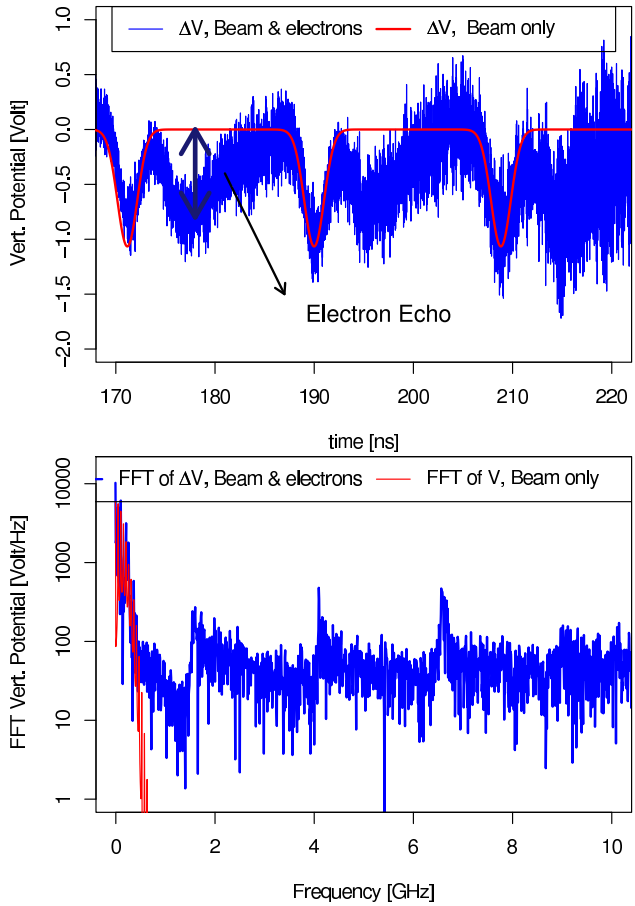

Figure 8: Top: The VORPAL pseudo voltage between the top and bottom plate of a virtual BPM in a dipole, when the beam is displaced vertically by 2.5 mm. In this case where the $SEY = 2.2$ and therefore the EC is saturated. About one ns after the passage of the bunch, the EC re-arrange itself, producing an "echo" signal. Bottom: the Fourier transform of this signal, showing clearly the low frequency cutoff and the higher order mode for this elliptical cavity.

SUMMARY

The electron cloud in the Fermilab Main Injector has been simulated in details using a 3D, self-consistent code, VORPAL. This PIC code is relatively new to our EC community and has been bench marked against the existing POSINST code and current discrepancies are under study. Meanwhile, the self-consistency of our VORPAL results has been checked and details map of the EC density and electric field have been computed. Such field map could be included in the Synergia framework. While the uncertainty in the SEY is such that no accurate predictions for the EC

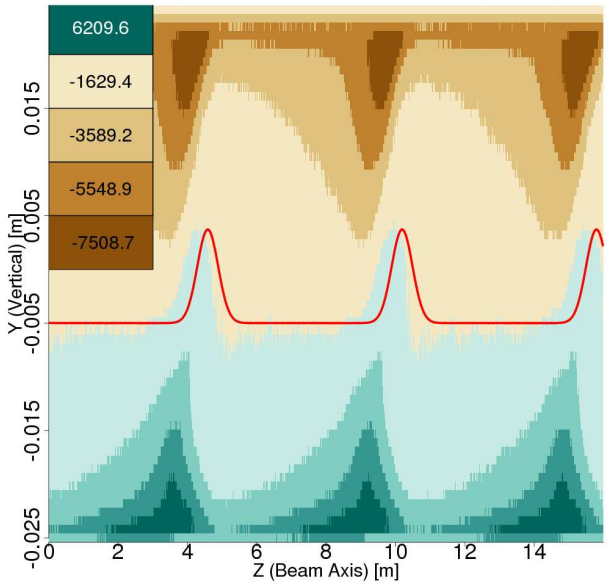

Figure 9: A color map of the projected electric field produced by both the proton bunch and the EC. The setup and beam conditions are those corresponding to the results presented on figure 4.

density can be made in the MI case, our results indicate that if the EC is thin enough not to cause beam instabilities it is then likely that the SEY is rather low ($\leq$ 1.36). In this case, our calculation shows that we should not see a dramatic increase of the EC during the project X era.

Despite the lack of precise predictions for the EC density, this simulation effort is worthwhile, as it provides guidance in establish a robust experimental program. More specifically, the value of the stray magnetic field at the RFA position must be determine. Since the SEY depends on the beam induced scrubbing, this crucial parameter must be determined *in-situ* and inside a magnetic field commensurate with the one used in the dipole or quadrupole. A dedicate set of two small dipoles equipped with instrumentation, retractable sample holder and an electron gun (to measure the SEY) should be installed in one of the available straight section of the MI.

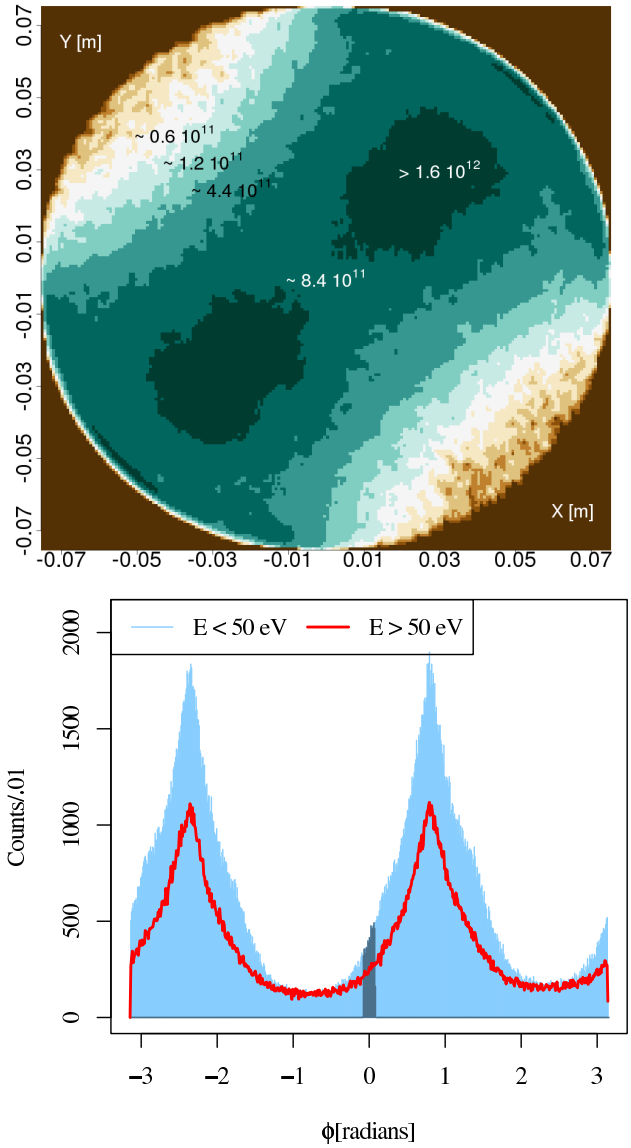

Figure 10: Top: A false color map of the EC density, transverse projection in the circular beam pipe supporting the RFA, as the EC is pinched by the passage of the bunch. The slits of the RFA are highlighted on the top of the cylindrical beam pipe. Bottom: Histograms of the azimuthal angle from the same data set. Again, the highlighted region is where the EC is sampled.

Acknowledgments

We thank Jim Amundson and Bob Zwaska from the Fermilab APC group for very productive discussions on the analysis of the data generated by VORPAL. Xiaolong Zhang ran successfully the POSINST code for the benchmark. We also acknowledge the other members of the VORPAL team: D. Alexander, K. Amyx, T. Austin, G. I. Bell, D. L. Bruhwiler, R. S. Busby, J. Carlsson, E. Cormier-Michel, Y. Choi, B. M. Cowan, D. A. Dimitrov, M. Durant, A. Hakim, B. Jamroz, D. P. Karipides, M. Koch, A. Likhanskii, M. C. Lin, J. Loverich, S. Mahalingam, P. Messmer, P. J. Mullowney, C. Nieter, K. Paul, I. Pogorelov, V. Ranjbar, C. Roark, B. T. Schwartz, S. W. Sides, D. N. Smithe, A. Sobol, D. J. Wade-Stein, G. R. Werner, N. Xiang, C. D. Zhou.

This work was supported by the United States Department of Energy under contract DE-AC02-07CH11359 and the ComPASS project funded through the Scientific Discovery through Advanced Computing program in the DOE Office of High Energy Physics. This research used resources of the National Energy Research Scientific Computing Center, which is supported by the Office of Science

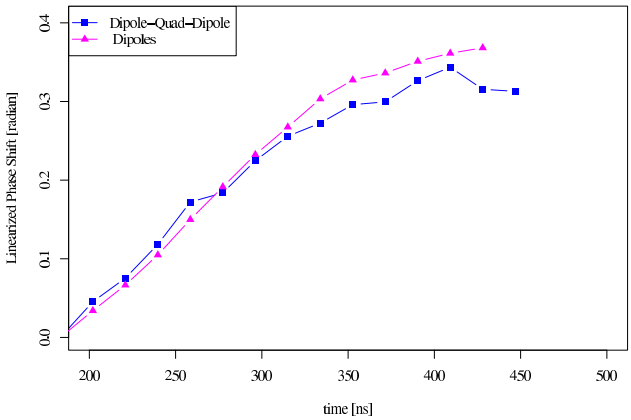

Figure 11: The simulate phase shift for the infinitely long dipole and for a more realistic implementation of a short section of the MI. The setup and beam conditions are those corresponding to the results presented on figure 4.

of the U.S. Department of Energy under Contract No. DE-AC02-05CH11231. This research used resources of the Argonne Leadership Computing Facility at Argonne National Laboratory, which is supported by the Office of Science of the U.S. Department of Energy under contract DE-AC02-06CH11357.

REFERENCES

[1] Phys. Rev. ST Accel. Beams 7, 124801 (2004)

[2] A. Z. Ghalam *et al.*, Phys. Plasmas 13, 056710 (2006)

[3] M. T. Pivi and M. A. Furman, Phys. Rev. ST Accel. Beams **6**, 034201 (2003).

[4] M.A. Palmer *et al.*, "Electron Cloud at Low Emittance in CesrTA", IPAC10, Kyoto, Japan, May 2010

[5] S. Holmes, "Project X: A multi-MW proton source at Fermilab" IPAC10, Kyoto, Japan, May 2010 http://accelconf.web.cern.ch/AccelConf/IPAC10/talks/tuyra01_talk.pdf

[6] A. Ghalam *et al.*, "3-D parallel simulation of continuous beam-cloud interactions", in *Proceedings of the 31st ICFA Beam Dynamics Workshop: Electron Cloud Effects*, Napa, CA, 2004, edited by M. Furman, SLAC-PUB-10751 (ECLOUD04).

[7] X. Zhang *et al*, FERMILAB-CONF-07-214-AD (June 2007), Proceedings of Particle Accelerator Conference (PAC07), Albuquerque, New Mexico, 25-29 Jun 2007, pp 3501 http://accelconf.web.cern.ch/AccelConf/p07/PAPERS/THPAN117.PDF

[8] C.Y. Tan, K.L. Duel, R. Zwaska, (Fermilab) . FERMILAB-CONF-09-141-AD, Apr 2009. 3pp. Presented at Particle Accelerator Conference (PAC 09), Vancouver, BC, Canada, 4-8 May 2009.

[9] N. Eddy *et al*, FERMILAB-CONF-09-168-AD (May 2009) 3p. Presented at Particle Accelerator Conference (PAC 09), Vancouver, BC, Canada, 4-8 May 2009.

[10] C. Yim Vallgren,*et al.*, "Low secondary electron yield carbon coatings for electron cloud mitigation in modern particle accelerators", IPAC10, Kyoto, Japan, May 2010.

[11] C. Nieter and J. R. Cary,"VORPAL: a versatile plasma simulation code", J. Comp. Phys. 196, 448-472 (2004).

[12] The Fermilab Main Injector Technical Design Handbook, http://www-fmi.fnal.gov/fmiinternal/MI_Technical_Design/index.html and The Main Injector Rookie Book, http://www-bdnew.fnal.gov/operations/rookie_books/Main_Injector_v1.1.pdf.

[13] B. Henrist *et al.*, Proceedings of EPAC 2002, Paris, France, p. 2553 http://cern.ch/AccelConf/e02/PAPERS/WEPDO014.pdf

[14] N. Hilleret *et al.*, Proceedings of EPAC 2000, Vienna, Austria, p. 217 http://cern.ch/AccelConf/e00/PAPERS/THXF102.pdf

[15] J. R. Zagel *et al* Proceedings of the Particle Accelerator Conference, Vancouver, Canada, p. 2166 http://cern.ch/AccelConf/pac97/papers/pdf/5P052.PDF

[16] Sauli, F., Principles of Operation of Multiwire Proportional and Drift Chambers, CERN 77-09, 3/5/1977

[17] Ed Barsotti *et al* Proceedings of the 1999 Particle Accelerator Conference, New York, 1999 http://cern.ch/AccelConf/p99/PAPERS/WEA149.PDF

[18] I. Kourbanis and D. Capista Private communication, March 2010

[19] Stephen D. Holmes, Proceedings of the Particle Accelerator Conference, Vancouver, Canada, p. 47 http://cern.ch/AccelConf/pac97/papers/pdf/2B001.PDF

[20] P. Adamson *et al*, Proceedings of the 2005 Particle Accelerator Conference, Knoxville, Tennessee http://cern.ch/AccelConf/p05/PAPERS/MPPP015.PDF

[21] M. A. Furman and M. T. Pivi, Phys. Rev. ST Accel. Beams **5**, 124404 (2002).

[22] . H. Stoltz and M. A. Furman and J.-L. Vay and A. W. Molvik and R. H. Cohen, "Numerical simulation of the generation of secondary electrons in the High Current Experiment", *Phys. Rev. ST Accel. Beams*, **6**, 054701, doi:10.1103/PhysRevSTAB.6.054701, 2003.

[23] VORPAL reference manual, v4.0, p. 86.

[24] Wolfgang S. M. Werner *et al* Phys. Rev. **B 78**, 233403 (2008).

[25] Arnold Shih and Charles Hor, IEEE Transactions on Electron Devices, Vol 40, **4**, April 1993.

[26] M. A. Furman, private communication in the context of the Compass Collaboration, 2008.

[27] J.F. Amundson *et al* Proceedings of Hadron 2008, Nashville, Tennesse, http://accelconf.web.cern.ch/AccelConf/HB2008/papers/wga08.pdf

[28] Kiran Sonnad *et al*, "Simulation and analysis of microwave transmission through an electron cloud, a comparison and results." PAC'07, THPAS008, May 2007, Albuquerque, New Mexico, p. 3525, `http://www.JACoW.org`.

MODELING ELECTRON CLOUD BUILDUP AND MICROWAVE DIAGNOSTICS USING VORPAL *

S. A. Veitzer†, Tech-X Corporation, Boulder, CO, 80303 USA
K. G. Sonnad‡, Cornell University, Ithaca, NY 14853, USA
P. L. G. LeBrun§, Fermilab, Batavia, IL 60510, USA
P. H. Stoltz¶, Tech-X Corporation, Boulder, CO, 80303 USA

Abstract

Electron cloud effect may seriously limit future accelerator performance when electron plasmas build up enough to cause instabilities in beams. Detailed simulations of electron cloud buildup, effects on beams, and mitigation will increase future accelerator performance and provide aid in the effective design of future accelerators. We present results of recent VORPAL simulations directed at modeling of microwave diagnostic experiments for measuring electron cloud effect. We focus on the effects of spatial non-uniformity of electron clouds on phase shift measurements and on directly correlating observed side-band amplitudes with cloud density.

SIMULATION OF ELECTRON CLOUDS ENHANCES ACCELERATOR PERFORMANCE

VORPAL

The VORPAL [1] code, a 3D finite-difference time-domain (FDTD) electromagnetics code, is designed for massively parallel distributed computing as well as for running in serial on desktop computers. Domain decomposition, a technique in which a large computational physical domain is split up into smaller pieces, which are then distributed on many different processes, is a powerful method for parallel computing, and is used extensively in VORPAL in order to improved computational performance and enable researchers to address very large simulation problems with short time scale resolution. VORPAL is appropriate for simulating traveling-wave diagnostics of electron clouds, both because it has the ability to span large spatial scales (determined by the system geometry) as well as short time scales (determined by the frequency of the rf and the spatial resolution), and because it can capture 3-Dimensional effects, such as the role of quadrupole magnets on electron density profiles. VORPAL also includes full models for complex electromagnetic-particle-boundary interactions, including embedded cut-cell geometry (2nd order accurate for the calculation of EM fields), self-consistent EM fields, including the effects of space charge, secondary electron emission, and self-consistent kinetic particle motion.

Figure (1) shows a typical VORPAL simulation layout. The beam pipe can be constructed with different cross-sections, such as circular, elliptical, or rectangular, depending on the system being modeled. The ends of the simulation domain contain Matched Amplitude Layers (MALs) or Perfectly Matched Layers (PMLs) which absorb EM waves and damp them out so that there are not numerical reflections off the end of the simulation domain. The electron cloud is represented by kinetic particles which evolve under the influence of electric and magnetic fields from various sources, such as a simulated rf signal traveling down the beam pipe, a beam current, externally defined magnetic fields, and space charge. Typically, an artificial current density at one end of the simulation, oscillating at the rf frequency, is added to generate a traveling rf signal, which passes through the electron cloud and can be measured on the other side. Phase shifts induced in this rf signal can be measured by comparing simulations with and without an electron cloud. In addition, long time-scale simulations to address electron cloud buildup under different conditions (external magnetic field configurations, secondary electron yield profiles, simulation geometry) have been carried out using a similar simulation setup, and are reported elsewhere [2].

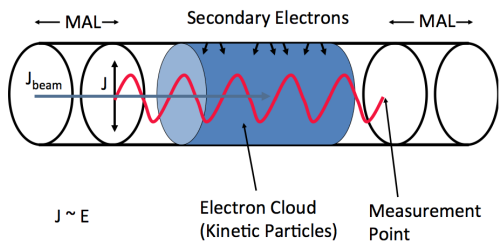

Figure 1: Typical diagram of a VORPAL electron cloud and microwave diagnostic simulation.

Simulation of Traveling Wave rf Diagnostics

In the simulation setup described above, traveling rf waves are emitted from the source current in both directions. The backward-propagating wave is almost immediately absorbed by the MAL or PML which is specifi-

* Part of this work was performed under the auspices of the Department of Energy as part of the ComPASS SCiDAC project (DE-FC02-07ER41499) and through the Small Business Innovation Research program, as well as through a subcontract from Cornell University

† veitzer@txcorp.com
‡ kgs52@cornell.edu
§ lebrun@fnal.gov
¶ pstoltz@txcorp.com

cally placed at the ends of the simulation region to absorb the waves without significant reflections. The forward-propagating wave travels through the electron cloud and is absorbed by a MAL or PML on the other end of the simulation. Measurement of the wave amplitude and phase is done just upstream of the absorbing layer. Phase shifts due to an electron cloud can be measured by conducting two simulations, one with electrons and one without, and then directly comparing the two resulting time series' using simple trigonometric expansions.

For uniform density clouds, theory predicts that the phase shift per unit length is

$$\frac{\Delta\Phi}{\Delta L} = \frac{\omega_p^2}{2c\left(\omega^2 - \omega_c^2\right)^{1/2}} \tag{1}$$

where ω is the rf frequency, ω_c is the cutoff frequency, and $\omega_p = \sqrt{n_e e^2/\epsilon_0 m_e}$ is the plasma frequency. Simulations for uniform density clouds [3] agree well with the linear theory, as is shown in Fig. (2).

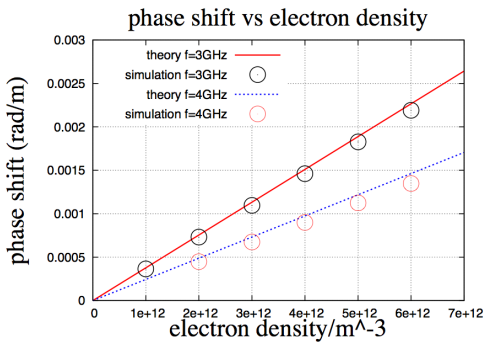

Figure 2: Phase shift against cloud density for uniformly distributed clouds. Simulated phase shifts correspond well with linear theoretical predictions. Figure reproduced from [3].

Cyclotron resonances have also been measured using VORPAL simulations with a similar setup, but with an additional externally applied magnetic field. A transversely directed dipole magnetic field will excite an upper-hybrid resonance if the applied field is normal to the rf electric field. Since the plasma density is low, the cyclotron frequency is nearly the same as the upper hybrid frequency, and is given by

$$\omega_{uh} \approx \omega_{ce} = \frac{qB}{m_e c} \tag{2}$$

Researchers [4] have simulated the cyclotron resonance using VORPAL by performing simulations of the transmission of TE_{11} and TM_{01} waves through cold electron clouds with externally applied dipole fields that are oriented in different directions and with different strengths. Figure (3) shows a comparison of these simulations for TE_{11} waves with an experimental measurement made at the PEP II facility [5].

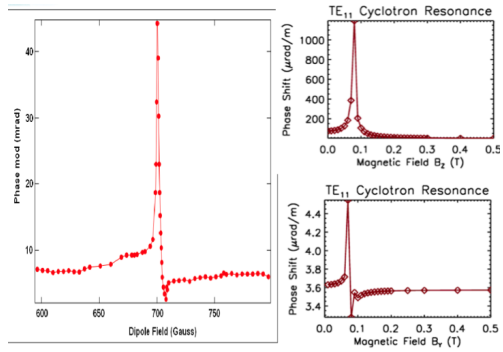

Figure 3: Cyclotron resonance in electron cloud-induced phase shifts. The left hand plot is reproduced from [5], from an experiment on the positron ring of PEP-II. The right hand plots show simulated phase shifts measured when the magnetic field is normal to the rf electric field (B_z) and parallel to the rf electric field direction (B_y). Small shifts in the second case are due to discretization errors in the simulation, and are on the order of 0.4%.

NON-UNIFORM DENSITY CLOUDS AND CONSEQUENCES FOR TRAVELING WAVE EXPERIMENTS

Theoretical models for phase shifts induced by electron clouds in traveling rf experiments typically assume that the clouds themselves are spatially uniform. However, cloud density evolves and grows as bunches accelerate electrons to the beam pipe walls, creating secondary electrons, and clouds typically disappear on a beam revolution time scale as gaps in the bunch train provide enough time for the cloud to relax and electrons to be reabsorbed. Even when averaged over a bunch-crossing or revolution time scale, the spatial distribution of electrons in a cloud is not necessarily uniform, as is demonstrated in Figure (4). The figure shows integrated cross sections of particle positions for four different magnetic field configurations and three different times in VORPAL simulations in an elliptical beam pipe section (Main Injector). The first column represents the time of first bunch crossing, 17 ns into the simulation. The middle and right-hand columns are snapshots of electron distributions at 500 ns and 1000 ns respectively. The top row in the figure corresponds to a simulation with no applied magnetic field, and the oscillating effect of bunch crossings can be seen. The second row shows that a modest solenoidal field (10 G in this case) can be effective in confining secondary electrons close to the beam pipe walls. However, the third row shows that an additional small transverse dipole field (10 G in the vertical direction here) negates the effect of the solenoidal field. Finally, the bottom row shows that a very non-uniform banded structure appears when a significant dipole field is attached. In this case a 2350 G vertical dipole field is applied to the simulations. Note that the cross section is elliptical in these simulations, with an aspect ratio of nearly 2:1, which ex-

plains the increased density near the top and bottom poles in some of the plots.

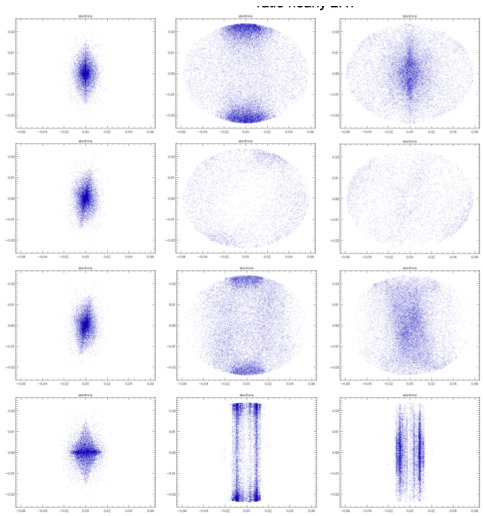

Figure 4: Non-uniformity in electron cloud distributions depends on the magnetic field configuration. A comparison of different VORPAL simulations at 17 ns, 500 ns, and 1000 ns (columns 1, 2, and 3 respectively). Magnetic configurations are (top) no external fields, (second row) 10 G solenoidal field out of the plane, (third row) 10 G solenoidal and vertical dipole fields, and (bottom) 2350 G vertical dipole field.

Experimental determination of electron cloud densities using traveling wave rf diagnostics do not directly measure phase shifts such as can be done in simulations. Typically traveling wave experiments will observe side bands at multiples of the beam revolution frequency because over long time scales the electron cloud is modulated because gaps in the bunch train allow sufficient time for the cloud to relax and the electrons to be absorbed into the beam pipe walls. The amplitude of observed side bands depends on the cloud density, and as such the ratio of the side band amplitude to the carrier amplitude is a good relative measurement of the cloud density. However, it is very difficult to deduce absolute density from side band measurements, because the theoretical treatment for traveling wave rf diagnostics assumes uniform density clouds.

Inasmuch as phase shifts are relatively larger in spatial locations where the transverse electric field of the rf are big, it may be possible to use higher order rf modes to characterize non-uniformity in electron cloud densities. For example, the lowest order mode and circular cross section beam pipe, TE_{11}, has oscillates with a spatial pattern that has a large transverse E component around the center of the beam pipe, as is depicted in figure (5). The direction of propagation here is the X-direction, so large electric field components in the Y and Z directions indicated a TE mode.

To test whether higher order modes can measure non-uniformity in electron clouds, we performed a large number of numerical experiments with different rf modes, and

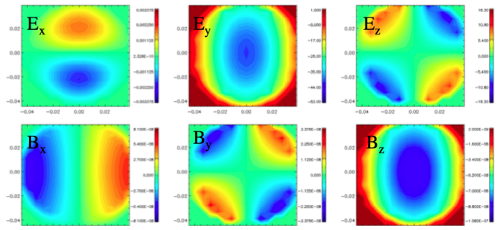

Figure 5: Electromagnetic field components for a TE_{11} in a circular cross section beam pipe.

computed phase shifts for different non-uniform cloud densities. To do this, we arranged electrons in concentric rings, as is depicted in figure (6).

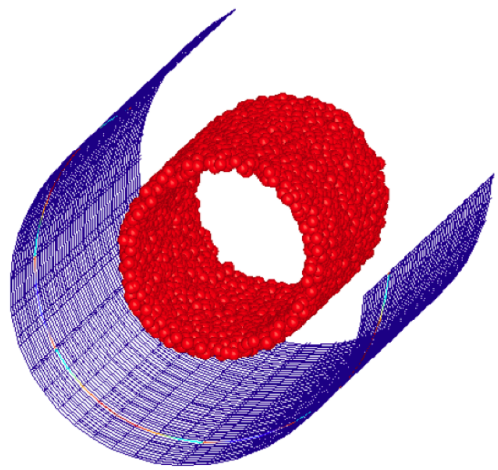

Figure 6: Typical simulation design for measuring electron cloud nonuniformity using phase shifts induced in higher order modes.

We then propagated higher order modes through the rings of electrons and computed the phase shifts using techniques described above. The results are shown in figure (7). In the figure, the phase shifts are plotted against the radius of the ring of electrons that makes up the cloud. Phase shifts do show a strong dependence on the location of the electron cloud, and in addition, the phase shift for a given cloud radius depends on the rf mode in a way that reflects the spatial pattern of the rf electric field. This analysis suggests that it might be possible to use simultaneous injection of multiple modes, both TE and TM, to measure non-uniformity in cloud density. However, there are technical obstacles to this related to power transmission and detection of higher order modes. In addition, experiments with higher order modes are likely to exhibit greater rf attenuation due to the higher frequencies involved. This is also problematic because amplitude modulation, and the loss of rf power to lower-frequency modes in not distinguishable from phase modulation.

The bottom-right plot in figure (7) is an analysis of the phase shifts for a TE_{13} mode, where the electrons in the right have a Gaussian profile, rather than being uniformly

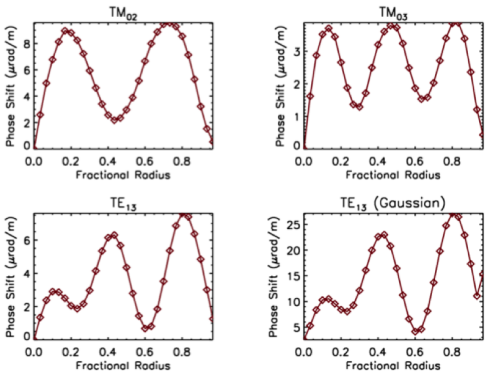

Figure 7: Higher-order mode phase shifts induced in non-uniform electron clouds as a function of radial location of the electron cloud rings.

distributed, but with the same average electron density over the ring. Comparison with the bottom-left plot shows that the exact form of the cloud is not important, but rather the radial location of cloud is the dominant factor in determining the phase shift for higher order modes.

DETERMINATION OF CLOUD DENSITY FROM SIDE BAND MEASUREMENTS

The deduction of electron cloud densities from traveling wave sideband measurements is difficult experimentally. There are a number of reasons for this, including (1) Theoretical considerations assume that the average cloud density is uniform, (2) Reflections of rf and other structural effects in the beam pipe means that the path length of the rf, and thus the amount of cloud sampled by the rf, is not accurately known, (3) amplitude modulation and loss of transmitted power is not distinguishable from phase modulation.

Straightforward time-domain simulation of electron cloud modulation is also difficult. In order to resolve side bands at the beam revolution frequency, overall simulation time needs to be at least on the order of a revolution period. However, this time scale is very long compared to a typical simulation time step, which needs to be small enough to resolve the rf wave. For instance, to achieve 10 kHz resolution, at least $200\mu s$ of overall simulation time is needed. With a 1 ps time step, needed to resolve a ~ 2 GHz rf signal, requires 2×10^8 time steps. In addition to long simulation times, numerical inaccuracies may cause problems with such long simulation times.

One possible solution to this problem is to modulate the electron weights in simulations at the revolution frequency, which will allow for the reconstruction of the spectra and associated side bands with much shorter simulation times. An example of this method is shown in figure (8). Three different cloud shapes were considered, and the particle weights were harmonically modulated at 10% of the carrier frequency (1.6 GHz). Thus side bands are observed at intervals of 160MHz from the carrier, as can be seen in the figure. As expected, the round and rectangular clouds showed about the same side band amplitude, while the striped cloud had a significantly lower side band amplitude. This is due to the non-uniformity effects described earlier, where the rf signal interacts with the cloud primarily where the transverse electric field of the rf is greatest.

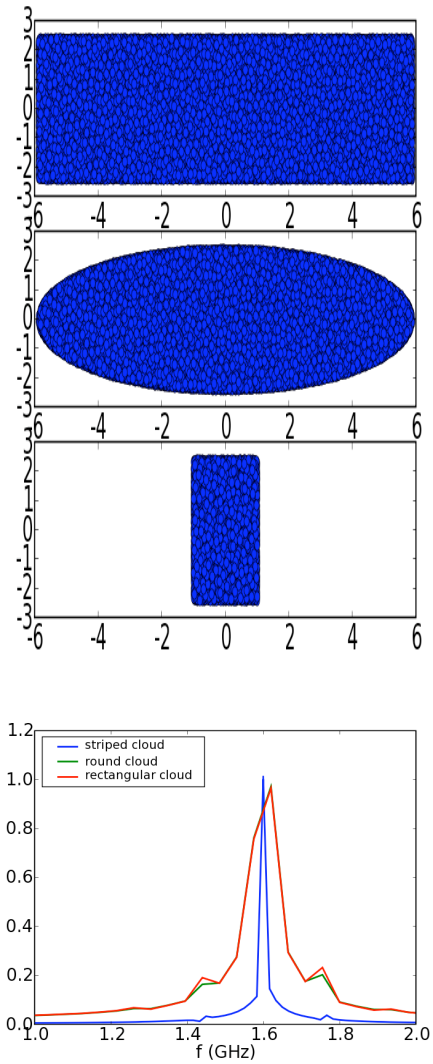

Figure 8: Simulated Fourier spectra for three different electron cloud shapes using explicit particle weighting modulation.

While the method of harmonic modulation of particle weights can reduce simulation times, the simulations are still subject to numerical instabilities due to grid heating for longer simulation times. A solution to this numerical problem is to replace simulation particles with an equivalent plasma dielectric substance. Since it is the dielectric properties of the electron plasma that induces phase shifts, a linear plasma dielectric model for the electrons can be used to effectively model traveling TE wave diagnostics.

The advantage to a plasma dielectric model is that one can avoid doing particle pushes altogether, which is generally the most time consuming part of a simulation. Thus simulations can be done which only involve field updates. The disadvantage is that buildup of the electron cloud can not be modeled with dielectrics alone. Also, external magnetic fields complicate the model somewhat, requiring a dielectric tensor instead of a scalar dielectric constant. Also, the linear assumption will break down at plasma densities above about $1.0e^{17}$ for these types of simulations. However, typical electron cloud densities are several orders of magnitude below this value. This advanced model is currently being developed [6], and will provide both greater numerical stability for long simulations, as well as improving the performance of the simulations.

References

[1] C. Nieter and J. R. Cary, "VORPAL: A versatile plasma simulation code", *J. Comput. Phys.*, **196**, pp. 448-473, 2004.

[2] P. L. G. Lebrun et al., "Accurate Simulation of the Electron Cloud in the Fermilab Main Injector with VORPAL", this issue.

[3] K. G. Sonnad, M. A. Furman, J. R. Cary, P. H. Stoltz, and S. A. Veitzer, "Simulation of the Dynamics of Microwave Transmission Through an Electron Cloud", *Proc. PAC 2007*, THPAS008, Albuquerque, NM, 2007.

[4] S. A. Veitzer, P. H. Stoltz, K. G. Sonnad, and J. M. Byrd, "Modeling Microwave Transmission in Electron Clouds", *Proc. PAC 2009*, 3486-FR5PFP089, Vancouver, B.C., 2009.

[5] M. T. F. Pivi et al., "Microwave Transmission Measurement of the Electron Cloud Density in the Positron Ring of PEP-II", *Proc. EPAC 2008*, MOPP065, Genoa, Italy, 2008.

[6] S. A. Veitzer, D. N. Smithe, and P. H. Stoltz, "Advanced Modeling of TE Microwave Diagnostics of Electron Clouds", *Proc. PAC 2011*, New York, N.Y., 2011.

TRAPPING OF ELECTRON CLOUD IN ILC/CESRTA QUADRUPOLE AND SEXTUPOLE MAGNETS

L. Wang and M. Pivi, SLAC, Menlo Park, CA 94025, U.S.A.

Abstract

The Cornell Electron Storage Ring (CESR) has been reconfigured as an ultra low emittance damping ring for use as a test accelerator (CesrTA) for International Linear Collider (ILC) damping ring R&D [1]. One of the primary goals of the CesrTA program is to investigate the interaction of the electron cloud with low emittance positron beam to explore methods to suppress the electron cloud, develop suitable advanced instrumentation required for these experimental studies and benchmark predictions by simulation codes. This paper reports the simulation of the electron-cloud formation in CESRTA and ILC quadrupole and sextupole magnets using the 3D code CLOUDLAND. We found that electrons can be trapped with a long lifetime in a quadrupole and sextupole magnet due to the mirror field trapping mechanism. We study the effects of magnet strength, bunch current, ante-chamber effect, bunch spacing effect and secondary emission yield (SEY) in great detail.

INTRODUCTION

The development of an electron cloud in magnets is the main concern where a weak solenoid field is not effective. Quadrupole and sextupole magnets have mirror field configurations which may trap electrons by the mirror field trapping mechanism [2]. Fig.1 shows the orbit of a trapped electron in a quadrupole magnet. The electron makes gyration motion (called transverse motion) and also moves along the field line (called longitudinal motion). At the mirror point (middle of the field line), there is a maximum longitudinal energy and minimum transverse energy. When the electron moves away from the mirror point, its longitudinal energy reduces and the transverse energy increases as the magnetic field increases. If the magnetic field is strong enough, the longitudinal energy becomes zero at one point and then the electron is turned back by the strong field. Note that the electrons are trapped in the region near the middle of the field lines. Although all quadrupole and sextupole magnets can trap electrons in principle, the trapping mechanism is also greatly sensitive to the detail dynamics of the electrons [3]. Both the positron beam and the spacing charge force of electron cloud itself play important roles. This paper reports the simulation of electron cloud in CESRTA/ILC quadrupole and sextupole magnets. Table 1 shows the main parameters used in the simulation.

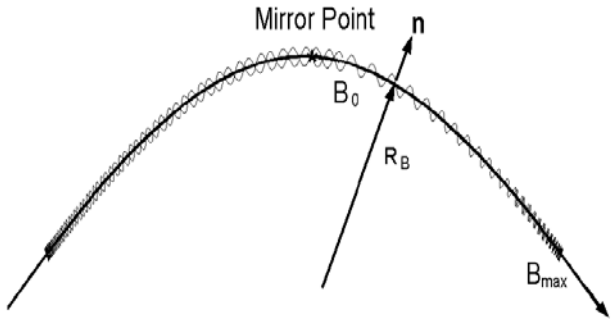

Fig.1: Trapping of an electron by a mirror field (quadrupole field here) from CLOUDLAND code

Table 1: Main simulation parameters for CESRTA and ILC positron damping ring

Description	CESRTA	ILC
Beam energy (GeV)	5.289	5.0
Circumference (m)	768.43	3238
Bunch length (mm)	15.0/17.24	6.0
Beam size (mm)	1.56/0.15	0.27/0.005
Bunch spacing (ns)	14	3/6
Bunch number per train	45	45
Bunch intensity ($\times 10^{10}$)	0.75~1.6	2.1

TRAPPING IN CESRTA QUADRUPOLE

In principle, electron cloud can be trapped in a quadrupole magnet due to the mirror field trapping. However, certain conditions are required for a deep trapping [3]. Electron cloud in a quadrupole magnet is sensitive to other parameters besides secondary emission, bunch current and beam filling pattern. Fig. 2 shows the build-up of the electron cloud in a quadrupole magnet with a field gradient of 0.517 *T/m*. The beam has one bunch train consisting of 45 bunches followed by a long train gap of 1.93μs. The electron cloud reaches saturation level after 10 turns (25μs). In contrast to the dipole magnet case, where electrons couldn't survive such long train gap, the electrons in quadrupole magnets surviving from the long train gap are trapped electrons. About 50% electrons can survive from the long gap as shown in the figure. Fig. 3 shows the evolution of an electron cloud during the train gap. The 1st picture in the figure is the

* Work supported by the U.S. Department of Energy under contract DE-AC02-76SF00515 and DE-FC02-08ER41538
# wanglf@slac.stanford.edu

electron cloud just after the passage of the last bunch along the bunch train. The positron bunches see an electron cloud like an Octupole field pattern in this case because the trapped electrons near the mirror field region are added to the quadrupole field pattern. After about 280 *ns*, only the electrons located at the minimum field region of the mirror field lines are survived, which shows excellent agreement with mirror field trapping mechanism.

FIG. 4 and 5 shows the build-up and evolution of electron cloud during the train gap with a field gradient of 9.2 *T/m*. Other parameters are the same as Fig. 2 and 3. Differently in this case, we can clearly see the quadrupole pattern: electrons moving along the magnetic field lines. The stronger magnetic field makes the trapped electrons closer to the beam, and therefore there is a larger electron density near the beam. As a result, these trapped electrons are more important for the beam dynamics. Note that there is a similar average electron density with the two field gradients.

FIG. 6 shows the bunch current effect with a field gradient of 1.0 *T/m*. There is a slow build-up for low bunch current. It is interesting that the peak average electron density at the end of the bunch train is close to a linear function of the bunch current. On the other hand, the electron density near the beam is a cubic function of bunch current as shown in the figure.

In a quadrupole magnet, there is a large electron flux near the middle the magnet poles as shown in FIG. 3 and 5. Note that the trapped electron cloud in FIG. 3 doesn't contribute a large electron flux at the surface of the beam pipe because they are trapped inside the beam chamber. The simulated electron flux has large peak at the center of the magnets poles (not shown here). This qualitatively agrees with the observation in CESRTA [4]. The trapped electron cloud in quadrupole magnet also has been observed experimentally in PSR [5].

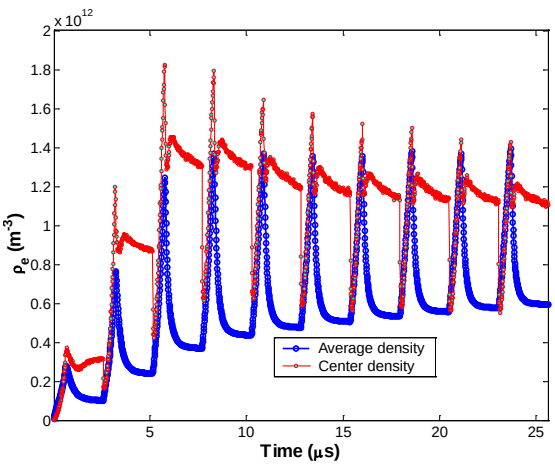

FIG. 2. Electron build-up in a quadrupole magnet with a field gradient of 0.517*T/m*.

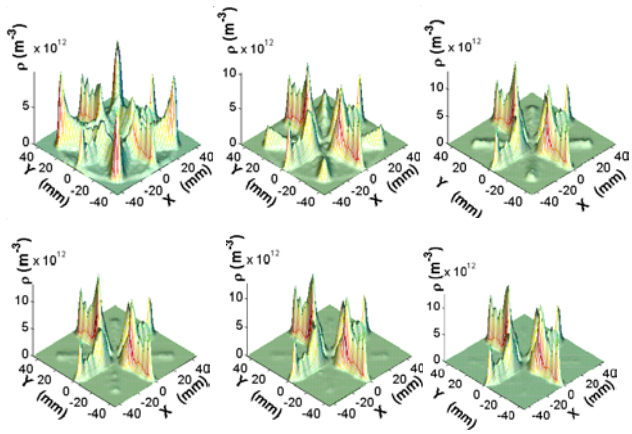

FIG. 3. Evolution of electron cloud during the train gap, frames separated by Δt=70 *ns*. Parameters used for simulation: Bunch length 17.24 *mm*, bunch current 1.0 *mA*, bunch spacing 14 *ns*, field gradient 0.517 *T/m*, peak SEY 2.0, energy at peak SEY 310 *eV*, photon flux 0.21 photons/m/particle, reflectivity 20%.

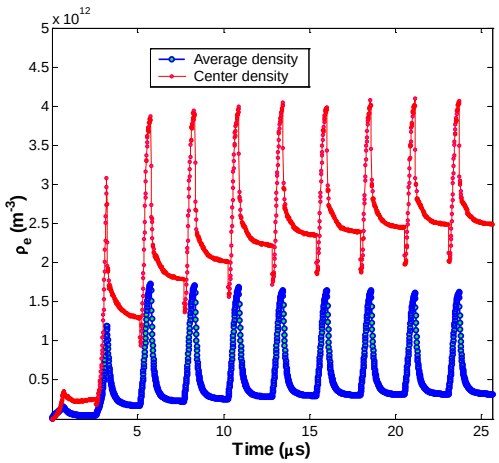

FIG. 4. Electron build-up in a quadrupole magnet with a field gradient of 9.2 T/m.

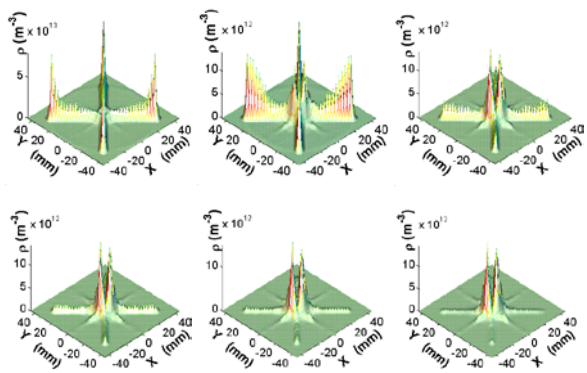

FIG. 5. Evolution of electron cloud during the train gap with a field gradient of 9.2 T/m. Other Parameters are the

same as those in Fig. 3. Frames are separated by Δt=70 *ns*.

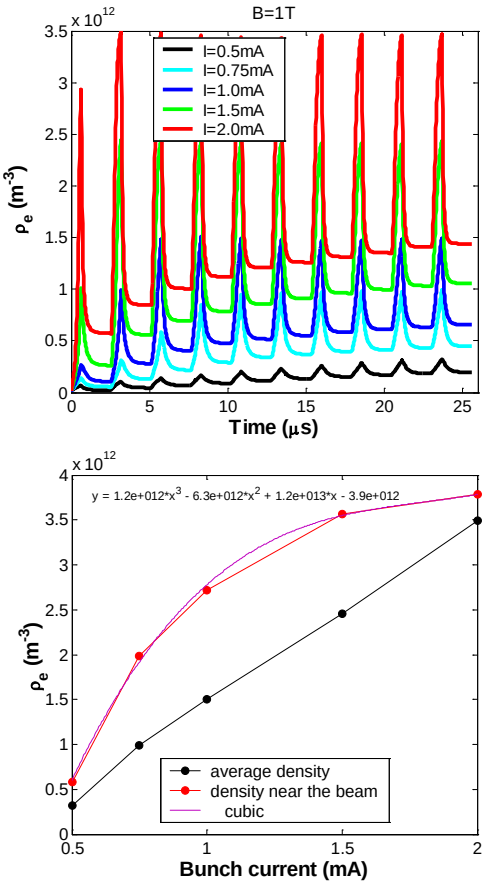

FIG. 6. Bunch current effect on electron build-up (top) and peak electron density (bottom) in a quadrupole magnet with a field gradient of 1.0 T/m

TRAPPING OF ELECTRON CLOUD IN ILC QUADRUPOLE AND SEXTUPOLE

Many configurations have been studied for ILC positron damping ring in order to optimize the electron cloud effect on the beam dynamics, for instance, the ring circumference, bunch spacing, ante-chamber effect, coating (SEY) effect. In this study, we only study 3km ring. We systematically scan the following parameters: bunch spacing from 3ns to 6ns, SEYs from 0.9 to 1.4, and ante-chamber protection effect of 0%, 90% and 98%, respectively. FIG. 7 shows the build-up of electron cloud in ILC quadrupole magnet without ante-chamber effect for different SEYs and bunch spacing. FIG. 8 shows the build-up of electron cloud with 98% ante-chamber reduction effect for different SEYs and bunch spacing. A larger number of electrons (30%~70%) can be trapped and survive from the long train gap and there is a slow build-up and slow decay comparing with electron in a dipole magnet. In general, it takes several bunch trains (even turns in CESRTA case) for the electron cloud to get saturation level. It saturates quickly without ante-chamber as expected due to the large photons flux.

The maximum electron densities along the bunch train with various configurations are listed in Table 2-5. Electron density in sextupole is lower than that in the quadrupole magnet. Here we discuss the electron in quadrupole magnet only. There is a larger (a factor 2.3~1.6) average electron density in 3ns spacing case comparing with 6ns spacing. The electron density near the beam is also always smaller with a 6ns bunch spacing beam.

The effect of SEY is significant with ante-chamber while it become less effective without ante-chamber because the strong space charge force limits the saturation density. In all cases, there is a larger density for a larger SEY. And there is a long saturation time for low SEYs.

The effect of ante-chamber is complicated by the space charge effect. Antechamber is effective in reduction of the electron cloud density when SEY is small (<=1.0); On the other hand, its mitigation effect becomes smaller with a larger SEY because the secondaries are dominant. With ante-chamber, there is always a small average electron density. However when SEY is larger (>1.2) the density near the beam can be larger comparing without ante-chamber case. Simulation shows there is a different electron distribution with and without ante-chamber protection effect. Detail study finds the space charge effect without ante chamber play a very important role on the electron distribution. FIG. 9 shows the electron distribution with ante-chamber protection effect. There is a large density around the beam. However, there is a lower density near the beam without ante-chamber as shown in FIG.10. The space charge force reduces the density near the beam in this case. In a short summary, the ante chamber has to be coated to reduce its SEY in order to take its advantage of reduction of the photons. With a SEY>1.1, the ante-chamber doesn't reduce the electron density near the beam!

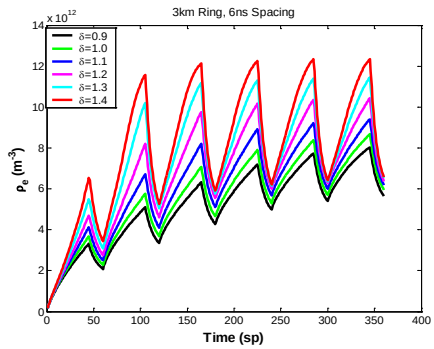

(a)

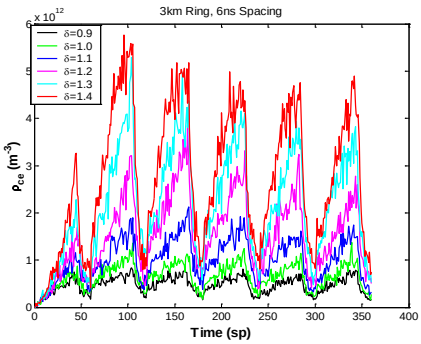

(b)

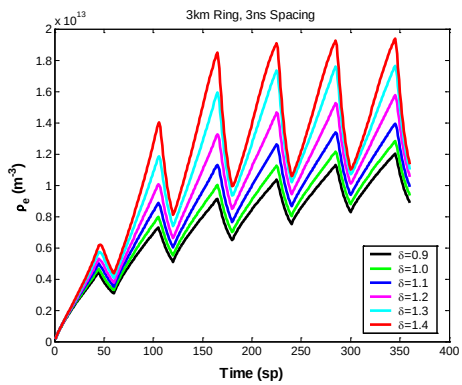

(c)

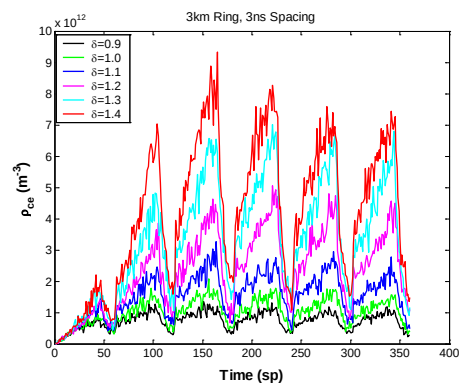

(d)

FIG. 7. Electron build-up in the ILC quadrupole magnet without ante-chamber protection. (a) 6ns spacing, average density; (b) 6ns spacing, electron density near the beam; (c) 3ns spacing, average density; (d) 3ns spacing, electron density near the beam

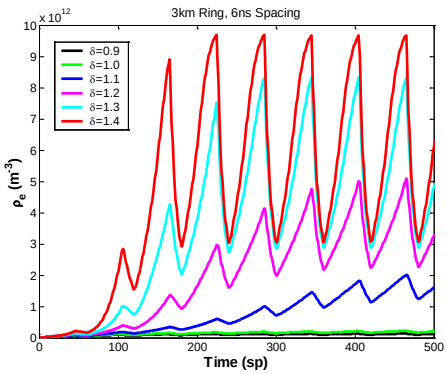

(a)

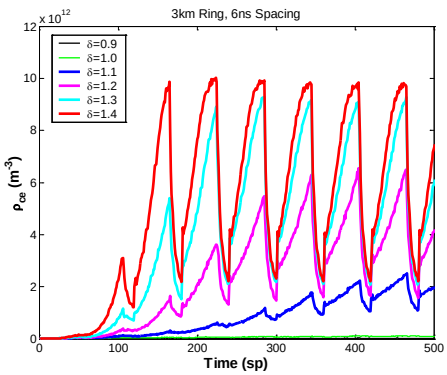

(b)

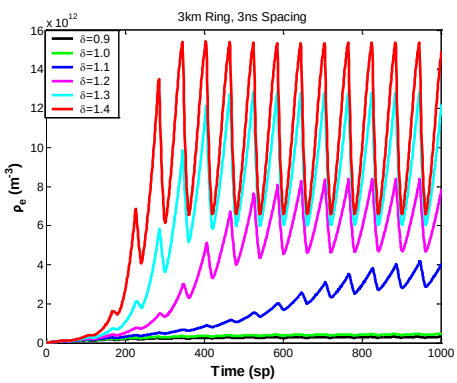

(c)

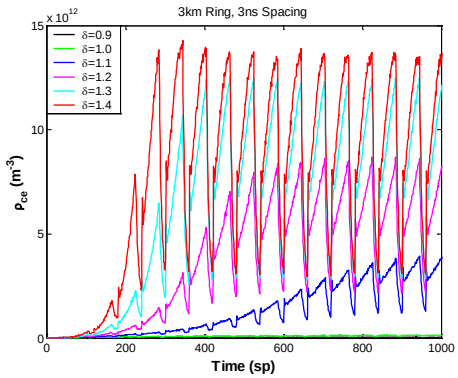

(d)

FIG. 8. Electron build-up in the ILC quadrupole magnet with 98% reduction of photons due to the ante-chamber. (a) 6ns spacing, average density; (b) 6ns spacing, electron density near the beam; (c) 3ns spacing, average density; (d) 3ns spacing, electron density near the beam

Table 2: Peak average density in ILC quadrupole magnet (1×10^{12}m^{-3})

SEY	Antechamber protection =0%		Antechamber protection =90%		Antechamber protection =98%	
	3ns spacing	6ns spacing	3ns spacing	6ns spacing	3ns spacing	6ns spacing
0.9	12.0	8.04	1.64	0.70	0.315	0.136
1.0	12.8	8.70	2.20	1.0	0.466	0.260
1.1	13.85	9.41	4.82	2.38	4.30	2.20
1.2	15.74	10.44	8.70	5.25	8.40	5.13
1.3	17.50	11.45	13.2	8.58	12.8	8.35
1.4	19.20	12.35	15.8	9.97	15.37	9.7

Table 3: Peak central density in ILC quadrupole magnet (1×10^{12}m^{-3})

SEY	Antechamber protection =0%		Antechamber protection =90%		Antechamber protection =98%	
	3ns spacing	6ns spacing	3ns spacing	6ns spacing	3ns spacing	6ns spacing
0.9	1.0	0.67	0.18	0.11	0.035	0.020
1.0	1.6	0.9	0.55	0.35	0.135	0.14
1.1	2.2	1.5	3.25	2.2	4.0	2.75
1.2	4.4	2.6	7.5	6.0	8.7	6.55
1.3	6.7	3.8	11.5	8.5	12.4	9.2
1.4	7.5	4.9	13.0	9.5	13.6	9.9

Table 4: Peak average density in ILC sextupole magnet (1×10^{12}m^{-3})

SEY	Antechamber protection =0%		Antechamber protection =90%		Antechamber protection =98%	
	3ns spacing	6ns spacing	3ns spacing	6ns spacing	3ns spacing	6ns spacing
0.9	11.3	6.4	1.07	0.52	0.2	0.10
1.0	>11.8	7.05	1.2	0.605	0.22	0.116
1.1	>12.4	7.75	>1.35	0.73	0.248	0.135
1.2	>13.2	>8.46	>1.55	0.94	0.290	0.174
1.3	>13.8	>9.3	1.95	1.56	0.354	0.303
1.4	14.8	10.2	3.03	3.25	0.65	>2.0

Table 5: Peak central density in ILC sextupole magnet (1×10^{12}m^{-3})

SEY	Antechamber protection =0%		Antechamber protection =90%		Antechamber protection =98%	
	3ns spacing	6ns spacing	3ns spacing	6ns spacing	3ns spacing	6ns spacing
0.9	0.55	0.40	0.06	0.05	0.01	0.008
1.0	0.60	0.50	0.08	0.07	0.014	0.012
1.1	0.70	0.55	0.1	0.085	0.018	0.016
1.2	0.90	0.75	0.145	0.150	0.026	0.025
1.3	1.3	0.9	0.24	0.370	0.05	0.075
1.4	1.4	1.1	0.76	1.14	0.18	>1.0

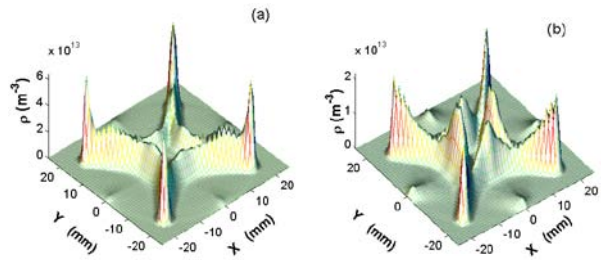

FIG. 9. Electron cloud distribution in ILC quadrupole, parameters used in simulation: 3km ring, 6ns bunch spacing with 98% ante-chamber reduction effect. (a) at the end of the bunch train (b) survived(trapped) electrons from the last bunch train.

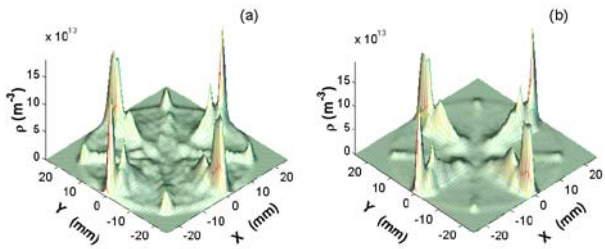

FIG. 10. Electron cloud distribution in ILC quadrupole, parameters used: 3km ring, 6ns bunch spacing without ante-chamber reduction effect. (a) at the end of the bunch train (b) survived(trapped) electrons from the last bunch train.

SUMMARY

We find large number of (up to 70%) deep trapped electrons in quadrupole and sextupole magnet of CesrTA and ILC positron damping ring. Simulations show that the electron cloud in a quadrupole magnet can be deeply trapped by the mirror field. The simulation results agree with the theory well. The trapped electrons can survive the long train gaps gap of 1.93μs. The distribution of trapped electrons strongly depends on the field and beam parameters. We found more electrons can be confined near the beam with a stronger magnetic field gradient. Due to the trapping, electrons in quadrupole and sextupole magnet, there is a slow decay of the electron

density during the train gap and the build-up is slow. It takes up to more than 10 bunch train/turns to reach saturation level and the saturated density near the beam can be large. Theretofore, the long lifetime electron in quadrupole can be important for the beam dynamics. Moreover, CESR-TA has strong magnetic field gradient which causes the trapped electrons closer to the beam. This may explain the observation of the effect of the long life time electron in CESR-TA[6].

We systematically study the effect of bunch spacing, SEYs and ante-chamber effect for ILC damping ring. There is lower density for 6 *ns* bunch spacing and ante-chamber is effective on reduction of the electron density only when SEY is small (<1.1). The secondary electron is dominant with a large SEY. Another important finding is that the strong space charge can significantly change the distribution of the electron cloud. It reduces the electron density near the beam. This makes the ante-chamber less attractive when SEY is large. In a summary, the quadrupole and sextupole need to be coated to reduce the SEYs in order to take advantage of the reduction of the photon flux.

ACKNOWLEDGMENTS

We thank J. Calvey, G. Dugan, B. Macek and M. Palmer for providing the input data of CESR-TA and fruitful discussions.

REFERENCES

[1]M. Palmer, et al. IPAC2010 proceedings.
[2] D. Jackson, Classical Electrodynamics.
[3]L. Wang, H. Fukuma, S. Kurokawa, K. Oide, Physical Review E, 66, 036502(2002).
[4] J. Calvey, in these proceedings.
[5] B. Macek, in these proceedings.
[6] G. Dugan, in these proceedings.

ELECTRON CLOUD STUDIES IN THE FERMILAB MAIN INJECTOR USING MICROWAVE TRANSMISSION*

J. C. Thangaraj#, N. Eddy, B. Zwaska, J. Crisp, I. Kourbanis, K. Seiya, Fermi National Accelerator Laboratory, Batavia, IL 60510, U.S.A.

Abstract

In this paper, we present recent results from our measurement at the Fermilab Main Injector through microwave transmission in a beam pipe. We present three types of measurement techniques. In the first technique, we use time-resolved direct phase shift measurement to measure the e-cloud density. In the second and third techniques, we look for side bands in the frequency spectrum with or without frequency span by collecting turns of data. We present experimental results taken from MI40 and MI52 test section of the main injector.

INTRODUCTION

Project X is a multi-megawatt proton facility planned for construction at Fermilab. To achieve this goal, high current proton beam will have to be transported through the main injector [1]. The main injector is a synchrotron that accelerates 53 MHz proton bunches from 8 GeV to 120-150 GeV. During the passage of a high intensity proton bunch, low energy background electrons can interact with the proton bunch and develop instabilities. This could potentially limit the performance of the accelerator by increasing the vacuum pressure, emittance growth, shifting the tune of the machine among other things. Hence it is important to measure, model and mitigate electron cloud in such machines.

In this work, we report our results from measuring electron cloud density using microwave techniques in the main injector at the Fermilab. We begin with a brief introduction to the principle behind the measurement and then discuss three different techniques to measure e-cloud density. Finally, we summarize our results and conclude by suggesting future plans.

Microwave measurement Principle

By sending EM waves through an electron cloud of uniform distribution and measuring the phase shift of the EM waves, the electron cloud density can be measured. The phase shift φ of an electromagnetic wave of frequency ω through a uniform, cold plasma (of plasma frequency ω_p and density ρ) per unit length is given by [2]:

$$\frac{\emptyset}{L} = \frac{\omega_p^2}{2c\sqrt{\omega^2 - \omega_c^2}}; \quad \omega_p^2 = 4\pi\rho r_e c^2$$

where c is the speed of light, r_e is the classical electron radius, and ω_c is the cut-off frequency of the pipe. The above formula assumes that the e-cloud density is static but in the main injector and other machines, the e-cloud density varies as a function of time. The reason being the proton bunch which generates the electron cloud has a time pattern. Hence, the e-cloud density varies as a function of time. So, sending a carrier wave into the cloud should result in a phase-modulation of the carrier wave. In other words, in frequency spectrum, we expect to see sidebands to the carrier [3]. By measuring the amplitude of the sideband, in theory, we can estimate the electron cloud density.

Here we summarize three different techniques used to measure e-cloud density in the main injector. The three techniques are called as direct phase shift, sideband spectrum and zero span measurement. All these techniques are based on the same general principle of measuring the phase shift of the carrier wave. In the sideband spectrum measurement, we send a carrier wave (1.5 GHz) and any phase modulation will show up as a side band. In the zero span measurement, we set the spectrum analyzer to the expected side band frequency (measured using the sideband spectrum technique) and collect data over the full injector cycle. In other words, we make power measurement at a single frequency. Any increase in the amplitude of the signal at this frequency will then indicate phase modulation. The direct phase shift measurement is similar to microwave interferometry. The carrier is split into two paths: one is sent through the e-cloud and to the receiver while the other is sent directly to the receiver. At the receiver, both the signals are demodulated to baseband, mixed and the mixer output recorded in a scope and time averaged to yield the phase shift. We use a filter to minimize the beam induced AM. Additionally, as this signal occurs at random phase each turn with respect to the microwave carrier, it simply averages away out many turns.

*Operated by Fermi Reserach Alliance, LLC under Contract No. DE-AC02-07CH11359 with US Department of Energy
jtobin@fnal.gov

EXPERIMENTAL SETUP

Figure 1 shows the experimental setup of our experiments. The source consists of a signal generator, an amplifier while at the receiver the mixer detects the phase modulation. The details are mentioned in here [4].

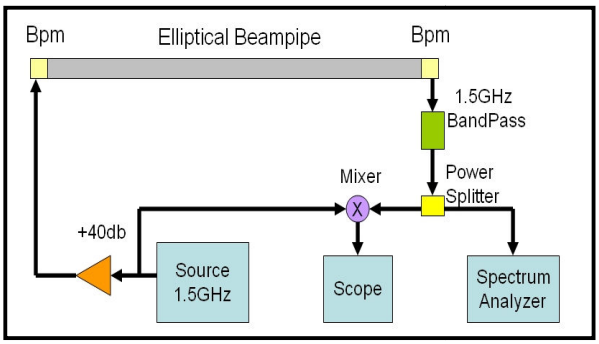

Figure 1: The experimental test setup showing the BPMs, which act as our antenna. The source is E4428C signal generator.

The BPMs used in our experiments are 25 cm long shorted stripline pickups. Fig 2 shows how they are connected to drive a TE11 mode.

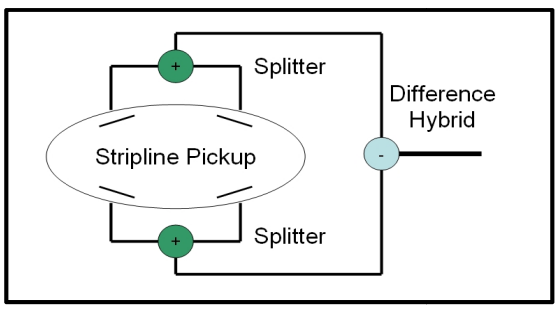

Figure 2: The BPM's connection are to cancel the common beam signal and couple TE11 mode.

Measurement location

The measurements for this work were done at several locations in the main injector. The locations were: MI 40 (Straight region), MI 52 Bend, MI 521(test). MI 40 is a straight section where the BPMs are separated by a drift region (15.1m). MI 52 is a bend region where the BPMs have two dipoles and their associated quads between them (12.9m). The bend field is 1.4T at 120GeV. Both these location have been upgraded to have high quality heliax cables for good signal transmission and reception. Both MI 40 and MI 52 have elliptical beam pipe and the cutoff frequency was just below 1.5 GHz. Recently, a test lattice (M521) of round beam pipe (6") of length 2m was installed for dedicated e-cloud studies.

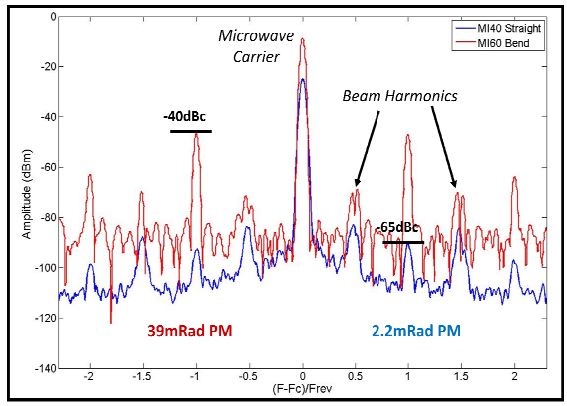

Figure 3: The figure shows the sideband spectrum measurement at MI 40 and MI 60 Bend region. The MI52 bend region shows a larger signal presumably due the strong e-cloud column due to the dipole fields.

Sideband spectrum measurement

Fig 3 shows the sideband spectrum measurement done at MI40 straight section and the MI 60 bend region. The proton beam signal and its harmonics constantly interfere with the measurements of the phase shift signal. So, the carrier frequency is chosen such that the signal is placed between the carrier and the 90 kHz beam harmonics. The increase in amplitude at the MI 60 bend may be due the presence of dipole which tends to increase the e-cloud density by trapping them along the field lines.

Zero span and Direct phase shift measurement

In the zero span measurement, the spectrum analyzer is set to the zero span mode. The phase shift signal from ramp to the extraction cycle of the main injector is recorded. This is shown in Fig 4. The transition indicates the time at which the bunch length of the proton bunch is at the minimum. The extract arrow indicates the end of the MI cycle. The lower trace shows the measurement without the carrier wave.

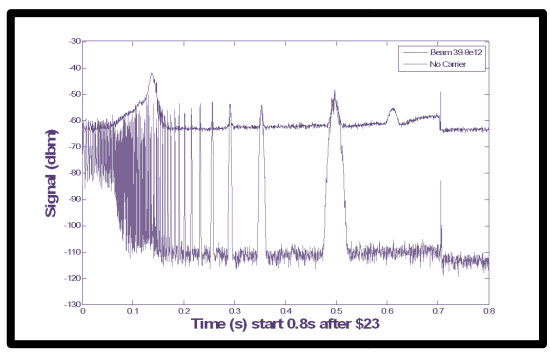

Figure 4: The upper trace shows the zerospan measurement at MI 52 Bend region.

At MI40 and MI60, direct phase shift measurements were done. The results are discussed elsewhere [5]. For our discussion we restrict ourselves to Fig 5, where we see that the phase-shift follows the proton beam signal and also indicating the growth in electron density in time.

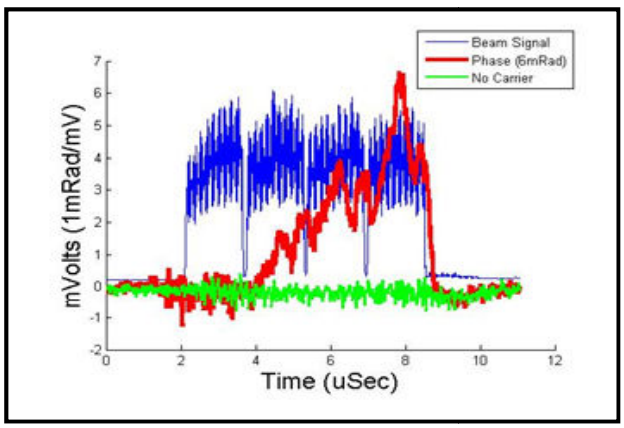

Figure 5: The red trace shows the phase shift signal while the blue trace shows the proton bunch structure. As time increases, the phase shift indicating increase in electron cloud density.

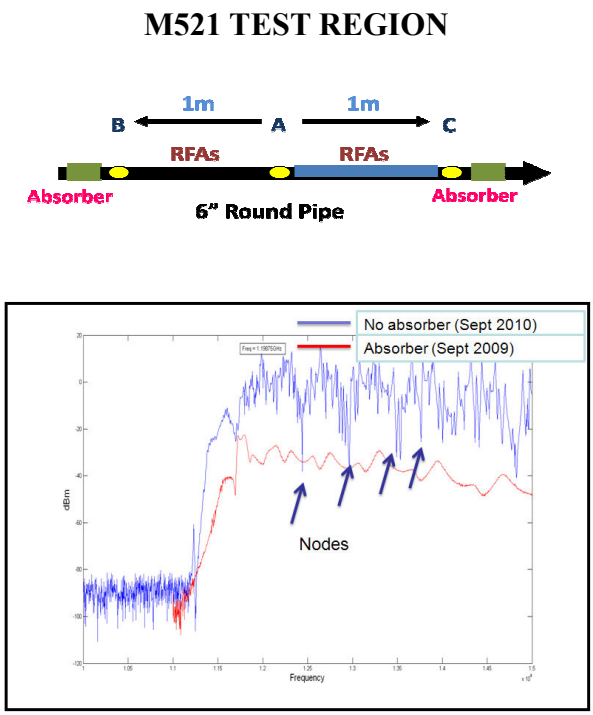

Figure 6: Showing the M521 test region (above) along with the transmission curve with and without the absorbers (below).

The top of Figure 6 shows the M521 test region. It consists of 2 m, 6 '' round beam pipe with BPMs A, B, C. The cutoff frequency for this section of the beam lattice is about 1.2 GHz. The bottom figure in Figure 6 shows the transmission curve with and without the absorbers. Removing the absorbers not only increased the transmission but many reflection nodes were observed. This seems to indicate that the phase shift may be amplified due to spurious reflections and making the absolute electron density measurement difficult. Currently, experiments are being designed to take advantage of the reflection to make a localized density measurement [6]. By deliberately using reflection, we can setup an experiment to measure the amplification factor and thus calculate the electron cloud density. Without the absorbers, we get reflections leading to standing waves. The microwave sees a phase shift each time is passes through the e-cloud, so this can lead to an amplification of the phase shift. Note this is impacted by how the vectors add, but in general if there is an amplification of the carrier (constructive), then the phase shift will also be amplified.

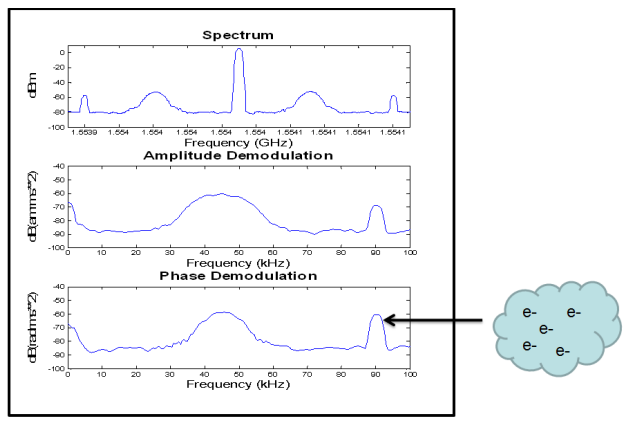

Figure 7: Side spectrum measurement at MI 521.The top plot shows the side spectrum, the middle plot shows the amplitude demodulation and the bottom plot shows the phase demodulation of the received signal

Fig 7 shows the results of the measurement done at M521. The sideband indicates that the signal has been modulated. Since we always have some AM modulation indicated by the middle plot, the plausible reason for the observed phase modulation (bottom plot) is due the presence of electron cloud.

SUMMARY AND CONCLUSION

Electron cloud density measurements using microwave techniques has been tested at three locations in the main injector using three different techniques. All the techniques show electron cloud formation in the main

injector at transition and more specifically stronger electron cloud density at the bend region. A side band spectrum measurement on the e-cloud test lattice also indicated electron cloud formation. Though these techniques are successful in indicating electron cloud formation, it is still difficult to make an absolute measurement due to reflections. A reflection based technique based on resonance cavity is being developed at Fermilab and will be tested at a location in the main injector with longer path length.

REFERENCES

[1] I. Kourbanis et al., "Current and Future High Power operation of Fermilab Main Injector", Fermilab Note, fermilab-conf-09-151-ad

[2 K. Sonnad et al., "Simulation and Anlaysis of Microwave transmission through an electron cloud, a comparison of results", Proceedings of PAC'07.

[3] F. Caspers et al., "The CERN SPS experiment on microwave transmision through the beam pipe", Proceedings of PAC'05.

[4] J. Crisp et al., "Measurement of electron cloud density with microwaves in the Fermilab main injector", DIPAC'09, Basel, Switzerland TUPB23; http://www.JACoW.org

[4] N. Eddy et al., "Measurement of electron cloud development in the Fermilab main injector using microwave transmission", PAC'09, Vancouver, May 2009, ID-3312; http://www.JACoW.org

[6] C. Tan, "Measuring electron cloud density with trapped modes", Fermilab note (unpublished)

The Ecloud Measurement Setup in the Main Injector*

C.Y. Tan†, M. Backfish, R. Zwaska, Fermilab, Batavia, IL 60504, USA

Abstract

An ecloud measurement setup was installed in a straight section of the Main Injector in 2009. The goal of the setup was to compare the characteristics of different beam pipe coatings when subjected to proton beam. The setup consists of one coated and one uncoated beam pipe with the same physical dimensions installed at the same location. Four RFAs (retarding field analyzers) and three BPMs (beam position monitors) used for microwave measurements have been used to measure the ecloud densities. The RFAs have performed very well and have collected both the time evolution and energy distribution of the ecloud for bare and two types of beam pipe coatings.

INTRODUCTION

Ecloud has been observed in many high intensity accelerators which can limit the amount of current that can be stored in them. In particular, for ProjectX, the amount of beam current that will be stored in the MI (Main Injector) will be $\sim 160 \times 10^{12}$ protons while the present maximum intensity is $\sim 45 \times 10^{12}$ protons which is about $3.5\times$ less beam. Although ecloud has been observed in the MI, it has not caused instabilities at the present running conditions. However, there is no guarantee that instabilities caused by ecloud will not be a problem at ProjectX intensities. Therefore, a program has been started to study the ecloud effects with both computer simulations and experiments.

In this papers, we will be focusing our attention on how coatings can affect the production of secondary electrons. We have installed an ecloud measurement setup in a straight section of MI which consists of one coated and one uncoated beam pipe with the same physical dimensions and at the same location, together with four retarding field analyzers (RFAs) and three sets of beam position monitors (BPMs) which can be used for the microwave measurements.

In the following sections we will introduce the installed setup and discuss the design of the RFAs and briefly touch on the microwave measurements. The experimental results of both titanium nitride (TiN) and amorphous carbon (aC) coated beam pipes when conditioned by proton beams will also be discussed here.

* Operated by Fermi Research Alliance, LLC under Contract No. DE-AC02-07CH11359 with the United States Department of Energy.

† cytan@fnal.gov

MAIN INJECTOR

The MI is a 2 mile ring which nominally ramps protons from 8 GeV to 120 GeV for the experiments and for anti-proton production or at 150 GeV for proton or anti-proton injection into the Tevatron. Figure 1 shows a bird's eye view of the Fermilab site and MI-52 where the ecloud measurement setup is located.

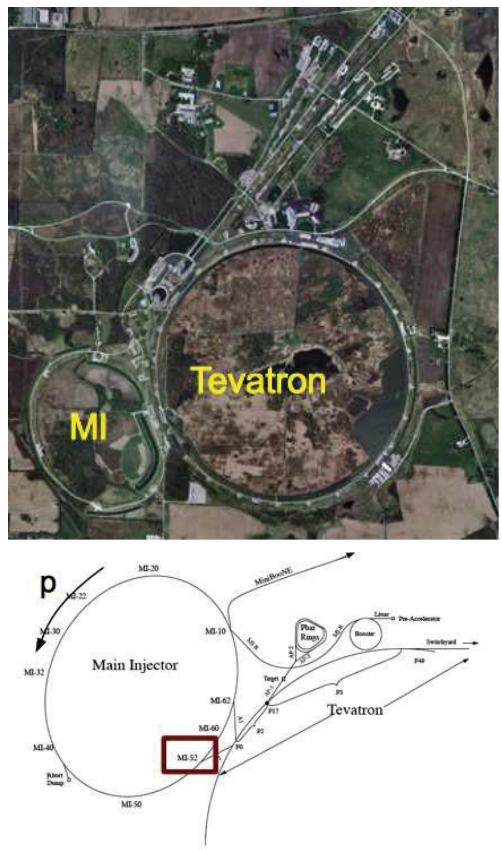

Figure 1: A bird's eye view of the Fermilab site and MI-52 where the the ecloud measurement setup is located.

The MI has many modes of operation. The highest proton intensity 40×10^{12} protons is achieved for the NuMI (Neutrinos from the Main Injector) experiment. In normal operations, NuMI is spilled from MI every 2.2s.

THE ECLOUD MEASUREMENT SETUP

The ecloud measurement setup is shown in Figure 2. The coated and uncoated beam pipes are 6" in diameter and are each 1 m long. The detectors on the setup are:

- RFAs. There are four RFAs installed. Three of the

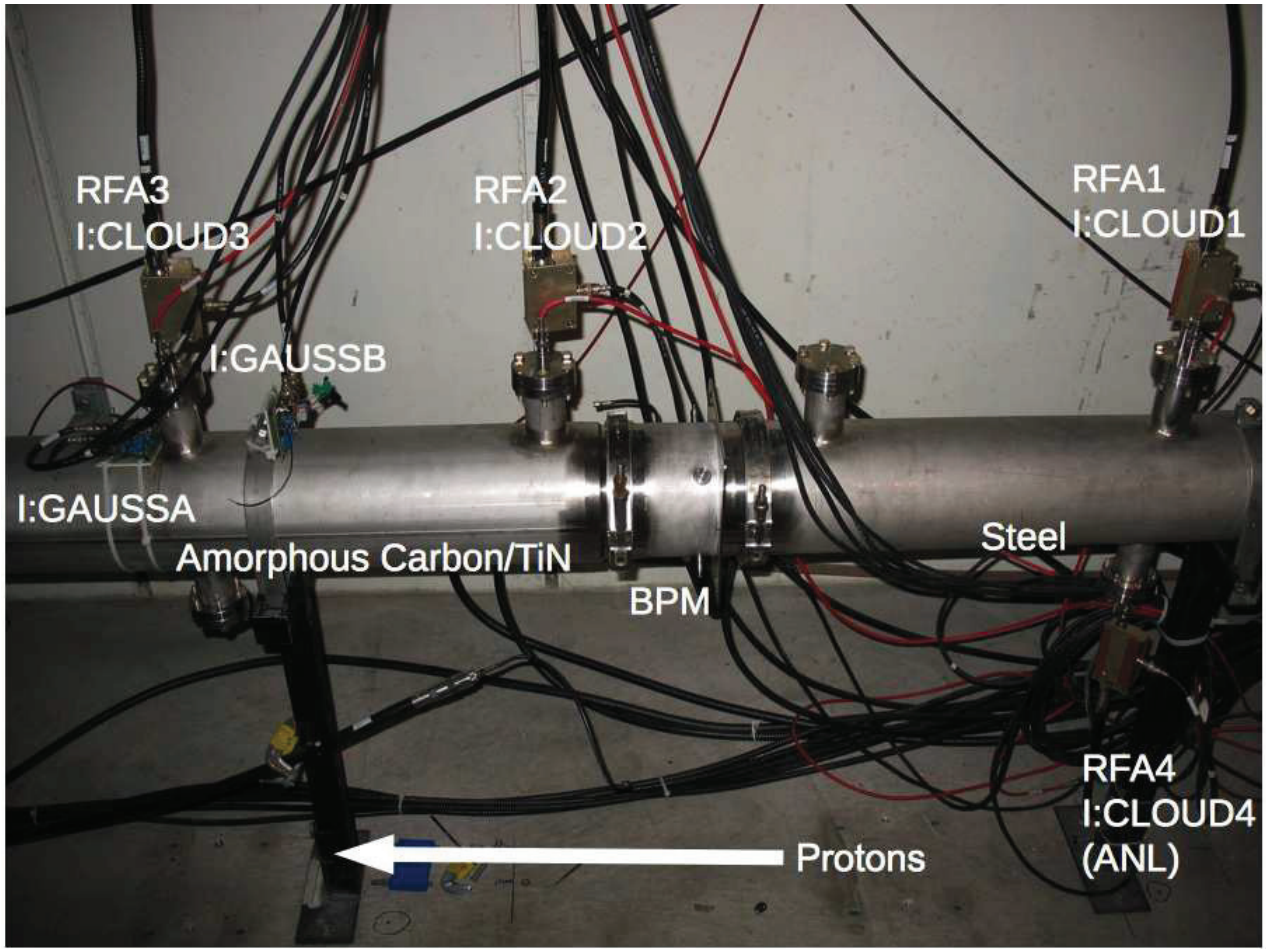

Figure 2: The ecloud measurement setup at MI-52. There are four RFAs and 3 BPMs (only one is shown here). The beam pipe is 6" in diameter and the coated and uncoated beam pipes are each 1 m long.

RFAs are FNAL (Fermi National Accelerator Laboratory) style which we will discuss below and one ANL (Argonne National Laboratory) style used for comparison.[1] The placement of the RFAs are shown in Figure 3.

- Magnetic Probes. Two magnetic probes which we have designed to be non-directional are called `I:GAUSSA` and `I:GAUSSB` in Figure 2.
- BPMs. Three BPMs are located at the positions shown in Figure 3. The BPMs are used in the microwave method for measuring ecloud densities.[2] Microwave absorbers were installed for the TiN coated beam pipe experiment. They were removed when we replaced the TiN coated beam pipe with aC.

RFAs

The design of the RFAs have been discussed in [3]. We will only highlight the reasons why certain choices were made in its design here. The RFA and its high gain amplifier are shown in Figure 4 and Figure 5 show how the amplifier is directly connected to the RFA.

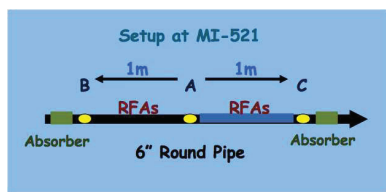

Figure 3: This is a cartoon of the measurement setup shown in Figure 2. Note that the absorbers were removed when the aC coated beam pipe was installed. (Courtesy of N. Eddy)

- Improved Sensitivity Using SIMION[4], we optimised our design so that it improved its sensitivity compared to the ANL RFA. The improvements are
  - a larger collecting surface area.
  - a cup rather than a flat surface for collecting the electrons.
  - a geometry which focuses the electrons onto the cup with the grid.
  - reduction in the number of grids to one because each grid reduces sensitivity by about 20%.

Our *in situ* ecloud measurements, show that our RFA is almost 2× more sensitive than the ANL RFA.

- High Gain Amplifier A specially designed radhard, high gain amplifier with a 3 kHz low pass filter (LPF) is directly connected to the RFA. The 3 kHz LPF has been chosen because previous measurements show that there is strong 10 kHz in the MI tunnel. The LPF attenuates this noise to better than 40 dB. The electronics also has bypass relays so that the signal can be monitored if the amplifier becomes saturated.
- High quality cables All the signal cables are heliax cables which are isolated from the beam pipe and grounded in the relay racks upstairs in the service building. Only grounding upstairs prevents ground loops and reduces ramp noise which can contaminate the ecloud signals.

One limiting factor in the design is that we need to bias the grid at 20V because electrons will bounce off the RFA without this bias. From bench experiments, we find that 20V is sufficient for electron beam energies up to 600 eV. Unfortunately, for energy spectrum measurements, this will limit us to above 20 eV electrons.

Magnetic Probes

Computer simulations with POSINST and VORPAL and bench experiments have shown that a magnetic field can both affect the collection efficiency of the RFAs and the electron cloud distribution.[5]

We built two axis independent magnetic probes to measure the B-field in our setup. Figure 5 shows how the two probes are installed in the setup. The probes show that the B-field follows the MI ramps and gets to a value between 5 to 6 gauss at flattop. See Figure 6.

We also covered up the coated beam pipe with mumetal to shield it from the B-field. There are small differences between the shielded and unshielded results. Figure 8 shows the before and after effects on the RFA signal located in the TiN coated section. It is clear from here that a pedestal appears at the ramp flattop.

Microwave Setup

There are three BPMs in the setup which are used as microwave antennæ for the transmission or reception of RF (radio frequency). A typical microwave setup is shown in Figure 7. Unfortunately, no phase shift has been measured when there are microwave absorbers at the end of the setup. This is because the present setup is only 2 m long and without any reflections, the phase shift is so small that it cannot be measured. On the other hand, after the microwave absorbers were removed, multiple reflections are supported in the setup and our measurements do show a phase shift from ecloud. However, more work needs to be done to understand how to correlate the phase shift to ecloud density. [6].

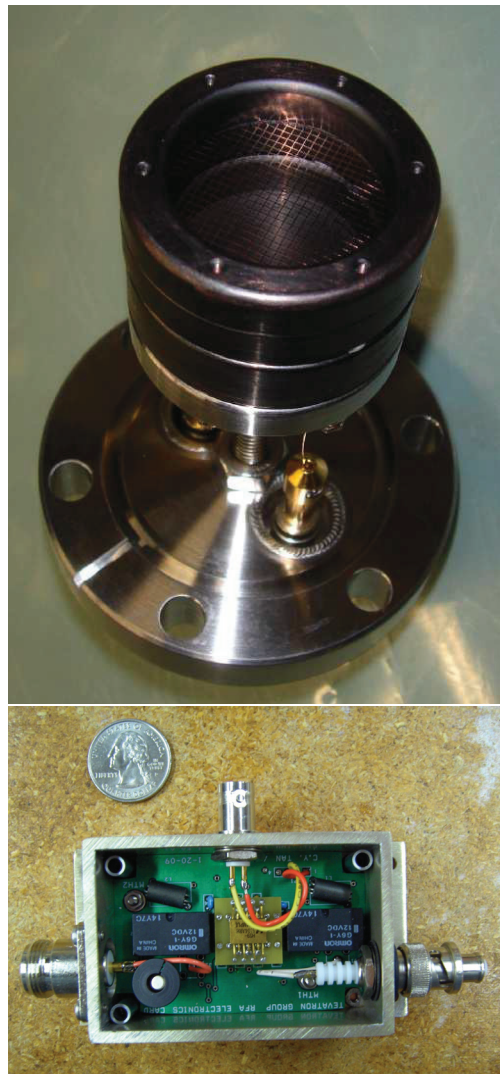

Figure 4: The FNAL RFA and the amplifier package. On the amplifier package, the gold colored integrated circuit (HS-5104ARH) is the radhard operational amplifier and the two black rectangular packages are the bypass relays. Figure 5 shows how the amplifier is directly connected to the RFA.

EXPERIMENTAL RESULTS

We will compare the RFA measurements for steel, TiN and aC in this section. We remind the reader that the locations and beam coating types are shown in Figure 2.

Figure 8 shows the typical signal that is seen on the RFAs for steel and TiN coated beam pipes. (Note: in this plot and Figures 10 and 11, the span of the plots cover part of the MI cycle which is 2.2s. The RFA data from each cycle are superimposed.) The maximum electron current that we see in the RFA signal occur soon after transition which is at 20.48 GeV. Note: for convenience we will call the "maximum electron current" measured on the RFA "dips".

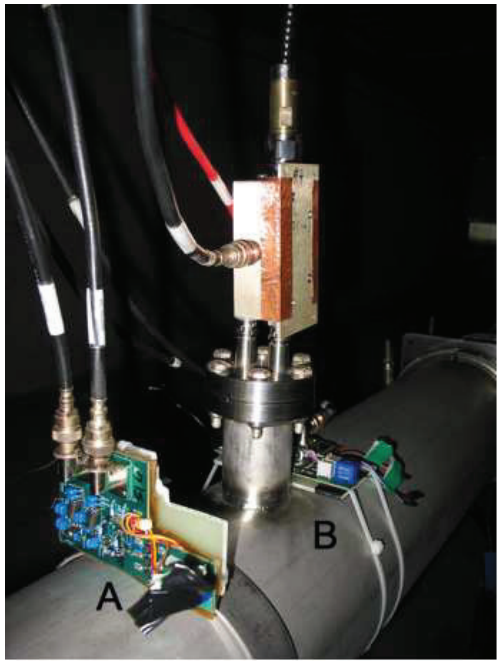

Figure 5: Two probes are installed in the setup labelled A and B here. The RFA amplifier is directly connected to the RFA in the tunnel.

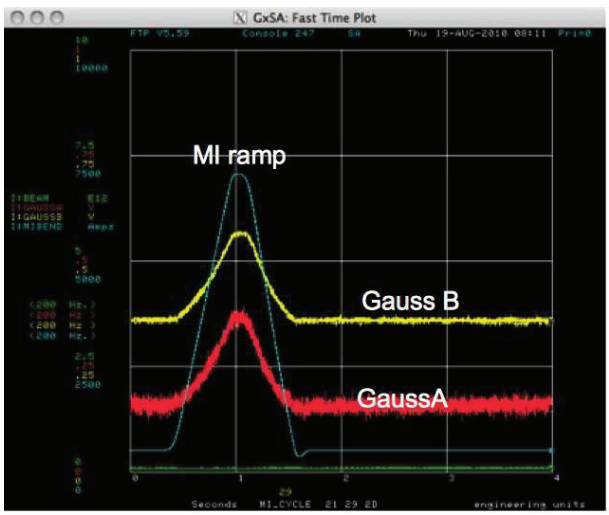

Figure 6: The B-field on the setup follows the MI ramp. The maximum field is between 5 to 6 gauss at flattop.

Comparing TiN, aC and Steel

Figure 10 is a signal comparision between TiN, aC and steel. There is a very strong double dip structure on CLOUD3 (aC) which is absent on CLOUD1 (steel). In this figure, the amplifier on CLOUD3 is turned on while it is off for CLOUD1. The same double dip structure is seen whether the amplifiers are on or off. Figure 11 shows a snapshot of the RFA signals after aC has been somewhat conditioned and the double dip structure vanishes.

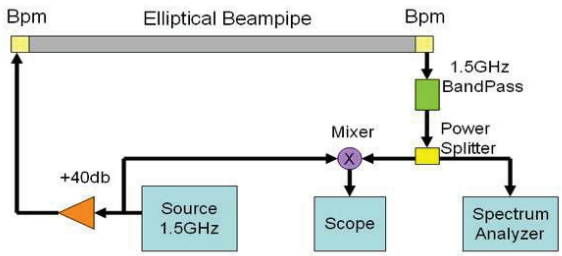

Figure 7: The microwave setup used for microwave measurements. Unfortunately, the length of the setup precluded this method. (Courtesy of N. Eddy)

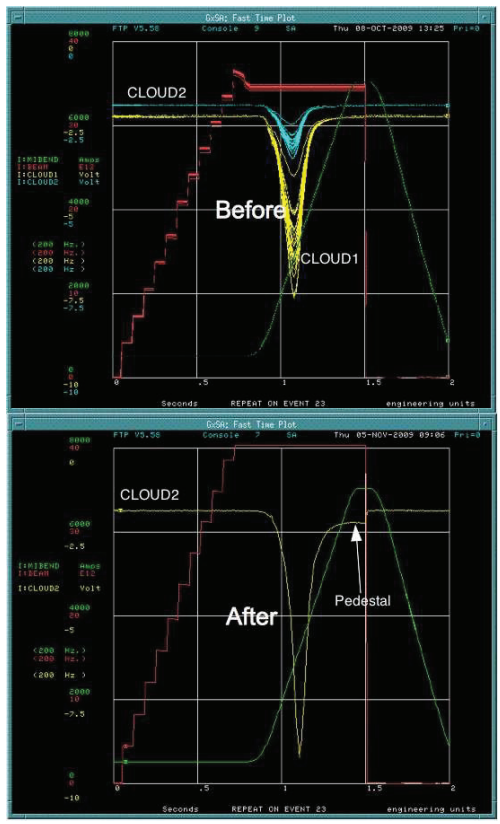

Figure 8: These are typical RFA signals on TiN and steel with the ampifiers on. The before picture compares CLOUD1 (yellow) on steel and CLOUD2 (cyan) on TiN. The after picture is when the TiN beam pipe is wrapped in mumetal. There is a clear pedestal in the RFA signal at flattop indicated by the arrow. (The red trace is the beam current and the green trace is the MI ramp.)

Tracking Conditioning

We refer to Figure 9 for how conditioning of the beam pipe is tracked. Using steel (green curve) as our example, we see a small amount of ecloud until the current in MI is about 30×10^{12} protons. When the MI current is increased from 30×10^{12}, we see that the ecloud signal takes off very quickly. The result is a curve that takes the shape of a

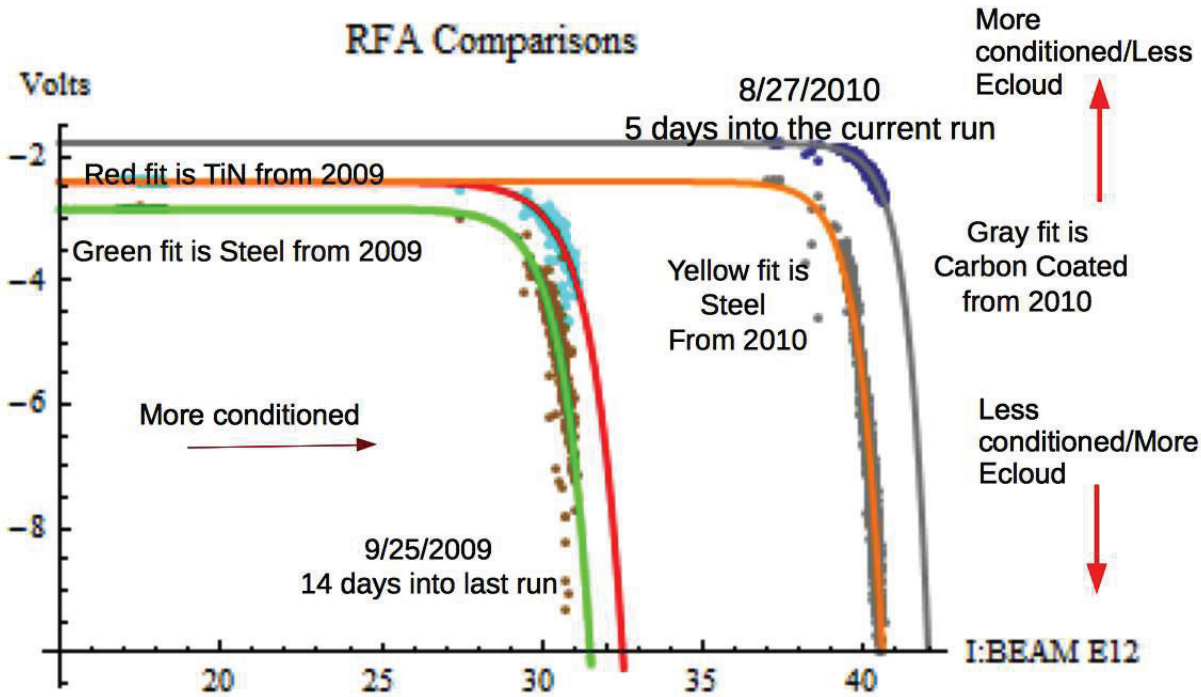

Figure 9: This is a comparision between TiN, steel for the first run and aC, steel for the current run. The beam pipe appears to condition faster after 5 days for aC, steel than TiN, steel after 14 days because of the higher initial intensity in MI.

"knee". The location of the "knee" is a very good way to track the threshold current for ecloud because as the beam pipe is conditioned, the curve flattens out at that conditioning intensity. When the intensity of MI is increased, a new curve (for example the yellow curve) with a knee coincident with the higher MI intensity is formed. And again, as the beam pipe is conditioned at this intensity, the curve flattens out. Therefore, as the beam pipe gets more conditioned, the knee moves towards the right and thus by tracking the knee we can see how the threshold current in MI evolves as a function of electron exposure.

All the necessary data for tracking conditioning is data logged and analyzed offline with the following procedure (also see Figure 12):

- conditioning is tracked by data logging the dips in the RFA (Figure 12(a)) signals and plotting them (Figure 12(b)).
- The knee from Figure 12(b) is tracked and forms the ordinate of Figure 12(d). Each dip is integrated to get a total charge. This forms the abscissa of Figure 12(d).
- Figure 12(d) is the conditioning plot.

The knee in Figure 12(b) for the first run where TiN and steel beam pipes were used and for the current run where aC and steel beam pipes are used are shown in Figure 9. It appears that aC and steel in this current run has conditioned better after 5 days compared to TiN and steel in the previous run after 14 days. However, this is accounted for by the higher initial MI intensity for the present run.

The conditioning curves for TiN and steel are shown in Figure 13. The signal gets very small for TiN after $\sim 3.5 \times 10^{17}$ are absorbed — this is the "hook" in the plot. However, there is still a strong ecloud signal in the steel beam pipe despite having absorbed more than twice the number of electrons (Note: the TiN conditioning curve shown in the talk is incorrect.)

The conditioning curve for aC, steel is much more interesting. There was a vacuum leak near RFA3 which affected the aC properties. After the leak, the aC at this location seems to follow the steel condition curve rather than the aC conditioning curve at the RFA2 location. We spoke to the vacuum group and found that the leak only got up to 10^{-6} torr (normal vacuum $\sim 10^{-8}$ torr) before gate valves closed. The repair was done in atmosphere and normal procedures were followed. Figure 14 shows the clear drop in the conditioning curve after the vacuum incident for aC at the RFA3 location. Note that as of this writing we only have 1 month worth of aC data compared to 1 year of TiN data.

Ecloud Energy Spectrum

The ecloud spectrum has been measured for TiN, aC and steel at RFA1, RFA2 and RFA3. The measurements are shown in Figure 15. We are unable to measure the energy below 20 eV because we need to bias the grid of the RFAs

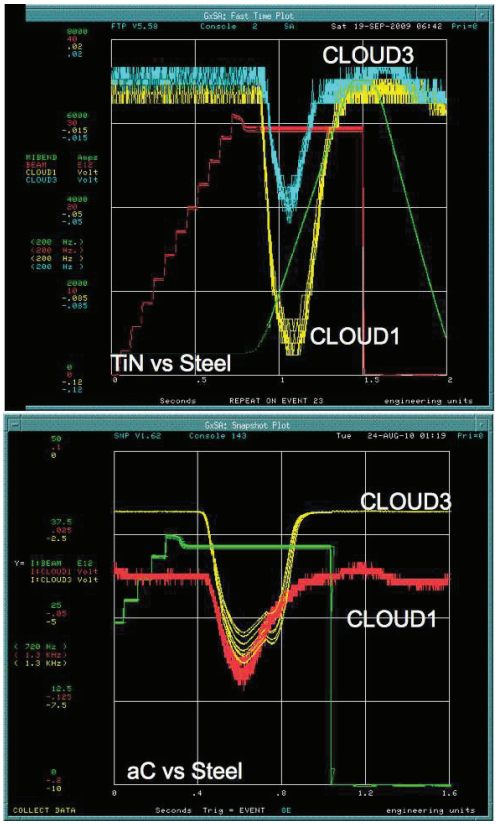

Figure 10: These two figures compare the TiN, aC and steel signals on CLOUD1 and CLOUD3. There is a strong double dip structure from CLOUD3 with aC installed. This double dip structure is not seen on CLOUD1. Note: On this figure only CLOUD3 on aC have the amplifiers on.

by 20V. No errorbars are shown in these graphs at this time because they data is still being analyzed. The negative fraction for the RFA3 spectrum for the region midway between the TiN beam pipe and steel beam pipe has a negative fraction which is unphysical. These negative values should be consistent with zero with the errorbars included.

CONCLUSION

The ecloud setup in MI-52 has yielded many important results which will guide us in deciding which type of coatings will be necessary for ProjectX. At least from our experimental results so far, TiN and aC seem to have very similar performances in ecloud mitigation. A fortuitous vacuum leak at our test location also show that aC may not be very robust. Steel, on the other hand, even after ~ 1 year of exposure to electrons is still conditioning and still shows ecloud buildup.

REFERENCES

[1] R.A. Rosenberg and K.C. Harkay, "A Rudimentary Electron Energy Analyer for Accelerator Diagnostics", Nucl. Instrum. Methods, **A453**, 507 (2000).

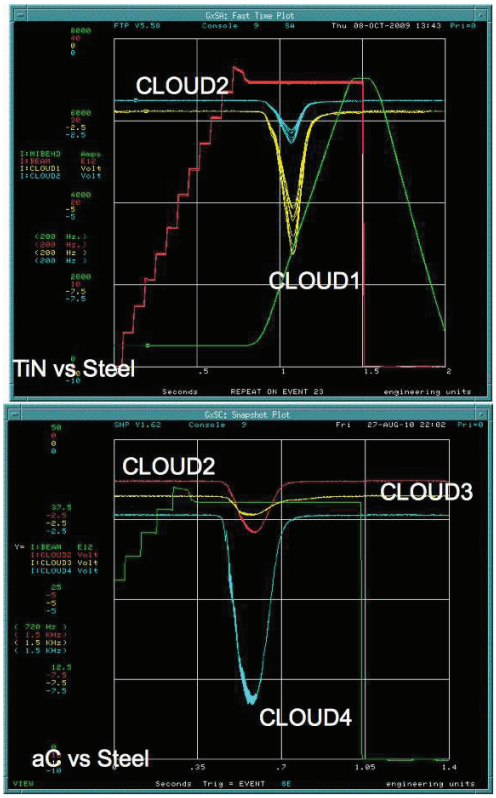

Figure 11: As time evolves, the double dip structure on CLOUD3 (aC) vanishes and the signals on all the RFAs get smaller.

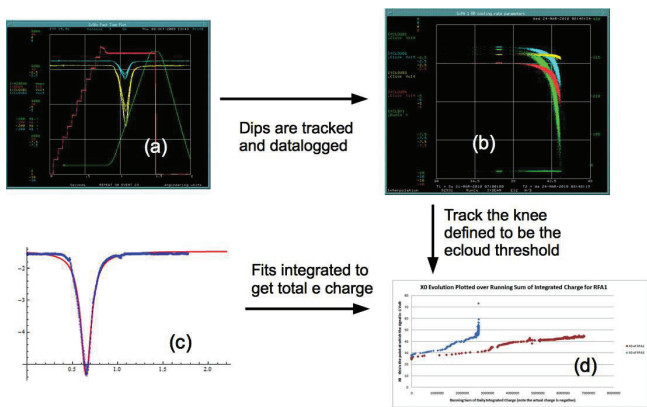

Figure 12: This figure shows how conditioning of the beam pipe is tracked. See text for details.

[2] N. Eddy *et al*, "Measurement of Electron Cloud Development in the Fermilab Main Injector Using Microwave Transmission, PAC2009, Vancouver, May 2009, WE4GRC02.

[3] C.Y. Tan *et al*, "An Improved Retarding Field Analyzer for Electron Cloud Studies", PAC'2009, Vancouver, May 2009, TH5RFP041.

[4] SIMION 8.0.4, `http://www.simion.com`.

[5] P.L.G. Lebrun, "Simulation of the electron cloud in the Fermilab Main Injector using VORPAL", these proceedings.

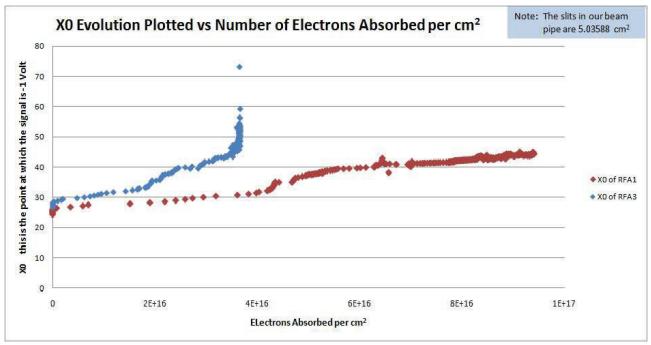

Figure 13: The conditioning curve for TiN and steel. The RFA signal on the TiN becomes very small after about 3.5×10^{17} are absorbed while the steel continues to condition.

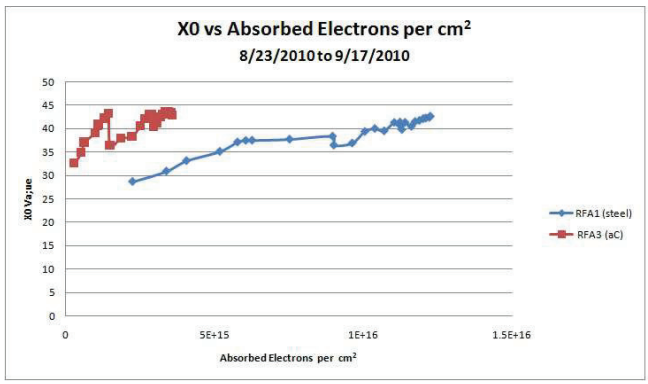

Figure 14: After the vacuum incident, there is a sharp drop in the conditioning curve of aC. Note that as of this writing we only have 1 month worth of aC data compared to 1 year of TiN data.

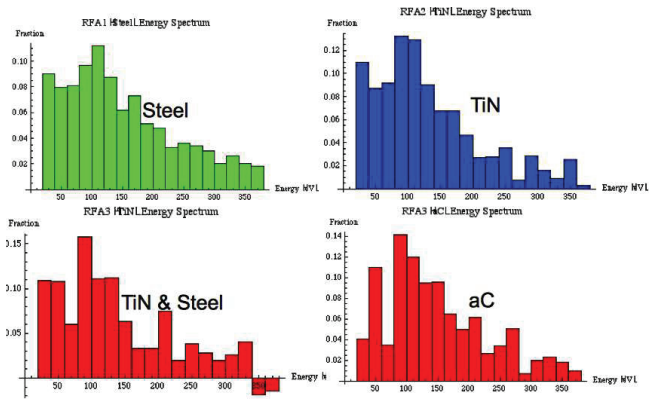

Figure 15: The energy spectrum of the ecloud collected for TiN, aC and steel at RFA1, RFA2 and RFA3. The negative fraction for the case of the RFA3 spectrum which is for the region between TiN coated beam pipe and steel beam pipe is probably consistent with zero after the error bars are included.

[6] C. Thangaraj, "Electron Cloud Studies in the Fermilab Main Injector using Microwave Transmission", these proceedings.

ANALYSIS OF THE ELECTRON CLOUD DENSITY MEASUREMENT WITH RFA IN A POSITRON RING*

K. Kanazawa#, H. Fukuma, KEK, Tsukuba, Ibaraki, Japan
J. Puneet, The Graduate Universiry for Advanced Studies, Tskuba, Ibaraki, Japan

Abstract

In a positron ring such as KEKB LER, clouding electrons receive an almost instantaneous kick from circulating bunches. Therefore, high energy electrons in the cloud are produced locally around the beam just after the interaction with the bunch. The authors gave an estimation of their density using a high energy electron current measured with RFA and a calculated volume neglecting their initial velocity before the interaction with the bunch [1][2]. To evaluate the accuracy of this estimation, the process of the measurement is analyzed using the phase space density for the motion of electrons in the transverse plane of the beam. The expressions that can evaluate the accuracy of the estimation with the help of simulation are obtained. One of the authors has shown that the accuracy for a drift space is within ±5% error [3]. For other applications such as in a solenoid field or in a quadruple field, the evaluation is not yet given. In addition to this discussion, some examples of the estimation of the electron cloud density with RFA are shown.

INTRODUCTION

The electron cloud in the accelerator ring of positively charged particles is one of serious obstacles to achieve a stable low emittance beam. The study of the electron cloud to clarify and to mitigate the effect is now a major issue for the design of the positron damping ring of ILC or for the upgrade of LHC. The positron storage ring of KEK B-Factory (LER), which was shutdown June 2010, had been suffering from the electron cloud problem in increasing the stored current to achieve a higher luminosity. During the study of the electron cloud in LER, a simple idea to estimate the density with a retarding field analyzer (RFA) attached to a vacuum chamber is developed.

The idea arises from the efforts to explain the measurement in a drift space. Most of bunches in LER are spaced by 6 ns (3 bucket space). The typical bunch population during collision experiment is around 7×10^{10}. The major part of electrons arrive at an RFA have low energies less than 20 eV. A time-resolved observation shows these low energy electrons arrive almost continuously except large train gaps. On the other hand high energy electrons, for example, with energies more than 2 keV, are observed as a rapidly changing current which has regular peaks corresponding to the bunch pattern [1].

Obviously the peak consists of electrons which get their energy through the interaction with the high electric field near a circulating bunch. Since the electric field of a relativistic positron bunch is contracted into the transverse plane of the beam, the resulting acceleration occurs essentially in this plane. The radius of the transverse area, where these high energy electrons stayed just before the interaction with the bunch, can be calculated from the bunch charge and the retarding bias with sufficient precision. A possible ambiguity due to the initial energies of electrons is small because the energy of most electrons before the interaction is less than few×10 eV. If the retarding bias is set so that electrons in the corresponding area can reach the duct wall before the next bunch arrives, from the pulse of electron current the density near the beam (and in front of the bunch) can be known. Usually, an RFA is set behind a small aperture of the duct wall. Therefore it cannot receive the whole electrons of the area but observes a finite portion of it. The estimation of this observed area is not simple because of the initial energies of electrons [3]. The point of our idea is to propose an approximation for the observed area to use the area obtained by assuming electrons are at rest before the interaction. Using the calculated observed area, the near beam electron cloud density (just before the interaction with a bunch) is estimated as:

$$\text{Density} = \frac{\text{No. of electron per bunch}}{\text{Observed area} \times \text{Detector length}}. \qquad (1)$$

This idea was first applied to drift spaces and gave a reasonable estimation of density [1]. The idea is further developed to apply for the measurement in a solenoid field and in a quadrupole magnetic field. The resulting estimation of the electron cloud density seems also reasonable [2].

In the following, the process of the high energy electron measurement with RFA is analysed using the phase space density of electrons and how the validity of the approximation adopted in our estimation can be checked with the help of the simulation on electron motion is shown. In addition the result of the density estimations under different types of a magnetic field is

*Work supported by The Japan/US Cooperation Program
#ken-ichi.kanazawa@kek.jp

summarized to give an idea for modelling the condition in simulation.

ANALYSIS OF MEASUREMENT WITH BIASED RFA

The goal of this section is to relate the number of electrons measured with a biased RFA with the density of the cloud just before the interaction with a circulating bunch, following the line of thought in the previous section. We use the density in the μ-space. Since the motion of electrons in a positron ring is nearly confined in the transverse plane to the beam, the form of the density in the six dimensional phase space (Ω) can be assumed to be,

$$\Omega(v_x, v_y, v_z, x, y, z, t) = \delta(v_z)\rho(v_x, v_y, x, y, t). \quad (2)$$

At a certain location of an accelerator ring, special timings are specified. The time just before a circulating bunch arrives at the location is t_0, just after the bunch passes is t_1, and at t_B, the next bunch arrives.

At $t = t_1$, most high energy electrons are produced around the beam after the interaction with a positron bunch. We define a circular region S_0 that covers most, for example 99%, of the position (at $t = t_0$) of those electrons which get energies higher than certain value (= retarding bias) at $t = t_1$. Then we define some functions on this region.

Average density around the beam at $t = t_0$,

$$\rho_{AV} = \frac{1}{S_0 L}\int dv_x dv_y \int \rho(v_x, v_y, x, y, t_0) L dx dy. \quad (3)$$

Spatially averaged velocity distribution around the beam at $t = t_0$,

$$D(v_x, v_y) = \frac{1}{\rho_{AV} S_0 L}\int_{S_0} \rho(v_x, v_y, x, y, t_0) L dx dy. \quad (4)$$

This D is normalized as,

$$\int D(v_x, v_y) dv_x dv_y = 1. \quad (5)$$

Using these two functions, we rewrite the density function as,

$$\rho(v_x, v_y, x, y, t_0) = \rho_{AV} D(v_x, v_y) + \Delta(v_x, v_y, x, y, t_0). \quad (6)$$

The newly introduced function Δ satisfies in the S_0,

$$\int dv_x dv_y \int_{S_0} \Delta(v_x, v_y, x, y) dx dy = 0. \quad (7)$$

Now we relate the density at $t = t_0$ to the number of electrons per positron bunch observed with a biased RFA. For this we think as follows: the position of electrons that have a velocity (v_x, v_y) at $t = t_0$ and then observed with a biased RFA fill a specified region $S(v_x, v_y, t_0)$ with in S_0. We assume the bias of an RFA is set so that all electrons in $S(v_x, v_y, t_0)$ reaches an RFA before $t = t_B$. Then the number of observed electrons within the velocity space volume $dv_x dv_y$ around (v_x, v_y) is given by,

$$dN_e = dv_x dv_y \int_{S(v_x, v_y, t_0)} \rho(v_x, v_y, x, y, t_0) L dx dy. \quad (8)$$

Therefore, the total number of electrons per positron bunch observed with a biased RFA is,

$$N_e = \int dv_x dv_y \int_{S(v_x, v_y, t_0)} \rho(v_x, v_y, x, y, t_0) L dx dy. \quad (9)$$

To see the assumptions in our model more clearly in this formalism, we introduce Eq. (6) in this expression. Then we get,

$$\begin{aligned} N_e &= \int \rho_{AV} D(v_x, v_y) dv_x dv_y \int_{S(v_x, v_y, t_0)} L dx dy \\ &\quad + \int dv_x dv_y \int_{S(v_x, v_y, t_0)} \Delta(v_x, v_y, x, y) L dx dy \\ &= \rho_{AV} L \int S(v_x, v_y, t_0) D(v_x, v_y) dv_x dv_y \\ &\quad + \int dv_x dv_y \int_{S(v_x, v_y, t_0)} \Delta(v_x, v_y, x, y) L dx dy \\ &= \rho_{AV} L \cdot (\text{averaged observed area}) \\ &\quad + \begin{pmatrix} \text{correction mainly due to} \\ \text{the spatial nonuniformity} \end{pmatrix} \end{aligned} \quad (10)$$

According to this formalism, approximations adopted in our model are expressed as,

$$\begin{aligned} S &\equiv \int S(v_x, v_y, t_0) D(v_x, v_y) dv_x dv_y \cong S(0,0,t_0) \\ R &\equiv \frac{\int dv_x dv_y \int_{S(v_x, v_y, t_0)} \Delta(v_x, v_y, x, y) L dx dy}{\rho_{AV} S L} << 1 \end{aligned} \quad (11)$$

All quantities appeared in this expression can be calculated by the simulation on the electron motion. Then we will have an evaluation on the accuracy of our estimation. Of course, by direct comparison between the

estimated density and the simulated density, we can evaluate the accuracy of the measurement. In this case, however, such factor as the efficiency of an RFA comes into as an ambiguity. To see the validity of physics included in our idea, above evaluation is superior.

For a drift space, one of the authors has shown [3],

$$S \approx S(0,0,t_0)\times(1\pm 0.05), \quad R \approx 0.01 \tag{12}$$

Thus, our working model gives sufficiently good estimation of the density in a drift space.

ESTIMATED ELECTRON CLOUD DENSITY

The measurement of the electron cloud density was performed for several bunch patterns. Here, the results for 6 ns bunch spacing are presented. In LER the bunch current of 1 mA corresponds to the bunch population of 6.3×10^{10}. The vacuum duct is made of OFC.

The number of electrons that enter an RFA per bunch is calculated from DC current measured by RFA, so it is average. The density is obtained by estimating $S(0,0,t_0)$ for a given geometry of measurement. The efficiency of the RFA is assumed to be determined by geometry only.

The estimated density corresponds to the density close to the beam and just before the interaction with a bunch.

In a Drift Space

In a drift space, RFA is attached to a pump port. The schematic view is given in Fig. 1. The pump port is separated from the beam with a grid that has deep slots facing the beam which are backed up with thin bars.

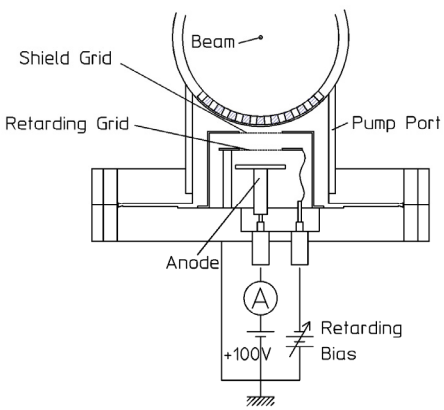

Figure 1: Schematic view if RFA at a pump port.

For a drift space, we use an analytical expression for $S(0,0,t_0)$ given by assuming a point bunch,

$$S(0,0,t_0) = Fr_e^{\,2} N_B^{\,2} \frac{m_e c^2}{eV_b}, \tag{13}$$

where F is a reduction factor determined by the geometry of measurement and in general by the detector efficiency. In this example, only geometrical condition is considered. The remaining factor is an cross sectional area that is limited by the bias of an RFA (V_b).

Figure 2 shows an example of density estimation in a drift spaces. The effect of various surface coating is compared. The location of this measurement is in the middle of 200m straight section. The last bending magnet in the arc is nearly 100m far. Therefore the direct synchrotron radiation is negligible. The divergence of the density at low bunch currents is not real. It is because the detection limit is given as a constant current. The density is of the order of 10^{-11} m^{-3} and smaller than an arc section (typically ~10^{-12} m^{-3}, not shown here). This is due to the difference of the intensity of direct synchrotron radiation. The bump at around the bunch current of 0.9 mA is considered as a kind of trapping effect which depends on the bunch space.

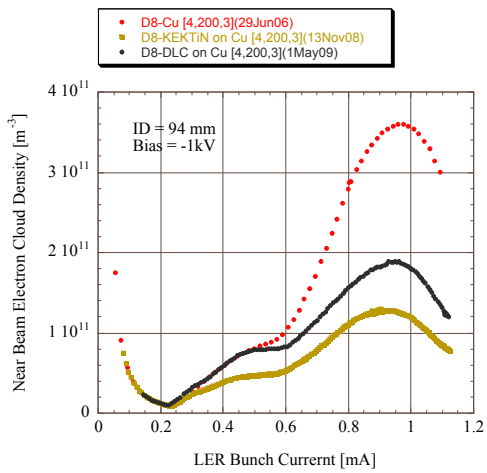

Figure 2: An example of the density estimation in a drift space. The effect of TiN coating and DLC (Diamond Like Carbone) is compared with copper surface.

In a Solenoid Field

In a solenoid field, electrons accelerated in the neighbour of a bunch must have an energy larger than a certain value to reach the duct wall, which is determined by the radius of the beam duct and the intensity of the magnetic field. For the detector on the duct wall, energy selection is thus automatic. The opening of the detector is set vertically to the wall and hidden in a groove of the wall. The detector needs in principle only a collector. However, actually it also has a retarding grid which is used to reject electrons migrating along the wall (Fig. 3).

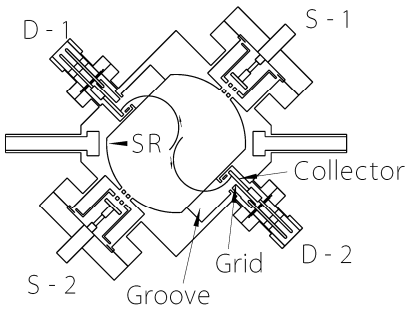

Figure 3: Cross section of the detector system for the measurement in a solenoid field. Detectors S-1 and S-2 are a standard RFA and are used to estimate the density without a solenoid field. Detectors D-1 and D-2 are used under a solenoid field. The diameter of the duct is 92 mm. Typical orbits of the electron which the detectors are expected to catch are shown. SR shows the location exposed to direct synchrotron radiation.

The observed area is calculated using a number of subroutines of CLOUDLAND [4]. At first, electrons are stationed on the grid of 0.1 mm by 0.1 mm in the transverse plane of the beam. Then, the motion of electrons after the interaction with a bunch is numerically traced. The initial position of electrons that enter the detector within 6 ns after passing of a bunch is marked on the grid. The time limit of 6 ns is selected for the present operational pattern of LER. The real size of a bunch at the location of measurement is used in the calculation. The bunch length is 6 mm.

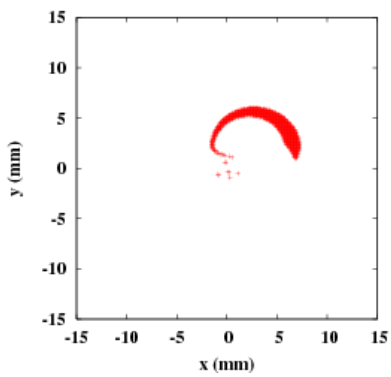

Figure 4: The observed area in a solenoid field. The bunch passes the centre (0, 0). The solenoid field is 50 G. The location of the detector is downward (different from Fig. 3).

Figure 4 shows the observed area for a solenoid field for the bunch current of 1.2 mA and B = 50 G. The area is confined around the beam as expected. Note in Fig. 4, the direction of the detector is downward. The observed area was calculated for different bunch currents and fitted by a polynomial of the bunch current. For both cases the area is nearly proportional to the square of the bunch current.

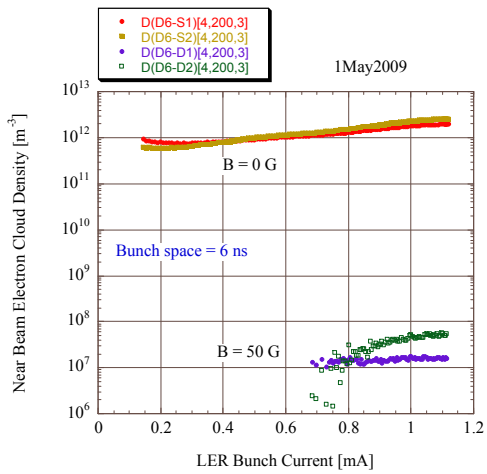

Figure 5: Electron cloud density with and without a solenoid field.

The solenoid coil with the inner diameter of 400 mm and the length of 530 mm was prepared to produce the central field of 50 G. The density without a solenoid field is estimated by standard RFAs. Under the solenoid field, two detectors D-1 and D-2 (see Fig. 3) show a large difference in measured currents. The ratio of both current is independent of bunch patterns. The difference is due to a background current that is proportional to the total beam current and is independent of bunch patterns. It is larger in the detector D-2 whose opening faces the surface directly illuminated by synchrotron radiation. This background was understood to be photo-electrons due to the reflected synchrotron radiation which are produced on the grid that is biased -100 V. For the estimation of cloud density, this background is subtracted. The remaining currents become similar for both detectors.

Figure 5 shows the comparison of the densities as a function of the LER bunch current, with and without a solenoid field. By applying the solenoid field of 50 G, the density becomes lower by four orders of magnitude. The effectiveness of the solenoid field is first demonstrated by the direct measurement of cloud density. The estimated density can be the upper limit of the central density. Simulations give the upper limit of 10^6 m^{-3} [5].

In a Quadrupole magnet

In a quadrupole magnetic field, electrons accelerated towards the magnet pole move spirally around the B-axis shown in Fig. 2, losing their energy along this axis to the

spiral motion around this axis. An RFA is set in front of the magnet pole. Only here, electrons from the neighbour of the beam can be observed. The retarding bias of the RFA selects longitudinal energies along the above mentioned axis (Fig. 6).

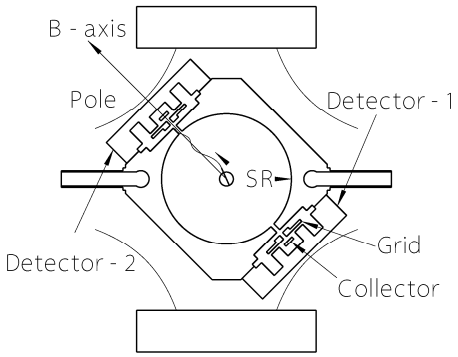

Figure 6: Cross section of the detector for a quadruple magnet. The detector opening is in front of the magnet pole. A sketch of an electron orbit that enters the detector is shown. The diameter of the duct is 94 mm. SR shows the location exposed to direct synchrotron radiation.

The observed area for a quadruple magnetic field case is calculated similarly as the case in a solenoid field. Figure 7 shows the result for a quadrupole magnetic field for the bunch current of 1.2 mA and the field gradient of -3.32 Tm^{-1}. The direction of the detector is up-left. The big 'island' in Fig. 7 is an expected region by rough analysis. The small islands correspond to electrons that get longitudinal velocity (normal to the figure) after the interaction with a bunch. In estimating an observed area, all points are included.

Figure 8 shows the density estimation in the quadrupole magnet QA1RP.Two detectors give different estimations of density though the general feature of two curves looks similar. This difference is observed to be sensitive to the position of beam orbit. It was not tried to adjust the beam to match the two curves. The green squares are the densities calculated by CLOUDLAND. Agreement with simulation is rather good for our way of approximation. From simulation, it has been long claimed that the central density in a quadrupole magnet is about two orders of magnitude lower than a typical drift space density. This measurement confirmed the assertion for the first time.

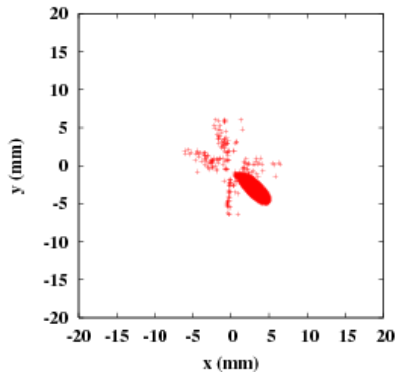

Figure 7: The observed area in a quadruple magnetic field. The field gradient is -3.32 Tm^{-1}. The location of the detector is top-left. Electrons whose energy of the motion in the direction normal to the detector is larger than 1 keV are selected (not selected by the total energy).

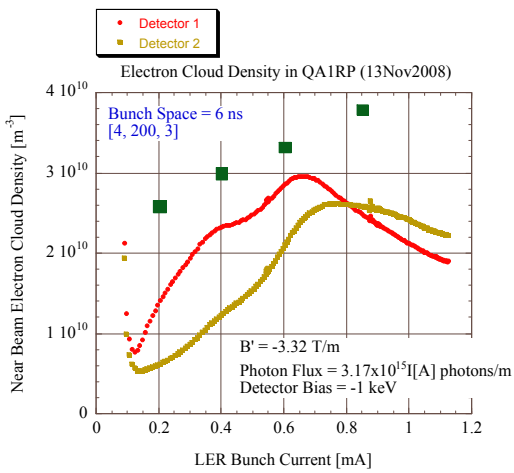

Figure 8: Electron cloud density in the quadrupole magnet QA1RP.

SUMMARY

We proposed an idea to estimate the electron cloud density using a high energy electron current measured with RFA and a calculated volume neglecting their initial velocity before the interaction with the bunch. To evaluate the accuracy of this estimation, the process of the measurement is analyzed using the phase space density for the motion of electrons in the transverse plane of the beam. The expressions that can evaluate the accuracy of the estimation with the help of simulation are obtained. One of the authors has shown that the accuracy for a drift space is within ±5% error [3]

Estimated densities in a drift space give reasonable values. Based on our idea, it is found that the near beam cloud density is reduced by more than four orders of

magnitude when a solenoid field of 50 G is applied. The estimated density in a quadrupole magnet is close to the value obtained by simulation.

Judging from these estimated densities, our idea seems to provide one of a reasonable method to estimate the local electron cloud density. The evaluation of the accuracy for measurements in a solenoid field and in a quadrupole magnet still remains.

ACKNOWLEDGEMENT

The authors wish to express sincere thanks to H. Hisamatsu for his preparation of detector electronics and to M. Tobiyama for his effort to stabilize stored beam during measurement.

REFERENCES

[1] K. Kanazawa, H. Fukuma, H. Hisamatsu, and Y. Suetsugu, "Measurement of the Electron Cloud Density around the Beam", PAC'05, Knoxville, Tennessee, June 2005, FPAP007, p. 1054 (2005); http://www.JACoW.org.

[2] K. Kanazawa, and H. Fukuma, "Measurement of the Electron Cloud Density in a Solenoid Coil and a Quadrupole magnet at KEKB LER", IPAC'10, Kyoto, Japan, May 2010, TUPD041, p. 2015 (2010); http://www.JACoW.org.

[3] P Jain, H. Fukuma, K. Kanazawa, and Y. Suetsugu, "Analysis of the Measurement of Electron Cloud Density under Various Beam-optics Elements in KEKB LER", IPAC'10, Kyoto, Japan, May 2010, TUPC050, p. 1835 (2010); http://www.JACoW.org.

[4] L. F. Wang, H. Fukuma, K. Ohmi, S. Kurokawa, K. Oide, and F. Zimmermann, "Numerical Study of the Photoelectron Cloud in KEKB Low Energy Ring with a Three-Dimensional Particle in Cell Method", Phys. Rev. ST-AB 5 (2002) 124402.

[5] L. Wang, H. Fukuma, K. Ohmi, and Y. Suetsugu, "3D Simulation of Photoelectron Cloud", PAC'01, Chicago, Illinois, June 2001, FOAB010, p. 701 (2001); http://www.JACoW.org.

STATUS OF COLDDIAG: A COLD VACUUM CHAMBER FOR DIAGNOSTICS

S. Gerstl[#], T. Baumbach, S. Casalbuoni, A. W. Grau, M. Hagelstein, D. Saez de Jauregui,
Karlsruhe Institute of Technology (KIT), Karlsruhe, Germany,
C. Boffo, G. Sikler, BNG, Würzburg, Germany,
V. Baglin, CERN, Geneva, Switzerland,
M. P. Cox, J. C. Schouten Diamond, Oxfordshire, England,
R. Cimino, M. Commisso, B. Spataro, INFN/LNF, Frascati, Italy,
A. Mostacci, Rome University La Sapienza, Rome, Italy,
E. J. Wallén, MAX-lab, Lund, Sweden,
R. Weigel, Max-Planck Institute for Metal Research, Stuttgart, Germany,
J. Clarke, D. Scott, STFC/DL/ASTeC, Daresbury, Warrington, Cheshire, England,
T. W. Bradshaw, STFC/RAL, Chilton, Didcot, Oxon, England,
R. M. Jones, I. R. R. Shinton, University Manchester, Manchester, England

Abstract

One of the still open issues for the development of superconducting insertion devices is the understanding of the beam heat load. With the aim of measuring the beam heat load to a cold bore and the hope to gain a deeper understanding in the beam heat load mechanisms, a cold vacuum chamber for diagnostics is under construction. The following diagnostics will be implemented:

i) retarding field analyzers to measure the electron energy and flux,
ii) temperature sensors to measure the total heat load,
iii) pressure gauges,
iv) mass spectrometers to measure the gas content.

The inner vacuum chamber will be removable in order to test different geometries and materials. This will allow the installation of the cryostat in different synchrotron light sources. COLDDIAG will be built to fit in a short straight section at ANKA. A first installation at the synchrotron light source Diamond is foreseen in June 2011. Here we describe the technical design report of this device and the planned measurements with beam.

INTRODUCTION

Superconducting insertion devices (IDs) have higher fields for a given gap and period length compared with the state of the art technology of permanent magnet IDs. This technological solution is very interesting for synchrotron light sources since it permits to increase the brilliance and/or the photon energy at moderate costs. One of the key issues for the development of superconducting IDs is the understanding of the beam heat load to the cold vacuum chamber.

[#]stefan.gerstl@kit.edu

Possible beam heat load sources are:

1) synchrotron radiation,
2) resistive wall heating,
3) electron and/or ion bombardment,
4) RF effects.

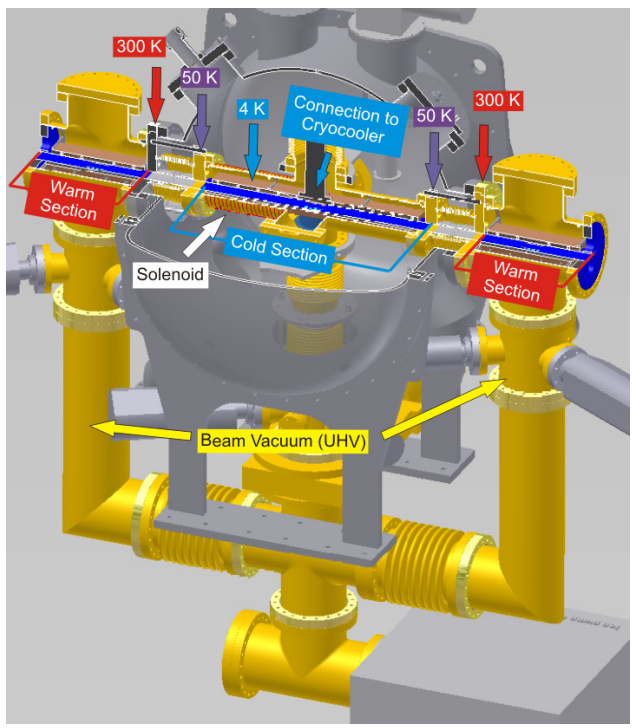

Figure 1: Sketch of the cryostat

The values of the beam heat load due to synchrotron radiation and resistive wall heating have been calculated

and compared for the cold vacuum chambers installed at different light sources with the measured values. The disagreement between beam heat load measured and calculated is not understood [1, 2, 3].

THE VACUUM CHAMBER

COLDDIAG consists of a cold vacuum chamber located between two warm sections (fig. 1), one upstream and one downstream. This will allow to observe the influence of synchrotron radiation on the beam heat load and to make a direct comparison of the cryogenic and room temperature regions.

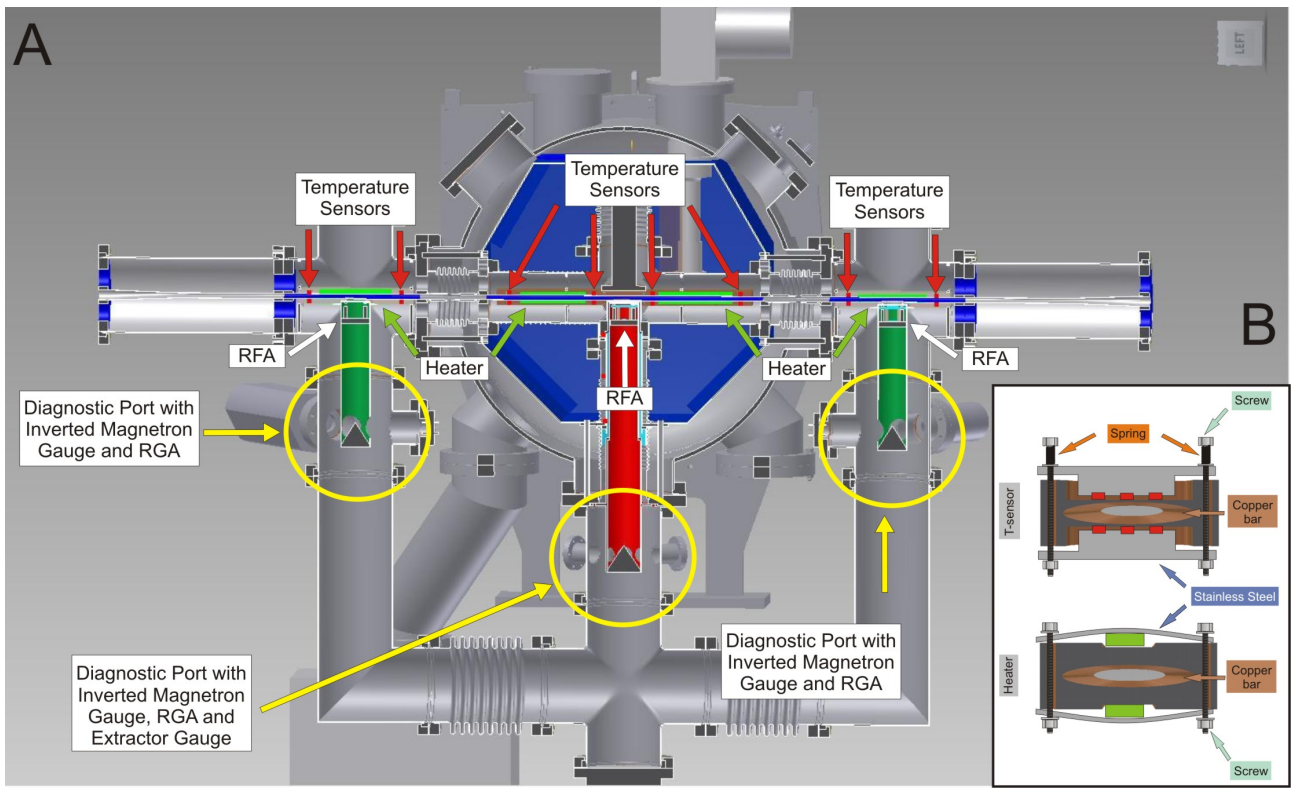

Figure 2a, b: Overview of the diagnostics installed in COLDDIAG

Studies performed with the cold bore superconducting undulator installed at the synchrotron radiation source ANKA suggest that the main contribution to the beam heat load is due to secondary electron bombardment. The electron bombardment model appears to be consistent with the beam heat load and the dynamic pressure rise observed for bunch lengths of about 10 mm [2]. Low energy electrons (few eV) are accelerated by the electric field of the beam towards the wall of the vacuum chamber, introducing heat to the cold liner and causing non-thermal desorption of gas from the cryogenic surface.
In order to gain a quantitative understanding of the problem and to find effective remedies we have designed a cold vacuum chamber for diagnostics [3] together with the company Babcock Noell to be installed in synchrotron light sources. The goal is to measure the heat load, the pressure, the gas content and the flux and spectrum of the low energy electrons bombarding the wall.
A first installation in the Diamond Light Source is foreseen for June 2011. In the following we describe the technical design report of this device and the planned measurements with beam.

The electron beam will go through a liner designed to be exchangeable. The first liner that will be tested at Diamond will be a copper bar with an elliptical cross section and 50 µm of copper plating on top to simulate the design of the installed wigglers at Diamond and the insertion devices used at ANKA. For the diagnostic port in the cold section a design based on the COLDEX device [4] was chosen. The diagnostic devices are connected to the cold liner through a warm tube to avoid gas condensation along the path between liner and diagnostic device.
The vacuum system of COLDDIAG consists of two volumes: the isolation vacuum and the beam vacuum (UHV). A DN100 CF stainless steel 6-way cross separates the two vacua (fig. 1). The beam vacuum (fig.1 marked in yellow) includes all the diagnostic devices as well as the liner. This volume will be pumped with a 500 l/min ion pump. In addition during cold operation the cold bore of the chamber works like a cryopump. A base

pressure of about 10^{-11} mbar is expected in the UHV vacuum in absence of the beam. The usage of bellows allows for the thermal shrinkage of the cold parts as they cool down. The bellows are optimized to minimize the heat transfer. They are also equipped with RF-fingers.

In order to simulate the liner of superconducting insertion devices the liner must be cooled down to reach 4.2 K in absence of beam. COLDDIAG is cryogen-free and cooled by a Sumitomo RDK-415D cryocooler. The system has 3 temperature regimes: 300 K, 50 K at the radiation shield, and 4 K at the liner. Calculations of thermal radiation and conductance show a heat load of 44.4 W on the shield at 50 K, and 0.65 W on the cold liner at 4.2 K. With a maximum cooling power of 35 W at 50 K at the 1st stage of the cryocooler and 1.5 W at 4.2 K at the 2nd stage one cryocooler is anticipated to be enough to obtain 4.2 K on the liner in absence of beam.

In order to suppress the low energy electrons bombarding the wall, a solenoid on the beam axis producing a maximum field of 100 Gauss will be wound around on one of the long arms of the cold UHV cross (symbolized by the red spiral in fig. 1).

DIAGNOSTICS

The following diagnostics will be implemented:

i) temperature sensors to measure the total heat load,
ii) retarding field analyzers to measure the electron flux,
iii) pressure gauges,
iv) and mass spectrometers to measure the gas composition.

In total 38 temperature sensors will allow to monitor the status of the chamber and measure the beam heat load. Eight calibrated Hereaus C220 PT100 sensors in each of the warm sections and 16 calibrated Lakeshore Cernox 1050-SD in the cold section are separated by only 1 mm of copper from the copper plated surface to place them as near as possible to the beam (fig. 2a, b). The spatial distribution will give us the possibility to measure not only the beam heat load but also the heat distribution on the liner. To calibrate the temperature sensors to the beam heat load we use 6 ceramic heaters, one in each warm section and 4 in the cold section. The heaters simulating the heating from the beam are made of a thin stainless steel foil between a sapphire and a Macor plate (fig. 2a, b).

In each of the connection pipes, between the liner and the diagnostic ports a small half moon shaped retarding field analyzer (RFA) will be placed to obtain the electron flux of the electrons impinging the wall. During calibration of a similar RFA for the ANKA storage ring at

INFN in Frascati it turned out, that it is not possible to obtain the electron distribution with the current setup [5]. This might be due to a background of secondary electrons produced inside the RFA. At the moment we are testing an improved setup using a lock-in technique. To solve the problem of the secondary electrons produced in the RFA we use an AC voltage inductively coupled to the retarding grid and detect the signal on the collector plate. With this setup we can directly acquire the first derivative of the electron current on the collector, which gives us the electron energy distribution.

At each of the three diagnostic ports, an inverted magnetron gauge (minimal measurable pressure 10^{-10} mbar) and a residual gas analyzer will be installed, to monitor the total pressure and the gas composition of the beam vacuum. The middle diagnostic port will also be equipped with an extractor gauge, which is more sensitive than the inverted magnetron gauges (minimal measurable pressure 10^{-11} mbar).

Through the middle diagnostic port also it will be possible to inject different gases. Therefore a heated high precision all metal leak valve, which allows to control the gas flow to the chamber down to 10^{-10} mbar*l/s was chosen. To study the effect of the injected gases under controlled conditions a defined amount of molecules must be homogeneously deposited on the cold liner. To do so we warm up the liner with the installed heaters to about 150 K. This will clean the liner surface as the boiling point of the most gases in the storage ring is below this temperature. Together with the cool down of the liner the gas will be injected until cryopumping of the cold surface starts. At this point, which will show up as a dramatic pressure decrease, the gas injection will be stopped. In several offline tests the amount of deposited gas will be checked by warming up the liner again and measuring the pressure increase of the adsorbed gas with the RGA's.

PLANNED MEASUREMENTS

During normal user operation the temperature, electron flux, pressure and gas composition will be monitored to collect statistics. During machine physics at Diamond we plan to change:

1) the average beam current to compare the beam heat load data with synchrotron radiation and resistive wall heating predictions,
2) the bunch length to compare with resistive wall heating predictions,
3) the filling pattern in particular the bunch spacing to test the relevance of the electron cloud as heating mechanisms,
4) beam position to test the relevance of synchrotron radiation and the gap dependence of the beam heat load,
5) inject different gases naturally present in the beam vacuum (H_2, CO, CO_2, CH_4) to understand the influence of the cryosorbed gas layer on the beam heat load and

eventually identify the gases to be reduced in the beam vacuum.

SUMMARY

In this paper we reported about the design and the foreseen diagnostic devices of COLDDIAG. First tests of the experimental setup will take place at ANKA after delivery in January 2011. A first installation of COLDDIAG at an electron storage ring is planned for June 2011 in the Diamond Light Source.

REFERENCES

[1] E. Wallèn, G. LeBlanc, Cryogenics 44, 879 (2004).
[2] S. Casalbuoni et al., Phys. Rev. ST Accel. Beams 10, 093202 (2007).
[3] S. Casalbuoni et al., Proceedings of EPAC08.
[4] V. Baglin et al., Vacuum 73, 201-206 (2004).
[5] D. Saez de Jauregui et al., Proceedings of PAC 2009, Vencouver, Canada

ILC Damping Rings: Benefit of the Antechamber or: Antechamber vs. SEY*

M. A. Furman,† Center for Beam Physics, LBNL, Berkeley, CA 94720,
and CLASSE, Cornell University, Ithaca, NY 14853

Abstract

We present simulation results of the build-up of the electron-cloud density n_e for the two proposed ILC damping ring lattices, DC04 and DSB3, with particular attention to the potential benefit of an antechamber. We examine a field-free region and a dipole bending magnet, with or without an antechamber. We assume a secondary electron emission model for the chamber surface based on approximate fits to measured data for TiN, except that we let the peak value of the secondary emission yield (SEY), $\delta_{\max}$, be a variable. We conclude that there is a critical value of $\delta_{\max}$ below which the antechamber provides a substantial benefit, roughly a factor ~ 40 reduction in n_e relative to the case in which $\delta_{\max}$ exceeds the critical value. We estimate the steady-state value of n_e as a function of $\delta_{\max}$, and thereby obtain the critical value of $\delta_{\max}$ for all cases considered. Thus, from the perspective of the electron-cloud effect, the inclusion of an antechamber in the design is justified only if $\delta_{\max}$ is below the critical value.

The results presented here constitute a slight extension of those previously presented in March and September, 2010 [1, 2].

INTRODUCTION AND ASSUMPTIONS

The desire to limit the potentially serious adverse consequences from the electron cloud effect (ECE) in the proposed ILC positron damping ring has led to the consideration of adding an antechamber to the vacuum chamber [3], a design decision similar to the one adopted many years ago for the positron ring of the PEP-II collider [4]. The antechamber provides the obvious benefit of extracting from the vacuum chamber a large fraction η (η =antechamber clearing efficiency) of the synchrotron-radiated photons, which are therefore unavaliable to generate photoelectrons.

Fighting against the photon clearing effect of the antechamber is the process of secondary electron emission off the walls of the chamber. The number of secondary electrons grows in time in a compound fashion, and can therefore readily negate the clearing effect of the antechamber. The secondary electron density is a nonlinear function of bunch intensity and of $\delta_{\max}$, and exhibits threshold behavior in both of these variables, hence the resulting balance between the antechamber and the SEY of the chamber material is non-trivial.

* Work supported by the US DOE under contract DE-AC02-05CH11231 and by the CESRTA program. Invited talk presented at the ECLOUD10 Workshop (Cornell Univerity, Oct. 8-12, 2010).

† mafurman@lbl.gov

We consider both proposed lattices, DC04 ($C = 6$ km) and DSB3 ($C = 3$ km), and for each of these we examine field-free regions and dipole bending magnets. For each case, we simulate the build-up with and without an antechamber of clearing efficiency $\eta = 98\%$ (Fig. 1). In all cases we set the bunch spacing $t_b = 6$ ns, and then repeat the analysis for most cases for $t_b = 3$ ns. The beam energy and bunch intensity are fixed throughout. The SEY function $\delta(E_0)$ used here is shown in Fig. 2. The emission spectrum corresponds, approximately, to that of TiN, but we let $\delta_{\max}$ be an adjustable input parameter on the range $0 - 1.4$. A detailed set of parameters is listed in Tables 1-2.

This being a build-up simulation, the beam is a prescribed (non-dynamical) function of space and time, with bunches of specified sizes, intensity and spacing. The fill pattern simulated consists of 5 trains, as defined in Table 1, whether the bunch spacing is 3 or 6 ns. The electrons, on the other hand, are fully dynamical. The analysis is carried out with the electron-cloud build-up code POSINST [5–8].

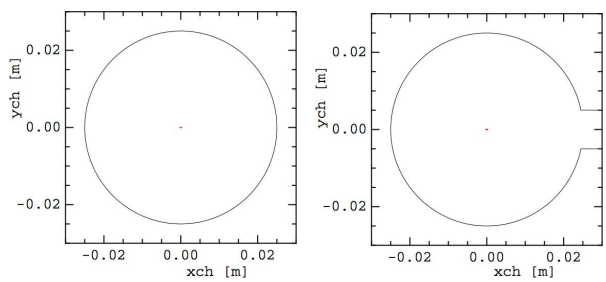

Figure 1: Cross section of the vacuum chamber, without and with an antechamber. The red dot at the center represents the approximate one-sigma beam profile.

RESULTS

Figure 3 shows the build-up of n_e for a field-free section when $t_b = 6$ ns. It is clear that (1) n_e reaches steady state for all values of $\delta_{\max}$ examined, (2) the steady-state value is slightly larger for DSB3 than for DC04, and (3) when an antechamber is present, the steady-state value of n_e is a factor ~ 40 lower than the no-antechamber case.

Figure 4 shows the corresponding results for a dipole bending magnet. In this case, one sees that the antechamber also provides a protection factor of ~ 40 only if $\delta_{\max}$ is sufficiently low: the critical value of $\delta_{\max}$ is ~ 1.2 for DC04, and ~ 1.1 for DSB3. If $\delta_{\max}$ exceeds this value, the build-up runs away in time until it reaches the level of the

Table 2: Input parameters that vary from DC04 to DSB3.

	DC04		DSB3	
Circumference [m]	6476.4		3238.2	
Harmonic no.	14042		7021	
n'_γ [photons/e$^+$/m]	0.33		0.47	
n'_e [photo-el./e$^+$/m] (w/o antechamber)	0.033		0.047	
n'_e [photo-el./e$^+$/m] (w. antechamber)	0.66×10^{-3}		0.94×10^{-3}	
	field-free	bend	field-free	bend
Tr. bunch sizes (σ_x, σ_y) [μm]	(360,6)	(260,6)	(270,6)	(110,5)
Dipole field B [T]	0	0.27	0	0.36

Table 1: Assumed global parameters.

Ring and beam	
Beam energy	$E_b = 5$ GeV
Bunch population	$N_b = 2 \times 10^{10}$
RMS bunch length	$\sigma_z = 5$ mm
RF frequency	650 MHz
Bunch train:	
if $t_b = 6.154$ ns: 45 bunches (spacing = 4 buckets)	
$+(15 \times 4 = 60)$ empty buckets	
if $t_b = 3.077$ ns: 45 bunches (spacing = 2 buckets)	
$+(15 \times 2 = 30)$ empty buckets	
Fill pattern simulated	$5 \times$ (train+gap)
Chamber radius	$a = 2.5$ cm
Antechamber full height (if present)	$h = 1$ cm
Antechamber clearing efficiency	$\eta = 98\%$
Quantum efficiency of chamber	QE=0.1
Radiation vertical spot size at wall	$\sigma_y = 1$ mm
Photon reflectivity	$R = 0.9$ *
Peak SEY values explored:	
$\delta_{\max} = 0, 0.9, 1.1, 1.2, 1.3, 1.4$	
Electron energy at $\delta_{\max}$	$E_{\max} = 296$ eV
SEY at $E = 0$	$\delta(0) = 0.31 \times \delta_{\max}$
Simulation parameters	
Primary macroelectrons/bunch	1,000
Max. no. of macroelectrons	20,000
Bunch profile	3D gaussian
Full bunch length	$L_b = 5\sigma_z$
Integration time step Δt:	
during bunch: 1.25×10^{-11} s $= 9$ kicks/L_b	
outside bunch: $(2.4 - 2.5) \times 10^{-11}$ s	
Space-charge grid	64×64
Grid cell size	$(5\text{ cm})/64 = 781\ \mu m$

* This implies that, if there is no antechamber, a fraction $1 - R = 0.1$ of the photoelectrons are generated localized at the right "edge" of the chamber. If there is an antechamber, the fraction of the photoelectrons that are generated localized at the right "edge" of the chamber (just above and below the slot) is 5.7×10^{-8}.

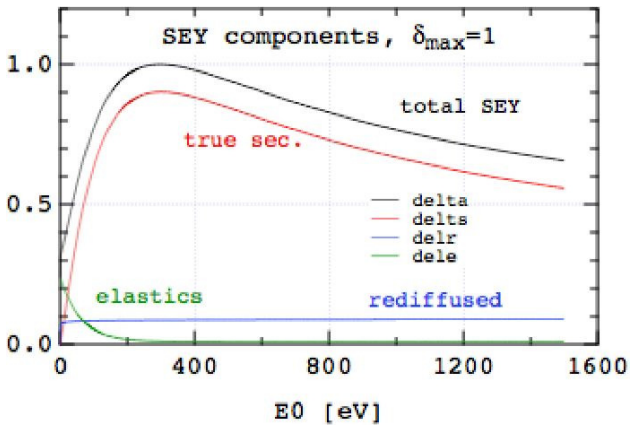

Figure 2: The three main components of the SEY function $\delta(E_0)$, for the case $\delta_{\max} = 1.0$. For other values of $\delta_{\max}$, the three components are scaled by a common factor.

no-antechamber case.[1] In the above-mentioned field-free case, we conclude therefore that the critical value of $\delta_{\max}$ exceeds 1.4, the highest value we exercised. There are simple physical arguments, and plenty of experience in other contexts, that indicates that there is always a critical value of $\delta_{\max}$. Table 3 lists the estimated values of $\delta_{\max}$ for all cases considered in this note.

Figures 5 and 6 compare the build-up for the 3-ns bunch spacing (top plots) with the previously described 6-ns spacing cases (bottom plots), for the DSB3 lattice. One sees the same qualitative features as before, except that the steady-state value of n_e for the 3-ns case is roughly twice that for the 6-ns case.

Tables 4-9 present our results in digitized form for n_e as a function of $\delta_{\max}$. Tables 4-5 summarize the estimated values of the average n_e at saturation, corresponding to the figures above. Tables 6 and 7 show the estimated value of the electron density in the neighborhood of the beam, namely within the 10-σ beam ellipse about the center of the chamber, rather than the overall density. In this case the density is averaged over the bunch length. Finally, Tables

[1] While we have not verified this statement by explicit calculation, we believe it is correct based on basic physical arguments.

Table 3: Critical value of $\delta_{\max}$.

DC04				DSB3			
$t_b = 3$ ns		$t_b = 6$ ns		$t_b = 3$ ns		$t_b = 6$ ns	
field-free	bend	field-free	bend	field-free	bend	field-free	bend
not done	not done	>1.4	∼1.2	∼1.3	∼1.1	>1.4	∼1.1

8 and 9 show the estimated electron density also within the 10-σ beam ellipse, except that these values are now the instantaneous values just before the arrival of the bunch at the location being analyzed. These instantaneous 10-σ beam ellipse values of n_e are typically used as inputs to beam dynamics simulations used to study the effects of the electron cloud on the beam (these fall outside the scope of the pressent investigation).

CONCLUSIONS AND DISCUSSION

In general terms, we conclude that:

1. n_e in DSB3 is larger than in DC04 by $10 - 20\%$.
2. The 10-σ front-bunch-density is comparable to the average n_e (within a factor 2 or less).
3. If no antechamber is present:
   (a) n_e has a generally smooth, monotonic dependence on $\delta_{\max}$ in the range examined.
   (b) n_e is $\sim 2\times$ higher for $t_b = 3$ ns than for $t_b = 6$ ns.
4. With antechamber:
   (a) n_e has a 1st-order phase transition as a function of $\delta_{\max}$.
   (b) The critical value of $\delta_{\max}$ is in the range $\sim 1.0-1.3$ (see Table 3), depending on the details of the case examined.
5. If $\delta_{\max}$ is below its critical value, the antechamber reduces n_e by factor ~ 40 relative to no-antechamber case.
6. If $\delta_{\max}$ exceeds its critical value, the antechamber offers no protection.

For the larger values of $\delta_{\max}$ examined, especially if there is no antechamber, the estimated value of n_e is within the range of what is expected to lead to beam instability [3]. For this reason, a more careful assessment might be indicated in order to ascertain with more confidence the regime of the ILC positron damping ring vis-à-vis the ECE.

For example, the sensitivity of our results to the details of secondary emission mode have not been explored here, except for $\delta_{\max}$. It seems desirable to vary $E_{\max}$ by $\pm 20\%$ and see what happens, since this parameter is not precisely known. Ditto for the secondary electron spectrum composition (true secondaries vs. rediffused vs. elastically backscattered electrons). We have also not explored the sensitivity to the antechamber height h, which determines the clearing efficiency η. By exercising both η and $\delta_{\max}$ one would determine the interesting phase diagram $\eta - \delta_{\max}$.

The numerical convergence of our results has been only partly checked. In most cases, we found that 5 trains is sufficiently long for n_e to sensibly reach steady state, provided $\delta_{\max}$ is low enough. A more accurate determination of the critical value of $\delta_{\max}$ for each case would require running the simulation for longer than 5 trains. If we increase the integration time step Δt by a factor of 3, the results do not change much, except for the "runaway cases" pertaining to the bending magnets with antechamber and $\delta_{\max}$ large enough that n_e does not reach steady state by the end of the 5th bunch train. The dependence on the space-charge grid has not been checked, but a 64×64 grid has given quite stable results in other contexts. Ditto for number of macroparticles. The photon reflectivity parameter R has not been exercised, although it is known that high values, such as $R = 0.9$ used in all cases here, tends to yield pessimistic (ie. higher) values for n_e than low values in bending magnets. A fairly accurate value of R might be determined via the program Synrad3D [9]. Finally, we have not assessed the ECE in quads, wigglers, and other regions of the machine. Traditionally, these regions do not contribute significantly to the ECE relative to the bending magnets and field-free regions, although the ILC positron damping ring is probably the first exception to this rule, given the importance of the wigglers.

ACKNOWLEDGMENTS

I am indebted to M. Pivi, M. Palmer and G. Dugan for discussions.

REFERENCES

[1] M. A. Furman, "Status of Ecloud Build-Up Simulations for the ILC DRs," ILC Ecloud Task Force collaboration meeting, 10 March 2010.

[2] M. A. Furman, "Status of Ecloud Build-Up Simulations for the ILC DRs: 3 ns Bunch Spacing," ILC Ecloud Task Force collaboration meeting, 22 Sepember 2010.

[3] M. Pivi, these proceedings.

[4] "PEP-II: An Asymmetric B Factory–Conceptual Design Report," June 1993, LBL-PUB-5379/SLAC-418/CALT-68-1869/UCRL-ID-114055/UC-IIRPA-93-01.

[5] M. A. Furman and G. R. Lambertson, "The electron-cloud instability in the arcs of the PEP-II positron ring," LBNL-41123/CBP Note-246, PEP-II AP Note AP 97.27 (Nov. 25, 1997). Proc. *Intl. Workshop on Multibunch Instabilities in Future Electron and Positron Accelerators "MBI-97"* (KEK, 15-18 July 1997; Y. H. Chin, ed.), KEK Proceedings **97-17**, Dec. 1997, p. 170.

[6] M. A. Furman and M. T. F. Pivi, "Probabilistic model for the simulation of secondary electron emission," LBNL-49771/CBP Note-415 (Nov. 6, 2002). PRST-AB **5** 124404 (2003), http://prst-ab.aps.org/pdf/PRSTAB/v5/i12/e124404.

[7] M. A. Furman and M. T. F. Pivi, "Simulation of secondary electron emission based on a phenomenological probabilistic model," LBNL-52807/SLAC-PUB-9912 (June 2, 2003).

[8] M. A. Furman, "The electron-cloud effect in the arcs of the LHC," LBNL-41482/CBP Note 247/LHC Project Report 180 (May 20, 1998).

[9] G. Dugan, S. Milashuk and D. Sagan, "Synrad3D Photon Propagation and Scattering Simulation," these proceedings.

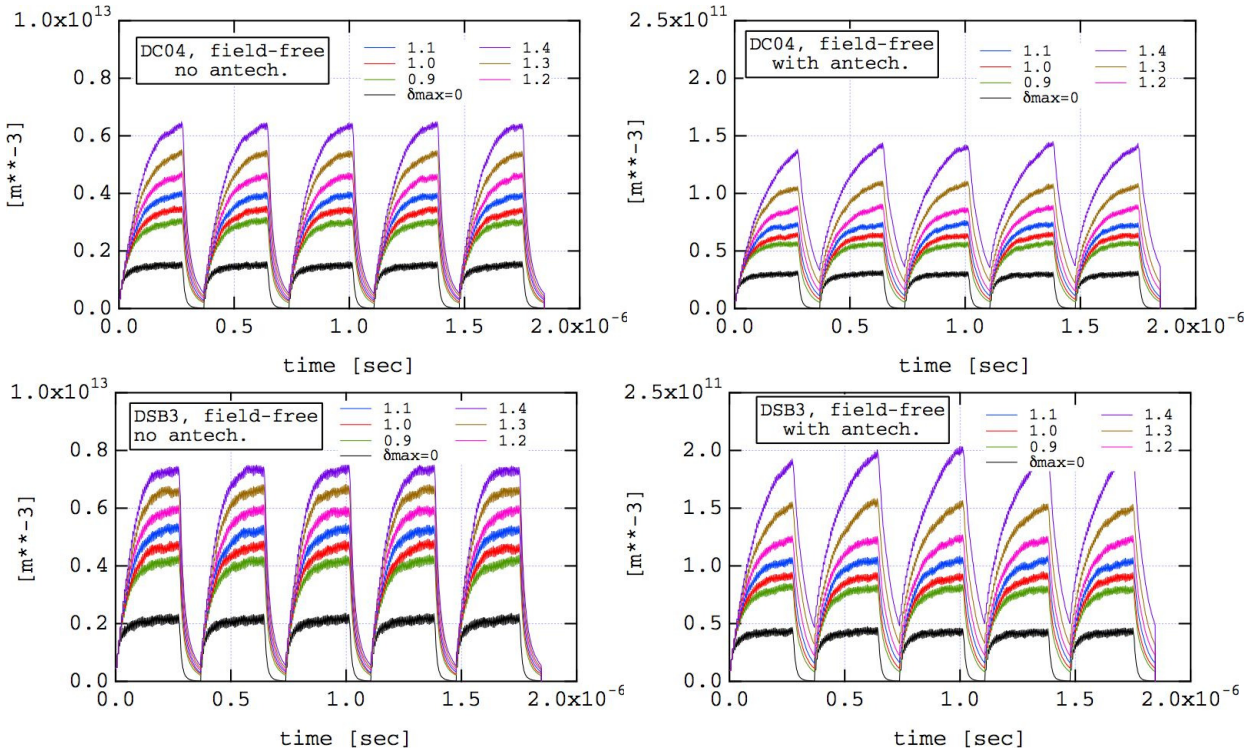

Figure 3: Electron-cloud density averaged over the chamber cross section vs. time for a field-free region and $t_b = 6$ ns. Top: DC04; bottom: DSB3. Note that the vertical scale of the right plots (with antechamber) is a factor 40 lower than in the left ones.

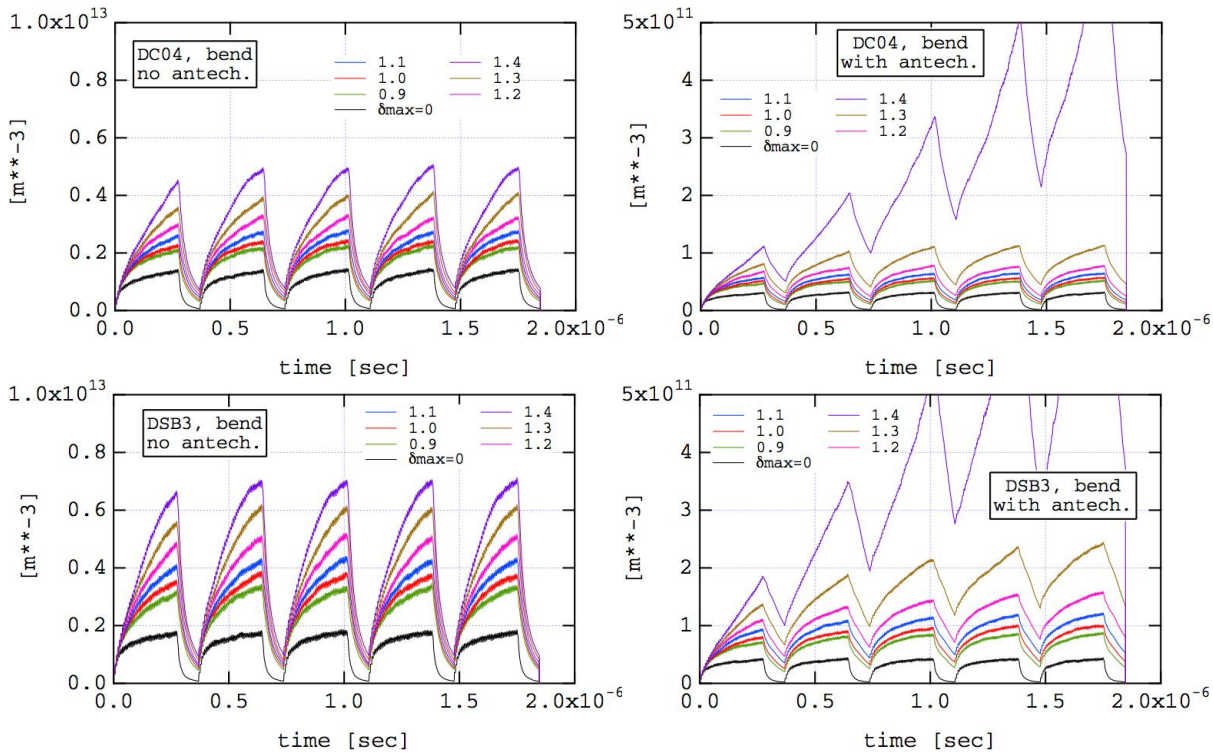

Figure 4: Electron-cloud density averaged over the chamber cross section vs. time for a dipole bending magnet and $t_b = 6$ ns. Top: DC04; bottom: DSB3. Note that the vertical scale of the right plots (with antechamber) is a factor 20 lower than in the left ones.

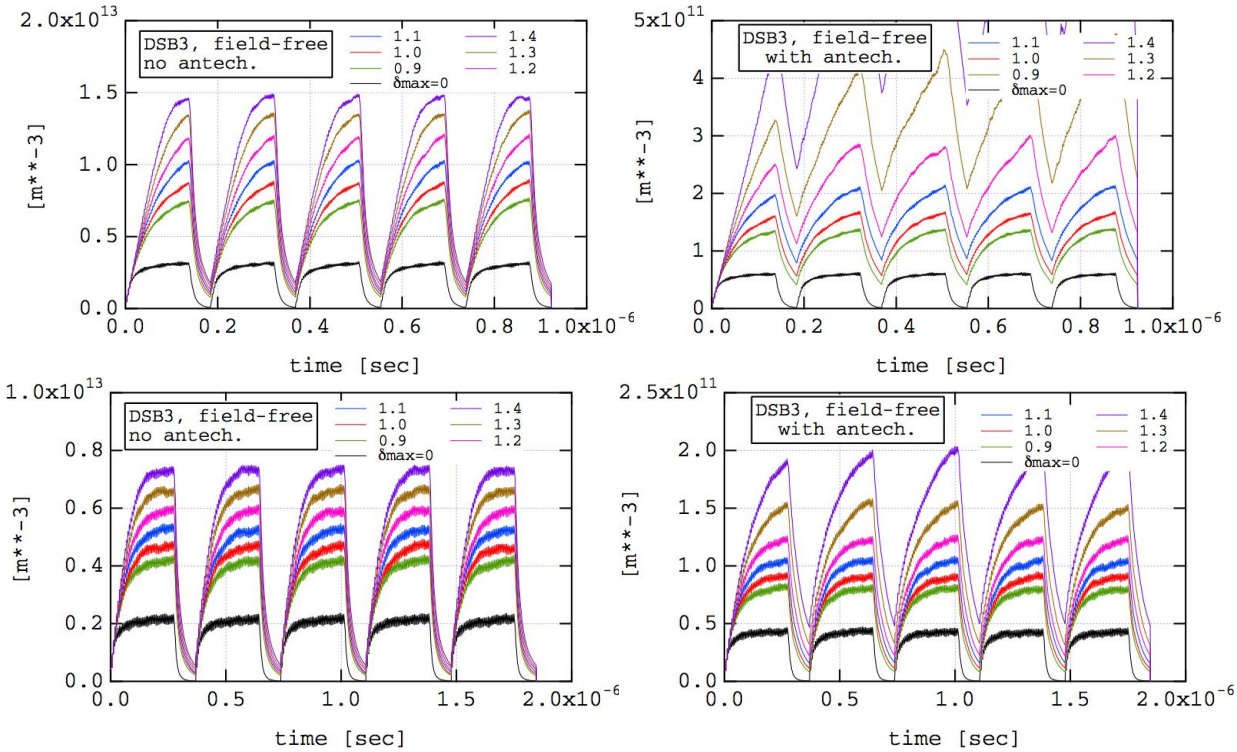

Figure 5: Electron-cloud density averaged over the chamber cross section vs. time for a field-free region for the DSB3 lattice. Top: $t_b = 3$ ns; bottom: $t_b = 6$ ns. Note that the vertical scale of the right plots (with antechamber) is a factor 40 lower than in the left ones.

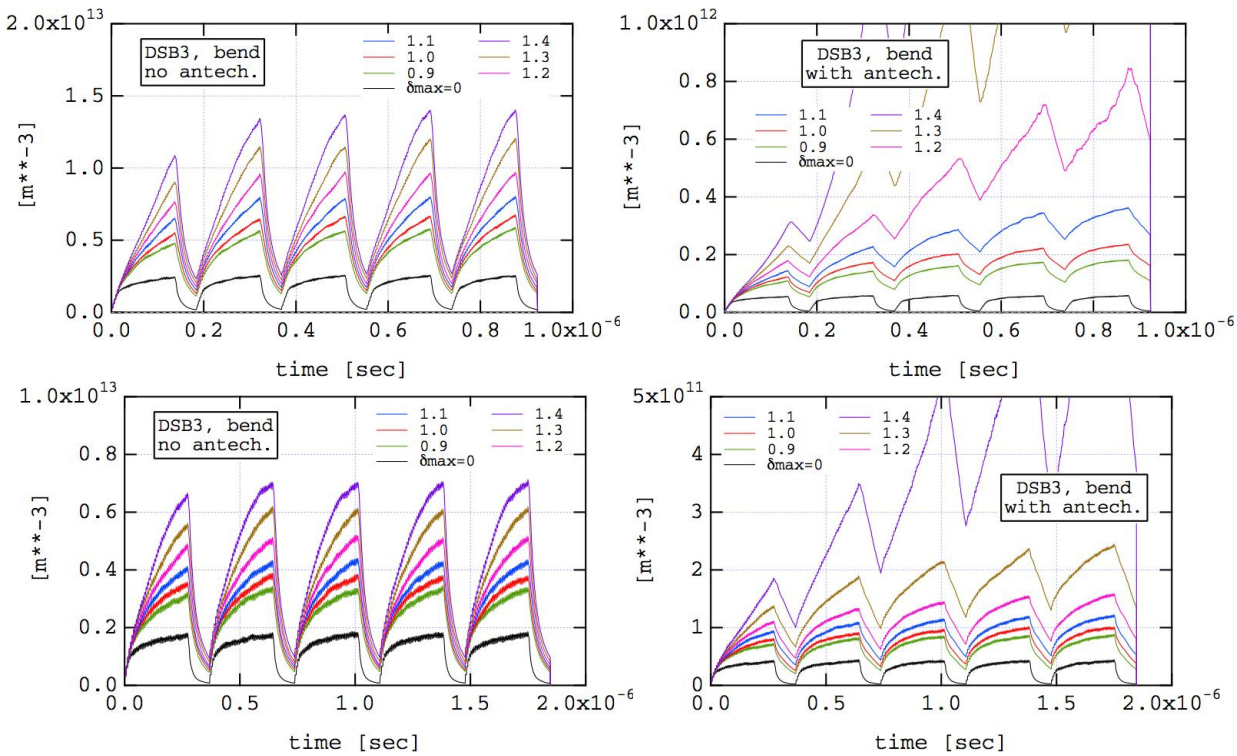

Figure 6: Electron-cloud density averaged over the chamber cross section vs. time for a dipole bending magnet for the DSB3 lattice. Top: $t_b = 3$ ns; bottom: $t_b = 6$ ns. Note that the vertical scale of the right plots (with antechamber) is a factor 20 lower than in the left ones.

Table 4: Overall n_e at saturation* for $t_b = 6$ ns (units: 10^{12} m^{-3})

	DC04				DSB3			
	field-free		bend		field-free		bend	
$\delta_{\max}$	antech.	no antech.	antech.	no antech.	antech.	no antech.	antech.	no antech.
0.0	0.031	1.5	0.032	1.4	0.044	2.2	0.045	1.8
0.9	0.056	3.0	0.054	2.2	0.081	4.3	0.090	3.3
1.0	0.064	3.4	0.058	2.4	0.092	4.6	0.10	3.7
1.1	0.073	3.9	0.065	2.8	0.10	5.3	0.12	4.3
1.2	0.087	4.7	0.079	3.2	0.12	6.0	0.16	5.1
1.3	0.10	5.4	0.11	4.1	0.15	6.6	> 0.2	6.1
1.4	0.14	6.3	> 0.8	5.0	0.20	7.3	> 1	7.0

* Saturation means here "at the end of the last (5th) train of bunches."

Table 5: DSB3: overall n_e at saturation* (units: 10^{12} m^{-3})

	$t_b = 3$ ns				$t_b = 6$ ns			
	field-free		bend		field-free		bend	
$\delta_{\max}$	antech.	no antech.	antech.	no antech.	antech.	no antech.	antech.	no antech.
0.0	0.06	3.2	0.06	2.5	0.044	2.2	0.045	1.8
0.9	0.14	7.7	0.18	5.8	0.081	4.3	0.090	3.3
1.0	0.17	9.0	0.23	6.7	0.092	4.6	0.10	3.7
1.1	0.22	10.1	0.36	7.9	0.10	5.3	0.12	4.3
1.2	0.3	12.1	>0.85	9.6	0.12	6.0	0.16	5.1
1.3	0.5	13.8	>2.75	12	0.15	6.6	>0.2	6.1
1.4	>1.2	15	>5	14	0.20	7.3	>1	7.0

* Saturation means here "at the end of the last (5th) train of bunches."

Table 6: n_e within 10 beam σ's at saturation,* averaged over bunch length, for $t_b = 6$ ns (units: 10^{12} m^{-3})

	DC04				DSB3			
	field-free		bend		field-free		bend	
$\delta_{\max}$	antech.	no antech.	antech.	no antech.	antech.	no antech.	antech.	no antech.
0.0	0.08	5.0	0.01	0.6	0.12	9	0.015	0.7
0.9	0.18	10	0.035	1.6	0.22	14	0.03	1.5
1.0	0.20	11	0.046	1.6	0.26	14	0.04	2.0
1.1	0.22	14	0.065	3.1	0.31	19	0.09	2.3
1.2	0.25	15	0.11	4.5	0.41	20	0.05	3.0
1.3	0.35	16	0.25	6.0	0.48	23	0.2	3.5
1.4	0.44	20	>4	8.0	0.62	24	>0.6	4.5

* Saturation means here "at the end of the last (5th) train of bunches." These data have large statistical errors, $\sim 50\%$ or more.

Table 7: DSB3: n_e within 10 beam σ's at saturation* (units: 10^{12} m^{-3})

	$t_b = 3$ ns				$t_b = 6$ ns			
	field-free		bend		field-free		bend	
$\delta_{\max}$	antech.	no antech.	antech.	no antech.	antech.	no antech.	antech.	no antech.
0.0	0.2	10	0.02	0.8	0.12	9	0.015	0.7
0.9	0.5	25	0.06	2	0.22	14	0.03	1.5
1.0	0.5	28	0.07	2.2	0.26	14	0.04	2.0
1.1	0.7	30	0.12	3	0.31	19	0.09	2.3
1.2	0.75	30	0.2	3.5	0.41	20	0.05	3.0
1.3	>1.4	35	>0.3	4	0.48	23	0.2	3.5
1.4	>3	40	>0.3	5	0.62	24	>0.6	4.5

* Saturation means here "at the end of the last (5th) train of bunches." These data have large statistical errors, $\sim 50\%$ or more.

Table 8: n_e at bunch front within 10 beam σ's for $t_b = 6$ ns* (units: 10^{12} m^{-3})

	DC04				DSB3			
	field-free		bend		field-free		bend	
$\delta_{\max}$	antech.	no antech.	antech.	no antech.	antech.	no antech.	antech.	no antech.
0.0	0.024	1.2	0.023	1.0	0.034	1.7	0.031	1.3
0.9	0.044	2.3	0.038	1.6	0.063	3.2	0.063	2.4
1.0	0.050	2.6	0.042	1.8	0.070	3.6	0.073	2.6
1.1	0.057	3.0	0.048	1.9	0.081	4.0	0.086	2.9
1.2	0.066	3.4	0.056	2.2	0.94	4.5	0.10	3.4
1.3	0.080	3.9	0.079	2.6	0.11	5.0	>0.2	3.9
1.4	0.10	4.5	>0.3	3.1	0.14	5.6	>0.3	4.6

* These data have large statistical errors, $\sim 50\%$ or more. Within these errors, there is no difference between the time-averaged density and the instantaneous density at the last bunch in the train.

Table 9: DSB3: n_e at bunch front within 10 beam σ's (units: 10^{12} m^{-3})

	$t_b = 3$ ns				$t_b = 6$ ns			
	field-free		bend		field-free		bend	
$\delta_{\max}$	antech.	no antech.	antech.	no antech.	antech.	no antech.	antech.	no antech.
0.0	0.1	5	0.02	0.6	0.034	1.7	0.031	1.3
0.9	0.25	10	0.04	1.6	0.063	3.2	0.063	2.4
1.0	0.28	11	0.05	2.3	0.070	3.6	0.073	2.6
1.1	0.35	13	0.1	1.9	0.081	4.0	0.086	2.9
1.2	0.45	15	0.12	3.0	0.94	4.5	0.10	3.4
1.3	0.64	16	0.23	3.3	0.11	5.0	>0.2	3.9
1.4	>1.2	16	>0.7	4.4	0.14	5.6	>0.3	4.6

* These data have large statistical errors, $\sim 50\%$ or more. Within these errors, there is no difference between the time-averaged density and the instantaneous density at the last bunch in the train.

CESRTA PRELIMINARY RECOMMENDATIONS FOR THE ILC POSITRON DAMPING RING

M. Palmer, Cornell University - CLASSE

Abstract

The first phase of the CesrTA experimental program is now complete. Electron cloud research over the course of the last 2.5 years has focused on two principle topics. The first is the characterization of methods to mitigate the electron cloud build-up in each of the magnetic field regions of concern for damping ring design. The second is the characterization of the cloud's impact on ultra-low emittance beams. Our intent is now to incorporate these results into the technical design of the positron damping ring for the International Linear Collider. Implications for the ILC DR design will be discussed.

While no paper is available here, two references were published recently covering our recommendations:

M. T.F. Pivi, L. Wang, L. E. Boon, K. C. Harkay, J. A. Crittenden, G. Dugan, M. A. Palmer, T. Demma, S. Guiducci, M. A. Furman, K. Ohmi, K. Shibata, Y. Suetsugu, J. Urakawa, C. Yin Vallgren, "Recommendation for Mitigations of the Electron Cloud Instability in the ILC", Proceedings of IPAC 2011, San Sebastian, Spain.

J. A. Crittenden, J. V. Conway, G. Dugan, M. A. Palmer, D. L. Rubin, L. E. Boon, K. C. Harkay, M. A. Furman, S. Guiducci, M. T.F. Pivi, L. Wang, "Investigation into Electron Cloud Effects in the ILC Damping Ring Design", Proceedings of IPAC 2012, New Orleans, Louisianna, USA.

SIMULATION OF ELECTRON CLOUD INDUCED INSTABILITIES AND EMITTANCE GROWTH FOR CESRTA*

M. T. F. Pivi, SLAC, Menlo Park CA,
K. G. Sonnad, G. Dugan, M. A. Palmer, CLASSE Cornell University, Ithaca NY

Abstract

The program CMAD is being used to study single bunch instabilities induced by electron clouds. In the results presented in this paper, we studied the motion of the bunch centroid, the emittance evolution and motion of single test particles within the bunch. A series of studies were performed with varying cloud densities. The spectrum of centroid motion which showed indications of head tail motion was closely examined. The emittance evolution of the beam was computed. The trajectories of single test particles were analyzed qualitatively.

INTRODUCTION

CMAD is a two species Particle-in-cell (PIC) program capable of studying interactions between beams and electron clouds [2]. A comparison between results from CMAD and other similar codes has been carried out [1] for some simple cases. In this paper, we have performed similar simulations with several additional features included. All of them represent the parameters and conditions that occurred in CesrTA during experiments being carried out to study the influence of electron clouds on the dynamics of positron beams. Several features such as head tail motion and beam emittance calculations show similar features as to what has already been observed [3].

In observations, we have typically used trains varying from 20 to 45 bunches with a 14 ns spacing. Depending upon its properties, each bunch creates a certain amount of cloud and as a result the lagging bunches experience a higher cloud density compared to the leading ones. CesrTA instrumentation has the ability to observe the turn by turn position and the beam size of each of the bunches. CMAD tracks a single bunch and so in order to simulate the effect of different bunches along the train, we need to perform a set of independent calculations with varying prespecified cloud densities. The cloud densities seen by the different bunches can be estimated from build up codes or by the observed tune shifts. The tune shifts calculated from build up simulations have agreed well with observed tune shifts [4]. CMAD starts with a uniform distribution of electrons while work is underway to have the program be able to use any distribution as an initial condition.

In the results presented in this paper, we used a 2.08GeV beam, which is the energy most of the experiments have been performed so far. In these simulations, particles are tracked across the full lattice, where each element of non-zero length in the lattice consists of a cloud-beam "interacting point". Thus, the simulation takes into account the variation of the beam size based upon the beta function and dispersion all around the ring. In the model, the bunch had 96 slices, and the charge from each slice was distributed over a 128×128 grid, with 300000 macro particles (positrons) and 100000 macro electrons. The bunch current used was 1mA, corresponding to 1.6×10^{10} positrons. The bunch length was 12.2mm, vertical emittance was 20pm and horizontal emittance 2.6nm. The relative energy spread was 8.12×10^{-4}. The betatron tunes were 14.57 (horizontal) and 9.62 (vertical). The synchrotron tune was 0.055. The chromaticities were 0.6 (horizontal) and 2.3 (vertical) in units of $dQ/(dp/p)$. Overall, care was taken to match the parameters as closely as possible to the machine conditions that existed during the time of one of the observations made at CesrTA.

MOTION OF BUNCH CENTROID

In this section, we show the behavior of the centroid motion for varying cloud densities. The bunch initially had no offset. Nevertheless, the finite number of macro particles, however large, are enough to trigger a self excitation of the centroid motion, that increases with cloud density. A very similar trend in the self excitation has been seen in measurements. Of course, the mechanism of the initial perturbation in the beam offset is different in experiments, *ie* it is not numerical. The self excitation is produced by nonlinear coupling between the two transverse degrees of freedom. In addition, the effect of longitudinal motion would also play a role due to the presence of dispersive coupling between the longitudinal and horizontal motion.

Figure 1 shows the horizontal bunch displacement with respect to the initial beam size. We do not see a significant variation in oscillation amplitude with cloud density. For lower cloud densities, of the order of $1 \times 10^{10}/m^3$ shown in Fig 1a we do not see any significant self excitation. For cloud densities an order of magnitude higher, *ie* $\sim 1 \times 10^{11}/m^3$ shown in Fig 1b there is a clear indication of self excitation. In the next level of cloud densities, Fig 1c, we see that the all bunches get excited to about the same amplitude, but the transient state to reach the final amplitude of oscillation is longer in duration for the lower densities within this category of electron densities.

Figure 2 shows the vertical bunch displacement with respect to the initial beam size. for the same values of cloud densities. These show that the extent of self excitation

* Work supported by DOE grant DE-FC02-08ER41538, NSF grant PHY-0734867

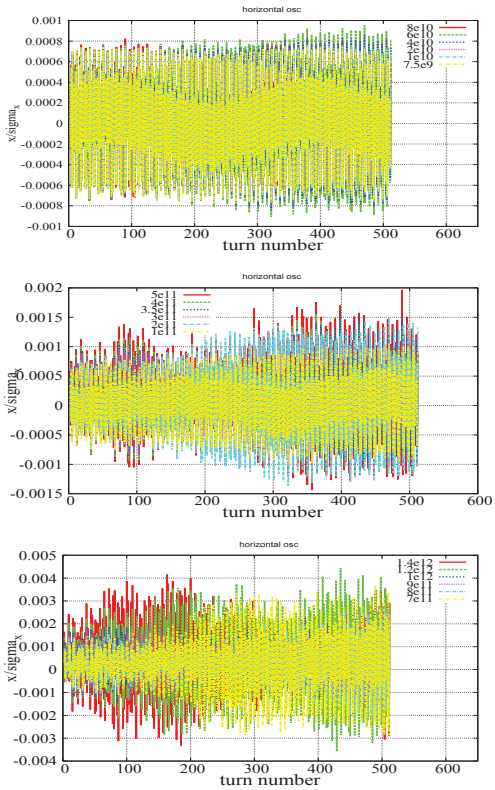

Figure 1: Motion of vertical bunch centroid for varying cloud densities.

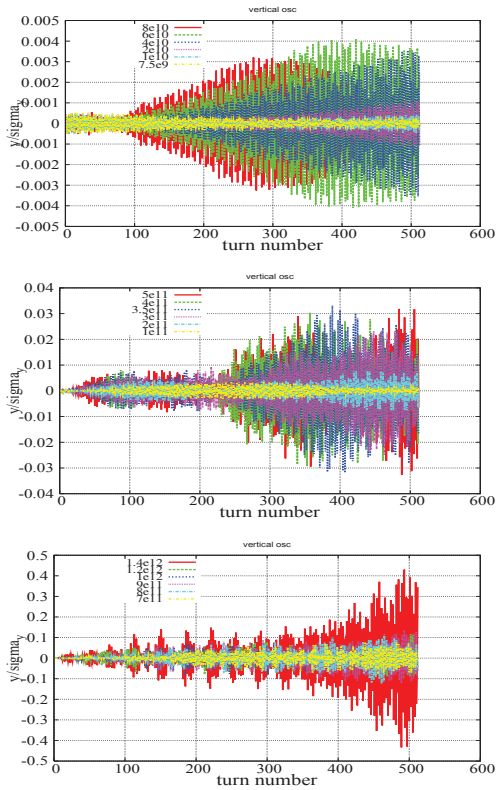

Figure 2: Motion of horizontal bunch centroid for varying cloud densities.

clearly grows with cloud density. In some cases, we also see stages of damping induced by the electron clouds. The oscillation clearly becomes more chaotic as the cloud density increases. It is expected that the horizontal motion is more stable than the vertical given that the horizontal size of the beam is larger by about a factor of 100.

Figures [3,4] show the spectrum of the centroid motion of the bunches under varying cloud densities. In Fig 4, we see that the betatron tune is gradually shifted with increasing cloud densities. The synchrotron sidebands are clearly noticeable, indicative of headtail motion. We clearly see the first order sidebands, which are spaced from the betatron peak by the value of the synchrotron frequency. These represent the so called $m = \pm 1$ mode. Additionally, second order sidebands, spaced by twice the synchrotron frequency value from the betatron peaks are visible at higher cloud densities. These are representative of the $m = \pm 2$ mode of the headtail interaction. We also see that the betatron tune splits with one component remaining at the "unshifted" tune. This splitting has not been observed in experiments, which is likely because the simulations currently do not model the evolution of the electron density in the vicinity of the beam accurately enough. We are currently working toward a more realistic model to account for the density evolution of the cloud during the bunch passage. Figure 3 shows the spectrum of the horizontal motion. We see the presence of synchrotron sidebands, although they are weaker. The tune shift is not visible simply because it is too small and the resolution of the spectra, resulting from 512 turns is not fine enough. It may be noted that while in simulations we are able to isolate the horizontal and vertical motion well enough, observed signals from BPMs always contain a mixture of features of motion from both the transverse planes. Nevertheless, these signals have revealed the same essential features shown by simulations.

Figure 5a shows a summary of the heights of the left and right sidebands along with the heights of the vertical betatron peaks for different cloud densities. We see that a transition in the relative height of at least one of the sideband peaks occurs at cloud densities of 3.5×10^{11} and 4×10^{11}. For cloud densities beyond these values, we see that both the sideband heights remain relatively close to the betatron peak heights. Figure 5b shows the position of the betatron and both the sideband peaks in tune space. We see the gradual shift in betatron tune. Additionally, we see that the sideband peaks are consistently spaced away from the betatron peak by the value of the synchrotron frequency. It has been observed at KEK [5] that, due to coupling between lower and higher order headtail modes, the sidebands belonging to the two orders would drift toward each other and even combine into one. On the other hand, our simulation results are consistent with what has been observed at CesrTA under the same conditions. It is likely that the mode coupling described above would become observable

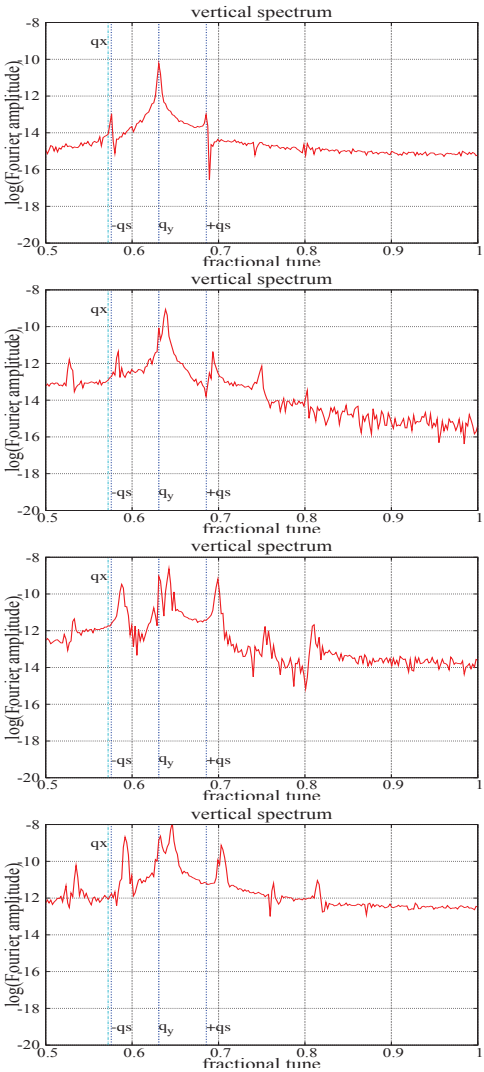

Figure 3: Spectrum of vertical bunch motion for varying cloud densities. From top to bottom (a)6e10 (b)3e11 (c)6e11 (d)8e11 electrons per m^3

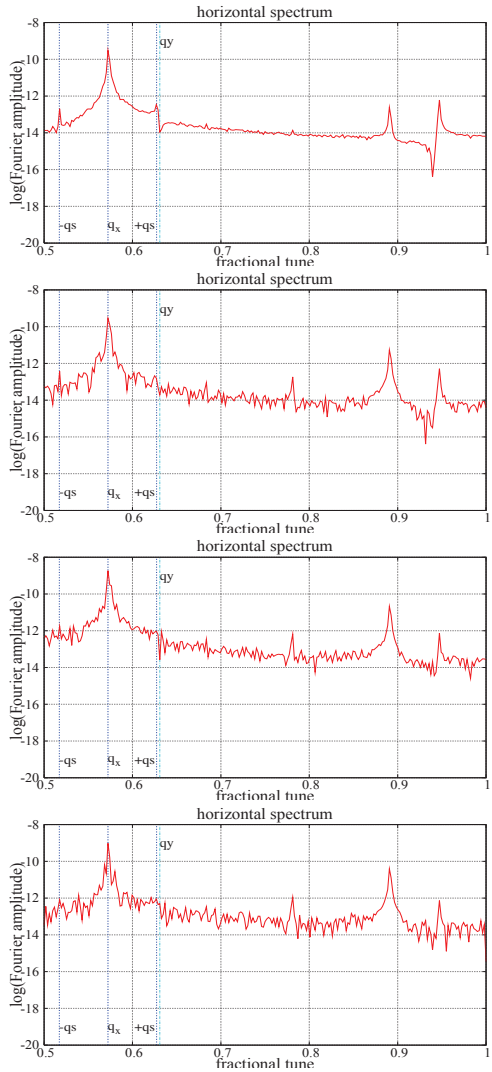

Figure 4: Spectrum of vertical bunch motion for varying cloud densities. From top to button (a)6e10 (b)3e11 (c)6e11 (d)8e11 electrons per m^3

at higher bunch currents and cloud densities. This is yet to be confirmed as to what the conditions at CesrTA should be to observe such a mode coupling.

CALCULATION OF EMITTANCE GROWTH RATE

Figure [6] shows the horizontal emittance growth rate of the bunches. We clearly see that the emittance growth rate increases with increased cloud density. The horizontal growth rate is very small. At such small values, one might need to factor in a contribution to numerical noise. Nevertheless, we clearly see that the growth rate increases with increased cloud density. Figure [7] shows the vertical emittance growth rate. The vertical emittance undergoes a higher growth rate due to its smaller initial value. One would expect a smaller contribution from numerical noise in this case. In general, we need to perform simulations with varying computational parameters, such as grid spacing, macro particles, and extent of the cloud to get a better quantitative idea of a possible contribution from numerical noise on emittance growth.

Despite the uncertainty in estimating the emittance growth rate, we see a definite increase in this quantity in correspondence with the height of the sidebands which is consistent with observations from X-ray beam size monitors (BSMs) at CesrTA. However, it must be noted that the BSMs measure the beam size after the beam has reached a quasi-equilibrium state, while in simulations we are, in the first 500 turns still looking at a transient state, with the emittance still growing linearly. In order to make a closer comparison between experiments and simulations, one needs to calculate the quasi equilibrium emittance. This would require including the effect of radiation damping and quantum excitations and tracking the beam for several damping times. The damping time of the CesrTA

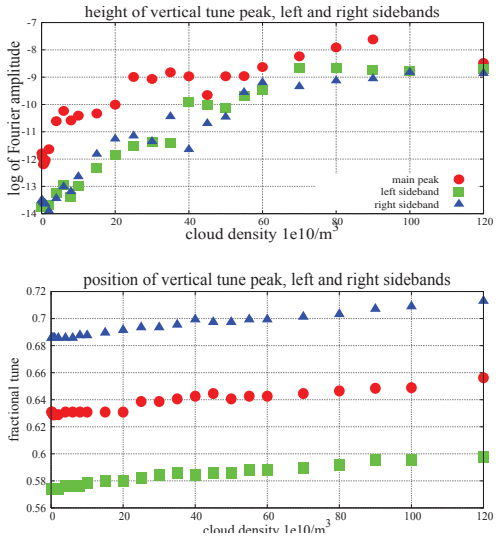

Figure 5: Plots showing relative heights of betatron and sideband peaks (above) and relative position of the peaks in tune space

2GeV configuration is about 21000 turns.

MOTION OF INDIVIDUAL PARTICLES

We have observed the motion of individual test particles in order to study their confinement properties for varying cloud densities and also how their oscillation frequency varies with change in oscillation amplitude. Although it would be difficult to determine these quantities experimentally. probing into such details with the help of simulations can provide a lot of insight into the underlying physical processes and the mechanisms that drive the beams unstable in the presence of electron clouds.

In Figs 8 and 9, we show the transverse phase space trajectory of particles of particles initially at $x = 0.1 \times \sigma_x$, $y = 0.1 \times \sigma_y$ and $z = 0.1 \times \sigma_z$. The small initial offset ensures that coupling between the three degrees of freedom, if present affects the dynamics of the particle motion. The variation of the tune with oscillation amplitude for various cloud densities can in principle be estimated with the help of such single particle trajectories.

The horizontal motion, shown in Fig 8 indicates that motion in this plane is fairly regular and lies on the invariant ellipse. On the other hand, in Fig 9 which shows motion in the vertical plane, we clearly see that the particles stray away from the ellipse as the electron density increases. We plan to extend the analysis of single particle trajectories beyond just phase space traces. For example, one could do a frequency spectrum analysis to look for evidence of linear and nonlinear coupling between the respective degrees of freedom, the oscillation frequencies of the so called radial and angular modes for each degree of freedom and several other details associated with single particle motion can also be examined.

CONCLUSION

We have made a systematic study of the influence of electron clouds on the dynamics of positron beams at CesrTA. We have looked into the motion of the beam at different levels of resolution. This included the centroid motion, the emittance evolution and motion of individual particles within the beam. The spectrum of the centroid motion was studied carefully. The spectra of the centroid motion had prominent synchrotron sidebands off the betatron tunes, indicating head-tail motion. The height of the sidebands increased with increasing cloud density and this was accompanied by the appearance of higher order sidebands, especially in the spectra of the vertical motion. Work is underway to examine the motion of individual slices and how they differ according to position along the length of the bunch.

A summary of synchrotron sideband heights for various cloud densities revealed that there was transition in the side band intensity at a density of about $3 - 4 \times 10^{11}$. This has been consistent with observation. It should be noted that in experiments, there is a noise floor that buries the sideband peaks at lower cloud densities, but these are still visible in simulations, where the data has far less noise.

The beam emittance calculation clearly showed that the rate of growth of the emittance grew with increased cloud

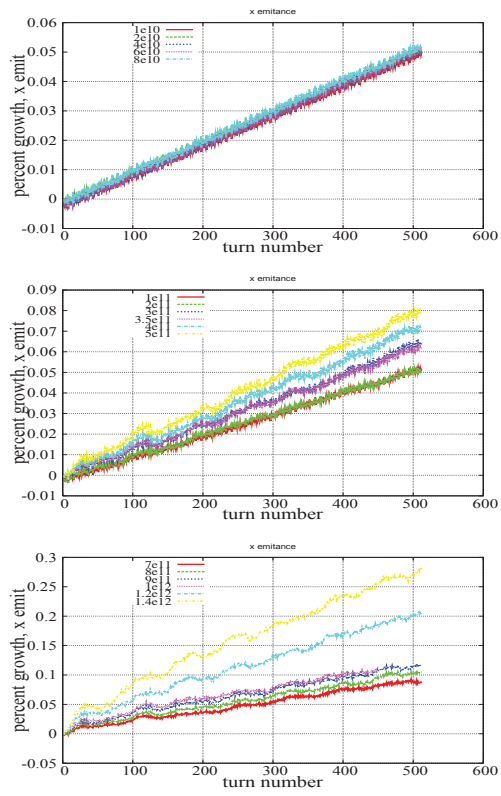

Figure 6: Emittance growth rate for varying cloud densities and a summary of sidebands heights along with the betatron peak heights

density. The growth was always linear, *ie*, a transition to an exponential growth rate was not seen under the given conditions. The simulations were not performed long enough to see see at what values the emittances saturated. It is likely that the final emittance is determined by the influence of radiation damping and quantum excitations, coupled with the electron effect. These additional features are yet to be included in the simulations. It would be challenging to be able to be able observe transient effects in experiments, although such a comparison would be very informative, especially with regard to estimating the contribution of numerical noise in the simulations. If numerical noise is a prominent factor, it will be sensitive to computational parameters such as grid size and number of macro particles. The dependence on these parameters needs to be examined more closely in future. Calculation of the single particle motion showed that the horizontal motion was fairly regular over a range of cloud densities while the vertical motion became increasingly chaotic with increased cloud density.

In conclusion, we state that CMAD has been able to reproduce several features of the dynamics of positron beams also observed in experiments. Study was performed for a parameter set corresponding to one set of observations at CesrTA. We need to extend this study to other conditions at which observations have been made and will be made in future. At the same time work needs to be done to include more features in CMAD in order to get a closer quantitative agreement with observations.

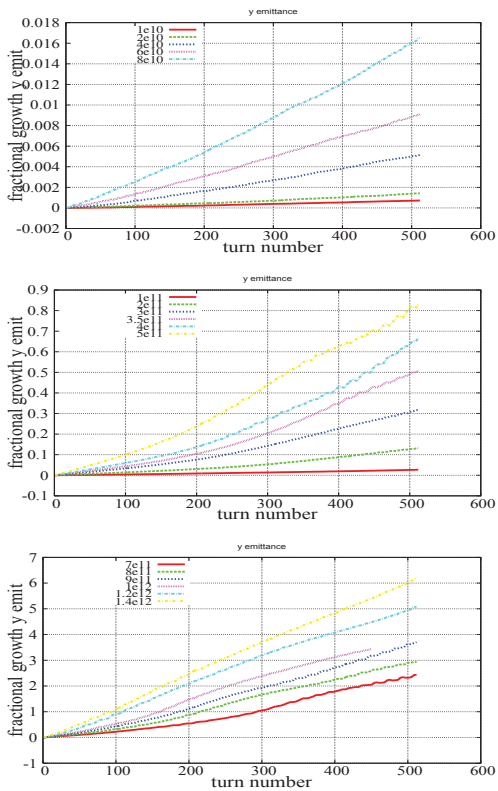

Figure 7: Emittance growth rate for varying cloud densities and a summary of sidebands heights along with the betatron peak heights

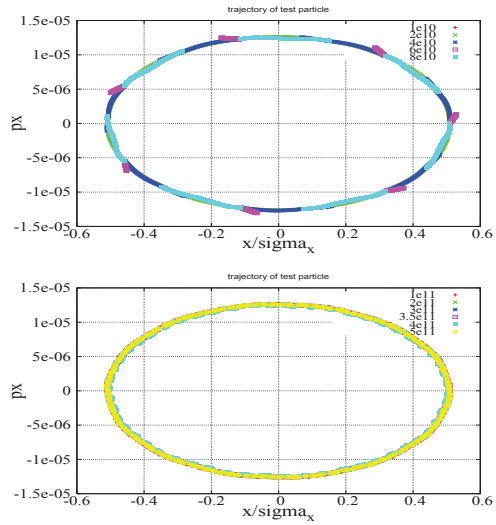

Figure 8: Single particle trajectory in horizontal phase space

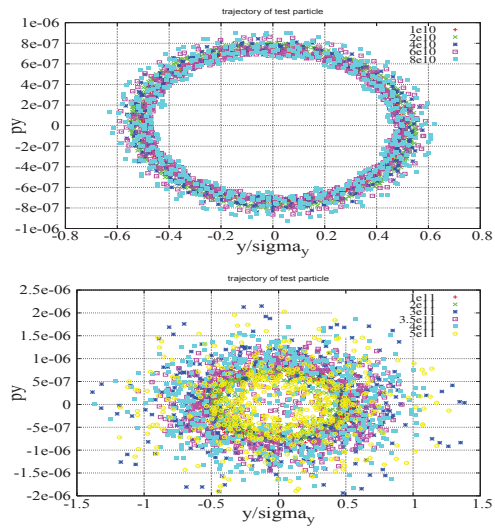

Figure 9: Single particle trajectory in vertical phase space

REFERENCES

[1] K. G. Sonnad *et al*, In these proceedings

[2] M. T.F. Pivi, Proceedings of PAC 2007, Session THPAS066

[3] M. G. Billing, *et al* In these proceedings

[4] D. L. Kreinick *et al*, In these proceedings

[5] J. W. Flanagan, K. Ohmi, H. Fukuma, S. Hiramatsu, M. Tobiyama and E. Perevedentsev, Phys. Rev. Lett. 94, 054801 (2005)

This research used resources of the National Energy Research Scientific Computing Center, which is supported by the Office of Science of the U.S. Department of Energy under Contract No. DE-AC02-05CH11231.

List of Authors

Italic papercodes indicate primary authors

— Z —

Institutes List

Argonne National Laboratory
- Harkay, K.
- Ivanyushenkov, Y.
- Kustom, R.
- Moog, E.
- Rosenberg, R.
- Trakhtenberg, E.

Babcock Noell GmbH (BNG)
- Boffo, C.
- Sikler, G.

Brookhaven National Laboratory
- Blaskiewicz, M.
- Brennan, J.
- Fischer, W.
- Hershcovitch, A.
- Liaw, C.
- Meng, W.

CERN
- Baglin, V.
- Calatroni, S.
- Chiggiato, P.
- Costa Pinto, P.
- Hofle, W.
- Neupert, H.
- Rumolo, G.
- Salvant, B.
- Shaposhnikova, E.
- Taborelli, M.
- Tomas, R.
- Vollenberg, W.
- Yin Vallgren, C.
- Zimmermann, F.

CNR-IOM
- Giglia, A.
- Mahne, N.

California Polytechnic State University
- Holtzapple, R.
- Randazzo, M.

Cockcroft Institute
- Jones, R.
- Shinton, I.

Cornell University - CLASSE
- Alexander, J.
- Asner, D.
- Billing, M.
- Calvey, J.
- Conolly, C.
- Conway, J.
- Crittenden, J.
- Dugan, G.
- Eggert, N.
- Fontes, E.
- Greenwald, S.
- Hopkins, W.
- Kim, J.
- Kreinick, D.
- Kreis, B.
- Leong, Z.
- Li, Y.
- Liu, X.
- Lyndaker, A.
- Makita, J.
- Medjidzade, V.
- Meller, R.
- Moore, T.
- Palmer, M.
- Peterson, D.
- Ramirez, G.
- Rendina, M.
- Revesz, P.
- Rider, N.
- Rubin, D.
- Sagan, D.
- Savino, J.
- Schwartz, R.
- Seeley, R.
- Shanks, J.
- Sikora, J.
- Sonnad, K.
- Strohman, C.
- Strohman, S.
- Tigner, M.
- Williams, H.
- Yanay, Y.

DESY
- Wanzenberg, R.

Diamond Light Source Ltd (Diamond)
- Cox, M.
- Schouten, J.

Fermilab
- Backfish, M.
- Capista, D.
- Crisp, J.
- Eddy, N.
- Kourbanis, I.
- Lebrun, P.
- Seiya, K.
- Spentzouris, P.
- Tan, C.
- Thangaraj, J.

- Valerio, L.
- Zwaska, R.

GSI
- Franchetti, G.

HCEI
- Sochugov, N.

Harvard University
- Hammond, K.

INFN/LNF
- Cimino, R.
- Commisso, M.
- Demma, T.
- Grosso, D.
- Mostacci, A.
- Spataro, B.

KEK
- Flanagan, J.
- Fukuma, H.
- Jin, H.
- Kanazawa, K.
- Kato, S.
- Nishiwaki, M.
- Ohmi, K.
- Suetsugu, Y.
- Susaki, Y.
- Yusuke, S.

Karlsruhe Institute of Technology
- Baumbach, T.
- Casalbuoni, S.
- Gerstl, S.
- Grau, A.
- Hagelstein, M.
- Saez de Jauregui, D.
- Schleede, S.
- Tavares, P.

LANL
- Macek, R.
- McCrady, R.
- Rybarcyk, L.
- Spickermann, T.
- Zaugg, T.

LBNL
- Byrd, J.
- Celata, C.
- De Santis, S.
- Furman, M.
- Penn, G.
- Secondo, R.
- Vay, J.
- Venturini, M.

Lund University - MAX-Lab
- Wallen, E.

Max-Planck Institute for Metal Research, Stuttgart
- Weigel, R.

ORNL
- Holmes, J.

PVI
- Custer, A.
- Erickson, M.
- Jamshidi, N.
- Poole, H.

Purdue University
- Boon, L.
- Garfinkel, A.

SLAC National Accelerator Laboratory
- Bullitt, A.
- Fox, J.
- Mastorides, T.
- Ndabashimiye, G.
- Pivi, M.
- Rivetta, C.
- Turgut, O.
- Wang, L.

Science and Technology Facilities Council (STFC/DL/ASTeC) Daresbury Laboratory Accelerator Science and Technology Centre
- Clarke, J.
- Scott, D.

Science and Technology Facilities Council (STFC/RAL) Rutherford Appleton Laboratory
- Bradshaw, T.

Tech-X Corporation
- Stoltz, P.
- Veitzer, S.

TechSource, Inc.
- Browman, A.
- Macek, R.
- McCrady, R.
- Zaugg, T.

The Graduate University for Advanced Studies
- Jain, P.

University of California at Los Angeles
- Omcikus, N.

University of Colorado Boulder
- Cary, J.

Participants List